2021, Vol. 80, No. 3, pp. 477–744

FOLIA MORPHOLOGICA

August 2021

ISSN 0015–5659
eISSN 1644–3284
Impact Factor: 1.183

POLISH ANATOMICAL SOCIETY

FOLIA MORPHOLOGICA

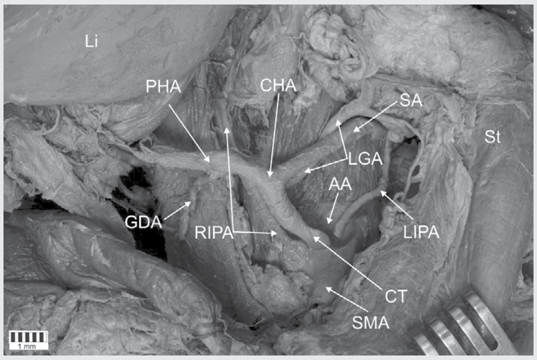

Vol. 80 2021 No. 3

VIA MEDICA

https://journals.viamedica.pl/folia_morphologica

FOLIA MORPHOLOGICA

An international multidisciplinary journal devoted to fundamental research in the morphological sciences
Official Journal of the Polish Anatomical Society
(a Constituent Member of European Federation for Experimental Morphology — EFEM)

EDITOR-IN-CHIEF
Janusz Moryś
Department of Anatomy and Neurobiology
Medical University of Gdańsk

https://journals.viamedica.pl/folia_morphologica

See our website for information on manuscript status, aims and scope, instructions for authors as well as editorial board.

Folia Morphologica

Publishing, Subscription and Advertising Office:
VM Media sp. z o.o. VM Group sp.k., Grupa Via Medica
ul. Świętokrzyska 73, 80–180 Gdańsk, Poland
tel. (+48 58) 320 94 94, fax (+48 58) 320 94 60
Managing editor
Joanna Niezgoda
e-mail: joanna.niezgoda@viamedica.pl
Cover designer
Sylwia Scisłowska

The journal is published at: www.fm.viamedica.pl in one volume per year consisting of four numbers. Subscription rates: Paper subscription, 4 issues incl. package and postage institutional — 140 euro. The above prices are inclusive of regular postage costs. Payment should be made to: VM Media sp. z o.o. VM Group sp.k., Grupa Via Medica, Bank BGŻ Paribas SA account number: 15 1600 1303 0004 1007 1035 9021; SWIFT: PPABPLPK. Single issues, subsriptions orders and requests for sample copies should be send to e-mail: prenumerata@viamedica.pl. Electronic orders option available at: https://journals.viamedica.pl/folia_morphologica. The publisher must be notified of a cancellation of access to electronic version not later then two months before the end of a calendar year. After that date electronic access will be automatically prolonged for another year.

Folia Morphologica is the official journal of the Polish Anatomical Society. For information about the Society, please contact: Prof. Marek Grzybiak, Department of Clinical Anatomy, Medical University of Gdansk, ul. Dębinki 1, 80–211 Gdańsk, Poland, tel: +48 58 349 14 22, e-mail: grzybiak@gumed.edu.pl

Editorial policies and author guidelines are published on journal website: https://journals.viamedica.pl/folia_morphologica

Legal note: https://journals.viamedica.pl/folia_morphologica/about/legalNote

Folia Morphologica is indexed by: BIOSIS Previews, CAS, CINAHL, CrossRef, Dental Abstracts, EBSCO, Elsevier BIOBASE, EMBIOLOGY, FMJ, Google Scholar, Index Copernicus (154.80), Index Medicus/MEDLINE, Index Scholar, Polish Ministry of Education and Science (70), NCBI/National Center for Biotechnology Information, Polish Medical Bibliography, Scopus, SJR, Thomson Reuters, Thomson Scientific Products — Biological Abstracts, Ulrich's Periodicals Directory, Veterinary Bulletin, WorldCat and Zoological Record. Position in Index Copernicus ranking systems is available at: www.indexcopernicus.com. Current Impact Factor of Folia Morphologica (2020) is 1.183.

ISSN 0015–5659
eISSN 1644–3284

20-0809.003.001

FOLIA MORPHOLOGICA

Editor-in-Chief
JANUSZ MORYŚ
Department of Anatomy and Neurobiology, Medical University of Gdańsk
ul. Dębinki 1, 80–211 Gdańsk, Poland
tel. (+48 58) 349 1401, fax (+48 58) 349 1421, e-mail: jmorys@gumed.edu.pl

VIA MEDICA

REVIEW ARTICLE

Folia Morphol.
Vol. 80, No. 3, pp. 477–486
DOI: 10.5603/FM.a2019.0129

ISSN 0015–5659
eISSN 1644–3284
journals.viamedica.pl

New Terminologia Anatomica: cranium and extracranial bones of the head

P.P. Chmielewski

Division of Anatomy, Department of Human Morphology and Embryology, Faculty of Medicine, Wroclaw Medical University, Wroclaw, Poland

[Received: 12 October 2019; Accepted: 17 November 2019; Early publication date: 3 December 2019]

In 2019, the updated and extended version of Terminologia Anatomica was published by the Federative International Programme for Anatomical Terminology (FIPAT). This new edition uses more precise and adequate anatomical names compared to its predecessors. Nevertheless, numerous terms have been modified, which poses a challenge to those who prefer traditional anatomical names, i.e. medical students, teachers, clinicians and their instructors. Therefore, there is a need to popularise this new edition of terminology and explain these recent changes. The anatomy of the head, including the cranium, the extracranial bones of the head, the soft parts of the face and the encephalon, poses a particular challenge for medical students but also engenders enthusiasm in those of them who are astute learners. The new version of anatomical terminology concerning the human skull (FIPAT 2019) is presented and briefly discussed in this synopsis. The aim of this article is to present, popularise and explain these interesting modifications that have recently been endorsed by the FIPAT. Based on teaching experience at the Division of Anatomy/Department of Anatomy at Wroclaw Medical University, a brief description of the human skull is given here. This text can be useful to medical students, teachers, authors and researchers who might want to use the current version of anatomical terminology concerning the human skull. (Folia Morphol 2021; 80, 3: 477–486)

Key words: anatomical terminology, anatomical nomenclature, bones of the head, cranium, skull, Nomina Anatomica, Terminologia Anatomica

INTRODUCTION

The skeleton of the head consists of the cranium and the extracranial bones of the head, i.e. the mandible and the hyoid bone [5]. The cranium consists of two parts, i.e. the cerebral cranium called **neurocranium** and the visceral cranium called **viscerocranium**. The term *splanchnocranium* is not used. Both parts of the cranium are composed of individual bones that are joined by cranial sutures and cranial syndesmoses. Noteworthy, the cranium is *not* the entire skeleton of the head. Although the traditional term 'skull' has been discarded in order to classify the mandible as one of the extracranial bones of the head, the skull consists of the cranium and the mandible. In physical anthropology and osteology, the following terms are often used: *cranium* (the skull), *calvarium* (the brain case), *calvaria* (the skull vault), *calva* and *calotta* (the skull cap).

In early ontogeny, cranial bones develop in connective tissue as membrane bone (Me) forming **desmocranium**, which is called the calvaria at the later stages of ontogeny. Bone that develops in cartilage (C)

Address for correspondence: Dr. P.P. Chmielewski, PhD, Division of Anatomy, Department of Human Morphology and Embryology, Faculty of Medicine, Wroclaw Medical University, ul. Chałubińskiego 6a, 50–368 Wrocław, Poland, e-mail: piotr.chmielewski@umed.wroc.pl

constitutes the cartilaginous part of embryological cranium, i.e. **chondrocranium**, that later forms the cranial base. If some parts of a bone develop in membrane and other parts develop in cartilage, the term a mixed bone (Mi) is used [6].

Based on developmental biology and comparative anatomy, the bones of the head can be divided into three types: (1) bones forming the calvarium (the brain case), including bones developing in membrane that form **the calvaria** (the skull vault) and bones developing in cartilage that form **the cranial base** (basicranium, the skull base; *basis cranii* in Latin), (2) bones associated with the nasal capsule that develop in connective tissue (i.e. the nasal bone, the lacrimal bone and the vomer) and bones that develop in cartilage (i.e. the ethmoid bone and the inferior nasal concha) and (3) bones that develop from the visceral arches that can be divided into two groups: (a) immobile bones, i.e. the maxilla, the zygomatic bone and the palatine bone, and (b) mobile bones, i.e. the mandible, the hyoid bone and the auditory ossicles, *ossicula auditus seu ossicula auditoria* in Latin [5, 6].

THE FRONTAL BONE

In adults, the anterosuperior aspect of the cranium forming the forehead is composed of one pneumatised bone, i.e. **the frontal bone** (***os frontale***, from 'frons' meaning 'the bone of the forehead', Me), which encases the cranial cavity anteriorly and contributes to the formation of the calvaria, although this bone is made up of two separate portions at birth and in some individuals throughout life (then the frontal suture, *sutura frontalis persistens seu sutura metopica*, is present) [8].

The frontal bone consists of: (1) the unpaired **squamous part** of the frontal bone (*squama frontalis*), (2) the paired **orbital part** of the frontal bone (*pars orbitalis ossis frontalis*) and (3) the unpaired **nasal part** of the frontal bone (*pars nasalis ossis frontalis*). The squama has three surfaces, i.e. the external, internal (inner, cerebral) and temporal surface [4, 5]. Two centres of ossification are visible on the external surface of the squamous part as two **frontal eminences** (frontal tubers, frontal tuberosities) that are situated over the frontal sinuses. The term 'frontal eminence' (***eminentia frontalis***) is believed to be more appropriate than 'frontal tubers' as these elevations are subtle in men and more pronounced but not prominent in women. Therefore, this term has recently been changed by the Federative International Programme for Anatomical Terminology (FIPAT) [cf. 4, 5]. The superciliary arches are situated above the supraorbital margins (previously referred to as the supraorbital borders or ridges) which form the inferior border of the squamous part.

The internal (inner) surface of the frontal bone has poorly defined **impressions for cerebral gyri** (***impressiones gyrorum*** *seu impressions digitatae*) [5], eminences of cerebral sulci (*juga cerebralia*) and inconstantly present arterial grooves (*sulci arteriosi*). In the midline, there is **the groove for the superior sagittal sinus** (*sulcus sinus sagittalis superioris*) that is inferiorly continuous with **the frontal crest** (*crista frontalis*) that reaches to **the foramen caecum of the frontal bone** (*foramen caecum ossis frontalis*). Although this small foramen is sometimes not blind (in about 1% of cases) and then it can transmit a small vein from the nasal mucous membrane to the superior sagittal sinus, this well-established term has not been changed by the FIPAT [5], which is a sensible decision.

The temporal surface of the frontal bone forms the anterior part of the temporal fossa (*fossa temporalis*) that is located posterior to the zygomatic process of the frontal bone. This surface is separated from the external surface of the frontal bone by the temporal line (*linea temporalis*) that converges to the supraorbital margin to form the zygomatic process.

The nasal part is situated between the two orbital parts where the squama projects inferiorly. This is the smallest part of the frontal bone and it demarcates anteriorly **the ethmoidal notch** (***incisura ethmoidea*** *seu incisura ethmoidalis*) [5] in an arch-like fashion. The pointed median structure projecting downwards and forwards from the nasal part of the frontal bone towards the nasal bones is called **the nasal spine of the frontal bone** (*spina nasalis ossis frontalis*) [5]. This term has been changed by the FIPAT as this spine should be clearly distinguished from other nasal spines.

Table 1 provides examples of how the modern version of the anatomical terminology (FIPAT 2019) differs from its predecessors (FCAT 1998 and FIPAT 2011).

THE SPHENOID BONE

The unpaired and pneumatised bone that forms the central part of the cranial base is termed ***os sphenoideum*** *seu os sphenoidale* (**sphenoid(**al) **bone**, Mi), although the shorter and traditional term was *os sphenoides* [1–5]. The shape of this bone resembles a flying bat with its wings extended or a flying wasp [3]. Hence, the historical names *os vespiforme*,

Table 1. Comparison of terms from Terminologia Anatomica (1998, 2011) and New Terminologia Anatomica (2019) concerning the skull

Terminologia Anatomica (2019)	Terminologia Anatomica (1998, 2011)	English Equivalent (2019)
Alveoli dentales mandibulae	Alveolus dentalis	Dental alveoli of mandible
Alveoli dentales maxillae	Alveolus dentalis	Dental alveoli of maxilla
Apertura externa canalis carotidis	Apertura externa canalis carotici	External opening of carotid canal
Apertura interna canalis carotidis	Apertura interna canalis carotici	Internal opening of carotid canal
Bulla ethmoidea ossea	Bulla ethmoidalis	Bony ethmoidal bulla
Canalis carotidis	Canalis caroticus	Carotid canal
Canalis facialis	Canalis nervi facialis	Facial canal
Canalis hypoglossus	Canalis nervi hypoglossi	Hypoglossal canal
Cellulae ossis ethmoidei	Cellulae ethmoidales	Cells of ethmoid bone
Choana cranii	Choana	Choana of cranium
Condylus mandibulae	Caput mandibulae	Mandibular condyle
Crista ethmoidea maxillae	Crista ethmoidalis	Ethmoidal crest of maxilla
Crista ethmoidea ossis palatini	Crista ethmoidalis	Ethmoidal crest of palatine bone
Crista petrosa	Crista petrosa*	Petrous ridge
Crista sphenoidea	Crista sphenoidalis	Sphenoidal crest
Crista supramastoidea	Crista supramastoidea*	Supramastoid crest
Foramen alveolare inferius	Foramen mandibulae	Inferior alveolar foramen
Foramen ethmoideum anterius	Foramen ethmoidale anterius	Anterior ethmoidal foramen
Foramen ethmoideum posterius	Foramen ethmoidale posterius	Posterior ethmoidal foramen
Hiatus semilunaris osseus	Hiatus semilunaris	Bony semilunar hiatus
Infundibulum ethmoideum osseum	Infundibulum ethmoidale	Bony ethmoidal infundibulum
Jugum sphenoideum	Jugum sphenoidale	Sphenoidal yoke
Lingula sphenoidea	Lingula sphenoidalis	Sphenoidal lingula
Os ethmoideum	Os ethmoidale	Ethmoid(al) bone
Os sphenoideum	Os sphenoidale	Sphenoid(al) bone
Recessus sphenoethmoideus cranii	Recessus sphenoethmoidalis	Sphenoethmoidal recess of cranium
Rostrum sphenoideum	Rostrum sphenoidale	Sphenoidal rostrum
Sulcus carotidis	Sulcus caroticus	Carotid sulcus
Sulcus chiasmaticus	Sulcus prechiasmaticus	Chiasmatic sulcus

os sphexoideum and *os sphecoides* (from the Greek words 'vespa' and 'sfex', which means 'a wasp'). Interestingly, the name 'sphenoid(al)' has appeared by mistake. In Galen's manuscripts, this bone was referred to as the 'sphecoid bone', which means the 'bone that resembles a wasp', but the copyist made a mistake and wrote 'sphenoid', in Greek 'sfen' means a 'wedge' [6].

The sphenoid has several parts: **the body of the sphenoid bone** (***corpus ossis sphenoidei*** *seu corpus ossis sphenoidalis*) [5], **the greater wings** (***alae majores ossis sphenoidei*** *seu alae majors ossis sphenoidalis*), **the lesser wings** (***alae minores ossis sphenoidei*** *seu alae minores ossis sphenoidalis*) and **the pterygoid process** (*processus pterygoideus*). The body of the sphenoid bone is cuboid in shape and has six surfaces. The anterior surface bears **the sphenoidal crest** (***crista sphenoidea*** *seu crista sphenoidalis*) [5], a ridge that is a part of the superior wall of the nasal cavity. This crest continues down towards **the sphenoidal rostrum** (***rostrum sphenoideum*** *seu rostrum sphenoidale*) [5]. A thin and curved plated called **the sphenoidal concha** (***concha sphenoidea*** *seu concha sphenoidalis*) [5] can be observed on both sides. Laterally, there are small openings called **openings of sinus of sphenoid(al) bone** (***apertura sinus ossis sphenoidei*** *seu apertura sinus ossis sphenoidalis*) [5].

Although the preferred name for this bone is 'sphenoid' and the term 'sphenoidal' is a synonym, only the latter is used in two compounds (i.e. 'sinus of sphenoidal bone' and 'opening of sinus of sphenoidal bone'), which is rather surprising. This is an example of inconsistencies in the new edition of Terminologia Anatomica. The posterior surface fuses with the occipital bone to form the sphenooccipital synchondrosis. The superior surface has *planum sphenoideum et jugum sphenoideum* that lie in front of **the chiasmatic sulcus** (***sulcus chiasmaticus***) [cf. 4, 5]. The sella turcica is bounded anteriorly by the tuberculum sellae and posteriorly by the dorsum sellae. A depression for the pituitary gland (*glandula pituitaria seu hypophysis*) is called **hypophysial** (UK)/ /**hypophyseal** (US) **fossa** (*fossa hypophysialis* in Latin) [5], although this is inconsistent with the name of this gland both in Latin and English. The medial ends of the posterior edges of the lesser wings have anterior clinoid processes (sing. *processus clinoideus anterior*) because they are located in the vicinity of the anterior part of the hypophysial fossa. The lateral parts of the dorsum sellae that project forwards are termed posterior clinoid processes (sing. *processus clinoideus posterior*). The inconstantly present middle clinoid process (*processus clinoideus medius*) can be sometimes observed on both sides of the sella turcica.

Each greater wing has five surfaces: the cerebral surface, the temporal surface, the infratemporal surface, the maxillary surface and the orbital surface. The part of this bone that lies in front of the chiasmatic sulcus (*sulcus chiasmaticus seu sulcus prechiasmaticus seu sulcus praechiasmaticus* in Latin, traditionally termed *sulcus chiasmatis*) [7] and connects the lesser wings is currently called ***jugum sphenoideum*** *seu jugum sphenoidale* [5]. Interestingly, the sulcus that stretches from the foramen lacerum to the medial side of the anterior clinoid process, lying laterally on both sides of the sella turcica, is officially termed ***sulcus carotidis*** *seu sulcus caroticus* [5].

The lesser wings are two flat and small triangular plates arising by two roots from the anterosuperior edge of the body of the sphenoid bone. At the base of each lesser wing, medially to the anterior clinoid process, there is a bony canal for the optic nerve (CN II), which is called **the optic canal** (*canalis opticus*). The superior orbital fissure (*fissura orbitalis superior*) can be found between the greater and lesser wings where nerves and veins pass.

The paired **pterygoid process** drops vertically downwards from the junction of the body of the sphenoid bone with the greater wings. Each of them is made up of two laminae: **the medial pterygoid plate** (*lamina medialis*) and **the lateral pterygoid plate** (*lamina lateralis*) [5]. Between these plates the pterygoid fossa (*fossa pterygoidea*) can be observed at the posterior aspect. Anteriorly, these plates fuse in the vicinity of the *sulcus palatinus major ossis palatini*. Since the pterygoid processes are not involved, the term *sulcus pterygopalatinus* was discarded. The base of this process is pierced by the pterygoid canal (*canalis pterygoideus*) whose anterior opening communicates with the pterygopalatine fossa. An oblong depression at the root of the medial pterygoid plate is called the scaphoid fossa (***fossa scaphoidea***, previously known as *fossa scaphoides*). The tensor veli palatini originates from its lateral end. **The pterygospinous process** (***processus pterygospinosus***) [5] is a small and inconstantly present spine that extends from the posterior border of the lateral pterygoid plate where the pterygospinous ligament (*ligamentum pterygospinale*) attaches.

THE ETHMOID BONE

The unpaired and pneumatised bone of the *neurocranium* (although developmentally and topographically this bone belongs to the *viscerocranium* as it develops as C within the nasal capsule from three centres) that is located in the superior, medial and lateral parts of the nasal cavity is termed **the ethmoid**(al) **bone**, ***os ethmoideum*** *seu os ethmoidale* (from the Greek word '*ethmos*' meaning a 'sieve'), although the shorter and traditional name for this bone is *os ethmoides* [3–5].

Two bony plates of this bone include: (1) **the cribriform plate** and (2) **the perpendicular plate**. The cribriform plate is the horizontal plate that is perforated by numerous **cribriform foramina** (*foramina cribrosa*) [5] transmitting the olfactory nerve (*nervus olfactorius*, CN I) from the nasal mucous membrane to the olfactory bulb. This plate fills the ethmoidal notch between the orbital parts of the frontal bone and forms part of the roof of the nasal cavity and the middle part of the anterior cranial fossa. The small bony crest, rising above the cribriform plate and resembling a cock's comb, which gives attachment to the anterior part of the falx cerebri in the anterior cranial fossa, is called the crista galli. The perpendicular plate has two parts, i.e. the smaller superior part above the cribriform plate and the larger inferior part below this plate. This plate descends as the upper part of the nasal septum. Its anterosuperior part articulates with the nasal spine of the frontal bone and the nasal bones. Its anteroinferior border articulates with the septal cartilage. The posterior border is directed towards the sphenoidal crest, and the inferior border articulates with the vomer.

The main and paired part of this bone that lies on each side of the perpendicular plate is called ***labyrinthus ethmoideus*** *seu ethmoidalis* (**ethmoidal labyrinth** or so-called 'pannier' of this bone) [5]. This box-shaped and pneumatised portion contains anterior, middle and posterior groups of air cells in paper-thin compartments. The walls of these cellular cavities are so thin and delicate that they are often broken in the disarticulated bone. They are closed by adjacent bones in the intact cranium. Noteworthy, these air cells are currently termed ***cellulae ossis ethmoidei*** *seu cellulae ethmoideae osseae* but not '*cellulae ethmoidales*' [5]. The superior surface of the labyrinth has a number of incompletely closed cells. Their walls are completed in the articulated cranium by the edges of the ethmoidal notch of the frontal bone. Crossing this surface on each side are two groves that are converted into canals by articulation with the frontal bone; these are **the anterior ethmoidal foramen** (*foramen ethmoideum anterius seu foramen ethmoidale anterius*; old term *canalis orbitocranialis*) [5] and **the posterior ethmoidal foramen** (*foramen ethmoideum posterius seu foramen ethmoidale posterius*; old term *canalis orbitoethmoideus*) [5] which open on the medial wall of the orbit. The inferior surface of the labyrinth articulates with the maxilla and the palatine bone. The anterior surface of the labyrinth is covered by the lacrimal bone and the upper part of the frontal process of the maxilla. The posterior surface of the labyrinth presents large and irregular cellular cavities that are closed by articulation with the sphenoidal conchae and orbital processes of the palatine bones. The lateral surface of the labyrinth is termed ***lamina orbitalis labyrinthi ethmoidei*** or **the orbital plate of the ethmoidal labyrinth** (previously referred to as *lamina papyracea*). It constitutes the main part of the medial orbital wall and it covers the middle and posterior ethmoidal cells. This plate articulates anteriorly with the lacrimal bone, posteriorly with the sphenoid bone, superiorly with the orbital plate of the frontal bone and inferiorly with the maxilla and the orbital process of the palatine bone. The medial surface of the labyrinth forms the lateral wall of the nasal cavity. The anterior elevation that is formed by an especially large ethmoidal air cell is termed the **bony ethmoidal bulla** (***bulla ethmoidea ossea*** *seu bulla ethmoidalis*) [5]. This bulla compresses **the bony ethmoidal infundibulum** (***infundibulum ethmoideum osseum*** *seu infundibulum ethmoidale osseum*) [5], i.e. a deep and curved passage where the anterior ethmoidal cells open.

THE OCCIPITAL BONE

The unpaired bone that forms the posteroinferior part of the *neurocranium* is **the occipital bone** (***os occipitale***, Mi). Thus, it is a part of the calvaria and a part of the cranial base. This bone is made up of four parts that encircle the foramen magnum, i.e. **the squamous part** of the occipital bone (*squama occipitalis*), **the basilar part** of the occipital bone (*pars basilaris ossis occipitalis*) and the paired **lateral part** (clinically, the 'condylar part') of the occipital bone (*pars lateralis ossis occipitalis*) [6]. The squamous part has two surfaces, which remain unnamed, i.e. the convex external surface and the concave internal surface. The former has a site of appearance of the ossification nucleus in the centre where the bone is most convex which is called the external occipital protuberance (*protuberantia occipitalis externa*). There are two ridges that diverge laterally from this site that are called **superior nuchal lines** (sing. ***linea nuchalis superior***), although the previous term (*linea nuchae superior*) is often used. **Supreme (highest, Terminologia Anatomica 1998) nuchal lines** (sing. ***linea nuchalis suprema***, previously *linea nuchae suprema*) [cf. 4, 5] are encountered above and parallel and are less conspicuous. The trapezius muscle attaches between these two paired lines. Transverse ridges between the superior nuchal lines and the foramen magnum are called **inferior nuchal lines** (sing. ***linea nuchalis inferior***, previously *linea nuchae inferior*). The external occipital crest descends from the external occipital protuberance towards the foramen magnum.

The internal (inner, cerebral) surface of the squamous part bears **the cruciform eminence** (***eminentia cruciformis***, previously *eminentia cruciata*) [5] that gives rise to the groove for the transverse sinus passing laterally on each side, the ascending grove for the superior sagittal sinus and the internal occipital protuberance (*protuberantia occipitalis interna*) in the middle from which the internal occipital crest (crista occipitalis interna) descends to the posterior semicircumference of the foramen magnum. The upper depressions for the occipital lobes of the cerebrum are called cerebral fossae (sing. *fossa cerebralis*) and the lower depressions for the cerebellum are called cerebellar fossae (sing. *fossa cerebellaris*). Each lateral part contributes to the union of the cranium with the vertebral column and therefore carries the occipital condyle (*condylus occipitalis*) on its inferior surface. Interestingly, the name for the short canal that is located at the base of the occipital condyle, i.e. posteroinferiorly to the jugular tubercle and between the jugular process and the occipital condyle has been changed from *canalis nervi hypoglossi* to ***canalis hypoglossus***, **hypoglossal canal** in English [5]. Similar changes occurred in respect of other bony canals for nerves. Interestingly, the small and shallow depression that is sometimes present at the dorsal aspect of the *foramen magnum* in the midline between the cerebellar fossae at the lower end of the internal occipital crest, is officially termed ***fossa vermiana***, i.e. **the vermian fossa** in English [5], which is a traditional term, although the term *eminentia triangularis* is also used in the anatomical literature for its common variant. The basilar part fuses with the body of the sphenoid bone at age 18 to form a single bone and a smooth and sloping area for the medulla oblongata and the pons, i.e. *clivus*, this bone is sometimes referred to as *os basilare* [6].

THE PARIETAL BONES

The parietal bone (***os parietale***, from 'paries' meaning 'wall', Me) is a paired bone that forms the middle part of the calvaria (the skull vault). It has **the external surface** and **the internal surface** and **four borders** (frontal, sagittal, occipital and squamosal – not 'squamous') that are separated by **four angles** (frontal, occipital, mastoid and sphenoidal). The prominence that is located near the midline of the external surface is called **the parietal eminence** (or parietal tuber), ***eminentia parietalis*** *seu tuber parietale* [5]. The curved line for the attachment of the temporalis is termed the inferior temporal line (*linea temporalis inferior*) and the curved line for the attachment of the temporal fascia is termed the superior temporal line (*linea temporalis superior*). In the vicinity of the posterosuperior part of the parietal bone there is a small opening for an emissary vein called the parietal foramen (*foramen parietale*).

THE TEMPORAL BONES

The temporal bone (***os temporale***, Mi, from the Latin word '*tempus*' meaning 'time', so this is the 'time bone' just like the temporalis is the 'time muscle'; noteworthy, first grey hairs often appear in the pertinent region of the head, which is a critical juncture in life) contributes to the formation of the lateral wall and the base of the cranium. The structure of this bone is complicated because it contains important nerves, vessels and peripheral receptors for both the special sense of hearing and the maintenance of equilibrium. A number of muscles and ligaments attach to this bone. It also articulates with the mandible by a movable joint, i.e. the temporomandibular joint (TMJ).

Developmentally, each temporal bone consists of three parts: **the squamous part** (*pars squamosa*), **the petrous part** (*pars petrosa*, including the mastoid part, *pars mastoidea*) and **the tympanic part** (*pars tympanica*) [6]. In clinical anatomy, the mastoid part and the 'styloid part' are sometimes distinguished. Noteworthy, the mastoid part does not have a nucleus for independent ossification and arises from the petrous part, while the styloid part comprises **the styloid process** (from the Greek word 'stylos' meaning a 'pillar') which together with the stylohyoid ligament is a remnant of the second visceral arch [6]. Therefore, this traditional and clinical description is unfortunate from an embryological standpoint.

The squama is a thin, vertical and often translucent plate that forms the anterosuperior part of this bone. Its smooth external surface is called the **temporal surface** (*facies temporalis ossis temporalis*). This surface affords attachment to the temporalis muscle and is marked posteriorly by the middle temporal artery grooving ***sulcus arteriae temporalis mediae***. **The mandibular fossa** (the glenoid fossa of the temporal bone, *fossa mandibularis*) is bounded anteriorly by **the articular tubercle** (*tuberculum articulare*) and articulates with the mandibular condyle to form the TMJ. **The cerebral surface** bears marks of the brain and arteries, i.e. *impressiones gyrorum* (*seu digitatae*), *juga cerebralia et sulci arteriosi*.

The zygomatic process of the temporal bone (*processus zygomaticus ossis temporalis*) is a narrow bony arch that projects forwards from the inferior part of the squama to join the temporal process of the zygomatic bone and form **the zygomatic arch** (*arcus zygomaticus*).

The zygomatic process has two roots, i.e. the anterior root (the articular tubercle) and the posterior root, with the mandibular (glenoid) fossa between them, and two borders, i.e. the thin superior border that serves for the attachment of the temporal fascia and the inferior border that affords attachment to some fibres of the masseter. Interestingly, the traditional name for the crest that projects posteriorly as the continuation of the suprameatic line stretching from the base of the zygomatic process, forming the posteroinferior border of the temporal fossa, has been endorsed by the FIPAT and is officially termed **supramastoid crest** (***crista supramastoidea***) [5].

The longest bony canal of the temporal bone that originates on the floor of the internal acoustic meatus (internal auditory canal), stretching laterally to the axis of the petrous part and ending with the *foramen stylomastoideum* (stylomastoid foramen) is officially termed ***canalis facialis*** *seu canalis nervi facialis* (**facial canal** in English) [5] to match other similar modifications. Interestingly, the widest canal of the temporal bone is termed ***canalis carotidis*** *seu canalis caroticus* and the official names for its two openings are: ***apertura externa canalis carotidis*** *et* ***apertura interna canalis carotidis*** (*seu apertura externa canalis caroticus et aperture interna canalis caroticus,* respectively) [5].

THE FACIAL BONES

The facial bones are either associated with the nasal capsule or immobile (fixed) bones that are derived from the visceral arches, see Introduction. The mandible is neither part of the cranium nor part of the facial skeleton. Therefore, it has been classified as the extracranial bone of the head [5].

The nasal bone (*os nasale*) is a small and paired bone that has two unnamed surfaces, i.e. the external and the internal surface and four unnamed borders, i.e. superior, inferior, medial and lateral. It joints the contralateral bone to form the skeletal support for the *nasus externus*. Only two terms in the new edition of Terminologia Anatomica [5] refer to this bone, i.e. **the ethmoidal groove** (***sulcus ethmoideus*** *seu sulcus ethmoidalis*) and the nasal foramen (foramen nasalis). These bones are remarkably variable in different people

The lacrimal bone (*os lacrimale*) is a paired and exceptionally small and fragile bone of the face that is located in the anterior part of the medial wall of the orbit, just behind the frontal process of the maxilla. This bone presents two unnamed surfaces and four unnamed borders. Thus, this bone resembles an open booklet and the spine-like part is termed **the posterior lacrimal crest** (*crista lacrimalis posterior*). To the front of this crest runs **the lacrimal groove** (*sulcus lacrimalis ossis lacrimalis*). Together with the adjacent groove and the anterior lacrimal crest of the frontal process of the maxilla they form **the fossa for the lacrimal sac**, *fossa sacci lacrimalis* (Terminologia Anatomica, section Orbita) [5]. The posterior lacrimal crest ends inferiorly in a small bony hook termed **the lacrimal hamulus** (*hamulus lacrimalis*) which articulates with the lacrimal tubercle of the maxilla.

The zygomatic bone (***os zygomaticum***, after Riolan), which is casually referred to as the 'cheekbone' (*os malare*) and 'zygoma' (Galen) in clinical anatomy, is a paired bone that is one of the strongest bones of the cranium [6]. It connects the frontal bone with the temporal bone, thereby contributing to the **zygomatic arch** (*arcus zygomaticus*), i.e. the site of origin of the masseter, and strengthening the facial skeleton. Its central part is often referred to as the 'body of the zygomatic bone' (*corpus ossis zygomatici*) in clinical anatomy, although this term remains unofficial [5] and has not been endorsed by the FIPAT. The body has three surfaces, i.e. the surface and **the zygomaticofacial foramen** (*foramen zygomaticofaciale*). The zygomatic bone presents three surfaces, i.e. **the lateral** (malar), **orbital** and **temporal** surfaces, five borders and two processes, i.e. the superior **frontal process** which articulates with the zygomatic process of the frontal bone and the lateral **temporal process** which articulates with the zygomatic process of the temporal bone.

The maxilla is a paired, pneumatised and the largest bone of the face [6]. This bone comprises **the body of the maxilla** (*corpus maxillae*) with its four surfaces, i.e. anterior, infratemporal, nasal and orbital, and **four processes of the maxilla**, i.e. **the frontal process**, **the zygomatic process**, **the palatine process** and **the alveolar process**. The body contains a large sinus called **the maxillary sinus** (***sinus maxillae*** *seu sinus maxillaris osseus*) [5], which communicates with the nasal cavity through an opening on the medial (nasal) wall of the maxilla that is termed **hiatus of maxilla** (***hiatus maxillae*** *seu hiatus maxillaris osseus*) [5]. Posterior to the frontal process and anterior to this hiatus, **the lacrimal groove of maxilla** (*sulcus lacrimalis maxillae*) can be observed, which together with the lacrimal bone and the inferior nasal concha form **the nasolacrimal canal** (*canalis nasolacrimalis*). The anterior (traditionally termed 'malar') surface (*facies anterior maxillae*) has the infraorbital foramen (*foramen infraorbitale*) and the canine fossa (*fossa* *canina*) below, where the Levator anguli oris origins. The infratemporal surface (*facies infratemporalis maxillae*) is separated from the anterior surface by the zygomatic process and has several small perforations for the nerves and vessels to the upper teeth. **The maxillary tuberosity** (***tuber maxillae*** *seu eminentia maxillae*) [5] is a rounded and roughened elevation on the infratemporal surface of the body of the maxilla that is located posterior to the most distal molar of the maxillary arch. This important landmark is perforated **by the posterior superior alveolar foramina** (*foramina alveolaria superiora posteriora*), where the posterior superior alveolar nerve along with blood vessels enter the bone from the posterior. The nasal surface is continuous inferiorly with the superior surface of the palatine process. The orbital surface of the body is flat, smooth and triangular in shape. The lacrimal notch (*incisura lacrimalis*) is located just behind the frontal process. The infraobrital groove (*sulcus infraorbitalis*) originates in the vicinity of the posterior border of the orbital surface and is anteriorly converted into the infraorbital canal (*canalis infraorbitalis*) which opens on the anterior surface as the infraorbital foramen (*foramen infraorbitale*). **The frontal process of the maxillae** (*processus frontalis maxillae*) projects upwards and joints the nasal part of the frontal bone. Its lateral surface is divided into two parts by **the anterior lacrimal crest** (*crista lacrimalis anterior*), which is continuous downwards with the infraorbital margin. **The zygomatic process of the maxillae** (*processus zygomaticus maxillae*) articulates with the zygomatic bone. **The palatine process** (*processus palatinus*) forms most (about three quarters) of the hard bony palate by joining the contralateral process in the midline where **the nasal crest of maxilla** (*crista nasalis maxillae*) rises on the superior surface. This part faces the nasal cavity and articulates with the inferior edge of the vomer. Both openings that lead into **the incisive canals** (*canales incisivi*) are located in the vicinity of the anterior end of the nasal crest on the superior surface. **The alveolar process** (*processus alveolaris maxillae*) is the thickest and most spongy part of the maxilla. Its inferior border is called the alveolar arch of the maxilla (arcus alveolaris maxillae). This part has eight **dental alveoli** or dental sockets **of the maxilla** (*alveoli dentales maxillae*) for the eight upper teeth.

The palatine bone (*os palatinum*) is an L-shaped bone that is situated in the posterior part of the nasal cavity, between the maxilla and the pterygoid process of the sphenoid bone. Each palatine bone extends from the posterior quarter of the hard palate to the floor of the orbit. It also contributes to the formation of the floor and lateral wall of the nasal cavity. It enters into the formation of the pterygopalatine, pterygoid and infratemporal fossae [6]. Thus, although this bone is small, it contributes to the formation of some of the cranial cavities, including the orbit, the oral cavity, the nasal cavity and the three fossae. Each palatine bone has two plates, i.e. **the horizontal plate** (*lamina horizontalis ossis palatini*, previously *lamina palatina ossis palatini*) and **the perpendicular plate** (*lamina perpendicularis ossis palatini*). The former complements the palatine process posteriorly to form the hard bony palate. Its medial border meets the medial border of the contralateral bone to form the nasal crest with the vomer between its lips. The latter is longer and adjoins the nasal surface of the maxilla. On its nasal surface it has ethmoidal and conchal crests. The palatine bone has three processes, i.e. the pyramidal process (processus pyramidalis), which projects posteriorly and laterally from the junction of the horizontal and perpendicular plates, the larger **orbital process** (*processus orbitalis*) and the smaller **sphenoidal process** (***processus sphenoideus*** *seu processus sphenoidalis*) [5] with **the sphenopalatine notch** (*incisura sphenopalatina*) between them. The sphenoid bone covers this notch and converts it into **the sphenopalatine foramen**.

The inferior nasal conchae (*concha nasalis inferior*), previously termed the 'inferior nasal turbinate', is a paired curved bony plate that extends horizontally along the lateral wall of the nasal cavity. Unlike the other conchae (parts of the ethmoid bone), this is an independent bone. It has three processes: **maxillary** (*processus maxillaris*), **lacrimal** (*processus lacrimalis*) and **ethmoidal** (*processus ethmoidalis*). This bone has two surfaces (lateral and medial), two borders (superior and inferior) and two extremities.

The vomer (*vomer*, after Fallopio, Bartholin used the term *aratrum*, both these terms refer to the fact that this bone resembles the Roman ploughshare) is an unpaired and roughly quadrilateral plate that forms part of the bony nasal septum [6]. Its superior edge is thicker that the other edges and embraces the sphenoidal rostrum with the wings called *alae vomeris* (sing. **ala of vomer**, ***ala vomeris***). The upper half of the anterior edge articulates with the perpendicular plate of the ethmoid, and the lower part with the cartilaginous nasal septum. The inferior edge articulates with the nasal crest of the maxilla and the palatine bone. The free posterior edge constitutes the free posterior border of the bony nasal septum separating the right and left posterior nasal aperture of cranium, i.e. right and left **choana of cranium** (***choana cranii*** in Latin) [5].

EXTRACRANIAL BONES OF THE HEAD: THE MANDIBLE

The mandible (*mandibula*, which is derived from the Latin word *mandere*, which means 'to chew, masticate or devour') is classified as the extracranial bone of the head [5] and the only mobile skull bone. This is the largest and the strongest facial bone that is heavily formed to carry the lower teeth and the muscles of mastication [6]. This bone affords attachment to the muscles of the tongue and floor of the mouth. Its horseshoe shape is determined by its development and function.

The body of the mandible (*corpus mandibulae*) has two unnamed surfaces: *facies externa* and *facies interna*. On the external surface in the midline there is a vertical ridge where two halves are fused to form the junction called ***symphysis*** (syndesmosis) ***mandibulae seu menti*** [5]. In general, the structure and relief of the body are determined by the teeth and the function of this part which form the mouth. The inferior border is called **the base of the mandible** (***basis mandibulae***). The upper part, i.e. **the alveolar part** (***pars alveolaris mandibulae***) bears lower teeth. Consequently, the alveolar arch has **the dental alveoli** (***alveoli dentales mandibulae***) with the interalveolar septa (***septa interalveolaria mandibulae***) with **the interradicular septa** (***septa interradicularia mandibulae***) that can be found in some alveoli. Corresponding depressions for the former septa that are visible on the external surface of the body are called **the alveolar yokes of mandible** (***juga alveolaria mandibulae***). On the external surface of the body there is a ridge at the symphysis, which is known as **the mental protuberance** (***protuberantia mentalis***). **The mental tubercle** (***tuberculum mentale***) lies on each side of this protuberance. Laterally, there **is the mental foramen** (***foramen mentale***), which is an opening of **the mandibular canal** (***canalis mandibulae***), transmitting nerves and vessels. To the back of the mental foramen is **the oblique line** (***linea obliqua mandibulae***), which runs upwards. **Two mental spines** or 'genial tubercles' (***spinae mentales — spina mentalis superior et inferior***) project from the inner surface of the symphysis as the side of attachment of the genioglossus muscle. Inferiorly and on both sides of the mental spine lies **the digastrics fossa** (***fossa digastrica***) as the side of attachment of the digastric muscle. **The mylohyoid line** (***linea mylohyoidea***) runs backwards and upwards and passes obliquely towards the ramus.

The ramus of the mandible or 'mandibular ramus' (***ramus mandibulae***) is quadrilateral in shape and has two surfaces, i.e. the external and internal surfaces (facies lateralis et medialis), four unnamed borders (superior, inferior, anterior et posterior) and two processes (***processus coronoideus mandibulae*** et ***processus condylaris***). On the inner surface of the ramus is **the inferior alveolar foramen** (foramen alveolare inferius, previously 'foramen mandibulae') [5], leading to the mandibular canal mentioned above. The medial edge of this foramen projects as the lingula mandibulae, to which the sphenomandibular ligament attaches. **The mylohyoid groove** (***sulcus mylohyoideus***) originates behind the lingula and passes downwards and forwards. The inferior and posterior borders of the ramus arise from the body obliquely and posteriorly to form **the angle of the mandible** or 'mandibular angle' (***angulus mandibulae***). The anterior border of the ramus bears **the temporal crest** (***crista temporalis***) [5], where the temporalis attaches. The superior border has two processes: the condylar process has **the mandibular condyle** (***condylus mandibulae*** seu caput mandibulae seu *capitulum mandibulare*) [5] which is covered by cartilage. The condyle or head is continuous with the neck of the mandible (collum mandibulae) which has **the pterygoid fovea** (***fovea pterygoidea***) on its inner surface. **The coronoid process of the mandible** (***processus coronoideus mandibulae***) [5] is the 'muscular' and anterior process that has a rough area for attachment of the temporalis muscle. Both processes are separated by **the mandibular notch** (***incisura mandibulae***).

EXTRACRANIAL BONES OF THE HEAD: THE HYOID BONE

The hyoid bone (***os hyoideum***, previously *os hyoides*), named from its resemblance to the Greek letter U, is situated at the base of the tongue, between the mandible and the larynx, and is suspended from the tips of the styloid processes by the stylohyoid ligaments. It consists of **the body** (***corpus ossis hyoidei***) and two pairs of horns, i.e. the lesser horns and the greater horns, ***cornu minus*** *et* ***cornu majus ossis hyoidei***, respectively.

CONCLUSIONS

The new terminology concerning the cranium and the extracranial bones of the head uses more appropriate anatomical terms. Although the old tradition has been respected, more precise and anatomically adequate terms are currently being used. Therefore, the new version of the anatomical terminology deserves attention and should be used in both didactic and clinical practice.

Conflict of interest: None declared

REFERENCES

1. Chmielewski PP. New Terminologia Anatomica highlights the importance of clinical anatomy. Folia Morphol. 2020; 79(1): 15–20, doi: 10.5603/FM.a2019.0048, indexed in Pubmed: 31025701.
2. Chmielewski PP, Strzelec B. Should Terminologia Anatomica be revised and extended? A critical literature review. Folia Morphol. 2020; 79(1): 1–14, doi: 10.5603/FM.a2019.0047, indexed in Pubmed: 31025702.
3. Chmielewski PP, Domagała ZA. Terminologia Anatomica and its practical usage: pitfalls and how to avoid them. Folia Morphol. 2020; 79(2): 198–204, doi: 10.5603/FM.a2019.0086, indexed in Pubmed: 31411339.
4. FIPAT. Terminologia Anatomica. International Anatomical Terminology. 2nd edition. Georg Thieme Verlag, 2011.
5. FIPAT. Terminologia Anatomica. International Anatomical Terminology. 3rd edition. Georg Thieme Verlag, 2019.
6. Prives M, Lysenkov N, Bushkovich V. Human anatomy. MIR Publishers, Moscow 1985.
7. Strzelec B, Chmielewski PP, Gworys B. The Terminologia Anatomica matters: examples from didactic, scientific, and clinical practice. Folia Morphol. 2017; 76(3): 340–347, doi: 10.5603/FM.a2016.0078, indexed in Pubmed: 28026851.
8. Zdilla MJ, Russell ML, Koons AW, et al. Metopism: a study of the persistent metopic suture. J Craniofac Surg. 2018; 29(1): 204–208, doi: 10.1097/SCS.0000000000004030, indexed in Pubmed: 29049140.

VIA MEDICA

REVIEW ARTICLE

Folia Morphol.
Vol. 80, No. 3, pp. 487–504
DOI: 10.5603/FM.a2021.0079

ISSN 0015–5659
eISSN 1644–3284
journals.viamedica.pl

Role of brain-derived neurotrophic factor in shaping the behavioural response to environmental stressors

E. Badowska-Szalewska[1], G. Lietzau[1], J. Moryś[1, 2], P. Kowiański[1, 2]

[1]*Department of Anatomy and Neurobiology, Faculty of Medicine, Medical University of Gdansk, Poland*
[2]*Institute of Health Sciences, Pomeranian University of Slupsk, Poland*

[Received: 28 July 2021; Accepted: 5 August 2021; Early publication date: 7 August 2021]

Brain-derived neurotrophic factor (BDNF) is an important neurotrophin involved in an integration of the brain activity in physiological and pathological conditions, with formation of a short- and long-term functional and structural neuroplasticity. This process proceeds, with a changeable dynamics, in the subsequent stages of ontogenesis. In addition to many other functions in the central nervous system, BDNF is also involved in shaping a response to stress stimuli in the form of precisely adjusted behavioural reactions involving the limbic system, and the endocrine system with stimulation of the hypothalamic-pituitary-adrenal axis (HPA). Although almost every stressor increases the activity of the HPA, the neuronal response to it can vary substantially. This may be due to involvement of different neurotransmitter pathways, neuromodulators and neurohormones, as well as changes in gene expression. It is widely accepted that BDNF synthesis and secretion are modulated by stress. Furthermore, age is an important factor influencing the BDNF expression in response to different stressors. In this work, we focused on the analysis of the role of mild stressful stimuli, which commonly occur in the natural environment, on changes in BDNF expression at various stages of ontogenetic development. Although, the presented data comes from animal studies, probably similar mechanisms of stress regulation are also present in humans.

This comprehensive review shows that the influence of stressors on the BDNF expression depends on many factors, including a type and duration of a stressor, time of neurotrophin detection, animal's resistance to stress, brain area, and genotypic characteristics of an individual. A more detailed understanding of the mechanisms shaping stress reactions, including the role of BDNF, may be of both theoretical and practical importance, allowing designing more effective strategies for preventing and treating stress itself and the stress-related disorders. (Folia Morphol 2021; 80, 3: 487–504)

Key words: aging, brain-derived neurotrophic factor (BDNF), glucocorticoids, ontogenesis, stress

Address for correspondence: G. Lietzau, PhD, Department of Anatomy and Neurobiology, Faculty of Medicine, Medical University of Gdansk, ul. Dębinki 1, 80–211 Gdańsk, Poland, tel: +48 58 349 1819, e-mail: grazyna.lietzau@gumed.edu.pl

INTRODUCTION

Animal behaviour is a result of a coordinated action of functional systems within the central nervous system (CNS). The behaviour is a consequence of a reaction to external stimuli of different modalities, as well as the effect of a response to constantly changing parameters of internal environment in the organism. Finally, it is a consequence of elaborated reactions resulting from the conscious integration of stimuli in the brain cortical areas, reflexes, and instinctive or emotional reactions arising in subcortical structures of the brain. Stress stimuli of various natures, constantly affecting the body, play an important role in shaping the behaviour. Therefore, answering to these stimuli is an integral part of functioning in the natural environment. The reaction to stressful stimuli requires involvement and activation of many systems. In addition to the sensory and motor systems, they include the vegetative, endocrine and limbic systems, as well as various neurotransmitters, neuromodulators and signalling pathways, leading to changes in expression of transcription factors and gene activation. It is worth noting that the reaction to stressful stimuli is plastic and depends on interaction of numerous external and internal factors. It also changes its characteristics along ontogenetic development. One of the important factors shaping the response to stressful stimuli is brain-derived neurotrophic factor (BDNF). Despite systematic research, the role of this factor in shaping responses to different types of stressors at various stages of ontogenetic development is not fully elucidated. In research on the role of this factor many experimental models have been introduced to approximate the conditions of the stressors' action in the natural environment. This review summarises the current knowledge on the role of BDNF in stress at various stages of ontogenesis. A brief overview of the most commonly used tests to assess the expression of BDNF in response to stress stimuli is also presented.

STRESS REACTION MECHANISMS INTEGRATE FUNCTIONS OF THE ENDOCRINE, LIMBIC AND AUTONOMIC SYSTEMS

One of the most important functions of the nervous system is perception and transfer of information from both external and internal environment to the complex functional systems of the brain. This enables integration of stimuli and maintenance of physiological homeostasis, as well as elaboration of an adequate behavioural response. One of the most important systems involved in these processes is the hypothalamic-pituitary-adrenal axis (HPA) [67, 112, 157, 162]. Hypothalamus enables transfer and integration of neurogenic signals to the endocrine, limbic and autonomic systems. Within hypothalamus, the paraventricular nucleus (PVN) and, to a lesser extent, the supraoptic nucleus (SON) are the two areas involved in the stress response initiation [26, 169] and shaping this reaction, depending on the stressors' specificity [52, 105].

Taking into account the anatomical aspects related to the stimuli transfer between different functional systems in the brain, it can be suggested that influence of stressors on the HPA occurs in two ways: direct and indirect. The first one is used by physical stressors activating HPA directly [42, 67]. The second one is used by emotional stressors, influencing the HPA through activation of important structures of the limbic system, such as amygdala and hippocampus [23, 55, 130]. Activation of hypothalamus results in a rapid secretion of corticotrophin releasing hormone (CRH) — from the small cellular part of the PVN, and arginine-vasopressin (AVP) — from the large cellular part of this nucleus and from the supraoptic nucleus (SON). It is followed by a release of the adrenocorticotropic hormone (ACTH) from the pituitary gland [15, 108] and, ultimately, glucocorticoids or corticosterone from the adrenal cortex [69, 112]. Glucocorticoids, due to the negative feedback, influence hypothalamus and pituitary gland and inhibit the production of CRH and ACTH, respectively. This, in turn, results in reduction the HPA activity [68]. Despite the adaptive action of glucocorticoids in the short term, their long-term action lowers the body's ability to cope with stress and may affect the synaptic plasticity [100, 102].

INTERACTION OF GLUCOCORTICOIDS, NEUROTRANSMITTERS, AND BDNF IS NECESSARY TO ELABORATE THE STRESS REACTION

Stress may evoke changes in BDNF expression through signalling pathways triggered by glucocorticosteroids (glucocorticoids) [48, 86]. Barbany and Persson [16] reported that excessively high or low levels of glucocorticoids may alter the BDNF expression. It has been suggested that BDNF may reduce some of the negative effects of glucocorticoids [90] and its direct administration is able to restore the stress-reduced content of this neurotrophin, e.g. in the hippocampus [27, 82]. However, the results of these studies are inconclusive and not commonly accepted [63]. The interaction between glucocorticoids and BDNF can occur, among others, through their influence on expression of the TrkB receptor [72]. The studies conducted in animals with adrenalectomy (removal of adrenal glands) indicated that glucocorticoids negatively affected the BDNF expression in hippocampus and other cortical areas [71, 119, 150, 151]. However, adrenalectomy does not completely block the effects of stress on the BDNF concentration [151]. There is evidence that other factors, such as interleukin-1β, also contribute to the changes in the BDNF expression in hippocampus [17]. Also the animal activity is an important factor regulating the BDNF production in the rat hypothalamus [97]. The regulation involves classical neurotransmitters, such as glutamate, acetylcholine, serotonin and GABA [65, 76, 96]. It has been suggested that whereas glutamate, acetylcholine and serotonin increase the BDNF expression, GABA reduces its content in the CNS.

BDNF CONTRIBUTES TO MODIFICATION OF THE HPA ACTIVITY IN STRESS CONDITIONS

The role of stress as modulator of BDNF synthesis and release is well documented [108, 109]. The long-term stress affects the expression of genes responsible for signalling pathways related to glucocorticoids and neurotrophins, among them also BDNF [51, 54, 114, 159, 178]. Transcription of BDNF is under control of promoters which react differently to endogenous and exogenous stimuli (e.g. glucocorticoids and environmental factors, respectively) [80]. These stimuli are also responsible for triggering epigenetic modifications [155]. It is believed that epigenetic processes cause long-lasting or permanent changes in BDNF gene expression, which is reflected in the behavioural responses occurring during early development [130, 168]. Methylation of the BDNF gene is an important epigenetic process affecting its expression, thus inducing changes in the protein content initiated by stress. However, the consequences of this modification are differently interpreted by some authors [114]. The reason for this could be epigenetic changes at different loci within the same gene [91]. Additionally, there is evidence showing that changes in BDNF expression were also related with age [91]. It has been suggested that epigenetic modification of BDNF gene may be responsible for an occurrence of some pathologies induced by chronic stress, such as mental disorders or cognitive decline [167, 177]. Animal studies showed that chronic social stress in mice reduced BDNF expression in the hippocampus as a result of methylation within its gene [156].

Brain-derived neurotrophic factor plays an important role in integrating neuronal and endocrine responses to different stressors [140]. This is due to the direct influence of this neurotrophin on the HPA [73, 154]. Studies showed that both endogenous (already existing pool) and *de novo* synthesised BDNF regulated the HPA functioning and elaboration of an adaptive stress response [108]. It has been shown that a single injection of BDNF causes activation of the HPA [58]. Importantly, by modifying the HPA activity, BDNF facilitates adaptation to environmental conditions [140] and contributes to the maintenance of the physiological homeostasis [154]. By counteracting the adverse effects of glucocorticoids, BDNF is an important factor reducing the stress-induced psychosocial and psychological symptoms [90]. As mentioned before, the BDNF function in response to stressors relays on regulation of synthesis and release of hormones and neuropeptides, such as CRH and AVP in PVN and SON [4, 58, 97, 119]. The stress-induced increase in the BDNF concentration stimulates AVP and CRH synthesis [58, 97, 119]. It may also affect the intracellular content of neuropeptides [58].

REGULATORY ROLE OF BDNF IN SHAPING THE BEHAVIOURAL RESPONSE IS DETERMINED BY NEURONAL ACTIVITY AND FUNCTION, AS WELL AS STAGE OF ONTOGENETIC DEVELOPMENT

Brain-derived neurotrophic factor has important regulatory functions in neurons within the CNS, regardless of the stage of ontogenetic development [154]. The role of this neurotrophin is related to the activity of neural networks and synaptic plasticity, and it can differ depending on the stage of ontogenesis [58, 60, 90, 93, 146]. Neural activity affects the BDNF gene transcription, as well as synthesis of the BDNF protein. It also determines an expression of TrkB receptor, which is one of the most important signal transducers of this neurotrophin [61].

In the earliest stage of ontogenetic development, BDNF is involved in differentiation of neural stem cells into neurons, their growth and maturation [31, 175]. This is a consequence of BDNF regulatory function upon cell proliferation and migration, neuronal survival, as well as maturation of the axodendritic system and synaptogenesis [123, 175].

In the mature brain, BDNF regulates synaptic transmission [160] and has a protective function upon neurons [7, 89]. Consequently, BDNF has a role in promoting learning, cognitive and memory skills, as well as reduction of anxiety [37, 38]. During aging, BDNF is responsible for preventing neuronal degeneration, as well as for an enhancement of the regenerative and repair processes [98, 145, 154]. In many brain areas, including limbic structures such as hippocampus, amygdala and the hypothalamic nuclei, BDNF has been suggested to modulate the behavioural responses to stress [109, 116, 119]. However, its role in this process differs depending on the stage of development and brain area [93].

The variety of BDNF functions in the CNS suggests that alterations in the expression of this neurotrophic factor could be involved in the pathophysiology of the stress-related behaviours caused by long-term effects of stressful stimuli, such as orientation, memory and cognition disturbances and mental illnesses, such as depression, Parkinson's, Alzheimer's and Huntington's diseases [5, 104, 114]. Therefore, BDNF could be considered in future research on therapeutic agents aimed at treatment of several stress-related disorders.

CHANGES IN BDNF EXPRESSION DURING ONTOGENESIS AFFECT STRESS REACTIONS

Stimulation of the CNS with a mild stress evokes multidirectional effects. One of the ways in which this modification occurs is through activation of the HPA and its relationship with BDNF. This is indirectly related to involvement of BDNF in development of synaptic plasticity [58, 60, 79]. The intensity of this process varies during different stages of ontogenesis, which can be a consequence of changes in BDNF concentration [58, 108]. Following, we briefly discuss the CNS effects induced by the selected mild stressors (i.e. causing neither structural damage nor pain) often present in the animal's natural environment.

Early development

An early developmental stage, in rodents lasting approximately 2 weeks after birth, is called a stress hypo-responsive period (SHRP) [87, 132, 137]. During this time, activation of the HPA and a complete development of the stress response occur only after action of very strong psychological or physical stimuli [43, 139]. One can suspect that attenuation of the stress response during that time may protect the developing brain from negative effects of stress hormones (e.g. glucocorticoids) [132]. The high threshold of the HPA activation could be a consequence of the incomplete development of structures which control the stress response, one of which is PVN [125, 128]. It is also associated with a less efficient cooperation of the structures controlling the HPA [44].

Stress in the early period of life negatively affects development and functioning of the brain. It may be responsible for inducing anxiety, depression, and aggression also persisting later in life [2, 29, 70, 166]. However, in general, connection of stress occurring in the early life with psychopathological symptoms observed in adulthood is poorly understood and requires further research [167].

Maternal separation and social isolation. Maternal separation (MS) and social isolation (SI) are regarded as the most common causes of stress in the early life. Early periodic postpartum MS, as well as siblings SI are examples of stress that can cause disturbances in the HPA activity resulting in structural and functional impairments in later life [122, 126, 174, 177]. These two forms of stress in the early life also affect the BDNF mRNA and protein levels. The long-term MS-induced changes in the BDNF expression level in the hippocampus [21, 41] have been linked to learning and memory disorders [2, 30, 70, 174]. Ohta Ken-ichi et al. [111] showed that a long-term separation (6-h) from a mother, between postnatal day P2 and P20, reduced the expression of the BDNF genes in hippocampus of the Sprague-Dawley rats at P7. However, it had no effect on BDNF-ERK signalling after P14. MS between P2 and P14 induced a transient increase in the BDNF levels in hippocampus, prefrontal cortex [126], and amygdala of the Wistar rats [34]. Other studies showed that an early weaning (during the first week of life) had no effect on the BDNF levels in hippocampus [179]. BDNF increase was observed in the olfactory bulb, where this neurotrophic factor may play an important role in learning of the olfactory association [179]. The results confirm that stress sensitivity is lower and the HPA axis response is decreased in the early postnatal period [87, 132]. They also suggest that period of hyporesponsiveness to stress and duration of the postpartum MS may be important factors inducing changes in the BDNF expression in the various brain regions. It has been assumed that BDNF plays an important role in neuroprotection [92]. Hence, an increase of its expression could counteract the effects of MS. However, there are data indicating that MS induced a decrease in the BDNF expression within 3 weeks after birth [33]. This stressor also induced a reduction in the BDNF mRNA in P16, followed by an increase in P30 and P60 in hippocampus [83] and in the medial prefrontal cortex (mPFC) of Wistar rats [174]. A long-term MS induces reduction in the number of dendritic spines and delay in maturation of the pyramidal neurons in hippocampus [111]. Thus, the MS may influence the BDNF-associated signalling during synaptogenesis [111]. These processes and an increased apoptosis coexist in the early postnatal period [29]. These observations indicate that the MS-induced abnormalities in hippocampus are associated with disturbances in the BDNF signalling pathway during the early brain development [111]. Studies showed that the burden of MS in rodents was responsible for changes in BDNF expression in adulthood and aging, often leading to emotional and cognitive disturbances [122]. Hence, MS causes a decrease in the BDNF concentration, which may lay at the basis of some characteristic functional disorders. A potential factor contributing to these processes are epigenetic changes in the BDNF gene, which may increase susceptibility to stress later in life [141].

In adult and older rodents, the long-term MS also resulted in reduction of BDNF expression in hippocampus [2, 45, 94, 152]. Furthermore, in adult rats, a decrease in BDNF was observed in amygdala [124] and prefrontal cortex [126]. However, in adult rats additionally subjected to prolonged swimming stress, no further reduction in BDNF expression in the prefrontal cortex was reported [126]. It is possible that a decrease in BDNF expression in the CNS early in life can result in an impairment of the plasticity mechanisms later on.

The results of studies investigating changes in BDNF expression after MS are not equivocal. Récamier-Carballo et al. [122] observed an increase in BDNF concentration in hippocampus and amygdala and a decrease in the frontal cortex in adult mice after the long-term MS. Study by Greisen et al. [62] showed an increase in BDNF concentration in hippocampus in adult rats subjected previously to MS in their early life, although they found no changes in the frontal cortex and PVN. On the contrary, van Zyl et al. [164] showed no effect of MS and a restraint stress on BDNF content in hippocampus of adult rats. These differences could be explained by the selection of various species and strains of experimental animals, differences in the experimental conditions and protocols concerning for example the time-point of the expression measurement of the neurotrophic factor.

Thus, various changes in BDNF expression were demonstrated in different brain areas, both in animals after MS and those subjected to additional stress in adulthood. This suggests the complexity of the regulatory mechanisms. The increase in BDNF expression in hippocampus of rats after MS could be a compensatory response to neonatal separation, keeping neurogenesis unchanged in adult animals. Reports on the SI effects on the CNS and especially their pathophysiological consequences are not equivocal. Biggio et al. [21] have shown that both 3 h MS between P3 and P14 and SI after weaning induce a significant reduction in BDNF expression in hippocampus of Sprague-Dawley rats. Despite the opinion that early SI exacerbates responses to stressors [167], its effects in adulthood are poorly understood.

Maturation

The maturation (from P14 to P90) is a phase of a rapid structural and functional changes relaying on an intense development and reorganization of brain structures, including final shaping of their connections. In this phase, the structures involved in the stress response undergo further development. During this period, they are more sensitive to aversive stimuli then in the adulthood [99, 106]. In adolescence, a response of the HPA to stressors is increased and prolonged [9, 93, 107]. This results in an increased concentration of glucocorticoids and a prolonged time of their secretion after a repeated exposure to a stressor [99, 165]. It may be a consequence of the incomplete development of the HPA feedback inhibition [59, 93]. According to some authors, this can explain the insufficient control of its activity [9, 93, 99]. Numerous studies have shown that exposure to potentially traumatic stressors in adolescence has a significant impact on the further development of brain structures and formation of their connections [9, 36, 158]. In development, stress triggers processes resulting in permanent changes in the neuronal plasticity and efficiency of the synaptic connections, which require the BDNF activity [18, 63]. Many authors emphasize that changes of environmental conditions influencing sexually immature animals, with not completely formed neuroendocrine regulatory mechanisms and neuronal connections, may lead to the long-term physiological and behavioural dysfunctions [24, 66].

Predator odour and social isolation. The predator smell is a strong, unconditional and psychogenic stressor for the rodents [18, 153, 180]. Animals exposed to this stressor demonstrate changes in activity, long-lasting and augmented anxiety behaviour [153, 180]. They are accompanied by an increased level of glucocorticoid release and an altered BDNF concentration [18]. The nature of the response to a predator's threat early in life is a species-specific feature. It is often associated with development of defensive behaviour and sensitivity to stress during later development [18, 153, 180].

Bazak et al. [18] assessed BDNF expression in the frontal associative cortex, CA1, CA3 sectors of hippocampus and the dentate gyrus (DG), after a single (10 min) and multiple exposures to a predator urine scent in the Sprague-Dawley rats at P24. The experiment was repeated at P60. It was found that both the early and late effects of the stressor induced a significant reduction in the BDNF mRNA and BDNF protein levels in the hippocampal CA1. The effect of re-exposure to stress was greater in rats exposed to the same stressor again, indicating a cumulative effect of this kind of stimulus.

Exposure to a chronic psychosocial stress may also alter the BDNF expression. A long-term SI caused changes in functioning of the HPA and an increase of anxiety and depressive behaviours [177]. They were accompanied by a reduction of the BDNF mRNA and BDNF protein concentration in hippocampus of the adolescent rodents. This suggests an important role of this type of stressor in the regulation of the BDNF content in the limbic system and, thus, in shaping the adequate behavioural responses during further stages of ontogenesis. However, consequences of these processes for the synaptic plasticity and the brain structure in the adulthood remain unknown.

Chronic mild stress. Several procedures can induce mild forms of stress. Among the most frequently used are: temporary deprivation of food or water, overcrowding in a cage, social isolation, using a soaked sawdust in a cage or tilting frames (45°), inversion of the light/dark cycle, and a short-term (5 min) forced swimming test [155]. These stressors applied in the Spraque-Dawley rats resulted in a reduction of BDNF mRNA in hippocampus and an induction of morphological and functional changes in the spino-dendritic system [155]. A decrease in the BDNF mRNA expression in hippocampus was also reported after application of a chronic, unpredictable, mild stress, in form of the open field test, for 8 to 28 days, in 2-month-old Spraque-Dawley rats [142]. These results confirm the possibility of using many types of mild stressors in modelling responses to harmless stimuli present in the natural environment of rodents. This gives the possibility of their use in studies on behavioural responses in animals at different ages and under influence of stimuli of various nature and duration.

Immobilisation. An immobilisation stress (IM) induces the BDNF expression [95]. It is responsible for the structural plasticity changes in hippocampus and amygdala, i.e. areas involved in development of cognitive and affective symptoms of stress [136]. The effects of an acute and chronic immobilisation stress on the level of BDNF expression were observed in the 8-week-old Wistar rats [84]. A day following 2 h immobilisation, the BDNF level increased in neurons of the basolateral amygdala (BLA), although it did not change in the CA3 sector of hippocampus. However, after a long-term (8 h) immobilisation, the BDNF level increased in the BLA and decreased in CA3. Additionally, the BLA neurons hypertrophy and the hippocampal CA3 neuronal atrophy were observed. In line with these results, Ueyama et al. [161] reported a reduction of the BDNF mRNA level after 8 h immobilisation stress in hippocampus of the 6-week-old male Wistar rats.

Forced swimming. A forced swimming (FS) stress is a type of stimulus experienced by rats in their natural environment [40]. Chronic FS combines psychological stimuli of novelty and an aquatic environment with a physical stimulus in the form of the forced motor activity [42]. In the 2-month-old juvenile Sprague-Dawley rats, a short-term (10 min) FS test in cold water caused a rapid increase in the BDNF mRNA and BDNF protein concentration in hippocampus, already 15 min after the end of stimulation. However, after chronic FS (10 min/21 days in 25°C water), the BDNF mRNA and protein expression in hippocampus decreased after 60 min from its termination [143]. Badowska-Szalewska et al. [13] assessed the effects of the long-term FS (15 min/21 days in 22°C water) on the density of BDNF-containing neurons in the pyramidal layer of the hippocampal CA1, CA3 sectors and the granular neurons of DG, as well as in SON and PVN nuclei of the hypothalamus, in juvenile (P28) and middle-aged (P360) Wistar rats [13, 53]. They reported a decrease in the density of the BDNF-ir neurons in CA1 and DG and in the nuclei of the hypothalamus.

It was concluded that the type of the stressor determined the changes in number of the BDNF-ir cells in juvenile rats. The different density of BDNF-ir in juvenile versus middle-aged rats can be explained by age-related changes in the demand for BDNF [13, 53]. Exposure to a mild long-term stress early in life is believed to attenuate the HPA inhibition, which may lead to an increase in the glucocorticoid levels [74, 99], as well as to a decrease in BDNF expression. Importantly, this may result in an impairment of the neuroplasticity and of the normal brain development at subsequent stages of ontogenesis. Consequently, this may also initiate formation of improper behavioural reactions during subsequent life periods.

High light-open field stress. The high light-open field (HL-OF) test reflects conditions in which the rats actively explore a new environment [46, 53]. The aversive stimulus in the form of a bright light can trigger emotional reactions and anxiety behaviours [64, 118]. However, a chronic exposure to HL-OF (15 min/21 day cycle), changed the density of the BDNF-ir neurons neither in the large-cell (PVm) and small-cell (PVp) part of the PVN, nor in the SON of the hypothalamus, in the Wistar rats in P28 [53]. This can be explained by an adaptation to the particular types of stressors [46]. According to some authors, it may be the result of the BDNF-dependent plasticity within particular brain structures, and it suggests a protective role of BDNF in the neurons of these areas [146].

Adulthood

Reaching a complete morphological and functional maturity the animal's activity and behaviour becomes characteristic for the adult representatives of particular species. This is related to the intensification of its interaction with the surrounding environment and, thus, an increased susceptibility to the stressful stimuli. As a result, in stress studies on adult animals a wide range of tests approximating the impact of stressors occurring in the natural environment is used [4, 6, 58, 108, 119]. Adulthood is characterised by the HPA functional efficiency [6, 58]. Most of studies investigating the role of BDNF in hypothalamus and/ /or other structures involved in the HPA regulation in response to stress are performed in the adult rats.

It is worth mentioning that neurogenesis in the adult brain occurs in two main areas, the subventricular zone of the lateral ventricles and the subgranular zone of the dentate gyrus of the hippocampus [39]. Especially the latter area of proliferation is important for the proper shaping of processes related to spatial and contextual memory of stress-related events and reactions [49, 50, 101]. The effect of stressful stimuli is related to the reduction of neurogenesis and, consequently, it is also associated with a decrease in BDNF expression [47]. A further consequence of these processes is the disturbance of structural and functional plasticity in the hippocampus.

Restraint and immobilisation. Restraint and immobilisation stresses (RS and IM, respectively) combine the effects of psychological and physical stimuli [32, 147]. This combination of stressors occurs sporadically in the natural environment of rats. As expected, a complete immobilisation of an animal is more aversive than restricting its movements. Most studies on the effect of such stimulation on BDNF expression were focused on hippocampus. However, the results of studies investigating the BDNF mRNA and its protein level after stimulation by the acute or chronic RS or IM are unequivocal and inconclusive. Both acute (6 h) RS and chronic RS (lasting from 1 to 3 weeks) induced a marked reduction in the BDNF mRNA levels in hippocampus of the Sprague-Dawley rats [107] and C57BL/6J mice, and BALB/cJ mice [3]. Similarly, a decrease in BDNF level in the hippocampal pyramidal cell layer and in the granular layer of the DG was reported after 1 day in the 4 h/3days RS rat model [172]. In line with the previous results, Xu et al. [171] observed a decrease in BDNF expression and the neuronal proliferation in hippocampus after long-term (6 h/14 days) RS. Other authors showed that although the chronic RS leads to decrease in BDNF and the BDNF mRNA expression in the hippocampal CA3, it could initiate its increase in the BLA [19]. A significant decrease in the BDNF level after a single 3 h RS was also observed in the prefrontal cortex (PFC) of the Wistar rats [120]. However, Naert et al. [108] showed an increase in BDNF levels after chronic RS (3 h/21 days), not only in the hippocampus but also in the hypothalamus and pituitary gland in the Sprague-Dawley rats. Interestingly, there are also reports stating that an acute (3 h) and chronic (6 h/14 days) RS did not induce any changes in the BDNF mRNA levels or BDNF protein concentration in hippocampus and amygdala [121, 127].

Immobilisation for 2 h caused a decrease in the level of BDNF mRNA in hippocampus in the Sprague-Dawley rats, immediately after the end of the experiment [176]. Chronic IM reduced the BDNF levels and BDNF immunoreactivity in the hippocampal pyramidal neurons, as well as in the DG granular neurons, in the Sprague-Dawley rats [173]. A comparison of the effect of 7-day vs. 21-day IM on the BDNF level in the C57BL/6J mice showed that after 21 days of this type of stress the BDNF level in hippocampus was lower than in the 7-day group [25].

The available data suggest an importance of the time of BDNF concentration measurement after performing the experiment, stressing the possibility of its fluctuations. Marmigère et al. [95] have shown that after a short-term (15 or 60 min) IM the BDNF mRNA level increased rapidly and then decreased approximately 2–3 h after the stressor termination. Similarly, after 180 min exposure to IM, BDNF expression initially increased, then decreased to the level observed in the control group [95]. Moreover, it was also revealed that IM as a stressor can transiently increase BDNF expression, despite high levels of stress hormones [95]. These observations suggest that the rapid changes in BDNF concentration in hippocampus may be a part of the strong compensatory response triggered to maintain homeostasis, or suggest induction of the neuronal plasticity mechanisms triggered in animals when confronted with new stimuli.

Interesting effects on BDNF expression were observed in experiments with combination of stress and learning stimuli. In response to both acute and repeated IM stress, BDNF expression decreased in hippocampus [133]. However, animals additionally subjected to learning showed an increased expression of BDNF in comparison to those which were only stressed. Thus, learning and stress have the opposite effect on BDNF level and the effect of learning, leading to an increase in BDNF, is outweighing the stress effect. This observation may be of important practical significance for modifying animals' behaviour.

An analysis of impact of the IM on the level of the BDNF mRNA in various brain areas showed significant differences between them. One-time 2 h or 8 h immobilisation, as well as chronic (2 h/day, for 7 days) immobilisation caused a decrease in the BDNF mRNA level not only in the hippocampal sectors, DG but also in hypothalamus and several cortical areas of the Sprague-Dawley and Fischer 344/N rats [149–151]. On the other hand, a short-term (15 min) IM caused a significant increase in the BDNF mRNA and protein expression in PVN and SON in hypothalamus [119]. Numerous studies showed that both short-term (2 h) and longer, repeated (7 days/2× daily) immobilisation increased the level of BDNF mRNA in the PVN, lateral part of the hypothalamus and pituitary in the Sprague-Dawley and Fischer 344/N rats [149–151]. Fluctuations in the BDNF content, resulting from changes in the expression of genes regulated by the concentration of stress hormones, may contribute to alterations in a density of dendritic spines in structures of the limbic system [19]. A consequence of decreased BDNF expression may be structural changes and neuronal loss [148].

The diversity of the presented results, and a high dependence of BDNF level on duration of exposure to the stressor and its type, suggests the existence of complex regulatory mechanisms responsible for expression of BDNF mRNA and its protein in the CNS. One can expect significant differences in these mechanisms among various brain areas.

Social stress, social defeat stress. Pattern of BDNF expression in rodents, resulting from changing social hierarchy and living conditions modified in experiments, were the subject of previous studies [10, 134, 138]. Modified housing conditions and social hierarchy in the experimental animals (social stress) are natural stressors that can influence physiological parameters and behaviour [134]. A short-term (10 min) social stress in mice led to a decrease in BDNF mRNA content, 24 h after stimulation, in the CA1, CA3 sectors of hippocampus, DG, BLA, piriform cortex, thalamus and hypothalamus [116]. The BDNF mRNA levels normalised after approximately 5 days. According to the authors, the BDNF changes may be responsible for reactions relaying on inhibition of the territory defence behaviours and anxiety.

Changes in housing conditions and social stress are long-term acting stressful factors [10, 138]. Neither 7 nor 21 days of the social stress, based on exchanging animals in cages, influenced the BDNF level in hippocampus in C57BL/6J mice [25]. An exposure of the NMRI mice to 4 weeks of an intermittent stressor (by placing animals in a new cage or social hazard conditions) increased the BDNF expression in hippocampus among the socially endangered animals, but not in the mice placed in a new cage [113]. This can be explained by the role of BDNF in supporting mechanisms promoting behaviour related to defence of territory and offspring.

Other interesting observations come from studies conducted in a model which mimics conditions of the "isolation syndrome" and is based on depriving animals of social stimuli by placing them individually in cages [163]. The assessment of BDNF levels in hippocampus, frontal cortex, hypothalamus, striatum and midbrain in C57BL/6J mice subjected to long-term social stress or social deprivation showed significant differences compared to the group with a stable social structure [20]. In the group of animals subjected to the social deprivation, an increased activity of the HPA and a lower level of BDNF were demonstrated in the examined brain areas, in comparison to animals from the group with the stable social structure. Thus, the chronic social deprivation, as opposed to the social instability, has been found to lead to emotional disturbance and neuroendocrine activation, combined with decreased BDNF levels [20]. In order to evaluate the effect of a long-term, 8 weeks partial social isolation on BDNF changes in hippocampus, the concentration of this neurotrophic factor was measured in the Sprague-Dawley rats placed in cages either single or in pairs [134]. Lower concentrations of the BDNF protein were present in the animals living in isolation. Reduction in the level of BDNF mRNA and protein after the chronic social isolation (social defeat stress) in rodents' hippocampus has also been reported by other authors [156, 177]. A recent study by Viana Borges et al. [167] presenting a comparison of the effects of a social isolation (breeding in isolation) and a social support (breeding in pairs) on the level of BDNF in hippocampus of the Wistar rats additionally subjected to chronic unpredictable stress (CUS) confirmed the above-mentioned results. Furthermore, in animals subjected to isolation the decrease in the BDNF level in hippocampus was accompanied by the long-term memory impairment [167]. Therefore, higher expression of BDNF in animals living in social groups indicates the important role of this factor in stimulation of the mechanisms developing social relationships and maintaining mental health [35]. It has also been suggested that a social support may contribute to protecting against some effects of the stress-induced epigenetic modulation of BDNF genes [167]. This may be manifested by the preservation of cognitive functions. However, the detailed explanation of these regulatory mechanisms requires further research.

Predator odour. To assess reactions caused by fear of predators (predator scent stress), a test involving exposure of rodents to a smell of predator urine has been developed [80, 81]. After a single, short-term (10 min) exposure to the stress factor, the level of BDNF mRNA in the CA1 sector of hippocampus was assessed 7 days after the exposure. Cat smell increased anxiety behaviour, which correlated with the long-term decline in BDNF mRNA [81]. It has been suggested that the action of the aforementioned stressor, via changes in BDNF expression, may lead to remodelling of the neuronal connections in hippocampus [81].

Chronic mild stress. In order to simulate unpredictable situations that may occur in the rodents environment, a model of chronic mild stress (CMS) was developed [170]. This model reflects many types of stimuli inducing anxiety behaviour. However, occasionally changes in physiological parameters and behavioural responses after its use are ambiguous. In hippocampus of the rats exposed to CMS an increase in the BDNF mRNA expression was reported, not a decrease, as it could be expected, despite a behavioural response resembling depression [85]. Other authors have reported reduced [78] or increased anxiety [77] after using this stress model. It has been suggested that this type of stressor affects emotional behaviour and, indirectly, also the activation of the HPA and the level of BDNF [110]. The substantial discrepancies in the results may be due to the interplay of different neurobiological variables. This means that various signalling pathways responsible for regulation of the BDNF expression may be activated, adapting the brain to different situational contexts and emotional states.

Osmotic stress. The sensitivity of the hypothalamic nuclei to the osmotic stimuli was the basis for elaboration of a test which is useful for detection of the BDNF protein and mRNA level changes [4, 6, 28]. Three and 4.5 h after intraperitoneal administration of 3 mL of hypertonic 1.35% NaCl solution, an increase in the BDNF mRNA and BDNF protein concentration in the PVN and SON was reported in the Sprague-Dawley and Wistar rats [4, 6, 28]. The obtained results suggest the existence of a mechanism regulating the BDNF content, associated with sensitive to the osmotic stimuli areas located in hypothalamus.

Forced swimming. There is a documented evidence that the FS is responsible for inducing compensatory homeostatic mechanisms to prevent or reduce cytokine activation during a stress response [115, 117]. Although mechanisms of such reactions are not completely understood, there are premises indicating that neurotransmitter systems (e.g. glutamatergic or monoaminergic) as well as the HPA axis are involved [115, 117]. Interestingly, studies showed that both a single (20 min) and a chronic (20 min/21 day) FS episodes did not cause changes in the density of BDNF-ir neurons in the PVN and SON nuclei in hypothalamus of the adult Wistar rats [12]. One can assume that the relatively low harmfulness of the applied stimulus could have prevented changes in the density of BDNF-ir neurons.

High light-open field stress. HL-OF is a relatively strong stressor which may initiate structural and functional changes in several brain areas [64, 118]. The numerical density of BDNF-ir neurons in the PVN and SON was analysed in the Wistar rats undergoing HL-OF [12]. After a single 20 min exposure to HL-OF, an increase in BDNF-ir in the SON was observed, which most likely was related to an increase in the level of neurohormones (e.g. AVP), synthesized depending on the HPA axis activity. However, the long-term 21-day stimulation with HL-OF did not affect the density of BDNF-ir neurons. One can presume that the activity of the HPA was not maintained at a sufficiently high level for such a long period of time or that the experimental animals adapted to this type of stressor.

Aging

It is commonly accepted that animal's response to stress changes with age [93, 115]. Aging is a life period related with apparent changes of many functions of the limbic system and the neuroendocrine activity [112, 115]. One of the consequences of aging is an increased lability of the HPA, which can lead to changes in its activation [22, 103, 115]. This is due to an impairment of the controlling the stress response mechanisms regulating the HPA activity which involve several brain structures, among which the most important are hypothalamus, hippocampus, and amygdala [115, 144, 146]. All this limits the ability to response adequately to stress [112, 115]. The dysregulation of the system controlling stress response is manifested by a decreased inhibition of the HPA activity and termination of the stress response [57, 115].

An impairment of the negative feedback regulatory mechanisms of the HPA significantly modifies the action of glucocorticoids and their receptors [115]. It also influences the stress-dependent synthesis and secretion of the other neurohormones such as catecholamines [14, 93, 129], and increases the neuronal sensitivity to apoptosis [30, 131]. Importantly, during aging a stronger stimulus is required to induce a stress response, which in some cases may even increase the intensity of the reaction [112]. Finally, there are compensatory mechanisms activated during aging that enable adaptation to changing environmental conditions [56]. Activation of systems involved in the stress response was observed even in the absence of the stressor, which could be regarded as a state of readiness [56].

Immobilisation and chronic mild stress. Data about changes in BDNF expression in aging animals under influence of a mild stressor is still incomplete. Immobilisation reduced BDNF expression in hippocampus in older rodents [149]. This effect was present both after short- and long-term immobilisation. In the 24 month-old Fischer 344/N rats, a decrease in the BDNF mRNA in the DG was observed immediately after 2 h immobilisation [149]. The chronic immobilisation (2 h/7 days) reduced the BDNF mRNA in hippocampus in old (24 month) male Fischer 344/N rats [148].

A CUS model has been used to evaluate changes in BDNF expression in hippocampus [88, 142]. After an exposure of different duration (up to 28 days) on chronic unpredictable mild stress, a decrease in the BDNF mRNA expression in hippocampus was reported in the 22-month-old Sprague-Dawley rats [142]. Similarly, a 3-week exposure to CUS induced a decreased expression of BDNF in the hippocampal CA3 and DG in the 15-month-old Wistars [88]. A mild stress-induced decrease in BDNF expression in the hippocampal neurons is of a particular importance due to enhancement of changes in cognitive functions, learning, and memory during aging [1]. They could be a result of the impaired long-term synaptic enhancement observed at this stage of ontogenesis [8, 75]. Less effective synaptic transmission prevents repeated neuronal stimulation which, in turn, may result in receptor desensitization and finally, prevents neuronal damage [154]. This process can be regarded as one of the positive compensatory mechanisms preventing structural and functional damage in the CNS during aging.

Forced swimming. The FS is useful for assessing changes in BDNF expression during aging. A short-term stressor of 10 min swimming in cold water at 4°C induced a rapid increase in BDNF and the BDNF mRNA in hippocampus in the 22-month-old Sprague-Dawley rats, already 15 min after its completion [143]. A long-term FS of 10 min for 21 days in 25°C water reduced expression of the BDNF mRNA and protein after 60 min [143]. FS stimulation was also used to assess changes in the density of BDNF-ir neurons of the hippocampal pyramidal cell layer of CA1, CA3, and granular neurons in DG, and in the PVN and

SON nuclei of hypothalamus in P360 and P720 Wistar rats [11–13, 53]. After 20 min FS, an increase in the density of BDNF-ir neurons in CA2 and CA3 sectors of hippocampus was reported in the aged animals (P720) [11]. However, no difference was observed in the density of BDNF-ir neurons after exposure to chronic FS of 20 min/21 days in P360 and P720 age groups compared to the control groups [11–13, 53]. The explanation of these results may provide a hypothesis assuming that the increase in expression of neurotrophins, including BDNF, after a short-term stress may be associated with the consolidation of information about a harmless event in order to prepare the future response to a new stressful stimulus [95]. The lack of increase in BDNF expression after prolonged stimulation with a harmless stimulus can be also explained by habituation.

High light-open field stress. An effect of stimulation with the HL-OF stressor on the density of BDNF-ir neurons was assessed in the pyramidal cell layer in the CA1, CA2, CA3 sectors of hippocampus, granule cells layer in the DG, and in the PVN and SON nuclei of hypothalamus in the Wistar rats [11, 12, 53]. While after exposure to an acute 20 min stress the density of BDNF-ir neurons increased in CA1–CA3 regions of hippocampus, it decreased in the PVN in P720 [11, 12]. However, a chronic 21-day HL-OF stimulation did not change the density of BDNF-ir neurons in the examined brain structures in both P360 and P720 [11, 12, 53].

The increase in the density of BDNF-ir neurons after a single HL-OF stressor stimulation can be explained by the change in the HPA activation leading to the raised release of neurohormones. Interestingly, the increase in the BDNF-ir density of pyramidal neurons after the short-term stressor exposure may stimulate memory in the aged animals [135]. The above-mentioned "state of readiness" or alert, may be responsible for prevention of the reduction in BDNF level after the chronic stress in the older animals [56]. The repeated exposure to the same stressor may also cause habituation [88].

CONCLUSIONS

Although almost each stressor is believed to increase the activity of the HPA, the response of neurons to individual stressors varies considerably. This may result from the number of involved neurotransmitters, neurohormones and neurotrophic factors, including BDNF. Based on the presented data, one can conclude that the effect of stressful stimuli on BDNF expression in the various brain areas at the specific stages of the ontogenetic development depends on several factors, such as species and genotypic characteristics of experimental animals, and their individual resistance to stress. In addition, the psychophysical condition seems to be of great importance, as it determines the way of coping with the stressful situations. Important factors to consider that may affect the results of research on stress mechanisms are: a type of stressor used, an experimental model of stress, an analysed brain area, the precision of the BDNF detection method, time of assessment of the neurotrophin level after stress stimulation, the tested form of neurotrophin (precursor or mature form of BDNF) and, finally, the BDNF mRNA level. The presented data, on the one hand, indicate participation of BDNF in response to a wide range of stressors. On the other hand, they point to a different dynamics of changes in this neurotrophin level, depending on the type of stressor and the stage of ontogenetic development. Results of the studies using various experimental stress models indicate the multidirectional effect of BDNF on shaping the response to stress. Further studies are warranted to better understand the role of this neutrophin in the CNS during a stress response, and to consider its potential use in designing new, effective strategies of stress prevention or treatment.

Funding

This research was supported by funds provided by the Polish Ministry of Science and Higher Education (ST-11).

Conflict of interest: None declared

REFERENCES

1. Adlard PA, Engesser-Cesar C, Cotman CW. Mild stress facilitates learning and exercise improves retention in aged mice. Exp Gerontol. 2011; 46(1): 53–59, doi: 10.1016/j.exger.2010.10.001, indexed in Pubmed: 20951791.
2. Aisa B, Tordera R, Lasheras B, et al. Cognitive impairment associated to HPA axis hyperactivity after maternal separation in rats. Psychoneuroendocrinology. 2007; 32(3): 256–266, doi: 10.1016/j.psyneuen.2006.12.013.
3. Alfonso J, Frick LR, Silberman DM, et al. Regulation of hippocampal gene expression is conserved in two species subjected to different stressors and antidepressant treatments. Biol Psychiatry. 2006; 59(3): 244–251, doi: 10.1016/j.biopsych.2005.06.036, indexed in Pubmed: 16140276.
4. Aliaga E, Arancibia S, Givalois L, et al. Osmotic stress increases brain-derived neurotrophic factor messenger RNA expression in the hypothalamic supraoptic nucleus

with differential regulation of its transcripts. Relation to arginine–vasopressin content. Neuroscience. 2002; 112(4): 841–850, doi: 10.1016/s0306-4522(02)00128-8.
5. Allen S, Watson J, Shoemark D, et al. GDNF, NGF and BDNF as therapeutic options for neurodegeneration. Pharmacol Ther. 2013; 138(2): 155–175, doi: 10.1016/j.pharmthera.2013.01.004.
6. Arancibia S, Lecomte A, Silhol M, et al. In vivo brain-derived neurotrophic factor release and tyrosine kinase B receptor expression in the supraoptic nucleus after osmotic stress stimulus in rats. Neuroscience. 2007; 146(2): 864–873, doi: 10.1016/j.neuroscience.2007.01.057, indexed in Pubmed: 17346893.
7. Arancibia S, Silhol M, Moulière F, et al. Protective effect of BDNF against beta-amyloid induced neurotoxicity in vitro and in vivo in rats. Neurobiol Dis. 2008; 31(3): 316–326, doi: 10.1016/j.nbd.2008.05.012S0969-9961(08)00099-5, indexed in Pubmed: 18585459.
8. Artola A, von Frijtag JC, Fermont PCJ, et al. Long-lasting modulation of the induction of LTD and LTP in rat hippocampal CA1 by behavioural stress and environmental enrichment. Eur J Neurosci. 2006; 23(1): 261–272, doi: 10.1111/j.1460-9568.2005.04552.x, indexed in Pubmed: 16420435.
9. Avital A, Richter-Levin G. Exposure to juvenile stress exacerbates the behavioural consequences of exposure to stress in the adult rat. Int J Neuropsychopharmacol. 2005; 8(2): 163–173, doi: 10.1017/S1461145704004808, indexed in Pubmed: 15546500.
10. Avitsur R, Stark J, Dhabhar F, et al. Social disruption-induced glucocorticoid resistance: kinetics and site specificity. J Neuroimmunol. 2002; 124(1-2): 54–61, doi: 10.1016/s0165-5728(02)00010-3, indexed in Pubmed: 11958822.
11. BadowskaSzalewska E, Ludkiewicz B, Krawczyk R, et al. Comparison of the influence of two models of mild stress on hippocampal brainderived neurotrophin factor (BDNF) immunoreactivity in old age rats. Acta Neurobiologiae Experimentalis. 2017; 77(1): 68–76, doi: 10.21307/ane-2017-037, indexed in Pubmed: 28379217.
12. Badowska-Szalewska E, Ludkiewicz B, Krawczyk R, et al. Exposure to mild stress and brain derived neurotrophin factor (BDNF) immunoreactivity in the hypothalamic paraventricular (PVN) and supraoptic (SON) nuclei: Comparison between aged and adult rats. J Chem Neuroanat. 2016; 78: 57–64, doi: 10.1016/j.jchemneu.2016.08.007, indexed in Pubmed: 27565677.
13. Badowska-Szalewska E, Spodnik E, Klejbor I, et al. Effects of chronic forced swim stress on hippocampal brain-derived neutrophic factor (BDNF) and its receptor (TrkB) immunoreactive cells in juvenile and aged rats. Acta Neurobiol Exp. 2010; 70(4): 370–381, indexed in Pubmed: 21196945.
14. Bahtiyar S, Karaca KG, Henckens M, et al. Norepinephrine and glucocorticoid effects on the brain mechanisms underlying memory accuracy and generalization. Mol Cell Neurosci. 2020; 108: 103537, doi: 10.1016/j.mcn.2020.103537, indexed in Pubmed: 32805389.
15. Bale TL, Vale WW. CRF and CRF receptors: role in stress responsivity and other behaviors. Annu Rev Pharmacol Toxicol. 2004; 44: 525–557, doi: 10.1146/annurev.pharmtox.44.101802.121410, indexed in Pubmed: 14744257.
16. Barbany G, Persson H. Regulation of neurotrophin mRNA expression in the rat brain by glucocorticoids. Eur J Neurosci. 1992; 4(5): 396–403, doi: 10.1111/j.1460-9568.1992.tb00888.x, indexed in Pubmed: 12106347.
17. Barrientos RM, Sprunger DB, Campeau S, et al. Brain-derived neurotrophic factor mRNA downregulation produced by social isolation is blocked by intrahippocampal interleukin-1 receptor antagonist. Neuroscience. 2003; 121(4): 847–853, doi: 10.1016/s0306-4522(03)00564-5, indexed in Pubmed: 14580934.
18. Bazak N, Kozlovsky N, Kaplan Z, et al. Pre-pubertal stress exposure affects adult behavioral response in association with changes in circulating corticosterone and brain-derived neurotrophic factor. Psychoneuroendocrinology. 2009; 34(6): 844–858, doi: 10.1016/j.psyneuen.2008.12.018, indexed in Pubmed: 19181453.
19. Bennett MR, Lagopoulos J. Stress and trauma: BDNF control of dendritic-spine formation and regression. Prog Neurobiol. 2014; 112: 80–99, doi: 10.1016/j.pneurobio.2013.10.005, indexed in Pubmed: 24211850.
20. Berry A, Bellisario V, Capoccia S, et al. Social deprivation stress is a triggering factor for the emergence of anxiety- and depression-like behaviours and leads to reduced brain BDNF levels in C57BL/6J mice. Psychoneuroendocrinology. 2012; 37(6): 762–772, doi: 10.1016/j.psyneuen.2011.09.007, indexed in Pubmed: 21974975.
21. Biggio F, Pisu MG, Garau A, et al. Maternal separation attenuates the effect of adolescent social isolation on HPA axis responsiveness in adult rats. Eur Neuropsychopharmacol. 2014; 24(7): 1152–1161, doi: 10.1016/j.euroneuro.2014.03.009.
22. Boguszewski P, Zagrodzka J. Emotional changes related to age in rats: a behavioral analysis. Behav Brain Res. 2002; 133(2): 323–332, doi: 10.1016/s0166-4328(02)00018-9, indexed in Pubmed: 12110466.
23. Brunson KL, Khan N, Eghbal-Ahmadi M, et al. Corticotropin (ACTH) acts directly on amygdala neurons to down-regulate corticotropin-releasing hormone gene expression. Ann Neurol. 2001; 49(3): 304–312, indexed in Pubmed: 11261504.
24. Caldji C, Diorio J, Meaney M. Variations in maternal care in infancy regulate the development of stress reactivity. Biol Psychiatry. 2000; 48(12): 1164–1174, doi: 10.1016/s0006-3223(00)01084-2.
25. Capoccia S, Berry A, Bellisario V, et al. Quality and timing of stressors differentially impact on brain plasticity and neuroendocrine-immune function in mice. Neural Plast. 2013; 2013(971817), doi: 10.1155/2013/971817, indexed in Pubmed: 23606988.
26. Carrasco G, Van de Kar LD. Neuroendocrine pharmacology of stress. Eur J Pharmacol. 2003; 463(1-3): 235–272, doi: 10.1016/s0014-2999(03)01285-8, indexed in Pubmed: 12600714.
27. Castrén E, Kojima M. Brain-derived neurotrophic factor in mood disorders and antidepressant treatments. Neurobiol Dis. 2017; 97(Pt B): 119–126, doi: 10.1016/j.nbd.2016.07.010, indexed in Pubmed: 27425886.
28. Castren E, Thoenen H, Lindholm D. Brain-derived neurotrophic factor messenger RNA is expressed in the septum, hypothalamus and in adrenergic brain stem nuclei of adult rat brain and is increased by osmotic stimulation in the paraventricular nucleus. Neuroscience. 1995; 64(1): 71–80, doi: 10.1016/0306-4522(94)00386-j, indexed in Pubmed: 7708216.
29. Chen M, He G, Li Q. Maternal deprivation promotes hippocampal neuronal apoptosis via ERK1/2 signaling.

Front Biosci (Landmark Ed). 2018; 23: 1923–1932, doi: 10.2741/4681, indexed in Pubmed: 29772537.
30. Chen TT, Maevsky EI, Uchitel ML. Maintenance of homeostasis in the aging hypothalamus: the central and peripheral roles of succinate. Front Endocrinol (Lausanne). 2015; 6: 7, doi: 10.3389/fendo.2015.00007, indexed in Pubmed: 25699017.
31. Cheng A, Wang S, Cai J, et al. Nitric oxide acts in a positive feedback loop with BDNF to regulate neural progenitor cell proliferation and differentiation in the mammalian brain. Dev Biol. 2003; 258(2): 319–333, doi: 10.1016/s0012-1606(03)00120-9, indexed in Pubmed: 12798291.
32. Chiba S, Numakawa T, Ninomiya M, et al. Chronic restraint stress causes anxiety- and depression-like behaviors, downregulates glucocorticoid receptor expression, and attenuates glutamate release induced by brain-derived neurotrophic factor in the prefrontal cortex. Prog Neuropsychopharmacol Biol Psychiatry. 2012; 39(1): 112–119, doi: 10.1016/j.pnpbp.2012.05.018, indexed in Pubmed: 22664354.
33. Choy KH, de Visser Y, Nichols NR, et al. Combined neonatal stress and young-adult glucocorticoid stimulation in rats reduce BDNF expression in hippocampus: effects on learning and memory. Hippocampus. 2008; 18(7): 655–667, doi: 10.1002/hipo.20425, indexed in Pubmed: 18398848.
34. Chung EKY, Bian ZX, Xu HX, et al. Neonatal maternal separation increases brain-derived neurotrophic factor and tyrosine kinase receptor B expression in the descending pain modulatory system. Neurosignals. 2009; 17(3): 213–221, doi: 10.1159/000224631, indexed in Pubmed: 19546592.
35. Cirulli F, Berry A, Bonsignore LT, et al. Early life influences on emotional reactivity: evidence that social enrichment has greater effects than handling on anxiety-like behaviors, neuroendocrine responses to stress and central BDNF levels. Neurosci Biobehav Rev. 2010; 34(6): 808–820, doi: 10.1016/j.neubiorev.2010.02.008, indexed in Pubmed: 20171244.
36. Cohen H, Kaplan Z, Matar MA, et al. Long-lasting behavioral effects of juvenile trauma in an animal model of PTSD associated with a failure of the autonomic nervous system to recover. Eur Neuropsychopharmacol. 2007; 17(6-7): 464–477, doi: 10.1016/j.euroneuro.2006.11.003, indexed in Pubmed: 17196373.
37. Cowansage KK, LeDoux JE, Monfils MH. Brain-derived neurotrophic factor: a dynamic gatekeeper of neural plasticity. Curr Mol Pharmacol. 2010; 3(1): 12–29, do i: 10.2174/1874467211003010012, indexed in Pubmed: 20030625.
38. Cunha C, Brambilla R, Thomas KL. A simple role for BDNF in learning and memory? Front Mol Neurosci. 2010; 3: 1, doi: 10.3389/neuro.02.001.2010, indexed in Pubmed: 20162032.
39. Abdissa D, Hamba N, Gerbi A. Review Article on adult neurogenesis in humans. Translational Research in Anatomy. 2020; 20: 100074, doi: 10.1016/j.tria.2020.100074.
40. Dal-Zotto S, Martı O, Armario A. Influence of single or repeated experience of rats with forced swimming on behavioural and physiological responses to the stressor. Beh Brain Res. 2000; 114(1-2): 175–181, doi: 10.1016/s0166-4328(00)00220-5, indexed in Pubmed: 10996058.
41. Daskalakis N, Kloet ED, Yehuda R, et al. Early life stress effects on glucocorticoid-BDNF interplay in the hippocampus. Front Mol Neurosci. 2015; 8, doi: 10.3389/fnmol.2015.00068, indexed in Pubmed: 26635521.
42. Dayas CV, Buller KM, Crane JW, et al. Stressor categorization: acute physical and psychological stressors elicit distinctive recruitment patterns in the amygdala and in medullary noradrenergic cell groups. Eur J Neurosci. 2001; 14(7): 1143–1152, doi: 10.1046/j.0953-816x.2001.01733.x, indexed in Pubmed: 11683906.
43. de Kloet ER, Sibug RM, Helmerhost FM, et al. Stress, genes and the mechanism of programming the brain for later life. Neurosci Biobehav Rev. 2005; 29(2): 271–281, doi: 10.1016/j.neubiorev.2004.10.008, indexed in Pubmed: 15811498.
44. Dent G, Choi DC, Herman JP, et al. GABAergic circuits and the stress hyporesponsive period in the rat: ontogeny of glutamic acid decarboxylase (GAD) 67 mRNA expression in limbic-hypothalamic stress pathways. Brain Res. 2007; 1138: 1–9, doi: 10.1016/j.brainres.2006.04.082, indexed in Pubmed: 17276416.
45. Dimatelis JJ, Russell VA, Stein DJ, et al. Methamphetamine reversed maternal separation-induced decrease in nerve growth factor in the ventral hippocampus. Metab Brain Dis. 2014; 29(2): 433–439, doi: 10.1007/s11011-014-9481-z, indexed in Pubmed: 24407463.
46. Dubovicky M, Jezova D. Effect of chronic emotional stress on habituation processes in open field in adult rats. Ann N Y Acad Sci. 2004; 1018: 199–206, doi: 10.1196/annals.1296.023, indexed in Pubmed: 15240369.
47. Duman RS, Malberg J, Nakagawa S. Regulation of adult neurogenesis by psychotropic drugs and stress. J Pharmacol Exp Ther. 2001; 299(2): 401–407, indexed in Pubmed: 11602648.
48. Dwivedi Y, Rizavi HS, Pandey GN. Antidepressants reverse corticosterone-mediated decrease in brain-derived neurotrophic factor expression: differential regulation of specific exons by antidepressants and corticosterone. Neuroscience. 2006; 139(3): 1017–1029, doi: 10.1016/j.neuroscience.2005.12.058, indexed in Pubmed: 16500030.
49. Eisch A. Adult neurogenesis: implications for psychiatry. Prog Brain Res. 2002: 315–342, doi: 10.1016/s0079-6123(02)38085-3, indexed in Pubmed: 12432777.
50. Eisch AJ, Barrot M, Schad CA, et al. Opiates inhibit neurogenesis in the adult rat hippocampus. Proc Natl Acad Sci U S A. 2000; 97(13): 7579–7584, doi: 10.1073/pnas.120552597, indexed in Pubmed: 10840056.
51. Elliott E, Ezra-Nevo G, Regev L, et al. Resilience to social stress coincides with functional DNA methylation of the Crf gene in adult mice. Nature Neuroscience. 2010; 13(11): 1351–1353, doi: 10.1038/nn.2642, indexed in Pubmed: 20890295.
52. Engelmann M, Ludwig M. The activity of the hypothalamo-neurohypophysial system in response to acute stressor exposure: neuroendocrine and electrophysiological observations. Stress. 2004; 7(2): 91–96, doi: 10.1080/10253890410001677240, indexed in Pubmed: 15512852.
53. Ewa BS, Beata L, Ilona K, et al. Brain derived neurotrophic factor (BDNF) containing neurons in the hypothalamic paraventricular and supraoptic nuclei of juvenile and middle-aged rats after chronic stress. Int J Dev Neurosci. 2012; 30(2): 139–146, doi: 10.1016/j.ijdevneu.2011.12.001, indexed in Pubmed: 22178659.
54. Farrell C, O'Keane V. Epigenetics and the glucocorticoid receptor: A review of the implications in depression.

Psychiatry Res. 2016; 242: 349–356, doi: 10.1016/j.psychres.2016.06.022, indexed in Pubmed: 27344028.
55. Fenoglio KA, Brunson KL, Baram TZ. Hippocampal neuroplasticity induced by early-life stress: functional and molecular aspects. Front Neuroendocrinol. 2006; 27(2): 180–192, doi: 10.1016/j.yfrne.2006.02.001, indexed in Pubmed: 16603235.
56. Frolkis V. Stress-age syndrome. Mech Ageing Dev. 1993; 69(1-2): 93–107, doi: 10.1016/0047-6374(93)90074-2, indexed in Pubmed: 8104261.
57. Gilad G, Gilad V. Strain, stress, neurodegeneration and longevity. Mech Ageing Dev. 1995; 78(2): 75–83, doi: 10.1016/0047-6374(94)01529-u, indexed in Pubmed: 7596198.
58. Givalois L, Naert G, Rage F, et al. A single brain-derived neurotrophic factor injection modifies hypothalamo-pituitary-adrenocortical axis activity in adult male rats. Mol Cell Neurosci. 2004; 27(3): 280–295, doi: 10.1016/j.mcn.2004.07.002, indexed in Pubmed: 15519243.
59. Goldman L, Winget C, Hollingshead GW, et al. Postweaning development of negative feedback in the pituitary-adrenal system of the rat. Neuroendocrinology. 1973; 12(3): 199–211, doi: 10.1159/000122169, indexed in Pubmed: 4353346.
60. Gray JD, Milner TA, McEwen BS. Dynamic plasticity: the role of glucocorticoids, brain-derived neurotrophic factor and other trophic factors. Neuroscience. 2013; 239: 214–227, doi: 10.1016/j.neuroscience.2012.08.034, indexed in Pubmed: 22922121.
61. Greenberg ME, Xu B, Lu B, et al. New insights in the biology of BDNF synthesis and release: implications in CNS function. J Neurosci. 2009; 29(41): 12764–12767, doi: 10.1523/JNEUROSCI.3566-09.2009, indexed in Pubmed: 19828787.
62. Greisen MH, Altar CA, Bolwing TG, et al. Increased adult hippocampal brain-derived neurotrophic factor and normal levels of neurogenesis in maternal separation rats. J Neurosci Res. 2005; 79(6): 772–778, doi: 10.1002/jnr.20418, indexed in Pubmed: 15690366.
63. Groves JO. Is it time to reassess the BDNF hypothesis of depression? Mol Psychiatry. 2007; 12(12): 1079–1088, doi: 10.1038/sj.mp.4002075, indexed in Pubmed: 17700574.
64. Hale MW, Bouwknecht JA, Spiga F, et al. Exposure to high- and low-light conditions in an open-field test of anxiety increases c-Fos expression in specific subdivisions of the rat basolateral amygdaloid complex. Brain Res Bull. 2006; 71(1-3): 174–182, doi: 10.1016/j.brainresbull.2006.09.001, indexed in Pubmed: 17113944.
65. Heese K, Otten U, Mathivet P, et al. GABAB receptor antagonists elevate both mRNA and protein levels of the neurotrophins nerve growth factor (NGF) and brain-derived neurotrophic factor (BDNF) but not neurotrophin-3 (NT-3) in brain and spinal cord of rats. Neuropharmacology. 2000; 39(3): 449–462, doi: 10.1016/s0028-3908(99)00166-5, indexed in Pubmed: 10698011.
66. Heidbreder CA, Weiss IC, Domeney AM, et al. Behavioral, neurochemical and endocrinological characterization of the early social isolation syndrome. Neuroscience. 2000; 100(4): 749–768, doi: 10.1016/s0306-4522(00)00336-5, indexed in Pubmed: 11036209.
67. Herman JP, Figuieredo H, Mueller NK. Central mechanisms of stress integration: hierarchical circuitry controlling hypothalamo-pituitary-adrenocortical responsiveness. Front Neuroendocrinol. 2003; 24(3): 151–158, doi: 10.1016/j.yfrne.2003.07.001, indexed in Pubmed: 14596810.
68. Herman J, McKlveen J, Ghosal S, et al. Regulation of the hypothalamic pituitary adrenocortical stress response. Compr Physiol. 2016; 6(2): 603–621, doi: 10.1002/cphy.c150015, indexed in Pubmed: 27065163.
69. Herman J, Ostrander M, Mueller N, et al. Limbic system mechanisms of stress regulation: Hypothalamo-pituitary-adrenocortical axis. Prog Neuropsychopharmacol Biol Psychiatry. 2005; 29(8): 1201–1213, doi: 10.1016/j.pnpbp.2005.08.006, indexed in Pubmed: 16271821.
70. Huot R, Plotsky P, Lenox R, et al. Neonatal maternal separation reduces hippocampal mossy fiber density in adult Long Evans rats. Brain Res. 2002; 950(1-2): 52–63, doi: 10.1016/s0006-8993(02)02985-2, indexed in Pubmed: 12231228.
71. Jeanneteau F, Chao MV. Are BDNF and glucocorticoid activities calibrated? Neuroscience. 2013; 239: 173–195, doi: 10.1016/j.neuroscience.2012.09.017, indexed in Pubmed: 23022538.
72. Jeanneteau F, Garabedian MJ, Chao MV. Activation of Trk neurotrophin receptors by glucocorticoids provides a neuroprotective effect. Proc Natl Acad Sci U S A. 2008; 105(12): 4862–4867, doi: 10.1073/pnas.0709102105, indexed in Pubmed: 18347336.
73. Jeanneteau, FD, Lambert WM, Ismaili M, et al. DNF and glucocorticoids regulate corticotrophin-releasing hormone (CRH) homeostasis in the hypothalamus. Proc Natl Acad Sci U S A. 2012; 109(4): 1305–1310, doi: 10.1073/pnas.1114122109, indexed in Pubmed: 22232675.
74. Joëls M, Karst H, Alfarez D, et al. Effects of chronic stress on structure and cell function in rat hippocampus and hypothalamus. Stress. 2004; 7(4): 221–231, doi: 10.1080/10253890500070005, indexed in Pubmed: 16019587.
75. Kim JJ, Diamond DM. The stressed hippocampus, synaptic plasticity and lost memories. Nat Rev Neurosci. 2002; 3(6): 453–462, doi: 10.1038/nrn849, indexed in Pubmed: 12042880.
76. Knipper M, da Penha Berzaghi M, Blöchl A, et al. Positive feedback between acetylcholine and the neurotrophins nerve growth factor and brain-derived neurotrophic factor in the rat hippocampus. Eur J Neurosci. 1994; 6(4): 668–671, doi: 10.1111/j.1460-9568.1994.tb00312.x, indexed in Pubmed: 8025717.
77. Kompagne H, Bárdos G, Szénási G, et al. Chronic mild stress generates clear depressive but ambiguous anxiety-like behaviour in rats. Behav Brain Res. 2008; 193(2): 311–314, doi: 10.1016/j.bbr.2008.06.008, indexed in Pubmed: 18590771.
78. Kopp C, Vogel E, Rettori MC, et al. The effects of melatonin on the behavioural disturbances induced by chronic mild stress in C3H/He mice. Behav Pharmacol. 1999; 10(1): 73–83, doi: 10.1097/00008877-199902000-00007, indexed in Pubmed: 10780304.
79. Kowiański P, Lietzau G, Czuba E, et al. BDNF: A Key Factor with Multipotent Impact on Brain Signaling and Synaptic Plasticity. Cel Mol Neurobiol. 2017; 38(3): 579–593, doi: 10.1007/s10571-017-0510-4, indexed in Pubmed: 28623429.
80. Kozlovsky N, Kaplan Z, Zohar J, et al. Protein synthesis inhibition before or after stress exposure results in divergent

endocrine and BDNF responses disassociated from behavioral responses. Depress Anxiety. 2008; 25(5): E24–E34, doi: 10.1002/da.20366, indexed in Pubmed: 17828750.
81. Kozlovsky N, Matar MA, Kaplan Z, et al. Long-term down-regulation of BDNF mRNA in rat hippocampal CA1 subregion correlates with PTSD-like behavioural stress response. Int J Neuropsychopharmacol. 2007; 10(6): 741–758, doi: 10.1017/S1461145707007560, indexed in Pubmed: 17291374.
82. Krishnan V, Nestler EJ. The molecular neurobiology of depression. Nature. 2008; 455(7215): 894–902, doi: 10.1038/nature07455, indexed in Pubmed: 18923511.
83. Kuma H, Miki T, Matsumoto Y, et al. Early maternal deprivation induces alterations in brain-derived neurotrophic factor expression in the developing rat hippocampus. Neurosci Lett. 2004; 372(1-2): 68–73, doi: 10.1016/j.neulet.2004.09.012, indexed in Pubmed: 15531090.
84. Lakshminarasimhan H, Chattarji S. Stress leads to contrasting effects on the levels of brain derived neurotrophic factor in the hippocampus and amygdala. PLoS One. 2012; 7(1): e30481, doi: 10.1371/journal.pone.0030481, indexed in Pubmed: 22272355.
85. Larsen MH, Mikkelsen JD, Hay-Schmidt A, et al. Regulation of brain-derived neurotrophic factor (BDNF) in the chronic unpredictable stress rat model and the effects of chronic antidepressant treatment. J Psychiatr Res. 2010; 44(13): 808–816, doi: 10.1016/j.jpsychires.2010.01.005, indexed in Pubmed: 20172535.
86. Lee RS, Sawa A. Environmental stressors and epigenetic control of the hypothalamic-pituitary-adrenal axis. Neuroendocrinology. 2014; 100(4): 278–287, doi: 10.1159/000369585, indexed in Pubmed: 25427939.
87. Levine S, Huchton DM, Wiener SG, et al. Time course of the effect of maternal deprivation on the hypothalamic-pituitary-adrenal axis in the infant rat. Dev Psychobiol. 1991; 24(8): 547–558, doi: 10.1002/dev.420240803, indexed in Pubmed: 1773913.
88. Li Y, Ji Y, Jiang H, et al. Effects of unpredictable chronic stress on behavior and brain-derived neurotrophic factor expression in CA3 subfield and dentate gyrus of the hippocampus in different aged rats. Chin Med J (Engl). 2009; 122(13): 1564–1569, indexed in Pubmed: 19719949.
89. Lindvall O, Kokaia Z, Bengzon J, et al. Neurotrophins and brain insults. Trends Neurosci. 1994; 17(11): 490–496, doi: 10.1016/0166-2236(94)90139-2, indexed in Pubmed: 7531892.
90. Linz R, Puhlmann LMC, Apostolakou F, et al. Acute psychosocial stress increases serum BDNF levels: an antagonistic relation to cortisol but no group differences after mental training. Neuropsychopharmacology. 2019; 44(10): 1797–1804, doi: 10.1038/s41386-019-0391-y, indexed in Pubmed: 30991416.
91. Lopez JP, Mamdani F, Labonte B, et al. Epigenetic regulation of BDNF expression according to antidepressant response. Mol Psychiatry. 2013; 18(4): 398–399, doi: 10.1038/mp.2012.38mp201238, indexed in Pubmed: 22547115.
92. Lu B, Nagappan G, Guan X, et al. BDNF-based synaptic repair as a disease-modifying strategy for neurodegenerative diseases. Nature Rev Neurosci. 2013; 14(6): 401–416, doi: 10.1038/nrn3505, indexed in Pubmed: 23674053.
93. Lupien SJ, McEwen BS, Gunnar MR, et al. Effects of stress throughout the lifespan on the brain, behaviour and cognition. Nat Rev Neurosci. 2009; 10(6): 434–445, doi: 10.1038/nrn2639nrn2639, indexed in Pubmed: 19401723.
94. MacQueen G, Ramakrishnan K, Ratnasingan R, et al. Desipramine treatment reduces the long-term behavioural and neurochemical sequelae of early-life maternal separation. Int J Neuropsychopharmacol. 2003; 6(4): 391–396, doi: 10.1017/s1461145703003729, indexed in Pubmed: 14641986.
95. Marmigère F, Givalois L, Rage F, et al. Rapid induction of BDNF expression in the hippocampus during immobilization stress challenge in adult rats. Hippocampus. 2003; 13(5): 646–655, doi: 10.1002/hipo.10109, indexed in Pubmed: 12921353.
96. Marmigère F, Rage F, Tapia-Arancibia L. GABA–glutamate interaction in the control of BDNF expression in hypothalamic neurons. Neurochemistry International. 2003; 42(4): 353–358, doi: 10.1016/s0197-0186(02)00100-6, indexed in Pubmed: 12470709.
97. Marmigère F, Rage F, Tapia-Arancibia L. Regulation of brain-derived neurotrophic factor transcripts by neuronal activation in rat hypothalamic neurons. J Neurosci Res. 2001; 66(3): 377–389, doi: 10.1002/jnr.1230, indexed in Pubmed: 11746355.
98. Mattson MP, Maudsley S, Martin B. BDNF and 5-HT: a dynamic duo in age-related neuronal plasticity and neurodegenerative disorders. Trends Neurosci. 2004; 27(10): 589–594, doi: 10.1016/j.tins.2004.08.001, indexed in Pubmed: 15374669.
99. McCormick C, Mathews I, Thomas C, et al. Investigations of HPA function and the enduring consequences of stressors in adolescence in animal models. Brain Cogn. 2010; 72(1): 73–85, doi: 10.1016/j.bandc.2009.06.003, indexed in Pubmed: 19616355.
100. McEwen BS. Central effects of stress hormones in health and disease: Understanding the protective and damaging effects of stress and stress mediators. Eur J Pharmacol. 2008; 583(2-3): 174–185, doi: 10.1016/j.ejphar.2007.11.071, indexed in Pubmed: 18282566.
101. McEwen B. Effects of adverse experiences for brain structure and function. Biol Psychiatry. 2000; 48(8): 721–731, doi: 10.1016/s0006-3223(00)00964-1, indexed in Pubmed: 11063969.
102. McEwen BS. Structural plasticity of the adult brain: how animal models help us understand brain changes in depression and systemic disorders related to depression. Dialogues Clin Neurosci. 2004; 6(2): 119–133, doi: 10.31887/DCNS.2004.6.2/bmcewen, indexed in Pubmed: 22034132.
103. Meyza KZ, Boguszewski PM, Nikolaev E, et al. The effect of age on the dynamics and the level of c-Fos activation in response to acute restraint in Lewis rats. Behav Brain Res. 2007; 180(2): 183–189, doi: 10.1016/j.bbr.2007.03.007, indexed in Pubmed: 17452054.
104. Miranda M, Morici J, Zanoni M, et al. Brain-Derived neurotrophic factor: a key molecule for memory in the healthy and the pathological brain. Front Cell Neurosci. 2019; 13: 363, doi: 10.3389/fncel.2019.00363, indexed in Pubmed: 31440144.
105. Miyata S, Itoh T, Matsushima O, et al. Not only osmotic stress but also repeated restraint stress causes structural plasticity in the supraoptic nucleus of the rat hypothalamus. Brain Res Bull. 1994; 33(6): 669–675, doi: 10.1016/0361-9230(94)90231-3, indexed in Pubmed: 8193921.

106. Morrissey MD, Mathews IZ, McCormick CM. Enduring deficits in contextual and auditory fear conditioning after adolescent, not adult, social instability stress in male rats. Neurobiol Learn Mem. 2011; 95(1): 46–56, doi: 10.1016/j.nlm.2010.10.007, indexed in Pubmed: 20970512.
107. Murakami S, Imbe H, Morikawa Y, et al. Chronic stress, as well as acute stress, reduces BDNF mRNA expression in the rat hippocampus but less robustly. Neurosci Res. 2005; 53(2): 129–139, doi: 10.1016/j.neures.2005.06.008, indexed in Pubmed: 16024125.
108. Naert G, Ixart G, Maurice T, et al. Brain-derived neurotrophic factor and hypothalamic-pituitary-adrenal axis adaptation processes in a depressive-like state induced by chronic restraint stress. Mol Cell Neurosci. 2011; 46(1): 55–66, doi: 10.1016/j.mcn.2010.08.006, indexed in Pubmed: 20708081.
109. Naert G, Zussy C, Tran Van Ba C, et al. Involvement of endogenous brain-derived neurotrophic factor in hypothalamic-pituitary-adrenal axis activity. J Neuroendocrinol. 2015; 27(11): 850–860, doi: 10.1111/jne.12324, indexed in Pubmed: 26388293.
110. Nutt DJ, Stein DJ. Understanding the neurobiology of comorbidity in anxiety disorders. CNS Spectr. 2006; 11(10 Suppl 12): 13–20, doi: 10.1017/s1092852900025803, indexed in Pubmed: 17008826.
111. Ohta KI, Suzuki S, Warita K, et al. Prolonged maternal separation attenuates BDNF-ERK signaling correlated with spine formation in the hippocampus during early brain development. J Neurochem. 2017; 141(2): 179–194, doi: 10.1111/jnc.13977, indexed in Pubmed: 28178750.
112. Pardon MC. Stress and ageing interactions: a paradox in the context of shared etiological and physiopathological processes. Brain Res Rev. 2007; 54(2): 251–273, doi: 10.1016/j.brainresrev.2007.02.007, indexed in Pubmed: 17408561.
113. Pardon MC, Roberts RE, Marsden CA, et al. Social threat and novel cage stress-induced sustained extracellular-regulated kinase1/2 (ERK1/2) phosphorylation but differential modulation of brain-derived neurotrophic factor (BDNF) expression in the hippocampus of NMRI mice. Neuroscience. 2005; 132(3): 561–574, doi: 10.1016/j.neuroscience.2005.01.033, indexed in Pubmed: 15837118.
114. Park C, Rosenblat J, Brietzke E, et al. Stress, epigenetics and depression: A systematic review. Neurosci Biobehav Rev. 2019; 102: 139–152, doi: 10.1016/j.neubiorev.2019.04.010, indexed in Pubmed: 31005627.
115. Pedersen WA, Wan R, Mattson MP, et al. Impact of aging on stress-responsive neuroendocrine systems. Mech Ageing Dev. 2001; 122(9): 963–983, doi: 10.1016/s0047-6374(01)00250-0, indexed in Pubmed: 11348661.
116. Pizarro J, Lumley L, Medina W, et al. Acute social defeat reduces neurotrophin expression in brain cortical and subcortical areas in mice. Brain Res. 2004; 1025(1-2): 10–20, doi: 10.1016/j.brainres.2004.06.085, indexed in Pubmed: 15464739.
117. Plata-Salaman CR, Ilyin SE, Turrin NP, et al. Neither acute nor chronic exposure to a naturalistic (predator) stressor influences the interleukin-1beta system, tumor necrosis factor-alpha, transforming growth factor-beta1, and neuropeptide mRNAs in specific brain regions. Brain Res Bull. 2000; 51(12): 187–193, doi: 10.1016/s0361-9230(99)00204-x, indexed in Pubmed: 10709966.
118. Prut L, Belzung C. The open field as a paradigm to measure the effects of drugs on anxiety-like behaviors: a review. Eur J Pharmacol. 2003; 463(1-3): 3–33, doi: 10.1016/s0014-2999(03)01272-x, indexed in Pubmed: 12600700.
119. Rage F, Givalois L, Marmigère F, et al. Immobilization stress rapidly modulates BDNF mRNA expression in the hypothalamus of adult male rats. Neuroscience. 2002; 112(2): 309–318, doi: 10.1016/s0306-4522(02)00072-6, indexed in Pubmed: 12044449.
120. Ray B, Gaskins DL, Sajdyk TJ, et al. Restraint stress and repeated corticotrophin-releasing factor receptor activation in the amygdala both increase amyloid- precursor protein and amyloid- peptide but have divergent effects on brain-derived neurotrophic factor and pre-synaptic proteins in the prefrontal cortex of rats. Neuroscience. 2011; 184: 139–150, doi: 10.1016/j.neuroscience.2011.03.067, indexed in Pubmed: 21477639.
121. Reagan L, Hendry R, Reznikov L, et al. Tianeptine increases brain-derived neurotrophic factor expression in the rat amygdala. Eur J Pharmacol. 2007; 565(1-3): 68–75, doi: 10.1016/j.ejphar.2007.02.023, indexed in Pubmed: 17368617.
122. Récamier-Carballo S, Estrada-Camarena E, López-Rubalcava C. Maternal separation induces long-term effects on monoamines and brain-derived neurotrophic factor levels on the frontal cortex, amygdala, and hippocampus: differential effects after a stress challenge. Behav Pharmacol. 2017; 28(7): 545–557, doi: 10.1097/FBP.0000000000000324, indexed in Pubmed: 28704274.
123. Reichardt LF. Neurotrophin-regulated signalling pathways. Philos Trans R Soc Lond B Biol Sci. 2006; 361(1473): 1545–1564, doi: 10.1098/rstb.2006.1894, indexed in Pubmed: 16939974.
124. Réus G, Stringari R, Ribeiro K, et al. Maternal Deprivation Induces Depressive-like Behaviour and Alters Neurotrophin Levels in the Rat Brain. Neurochem Res. 2010; 36(3): 460–466, doi: 10.1007/s11064-010-0364-3, indexed in Pubmed: 21161589.
125. Rinaman L. Postnatal development of catecholamine inputs to the paraventricular nucleus of the hypothalamus in rats. J Comp Neurol. 2001; 438(4): 411–422, doi: 10.1002/cne.1324, indexed in Pubmed: 11559897.
126. Roceri M, Cirulli F, Pessina C, et al. Postnatal repeated maternal deprivation produces age-dependent changes of brain-derived neurotrophic factor expression in selected rat brain regions. Biol Psychiatry. 2004; 55(7): 708–714, doi: 10.1016/j.biopsych.2003.12.011, indexed in Pubmed: 15038999.
127. Rosenbrock H, Koros E, Bloching A, et al. Effect of chronic intermittent restraint stress on hippocampal expression of marker proteins for synaptic plasticity and progenitor cell proliferation in rats. Brain Res. 2005; 1040(1-2): 55–63, doi: 10.1016/j.brainres.2005.01.065, indexed in Pubmed: 15804426.
128. Rosenfeld P, Wetmore J, Levine S. Effects of repeated maternal separations on the adrenocortical response to stress of preweanling rats. Physiol Behav. 1992; 52(4): 787–791, doi: 10.1016/0031-9384(92)90415-x, indexed in Pubmed: 1409954.
129. Rosenzweig E, Barnes C. Impact of aging on hippocampal function: plasticity, network dynamics, and cognition. Prog Neurobiol. 2003; 69(3): 143–179, doi: 10.1016/s0301-0082(02)00126-0, indexed in Pubmed: 12758108.
130. Roth TL, Lubin FD, Funk AJ, et al. asting epigenetic influence of early-life adversity on the BDNF gene.

Biol Psychiatry. 2009; 65(9): 760–769, doi: 10.1016/j.biopsych.2008.11.028, indexed in Pubmed: 19150054.
131. Sapolsky R, Krey L, McEwen B. The adrenocortical axis in the aged rat: Impaired sensitivity to both fast and delayed feedback inhibition. Neurob Aging. 1986; 7(5): 331–335, doi: 10.1016/0197-4580(86)90159-4, indexed in Pubmed: 3024042.
132. Sapolsky R, Meaney M. Maturation of the adrenocortical stress response: Neuroendocrine control mechanisms and the stress hyporesponsive period. Brain Res Rev. 1986; 11(1): 65–76, doi: 10.1016/0165-0173(86)90010-x, indexed in Pubmed: 3011218.
133. Scaccianoce S, Del Bianko P, Caricasole, A, et al. Relationship between learning, stress and hippocampal brain-derived neurotrophic factor. Neuroscience. 2003; 121(4): 825–828, doi: 10.1016/s0306-4522(03)00514-1, indexed in Pubmed: 14580931.
134. Scaccianoce S, Bianco PD, Paolone G, et al. Social isolation selectively reduces hippocampal brain-derived neurotrophic factor without altering plasma corticosterone. Behav Brain Res. 2006; 168(2): 323–325, doi: 10.1016/j.bbr.2005.04.024, indexed in Pubmed: 16455145.
135. Schaaf MJ, De Kloet ER, Vreugdenhil E. Corticosterone effects on BDNF expression in the hippocampus. Implications for memory formation. Stress. 2000; 3(3): 201–208, doi: 10.3109/10253890009001124, indexed in Pubmed: 10938581.
136. Schafe G, LeDoux J. Memory consolidation of auditory pavlovian fear conditioning requires protein synthesis and protein kinase a in the amygdala. J Neurosci. 2000; 20(18): RC96–RC96, doi: 10.1523/jneurosci.20-18-j0003.2000, indexed in Pubmed: 10974093.
137. Schmidt MV, Enthoven L, Van der Mark M, et al. The postnatal development of the hypothalamic–pituitary–adrenal axis in the mouse. Int J Dev Neurosci. 2003; 21(3): 125–132, doi: 10.1016/s0736-5748(03)00030-3, indexed in Pubmed: 12711350.
138. Schmidt MV, Scharf SH, Liebl C, et al. A novel chronic social stress paradigm in female mice. Horm Behav. 2010; 57(4-5): 415–420, doi: 10.1016/j.yhbeh.2010.01.010, indexed in Pubmed: 20100488.
139. Schoenfeld NM, Leathem JH, Rabii J. Maturation of adrenal stress responsiveness in the rat. Neuroendocrinology. 1980; 31(2): 101–105, doi: 10.1159/000123058, indexed in Pubmed: 6248807.
140. Schulte-Herbruggen O, Chourbaji S, Muller H, et al. Differential regulation of nerve growth factor and brain-derived neurotrophic factor in a mouse model of learned helplessness. Exp Neurol. 2006; 202(2): 404–409, doi: 10.1016/j.expneurol.2006.07.002, indexed in Pubmed: 16914143.
141. Seo MiK, Ly NN, Lee CH, et al. Early life stress increases stress vulnerability through BDNF gene epigenetic changes in the rat hippocampus. Neuropharmacology. 2016; 105: 388–397, doi: 10.1016/j.neuropharm.2016.02.009, indexed in Pubmed: 26877199.
142. Shao SH, Shi SS, Li ZL, et al. Aging effects on the BDNF mRNA and TrkB mRNA expression of the hippocampus in different durations of stress. Chin J Physiol. 2010; 53(5): 285–293, doi: 10.4077/cjp.2010.amk056, indexed in Pubmed: 21793339.
143. Shi SS, Shao SH, Yuan BP, et al. Acute stress and chronic stress change brain-derived neurotrophic factor (BDNF) and tyrosine kinase-coupled receptor (TrkB) expression in both young and aged rat hippocampus. Yonsei Med J. 2010; 51(5): 661–671, doi: 10.3349/ymj.2010.51.5.661, indexed in Pubmed: 20635439.
144. Shoji H, Mizoguchi K. Acute and repeated stress differentially regulates behavioral, endocrine, neural parameters relevant to emotional and stress response in young and aged rats. Behav Brain Res. 2010; 211(2): 169–177, doi: 10.1016/j.bbr.2010.03.025, indexed in Pubmed: 20307586.
145. Silhol M, Arancibia S, Maurice T, et al. Spatial memory training modifies the expression of brain-derived neurotrophic factor tyrosine kinase receptors in young and aged rats. Neuroscience. 2007; 146(3): 962–973, doi: 10.1016/j.neuroscience.2007.02.013, indexed in Pubmed: 17391859.
146. Silhol M, Bonnichon V, Rage F, et al. Age-related changes in brain-derived neurotrophic factor and tyrosine kinase receptor isoforms in the hippocampus and hypothalamus in male rats. Neuroscience. 2005; 132(3): 613–624, doi: 10.1016/j.neuroscience.2005.01.008, indexed in Pubmed: 15837123.
147. Singh LK, Pang X, Alexacos N, et al. Acute immobilization stress triggers skin mast cell degranulation via corticotropin releasing hormone, neurotensin, and substance P: A link to neurogenic skin disorders. Brain Behav Immun. 1999; 13(3): 225–239, doi: 10.1006/brbi.1998.0541, indexed in Pubmed: 10469524.
148. Smith M. Hippocampal vulnerability to stress and aging: possible role of neurotrophic factors. Behav Brain Res. 1996; 78(1): 25–36, doi: 10.1016/0166-4328(95)00220-0, indexed in Pubmed: 8793034.
149. Smith M, Cizza G. Stress-induced changes in brain-derived neurotrophic factor expression are attenuated in aged Fischer 344/N rats. Neurobiol Aging. 1996; 17(6): 859–864, doi: 10.1016/s0197-4580(96)00066-8, indexed in Pubmed: 9363796.
150. Smith MA, Makino S, Kim SY, et al. Stress increases brain-derived neurotropic factor messenger ribonucleic acid in the hypothalamus and pituitary. Endocrinology. 1995; 136(9): 3743–3750, doi: 10.1210/endo.136.9.7649080, indexed in Pubmed: 7649080.
151. Smith MA, Makino S, Kvetnansky R, et al. Stress and glucocorticoids affect the expression of brain-derived neurotrophic factor and neurotrophin-3 mRNAs in the hippocampus. J Neurosci. 1995; 15(3): 1768–1777, doi: 10.1523/jneurosci.15-03-01768.1995, indexed in Pubmed: 7891134.
152. Solas M, Aisa B, Mugueta M, et al. Interactions between age, stress and insulin on cognition: implications for alzheimer's disease. Neuropsychopharmacology. 2010; 35(8): 1664–1673, doi: 10.1038/npp.2010.13, indexed in Pubmed: 20182419.
153. St-Cyr S, McGowan PO. Programming of stress-related behavior and epigenetic neural gene regulation in mice offspring through maternal exposure to predator odor. Front Behav Neurosci. 2015; 9: 145, doi: 10.3389/fnbeh.2015.00145, indexed in Pubmed: 26082698.
154. Tapia-Arancibia L. Physiology of BDNF: focus on hypothalamic function. Front Neuroendocrinol. 2004; 25(2): 77–107, doi: 10.1016/j.yfrne.2004.04.001, indexed in Pubmed: 15571756.
155. Tornese P, Sala N, Bonini D, et al. Chronic mild stress induces anhedonic behavior and changes in glutamate release, BDNF trafficking and dendrite morphology only in stress vulnerable rats. The rapid restorative action of ketamine.

Neurobiol Stress. 2019; 10: 100160, doi: 10.1016/j.ynstr.2019.100160, indexed in Pubmed: 31193464.
156. Tsankova NM, Berton O, Renthal W, et al. Sustained hippocampal chromatin regulation in a mouse model of depression and antidepressant action. Nat Neurosci. 2006; 9(4): 519–525, doi: 10.1038/nn1659, indexed in Pubmed: 16501568.
157. Tsigos C, Chrousos G. Hypothalamic–pituitary–adrenal axis, neuroendocrine factors and stress. J Psychosom Res. 2002; 53(4): 865–871, doi: 10.1016/s0022-3999(02)00429-4, indexed in Pubmed: 12377295.
158. Tsoory M, Cohen H, Richter-Levin G. Juvenile stress induces a predisposition to either anxiety or depressive-like symptoms following stress in adulthood. Eur Neuropsychopharmacol. 2007; 17(4): 245–256, doi: 10.1016/j.euroneuro.2006.06.007, indexed in Pubmed: 16889944.
159. Turecki G, Meaney MJ. Effects of the social environment and stress on glucocorticoid receptor gene methylation: a systematic review. Biol Psychiatry. 2016; 79(2): 87–96, doi: 10.1016/j.biopsych.2014.11.022, indexed in Pubmed: 25687413.
160. Tyler WJ, Perrett SP, Pozzo-Miller LD. The role of neurotrophins in neurotransmitter release. Neuroscientist. 2002; 8(6): 524–531, doi: 10.1177/1073858402238511, indexed in Pubmed: 12467374.
161. Ueyama T, Kawai Y, Nemoto K, et al. mmobilization stress reduced the expression of neurotrophins and their receptors in the rat brain. Neurosci Res. 1997; 28(2): 103–110, doi: S0168-0102(97)00030-8, indexed in Pubmed: 9220467.
162. Ulrich-Lai YM, Herman JP. Neural regulation of endocrine and autonomic stress responses. Nat Rev Neurosci. 2009; 10(6): 397–409, doi: 10.1038/nrn2647, indexed in Pubmed: 19469025.
163. Valzelli L. The “isolation syndrome” in mice. Psychopharmacologia. 1973; 31(4): 305–320, doi: 10.1007/BF00421275, indexed in Pubmed: 4582344.
164. van Zyl PJ, Dimatelis JJ, Russell VA. Behavioural and biochemical changes in maternally separated Sprague-Dawley rats exposed to restraint stress. Metab Brain Dis. 2016; 31(1): 121–133, doi: 10.1007/s11011-015-9757-y, indexed in Pubmed: 26555398.
165. Vázquez DM, Akil H. Pituitary-adrenal response to ether vapor in the weanling animal: characterization of the inhibitory effect of glucocorticoids on adrenocorticotropin secretion. Pediatr Res. 1993; 34(5): 646–653, doi: 10.1203/00006450-199311000-00017, indexed in Pubmed: 8284104.
166. Veenema A, Blume A, Niederle D, et al. Effects of early life stress on adult male aggression and hypothalamic vasopressin and serotonin. Eur J Neurosci. 2006; 24(6): 1711–1720, doi: 10.1111/j.1460-9568.2006.05045.x, indexed in Pubmed: 17004935.
167. Viana Borges J, Souza de Freitas B, Antoniazzi V, et al. Social isolation and social support at adulthood affect epigenetic mechanisms, brain-derived neurotrophic factor levels and behavior of chronically stressed rats. Behav Brain Res. 2019; 366: 36–44, doi: 10.1016/j.bbr.2019.03.025, indexed in Pubmed: 30880220.
168. Weaver IC, Cervoni N, Champagne F, et al. Epigenetic programming by maternal behavior. Nature Neurosci. 2004; 7(8): 847–854, doi: 10.1038/nn1276, indexed in Pubmed: 15220929.
169. Whitnall M. Regulation of the hypothalamic corticotropin-releasing hormone neurosecretory system. Prog Neurobiol. 1993; 40(5): 573–629, doi: 10.1016/0301-0082(93)90035-q, indexed in Pubmed: 8484004.
170. Willner P, Towell A, Sampson D, et al. Reduction of sucrose preference by chronic unpredictable mild stress, and its restoration by a tricyclic antidepressant. Psychopharmacology. 1987; 93(3): 538–564, doi: 10.1007/bf00187257, indexed in Pubmed: 3124165.
171. Xu H, Chen Z, He J, et al. Synergetic effects of quetiapine and venlafaxine in preventing the chronic restraint stress-induced decrease in cell proliferation and BDNF expression in rat hippocampus. Hippocampus. 2006; 16(6): 551–559, doi: 10.1002/hipo.20184, indexed in Pubmed: 16652337.
172. Xu H, Luo C, Richardson JS, et al. Recovery of hippocampal cell proliferation and BDNF levels, both of which are reduced by repeated restraint stress, is accelerated by chronic venlafaxine. Pharmacogenomics J. 2004; 4(5): 322–331, doi: 10.1038/sj.tpj.6500265, indexed in Pubmed: 15289796.
173. Xu H, Qing H, Lu W, et al. Quetiapine attenuates the immobilization-induced decrease of brain-derived neurotrophic factor in rat hippocampus. Neurosci Lett . 2002; 321(1-2): 65–68, doi: 10.1016/s0304-3940(02)00034-4, indexed in Pubmed: 11872258.
174. Xue X, Shao S, Wang W, et al. Maternal separation induces alterations in reversal learning and brain-derived neurotrophic factor expression in adult rats. Neuropsychobiology. 2013; 68(4): 243–249, doi: 10.1159/000356188, indexed in Pubmed: 24280707.
175. Yoshii A, Constantine-Paton M. Postsynaptic BDNF-TrkB signaling in synapse maturation, plasticity, and disease. Dev Neurobiol. 2010; 70(5): 304–322, doi: 10.1002/dneu.20765, indexed in Pubmed: 20186705.
176. Yun SJ, Park HJ, Yeom MJ, et al. Effect of electroacupuncture on the stress-induced changes in brain-derived neurotrophic factor expression in rat hippocampus. Neurosci Lett. 2002; 318(2): 85–88, doi: 10.1016/s0304-3940(01)02492-2, indexed in Pubmed: 11796192.
177. Zaletel I, Filipović D, Puškaš N. Hippocampal BDNF in physiological conditions and social isolation. Rev Neurosci. 2017; 28(6): 675–692, doi: 10.1515/revneuro-2016-0072, indexed in Pubmed: 28593903.
178. Zheng Yu, Fan W, Zhang X, et al. Gestational stress induces depressive-like and anxiety-like phenotypes through epigenetic regulation of BDNF expression in offspring hippocampus. Epigenetics. 2016; 11(2): 150–162, doi: 10.1080/15592294.2016.1146850, indexed in Pubmed: 26890656.
179. Zimmerberg B, Foote HE, Van Kempen TA. Olfactory association learning and brain-derived neurotrophic factor in an animal model of early deprivation. Dev Psychobiol. 2009; 51(4): 333–344, doi: 10.1002/dev.20373, indexed in Pubmed: 19308959.
180. Zoladz PR, Park CR, Halonen JD, et al. Differential expression of molecular markers of synaptic plasticity in the hippocampus, prefrontal cortex, and amygdala in response to spatial learning, predator exposure, and stress-induced amnesia. Hippocampus. 2012; 22(3): 577–589, doi: 10.1002/hipo.20922, indexed in Pubmed: 21538655.

VIA MEDICA

REVIEW ARTICLE

Folia Morphol.
Vol. 80, No. 3, pp. 505–513
DOI: 10.5603/FM.a2020.0106

ISSN 0015–5659
eISSN 1644–3284
journals.viamedica.pl

Current concepts on the morphology of popliteus tendon and its clinical implications

J. Zabrzyński[1, 2], G. Huri[3], A. Yataganbaba[3], Ł. Paczesny[1], D. Szwedowski[4], A. Zabrzyńska[5], Ł. Łapaj[2], M. Gagat[6], M. Wiśniewski[7], P. Pękala[8, 9, 10]

[1]Department of Orthopaedics, Orvit Clinic, Citomed Healthcare Centre, Torun, Poland
[2]Department of General Orthopaedics, Musculoskeletal Oncology and Trauma Surgery, University of Medical Sciences, Poznan, Poland
[3]Orthopaedics and Traumatology Department, Hacettepe Universitesi, Ankara, Turkey
[4]Orthopaedic Arthroscopic Surgery International (OASI) Bioresearch Foundation Milan, Italy
[5]Department of Radiology, Multidisciplinary Hospital, Inowroclaw, Poland
[6]Department of Histology and Embryology, Faculty of Medicine, Nicolaus Copernicus University in Torun, Collegium Medicum in Bydgoszcz, Poland
[7]Department of Normal Anatomy, Faculty of Medicine, Nicolaus Copernicus University in Torun, Collegium Medicum in Bydgoszcz, Poland
[8]International Evidence-Based Anatomy Working Group, Department of Anatomy, Jagiellonian University Medical College, Krakow, Poland
[9]Faculty of Medicine and Health Sciences, Andrzej Frycz Modrzewski Krakow University, Krakow, Poland
[10]Lesser Poland Orthopaedic and Rehabilitation Hospital, Krakow, Poland

[Received: 28 July 2020; Accepted: 11 August 2020; Early publication date: 2 September 2020]

In this review we described the anatomy and biomechanics of popliteus muscle and its tendon. Furthermore, we combined the anatomy with clinics and discussed a wide spectrum of disorders regarding the popliteus and its musculotendinous complex. There are three main anatomical regions of the popliteus musculotendinous complex: the proximal origin, the mid-portion, the distal part on the tibia. The unique localisation and various origins of the tendon, connected with structures such as fibular head, Wrisberg, Humphrey and posterior cruciate ligament, lateral meniscus, medial collateral ligament, give an implication to diagnosis and treatment. Popliteus dysfunction is often overlooked, that is the reason why diagnosis and treatment of its injuries is mostly insufficient. Repetitive or acute direct varus forces, when the tibia is in external rotation, and knee hyperextension or flexion with forced external rotation of the tibia, are the main mechanisms of trauma. Popliteus injuries mainly affect the athletic population and lead to severe activity limitations. Chronic disorders of the popliteus tendon, less known, are often described as tendinopathy and are frequently seen in runners. Their symptoms can mimic the lateral meniscal tears. On the other hand, high-energy traumatic injuries of the popliteus tendon often accompany complex, multi ligamentous injuries seen in competitive sports. We also presented the implication of popliteus tendon in knee arthroplasty, due to its particular exposition to iatrogenic trauma during surgery. The issues such as proper tibial component location and well-designed cut systems are crucial to avoid the popliteus impingement and preserve its structure. (Folia Morphol 2021; 80, 3: 505–513)

Key words: popliteus muscle, tendinopathy, posterolateral corner, popliteus reconstruction, popliteus tendon

Address for correspondence: J. Zabrzyński, MD, PhD, Orvit Clinic, ul. Marii Skłodowskiej-Curie 73, 87–100 Toruń, Poland, tel: +48 513094738, e-mail: zabrzynski@gmail.com

ANATOMY

Popliteus muscle originates from the lateral femoral condyle. It connects with the proximal fibula as a popliteofibular ligament and the posterior horn of the lateral meniscus as a tendinous attachment, and inserts into the posterior surface of tibia above the soleal line [8, 34]. Taylor and Bonney [48] in their comparative study concluded that the popliteus muscle is analogous to the deep portion of the pronator teres muscle. They both originated primitively from the fibula and the ulna, respectively. During the evolution, the origins of these muscles migrated proximally to the lateral femoral condyle and medial humeral epicondyle. Moreover, in reptiles and primitive mammals, the fibula articulates with the femur and subsequently, during the evolution, the fibula has moved distally to the proximal tibiofibular articulation [11].

The popliteus tendon, forming a strong cord, is intra-capsular structure that runs deep to the lateral collateral ligament (LCL), and passes through the popliteal hiatus [37]. Nevertheless, the popliteus tendon lies extra-articular and extra-synovial [19, 34]. The average total length of the popliteus tendon to its musculotendinous junction is 54.5 mm [26].

There are three main anatomical regions of the popliteus musculotendinous complex: the proximal origin (A), the mid-portion (B), the distal part on the tibia (C).

A. The proximal origin. The popliteus tendon passes beneath the LCL, and its fibres are attached to the popliteal groove, however, the main fascicle of fibres is inserted underneath the LCL (Fig. 1, 2) [50]. Moreover, it was found that the centre of the femoral insertion of the popliteus muscle–tendon complex is situated posterior and distal to the lateral epicondyle of femur [50].

B. The mid-portion. The popliteus complex has mainly the following origins: the small pit on the lateral femoral condyle, the posterior aspect of the fibrous capsule of the knee joint, the ligamentous band extending between the popliteal tendon and the superior portion of the posterior horn of the lateral meniscus and the popliteofibular ligament [34]. Moreover, the connections with the ligaments of Wrisberg and Humphrey, and the posterior cruciate ligament (PCL) were described [33]. The presence of a fibular attachment of the popliteus, known as popliteofibular (PFL) ligament, was described by numerous authors and is considered as part of the normal anatomy now [8]. Popliteomeniscal fascicles are synovial structures between the lateral meniscus and popliteus tendon. The

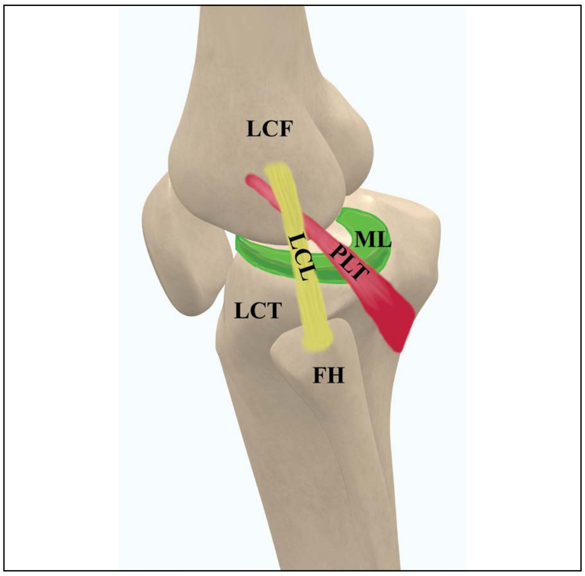

Figure 1. Scheme of the popliteus musculotendinous unit; FH — fibular head; LCF — lateral condyle of the femur; LCL — lateral collateral ligament; LCT — lateral condyle of the tibia; ML — lateral meniscus; PLT — popliteus tendon.

anterosuperior, posterosuperior, and posteroinferior popliteomeniscal fascicles, serve as struts, stabilising the posterior horn of the lateral meniscus [2, 37]. Nevertheless, numerous variabilities of the origins were observed [3]. Tria et al. [49], in cadaveric study, reported that 18/40 specimens (45%) had an isolated popliteus tendon insertion to the lateral femoral condyle, with no connection to the lateral meniscus. However, this results could be biased by the dissection technique or previous morbidities, and on the other hand, Aman et al. [2] revealed the presence of minimum 2/3 of popliteomeniscal fascicles in all examined by them cadaveric limbs. Disruption of the popliteomeniscal fascicles may lead to the abnormal mobility of the lateral meniscus. Simonnet et al. [42] identified the three types of meniscal attachments of the popliteus complex. The authors showed fewer alterations in the lateral meniscus and tibiofemoral cartilage in specimens with more popliteomeniscal fascicles. However, injuries to the popliteomeniscal fascicles are extremely difficult to identify by physical examination and even magnetic resonance imaging (MRI). The MRI is a well-established non-invasive imaging technique in recognition of normal popliteomeniscal fascicles; however, the gold standard for diagnosis and treatment of their tears is arthroscopy [17]. The popliteus tendon is localised in the posterolateral corner of the knee (PLC), in the bony groove, which also has an essential impact on further clinical

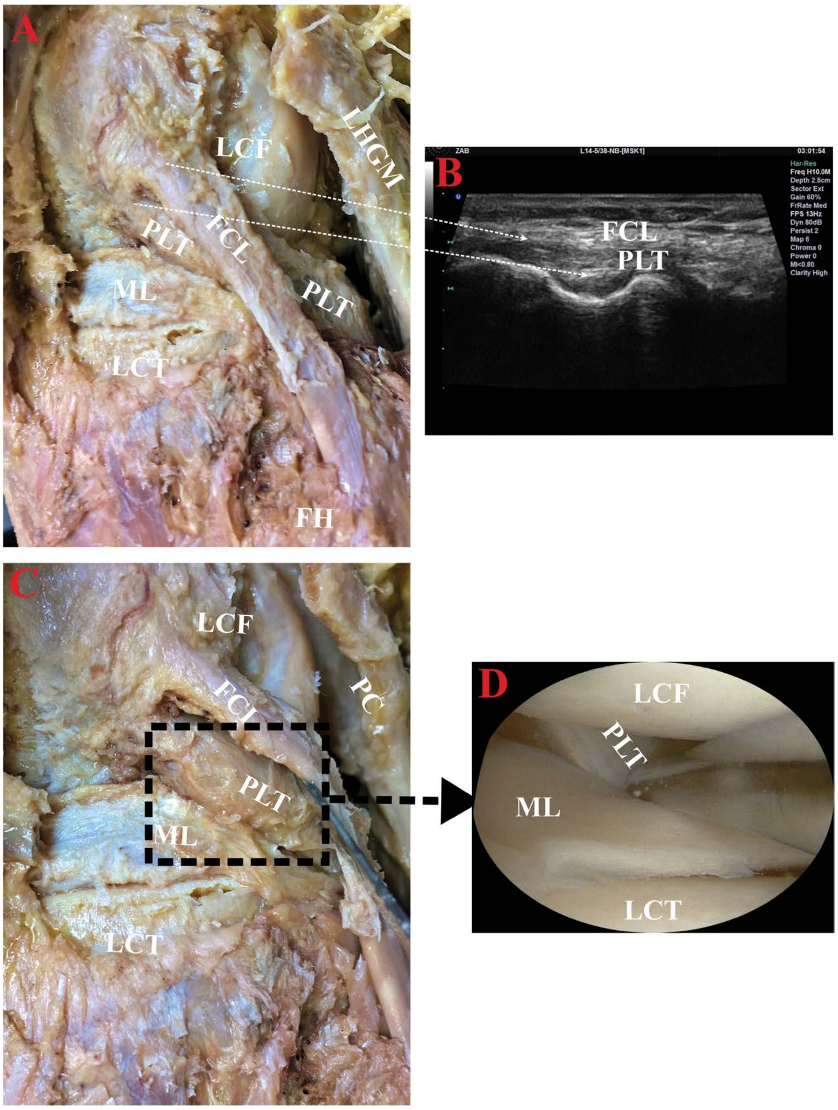

Figure 2. A. Lateral view of the knee joint showing the femoral attachments of popliteus tendon (PLT) and fibular collateral ligament (FCL) to the lateral condyle of the femur (LCF). The PLT passes beneath the FCL, which distal attachment is the fibular head (FH). Moreover, the relation between the lateral meniscus (ML) and the popliteus tendon is visible. Lateral condyle of the tibia (LCT); lateral head of the gastrocnemius muscle (LHGM); **B.** The sonographic scan of the lateral aspect of the knee joint with the proximal attachments of FCL and beneath the PLT origin; **C.** Lateral view of the knee joint showing the PLT and its relation to ML, the FCL is separated by the probe. Posterior capsule (PC); **D.** Arthroscopic view of the lateral compartment of the knee joint and the relations of the PLT to concomitant structures.

issues [11, 27]. The proximal part of the popliteus unit is separated from the lateral collateral ligament, capsule, and lateral femoral condyle by a synovial bursa. If the bursa becomes inflamed, a fluid collection can be seen on MRI or ultrasound imaging [12].

C. The distal part on the tibia. The muscle belly of the popliteus inserts above the soleal line at the proximal and posterior part of the tibia, forming the floor of popliteal fossa [13, 14]. Song et al. [43] with a three-dimensional reconstruction of the human knee showed that the popliteus tendon is divided into two bundles (medial and lateral) at the popliteal fossa. The popliteus muscle is composed of deep and superficial layers [37]. Some of its distal fibres are interconnected with fascial fibres attached to the distal region of the medial (tibial) collateral ligament (MCL) [33].

BIOMECHANICS

The popliteus complex acts as static and dynamic stabilizer of the knee joint. Its primary function is to rotate the femur externally when the foot is in contact with the ground and to internally rotate the tibia when the foot is not fixed, which is crucial while walking. During concentric activation, the popliteus internally rotates the tibia; contrary, during eccentric activation, it serves as a secondary restraint to external tibial rotation [33]. This dynamic and static resistance to external rotation is more noticeable, with higher degrees of knee flexion [39].

When the foot is in contact with the ground and the knee is in full extension, the knee is "locked", and initiation of the flexion of the joint requires the popliteus function. It plays a key role that unlocks the knee by rotating the femur externally on the tibia while the

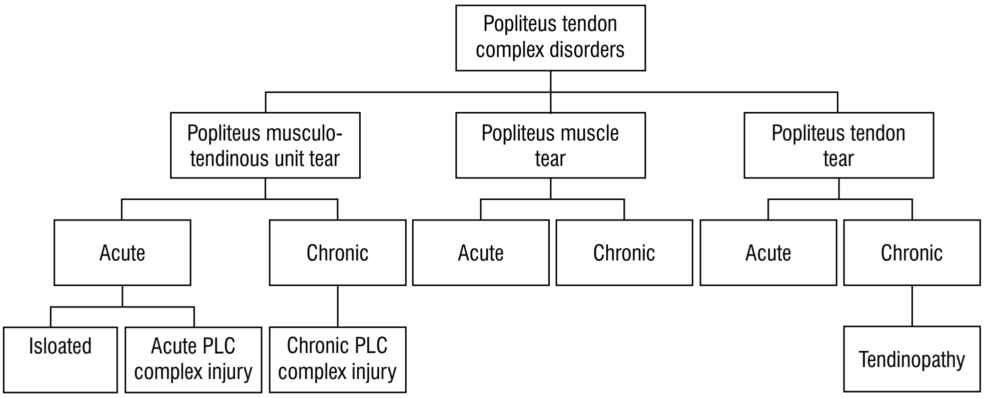

Figure 3. The general classification of the popliteus complex disorders; PLC — posterolateral corner of the knee.

knee is locked, facilitating the initial flexion [19]. Meanwhile, the popliteus' connections to the lateral meniscus and posterior capsule protect the lateral meniscus from impingement during movement. LaPrade et al. [27] defined the popliteus tendon as the "fifth major ligament of the knee". Some studies emphasized that popliteus helps PCL and quadriceps muscle carrying the load, which prevents the femur from excess dislocation. The connection between popliteus and PCL is provided by the Wrisberg and Humphrey ligaments and the main role plays the medial aponeurosis of the popliteus complex [35, 36]. In a biomechanical in vitro study, it has been shown that when the popliteus tendon is stretched with 50 N, the tibia rotates 4–5 degrees (°) while the knee is fully extended. The amount of rotation increases up to 12° as the knee is flexed 90° [23]. Moreover, authors transected the popliteofibular ligament, LCL, popliteus tendon sequentially during cyclic biomechanical testing. They noted gradually increased tibial external rotation with a lateral shift of the position of neutral tibial alignment. During the first 30-degree knee flexion, LCL contributes more to prevent the tibial varus, while the popliteus contributes more to limit the external rotation and posterior translation of the tibia [33].

CLASSIFICATION OF THE PATHOLOGY

Commonly, the popliteus muscle and tendon disorders are classified into isolated pathology of tendon, muscle belly and complex posterolateral corner injuries of the knee (Fig. 3). Posterolateral corner injuries are divided into three groups: A, B, and C, according to lesions occurring in different structures [13]. Type A involves the PFL and popliteus tendon; in this group, only an increase in the external tibial rotation is observed. In type B, the PFL, popliteus tendon, and LCL are affected. In this group, a lateral gapping occurs under the varus stress test at 30° of knee flexion along with an increase in tibial external rotation. In type C, the injury to the PFL, popliteus tendon, LCL, lateral capsule (avulsion) and cruciate ligament tear are observed. Severe varus instability at 30° of knee flexion and in extension is typical. The lack of a comprehensive, prognostic classification system was one of the concepts of the consensus on PLC of the knee presented by Chahla et al. [9]. A future classification system should allow differentiation between structure involved, the type of injury (avulsion versus intrasubstance), the chronicity, the treatment strategy, and it should reflect the prognosis.

MECHANISM OF TRAUMA

There are various types of specific pathomechanisms that cause popliteus injury. These are: a direct varus force when the tibia is in external rotation and knee hyperextension or flexion with forced external rotation of the tibia [11, 32, 38]. Brown et al. [6] emphasized that the mechanism of trauma is more complex than thought and still has unknown aspects. While the musculotendinous junction is the weakest part of the popliteus complex, the tendon is the most durable structure. The strength of the muscle belly is between these two. The tendon is susceptible to strain at the joint line or avulsion at its origin on the lateral femoral condyle. Moreover, complications related to the popliteus may also occur during total knee arthroplasty. Takubo et al. [47] revealed that the femoral origins of LCL and popliteus tendon are especially exposed to iatrogenic trauma during the knee arthroplasty, due to anatomic conditions. Furthermore, Takakashi et al. [45] demonstrated the special design of the cut systems, preserves the popliteus tendon, particularly endangered in a female cohort. The size of the tibial component in the knee arthroplasty also may have an impact on popliteus biomechanics and disorders. Bonnin et al. [5] presented in their cadaveric study, using the computed tomography, the importance of the tibial components location on the tibial plateau and the association with tibio-popliteus impingement. Regarding to knee arthroplasty and stability, Kesman et al. [22] showed that role of the popliteus complex in the stability of the knee joint during the arthroplasty was not clinically important and significant. Contrary, Cottino et al. [10] in their laboratory study showed that popliteus dissection caused both the lateral and medial instability of the knee joint; however, the greater impact was in the lateral compartment.

ISOLATED POPLITEUS TRAUMA AND TENDINOPATHY

Isolated injuries of the popliteus are rare and usually occur in athletes. Musculotendinous unit lesions are divided into three groups according to the severity of the trauma. Accordingly, grade-1 indicates microtrauma, while grade-3 corresponds to isolated high-energy injuries [30]. Repetitive stress and microtrauma can lead to popliteus tendinopathy. Patients present with persistent and chronic pain in the posterolateral region of the knee, around the popliteus insertion site on the femur, along the tendon and its attachment to the muscle belly [16, 19, 38]. In some cases, symptoms can mimic the lateral meniscal tear. Sometimes, there may be difficulty with walking on uneven ground or going up and down stairs [8]. As stated above, the function of the popliteal unit is to restrain the lateral femoral condyle movements and maintain its relationship with lateral tibial plateau. The downhill running or walking can exacerbate the pathology, causing increased stress on popliteus musculotendinous unit [36]. Patients can run for short distances, but posterolateral knee pain can develop with continued running. In sports such as basketball, tennis, and running, the balance between the femur and the tibia may be impaired due to the development of quadriceps failure. In this case, the load on popliteus increases, and an injury may occur.

COMPLEX POPLITEUS TRAUMA AND PLC INJURY

On the other hand, high-energy trauma can cause acute haemarthrosis and lateral knee pain. Depending on preserved stability of the joint, the isolated injury of the popliteus muscle-tendon unit should be evaluated. Avulsion of the femoral attachment of the popliteus has also been reported [31, 32]. This form of injury is rare (< 10%) and is often seen as part of complex knee injuries [19]. The structure of the posterolateral corner was once regarded as the "dark side of the knee" due to the complex and variable anatomy with inconsistent terminology used in the literature to describe the structures in this region [39]. However, in recent years, a significant contribution was made to understand the anatomy and biomechanics of the PLC [8]. Today, it is understood that inadequate diagnosis and treatment of injuries involving the posterolateral corner are associated with poor results and knee instability. Popliteus injury is seen in 60% to 68% of patients operated for posterolateral corner instability [20, 27]. Moreover, complete tears of popliteus unit usually are linked with multi-ligamentous injuries of the knee and subsequently need more advanced surgical procedures [8]. Cruciate ligament rupture (ACL or PCL) can mask the presence of PLC instability. Isolated ACL or PCL reconstruction without regard to PLC injury may result in graft failure. Posterolateral corner injuries are commonly associated with ACL or PCL rupture, but also medial compartment bone bruises [8, 15]. Inadequate reconstructive surgery, omitting the PLC deficiency, can lead to early degenerative changes of the knee joint [8, 43]. There are three major static stabilizers, known as primary stabilizers of the PLC: the fibular (lateral) collateral ligament, the popliteus tendon and the popliteofibular ligament [26, 39]. In recent studies, the group of structures forming the PLC were extended and according to these studies, the iliotibial tract, long and short heads of the biceps femoris muscle, mid-third lateral capsular ligament, fabellofibular ligament, also known as gastrocnemiofibular ligament, popliteofibular ligament, lateral meniscotibial ligament and posterior capsule also form the PLC [20, 46]. LCL and PFL act as static stabilizers against varus stress and external tibial rotation during knee flexion below 30°. Popliteus acts as a dynamic stabilizer against external rotation and posterior translation of the tibia [46]. The relationship between LCL and the insertion of popliteus on the lateral femur condyle has been studied in detail [46]. LCL is usually inserted in the postero-distal slope of the apex of the lateral epicondyle, while the popliteus is inserted to the anterior end of the popliteal sulcus [46].

DIAGNOSTICS

Tests that must be performed in evaluating PLC injuries and simultaneous popliteus injuries are: (1) varus stress test (in full extension: FCL, PLC and cruciate ligament injury; in 20–30° of knee flexion: FCL and potentially the secondary stabilizers of the PLC), (2) the dial test (conducted in 30 and 90° of knee flexion: an increase in the external tibial rotation of more than 10° in 30° of flexion compared to the opposite knee suggests PLC injury and an increase in the external tibial rotation of more than 10° in 30 and 90° of flexion compared to the opposite knee suggests PLC and PCL injury), (3) reverse pivot shift test (valgus force is applied when the knee is flexed at 90°, and the tibia is forced to external rotation, then the knee is slowly extended, if the subluxated lateral tibial plateau is reduced when the flexion is decreased to 35–40°, the test is positive), (4) the external rotation recurvatum test (the patient is in the supine position, knee joint extended, the great toe is grasped and the leg lifted from the table, while securing the femur to the table by applying gentle pressure to the anterior distal femur, recurvatum is measured by the amount of heel height in cm, test is performed bilaterally to compare) (Fig. 4) [8, 9].

If isolated popliteus pathology or complex PLC lesion is suspected after medical interview and physical examination, the proper radiological imaging is necessary. Firstly, standard radiographic imaging should be performed, including anteroposterior (AP), lateral (LAT), and sunrise views of the knee [16]. Stress radiographs are more sensitive for the diagnosis of PLC injuries; however, taking these radiographs can be challenging due to pain in the acute phase of injury.

LaPrade et al. [25] showed that isolated FCL rupture created an average of 2.7 mm gapping in the lateral joint space in the varus stress radiograph compared to the intact knee, and more than 4 mm gapping was associated with grade-3 PLC injury. MRI is essential to assess concomitant injuries and to determine the exact location of the injured structures [24]. Standard MRI sequences are often sufficient to evaluate complex knee injuries. Still, PLC structures can be better visualised using a coronal oblique plane view; however, one must be aware that PFL can be missed to the slice thickness. The popliteus musculotendinous complex lesions are detected in 1% of all knee MRI studies [19]. They may appear on MRI as an avulsion of the femoral attachment, an irregular contour of the tendon at the popliteal hiatus with surrounding high signal intensity changes due to oedema, or as swollen disorganised muscle fibres with high signal intensity changes within the popliteus muscle [19]. On the other hand, the avulsion of the head of the fibula (arcuate sign) may be an important indicator of posterolateral structures tear. This minor fractured bone fragment is often associated with popliteofibular and fabellofibular ligaments attachment rupture. Moreover, it is an important clinical predictor of posterolateral instability and surgical outcomes [17].

ANATOMICAL IMPLICATIONS INTO TREATMENT

Regarding the extent of pathology, popliteus injuries can be treated conservatively (grade-1–2 tears) or surgically (grade-3 tears and non-response to conservative treatment after three months).

Non-operative treatment is usually recommended for grade-1 and -2 of popliteus injury with good clinical outcomes [8]. Minimal radiographic changes at 8-year follow-up were found after conservative treatment with early mobilisation protocol [21].

Partial-thickness tendon or muscle tears can be treated with open or minimally-invasive debridement [21]. The intraarticular part of the surgery can be done arthroscopically with favourable outcomes [4, 16, 18]. However, in extra-articular cases, open surgery can be necessary depending on the level of stumps retraction. In avulsion injuries, it is necessary to fix the tendon the attachment site using a screw or anchor [7, 29, 31]. Isolated popliteus reconstruction can be performed in PLC injuries with primary external rotation instability pattern. Furthermore, early and aggressive treatment of grade-3 PLC injuries and surgical reconstruction improve long-term outcomes. It prevents persistent instability, varus thrust, chronic pain, and accelerated cartilage damage [39].

Doucet et al. [12] presented a clinical case of a patient with acute calcific tendinopathy of the popliteus tendon. On ultrasound imaging, hypoechoic changes specific to tendinopathy and calcification in the tendon were seen. The patient underwent ultrasound-guided glucocorticoid injection with good clinical results.

Persistent instability and poor functional outcomes were observed in grade-3 PLC injuries that were treated non-operatively [14]. Thus, several PLC surgical reconstruction techniques were described in the literature [8, 20, 27]. Better results are obtained when PLC injuries are repaired or reconstructed in the

Figure 4. The varus stress test in full extension (**A**) and in 20–30° of knee flexion (**B**). The reverse pivot shift test with the knee flexed to 90° (**C**) and slowly extended (**D**); **E, F.** The external rotation recurvatum test; **G.** The dial test.

acute stage [41]. Shelbourne et al. [40] reported that repairing the PLC by 4 weeks post-injury resulted in significantly better outcome than a repair performed between 4 to 6 weeks post-injury.

Non-anatomic reconstruction aims to provide posterolateral stability by applying tension on the uninjured posterolateral structures (extracapsular iliotibial band sling, augmentation technique, bicep tenodesis) [41]. Anatomic reconstruction of the injured LCL, popliteus tendon and PFL is recommended [41]. The reconstructive procedures tend to be more anatomical to restore the knee biomechanics. Stannard et al. [44] and Levy et al. [28] reported lower reoperation rates after PLC reconstruction than PLC repair. Ahn et al. [1] described a novel arthroscopic technique for anatomical reconstruction of the posterolateral corner of the knee joint. This technique reconstructs three key components (LCL, popliteus tendon, PFL) of the posterolateral corner. To obtain better results in the future, surgical techniques that allow early rehabilitation should be developed [8].

SUMMARY

Popliteus is an essential structure to maintain the knee stability with its sophisticated anatomical and biomechanical features. Its disorders are often overlooked in complex knee injuries. On the other hand, the isolated injuries of popliteus are less frequent, occur mainly in athletes and are characterised by pain around the insertion to the femur, along the tendon and its attachments to the local structures. Thus, in some cases the symptoms can mimic the lateral meniscal tear. Moreover, the imbalance between quadriceps muscle and posterolateral structures can lead to the increase of the load on the popliteus tendon, which can be observed in basketball, tennis, and downhill running. Further studies are needed to improve diagnosis and treatment outcomes, especially in isolated popliteus tendon pathology.

Conflict of interest: None declared

REFERENCES

1. Ahn JH, Wang JHo, Lee SY, et al. Arthroscopic-assisted anatomical reconstruction of the posterolateral corner of the knee joint. Knee. 2019; 26(5): 1136–1142, doi: 10.1016/j.knee.2019.07.009, indexed in Pubmed: 31402094.
2. Aman ZS, DePhillipo NN, Storaci HW, et al. Quantitative and qualitative assessment of posterolateral meniscal anatomy: defining the popliteal hiatus, popliteomeniscal fascicles, and the lateral meniscotibial ligament. Am J Sports Med. 2019; 47(8): 1797–1803, doi: 10.1177/0363546519849933, indexed in Pubmed: 31136201.
3. Bartonícek J. Rare bilateral variation of the popliteus muscle: anatomical case report and review of the literature. bartonic@fnkv.cz. Surg Radiol Anat. 2005; 27(4): 347–350, doi: 10.1007/s00276-005-0328-5, indexed in Pubmed: 16228109.
4. Blake SM. Popliteus tendon tenosynovitis. Commentary. Br J Sports Med. 2005; 39(12): e42, doi: 10.1136/bjsm.2005.019349, indexed in Pubmed: 16306488.
5. Bonnin MP, de Kok A, Verstraete M, et al. Popliteus impingement after TKA may occur with well-sized prostheses. Knee Surg Sports Traumatol Arthrosc. 2017; 25(6): 1720–1730, doi: 10.1007/s00167-016-4330-8, indexed in Pubmed: 27671286.
6. Brown TR, Quinn SF, Wensel JP, et al. Diagnosis of popliteus injuries with MR imaging. Skeletal Radiol. 1995; 24(7): 511–514, doi: 10.1007/BF00202148, indexed in Pubmed: 8545647.
7. Burstein D, Fischer D. Isolated rupture of the popliteus tendon in a professional athlete. Arthroscopy. 1990; 6(3): 238–241, doi: 10.1016/0749-8063(90)90081-n.
8. Chahla J, Moatshe G, Dean CS, et al. Posterolateral corner of the knee: current concepts. Arch Bone Jt Surg. 2016; 4(2): 97–103, indexed in Pubmed: 27200384.
9. Chahla J, Murray IR, Robinson J, et al. Posterolateral corner of the knee: an expert consensus statement on diagnosis, classification, treatment, and rehabilitation. Knee Surg Sports Traumatol Arthrosc. 2019; 27(8): 2520–2529, doi: 10.1007/s00167-018-5260-4, indexed in Pubmed: 30478468.
10. Cottino U, Bruzzone M, Rosso F, et al. The role of the popliteus tendon in total knee arthroplasty: a cadaveric study: SIGASCOT Best Paper Award Finalist 2014. Joints. 2015; 3(1): 15–19, indexed in Pubmed: 26151034.
11. Crum JA, LaPrade RF, Wentorf FA. The anatomy of the posterolateral aspect of the rabbit knee. J Orthop Res. 2003; 21(4): 723–729, doi: 10.1016/S0736-0266(02)00250-4, indexed in Pubmed: 12798074.
12. Doucet C, Gotra A, Reddy SM, et al. Acute calcific tendinopathy of the popliteus tendon: a rare case diagnosed using a multimodality imaging approach and treated conservatively. Skeletal Radiol. 2017; 46(7): 1003–1006, doi: 10.1007/s00256-017-2623-8, indexed in Pubmed: 28303297.
13. Fanelli GC, Larson RV. Practical management of posterolateral instability of the knee. Arthroscopy. 2002; 18(2 Suppl 1): 1–8, doi: 10.1053/jars.2002.31779, indexed in Pubmed: 11828342.
14. Geeslin AG, LaPrade RF. Location of bone bruises and other osseous injuries associated with acute grade III isolated and combined posterolateral knee injuries. Am J Sports Med. 2010; 38(12): 2502–2508, doi: 10.1177/0363546510376232, indexed in Pubmed: 20837553.
15. Geeslin AG, Moulton SG, LaPrade RF. A Systematic Review of the Outcomes of Posterolateral Corner Knee Injuries, Part 1: Surgical Treatment of Acute Injuries. Am J Sports Med. 2016; 44(5): 1336–1342, doi: 10.1177/0363546515592828, indexed in Pubmed: 26260464.
16. Guha AR, Gorgees KA, Walker DI. Popliteus tendon rupture: a case report and review of the literature. Br J Sports Med. 2003; 37(4): 358–360, doi: 10.1136/bjsm.37.4.358, indexed in Pubmed: 12893726.
17. Huang GS, Yu JS, Munshi M, et al. Avulsion fracture of the head of the fibula (the "arcuate" sign): MR imaging findings predictive of injuries to the posterolateral ligaments and posterior cruciate ligament. AJR Am J Roentgenol. 2003; 180(2): 381–387, doi: 10.2214/ajr.180.2.1800381, indexed in Pubmed: 12540438.
18. Huri G, Biçer OS. Unusual cause of knee locking. Case Rep Orthop. 2013; 2013: 837140, doi: 10.1155/2013/837140, indexed in Pubmed: 23476852.
19. Jadhav SP, More SR, Riascos RF, et al. Comprehensive review of the anatomy, function, and imaging of the popliteus and associated pathologic conditions. Radiographics. 2014; 34(2): 496–513, doi: 10.1148/rg.342125082, indexed in Pubmed: 24617694.
20. Jakobsen BW, Lund B, Christiansen SE, et al. Anatomic reconstruction of the posterolateral corner of the knee: a case series with isolated reconstructions in 27 patients. Arthroscopy. 2010; 26(7): 918–925, doi: 10.1016/j.arthro.2009.11.019, indexed in Pubmed: 20620791.

21. Kannus P. Nonoperative treatment of grade II and III sprains of the lateral ligament compartment of the knee. Am J Sports Med. 1989; 17(1): 83–88, doi: 10.1177/036354658901700114, indexed in Pubmed: 2929843.
22. Kesman TJ, Kaufman KR, Trousdale RT. Popliteus tendon resection during total knee arthroplasty: an observational report. Clin Orthop Relat Res. 2011; 469(1): 76–81, doi: 10.1007/s11999-010-1525-z, indexed in Pubmed: 20809169.
23. Krudwig WK, Witzel U, Ullrich K. Posterolateral aspect and stability of the knee joint. II. Posterolateral instability and effect of isolated and combined posterolateral reconstruction on knee stability: a biomechanical study. Knee Surg Sports Traumatol Arthrosc. 2002; 10(2): 91–95, doi: 10.1007/s00167-001-0269-4, indexed in Pubmed: 11914766.
24. LaPrade RF, Gilbert TJ, Bollom TS, et al. The magnetic resonance imaging appearance of individual structures of the posterolateral knee. A prospective study of normal knees and knees with surgically verified grade III injuries. Am J Sports Med. 2000; 28(2): 191–199, doi: 10.1177/03635465000280020901, indexed in Pubmed: 10750995.
25. LaPrade RF, Heikes C, Bakker AJ, et al. The reproducibility and repeatability of varus stress radiographs in the assessment of isolated fibular collateral ligament and grade-III posterolateral knee injuries. An in vitro biomechanical study. J Bone Joint Surg Am. 2008; 90(10): 2069–2076, doi: 10.2106/JBJS.G.00979, indexed in Pubmed: 18829903.
26. LaPrade R, Ly T, Wentorf F, et al. The Posterolateral Attachments of the Knee. Am J Sports Med. 2017; 31(6): 854–860, doi: 10.1177/03635465030310062101.
27. LaPrade RF, Wozniczka JK, Stellmaker MP, et al. Analysis of the static function of the popliteus tendon and evaluation of an anatomic reconstruction: the "fifth ligament" of the knee. Am J Sports Med. 2010; 38(3): 543–549, doi: 10.1177/0363546509349493, indexed in Pubmed: 20042547.
28. Levy BA, Dajani KA, Morgan JA, et al. Repair versus reconstruction of the fibular collateral ligament and posterolateral corner in the multiligament-injured knee. Am J Sports Med. 2010; 38(4): 804–809, doi: 10.1177/0363546509352459, indexed in Pubmed: 20118498.
29. Liu JN, Rebolledo BJ, Warren RF, et al. Surgical management of isolated popliteus tendon injuries in paediatric patients. Knee Surg Sports Traumatol Arthrosc. 2016; 24(3): 788–791, doi: 10.1007/s00167-016-4029-x, indexed in Pubmed: 26856317.
30. De Maeseneer M, Shahabpour M, Vanderdood K, et al. Posterolateral supporting structures of the knee: findings on anatomic dissection, anatomic slices and MR images. Eur Radiol. 2001; 11(11): 2170–2177, doi: 10.1007/s003300100983, indexed in Pubmed: 11702156.
31. Mirkopulos N, Myer TJ. Isolated avulsion of the popliteus tendon. A case report. Am J Sports Med. 1991; 19(4): 417–419, doi: 10.1177/036354659101900419, indexed in Pubmed: 1897662.
32. Nakhostine M, Perko M, Cross M. Isolated avulsion of the popliteus tendon. J Bone Joint Surg Br. 1995; 77(2): 242–244, indexed in Pubmed: 7706338.
33. Nyland J, Lachman N, Kocabey Y, et al. Anatomy, function, and rehabilitation of the popliteus musculotendinous complex. J Orthop Sports Phys Ther. 2005; 35(3): 165–179, doi: 10.2519/jospt.2005.35.3.165, indexed in Pubmed: 15839310.
34. Paraskevas G, Papaziogas B, Kitsoulis P. A study on the morphology of the popliteus muscle and arcuate popliteal ligament. Folia Morphol. 2006; 65(4): 381–384, indexed in Pubmed: 17171619.
35. Peduto AJ, Nguyen A, Trudell DJ, et al. Popliteomeniscal fascicles: anatomic considerations using MR arthrography in cadavers. Am J Roentgenol. 2008; 190(2): 442–448, doi: 10.2214/AJR.07.2643, indexed in Pubmed: 18212231.
36. Petsche TS, Selesnick FH. Popliteus tendinitis: tips for diagnosis and management. Phys Sportsmed. 2002; 30(8): 27–31, doi: 10.3810/psm.2002.08.401, indexed in Pubmed: 20086537.
37. Porrino J, Sharp JW, Ashimolowo T, et al. An update and comprehensive review of the posterolateral corner of the knee. Radiol Clin North Am. 2018; 56(6): 935–951, doi: 10.1016/j.rcl.2018.06.006, indexed in Pubmed: 30322491.
38. Quinlan JF, Webb S, McDonald K, et al. Isolated popliteus rupture at the musculo-tendinous junction. J Knee Surg. 2011; 24(2): 137–140, doi: 10.1055/s-0031-1275397, indexed in Pubmed: 21874950.
39. Rosas HG. Unraveling the posterolateral corner of the knee. Radiographics. 2016; 36(6): 1776–1791, doi: 10.1148/rg.2016160027, indexed in Pubmed: 27726747.
40. Shelbourne KD, Haro MS, Gray T. Knee dislocation with lateral side injury: results of an en masse surgical repair technique of the lateral side. Am J Sports Med. 2007; 35(7): 1105–1116, doi: 10.1177/0363546507299444, indexed in Pubmed: 17379923.
41. Shon OJ, Park JW, Kim BJ. Current concepts of posterolateral corner injuries of the knee. Knee Surg Relat Res. 2017; 29(4): 256–268, doi: 10.5792/ksrr.16.029, indexed in Pubmed: 29172386.
42. Simonnet ML, Rooze M, Feipel V. The proximal attachments of the popliteus muscle: a quantitative study and clinical significance. Surg Radiol Anat. 2003; 25(1): 58–63, doi: 10.1007/s00276-002-0093-7, indexed in Pubmed: 12677465.
43. Song Y, Xiong Y, Chen W, et al. Sectional anatomy and three-dimensional visualization of the posterolateral complex of the knee joint based on undeformed high-resolution sectional anatomical images. Anat Rec (Hoboken). 2018; 301(10): 1764–1773, doi: 10.1002/ar.23926, indexed in Pubmed: 30383338.
44. Stannard JP, Brown SL, Farris RC, et al. The posterolateral corner of the knee: repair versus reconstruction. Am J Sports Med. 2005; 33(6): 881–888, doi: 10.1177/0363546504271208, indexed in Pubmed: 15827360.
45. Takahashi A, Sugita T, Aizawa T, et al. Potential risk of excising the femoral insertion of the popliteus tendon during primary total knee arthroplasty: a biometric study. J Orthop Sci. 2015; 20(6): 1030–1035, doi: 10.1007/s00776-015-0773-x, indexed in Pubmed: 26362655.
46. Takeda S, Tajima G, Fujino K, et al. Morphology of the femoral insertion of the lateral collateral ligament and popliteus tendon. Knee Surg Sports Traumatol Arthrosc. 2015; 23(10): 3049–3054, doi: 10.1007/s00167-014-3059-5, indexed in Pubmed: 24839040.
47. Takubo A, Ryu K, Iriuchishima T, et al. The evaluation of the distance between the popliteus tendon and the lateral collateral ligament footprint and the implant in Total knee Arthroplasty using a 3-dimensional template. BMC Musculoskelet Disord. 2020; 21(1): 322, doi: 10.1186/s12891-020-03347-6, indexed in Pubmed: 32443975.
48. Taylor G, Bonney V. On the homology and morphology of the popliteus muscle: a contribution to comparative myology. J Anat Physiol. 1905; 40(Pt 1): 34–50, indexed in Pubmed: 17232661.
49. Tria AJ, Johnson CD, Zawadsky JP. The popliteus tendon. J Bone Joint Surg Am. 1989; 71(5): 714–716, indexed in Pubmed: 2732260.
50. Yang JH, Lim HC, Bae JiH, et al. Anatomic and isometric points on femoral attachment site of popliteus muscle-tendon complex for the posterolateral corner reconstruction. Knee Surg Sports Traumatol Arthrosc. 2011; 19(10): 1669–1674, doi: 10.1007/s00167-011-1442-z, indexed in Pubmed: 21328069.

VIA MEDICA

ORIGINAL ARTICLE

Folia Morphol.
Vol. 80, No. 3, pp. 514–519
DOI: 10.5603/FM.a2020.0095

ISSN 0015–5659
eISSN 1644–3284
journals.viamedica.pl

Is amygdala size correlated with stress?

M. Canbolat[1], M.F. Erbay[2], D. Şenol[1], C. Uçar[3], S. Yıldız[4]

[1]*Department of Anatomy, İnönü University, Malatya, Turkey*
[2]*Department of Radiology, İnönü University, Malatya, Turkey*
[3]*Department of Physiology, Adıyaman University, Adıyaman, Turkey*
[4]*Department of Physiology, İnönü University, Malatya, Turkey*

[Received: 18 June 2020; Accepted: 10 August 2020; Early publication date: 14 August 2020]

Background: *One of the important mechanisms that regulate the stress response of the body is hypothalamic pituitary adrenal axis. One of the structures activating this axis is amygdala. We have seen people around who react calmer and cooler to very stressful situations. Are people with smaller amygdala really calmer? Or, can we say that the bigger the amygdala, which is the trigger of the body's response to stress, the more a person panics? Aim of the study is to compare the saliva cortisol levels and amygdala volume.*
Materials and methods: *Study conducted with 63 male students. Magnetic resonance images of students were taken before their final exam to calculate amygdala volumes. Saliva samples of all students were taken two times to detect cortisol levels in saliva. First one was 20 days before the final exam and second one was on the exam day. We assumed that the students were stressful on exam day.*
Results and Conclusions: *No statistically significant correlation was found between saliva cortisol levels and amygdala volume in the study.* (Folia Morphol 2021; 80, 3: 514–519)

Key words: amygdala volume, saliva cortisol, stress, magnetic resonance images

INTRODUCTION

One of the most basic problems of today's human beings is stress. Stress, which is defined as the sensual tension [2, 35] that occurs as a result of the deterioration of physiological and spiritual well-being of the organism due to environmental factors, has negative influences on individuals' self-respect and productivity. Since stress plays a significant role in the occurrence of many diseases, one of the most important goals of health professionals is to eliminate stress and if this is not possible, to manage stress [22]. The response given by organism to stress in acute period is a useful tool that activates the resources of the organism to protect it against a dangerous situation [26]. Low levels of stress can even be instructional for the organism and can cause the organism to find new solutions to a problem [27]. What causes distress is the persistence and chronicity of stress. While acute and low intensity stress is useful for a person, chronic stress damages cognitive functions and neurological structures such as the hippocampus [10, 20].

One of the important mechanisms that regulate the stress response of the body in case of a stressful situation is hypothalamic pituitary adrenal axis (HPA axis) [29]. The function of HPA axis is sensing the external stimulus, assessing the stimulus and creating

Address for correspondence: Dr. M. Canbolat, Department of Anatomy, İnönü University Faculty of Medicine, 44280 Malatya, Turkey, tel: +090 5056682547, fax: +090 4223410036, e-mail: mustafa.canbolat@inonu.edu.tr

a fight-or-run response, completing the fight in the shortest time possible and bringing the organism back to its normal state. One of the structures activating this axis is amygdala. Amygdala is an almond-shaped subcortical structure in the temporal region of our brain. Amygdala, which is part of the limbic system, assesses the sensory direction of the external stimulus [31]. In addition, it realizes the activation or inhibition of responses like fear and anxiety [18]. It protects the organism from danger and enables its survival. It plays an active role in triggering emotions against external stimuli [32]. Amygdala assesses every situation and every object and makes this assessment roughly with questions such as "is it something that I like?", "can this harm me?", and if it is accepted as dangerous as a result of the assessment, amygdala starts the crisis situation. Long before an external sensory stimulus reaches the cortex after being filtered from the thalamus; it reaches the amygdala in a much faster way. By the time the sense has reached the cortex and has been assessed, amygdala has already started the process [16, 21]. When amygdala that has sensed the danger is activated, it sends a signal to hypothalamus and corticotrophin releasing factor (CRF) is released from the hypothalamus. CRF causes the pituitary to release adrenocorticotropic hormone (ACTH) and ACTH enables cortisol release from adrenal gland [11]. Cortisol regulates the physiological response of the organism against stress.

The thought that there might be an association between amygdala size and responses given under stress does not seem to be unreasonable because stimulating the amygdala causes fear and anxiety. We have seen people around who react calmer and cooler to very stressful situations. Are people with smaller amygdala really calmer? Or, can we say that the bigger the amygdala, which is the trigger of the body's response to stress, the more a person panics? In our study, our aim was to compare the saliva cortisol levels of healthy university students exposed to the same stressor and their amygdala size in order to find an answer to this question.

MATERIALS AND METHODS

Ethical approval for our study was obtained from the Malatya Clinical Researches Ethical Board (No. 2018/111). The participants in our study were informed about the study and they read and signed the informed consent form. We conducted our study with 63 male students from İnönü University, Faculty of Medicine who were not using cigarette, alcohol or drugs, who did not have any psychological disease, who did not have any seizures in childhood and later, who did not have any head trauma or surgical operation and who were right-handed. Median age of students were 21 (min: 19, max: 27) years.

We accepted 20 days before the final exam as relaxed period. Exam day is accepted as stressed period. We assumed that the students were stressed on exam day. To support this idea we used cortisol levels and State Trait Anxiety Inventory-I (STAI-I). The STAI-I was given to students during relaxed and stressed periods. Also saliva samples were taken during relaxed and stressed periods to detect cortisol levels in saliva. The STAI-I is one of the common scales to assess anxiety [4]. According to STAI-I, $\leq$ 36 points means "no anxiety", 37–42 points means "mild anxiety", $\geq$ 42 points means "high anxiety".

Neuroimaging

We got the magnetic resonance (MR) images of students a day before exam. 3T Siemens scanner (Skyra syngo MR E11 version, Germany) was used for neuroimaging. T1-weighted three-dimensional (3D) (MPRAGE) sequence was used in sagittal plane to get structural images and the following parameters were used: TE/TR: 2300 ms/2.32 s, flip angle: 8°, field of view: 240 mm^2, slice thickness: 0.9 mm. MR T1 data was downloaded from the scanner and by using different software, they were transferred and processed. MR images were kept in hdr and img formats. To do this, a personal computer on a 32-bit Dell PC, running Windows 10 operating system was used. Volume was calculated with mricloud (www.mricloud.org). Installation, configuration or training are not required to use the web based module. Through a web interface, mricloud volumetric analysis system functions remotely to provide a report including volumetric information from any submitted case.

Analysis saliva cortisol

Saliva samples of all students were taken before they entered the exam. Saliva samples were collected by using passive drool method [8]. Samples collected were kept in a laboratory freezer at –20°C. After thawing, the samples were centrifuged for 10 min at 4000 g and enzyme-linked immunosorbent assay (ELISA) analyses were conducted by using the supernatant.

Table 1. Values of cortisol levels and State Trait Anxiety Inventory-I (STAI-I) scores of volunteers

Variables	Relaxed		Stressed		P
	Median	Minimum–Maximum	Median	Minimum–Maximum	
Cortisol levels	8.34	2.87–24.16	15.45	2.99–122.78	0.000
STAI-I score	32	21–68	58	24–71	0.000

Table 2. Correlation analysis of amygdala volumes with cortisol level differences and State Trait Anxiety Inventory-I (STAI-I) score differences between relaxed and stressed periods

Variables	Test statistics	Cortisol difference	STAI-I score difference
Right amygdala volume	r	–0.120	0.120
	p	0.350	0.351
Left amygdala volume	r	–0.156	0.136
	p	0.222	0.287
Total amygdala volume	r	–0.146	0.120
	p	0.253	0.347

Table 3. Numbers of volunteers in relaxed and stressed periods according to State Trait Anxiety Inventory-I (STAI-I) scores

Period	STAI-I scores		
	< 36 (no anxiety)	37–42 (mild anxiety)	> 42 (high anxiety)
Relaxed	35 (55.6%)	19 (30.1%)	9 (14.3%)
Stressed	4 (6.3%)	6 (9.6%)	53 (84.1%)

All samples were diluted at 1:5 and assayed in triplicate by using the assay buffer. Carbonate buffer, pH 9.6 was used to dilute cortisol-bovine serum albumin stock solution (1 mg/mL) by ELISA procedure and this was added to 96-well microtiter plate at 200 μL/well. Later, the microtiter plate was incubated at +4°C for a night and washed 5 times with washing buffer by using an 8-channel pipette. Some of the binding places that did not include coating antigen were blocked for 2 hours at 37°C with blocking buffer (200 μL//well). Following the process of washing, diluted first Ab (antiserum) (40 μL/well) and standard solutions or samples (40 μL/well) were placed in duplicate and incubated at 37°C for 45 min. After the washing process, biotinylated anti-rabbit antibody (100 μL/well) was added and the plate was incubated at 37°C for 30 min. After washing for 5 times, Streptavidin peroxidase solution (100 μL/well) was added and the plate was incubated for 15 min at +4°C. Following another 5 times of washing, substrate solution (150 μL/well) was added to the plate and incubated in dark for 10 min. Following incubation, stop solution (50 μL/well) was also added and absorbance was measured at 450 nm by using the microplate reader. Inter-assay variation was found to be 7.8%, while inter-assay coefficients of variation was 5.6%.

Statistical analysis

Kolmogorov-Smirnov test was used to find out whether the data were normally distributed. The Wilcoxon paired-samples test was used to analyse the data which were not normally distributed. Spearman Rho correlation analysis was conducted on the data to find out how the cortisol level differed with amygdala volume and STAI-I scores. Minimum (min) and maximum (max) values of data which were not normally distributed were given with median. Mann-Whitney U test was performed to compare the right and left amygdala volumes. $P < 0.05$ values were considered as statistically significant. IBM SPSS Statistics 22.0 for Windows program was used in statistical analyses.

RESULTS

The median value of saliva cortisol increased in stressed period. Also STAI-I score increased in stressed period. The Wilcoxon paired-samples test was conducted on data and statistically significant increase was found in relaxed and stressed period saliva cortisol and STAI-I scores (Table 1).

As a result of Spearman rho correlation analysis of amygdala volumes and difference in cortisol values between relaxed period and stressed period, it was found that there was no correlation. Also there was no correlation between amygdala volumes and STAI-I score differences of relaxed and stressed periods (Table 2).

For the STAI-I score, there is a decrease in numbers of "no anxiety" and "mild anxiety" volunteers in stressed period compared to relax period. But there is a high increase in stressed period for the numbers of "high anxiety" volunteers compared to relax period (Table 3).

Table 4. Right, left and total amygdala volumes of volunteers

Variables	Amygdala volume [mm³]	P
Right amygdala	1974 (1533–2356)	0.000
Left amygdala	1781 (1480–2063)	
Total amygdala	3681 (3055–4349)	

Median value of the right amygdala volume of our volunteers was found as 1974 (1533–2356) mm^3, while the median value of their left amygdala volume was 1781 (1480–2063) mm^3. Median value of total amygdala volume of our volunteers was found 3681 (3055–4349) mm^3. Mann-Whitney U test was conducted on the data to find out whether the difference was significant. We found a statistically significant difference between the volumes of right and left amygdala (Table 4).

DISCUSSION AND CONCLUSIONS

For a high efficiency from personnel working in occupations with high stress; mainly security staff, surgeons and athletes; individuals need to be able to cope with these stressful situations. Of course, it is important to show quantitatively at the beginning of personnel choice whether the individual has such an ability. We conducted this study with the thought that we could obtain a parameter in the detection of personnel to be employed in the aforementioned stressful fields if we could find an association between amygdala volume and cortisol level.

In our study, we received the saliva cortisol level as an indicator of stress. As mentioned above, the ultimate product of the HPA axis, which is activated as a result of stress, is cortisol that is released in the circulation [17]. Cortisol level in saliva reflects the serum cortisol level [5, 13]. We chose to use saliva cortisol as an indicator of stress due to reasons such as its being non-invasive, not putting the samples in an extra stress and the ease of taking samples.

As a result of our study, we could not find an association between amygdala size and cortisol values we obtained from the samples as a quantitative parameter. In studies conducted, a big amygdala size has been associated with increased anxiety [1], being sensitive to negative experiences [6] and negative affectivity [9]. On the other hand, studies conducted in patients with unipolar depressive disorder have not shown a significant association between amygdala size and basal cortisol release [12, 25]. In another study conducted in patients with major depression, a positive correlation was found between amygdala size and average cortisol level [19]. In another study, a correlation was found between amygdala activities of university students exposed to the same stressor and the environment they lived in. While the bigger and more stressful place individuals lived in the more amygdala activity they had, subjects who lived in rural areas were found to have low amygdala activity [15]. Being exposed to the same stressor but responding differently can also be associated with amygdala size. In a study conducted with healthy female children, a positive correlation was found between fear and amygdala size [33]. In a study conducted on children who spent the first 2 years of their lives in an orphanage and who were exposed to abuse, amygdalae of these children were found to be big [30]. Observationally, individuals dealing with religious, mystic and meditative disciplines have a general state of calmness. In another study conducted, it has been put forward that meditation and yoga were associated with smaller amygdala [7].

Generally, studies conducted on patient groups have given different results. The common characteristic of these patient groups is having a chronic stress state. Exposition to this long-term stress, mostly since childhood, causes damages in limbic system structures such as amygdala [34] and hippocampus which have glucocorticoid receptor on them. However, our study was conducted on completely healthy young adults and the purpose of the study was to compare the cortisol level released against sudden stress and amygdala size.

Volumetric measurements have gained importance through imaging techniques. Symmetry or asymmetry of neuroanatomical structures distributed to both hemispheres is used as a prediction tool for clinicians in pathological processes [3]. An asymmetry is mentioned in the literature between right and left amygdala in terms of both function and size. In a meta-analysis [23] which examined 82 studies conducted on healthy individuals between 1990 and 2002 showed that the right amygdala size was bigger than that of the left amygdala. In our study, we found the right amygdala size statistically significantly bigger than that of the left hemisphere.

State-TraitAnxiety Inventory is one of the most used scales to assess anxiety. Anxiety has two components: state anxiety and trait anxiety [4]. In contrast trait anxiety, state anxiety shows psychological and physiological transient reactions directly associated with adverse situations at the given time [14]. So, we used state part of STAI to see anxiety scores of volunteers before exam. Occasional anxiety is part of life. People can feel anxious when faced with problems in work/school, before tests, before taking important decisions. Our volunteers got high anxiety scores before exam. Our findings are in line with the studies about exam stress [24, 28].

Conflict of interest: None declared

REFERENCES

1. Baur V, Hänggi J, Jäncke L. Volumetric associations between uncinate fasciculus, amygdala, and trait anxiety. BMC Neurosci. 2012; 13: 4, doi: 10.1186/1471-2202-13-4, indexed in Pubmed: 22217209.
2. Beheshtifar M, Hoseinifar H, Moghadam M. Effect procrastination on work-related stress. Eur J Econ Finance Admin Sci. 2011; 38: 59–64.
3. Duboc V, Dufourcq P, Blader P, et al. Asymmetry of the brain: development and implications. Annu Rev Genet. 2015; 49: 647–672, doi: 10.1146/annurev-genet-112414-055322, indexed in Pubmed: 26442849.
4. Fernández-Blázquez MA, Ávila-Villanueva M, López-Pina JA, et al. Psychometric properties of a new short version of the State-Trait Anxiety Inventory (STAI) for the assessment of anxiety in the elderly. Neurologia. 2015; 30(6): 352–358, doi: 10.1016/j.nrl.2013.12.015, indexed in Pubmed: 24484757.
5. Gatti R, Antonelli G, Prearo M, et al. Cortisol assays and diagnostic laboratory procedures in human biological fluids. Clin Biochem. 2009; 42(12): 1205–1217, doi: 10.1016/j.clinbiochem.2009.04.011, indexed in Pubmed: 19414006.
6. Gerritsen L, Rijpkema M, van Oostrom I, et al. Amygdala to hippocampal volume ratio is associated with negative memory bias in healthy subjects. Psychol Med. 2012; 42(2): 335–343, doi: 10.1017/S003329171100122X, indexed in Pubmed: 21740626.
7. Gotink RA, Vernooij MW, Ikram MA, et al. Meditation and yoga practice are associated with smaller right amygdala volume: the Rotterdam study. Brain Imaging Behav. 2018; 12(6): 1631–1639, doi: 10.1007/s11682-018-9826-z, indexed in Pubmed: 29417491.
8. Granger DA, Kivlighan KT, el-Sheikh M, et al. Salivary alpha-amylase in biobehavioral research: recent developments and applications. Ann N Y Acad Sci. 2007; 1098: 122–144, doi: 10.1196/annals.1384.008, indexed in Pubmed: 17332070.
9. Holmes AJ, Lee PH, Hollinshead MO, et al. Individual differences in amygdala-medial prefrontal anatomy link negative affect, impaired social functioning, and polygenic depression risk. J Neurosci. 2012; 32(50): 18087–18100, doi: 10.1523/JNEUROSCI.2531-12.2012, indexed in Pubmed: 23238724.
10. Kim EJ, Pellman B, Kim JJ. Stress effects on the hippocampus: a critical review. Learn Mem. 2015; 22(9): 411–416, doi: 10.1101/lm.037291.114, indexed in Pubmed: 26286651.
11. Koob GF. The role of CRF and CRF-related peptides in the dark side of addiction. Brain Res. 2010; 1314: 3–14, doi: 10.1016/j.brainres.2009.11.008, indexed in Pubmed: 19912996.
12. Kronenberg G, Tebartz van Elst L, Regen F, et al. Reduced amygdala volume in newly admitted psychiatric in-patients with unipolar major depression. J Psychiatr Res. 2009; 43(13): 1112–1117, doi: 10.1016/j.jpsychires.2009.03.007, indexed in Pubmed: 19394960.
13. Kudielka B, Hellhammer DH, Wüst S. Why do we respond so differently? Reviewing determinants of human salivary cortisol responses to challenge. Psychoneuroendocrinology. 2009; 34(1): 2–18, doi: 10.1016/j.psyneuen.2008.10.004.
14. Leal PC, Goes TC, da Silva LC, et al. Trait vs. state anxiety in different threatening situations. Trends Psychiatry Psychother. 2017; 39(3): 147–157, doi: 10.1590/2237-6089-2016-0044, indexed in Pubmed: 28813110.
15. Lederbogen F, Kirsch P, Haddad L, et al. City living and urban upbringing affect neural social stress processing in humans. Nature. 2011; 474(7352): 498–501, doi: 10.1038/nature10190, indexed in Pubmed: 21697947.
16. LeDoux J. The emotional brain, fear, and the amygdala. Cell Mol Neurobiol. 2003; 23(4-5): 727–738, doi: 10.1023/a:1025048802629, indexed in Pubmed: 14514027.
17. Lee DoY, Kim E, Choi MHo. Technical and clinical aspects of cortisol as a biochemical marker of chronic stress. BMB Rep. 2015; 48(4): 209–216, doi: 10.5483/bmbrep.2015.48.4.275, indexed in Pubmed: 25560699.
18. Lee SC, Amir A, Haufler D, et al. Differential recruitment of competing valence-related amygdala networks during anxiety. Neuron. 2017; 96(1): 81–88.e5, doi: 10.1016/j.neuron.2017.09.002, indexed in Pubmed: 28957678.
19. Malykhin N, Travis S, Sereshki A, et al. 132. Effects of cortisol on hippocampal subfields and centromedial amygdala volumes in healthy subjects and patients with major depressive disorder. Biol Psychiatry. 2018; 83(9): S54, doi: 10.1016/j.biopsych.2018.02.150.
20. Marin MF, Lord C, Andrews J, et al. Chronic stress, cognitive functioning and mental health. Neurobiol Learn Mem. 2011; 96(4): 583–595, doi: 10.1016/j.nlm.2011.02.016, indexed in Pubmed: 21376129.
21. Morris JS, Ohman A, Dolan RJ. A subcortical pathway to the right amygdala mediating "unseen" fear. Proc Natl Acad Sci U S A. 1999; 96(4): 1680–1685, doi: 10.1073/pnas.96.4.1680, indexed in Pubmed: 9990084.
22. Özel Y, Karabulut AB. Daily living and stress management. Turkish J Health Sci Res. 2018; 1(1): 48–56.
23. Pedraza O, Bowers D, Gilmore R. Asymmetry of the hippocampus and amygdala in MRI volumetric measurements of normal adults. J Int Neuropsychol Soc. 2004; 10(5): 664–678, doi: 10.1017/S1355617704105080, indexed in Pubmed: 15327714.
24. Ping LT, Subramaniam K, Krishnaswamy S. Test anxiety: state, trait and relationship with exam satisfaction. Malays J Med Sci. 2008; 15(2): 18–23, indexed in Pubmed: 22589620.
25. Schuhmacher A, Mössner R, Jessen F, et al. Association of amygdala volumes with cortisol secretion in unipolar depressed patients. Psychiatry Res. 2012; 202(2): 96–103,

doi: 10.1016/j.pscychresns.2011.09.007, indexed in Pubmed: 22698761.
26. Sharma D. Physiology of stress and its management. J Med Study Res. 2018; 1(1): 1–5, doi: 10.24966/msr-5657/100001.
27. Sharma M, Rush SE. Mindfulness-based stress reduction as a stress management intervention for healthy individuals: a systematic review. J Evid Based Complementary Altern Med. 2014; 19(4): 271–286, doi: 10.1177/2156587214543143, indexed in Pubmed: 25053754.
28. Spangler G. Psychological and physiological responses during an exam and their relation to personality characteristics. Psychoneuroendocrinology. 1997; 22(6): 423–441, doi: 10.1016/s0306-4530(97)00040-1.
29. Spiga F, Walker JJ, Terry JR, et al. HPA axis-rhythms. Compr Physiol. 2014; 4(3): 1273–1298, doi: 10.1002/cphy.c140003, indexed in Pubmed: 24944037.
30. Tottenham N, Hare TA, Quinn BT, et al. Prolonged institutional rearing is associated with atypically large amygdala volume and difficulties in emotion regulation. Dev Sci. 2010; 13(1): 46–61, doi: 10.1111/j.1467-7687.2009.00852.x, indexed in Pubmed: 20121862.
31. Tottenham N, Sheridan MA. A review of adversity, the amygdala and the hippocampus: a consideration of developmental timing. Front Hum Neurosci. 2009; 3: 68–77, doi: 10.3389/neuro.09.068.2009, indexed in Pubmed: 20161700.
32. Tufan AE, Yaluğ İ. Love phenomenon and neurobiology of love relations. Curr App Psychiatry. 2010; 2(4): 443–456.
33. van der Plas EAA, Boes AD, Wemmie JA, et al. Amygdala volume correlates positively with fearfulness in normal healthy girls. Soc Cogn Affect Neurosci. 2010; 5(4): 424–431, doi: 10.1093/scan/nsq009, indexed in Pubmed: 20150341.
34. Wang Q, Verweij EWE, Krugers HJ, et al. Distribution of the glucocorticoid receptor in the human amygdala; changes in mood disorder patients. Brain Struct Funct. 2014; 219(5): 1615–1626, doi: 10.1007/s00429-013-0589-4, indexed in Pubmed: 23748930.
35. Yıldız M, Güç K, Erdem S. Examine attitudes to cope with stress in terms of human values: a study on public employees. Sci J Turkish Military Academy. 2015; 25(1): 41–61.

VIA MEDICA

ORIGINAL ARTICLE

Folia Morphol.
Vol. 80, No. 3, pp. 520–526
DOI: 10.5603/FM.a2020.0096

ISSN 0015–5659
eISSN 1644–3284
journals.viamedica.pl

Is the middle cerebral artery bifurcation aneurysm affected by morphological parameters of bifurcation?

T. Benlice[1], A. Idil Soylu[1], Ö. Zel Terzi[2], F. Uzunkaya[1], H. Akan[1]

[1]Department of Radiology, OndokuzMayis University, Faculty of Medicine, Samsun, Turkey
[2]Department of Public Health, OndokuzMayis University, Faculty of Medicine, Samsun, Turkey

[Received: 10 June 2020; Accepted: 25 June 2020; Early publication date: 14 August 2020]

Background: *Aneurysm formation is a multifactorial process involving genetic, anatomical and environmental risk factors. A research focusing on the relationship between the presence of aneurysm and the morphology of the arteries will help in the pathogenesis and prediction of intracranial aneurysms. In this study, the relationship between the presence of aneurysm and various morphological parameters of aneurysm-related arteries was evaluated in patients with saccular middle cerebral artery (MCA) bifurcation aneurysm.*

Materials and methods: *The archival images of 74 patients (62.2% women) were evaluated retrospectively. In this study, the angle between the ipsilateral MCA M1 segment and the dominant truncus (Φ1), the angle between the M1 segment and the recessive truncus (Φ2), and the bifurcation angle (Φ1 + Φ2) were compared. Bilateral internal carotid artery (ICA), MCA M1 segment, dominant and recessive truncus diameters and these diameters ratios were compared with the aneurysmal side and the contralateral side without aneurysm.*

Results: *When the dominant truncus, recessive truncus angles and bifurcation angle were compared, a significant difference was found on the aneurysmal side ($p < 0.0001$). In the receiver operating characteristic analysis, when the bifurcation angle of 147.5° was accepted as the limit value, 78.4% sensitivity, 79.7% specificity, 79.5% positive predictive value and 78.7% negative predictive value were determined (area under the curve: 0.85).*

Conclusions: *Our study of the morphological features of arteries associated with MCA bifurcation aneurysms showed that the presence of MCA aneurysms was significantly associated with large bifurcation angles.* (Folia Morphol 2021; 80, 3: 520–526)

Key words: intracranial aneurysm, bifurcation morphology, haemodynamic changes

INTRODUCTION

Saccular intracranial aneurysms (IA) are potentially life-threatening vascular lesions. Due to the increase in the use of imaging techniques, 3–6% of the aneurysms can be detected during the non-ruptured stage [22]. Bifurcation of the middle cerebral artery (MCA), which is one of the most common localisations of IA, accounts for approximately 20% of all IAs [6]. Although many studies have been conducted on the

Address for correspondence: A. Idil Soylu, MD, OndokuzMayis University, Faculty of Medicine, Department of Radiology, 55139 Samsun, Turkey, tel: +90 362 3121919, fax: +90 362 4577146, e-mail: a.isoylu@gmail.com

pathogenesis and localisation of IAs, the factors associated with aneurysm are still poorly understood.

Aneurysm formation is a multifactorial process involving genetic, anatomical and environmental risk factors. Familial inheritance and environmental factors such as smoking, alcohol use, hyperlipidaemia and hypertension increase the risk of IA development [9, 17, 21]. In addition to genetic and environmental factors, arterial morphology is thought to play an important role in aneurysm formation. Haemodynamic stress in the arterial bifurcation region can trigger aneurysm formation by triggering focal degenerative mechanisms in the vessel wall. Therefore, a research focusing on the relationship between the presence of aneurysm and the morphology of the arteries will help in the pathogenesis and prediction of IAs [23].

In this study, the relationship between the morphological parameters of the arteries around the aneurysm and the presence of aneurysm in patients with MCA bifurcation aneurysm was evaluated by comparing with the normal contralateral side.

MATERIALS AND METHODS

This study was approved by the institutional ethics committee. The requirement of informed consent was waived, as this was a retrospective study.

Study population

Between July 2015 and December 2018, patients who underwent brain computed tomography angiography (CTA) for cerebral aneurysm or subarachnoid haemorrhage in our hospital were retrospectively analysed. One hundred and nine patients with MCA aneurysm were selected for the study. Thirty five patients were excluded from the study: 10 patients with artefact images, 1 patient with severe atherosclerotic stenosis in internal carotid artery (ICA), 6 patients with bilateral aneurysm, 4 patients with trifurcation in MCA, 3 patients with severe vasospasm due to subarachnoid haemorrhage, 2 patients with M3 segment aneurysm and 9 patients with M1 segment aneurysm. Finally, 74 patients were included in the study. In order to minimise the effect of genetic and environmental risk factors on the development of aneurysm, the aneurysmal side and the contralateral side without aneurysm were compared in the same patient. We excluded patients with trifurcation due to the very low number of patients.

CTA examinations

Multidetector computed tomography (MDCT) shots were performed with Light Speed 64 General Electric Discovery CT750HD 2015 (Milwaukee, Wisconsin, USA). After 60–100 mL Optiray (Dublin, Ireland), a non-ionic contrast agent, was administered at a rate of 3.5 mL/s; arterial phase cranial images with slice thickness of 0.625 mm, 120 kV, 400–500 mA, pitch 0.98 and rotation time 0.4 s were obtained from the skull base level to the vertex at 25 s.

Image interpretation

Image interpretation was performed using a workstation with OsiriX-64 bit software (Lite Digital Imaging and Communications in Medicine Viewer, version 5.6, Geneva, Switzerland). Images were examined independently by 2 radiologists. An interventional radiologist (A.I.S.) with 17 years of experience and a senior radiology resident (T.B., 5th year radiology resident) performed image interpretation. Multiplanar reformat series were reconstructed for each dataset. Axial, coronal, and sagittal reformatted images were interpreted as maximum intensity projections with 10 mm slice thickness and volume rendering techniques.

The definitions and measuraments of morphological parameters

Morphological measurements of the ICA supraclinoid segment, MCA M1 segment, dominant truncus and recessive truncus were taken. Aneurysmal bifurcation and non-aneurysmal contralateral MCA bifurcation were compared in terms of proximal and distal artery diameters, rates of these diameters, and bifurcation angles.

The MCA was segmented into three parts, M1 (originating from the terminal bifurcation of the ICA and terminating at the MCA bifurcation), dominant and recessive truncus (originating at the MCA bifurcation and terminating cerebral cortex). The larger trunk was considered the dominant trunk. ICA supraclinoid segment, MCA M1 segment, dominant truncus and recessive truncus diameters were measured on multiplanar reconstruction images. ICA supraclinoid segment diameter was measured 5 mm proximal to the ICA apex, MCA M1 segment diameter was measured 5 mm proximal to the bifurcation apex; superior and inferior truncus diameters were measured 5 mm proximal to the bifurcation apex. After adjusting the planes parallel to the axis of the artery in the sagittal and coronal planes, the diameter was measured in the axial plane. Where the shape of the vessel appears closest to the circle in a plane perpendicular to the diameter flow axis, it was averaged by measuring from 3 or 4 different axes.

In this study, the ratio of M1 diameter to the sum of the dominant and recessive truncus diameters was defined as DA, the ratio of upper truncus diameter to lower truncus diameter as KA, the ratio of dominant truncus diameter to M1 segment diameter as BA, the ratio of recessive truncus diameter to M1 segment diameter as CA and the ratio of M1 diameter to ICA diameter as LA.

The angle between the MCA M1 segment and the dominant truncus was called Φ1 and the angle between the MCA M1 segment and the recessive truncus was Φ2. The sum of the angles Φ1 and Φ2 was defined as the bifurcation angle. In each patient, the M1 segment plane continued laterally on the sagittal planes. The angle between this plane and the corresponding truncus plane was measured by angle measurement tool of the software. Φ1, Φ2 and bifurcation angle were recorded.

Interobserver reproducibility was evaluated in 15 randomly selected subjects. The mean interobserver difference was 0.06 ± 0.39% (95% limits of agreement), the mean intraobserver difference was 0.05 ± 0.32% (95% limits of agreement).

Statistical analysis

Statistical Package for Social Sciences for Windows, version 22 (SPSS Inc., Chicago, IL, USA) was used for statistical analysis. For the analysis of bifurcations, it was divided into two categories as the aneurysmal side and the contralateral side without aneurysm. Continuous variables with normal distribution were reported as mean ± standard deviation and continuous data with abnormal distribution were reported as median (minimum–maximum). Categorical variables were reported as frequency (%).

Pearson χ^2 test or Fisher's exact test were used to compare categorical variables. In the comparison of continuous variables, Student t test was used for continuous normally distributed data and Wilcoxon rank sum test was used for non-normally distributed data. They were tested independently.

In the statistical analysis of the study, p value < 0.05 was considered statistically significant. Receiver operating characteristic (ROC) curves were used to determine the optimal cut-off values of predictor.

Table 1. Bilateral comparison of artery diameter and diameter ratios associated with aneurysm

	Aneurysm side	Contralateral side	P
M1 segment diameter [mm]	2.2 ± 0.52	2.2 ± 0.52	0.82
Dominant truncus diameter [mm]	1.82 ± 0.45	1.81 ± 0.48	0.94
Recessive truncus diameter [mm]	1.23 ± 0.40	1.25 ± 0.41	0.82
ICA diameter [mm]	3.1 ± 0.64	3 ± 0.6	0.22
LA ratio	0.71 ± 0.14	0.74 ± 0.14	0.19
KA ratio	0.68 ± 0.17	0.70 ± 0.19	0.83
DA ratio	0.74 ± 0.14	0.74 ± 0.12	0.86
BA ratio	0.83 ± 0.18	0.82 ± 0.15	0.97
CA ratio	0.55 ± 0.14	0.56 ± 0.15	0.95

DA ratio — the ratio of M1 diameter to the sum of the dominant and recessive truncus diameters; KA ratio — the ratio of upper truncus diameter to lower truncus diameter; BA ratio — the ratio of dominant truncus diameter to M1 segment diameter; CA — the ratio of recessive truncus diameter to M1 segment diameter; LA — the ratio of M1 diameter to ICA diameter as LA

RESULTS

The study group consisted of 74 patients (62.2% female) aged between 24 and 79 years (mean age 58.41 years). 52.7% (39) of the aneurysms were on the right, while 47.3% (35) were localised to the left. 66.2% (49) of the aneurysms were not ruptured whereas 33.8% (25) were ruptured.

There was no statistically significant difference between ICA, MCA M1 segment, dominant and recessive truncus diameters and the ratios of these diameters in the aneurysmal side and in the contralateral bifurcation side as control group (Table 1).

The dominant truncus angle (Φ1) on the aneurysm side was 81.5 ± 33.1°, whereas this angle (Φ1) on the contralateral side was 55.8 ± 21.1° ($p < 0.0001$). The recessive truncus angle (Φ2) on the aneurysm side was 98.2 ± 30.9°, while this angle (Φ2) on the contralateral side was 68.2 ± 25.7° ($p < 0.0001$). The bifurcation angle on the aneurysm side was 179.7 ± ± 42.9°, as it was 124 ± 33.3° on the contralateral side ($p < 0.0001$). When the dominant, recessive truncus and bifurcation angles were compared to the aneurysm side and the contralateral side, it was found that the mean of all three angles on the aneurysm side was significantly higher ($p < 0.0001$) (Table 2).

The diagnostic feature of bifurcation angle for predicting aneurysm formation was examined by ROC curve analysis (Fig. 1). Significant limit value was determined. Then sensitivity, specificity, positive predictive value and negative predictive value were

Table 2. Middle cerebral artery (MCA) bifurcation angle measurements on ipsilateral and contralateral sides

	Aneurysmal MCA (n = 74)	Contralateral MCA (n = 74)	P
Φ1	81.5 ± 33.1	55.8 ± 21.1	< 0.0001
Φ2	98.2 ± 30.9	68.2 ± 25.7	< 0.0001
Bifurcation angle	179.7 ± 42.9	124.18 ± 33.37	< 0.0001

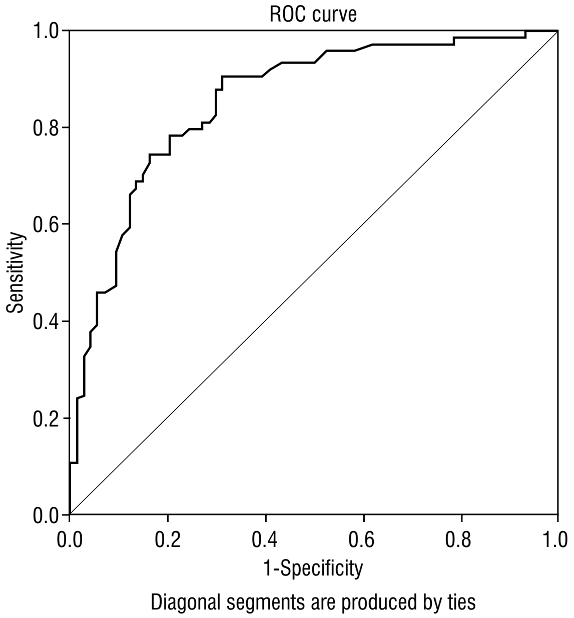

Figure 1. Diagnostic feature of the sum of upper and lower angle measurement for predicting aneurysm formation according to receiver operating characteristic (ROC) curve analysis.

Table 3. Diagnostic feature of bifurcation angle for predicting aneurysm formation, values of three angles obtained according to receiver operating characteristic curve analysis

Limit value	Sensitivity	Specificity	Positive predictive value	Negative predictive value
146.5	78.4%	78.4%	78.4%	78.4%
147.5	78.4%	79.7%	79.5%	78.7%
148.5	77%	79.7%	79.2%	77.6%

calculated for this value. In the evaluation of the area under the curve (AUC), when the type 1 error level was below 5%, the diagnostic value of the test was interpreted as statistically significant. In the ROC analysis, when the bifurcation angle of 147.5° was accepted as the limit value, 78.4% sensitivity, 79.7% specificity, 79.5% positive predictive value and 78.7% negative predictive value were determined (AUC: 0.85; Table 3).

DISCUSSION

The pathophysiological mechanism of IA formation is controversial. The development of IAs is associated with acquired factors such as smoking and hypertension, as well as with congenital and genetic factors [23]. If the patient has certain risk factors (female gender, smoking, alcohol, age and hypertension) or family history, aneurysm development is more likely [14]. However, it is almost impossible to predict precisely the localisation of the aneurysm, and thus the onset and early development of the aneurysm. In addition to the genetic and acquired factors mentioned above, haemodynamic stress is thought to play an important role in the formation of aneurysms by triggering focal degenerative mechanisms in the vessel wall [17]. Middle cerebral artery bifurcation has a very complex morphology due to angulations as well as varying diameters and variations of M1 segment and truncal branches. Because of this complex morphology, haemodynamic stress in different localizations of this structure is not homogeneous [18]. In order to minimise the confounding effects of acquired risk factors in our study, we compared the bifurcation in the aneurysmal side and contralateral side without aneurysm in the same patient. We excluded patients with bilateral aneurysms.

It is essential that the branching and bifurcation zones in the cerebral arteries are optimally arranged to generate a constant wall shear stress (WSS) by consuming minimum energy along the main artery and branches. Haemodynamic factors such as WSS are affected by the geometry of the vascular tree [3]. The optimal principle of minimum work minimises wall tension stress due to both vascular diameters and bifurcation angles [11]. Ingebrigtsen et al. [7] assumed that normal MCA bifurcations would follow the minimum work principles and the presence of an aneurysm would be associated with deviations from the optimum bifurcation geometry.

The bifurcation apex is the maximum stress zone in the artery due to the direct effect of blood flow. This region is exposed to high WSS variations that are believed to cause endothelial damage to the vessel wall. As the angle of bifurcation increases, the forces applied to the lateral branches try to balance each other more but compensate less for the forces applied to the apex of the parent artery [15]. It has been shown that high pressure caused by increased bifurcation angle in apex may be associated with endothelial dysfunction and aneurysm progression secondary to endothelial proliferation and apoptosis [8]. In their study, Roach et al. [15] found that aneurysms localised to wide bifurcation angles were associated with a large stagnation area and high WSS at the bifurcation apex. These haemodynamic changes could cause them to grow more than those settled in narrow-angle bifurcations [15]. Finlay et al. [4] described a collagen tendon-like medial pad that is thought to protect the bifurcation apex where flow is divided into side branches and has the highest WSS and spatial wall shear stress gradient (WSSG) [4]. Meng et al. [10] reported the presence of an "intimal pad" in the stroke area of the flow jet in the bifurcation. In both studies, it was found that as the bifurcation angles increased, the stroke area of the blood moved away from the bifurcation apex where the arterial wall was preserved, and the blood flow forming larger vortices needed a longer distance to return to the laminar state. This has been reported to cause greater damage to the vessel wall adjacent to the dense collagen fibre area. It has been reported that these dynamics changes in wide bifurcation angles lead to aneurysm formation as a result of high WSS and WSSG exposure in the vulnerable artery wall around the bifurcation apex [4].

The effects of MCA M1 segment, branch diameters and branch angles can be conceptualised as haemodynamics of the bifurcation point in the artery. Since the bifurcation angles are relatively larger in aneurysmatic bifurcations, we assume that blood flow has to make a deeper deviation at this point. In studies evaluating bifurcation geometry in Willis polygon, aneurysmal bifurcations have been reported to have wider bifurcation angles than non-aneurysmal bifurcations [2, 7]. Sadatomo et al. [16] reported that aneurysmal MCA bifurcations had narrower lateral angles than non-aneurysmal bifurcations in their studies evaluating MCA bifurcations. In this study, unlike other studies, the lateral angle which is accepted as the angle associated with the aneurysm, is complementary to the angle in other studies. Therefore, the correlation with the narrow angle was reported as the opposite of our study. In our study, truncal angles and bifurcation angles on the side of the aneurysmal MCA bifurcation were significantly wider than the control group ($p < 0.0001$).

Baharoğlu et al. [1] reported that changes in bifurcation vessel geometry were associated with increased risk of aneurysm formation by altering haemodynamic forces at the apex of the bifurcation in their study of localised aneurysms in MCA bifurcation. In this study, 140° for bifurcation angle (93% sensitivity and 93% specificity, AUC: 0.98), 69° for upper trunk angle (63% sensitivity and 96% specificity, AUC: 0.84) and 83° for lower trunk angle (78% sensitivity and 91% specificity, AUC: 0.91) have been reported [1]. Total bifurcation angle has been reported to perform best in differentiating aneurysmal and non-aneurysmal MCA. In another study, Gao et al. [5] reported that stent-mediated treatment effectively reduced the angle of bifurcation in the postoperative period and reduced wall damage caused by abnormal hemodynamic stress at the bifurcation apex. Therefore, not only the individual angles between the parent artery and the branches ($\Phi 1$ and $\Phi 2$), but also the bifurcation angle were examined. In our study, when the 147.5° bifurcation angle was accepted as the limit value, 78.4% sensitivity, 79.7% specificity, 79.5% positive predictive value and 78.7% negative predictive value were determined (AUC: 0.85). The data of our study is consistent with the results of the study of Baharoğlu et al. [1].

Our other hypothesis is that if the sum of the dominant and recessive truncus diameters forming the distal bed is larger than the diameter of the M1 segment, the blood can proceed freely without causing a haemodynamic imbalance in the distal bifurcation region, but in the opposite case the changing flow dynamics might trigger the development of the aneurysm. According to the principle of flow protection, the distal bed should be at least equal to the proximal so blood can flow freely without encountering a high resistance [12]. The smaller main vessel diameter causes higher jet flow at the bifurcation apex and increases the haemodynamic stress which the arterial wall is exposed [13]. Therefore, simple morphological parameters like large bifurcation angles, disproportionate diameters and haemodynamic changes, may be useful in predicting aneurysm formation in high-risk patients. In the study examining the relationship between anterior communicating artery (ACoA) formation and environmental geometry, a positive correlation was observed not only between A1 and A2 diameter ratio and aneurysm formation but also the incidence of A1 dominance to feed both A2 [20]. Soylu et al. [19] reported that increased contralateral ICA/A1 ratio, increased ipsilateral A1/A2 ratio and narrow bifurcation angle were the most important determinants for aneurysm development in their study evaluating the morphological factors affecting ACoA aneurysms. In this study, we did not find any significant difference when we compared ICA, M1 segment, dominant and recessive truncus diameters and the ratio of these diameters. In our study group, normal physiological flow pattern was present in M1 and its branches. Therefore there was no effect of flow rate in main and branch arteries on the development of aneurysm.

Limitations of the study

The main limitation of this study is related to retrospective design. We cannot conclude that a larger bifurcation angle causes aneurysm formation. Because of the lack of data on geometry before and after aneurysm formation, we cannot ignore the possibility that aneurysm formation affects adjacent vessel geometry. Therefore, all outcome about the parameters examined can only be related to the presence of aneurysm and are not necessarily predictors of the risk of occurrence. This study, it does not give information about the clinical course of the disease or haemodynamic properties of the flow. Also the measurements are performed manually in our study. Although the results vary slightly, this is a much more applicable technique in the clinical setting. Care is taken to avoid any changes in diameter measurements between observers but the resulting bias cannot be ruled out.

CONCLUSIONS

In conclusion, our study showed that the presence of MCA aneurysms was significantly associated with large bifurcation angles. In patients with clinical risk factors large bifurcation angle might be interpreted as additional risk factor. Measurement of these simple morphological factors can be easily performed by radiologists.

REFERENCES

1. Baharoglu MI, Lauric A, Safain MG, et al. Widening and high inclination of the middle cerebral artery bifurcation are associated with presence of aneurysms. Stroke. 2014; 45(9): 2649–2655, doi: 10.1161/STROKEAHA.114.005393, indexed in Pubmed: 25116869.
2. Bor AS, Velthuis BK, Majoie CB, et al. Configuration of intracranial arteries and development of aneurysms: a follow-up study. Neurology. 2008; 70(9): 700–705, doi: 10.1212/01.wnl.0000302176.03551.35, indexed in Pubmed: 18299521.
3. Can A, Ho AL, Dammers R, et al. Morphological parameters associated with middle cerebral artery aneurysms. Neurosurgery. 2015; 76(6): 721–6; discussion 726, doi: 10.1227/NEU.0000000000000713, indexed in Pubmed: 25734323.
4. Finlay HM, Whittaker P, Canham PB. Collagen organization in the branching region of human brain arteries. Stroke. 1998; 29(8): 1595–1601, doi: 10.1161/01.str.29.8.1595, indexed in Pubmed: 9707199.
5. Gao B, Baharoglu MI, Cohen AD, et al. Y-stent coiling of basilar bifurcation aneurysms induces a dynamic angular vascular remodeling with alteration of the apical wall shear stress pattern. Neurosurgery. 2013; 72(4): 617–29; discussion 628, doi: 10.1227/NEU.0b013e3182846d9f, indexed in Pubmed: 23277371.
6. Greenberg M. Handbook of Neurosurgery. 6th ed. New York 2006: 289–365.
7. Ingebrigtsen T, Morgan MK, Faulder K, et al. Bifurcation geometry and the presence of cerebral artery aneurysms. J Neurosurg. 2004; 101(1): 108–113, doi: 10.3171/jns.2004.101.1.0108, indexed in Pubmed: 15255260.
8. Kondo S, Hashimoto N, Kikuchi H, et al. Apoptosis of medial smooth muscle cells in the development of saccular cerebral aneurysms in rats. Stroke. 1998; 29(1): 181–189, doi: 10.1161/01.str.29.1.181, indexed in Pubmed: 9445349.
9. Longstreth WT, Nelson LM, Koepsell TD, et al. Cigarette smoking, alcohol use, and subarachnoid hemorrhage. Stroke. 1992; 23(9): 1242–1249, doi: 10.1161/01.str.23.9.1242, indexed in Pubmed: 1519278.
10. Meng H, Wang Z, Hoi Y, et al. Complex hemodynamics at the apex of an arterial bifurcation induces vascular remodeling resembling cerebral aneurysm initiation. Stroke. 2007; 38(6): 1924–1931, doi: 10.1161/STROKEAHA.106.481234, indexed in Pubmed: 17495215.
11. Murray CD. The physiological principle of minimum work applied to the angle of branching of arteries. J Gen Physiol. 1926; 9(6): 835–841, doi: 10.1085/jgp.9.6.835, indexed in Pubmed: 19872299.
12. Murray CD. The physiological principle of minimum work: I. The vascular system and the cost of blood volume. Proc Natl Acad Sci U S A. 1926; 12(3): 207–214, doi: 10.1073/pnas.12.3.207, indexed in Pubmed: 16576980.
13. Przelomski MM, Fisher M, Davidson RI, et al. Unruptured intracranial aneurysm and transient focal cerebral ischemia: a follow-up study. Neurology. 1986; 36(4): 584–587, doi: 10.1212/wnl.36.4.584, indexed in Pubmed: 3960339.
14. Raps EC, Rogers JD, Galetta SL, et al. The clinical spectrum of unruptured intracranial aneurysms. Arch Neurol. 1993; 50(3): 265–268, doi: 10.1001/archneur.1993.00540030031010, indexed in Pubmed: 8442705.
15. Roach MR, Scott S, Ferguson GG. The hemodynamic importance of the geometry of bifurcations in the circle of Willis (glass model studies). Stroke. 1972; 3(3): 255–267, doi: 10.1161/01.str.3.3.255, indexed in Pubmed: 5034974.
16. Sadatomo T, Yuki K, Migita K, et al. Differences between middle cerebral artery bifurcations with normal anatomy and those with aneurysms. Neurosurg Rev. 2013; 36(3): 437–445, doi: 10.1007/s10143-013-0450-5, indexed in Pubmed: 23354785.
17. Schievink WI, Schaid DJ, Rogers HM, et al. On the inheritance of intracranial aneurysms. Stroke. 1994; 25(10): 2028–2037, doi: 10.1161/01.str.25.10.2028, indexed in Pubmed: 8091449.

18. Shojima M, Oshima M, Takagi K, et al. Role of the bloodstream impacting force and the local pressure elevation in the rupture of cerebral aneurysms. Stroke. 2005; 36(9): 1933–1938, doi: 10.1161/01.STR.0000177877.88925.06, indexed in Pubmed: 16081858.
19. Soylu Aİ, Ozturk M, Akan H. Can vessel diameters, diameter ratios, and vessel angles predict the development of anterior communicating artery aneurysms: A morphological analysis. J Clin Neurosci. 2019; 68: 250–255, doi: 10.1016/j.jocn.2019.07.024, indexed in Pubmed: 31358430.
20. Tarulli E, Fox AJ. Potent risk factor for aneurysm formation: termination aneurysms of the anterior communicating artery and detection of A1 vessel asymmetry by flow dilution. Am J Neuroradiol. 2010; 31(7): 1186–1191, doi: 10.3174/ajnr.A2065, indexed in Pubmed: 20360345.
21. Taylor CL, Yuan Z, Selman WR, et al. Cerebral arterial aneurysm formation and rupture in 20,767 elderly patients: hypertension and other risk factors. J Neurosurg. 1995; 83(5): 812–819, doi: 10.3171/jns.1995.83.5.0812, indexed in Pubmed: 7472548.
22. Wardlaw JM, White PM. The detection and management of unruptured intracranial aneurysms. Brain. 2000; 123(2): 205–221, doi: 10.1093/brain/123.2.205.
23. Wiebers DO, Whisnant JP, Sundt TM, et al. The significance of unruptured intracranial saccular aneurysms. J Neurosurg. 1987; 66(1): 23–29, doi: 10.3171/jns.1987.66.1.0023, indexed in Pubmed: 3783255.

VIA MEDICA

ORIGINAL ARTICLE

Folia Morphol.
Vol. 80, No. 3, pp. 527–532
DOI: 10.5603/FM.a2020.0092
Copyright © 2021 Via Medica
ISSN 0015–5659
eISSN 1644–3284
journals.viamedica.pl

Analysis of posterior circulation diameters depending on age, sex and side by computed tomography angiography

M.N. Kocak[1, 2], R. Sade[2, 3, 4], M. Ay[2, 3], G. Polat[2, 3], B. Pirimoğlu[2, 3], A. Yalcin[5], S. Kapakin[6], I.M. Kabakus[7], M. Ur[8]

[1]*Department of Neurology, Medical Faculty, Ataturk University, Erzurum, Turkey*
[2]*Educational and Training Hospital, Ataturk University, Erzurum, Turkey*
[3]*Department of Radiology, Medical Faculty, Ataturk University, Erzurum, Turkey*
[4]*Clinical Research, Development and Design Application and Research Centre, Ataturk University, Erzurum, Turkey*
[5]*Department of Radiology, Medical Faculty, Binali Yildirim University, Erzincan, Turkey*
[6]*Department of Anatomy, Medical Faculty, Ataturk University, Erzurum, Turkey*
[7]*Department of Radiology and Radiological Science, Medical University of South Carolina, South Carolina, United States*
[8]*Siemens Healthcare, Istanbul, Turkey*

[Received: 18 June 2020; Accepted: 20 July 2020; Early publication date: 7 August 2020]

Background: *Posterior circulation of brain is important because of vital organs' blood supply provided by them. In this study, we evaluate the relationship of posterior circulation measurements with age, gender and side by using computed tomography angiography (CTA) images.*

Materials and methods: *A total 199 brain CTA examinations were retrospectively analysed for all posterior circulation arteries (vertebral artery, basilar artery, posterior cerebral artery [PCA], superior cerebellar artery [SCA], anterior inferior cerebellar artery, and posterior inferior cerebellar artery [PICA]) to compare the difference based on age, gender and side.*

Results: *There is no correlation between age and the mean diameters of all vessels ($p > 0.05$). The mean diameter of left vertebral artery was higher than right vertebral artery in all genders ($p = 0.004$ for males and $p < 0.001$ for females). The mean diameter of left SCA and PICA were higher than right SCA and PICA in females ($p = 0.032$ and $p = 0.027$, respectively). The mean diameters of basilar, left PCA, left SCA, left vertebral, right PCA, right SCA, right PICA and right vertebral artery were higher in males and that differences were statistically significant ($p < 0.001$, $p = 0.002$, $p = 0.006$, $p = 0.004$, $p = 0.001$, $p = 0.003$, $p = 0.002$, and $p = 0.006$, respectively).*

Conclusions: *The posterior circulation vessel diameter is not affected by aging. The mean diameters of basilar artery, both PCAs, both SCAs, right PICA, both vertebral arteries were higher in males. The mean diameter of left vertebral artery is higher than that of right vertebral artery in all genders.* (Folia Morphol 2021; 80, 3: 527–532)

Key words: cerebral arteries, cerebellar arteries, posterior circulation, morphometric measurements, computed tomography

Address for correspondence: Dr. R. Sade, Department of Radiology, Faculty of Medicine, Ataturk University, 25240 Erzurum, Turkey, tel: +90 555 3723339, fax: +90 442 2361014, e-mail: recepsade@yahoo.com

INTRODUCTION

Posterior circulation consists of vertebral, basilar, posterior cerebral, superior cerebellar, anterior inferior cerebellar and posterior inferior cerebellar arteries, as well as their branches. It is very variable and sometimes complex. Posterior circulation vascularizes the posterior part of the brain, in which many vital structures, such as the cerebellum, thalamus, and brainstem, are located. Although digital subtraction angiography (DSA) is the gold standard in vascular imaging, it has been shown that computed tomography angiography (CTA) has become as effective as DSA with the advances in technology [2]. A brain CTA examination is a non-invasive evaluation method. There are several morphologic studies which evaluate the brain arterial system [2, 6, 8, 12]. There are several studies investigating the variations in the posterior circulation system [2, 6, 11]; however, those involving the measurement of arterial diameter are limited in number [8, 13]. To our knowledge, the current study is the first in English language literature that explored the relationship between posterior circulation arteries and age, gender, and side simultaneously.

MATERIALS AND METHODS

This retrospective study included the data from the patient files gathered from the local picture archiving and communication systems between January 2019 and January 2020. A total of 256 brain CTA examinations were included. CTA examinations were performed on a 320-row detector computed tomography (CT) (Aquillion ONE Vision; Toshiba Medical Systems Corporation, Otawara, Japan), or a 256-row detector CT (Somatom® Definition Flash, Siemens Healthcare, Forchheim, Germany). The CT acquisition protocol was also performed with the following parameters: 0.5-s gantry rotation time, 0.5 mm slice thickness, 128 × × 0.6-mm or 192 × 0.6-mm collimation using a z-flying focal spot, 200 mAs tube current at 120 kVp tube voltage. For optimal intraluminal contrast enhancement, the delay time between start of contrast material administration and start of scanning was determined for each patient individually by using a bolus-tracking technique. A total of 60–75 mL iopromide (Ultravist 370 mg/mL, Bayer Schering Pharma, Berlin, Germany), an automatic injector was used (MCT Plus; Medrad, Pittsburgh, PA) over 15 s through an 18-gauge intravenous line placed into the right antecubital vein at a rate of 4–5 mL/s. The contrast produced a sensation of "hot flash". Immediately following the injection of the iodinated contrast, 50 mL saline was infused by the same injector via the same route.

The cases with trauma, tumour or vascular pathologies, paediatric cases, and repetitive examinations were excluded (Fig. 1). As a result, a total of 199 brain CTA examinations were evaluated on axial, coronal, or sagittal images by 2 radiologists with 3 and 10 years of neuroradiology experience. The diameter of the vertebral artery (VA) was measured on the intracranial segment (V4), 1 cm before the confluence. The diameters of the posterior cerebral artery (PCA) were measured on the P1 segment. If there was no P1 or V4 segment, the measurement was not performed. The diameter of the basilar artery (BA) was measured from the mid-part. The diameters of the superior cerebellar artery (SCA), anterior inferior cerebellar artery (AICA), and posterior inferior cerebellar artery (PICA) were measured from the proximal part (Fig. 2). The measurements and patients' demographic data were recorded.

Statistical analysis

Statistical analyses were performed using SPSS v. 22.0 (SPSS Inc., Chicago IL, USA). The suitability of the data for normal distribution was evaluated by the single-sample Kolmogorov-Smirnov test. Levene's statistics were used for the homogeneity analysis of group variances. The independent-samples t-test was conducted to determine the differences between male and female biometric measurements, and the paired-samples t-test was utilised to determine those between the left and right measurements of men and women. The significance level was accepted as $p < 0.05$.

RESULTS

The mean age of the patients was 48.55 ± 15.82 (range 18–91) years. Of the patients, 105 (52.76%) were female. The mean diameters were calculated as 3.34 ± 0.59 (range 1.35–5.3) mm for BA, 1.79 ± ± 0.47 (range 0.52–3.50) mm for the left PCA, 1.12 ± ± 0.33 (range 0.40–2.18) mm for the left SCA, 1.02 ± ± 0.34 (range 0.33–1.98) mm for the left AICA, 1.26 ± ± 0.36 (range 0.40–2.20) mm for the left PICA, 2.99 ± ± 0.70 (range 0.95–5.13) mm for the left VA, 1.76 ± ± 0.47 (range 0.80–2.94) mm for the right PCA, 1.06 ± ± 0.31 (range 0.36–2.10) mm for the right SCA, 0.95 ± ± 0.31 (range 0.30–1.76) mm for the right AICA, 1.18 ± ± 0.36 (range 0.43–2.56) mm for the right PICA, and 2.68 ± 0.71 (range 0.94–4.52) mm for the right VA.

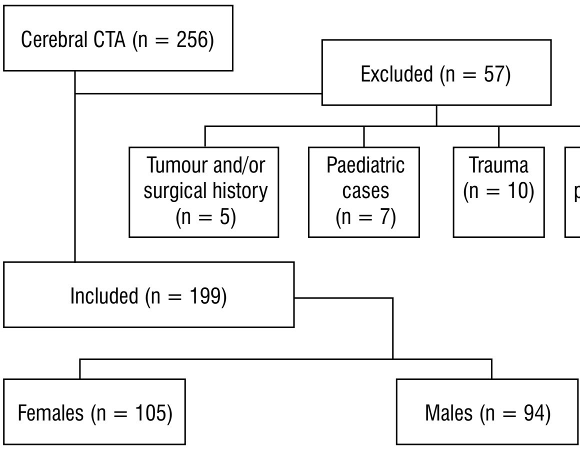

Figure 1. Study flow diagram; CTA — computed tomography angiography.

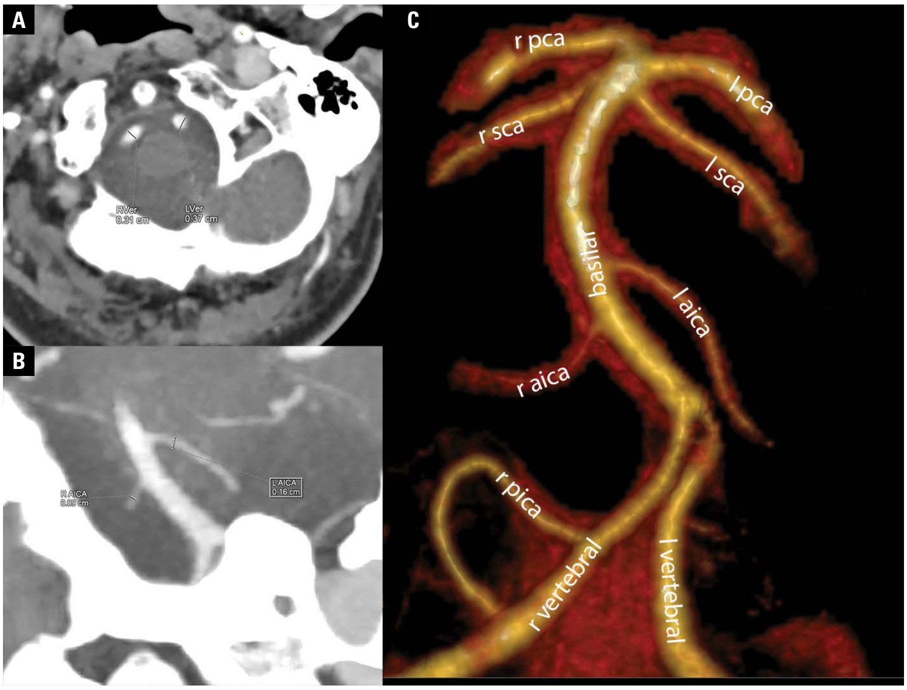

Figure 2. Axial (**A**), coronal (**B**) and three-dimensional volume rendered (**C**) computed tomography images of a 51-year-old male. The measurements of right vertebral artery (r vertebral) and left vertebral artery (l vertebral) are shown on axial image (B). The measurements of right anterior inferior cerebral artery (r aica) and left anterior inferior cerebral artery (l aica) are shown on axial image; r pica — right posterior inferior cerebellar artery; l pca — left posterior cerebral artery; r pca — right posterior cerebral artery; l sca — left superior cerebellar artery; r sca — right superior cerebellar artery.

There was no correlation between age and the mean diameters of any of the arteries ($p > 0.05$)

The mean diameters of BA, left PCA, left SCA, left VA, right PCA, right SCA, right PICA, and right VA were statistically significantly higher in males than in females (Table 1). Left foetal-type PCA was observed in 4 males and 5 females. Right foetal-type PCA was detected in 2 males and 2 females. There was no statistically significant difference in foetal-type PCA variations between the genders ($p = 0.95$). The left SCA could not be visualised in 1 male, the right SCA in 1 female, the left AICA in 34 males and 39 females, the right AICA in 30 males and 33 females, the left PICA in 2 males and 5 females, the right PICA in

Table 1. The intergroup comparison of the posterior circulation arteries measurements by gender

Artery	Gender	Number	Mean	Standard deviation	t	df	P
Basilar	Male	94	3.52	0.61	4.033	197	**0.000**
	Female	105	3.18	0.58			
Left PCA	Male	90	1.91	0.47	3.195	188	**0.002**
	Female	100	1.68	0.48			
Left SCA	Male	93	1.18	0.35	2.768	196	**0.006**
	Female	105	1.06	0.29			
Left AICA	Male	60	1.01	0.37	–0.155	124	0.877
	Female	66	1.02	0.3			
Left PICA	Male	92	1.30	0.37	1.520	190	0.130
	Female	100	1.22	0.35			
Left vertebral	Male	94	3.14	0.75	2.924	197	**0.004**
	Female	105	2.85	0.62			
Right PCA	Male	92	1.88	0.49	3.514	193	**0.001**
	Female	103	1.65	0.43			
Right SCA	Male	94	1.13	0.35	2.965	167	**0.003**
	Female	104	0.99	0.25			
Right AICA	Male	64	0.95	0.31	–0.137	134	0.892
	Female	72	0.96	0.31			
Right PICA	Male	92	1.26	0.38	3.065	187	**0.002**
	Female	97	1.10	0.32			
Right vertebral	Male	94	2.82	0.7	2.765	195	**0.006**
	Female	103	2.55	0.69			

PCA — posterior cerebral artery; SCA — superior cerebellar artery; AICA — anterior inferior cerebellar artery; PICA — posterior inferior cerebellar artery

2 males and 8 females, and the V4 segment of the right VA in 2 females.

The mean diameters of SCA, PICA, and VA were statistically significantly higher on the left side compared to the right side (Table 2). However, in gender-based subgroup analyses, a statistically significant result was observed in only 1 artery (VA) in both genders (Table 3). The mean diameters of SCA and PICA were higher on the left side in both males and females but the differences were not statistically significant in males (Table 3). The mean diameter of the left VA was higher than that of the right VA in both genders.

DISCUSSION

In this study, a total of 13 foetal-type PCA variations (6.53%) were observed, which is a lower percentage than reported in the literature [6, 11]. Han et al. [2] showed that CTA with 1-mm slice thickness underestimated cerebral arteries compared to DSA. In the current study, we used 0.5-mm slice thickness for CTA. Thus, we consider that our different results were due to our CT device being able to show smaller vessels. This is supported by similar results obtained from cadaver studies [9, 13]. Another explanation may be that there is a difference in the rate of variation in different societies. Further thin-slice CTA and cadaver studies on this subject can provide a better explanation.

In this study, the diameters of VA, BA, PCA, PICA and AICA were similar to the ranges in the literature (2.8 mm vs. 2.2–2.8 mm, 3.3 mm vs. 2.7–3.6 mm, 1.8 mm vs. 1.6–2.2 mm, 1.2 mm vs. 1.2–1.7 mm, and 1 mm vs. 1 mm, respectively) [4, 7, 8, 10, 12, 13]. However, the SCA diameter was lower than the literature range (1.1 mm vs. 1.3–1.4 mm) [1, 5, 7]. This could be related to the differences in the method (cadaver versus CTA), technique (1 mm vs. 0.5 mm slice thickness), or patient selection (inclusion and exclusion criteria).

Rai et al. [8] revealed that the vessel calibre was affected by age. However, Ichikawa et al. [3] found no correlation between age and vessel calibre. Furthermore Vitosevic et al. [12] showed that the calibre of BA was higher in the elderly but those of VA and

Table 2. The intergroup comparison of the posterior circulation arteries measurements by side

Artery	Side	Number	Mean	Standard deviation	t	df	P
PCA	Right	186	1.76	0.47	–0.624	185	0.533
	Left	186	1.78	0.49			
SCA	Right	197	1.06	0.31	–2.692	196	**0.008**
	Left	197	1.12	0.33			
AICA	Right	120	0.95	0.31	–1.657	119	0.100
	Left	120	1	0.32			
PICA	Right	187	1.18	0.36	–2.274	186	**0.024**
	Left	187	1.25	0.36			
Vertebral	Right	197	2.68	0.71	–4.816	196	**0.000**
	Left	197	2.9	0.7			

PCA — posterior cerebral artery; SCA — superior cerebellar artery; AICA — anterior inferior cerebellar artery; PICA — posterior inferior cerebellar artery

Table 3. The subgroup comparison of the posterior circulation arteries measurements by gender

Artery	Side	Number	Mean	Standard deviation	t	df	P
Male							
PCA	Right	88	1.86	0.49	–0.672	87	0.503
	Left	88	1.9	0.47			
SCA	Right	93	1.13	0.35	–1.619	92	0.109
	Left	93	1.18	0.35			
AICA	Right	56	0.95	0.31	–0.934	55	0.354
	Left	56	0.99	0.35			
PICA	Right	91	1.26	0.38	–0.939	90	0.350
	Left	91	1.30	0.37			
Vertebral	Right	94	2.82	0.7	–2.973	93	**0.004**
	Left	94	3.14	0.75			
Female							
PCA	Right	98	1.66	0.43	–0.192	97	0.848
	Left	98	1.67	0.48			
SCA	Right	104	0.99	0.25	–2.168	103	**0.032**
	Left	104	1.06	0.29			
AICA	Right	64	0.95	0.32	–1.393	63	0.169
	Left	64	1	0.31			
PICA	Right	96	1.1	0.32	–2.242	95	**0.027**
	Left	96	1.2	0.34			
Vertebral	Right	103	2.55	0.69	–3.962	102	**0.000**
	Left	103	2.86	0.63			

PCA — posterior cerebral artery; SCA — superior cerebellar artery; AICA — anterior inferior cerebellar artery; PICA — posterior inferior cerebellar artery

PCA were similar. In the current study, we observed no correlation between age and vessel calibre.

In this study, the mean diameters of BA, left PCA, right PCA, left SCA, right SCA, right PICA, left VA and right VA were higher in males. Rai et al. and Ichikawa et al. revealed similar results in that the mean diameters of BA and VA were higher in males [3, 8]. On the other hand, Vitosevic et al. [12] showed no diameter difference in BA by gender. However, the authors did not evaluate SCA, AICA, and PICA; therefore, we could not compare our results.

In this study, the mean diameters of SCA, PICA and VA were higher on the left side. Vitosevic et al. showed no statistically significant diameter difference in VA and PCA depending on the side [12]. However, several studies including the current study showed that the left VA diameter was higher than the right VA diameter [4, 7, 8, 10, 13]. Shrontz et al. [10] revealed that there was no diameter difference between the left and right sides for PCA, PICA, and AICA. Pai et al. [7] reported that the diameters of the left AICA and SCA were higher than those of the right side while two other studies showed no side-based diameter differences in SCA [1, 5]. The current study has both similarities and differences compared to the literature, which can be attributed to the differences in the technique used, number of patients evaluated, and the anatomical variations between the samples.

Limitations of the study

There are several limitations of this study. First, a CTA study cannot provide as comprehensive data as a cadaveric study. Second, we used the slice thickness as 0.5 mm; thus, we were not able to evaluate vessels that were smaller than 0.5 mm in diameter; however, 0.5 mm is the lowest available cross-sectional thickness of devices in current medical use. Another limitation concerns the small sample size. Finally, we excluded patients with vascular diseases, which may have affected our age-related evaluation.

CONCLUSIONS

A CTA examination is a valuable technique for vascular evaluation even in small vessels, such as PICA and AICA. The posterior circulation vessel diameter was not affected by normal aging. The mean diameters of the left VA were found to be higher than those of the right. Lastly, the mean diameters of BA, left PCA, right PCA, left SCA, right SCA, right PICA, left VA and right VA were higher in males compared to females.

Conflict of interest: None declared

REFERENCES

1. Garcia-Gonzalez U, Cavalcanti DD, Agrawal A, et al. Anatomical study on the "perforator-free zone": reconsidering the proximal superior cerebellar artery and basilar artery perforators. Neurosurgery. 2012; 70(3): 764–772, doi: 10.1227/NEU.0b013e3182351f8e, indexed in Pubmed: 21904251.
2. Han A, Yoon DY, Chang SKi, et al. Accuracy of CT angiography in the assessment of the circle of Willis: comparison of volume-rendered images and digital subtraction angiography. Acta Radiol. 2011; 52(8): 889–893, doi: 10.1258/ar.2011.110223, indexed in Pubmed: 21828003.
3. Ichikawa H, Mukai M, Takahashi N, et al. Dilative arterial remodeling of the brain with different effects on the anterior and posterior circulation: an MRI study. J Neurol Sci. 2009; 287(1-2): 236–240, doi: 10.1016/j.jns.2009.06.029, indexed in Pubmed: 19695577.
4. Karatas A, Yilmaz H, Coban G, et al. The anatomy of circulus arteriosus cerebri (circle of willis): a study in turkish population. Turk Neurosurg. 2016; 26(1): 54–61, doi: 10.5137/1019-5149.JTN.13281-14.1, indexed in Pubmed: 26768869.
5. Krzyżewski RM, Stachura MK, Stachura AM, et al. Variations and morphometric analysis of the proximal segment of the superior cerebellar artery. Neurol Neurochir Pol. 2014; 48(4): 229–235, doi: 10.1016/j.pjnns.2014.07.006, indexed in Pubmed: 25168320.
6. Li Qi, Li J, Lv F, et al. A multidetector CT angiography study of variations in the circle of Willis in a Chinese population. J Clin Neurosci. 2011; 18(3): 379–383, doi: 10.1016/j.jocn.2010.07.137, indexed in Pubmed: 21251838.
7. Pai BS, Varma RG, Kulkarni RN, et al. Microsurgical anatomy of the posterior circulation. Neurol India. 2007; 55(1): 31–41, doi: 10.4103/0028-3886.30424, indexed in Pubmed: 17272897.
8. Rai AT, Rodgers D, Williams EA, et al. Dimensions of the posterior cerebral circulation: an analysis based on advanced non-invasive imaging. J Neurointerv Surg. 2013; 5(6): 597–600, doi: 10.1136/neurintsurg-2012-010549, indexed in Pubmed: 23178224.
9. Sahni D, Jit I, Lal V. Variations and anomalies of the posterior communicating artery in Northwest Indian brains. Surg Neurol. 2007; 68(4): 449–453, doi: 10.1016/j.surneu.2006.11.047, indexed in Pubmed: 17905073.
10. Shrontz C, Dujovny M, Ausman JI, et al. Surgical anatomy of the arteries of the posterior fossa. J Neurosurg. 1986; 65(4): 540–544, doi: 10.3171/jns.1986.65.4.0540, indexed in Pubmed: 3760965.
11. van der Lugt A, Buter TC, Govaere F, et al. Accuracy of CT angiography in the assessment of a fetal origin of the posterior cerebral artery. Eur Radiol. 2004; 14(9): 1627–1633, doi: 10.1007/s00330-004-2333-1, indexed in Pubmed: 15127219.
12. Vitosevic F, Rasulic L, Medenica SM. Morphological characteristics of the posterior cerebral circulation: an analysis based on non-invasive imaging. Turk Neurosurg. 2019; 29(5): 625–630, doi: 10.5137/1019-5149.JTN.22661-18.1, indexed in Pubmed: 29694661.
13. Wijesinghe P, Steinbusch HWM, Shankar SK, et al. Circle of Willis abnormalities and their clinical importance in ageing brains: A cadaveric anatomical and pathological study. J Chem Neuroanat. 2020; 106: 101772, doi: 10.1016/j.jchemneu.2020.101772, indexed in Pubmed: 32165168.

VIA MEDICA

ORIGINAL ARTICLE

Folia Morphol.
Vol. 80, No. 3, pp. 533–541
DOI: 10.5603/FM.a2020.0099

ISSN 0015–5659
eISSN 1644–3284
journals.viamedica.pl

Evaluation of the greater occipital nerve location regarding its relation to intermastoid and external occipital protuberance to mastoid process lines

T. Huanmanop[1], I. Issara[2], S. Agthong[1], V. Chentanez[1]

[1]Department of Anatomy, Faculty of Medicine, King Chulalongkorn Memorial Hospital, Chulalongkorn University, Bangkok, Thailand
[2]Medical Science Programme, Faculty of Medicine, King Chulalongkorn Memorial Hospital, Chulalongkorn University, Bangkok, Thailand

[Received: 22 June 2020; Accepted: 7 August 2020; Early publication date: 22 August 2020]

Background: *Localisation of the greater occipital nerve (GON) is essential for the achievement of several procedures performed in the occipital region especially the treatment of occipital neuralgia. This study proposed to investigate the location of GON subcutaneous (Sc) and semispinalis capitis (SSC) piercing points related to the intermastoid and external occipital protuberance (EOP) to mastoid process (MP) lines.*
Materials and methods: *The Sc piercing point, relation to SSC and obliquus capitis inferior (OCI) muscles of 100 GONs from 50 cadaveric heads (23 males, 27 females) were dissected. Distances from EOP to MP (EM line) on both sides and between MPs (MM line) were measured. Perpendicular lines from Sc and SSC piercing points to EM and MM lines were created and measured. Distances from EOP to the perpendicular lines of SSC piercing point and from MP to the perpendicular lines of Sc piercing point were measured and calculated into percentage of EM and MM length, respectively.*
Results: *Three types of Sc piercing points (I, II and III) were obtained. The percentage of GON piercing trapezius muscle (TP) (type I), aponeurosis of TP (type II) and aponeurosis between TP and sternocleidomastoid muscle (SCM) (type III) were 2, 67 and 31, respectively. In addition, 95% of GON pierced SSC, 2% pierced its tendinous band and 3% travelled between its medial fibres and the nuchal ligament. 94% of the GON turned around the lower edge of the OCI, while 6% pierced the lower edge of this muscle. Sc piercing point was always located above the MM line, but it could be above, below or on the EM line. In contrast, all of the SSC piercing points were located below the EM line except in one specimen, but it could be above, below or on the MM line. Therefore, the MM and EM lines were used as reference lines for locating the Sc and SSC piercing points, respectively. The mean EM line length was 81.26 ± 5.26 mm with statistically significant differences between genders and sides in female. The mean MM line length was 121.77 ± 8.54 mm with a statistically significant difference between genders. Sc piercing point could be located at 44% of MM line length from ipsilateral MP with a mean vertical distance of 18 mm. No statistically significant difference was found between genders and sides in these parameters, but a statistically significant difference was found in the percentage of MB to MM line between type III and type I (p = 0.02). SSC piercing point of all types could be located at the point of 25% of EM line length from EOP with*

Address for correspondence: V. Chentanez, MD, PhD, Department of Anatomy, Faculty of Medicine, King Chulalongkorn Memorial Hospital, Chulalongkorn University, Bangkok 10330, Thailand, tel: 66-860701084, e-mail: fmedvct@gmail.com

a vertical distance of 18 mm below EM line. No statistically significant difference was found between genders, sides and types of both piercing points.

***Conclusions:** MM and EM lines are potential reference lines for locating the Sc and SSC piercing points of GON, respectively.* (Folia Morphol 2021; 80, 3: 533–541)

Key words: external occipital protuberance, greater occipital nerve, localisation, mastoid process, piercing point, semispinalis capitis muscle, trapezius muscle

INTRODUCTION

According to the definition of the International Headache Society (IHS) in 2004, occipital neuralgia (ON) is described as a paroxysmal shooting or stabbing pain of the occipital area innervated by the greater occipital nerve (GON), lesser occipital nerve (LON) and third occipital nerve [9]. Several aetiologies of ON including trauma, tumours, infection, degenerative changes and anatomical features were reported [4]. Anatomic consideration of ON especially the localization of GON, LON and third occipital nerve were reviewed and further investigated [4, 6, 14–19, 21–24]. Entrapment of GON was reported to correlate with ON in a majority of cases [8, 10]. GON derives from the medial branch of posterior ramus of the second cervical spinal nerve and emerges between axis and obliquus capitis inferior (OCI) then ascends through the semispinalis capitis (SSC) and pierces the trapezius (TP) to the subcutaneous tissue of the occipital region. Possible sites of the GON irritation and entrapment are also reported including the point at which the nerve emerged between the atlas and the axis [20] and the point where the GON pierces the OCI, SSC and TP muscles [2, 23]. Moreover, Janis et al. (2010) [11], reported six major compression points along its course in 25 fresh cadaveric heads which were: between the SSC and OCI, at the entrance and the exit from the SSC, at the entrance and exit from the TP and at the crossing point with the occipital artery. Treatment options of ON include posture correction, pharmacological treatment, local anaesthetic injection, botulinum toxin infiltrations, pulse radiofrequency therapy and surgery [1, 5]. Occipital nerve block using a local anaesthetic with corticosteroids was injected at 2 cm lateral and 2 cm inferior to the external occipital protuberance (EOP) for blocking the GON [13]. Jose et al. (2018) [12] evaluated the effectiveness of surgical decompression of GON at the level of SSC and TP tunnel in 11 patients suffering from ON. Complete elimination and significant relief of pain was reported in three and six patients respectively. Therefore, the anatomic variation of the course of the GON is essential for the treatment of ON. The subcutaneous (Sc) piercing point of GON is classified into two or three types based on whether it pierced TP muscle fibre (type I), TP aponeurosis (type II) or the aponeurosis between TP and sternocleidomastoid (SCM) muscles (type III) [3, 22, 24]. Furthermore, the localization of the Sc and SSC piercing points using bony landmarks and reference lines including EOP, MP, EOP-MP line, intermastoid (MM) line and superior nuchal line have been evaluated extensively by several methods of measurement [3, 7, 14, 16–18, 21, 23]. Major obstacles to locate the exact location of GON are the variations of its Sc and SSC piercing points. This study aimed to evaluate the location of Sc and SSC piercing points by using the appropriate surface landmarks and testing its significant differences between genders and sides. Moreover, statistical differences of the location between types and patterns of Sc and SSC piercing points were also analysed.

MATERIALS AND METHODS

This study was performed in 50 formalin-fixed Thai cadavers (23 male and 27 female) supported by the Department of Anatomy, Faculty of Medicine, Chulalongkorn University. The average age of the cadavers was 77 years (range 41–99). All cadavers did not have any damages or history of operation in the occipital region. A horizontal skin incision was made along the line joining the upper border of the auricles and a midline vertical incision was made downward. The skin was removed from medial to lateral. The piercing point of GON to subcutaneous tissue was identified. Then the TP was detached laterally to observe the pattern of the GON in relation to the SSC. Next, the SSC was detached laterally to follow the GON until the suboccipital triangle was identified. The type of the GON in relation to OCI was identified.

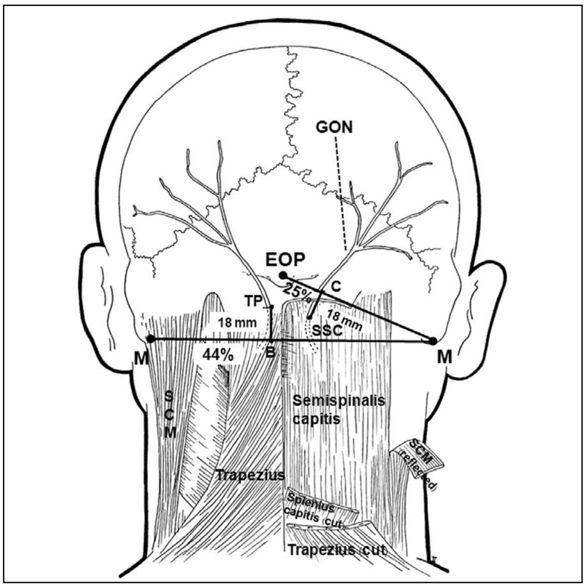

Figure 1. Schematic diagram illustrating the lines joining the three bony landmarks: external occipital protuberance and mastoid process (EM line), line between mastoid processes (intermastoid or MM line), the perpendicular lines from the subcutaneous piercing point to MM line (TP-B), semispinalis capitis piercing point to EM line (SSC-C) and surface localisation of GON; EOP — external occipital protuberance; GON — greater occipital nerve; M — mastoid process; SCM — sternocleidomastoid muscle; SSC — semispinalis capitis piercing point; TP — subcutaneous piercing point.

To determine the location of Sc and SSC piercing points, the most prominent point of EOP and lowest points of MP on both sides were identified and marked. Then, the lines joining these bony landmarks were created as EM and MM lines (Fig. 1). The locations of all piercing points were determined in relation to the EM and MM lines. The perpendicular lines from the Sc and SSC piercing points to the EM and to MM lines were created (Fig. 1). The length of EM line, MM line and the perpendicular line was measured using a standardised digital Vernier calliper (GuangLu® 0–100 mm; range 100 mm, resolution 0.01 mm). Each measurement was done twice and the average was used. The same digital Vernier calliper was used to assure measurement consistency. All measurements were done by the same investigator.

Statistical analysis

Statistical analysis was performed using Stata version 15.1 (Stata Corp. 2017 Stata Statistical Software: Release 15. College Station, TX: Stata Corp LLC). Mean and standard deviation (SD) of each parameter were obtained. Paired Student's t-test was used to examine the difference between right and left side, and unpaired Student's t-test was used to compare results between male and female. The statistical difference between types was analysed using One-Way ANOVA followed by Tukey test. For all analyses, an alpha level of 0.05 was adopted for statistical significance.

Ethical consideration

This cadaveric study has been approved by the Institutional Review Board (IRB) of the Faculty of Medicine, Chulalongkorn University (IRB NO. 594/59).

RESULTS

Sc and SSC piercing points of GON and its relation to OCI muscle

Three types of Sc piercing points of 100 GON were observed (Fig. 2). The prevalence of each type is shown in Table 1. The most frequent was type II, in which the GON pierced the aponeurosis of the TP (67%). Type I, in which the GON pierced the muscular part of TP was found in only 2%. GON pierced the aponeurosis between TP and SCM (type III) in 31%. Symmetrical type was observed in 54% of cases of type II and 18% of type III. The course of GON in the SSC as shown in Figure 2 was found in three patterns: piercing the muscle (95%), piercing its tendinous band (2%) and coursing between its most medial fibres and the nuchal ligament (3%). Symmetry was found in 94% of cases whose GON pierced the SSC muscle. GON turned around the lower edge of OCI in 94% and pierced the lower edge of OCI in 6% (Table 1). Symmetry was found in 90% and 2% of cases in both courses, respectively. In one cadaveric head, the right GON was split into 2 branches by SSC muscle fibre, then piercing the aponeurosis of TP. The left GON of that case split into 2 branches before piercing the TP.

Localisation of Sc and SSC piercing points

The results of Sc and SSC piercing points in relation to EM and MM lines are illustrated in Table 2. Observation data revealed that the Sc piercing point was always located above the MM line, but it could be above, below and on the EM line. Although, the SSC piercing points of all cases were located below the EM line except one male right GON, it could be above, below and on the MM line (Table 2). Therefore, the MM line was used as a reference line for locating the Sc piercing point and the EM line was suitable for locating the SSC piercing point. Aforementioned, the GON of both sides in one cadaver split into two branches. This cadaver was not included in the measurement. Therefore, all parameters were measured in

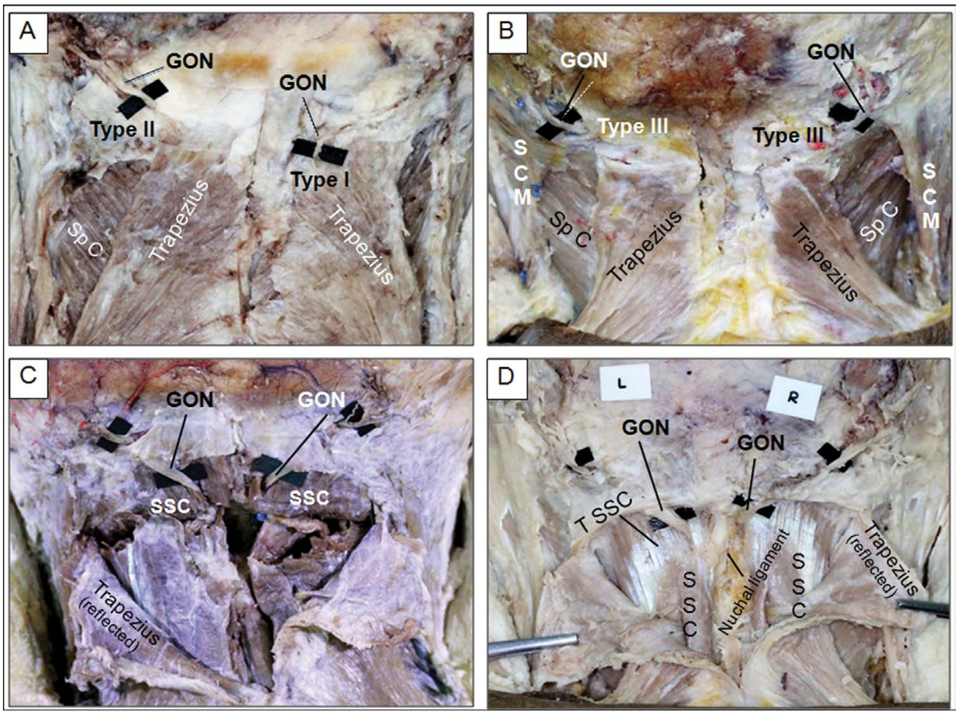

Figure 2. Posterior view of the occipital regions showing types of subcutaneous piercing points (**A, B**), patterns of semispinalis capitis piercing point (**C, D**). **A.** Right GON pierced the trapezius muscle (type I), left GON pierced the aponeurosis of trapezius muscle (type II); **B.** GONs of both sides pierced the aponeurosis between trapezius and sternocleidomastoid muscle (type III); **C.** GON of both sides pierced the semispinalis capitis muscle; **D.** Right GON coursed between the medial fibre of semispinalis capitis and nuchal ligament, left GON pierced the tendinous band of semispinalis capitis muscle; GON — greater occipital nerve; SCM — sternocleidomastoid muscle; SpC — splenius capitis; SSC — semispinalis capitis; T SSC — tendinous band of semispinalis capitis.

Table 1. Prevalence of subcutaneous piercing point type, patterns of semispinalis capitis (SSC) piecing point and the relation of greater occipital nerve to obliquus capitis inferior (OCI)

Type	Male (n = 23)		Female (n = 27)		Total N (%)
	Left, n (%)	Right, n (%)	Left, n (%)	Right, n (%)	
Subcutaneous piercing point					
Type I	0 (0%)	1 (1%)	1 (1%)	0 (0%)	2 (2%)
Type II	13 (13%)	14 (14%)	18 (18%)	22 (22%)	67 (67%)
Type III	10 (10%)	8 (8%)	8 (8%)	5 (5%)	31 (31%)
Semispinalis capitis piercing point					
Muscle	21 (21%)	21 (21%)	27 (27%)	26 (26%)	95 (95%)
Tendinous band	1 (1%)	1 (1%)	0 (0%)	0 (0%)	2 (2%)
Between SSC and Nuchal ligament	1 (1%)	1 (1%)	0 (0%)	1 (1%)	3 (3%)
Relation to OCI lower edge					
Turn around	23 (23%)	23 (23%)	24 (24%)	24 (24%)	94 (94%)
Piercing muscle	0 (0%)	0 (0%)	3 (3%)	3 (3%)	6 (6%)

49 cadavers. The results and analysis of the length of EM, MM, perpendicular line from Sc piercing point to MM line (TP-B), from MP to TP-B on MM line (M-B), perpendicular line from SSC piercing point to EM line (SSC-C) and from EOP to SSC-C on EM line (E-C) are illustrated in terms of mean ± SD in Table 3. The mean EM line length was 81.26 ± 5.26 mm with statistically significant differences between genders and sides. The mean MM line length was 121.77 ± 8.54 mm with a statistically significant difference between genders. The mean length of TP-B was 17.97 ± 5.8 mm and had no statistically significant difference between

Table 2. Prevalence of subcutaneous and semispinalis capitis piercing points in relation to the distance from external occipital protuberance to mastoid process (EM line) and distance between mastoid processes (MM line)

Gender	Subcutaneous piercing point						Semispinalis capitis piercing point					
	EM line			MM line			EM line			MM line		
	Above	Below	On	Above	Below	On	Above	Below	On	Above	Below	On
Male												
Left	11	8	3	22	0	0	0	22	0	15	7	0
Right	10	11	1	22	0	0	1	21	0	13	8	1
Total	21	19	4	44	0	0	1	43	0	28	15	1
Female												
Left	12	13	2	27	0	0	0	27	0	22	5	0
Right	12	14	1	27	0	0	0	27	0	23	4	0
Total	24	27	3	54	0	0	0	54	0	45	9	0

genders and sides. Moreover, there was no statistically significant difference of TP-B length between types of Sc piercing point. The mean M-B length was 53.96 ± ± 6.53 mm without a statistically significant difference between sides but with a statistically significant difference between genders ($p = 0.02$). The mean percentage of M-B to MM was 44.36 ± 4.52 without a statistically significant difference between genders and sides. However, there was a statistically significant difference of this parameter between type III and type I of Sc the piercing point ($p = 0.02$).

The mean length of SSC-C was 18.10 ± 5.13 mm perpendicular to EM line and had no statistically significant difference between genders and sides. Moreover, there was no statistically significant difference of this parameter between types of SC and SSC piercing points. The mean E-C length and percentage of E-C to EM was 20.49 ± 4.29 mm and 25.25 ± 4.83% respectively. There was no statistically significant difference of the percentage of E-C to EM between genders, sides and types of both piercing points.

DISCUSSION

The most common location of Sc piercing point in the aponeurosis of TP (type II) was reported in several previous studies [3, 22, 24]. A comparison of the prevalence of types of Sc piercing point, characteristic of SSC piercing point and its relation to OCI in the previous and current studies is illustrated in Table 4. Results of this study confirmed those of two previous reports [3, 24] that type II was the most common and type I was found in a lesser number. However, the finding of type III in 31% of cases was different from Won et al. (2018) (62.5%) [24]. The number of specimens and ethnicity may have an influence on the prevalence of each type. In addition, the GON was shown to pierce the SSC muscle in 95% of our cases. The rest pierced the tendinous band of SSC in 2% and travelled between SSC and nuchal ligament in 3%. This result was similar to those of the previous studies (Table 4). In addition, the prevalence of GON turning around the lower edge of OCI was the most common. Only one pervious study reported an atypical course of GON passing through the suboccipital triangle [18]. Tubbs et al. (2014) [22] reported 10 atypical courses of GON from 30 specimens; two cases of type II in which the GON pierced the lower edge of OCI, 5 cases of GON piercing the tendinous band of SSC which were type I (1 case) and type II (4 cases), and 3 cases of GON travelling between its most medial fibres and the nuchal ligament which were type I (1 case) and type II (2 cases). This study revealed 11 atypical courses of GON from 100 specimens. The prevalence was lower and included six cases of type II piercing the lower edge of OCI, one cases of type I and one case of type II piercing the tendinous band of SSC, and 3 cases of GON travelling between its most medial fibres and the nuchal ligament which were type II (2 cases) and type III (1 case). This issue is clinically important because atypical courses of GON might be associated with a higher incidence of nerve entrapment and ON [2, 23]. In general, the GON divided into 2 branches after exiting to the subcutaneous tissue but it could be split by the muscle fibre of SSC and often reconnected [6]. The splitting of GON before exiting to the subcutaneous tissue occurred on both sides of one male cadaveric head, where the right GON was split by SSC muscle fibre and pierced the aponeurosis of the TP without reconnection. The left GON split before piercing the aponeurosis of the TP. This variation

Table 3. The mean ± standard deviation length of EM, MM, TP-B, MB, SSC-C, E-C, percentage of EC/EM and MB/MM

	Gender	Side		Total	P
		Left	Right		
EM [mm]	Male (n = 22)	84.43 ± 4.35	85.16 ± 5.56	84.30 ± 5.01	0.09
	Female (n = 27)	77.61 ± 3.99	79.95 ± 3.79	78.78 ± 4.03	0.02*
	Total (n = 49)	80.22 ± 5.05	82.26 ± 5.31	81.26 ± 5.26	0.00*
	P	0.00*	0.00*		
MM [mm]	Male (n = 22)	–	–	127.18 ± 8.85	
	Female (n = 27)	–	–	117.36 ± 5.12	
	Total (n = 49)	–	–	121.77 ± 8.54	
	P			0.00*	
TP-B [mm]	Male (n = 22)	18.35 ± 3.93	17.92 ± 6.70	18.14 ± 5.43	0.77
	Female (n = 27)	17.77 ± 5.75	17.88 ± 6.59	17.82 ± 6.12	0.91
	Total (n = 49)	18.03 ± 4.97	17.90 ± 6.57	17.97 ± 5.8	0.87
	P	0.69	0.98		
MB [mm]	Male (n = 22)	55.72 ± 7.53	56.77 ± 6.65	56.25 ± 7.04	0.51
	Female (n = 27)	50.93 ± 6.72	53.28 ± 3.63	52.11 ± 5.48	0.05
	Total (n = 49)	53.08 ± 7.42	54.85 ± 5.44	53.96 ± 6.53	0.07
	P	0.02*	0.02*		
SSC-C [mm]	Male (n = 22 L, 21 R)	18.34 ± 5.28	19.09 ± 6.71	18.71 ± 5.96	0.51
	Female (n = 27)	18.23 ± 4.43	16.98 ± 4.28	17.61 ± 4.36	0.07
	Total (n = 49 L, 48 R)	18.28 ± 4.77	17.9 ± 5.51	18.10 ± 5.13	0.59
	P	0.94	0.19		
E-C [mm]	Male (n = 22)	20.23 ± 4.8	22.08 ± 4.68	21.15 ± 4.77	0.13
	Female (n = 27)	19.46 ± 3.61	20.45 ± 4.03	19.95 ± 3.82	0.15
	Total (n = 49)	19.80 ± 4.16	21.18 ± 4.36	20.49 ± 4.29	0.04*
	P	0.52	0.20		
EC/EM [%]	Male (n = 22)	24.21 ± 5.39	25.87 ± 4.88	25.04 ± 4.34	0.17
	Female (n = 27)	25.07 ± 4.39	25.56 ± 4.91	25.31 ± 4.23	0.52
	Total (n = 49)	24.68 ± 4.83	25.70 ± 4.85	25.25 ± 4.83	0.13
	P	0.54	0.83		
MB/MM [%]	Male (n = 22)	43.82 ± 5.09	44.69 ± 4.78	44.25 ± 3.97	0.50
	Female (n = 27)	43.37 ± 5.10	45.42 ± 2.76	44.39 ± 3.22	0.047*
	Total (n = 49)	43.57 ± 5.05	45.09 ± 3.78	44.36 ± 4.52	0.06
	P	0.76	0.51		

*Statistical significance; EM — distance from external occipital protuberance to mastoid process; MM — distance between mastoid processes; TP-B — perpendicular distance from subcutaneous piercing point to MM line; MB — distance from mastoid process of the ipsilateral side to the point of TP-B on MM line; SSC-C — perpendicular distance from subcutaneous piercing point to EM line; E-C — distance from external occipital protuberance to the point of SSC-C on EM line; EC/EM — percentage of EC to EM length; MB/MM — percentage of MB to MM length

should be made aware of when performing the GON block since anaesthetic could affect only one branch of the GON. Nevertheless, it was found in only 2% of specimens. Furthermore, symmetrical patterns of Sc and SSC piercing points were found in a high percentage, thus reducing the concern of asymmetry.

A comparison of locations of the GON in relation to EOP, midline, intermastoid (MM) and EM lines in the previous and current studies is demonstrated in Table 5 [3, 7, 14, 16–18, 21, 23]. The Sc piercing point was above MM line at a mean distance of 17.79 ± ± 5.80 mm and is similar to that of Güvençer et al. 2011 (17.1 ± 2.58 mm) [7]. However, dissimilarity might be due to the number of samples, method of measurement and ethnicities. Moreover, comparisons of GON location in each type of Sc and SSC piercing points were not taken into account in the previous studies. Our data revealed that the Sc piercing point

Table 4. Comparisons of the prevalence of subcutaneous piecing point type, patterns of semispinalis capitis (SSC) piercing point and relation of greater occipital nerve (GON) to obliquus capitis inferior (OCI) in this and previous studies

Authors, year	Bovim et al. 1991 [3]	Mosser et al. 2004 [17]	Natsis et al. 2006 [18]	Tubbs et al. 2014 [22]	Won et al. 2018 [24]	This study, 2020
Race	Norwegian	American	German	American	Korean	Thai
Number (sides)	20 (40)	20 (40)	40 (80)	15 (30)	28 (56)	50(100)
Pierce trapezius muscle (type I)	18 (45%)	–	–	5 (16.7%)	14 (50%)	2 (2%)
Pierce trapezius aponeurosis	22 (55%)	–	–	25(83.3%)	7 (12.5%)	67 (67%)
Pierce between trapezius and sternocleidomastoid	0 (0%)	–	–	0 (0%)	35 (62.5%)	31 (31%)
Pierce SSC muscle	36 (90%)	40 (100%)	–	22 (73.3%)	–	95 (95%)
Pierce tendinous band of SSC	0 (0%)	0 (0%)	–	5 (16.7%)	–	2 (2%)
Between SSC and nuchal ligament	4 (10%)	0 (0%)	–	3 (10%)	–	3 (3%)
Turn around lower edge of OCI	37 (92.5%)	–	76 (95%)	28 (93.3%)	–	94 (94%)
Pierce muscle of lower edge of OCI	3 (7.5%)	–	3 (3.75%)	2 (6.7%)	–	6 (6%)
Passes through suboccipital triangle	0 (0%)	–	1 (1.25%)	0 (0%)	–	0 (0%)

Data are shown as number (%).

was always located above the MM line, therefore, the intermastoid or MM line was used to locate the Sc piercing point which was similar to the result of Loukas et al, (2006) [16]. The Sc piercing point could be located approximately 44% (44.36 ± 4.52%) of the distance along MM line from the ipsilateral MP with a mean vertical distance of about 18 mm (17.97 ± ± 5.80 mm) (Fig. 1). No statistically significant difference was found between genders and sides. However, a statistically significant difference was found between type III and type I ($p = 0.02$). Nevertheless, type I was found only in 2% of cases. As previously mentioned in the results, Sc piercing points could be located either above, below and on the EM line similar to the result of Won et al. (2018) [24]. They located the Sc piercing point of GON by drawing a circle with a radius of 2 cm and divided into four equal sectors at the medial transaction point of EM line. The GON pierced the fascia within the circle in 85.7% of specimens and most frequently (42.9%) in the inferomedial sector of the circle [24]. Shin et al. (2018) [19] used a three-dimensional digitizer to locate the GON on the superior nuchal and EM line. The GON was on the medial third of EM line and 33.5 mm from the EOP on the superior nuchal line. They recommended the safe injection points on the EM line at about 3 cm from EOP, 1 cm inferior and parallel to the EM line and 3 cm from MP [19].

Tubbs et al. (2007) [21], reported that the GON pierced the SSC on an average of 2 cm superior to the intermastoid line, similar to Loukas et al. (2006) [16]. In contrast, our data revealed that GON might pierce the SSC above, below or on the MM line. Moreover, almost all of the SSC piercing points were located below the EM line (except one male right GON). Therefore, we decided to use the EM line to locate the SSC piercing point. The SSC piercing point of all types could be located at approximately 25% (25.25 ± 4.83%) of the distance along EM line from the EOP with a mean vertical distance of about 18 mm (18.10 ± 5.13 mm) below EM line (Fig. 1). No statistically significant difference was found between genders, sides and types of the piercing points. These morphometric data are useful for performing GON block or avoiding GON injury during procedures in the occipital region in Asian population.

CONCLUSIONS

Type and location of Sc piercing points, patterns and location of SSC piercing point and the relation of GON to OCI were examined in 50 embalmed cadaveric heads. Three types of Sc piercing points were found. The most prevalent was type II followed by type III and I, respectively. Sc and SSC piercing points were located with reference to the intermastoid (MM) and EOP to MP (EM) lines, respectively. Most parameters demonstrated no statistically significant differences between genders, sides and type of Sc and SSC piercing points. Knowledge of the anatomical variations of the GON piercing points and its location may optimize the efficacy and safety of relevant procedures in the occipital area.

Table 5. Comparison of distances from reference landmarks for greater occipital nerve localisation in this and previous studies

	Vital et al. 1989 [23]	**Bovim et al. 1991 [3]**	**Mosser et al. 2004 [17]**	**Natsis et al. 2006 [18]**	**Loukas et al. 2006 [16]**	**Tubbs et al. 2007 [21]**	**Güvençer et al. 2011 [7]**	**Kim et al. 2018 [14]**	**This study 2020**
N (sides)	9 (18)	20 (40)	20 (40)	40 (80)	100 (200)	12 (24)	??? (12)	30 (60)	49 (98)
Race	French	Norwegian	American	German	American	American	Turk	Korean	Thai
Distances from reference landmarks Subcutaneous piercing point									
Inferior to EOP [mm]	22.2	12	30	8.9 ± 2.4	–	–	15.1 ± 7.0	16.3 ± 5.9	–
Lateral to midline [mm]	31.8	24	15	Right: 35.4 ± 4.6 Left: 33.9 ± 4.8	38 (1.5–7.5)	40 (35–65)	47.9 ± 8.0	22.6 ± 7.4	–
Perpendicular distance to/above or below MM line [mm]	5–25 above	–	–	–	–	–	17.1 ± 2.8 above	–	17.97 ± 5.80 perpendicular
From MP [mm]	–	–	–	–	–	–	59.4 ± 2.3	–	–
% of MM line from MP	–	–	–	–	41 ± 3	–	–	–	44.36 ± 4.52
% of EM line	–	–	–	–	22 ± 2	–	–	–	–
Distances from reference landmarks Semispinalis capitis piercing point									
Inferior to EOP [mm]	37.3	37	Right: 29.1 ± 7.8 Left: 28.7 ± 6.6	27.2 ± 6.3	–	–	53.6 ± 5.0	27.7 ± 9.9	–
Lateral to midline [mm]	11.5	16	Right: 14.1 ± 4.4 Left: 13.8 ± 4.3	Right: 12.1 ± 2.4 Left: 12.0 ± 2.4	–	–	9.0 ± 1.9	13.1 ± 6.0	–
Perpendicular distance to/above or below MM line [mm]	0–15 below	–	–	–	20 (11–42) above	20 (15–33) above	11.5 ± 3.9 above	–	–
From MP [mm]	–	–	–	–	–	–	65.5 ± 5.9		
Perpendicular distance to/below EM line [mm]									18.10 ± 5.13 perpendicular
% of EM line from EOP	–	–	–	–	–	–	–	–	25.25 ± 4.83

EOP — external occipital protuberance; EM — external occipital protuberance to mastoid process; MM — intermastoid line; MP — mastoid process

Acknowledgements

The authors would like to express our sincere appreciation to all those who have donated their bodies for medical study and research. Special thanks are extended to Dr. Lita Tesapirat for statistical analysis and the technical staff of the Department of Anatomy, Faculty of Medicine, Chulalongkorn University for their support in cadaveric care.

Conflict of interest: None declared

REFERENCES

1. Barmherzig R, Kingston W. Occipital neuralgia and cervicogenic headache: diagnosis and management. Curr Neurol Neurosci Rep. 2019; 19(5): 20, doi: 10.1007/s11910-019-0937-8, indexed in Pubmed: 30888540.
2. Bogduk N. The clinical anatomy of the cervical dorsal rami. Spine (Phila Pa 1976). 1982; 7(4): 319–330, doi: 10.1097/00007632-198207000-00001, indexed in Pubmed: 7135065.
3. Bovim G, Bonamico L, Fredriksen TA, et al. Topographic variations in the peripheral course of the greater occipital nerve. Autopsy study with clinical correlations. Spine (Phila Pa 1976). 1991; 16(4): 475–478, doi: 10.1097/00007632-199104000-00017, indexed in Pubmed: 2047922.
4. Cesmebasi A, Muhleman MA, Hulsberg P, et al. Occipital neuralgia: anatomic considerations. Clin Anat. 2015; 28(1): 101–108, doi: 10.1002/ca.22468, indexed in Pubmed: 25244129.
5. Choi Il, Jeon SR. Neuralgias of the head: occipital neuralgia. J Korean Med Sci. 2016; 31(4): 479–488, doi: 10.3346/jkms.2016.31.4.479, indexed in Pubmed: 27051229.
6. Ducic I, Moriarty M, Al-Attar A. Anatomical variations of the occipital nerves: implications for the treatment of chronic headaches. Plast Reconstr Surg. 2009; 123(3): 859–863, doi: 10.1097/PRS.0b013e318199f080, indexed in Pubmed: 19319048.
7. Güvençer M, Akyer P, Sayhan S, et al. The importance of the greater occipital nerve in the occipital and the suboccipital region for nerve blockade and surgical approaches--an anatomic study on cadavers. Clin Neurol Neurosurg. 2011; 113(4): 289–294, doi: 10.1016/j.clineuro.2010.11.021, indexed in Pubmed: 21208741.
8. Hammond SR, Danta G. Occipital neuralgia. Clin Exp Neurol. 1978; 15: 258–270, indexed in Pubmed: 756019.
9. Headache Classification Subcommittee of the International Headache Society. The International Classification of Headache Disorders: 2nd ed. Cephalalgia. 2004; 24 Suppl 1: 9–160, doi: 10.1111/j.1468-2982.2003.00824.x, indexed in Pubmed: 14979299.
10. Hunter C, Mayfield F. Role of the upper cervical roots in the production of pain in the head. Am J Surg. 1949; 78(5): 743–751, doi: 10.1016/0002-9610(49)90316-5.
11. Janis JE, Hatef DA, Ducic I, et al. The anatomy of the greater occipital nerve: Part II. Compression point topography. Plast Reconstr Surg. 2010; 126(5): 1563–1572, doi: 10.1097/PRS.0b013e3181ef7f0c, indexed in Pubmed: 20639804.
12. Jose A, Nagori SA, Chattopadhyay PK, et al. Greater occipital nerve decompression for occipital neuralgia. J Craniofac Surg. 2018; 29(5): e518–e521, doi: 10.1097/SCS.0000000000004549, indexed in Pubmed: 29762321.
13. Juškys R, Šustickas G. Effectiveness of treatment of occipital neuralgia using the nerve block technique: a prospective analysis of 44 patients. Acta Med Litu. 2018; 25(2): 53–60, doi: 10.6001/actamedica.v25i2.3757, indexed in Pubmed: 30210238.
14. Kim HS, Shin KJ, O J, et al. Stereotactic topography of the greater and third occipital nerves and its clinical implication. Sci Rep. 2018; 8(1): 870, doi: 10.1038/s41598-018-19249-6, indexed in Pubmed: 29343808.
15. Kwon HJ, Kim HS, O J, et al. Anatomical analysis of the distribution patterns of occipital cutaneous nerves and the clinical implications for pain management. J Pain Res. 2018; 11: 2023–2031, doi: 10.2147/JPR.S175506, indexed in Pubmed: 30310306.
16. Loukas M, El-Dedfy A, Tubbs RS, et al. Identification of greater occipital nerve landmarks for treatment of occipital neuralgia. Folia Morphol. 2006; 65(4): 337–342, indexed in Pubmed: 17171613.
17. Mosser SW, Guyuron B, Janis JE, et al. The anatomy of the greater occipital nerve: implications for the etiology of migraine headaches. Plast Reconstr Surg. 2004; 113(2): 693–698, doi: 10.1097/01.PRS.0000101502.22727.5D, indexed in Pubmed: 14758238.
18. Natsis K, Baraliakos X, Appell HJ, et al. The course of the greater occipital nerve in the suboccipital region: a proposal for setting landmarks for local anesthesia in patients with occipital neuralgia. Clin Anat. 2006; 19(4): 332–336, doi: 10.1002/ca.20190, indexed in Pubmed: 16258972.
19. Shin KJ, Kim HS, O J, et al. Anatomical consideration of the occipital cutaneous nerves and artery for the safe treatment of occipital neuralgia. Clin Anat. 2018; 31(7): 1058–1064, doi: 10.1002/ca.23210, indexed in Pubmed: 29752841.
20. Stechison MT, Mullin BB. Surgical treatment of greater occipital neuralgia: an appraisal of strategies. Acta Neurochir (Wien). 1994; 131(3-4): 236–240, doi: 10.1007/BF01808620, indexed in Pubmed: 7754828.
21. Tubbs RS, Salter EG, Wellons JC, et al. Landmarks for the identification of the cutaneous nerves of the occiput and nuchal regions. Clin Anat. 2007; 20(3): 235–238, doi: 10.1002/ca.20297, indexed in Pubmed: 16944523.
22. Tubbs RS, Watanabe K, Loukas M, et al. The intramuscular course of the greater occipital nerve: novel findings with potential implications for operative interventions and occipital neuralgia. Surg Neurol Int. 2014; 5: 155, doi: 10.4103/2152-7806.143743, indexed in Pubmed: 25422783.
23. Vital JM, Grenier F, Dautheribes M, et al. An anatomic and dynamic study of the greater occipital nerve (n. of Arnold). Applications to the treatment of Arnold's neuralgia. Surg Radiol Anat. 1989; 11(3): 205–210, doi: 10.1007/BF02337823, indexed in Pubmed: 2588096.
24. Won HJ, Ji HJ, Song JK, et al. Topographical study of the trapezius muscle, greater occipital nerve, and occipital artery for facilitating blockade of the greater occipital nerve. PLoS One. 2018; 13(8): e0202448, doi: 10.1371/journal.pone.0202448, indexed in Pubmed: 30110386.

VIA MEDICA

ORIGINAL ARTICLE

Folia Morphol.
Vol. 80, No. 3, pp. 542–548
DOI: 10.5603/FM.a2020.0088

ISSN 0015–5659
eISSN 1644–3284
journals.viamedica.pl

Comparison of the histological structure of the tibial nerve and its terminal branches in the fresh and fresh-frozen cadavers

Ł. Warchoł[1], J.A. Walocha[1], E. Mizia[1], H. Liszka[1], M. Bonczar[2]

[1]*Department of Anatomy, Jagiellonian University Medical College, Krakow, Poland*
[2]*Intermed Medical Clinic, Zabierzow, Poland*

[Received: 7 June 2020; Accepted: 28 July 2020; Early publication date: 7 August 2020]

Background: *The aim of this study was to compare the histological structure (cross-sectional area [CSA] and number of nerve fascicles) of the distal part of the tibial nerve (TN) and its terminal branches (medial plantar nerve [MPN], lateral plantar nerve [LPN]) in the fresh and fresh-frozen cadavers using computer assisted image analysis.*

Materials and methods: *The TNs with terminal branches (MPN and LPN) were dissected from the fresh and fresh-frozen cadavers. Each nerve was harvested 5 mm proximally and respectively 5 mm distally from the TN bifurcation, marked, dehydrated, embedded in paraffin, sectioned at 2 μm slices and stained with haematoxylin and eosin. Then the specimens were photographed and analysed using Olympus cellSens software.*

Results: *The fresh cadavers' group comprised 60 feet (mean age 68.1 ± 15.2 years). The mean CSA and the number of nerve fascicles were respectively 15.25 ± 4.6 mm^2, 30.35 ± 8.45 for the TN, 8.76 ± 1.93 mm^2, 20.75 ± 7.04 for the MPN and 6.54 ± 2.02 mm^2, 13.40 ± 5.22 for the LPN. The fresh-frozen cadavers' group comprised 21 feet (mean age 75.1 ± 9.0 years). The mean CSA and the number of nerve fascicles were respectively 13.71 ± 5.66 mm^2, 28.57 ± 8.00 for the TN, 7.55 ± 3.25 mm^2, 18.00 ± 6.72 for the MPN and 4.29 ± 1.93 mm^2, 11.33 ± 1.93 for the LPN. Only LPNs showed statistical differences in the CSA and the number of nerve fascicles between examined groups ($p = 0.000$, $p = 0.037$, respectively). A positive correlation was found between donors age and tibial nerve CSA in the fresh cadavers group ($r = 0.44$, $p = 0.000$). A statistical difference was found between the MPN and LPN both in the CSA and the number of nerve fascicles ($p < 0.001$, $p < 0.001$, respectively).*

Conclusions: *The CSA and the number of nerve fascicles of the tibial and medial plantar nerves were similar in the fresh and fresh-frozen cadavers whilst different in the LPN. The TN showed increasing CSA with the advanced age in the fresh cadavers. The MPN had larger CSA and more nerve fascicles than the LPN.* (Folia Morphol 2021; 80, 3: 542–548)

Key words: tibial nerve, cross-sectional area, medial and lateral plantar nerves, fresh cadavers, fresh-frozen cadavers

Address for correspondence: Dr. Ł. Warchoł, Department of Anatomy, Jagiellonian University Medical College, ul. Kopernika 12, 31–034 Kraków, Poland, tel: +48 601 865 239, e-mail: l.warchol@uj.edu.pl

INTRODUCTION

The tibial nerve (TN) is a peripheral sensorimotor nerve arising as a branch of sciatic nerve bifurcation in the popliteal fossa [40]. It runs vertically on the tibialis posterior muscle together with the posterior tibial vessels. Postero-inferiorly to the medial malleolus it terminates emitting medial plantar nerve (MPN) and smaller lateral plantar nerve (LPN) [28]. The TN bifurcation level shows a great variability as so depending on the study its localisation is referred to the medial or lower located lateral malleolus [24, 43]. Most commonly it is described below the tip of the medial malleolus, inside the tarsal tunnel [42]. Tibial nerve and its branches provide innervation to the posterior lower leg, the muscles and skin of the sole of the foot [21].

For many years ankle arthroscopy has proved to be a useful diagnostic and therapeutic procedure for ankle and foot disorders. Although it is a minimally invasive surgery neurological complications are most frequently reported referring to the tibial, sural, superficial peroneal and deep peroneal nerves [1, 45, 47]. According to Freedman and Barron [13] all neurovascular impairments are caused by distractor pin or portal placement. In order to avoid iatrogenic injuries and to perform safe and reproducible arthroscopy constant training is highly recommended.

Nowadays necessity of constant practicing of surgical skills is emphasized by professionals [2]. They clearly highlight the superiority of fresh cadavers among any frozen or anatomically preserved. However, due to ethical and technical problems as well as limited access to the fresh bodies, fresh-frozen cadavers proved to be convenient surgical training model [35]. Because of their most lifelike features they are used by surgeons, orthopaedics, radiologists and anaesthesiologist to practice and improve operating skills [12, 17]. Fresh-frozen bodies also found application in the research and bioengineering, allowing development of new instruments and procedures.

The aim of this study was to compare the histological structure of the TN and its terminal branches in the fresh and fresh-frozen cadavers.

MATERIALS AND METHODS

The study was conducted on 60 lower limbs of the fresh cadavers and on 21 lower limbs of the fresh-frozen cadavers in the Department of Anatomy between December 2016 and March 2019. The group of fresh-frozen cadavers composed of already amputated lower limbs at the level of the knee originating from mixed donors with known medical record. The exclusion criteria were any deformation of the lower limb or the lower limb trauma, surgical or radiotherapeutic procedures of the lower limb, chronic disease of the lower limb in the medical record of the donor.

The research protocol was approved by the local Ethics Committee (Registry No. 122.6120.315.2016). The study has been performed in accordance with the ethical standards established in the 1964 Declaration of Helsinki and its later amendments.

Dissection technique

The incision was made in the midline between the tip of the medial malleolus and the Achilles tendon. It continued 10 cm proximally along the Achilles tendon and 10 cm distally curving anteriorly 2 cm below the tip of the medial malleolus. Upon dissecting the skin and the subcutaneous tissue the TN was visualised together with the posterior tibial artery and two posterior tibial veins. After meticulous dissection the TN, its bifurcation and LPN and MPN were exposed. The plantar nerves were marked 2 cm distally from the TN bifurcation point with the following pattern: blue thread — lateral plantar nerve, white thread — medial plantar nerve. The TN was left without any marking. Then 3 cm proximally to the bifurcation the TN was cut out from the main nerve trunk. Accordingly, 3 cm distally the MPN and LPN were cut out. The excised tibial nerve and its terminal branches were removed *en bloc* from the cadaver. The incision was closed with the running subcuticular suture. In the group of fresh-frozen cadavers the dissection was performed after thawing of the specimens overnight at room temperature. The harvesting was carried out by the same surgeon.

Preparation of histological slide

The excised block of nerves was fixed in a 10% solution of the formaldehyde (pH 7.4). After 2–5 days it was removed from the formaldehyde. The TN was cut transverse to the nerve axis 5 mm and 10 mm proximally to the TN bifurcation point as were the MPN and LPN 5 mm and 10 mm distally to the TN bifurcation point. Obtained 5 mm long nerve fragments were dehydrated separately and embedded in paraffin according to its initial marking. Each paraffin cube was transverse sectioned with the microtome providing one 2 μm thick slice. Subsequently each slice was stained with haematoxylin and eosin (Fig. 1).

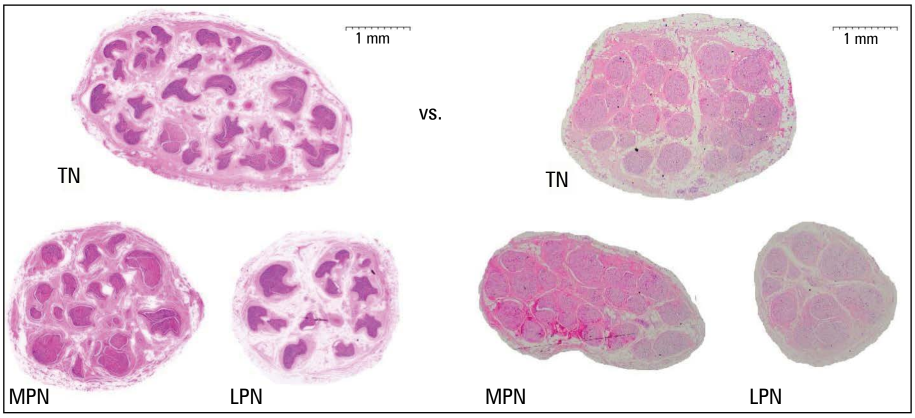

Figure 1. Cross-section of tibial nerve (TN), medial plantar nerve (MPN) and lateral plantar nerve (LPN) of the fresh cadaver (on the left) and fresh-frozen cadaver (on the right). Haematoxylin and eosin staining.

Table 1. Measured nerve parameters for tibial nerve, medial plantar nerve, and lateral plantar nerve — comparison between fresh and fresh-frozen cadavers

Measurement		Fresh cadavers					Fresh-frozen cadavers					P
		N	Mean ± SD	Median	Lower quartile (Q1)	Upper quartile (Q3)	N	Mean ± SD	Median	Lower quartile (Q1)	Upper quartile (Q3)	
Cross-sectional area [mm²]	Tibial nerve	60	15.25 ± 4.65	14.66	11.77	17.29	21	13.71 ± 5.66	12.84	9.50	16.15	0.094
	Medial plantar nerve	60	8.76 ± 1.93	8.45	7.19	9.90	21	7.55 ± 3.25	7.53	4.61	10.36	0.156
	Lateral plantar nerve	60	6.54 ± 2.02	6.44	5.12	7.41	21	4.29 ± 1.93	4.31	2.52	5.76	0.000
Number of nerve fascicles	Tibial nerve	60	30.35 ± 8.45	31.00	25.00	35.25	21	28.57 ± 8.00	31.00	22.00	35.00	0.403
	Medial plantar nerve	60	20.75 ± 7.04	20.00	16.00	25.00	21	18.00 ± 6.72	18.00	12.00	22.00	0.123
	Lateral plantar nerve	60	13.40 ± 5.22	13.50	10.75	15.00	21	11.33 ± 1.93	11.00	7.00	14.00	0.037

Numbers in bold indicate statistically significant differences between fresh and fresh-frozen cadavers ($p < 0.05$); SD — standard deviation

Micromorphometry

The cross-sectional area (CSA) and the number of nerve fascicles of the TN, MPN, and LPN were assessed using a light microscope (Olympus BX53, 20× magnification). Each cross-section was photographed (20× magnification), afterwards the CSA was measured semi-automatically using Olympus cellSens Standard 2.3 software with the producer's precision of 10 μm, whilst the number of nerve fascicles was calculated manually. Each slice was assessed once by the same pathologist. Then the values of the CSA and the number of nerve fascicles were tabulated according to the group (fresh or fresh-frozen cadavers).

Statistical analysis

Obtained data were statistically processed using descriptive statistics such as percentage, mean, median, standard deviation, upper and lower quartiles. A p-value of < 0.05 was considered as statistically significant. Two groups were compared using the Mann-Whitney test or t-test depending on normal distribution. To compare CSA and number of nerve fascicles between TN, MPN and LPN paired t-test or Wilcoxon rang test were used depending on whether data was normally distributed. Correlation coefficients were calculated to establish any statistical dependence between parameters. All analyses were performed using MedCalc version 16.8.

RESULTS

There were 30 fresh cadavers dissected (n = 60 lower limbs) with a mean age of 68.1 ± 15.2 (range from 27 to 91 years). 28 (46.7%) feet were female and 32 (53.3%) were male. In the group of fresh-frozen cadavers 21 lower limbs were dissected with a mean age of 75.1 ± 9.0 (range from 60 to 92 years). Twelve (57.1%) feet were female and 9 (42.9%) were male. The mean CSA and number of nerve fascicles of the TN, MPN, and LPN in the fresh and fresh-frozen groups are presented in Table 1. Gender differences between examined groups are presented in Table 2. In both examined groups males' tibial nerves showed larger CSA and more nerve fascicles than females'. Only LPNs showed statistical differences in the CSA

Table 2. Measured nerve parameters for tibial nerve, medial plantar nerve, and lateral plantar nerve — comparison by gender between fresh and fresh-frozen cadavers

Gender	Measurement		Fresh cadavers					Fresh-frozen cadavers					P
			N	Mean ± SD	Median	Lower quartile (Q1)	Upper quartile (Q3)	N	Mean ± SD	Median	Lower quartile (Q1)	Upper quartile (Q3)	
Women	Cross-sectional area [mm²]	Tibial nerve	28	12.27 ± 2.45	11.85	10.35	14.31	12	12.70 ± 3.90	13.46	9.28	15.27	0.802
		Medial plantar nerve	28	7.81 ± 1.41	7.37	6.70	9.10	12	7.77 ± 3.38	7.41	5.88	10.78	0.988
		Lateral plantar nerve	28	5.83 ± 1.25	5.77	4.61	6.86	12	4.47 ± 2.05	4.56	2.70	5.79	0.030
	Number of nerve fascicles	Tibial nerve	28	26.32 ± 8.87	25.00	19.50	34.00	12	28.08 ± 9.13	31.50	20.50	34.25	0.555
		Medial plantar nerve	28	17.71 ± 5.28	18.00	14.50	20.50	12	16.50 ± 7.23	17.00	12.00	19.75	0.426
		Lateral plantar nerve	28	11.50 ± 3.72	12.00	9.00	14.00	12	11.42 ± 7.23	9.00	6.00	14.25	0.417
Men	Cross-sectional area [mm²]	Tibial nerve	32	17.86 ± 4.57	17.10	15.02	19.90	9	15.06 ± 7.45	12.57	10.09	16.29	0.053
		Medial plantar nerve	32	9.58 ± 1.95	9.16	8.40	10.66	9	7.26 ± 3.25	7.64	4.61	9.83	0.092
		Lateral plantar nerve	32	7.17 ± 2.36	7.08	5.18	8.35	9	4.05 ± 1.86	3.35	2.28	5.66	0.001
	Number of nerve fascicles	Tibial nerve	32	33.88 ± 6.31	34.00	28.50	38.00	9	29.22 ± 6.67	30.00	25.00	35.00	0.119
		Medial plantar nerve	32	23.41 ± 7.37	22.50	17.50	29.50	9	20.00 ± 5.77	20.00	17.00	24.00	0.270
		Lateral plantar nerve	32	15.06 ± 5.81	14.50	12.50	16.50	9	11.22 ± 2.73	12.00	9.00	13.00	0.020

Numbers in bold indicate statistically significant differences between males and females ($p < 0.05$); SD — standard deviation

and number of nerve fascicles between examined groups. The LPN also proved statistical difference among males (CSA and number of nerve fascicles) and females (CSA) in fresh and fresh-frozen cadavers. In the fresh cadavers no statistically significant differences between right and left foot of the individual were found ($p > 0.05$). Such comparison was not possible to perform in the fresh-frozen cadavers as the examined lower limbs originated from different individuals. There is statistically significant difference between MPN and LPN in CSA and number of nerve fascicles in both groups ($p < 0.001$). CSA of the MPN confirmed to be 1.3 times and 1.8 times larger than the lateral plantar nerves' in the fresh and fresh-frozen specimens, respectively. The MPN also proved to have more nerve fascicles than the LPN in both examined groups. A positive correlation was noted between the age of donors and the CSA of the TN in the fresh cadavers group ($r = 0.44$, $p = 0.000$; Table 3).

DISCUSSION

The present study compares histological structure (CSA and number of nerve fascicles) of the distal part of the TN and its terminal branches (MPN and LPN) in the fresh and fresh-frozen cadavers assessed using computer-assisted measurements. Literature analysis shows that in the previous studies the CSA of the tibial nerve was evaluated by ultrasound or magnetic resonance imagining on the living patients or volunteers [5, 15, 22]. To the best of our knowledge this is the first publication analysing histological differences in peripheral nerves obtained from the fresh and fresh-frozen cadavers. It is also the first study revealing TN, MPN, and LPN CSA measured directly on the nerves harvested from the fresh cadavers. Furthermore no reference values for the CSA of the medial and lateral plantar are available in the literature.

In the present study the TN, MPN, and LPN harvested from the 60 fresh cadavers were compared to 21 collected from the fresh-frozen cadavers. The fresh

Table 3. Association between age and measured nerve parameters for tibial nerve, medial plantar nerve, and lateral plantar nerve in fresh and fresh-frozen cadavers

Measurement		Fresh cadavers			Fresh-frozen cadavers		
		N	R	P	N	R	P
Cross-sectional area [mm²]	Tibial nerve	60	**0.439**	**0.000**	21	0.112	0.629
	Medial plantar nerve	60	0.083	0.531	21	0.040	0.862
	Lateral plantar nerve	60	0.110	0.401	21	-0.045	0.847
Number of nerve fascicles	Tibial nerve	60	0.086	0.512	21	–0.161	0.485
	Medial plantar nerve	60	–0.224	0.085	21	–0.140	0.545
	Lateral plantar nerve	60	–0.104	0.428	21	–0.204	0.376

Numbers in bold indicate statistically significant age correlation ($p < 0.05$).

Table 4. Studies of the tibial nerve cross-sectional area (CSA) measured at the level of medial malleolus

	Group (n)	Mean age	CSA of the tibial nerve at the level of medial malleolus [mm²]	Reference range [mm²]	Type of study
He et al., 2019 [16]	40	55.2	11.6 ± 1.6	–	US 4–15 MHz
Lothet et. al., 2019 [25]	15	21.7	12.3	–	US 18 MHz
Bedewi et al., 2018 [5]	138	38.3	12.7 ± 4.5	2.0–30.0	US 18.5 MHz
Grimm et al., 2018 [15]	100	51.2	10.2 ± 2.0	–	US 14 MHz
Kronlage et al., 2017 [22]	60	30.5	8.1 ± 2.0*	4.0–12.1	MRI
Singh et al., 2017 [36]	75	39.5	12.4 ± 1.1	10.0–14.0	US 7–18 MHz
Kang et al., 2016 [20]	20	65.0	12.4 ± 2.9	–	US 7–12 MHz
Boehm et al., 2014 [7]	56	50.2	9.6 ± 2.2	9.0–10.2	US 12–15 MHz
Seok et al., 2014 [33]	94	43.9	12.1 ± 3.1	8.5–22.8	US 5–12 MHz
Riazi et al., 2012 [31]	43	46.8	17.7 ± 6.5	–	US 6–13 MHz
Tagliafico et al., 2012 [38]	58	47.0	9.6 ± 4.0	7.2–13.7	US 17.5 MHz
Cartwright et al., 2008 [11]	60	45.9	13.7 ± 4.3	5.1–22.3	US 15 MHz
Lee et al., 2005 [23]	24	57.4	12.0	–	US 10–12 MHz

*Measured at the proximal third of the calf; MRI — magnetic resonance imaging; US — ultrasonography

cadavers group composed of younger donors (mean age: 68.1 vs 75.1) and presented slightly higher values of CSA (TN: 15.25 vs. 13.71; MPN: 8.76 vs. 7.55; LPN: 6.54 vs. 4.29) and more nerve fascicles (TN: 30.35 vs. 28.57; MPN: 20.75 vs. 18.00; LPN: 13.40 vs. 11.33). Nevertheless tibial nerve CSA measured in both groups is in line with results of ultrasound and magnetic resonance imaging performed on living patients (Table 4). The statistical analysis proved that the tibial and medial plantar nerves are similar in the fresh and fresh-frozen groups. On the other hand the lateral plantar nerves appeared to be statistically different. Such discrepancy may be the result of anatomical differences of the examined nerves. The LPN is the smaller terminal branch of the TN bifurcation [21]. Because of that it may be suggested that freezing process does not alter larger nerves (TN, MPN) whilst impacts smaller ones (LPN). Although the differences proved to be statistically insignificant (except for LPN) their slightly decreased values in fresh-frozen cadavers is worth noticing. Besides micromorphometric assessment some differences between two examined groups appeared during its histological preparation. Fresh-frozen specimens showed grater stiffness and hardness of the nerve trunks, poorly stained with haematoxylin and eosin and revealed more artefacts in the microscopic analysis.

Decreased CSA of the assessed nerves may be explained by Bakhach [4] who described changes occurring in biological tissues during freezing using thermodynamic and biophysical laws. Emphasizing that water may reach up to 70% of tissues volume he examined its transfer between intra and extracellular compartments throughout crystallisation process. Intracellular formation and aggregation of ice crystals destroy its structures and cause mechanical stress on the cell walls resulting in deformation and fragmentation. Moreover water transition into a solid state leads to changes in extracellular chemical composition with the increased ion accumulation. Such concentration gradient between cell membrane makes water run out of the intracellular space causing its dehydration. These may elucidate rigidness of the nerve samples, artefacts in the microscopic assessment and slightly decreased CSA of the fresh-frozen cadavers registered in the present study.

Although fresh cadavers retain biomechanical features and are most suitable for the surgical training, they putrefy and are available only for the short time [3]. Searching for the best fresh body equivalent brought to many studies on its preservation [9, 12]. Along with proved advantages each method revealed some limitations, as so: formalin fixation makes the specimens stiff and discoloured, Thiel embalming requires infrastructure for the process and is not suitable for all tissues, fresh-freezing brings the risk of infection and needs time for thawing [39]. Nevertheless, fresh-frozen cadavers seem to be the most flexible and realistic [19]. They appeared to be even better than the virtual reality stimulator [34].

While literature provides comparative analysis of the fresh and fresh-frozen tendons [6, 18], bones [10, 26, 41], and osteochondral allografts, [29] there is lack of such comparison for the human peripheral nerves. Hohmann et al. [18] revealed that the long head of biceps tendons showed higher loads to failure and lower elasticity in the fresh-frozen samples when compared to the fresh specimens. At the same time fresh tendons were wider and presented larger CSA. On the contrary, Bitar et al. [6] state that fresh-frozen tendons of the semitendinosus muscle show no histological differences referring to the fresh ones. Similarly Panjabi et al. [30] deny any physical or histological changes in the fresh-frozen specimens. Opposite to that, Giannini et al. [14] noted an increased CSA in the fresh-frozen tendons of the posterior tibial muscles as well as increased stiffness and decreased ultimate load. An interesting study was performed by Zarb et al. [46] who analysed the quality of the magnetic resonance images of living patients', fresh-frozen and Thiel embalmed bones, ligaments, tendons and muscles of the ankle. The image quality of the fresh-frozen specimen appeared to be higher when compared to that of living patient. Unfortunately no nerves of the ankle were included in the research which might have been beneficial for the present study reference.

Fresh-frozen peripheral nerves were examined mostly in relation to their biomechanical properties [8, 44]. Stouthandel et al. [37] compared Thiel embalmed and fresh-frozen median nerves showing slight increase of CSA in the embalmed group, no significant difference in elasticity and similar biomechanical patterns. Enlarged CSA of the nerves preserved with the Thiel method is interpreted to be the result of the embalming fluid uptake. Sargon et al. [32] counted the myelinated nerve fibres of the fresh-frozen facial nerve terminal branches concluding that both fresh and fresh-frozen human specimens are better than formalin-fixed in order to perform the anatomic dissection and find tiny nerves.

To the best of our knowledge there has not been any publication which compared histological structure of the fresh-frozen human nerves to the fresh ones. As so, such analysis of the peripheral nerves together with biomechanical experiments may constitute a valuable subject for the future studies.

Albeit there were relatively high number of lower limbs examined in the present study (81 feet) their uneven distribution among the compared groups (60 vs. 21) and low number of fresh-frozen cadavers might have influenced the results. Only 9 males in the fresh-frozen cadavers group would have significantly hindered the gender comparison. Second limitation is the fact that lower limbs included in the group of fresh-frozen cadavers originated from different donors which impeded the intra-individual left-right comparison. Another restriction is the various age of the analysed groups which is proved to correlate with peripheral nerves CSA [15, 27]. Narrow range of age in the fresh-frozen cadavers (from 60 to 92 years) might have also biased the age correlation which was confirmed for the tibial nerve CSA in the fresh cadavers (range of age from 27 to 91 years). Therefore, for the sake of future studies, the authors would recommend to collect and compare specimens from the contralateral sides of the individual (followed by the left-right difference exclusion).

CONCLUSIONS

To conclude, the authors of the present study proved that freezing process alters tissue properties of the smaller nerves on top of impacting biomechanical features of the peripheral nerves. Histological structure of the larger nerves remains uninfluenced by the freezing process.

Conflict of interest: None declared

REFERENCES

1. Abdul-Jabar HB, Bhamra J, Quick TJ, et al. Iatrogenic posterior tibial nerve division during a combined anterior ankle arthroscopy with

an additional posterolateral portal. J Surg Case Rep. 2016; 2016(5): rjw097, doi: 10.1093/jscr/rjw097, indexed in Pubmed: 27197613.
2. András C, Josvai A, Gergely C, et al. The importance of daily fast fresh cadaver dissection (how can we organize it?). J Neurol Stroke. 2019; 9(1), doi: 10.15406/jnsk.2019.09.00336.
3. Arnout N, Myncke J, Vanlauwe J, et al. The influence of freezing on the tensile strength of tendon grafts : a biomechanical study. Acta Orthop Belg. 2013; 79(4): 435–443, indexed in Pubmed: 24205775.
4. Bakhach J. The cryopreservation of composite tissues. Organogenesis. 2014; 5(3): 119–126, doi: 10.4161/org.5.3.9583.
5. Bedewi MA, Abodonya A, Kotb M, et al. Estimation of ultrasound reference values for the lower limb peripheral nerves in adults: A cross-sectional study. Medicine (Baltimore). 2018; 97(12): e0179, doi: 10.1097/MD.0000000000010179, indexed in Pubmed: 29561431.
6. Bitar AC, Santos LA, Croci AT, et al. Histological study of fresh versus frozen semitendinous muscle tendon allografts. Clinics (Sao Paulo). 2010; 65(3): 297–303, doi: 10.1590/S1807-59322010000300010, indexed in Pubmed: 20360921.
7. Boehm J, Scheidl E, Bereczki D, et al. High-resolution ultrasonography of peripheral nerves: measurements on 14 nerve segments in 56 healthy subjects and reliability assessments. Ultraschall Med. 2014; 35(5): 459–467, doi: 10.1055/s-0033-1356385, indexed in Pubmed: 24764211.
8. Botero SS, Honecker S, Jmal H, et al. The biomechanical properties of 44 human digital collateral nerves from fresh frozen cadavers. J Cell Immunother. 2018; 4(1): 38–40, doi: 10.1016/j.jocit.2018.09.009.
9. Brenner E. Human body preservation - old and new techniques. J Anat. 2014; 224(3): 316–344, doi: 10.1111/joa.12160, indexed in Pubmed: 24438435.
10. Cartner JL, Hartsell ZM, Ricci WM, et al. Can we trust ex vivo mechanical testing of fresh--frozen cadaveric specimens? The effect of postfreezing delays. J Orthop Trauma. 2011; 25(8): 459–461, doi: 10.1097/BOT.0b013e318225b875, indexed in Pubmed: 21738060.
11. Cartwright MS, Passmore LV, Yoon JS, et al. Cross-sectional area reference values for nerve ultrasonography. Muscle Nerve. 2008; 37(5): 566–571, doi: 10.1002/mus.21009, indexed in Pubmed: 18351581.
12. Eisma R, Wilkinson T. From "silent teachers" to models. PLoS Biol. 2014; 12(10): e1001971, doi: 10.1371/journal.pbio.1001971, indexed in Pubmed: 25333490.
13. Freedman DM, Barron OA. Iatrogenic posterior tibial nerve division during ankle arthroscopy. Arthroscopy. 1998; 14(7): 769–772, doi: 10.1016/s0749-8063(98)70109-4, indexed in Pubmed: 9788378.
14. Giannini S, Buda R, Di Caprio F, et al. Effects of freezing on the biomechanical and structural properties of human posterior tibial tendons. Int Orthop. 2008; 32(2): 145–151, doi: 10.1007/s00264-006-0297-2, indexed in Pubmed: 17216243.
15. Grimm A, Axer H, Heiling B, et al. Nerve ultrasound normal values — Readjustment of the ultrasound pattern sum score UPSS. Clin Neurophysiol. 2018; 129(7): 1403–1409, doi: 10.1016/j.clinph.2018.03.036, indexed in Pubmed: 29729596.
16. He Y, Xiang Xi, Zhu BH, et al. Shear wave elastography evaluation of the median and tibial nerve in diabetic peripheral neuropathy. Quant Imaging Med Surg. 2019; 9(2): 273–282, doi: 10.21037/qims.2019.02.05, indexed in Pubmed: 30976551.
17. Hocking G, McIntyre O. Achieving change in practice by using unembalmed cadavers to teach ultrasound-guided regional anaesthesia. Ultrasound. 2010; 19(1): 31–35, doi: 10.1258/ult.2010.010040.
18. Hohmann E, Keough N, Glatt V, et al. The mechanical properties of fresh versus fresh/frozen and preserved (Thiel and Formalin) long head of biceps tendons: A cadaveric investigation. Ann Anat. 2019; 221: 186–191, doi: 10.1016/j.aanat.2018.05.002, indexed in Pubmed: 29879483.
19. Jansen S, Kirk D, Tuppin K, et al. Fresh frozen cadavers in surgical teaching: a gelatine arterial infusion technique. ANZ J Surg. 2011; 81(12): 880–882, doi: 10.1111/j.1445-2197.2010.05596.x, indexed in Pubmed: 22507413.
20. Kang S, Kim SeH, Yang SN, et al. Sonographic features of peripheral nerves at multiple sites in patients with diabetic polyneuropathy. J Diabetes Complications. 2016; 30(3): 518–523, doi: 10.1016/j.jdiacomp.2015.12.008, indexed in Pubmed: 26782023.
21. Koo GB, Lee JH, Jang JH, et al. Superficial course of the medial plantar nerve: case report. Anat Cell Biol. 2019; 52(1): 87–89, doi: 10.5115/acb.2019.52.1.87, indexed in Pubmed: 30984458.
22. Kronlage M, Schwehr V, Schwarz D, et al. Magnetic resonance neurography : normal values and demographic determinants of nerve caliber and T2 relaxometry in 60 healthy individuals. Clin Neuroradiol. 2019; 29(1): 19–26, doi: 10.1007/s00062-017-0633-5, indexed in Pubmed: 29030674.
23. Lee D, Dauphinée D. Morphological and functional changes in the diabetic peripheral nerve. J Am Podiatr Med Assoc. 2005; 95(5): 433–437, doi: 10.7547/0950433.
24. Lijoi F, Lughi M, Baccarani G. Posterior arthroscopic approach to the ankle: an anatomic study. Arthroscopy. 2003; 19(1): 62–67, doi: 10.1053/jars.2003.50003, indexed in Pubmed: 12522404.
25. Lothet EH, Bishop TJ, Walker FO, et al. Ultrasound-Derived nerve cross-sectional area in extremes of height and weight. J Neuroimaging. 2019; 29(3): 406–409, doi: 10.1111/jon.12590, indexed in Pubmed: 30582247.
26. Marieswaran M, Mansoori N, Digge VK, et al. Effect of preservation methods on tensile properties of human femur-ACL-tibial complex (FATC) - a cadaveric study on male subjects. Acta Bioeng Biomech. 2018; 20(4): 31–42.
27. Mizia E, Tomaszewski KA, Rutowicz B, et al. Computer-assisted assessment of the histological structure of the human sural nerve. Folia Morphol. 2014; 73(3): 292–297, doi: 10.5603/FM.2014.0046, indexed in Pubmed: 25242156.
28. Moore KL. Clinically Oriented Anatomy. 8th Edition, LWW 2017.
29. Pallante-Kichura AL, Chen AC, Temple-Wong MM, et al. In vivo efficacy of fresh versus frozen osteochondral allografts in the goat at 6 months is associated with PRG4 secretion. J Orthop Res. 2013; 31(6): 880–886, doi: 10.1002/jor.22319, indexed in Pubmed: 23362152.
30. Panjabi MM, Krag M, Summers D, et al. Biomechanical time-tolerance of fresh cadaveric human spine specimens. J Orthop Res. 1985; 3(3): 292–300, doi: 10.1002/jor.1100030305, indexed in Pubmed: 4032102.
31. Riazi S, Bril V, Perkins BA, et al. Can ultrasound of the tibial nerve detect diabetic peripheral neuropathy? A cross-sectional study. Diabetes Care. 2012; 35(12): 2575–2579, doi: 10.2337/dc12-0739, indexed in Pubmed: 23033242.
32. Sargon MF, Ogretmenoglu O, Gunenc Beser C, et al. Quantitative analysis of the terminal branches of facial nerve in fresh frozen head and neck specimens. Folia Morphol. 2014; 73(1): 24–29, doi: 10.5603/FM.2014.0004, indexed in Pubmed: 24590519.
33. Seok HY, Jang JH, Won SJ, et al. Cross-sectional area reference values of nerves in the lower extremities using ultrasonography. Muscle Nerve. 2014; 50(4): 564–570, doi: 10.1002/mus.24209, indexed in Pubmed: 24639103.
34. Sharma M, Horgan A. Comparison of fresh-frozen cadaver and high-fidelity virtual reality simulator as methods of laparoscopic training. World J Surg. 2012; 36(8): 1732–1737, doi: 10.1007/s00268-012-1564-6, indexed in Pubmed: 22484566.
35. Sharma M, Macafee D, Pranesh N, et al. Construct validity of fresh frozen human cadaver as a training model in minimal access surgery. JSLS. 2012; 16(3): 345–352, doi: 10.4293/108680812X13462882735818, indexed in Pubmed: 23318058.
36. Singh K, Gupta K, Kaur S. High resolution ultrasonography of the tibial nerve in diabetic peripheral neuropathy. J Ultrason. 2017; 17(71): 246–252, doi: 10.15557/JoU.2017.0036, indexed in Pubmed: 29375899.
37. Stouthandel MEJ, Vanhove C, Devriendt W, et al. Biomechanical comparison of Thiel embalmed and fresh frozen nerve tissue. Anat Sci Int. 2020; 95(3): 399–407, doi: 10.1007/s12565-020-00535-1, indexed in Pubmed: 32144646.
38. Tagliafico A, Cadoni A, Fisci E, et al. Reliability of side-to-side ultrasound cross-sectional area measurements of lower extremity nerves in healthy subjects. Muscle Nerve. 2012; 46(5): 717–722, doi: 10.1002/mus.23417, indexed in Pubmed: 23055313.
39. Thiel W. [The preservation of the whole corpse with natural color]. Ann Anat. 1992; 174(3): 185–195, indexed in Pubmed: 1503236.
40. Tomaszewski KA, Graves MJ, Henry BM, et al. Surgical anatomy of the sciatic nerve: A meta-analysis. J Orthop Res. 2016; 34(10): 1820–1827, doi: 10.1002/jor.23186, indexed in Pubmed: 26856540.
41. Unger S, Blauth M, Schmoelz W, et al. Effects of three different preservation methods on the mechanical properties of human and bovine cortical bone. Bone. 2010; 47(6): 1048–1053, doi: 10.1016/j.bone.2010.08.012, indexed in Pubmed: 20736094.
42. Warchoł Ł, Walocha JA, Mizia E, et al. Ultrasound-guided topographic anatomy of the medial calcaneal branches of the tibial nerve. Folia Morphol. 2021; 80(2): 267–274, doi: 10.5603/FM.a2020.0062, indexed in Pubmed: 32488855.
43. Warchoł Ł, Mróz I, Mizia E, et al. Vascular density of inferior tibiofibular joint - cadaveric experimental study. Folia Med Cracov. 2017; 57(1): 47–54, indexed in Pubmed: 28608862.
44. Wong YR, Pang X, Lim ZY, et al. Biomechanical evaluation of peripheral nerves after crush injuries. Heliyon. 2019; 5(4): e01557, doi: 10.1016/j.heliyon.2019.e01557, indexed in Pubmed: 31183426.
45. Young BH, Flanigan RM, DiGiovanni BF. Complications of ankle arthroscopy utilizing a contemporary noninvasive distraction technique. J Bone Joint Surg Am. 2011; 93(10): 963–968, doi: 10.2106/JBJS.I.00977, indexed in Pubmed: 21593373.
46. Zarb F, McNulty J, Gatt A, et al. Comparison of in vivo vs. frozen vs. Thiel cadaver specimens in visualisation of anatomical structures of the ankle on proton density Magnetic Resonance Imaging (MRI) through a visual grading analysis (VGA) study. Radiography (Lond). 2017; 23(2): 117–124, doi: 10.1016/j.radi.2016.12.004, indexed in Pubmed: 28390542.
47. Zengerink M, van Dijk CN, Zengerink M, et al. Complications in ankle arthroscopy. Knee Surg Sports Traumatol Arthrosc. 2012; 20(8): 1420––1431, doi: 10.1007/s00167-012-2063-x, indexed in Pubmed: 22669362.

VIA MEDICA

ORIGINAL ARTICLE

Folia Morphol.
Vol. 80, No. 3, pp. 549–556
DOI: 10.5603/FM.a2020.0083

ISSN 0015–5659
eISSN 1644–3284
journals.viamedica.pl

Anatomic characterisation of the parietal branches arising from the internal iliac artery in the foetal pig (*Sus scrofa domestica*)

H. Anetai[1], K. Tokita[2, 3], M. Sakamoto[3], S. Midorikawa-Anetai[2, 4], R. Kojima[2]

[1]*Department of Anatomy and Life Structure, School of Medicine, Juntendo University, Tokyo, Japan*
[2]*School of Physical Therapy, Faculty of Health and Medical Care, Saitama Medical University, Saitama, Japan*
[3]*Graduate School of Medicine, Saitama Medical University, Saitama, Japan*
[4]*Graduate School of Agricultural and Life Sciences, the University of Tokyo, Japan*

[Received: 16 May 2020; Accepted: 11 July 2020; Early publication date: 29 July 2020]

Background: *It is critical for surgeons to have a full understanding of the complex courses and ramifications of the human internal iliac artery and its parietal branches. Although numerous anatomical studies have been performed, not all variations at this site are currently understood. Therefore, we characterised these blood vessels in foetal pigs to provide additional insight from a comparative anatomical perspective.*

Materials and methods: *Eighteen half-pelvis specimens from foetal pigs were dissected and examined on macroscopic scale.*

Results: *Among our findings, we identified the internal iliac artery as a descending branch of the abdominal aorta. A very thick umbilical artery arose from the internal iliac artery. The superior gluteal, inferior gluteal, and internal pudendal arteries formed the common arterial trunk. Although the superior gluteal artery emerged from the common trunk from inside the pelvis, the inferior gluteal and internal pudendal arteries bifurcated at deep layer within the gluteus muscles after leaving pelvic cavity. We were unable to detect an typical obturator artery emerging from the internal iliac artery. A branch supplying the hip adductors was identified as arising from the inferior epigastric artery which itself was derived from the distal end of the external iliac artery.*

Conclusions: *We identified the anatomic characteristics of the internal iliac artery and its parietal branches in the foetal pig. Our findings provide new insight into the comparative anatomy of the internal iliac artery and will promote understanding of related morphogenetic processes.* (Folia Morphol 2021; 80, 3: 549–556)

Key words: hypogastric artery, pelvic artery, gross anatomy, comparative anatomy, anatomical variation, domestic animal

INTRODUCTION

The internal iliac artery arises from a bifurcation of the common iliac artery which generates numerous branches that feed the gluteal region, the medial compartment of thigh, and the intrapelvic viscera in humans [14, 15, 18, 26]. These branches are classified into two groups on the basis of the pattern of blood supply (Table 1). Group 1 includes the parietal

Address for correspondence: Mr. H. Anetai, Department of Anatomy and Life Structure, School of Medicine, Juntendo University, 2-1-1 Hongo, Bunkyo-ku, Tokyo 113-8421, Japan, tel: +81-3-5802-1023, fax: +81-3-5689-6923, e-mail: h-anetai@juntendo.ac.jp

Table 1. General anatomy of the parietal and visceral branches of the human internal iliac artery

Group	Artery	Main blood supply
Parietal branch	Superior gluteal artery	Gluteal muscles
	Inferior gluteal artery	Gluteal muscles
	Internal pudendal artery	Parietal wall of ischio-anal fossa
	Obturator artery	Hip adductor muscles
	Iliolumbar artery	Intrapelvic muscles
	Lateral sacral artery	Spinal cord
Visceral branch	(Cord of) umbilical artery	–
	Superior vesical arteries	Urinary organs
	Inferior vesical arteries	Urinary organs
	Artery to ductus deferens/uterine artery	Internal genitalia
	Middle rectal artery	Rectum

branches, which are the arteries that feed the parietal muscles, e.g., the gluteal and hip adductor muscles. Group 2 are the visceral branches that provide blood supply to the intrapelvic organs, including the internal genitalia, urinary organ, and the rectum. The superior gluteal (SG), iliolumbar and lateral sacral arteries typically arise from the posterior division of the internal iliac artery, while all other branches originate from the anterior division [15, 18].

The ramifications and courses characteristic of these branches of the internal iliac artery can be quite complex in human subjects, and there are many published studies that survey the anatomy of this region [1, 2, 8, 9, 17, 23, 24, 27, 30, 32, 36, 39, 41, 42]. The anomalies identified in the main parietal branches, the SG, inferior gluteal artery (IG), internal pudendal artery (IP), and obturator artery (Ob) have been a subject of great interest among anatomists and clinicians due to their morphological and surgical significance.

In the past few years, morphogenetic and topographic studies focused on the origin and course of variations identified among the parietal branches of the internal iliac artery have been subjected to conventional statistical analyses. As but one example, Honma et al. [17] examined the formation of an arterial ring in the human pelvic artery and suggested that specific ramifications of the parietal branches were associated with the site of disappearance of the arterial ring. Furthermore, previous study examined variations in the course taken by the SG, including its relationship with the lumbosacral plexus; we found that the route taken by the SG varied in accordance with the segmental variations of the lumbosacral plexus [4]. However, not all anatomical variations among the parietal branches are clearly understood; for example, the branching patterns and course variations observed among the IG and Ob have not been fully considered.

There are very few published studies that focus on embryologic and comparative anatomical descriptions of anomalies of the internal iliac artery and its parietal branches; likewise, precise embryological and anatomical descriptions of the internal iliac artery during foetal development have not been reviewed since 1919 [35]. Anatomic investigations of the internal iliac artery have been conducted in a several primate, rodent, and artiodactyl species, although very few comparative studies have emerged [2, 6, 13, 16, 21, 22]. As such, it is clear that the standard anatomy of the internal iliac artery with respect to commonalities shared with other mammalian species has not been fully addressed; strong basic findings would be crucial prior to any discussion of variations or aberrancies. In the present study, our goal was to identify the anatomical characteristics of the parietal branch arising from the internal iliac artery in a foetal pig (*Sus scrofa domestica*). This would be an important first step toward systematising all available information on the standard structure of the common parietal branches as well as the identification of specific findings characteristic of each species.

MATERIALS AND METHODS

The present study performed in 18 half-pelvis specimens (12 right and 6 left) from foetal pigs (*Sus scrofa domestica*) which had been used for anatomical studies as part of the curriculum of the Department of Physical Therapy, Faculty of Health and Medical Care, Saitama Medical University. In the present study, experiments involving animals were carried out in accordance with the Guidelines for Proper Conduct of Animal Experiments (Science Council of Japan), as revised in 2006.

All specimens were obtained as scientific teaching materials from Bio Corporation (Alexandria, MN, USA) and were embalmed with 1.8% formalin, 2.7% phenol, and 5.0% ethylene glycol. Additionally, the specimens were injected with red latex in the arterial systems. The distance between the crown and rump of the specimens was 30–35 mm.

The internal iliac artery and its parietal branches were identified through conventional macroscopic dissection procedures. The origin, course and dis-

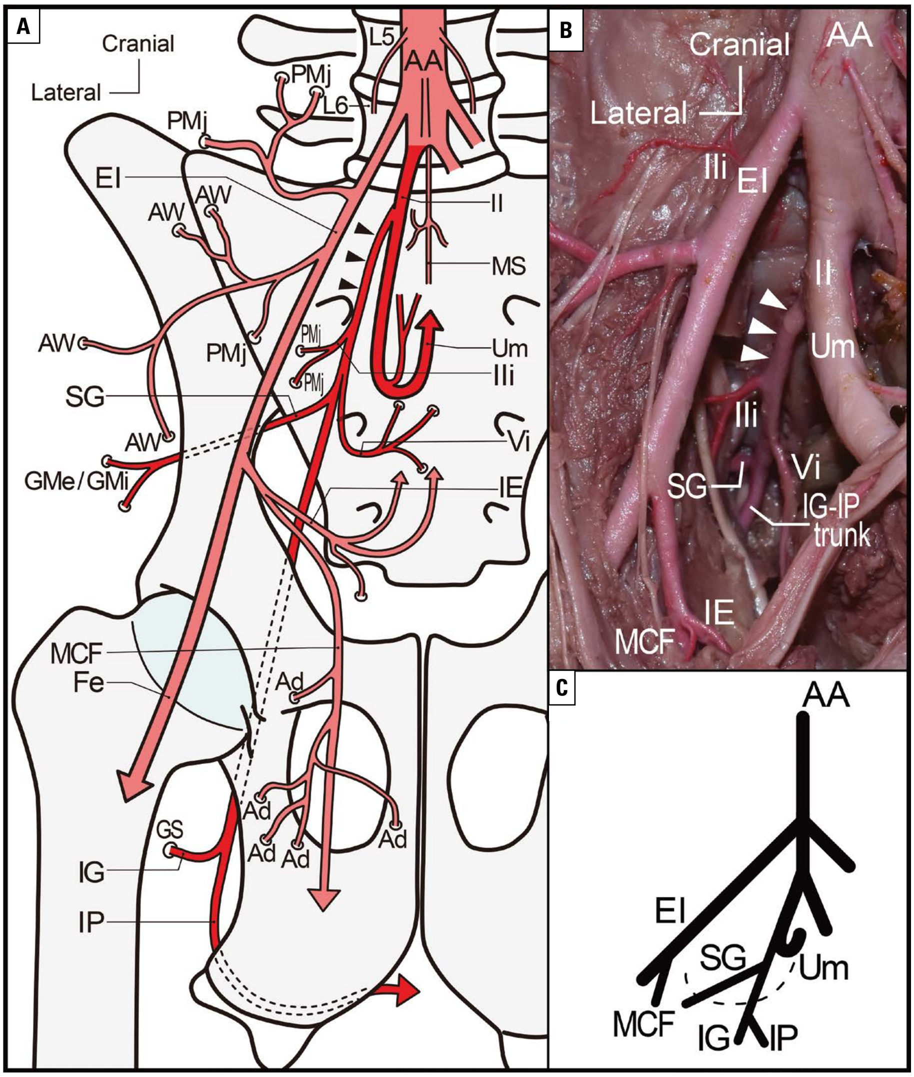

Figure 1. Typical ramification and branches from the iliac artery; **A.** Drawing of the iliac artery and peripheral structures in the foetal pig. The internal iliac artery and its branches are shown in bright red; **B.** Photograph of a dissected right iliac artery and peripheral structures in the foetal pig; **C.** Schematic of the arterial tree of dissected right iliac artery in the foetal pig. Black and white arrowheads indicate the common arterial trunk formed by the superior gluteal artery (SG), inferior gluteal artery (IG), and internal pudendal artery (IP). The dotted line indicates the outlet of the pelvic cavity; AA — abdominal aorta; Ad — hip adductor muscles; AW — abdominal wall; EI — external iliac artery; Fe — femoral artery; GMe — gluteus medius; GMi — gluteus minimus; GS — gluteus superficialis; IE — inferior epigastric artery; II — internal iliac artery; Ili — iliolumbar artery; L — lumbar vertebra; MCF — medial circumflex femoral artery; MS — medial sacral artery; PMj — psoas major; Um — umbilical artery; Vi — visceral branch.

tribution of the all parietal branches were recorded by accurate sketches and photographs that were organised following the classifications described by Adachi [1] and Yamaki et al. [42].

RESULTS

Ramifications of the iliac artery

In all cases examined, the external and internal iliac arteries arose directly from the abdominal aorta at the level of the last lumbar vertebra; there was no blood vessel corresponding to the common iliac artery in the foetal pig. The internal iliac artery descended from its point of origin into the pelvic cavity and then generated several branches. Its ramifications and the courses of several parietal branches were as shown in Figure 1. Of all branches, the umbilical artery extended from the internal iliac artery with a strong and consistent pattern. This artery first descended, and turned toward the umbilicus and ascended.

Ramifications, course, and distributions of SG, IG, and IP

In all 18 half-pelvis specimens, the SG, IG, and IP were the three main parietal branches that form the common arterial trunk (black and white arrowheads in Fig. 1A, B) that emerged from the internal iliac artery. The SG emerged from the common arterial trunk as an oblique descending branch. In the 15 of 18 specimens examined, the SG passed through the upper part of the sacral plexus, below the lumbosacral trunk and the suprapiriform foramen to reach gluteal muscles ("a" in Fig. 2 and Table 2). The relation of the SG course to the sacral plexus was nearly constant even in cases in which the root of the plexus shifted cranially or caudally due to a smaller or larger number of thoracolumbar vertebrae (Table 2).

The arterial trunk of the remaining two branches, the IP-IG trunk, descended and passed through the infrapiriform foramen to appear outside the pelvis.

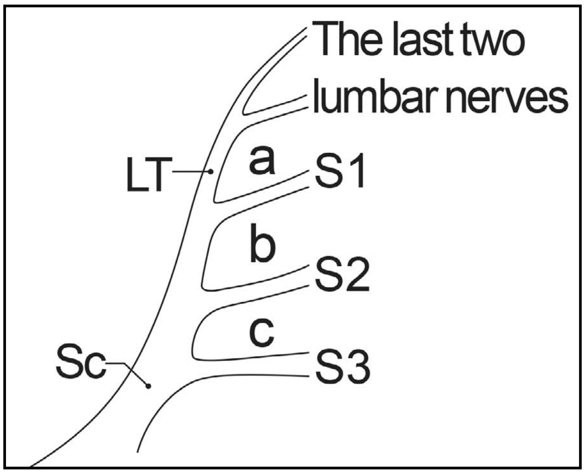

Figure 2. Positional relation of the gluteal artery route to the sacral plexus. The superior gluteal artery (SG) passed through the upper (a) or occasionally the middle part (b) of the sacral plexus. The lower part of the plexus was intersected by the atypical gluteal artery (c). The lumbosacral trunk consistently originated from the last two lumbar nerves; LT — lumbosacral plexus; S — root of the sacral nerves; Sc — sciatic nerve.

After leaving the pelvic cavity, the common arterial trunk divided immediately into two branches; the IG provided blood supply to the gluteus superficialis muscle from the deep surface along with the inferior gluteal nerve and the IP entered into the pudendal canal together with the pudendal nerve.

The origin, course, and distribution of the Ob

There was no Ob originating from the internal iliac artery. Although this artery as an extremely slender branch was occasionally detected as emerging from the common trunk or iliolumbar artery and descending toward the obturator foramen, it did not reach the obturator foramen and the hip adductors. Meanwhile, an arterial branch supplying blood to the hip adductor muscles, similar to the human Ob, was found to be arising from the inferior epigastric artery which extended from distal end of the external iliac artery (Fig. 1). This artery passed under the inguinal ligament and extended around hip adductors. Most of cases exhibited this single-branch anatomy save a few cases that exhibited two branches; this branch corresponded to the medial circumflex femoral artery that extended from the deep femoral artery observed generally in veterinary anatomy [28].

Other minor parietal branches

The iliolumbar artery arose from either the external and internal iliac arteries, and included multiple

Table 2. Number of thoracolumbar vertebra, origin of the lumbosacral trunk, and the course of the superior gluteal artery (SG), refer to Figure 2, in all 18 cases examined

Specimen number	Number of vertebrae		Total number of thoracolumbar vertebrae	Origin of the lumbosacral trunk	SG course
	Thoracic	Lumbar			
1	15	7	22		a
2	15	7	22		a
3	15	6	21		a
4	15	6	21		a
5	15	6	21		a
6	15	6	21		a
7	14	6	20		a
8	16	6	22		a
9	16	6	22	All originated from	b
10	14	7	21	the last two lumbar nerves	a
11	14	7	21		b
12	14	7	21		b
13	14	8	22		a
14	15	7	22		a
15	15	7	22		a
16	15	7	22		a
17	16	6	22		a
18	16	7	23		a

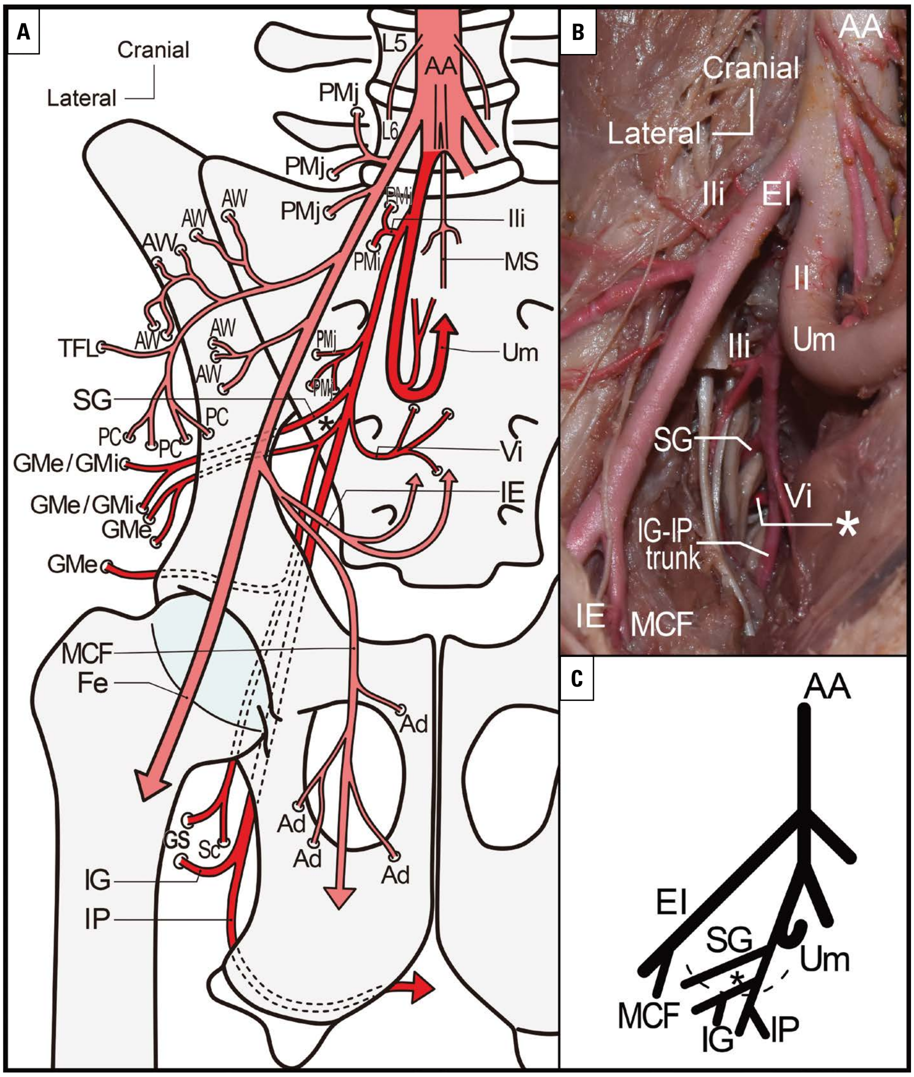

Figure 3. Atypical ramification and branches from the iliac artery; **A.** Drawing of right iliac artery and peripheral structures in the foetal pig. The internal iliac artery and its branches are shown in red; **B.** Photograph of the right iliac artery and peripheral structures in the foetal pig; **C.** Schematic of the arterial tree of the iliac artery in the foetal pig. Black and white asterisks denote the atypical gluteal artery. The dotted line shows the outlet of the pelvic cavity; AA — abdominal aorta; Ad — hip adductor muscles; AW — abdominal wall; EI — external iliac artery; Fe — femoral artery; GMe — gluteus medius; GMi — gluteus minimus; GS — gluteus superficialis; IE — inferior epigastric artery; IG — inferior gluteal artery; II — internal iliac artery; Ili — iliolumbar artery; IP — internal pudendal artery; L — lumbar vertebrae; MCF — medial circumflex femoral artery; MS — medial sacral artery; PC — panniculus carnosus; PMi — psoas minor; PMj — psoas major; Sc — sciatic nerve; SG — superior gluteal artery; TFL — tensor fasciae lata; Um — umbilical artery; Vi — visceral branch.

branches that provided blood supply to the psoas major, psoas minor, and iliacus muscles. The iliolumbar artery emerged from the common arterial trunk as a first branch and had a tendency to pass above or below the lumbosacral trunk.

Although the medial sacral artery arose from the posterior division of the lower end of the abdominal aorta as a well-developed long descending branch, the lateral sacral artery was absent.

Atypical gluteal artery

Of the 18 specimens examined, we identified 1 case with a second gluteal artery (black and white asterisks in Fig. 3A, B). In this case, the SG emerged from the common arterial trunk after the iliolumbar artery and a second gluteal artery was detected immediately distal to this point from remaining descending branch. The SG passed through the middle sacral plexus, between the ventral rami of S1 and S2 spinal roots ("b" in Fig. 2 and Table 2), and through the suprapiriform foramen to reach the gluteus muscles. By contrast, the atypical gluteal artery passed through the lower part of the sacral plexus, between the spinal roots of S2 and S3 ("c" in Fig. 2) as well as the suprapiriform foramen. After leaving the pelvic cavity, the atypical branch bifurcated immediately; one branch provided blood supply to the gluteus medius and the other distributed blood to the gluteus medius, gluteus superficialis muscles, and sciatic nerve (Fig. 3A). In this case, the IG and IP arose at the bifurcation of the IG-IP trunk after leaving the pelvic cavity as was typical for the 18 foetal pig specimens examined.

DISCUSSION

Origin of the parietal branch in the foetal pig

In the present study, the patterns of several parietal branches arising from the internal iliac artery were evaluated in the foetal pig. In all specimens, the SG, IG, and IP formed the common descending trunk; the SG emerged from the common arterial trunk in the pelvic cavity. Meanwhile, the remaining IG-IP trunk bifurcated into the IG and IP after leaving the pelvic cavity. This branching pattern observed in the foetal pig corresponds to type IV as classified by Adachi in his study of the human internal iliac artery [1], although Adachi's classification did not consider whether the trunk bifurcates to the IG and IP at a location inside or outside of pelvic cavity. According Yamaki's modification of Adachi's classification system, this pattern of ramification corresponds to type IV/group 4 and is detected in only 0.5% of human subjects [42]. Although several branching patterns of human internal iliac artery have been examined based on the morphogenetic analysis of the specific case of arterial ring formation, type IV/group 4 is an exception [17].

The IG has been identified as a persistent axial artery (which corresponds to the sciatic artery) in the lower extremity that develops in the primordial stage [5, 7, 12, 34, 35, 43]. The bifurcation of the common arterial trunk outside of pelvis reflects the fact that the IP originates from the IG. The IP originated from the IG in 40–90% in humans and there are remarkable variations among ethnic groups and specific published reports [1, 3, 9, 23, 32, 39]. Interestingly, in the ground squirrel (*Citellus citellus*), the IP originates from the external iliac artery [6]. To understand the branching patterns of the common arterial trunk formed by the IG and IP, it is clearly crucial to establish the origin of the IP.

Course of the SG

The SG typically passed through the upper sacral plexus, below the lumbosacral trunk; this is the case even if the root of the plexus and the lumbosacral trunk shift cranially or caudally due to a smaller or larger number of thoracolumbar vertebrae (Fig. 2, Table 2). We suggest that this observation implies that the course taken by the SG relates directly to the observed segmental variations in the plexus including the lumbosacral trunk; this observation reflects similar findings from human cadaveric dissections [4].

The atypical gluteal artery

The atypical gluteal artery arose from the descending common arterial trunk after the emergence of the typical SG; it passed through the lower part of the sacral plexus and between the spinal roots of S2 and S3 (Fig. 2). This artery distributed blood to the gluteus medius, gluteus superficialis muscles, and sciatic nerve after emerging from the suprapiriform foramen and dividing into two branches (Fig. 3A). According to its origin, course, and distribution, this atypical artery has the anatomical characteristics that are similar to those both the SG and the IG. However, the fact that it supplies the sciatic nerve indicates that this atypical artery corresponds more closely to the IG, because the artery feeding the sciatic nerve has been identified as a persistent form of the sciatic artery which was present in the primordial stages prior to birth [14, 18]. Analysis of this and other atypical cases may help toward our understanding of the morphogenesis of the sciatic artery.

Comparative anatomy of the internal iliac artery and its main parietal branches

The anatomy of the iliac artery has been evaluated in a several primate, artiodactyl, and rodent species; we have summarised the ramification patterns in Figure 4. As shown, the common iliac artery is absent in foetal pigs and llamas (*Lama glama*) [16], both of which belong to Artiodactyla. Although absence of the common iliac artery has been reported in human subjects, this anomaly is extremely rare [10, 25, 37]. Interestingly, aplasia of the common iliac artery has also been observed in other artiodactyls, including sheep (*Ovis aries*) and pampas deer (*Ozotoceros bezoarticus*) [11, 40] and as such, appears to be a phylogenetically defined phenomenon.

In both primates and rodents, the common iliac artery bifurcates into the external and internal iliac arteries (Fig. 4B, C). The SG has a tendency to emerge from the iliac artery before other main parietal branches; this branching pattern may reflect the fact that the SG originates from a root of the sciatic artery in humans during foetal development [35].

The IG and IP are frequently detected together and form the common arterial trunk; however, the IP can originate from the external iliac artery, as described above for ground squirrels. In progressive stage of human development *in utero*, the sciatic artery (which corresponds to the IG) and the IP were derived from a posterior division of the umbilical artery while the external iliac artery originates from the proximal part of the umbilical artery at a site in close proximity to the origin of the sciatic artery [35]. Therefore, the IP could originate from the IG and proximal part of the external iliac artery.

The medial circumflex femoral artery in the foetal pig provided blood to the hip adductors in place of the Ob. The medial circumflex femoral artery arose

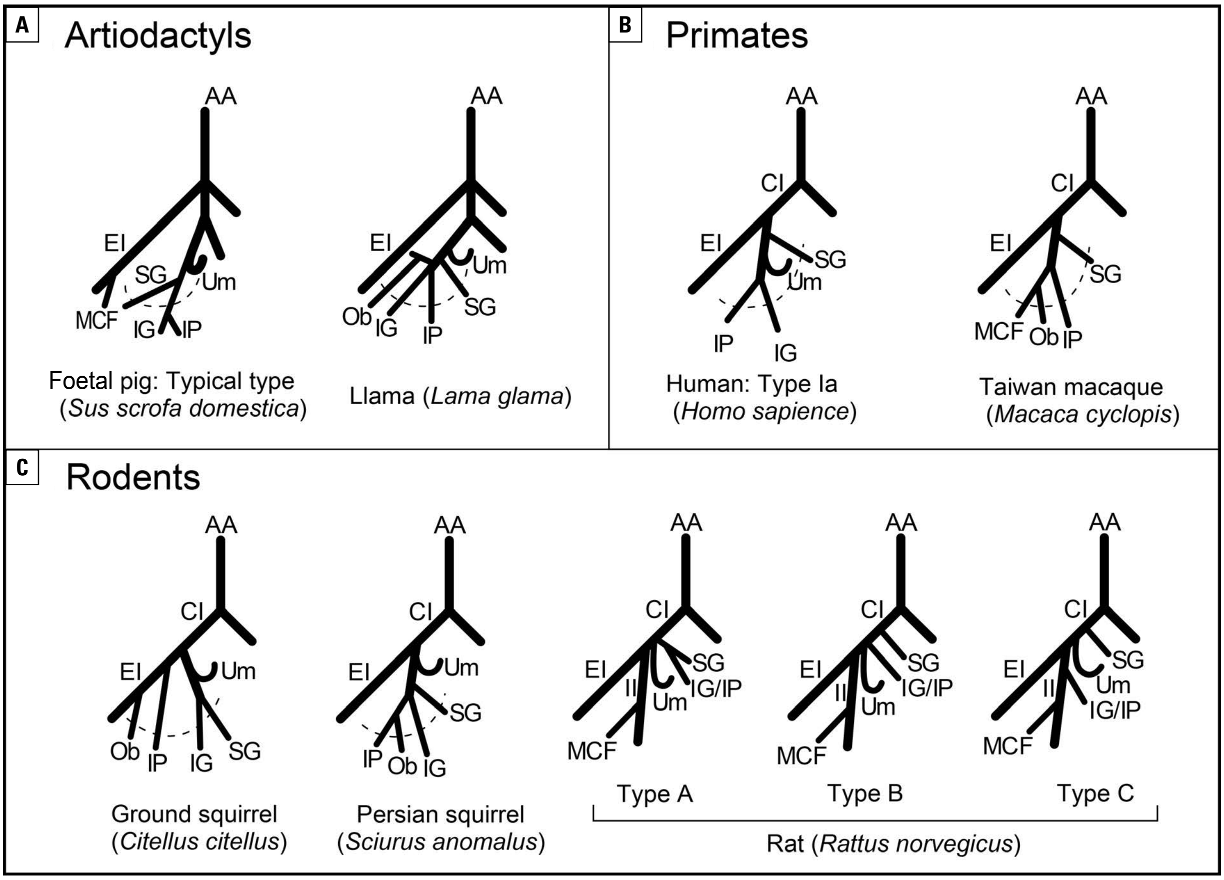

Figure 4. Summary of the ramification pattern of the iliac artery in several mammals including artiodactyls (**A**), primates (**B**), and rodents (**C**). Modified schematics of arterial tree of the internal iliac artery in each species, the foetal pig (present study), Llama (Graziotti, 2003), Human (Adachi, 1928), Taiwan macaque (Fujita, 1963), Ground squirrel (Blagojevic, 2013), Persian squirrel (Akibari, 2016) and Rat (Kigata and Shibata, 2019) are shown. The dotted line shows the outlet of the pelvic cavity; AA — abdominal aorta; CI — common iliac artery; EI — external iliac artery; II — internal iliac artery; IG — inferior gluteal artery; IP — internal pudendal artery; MCF — medial circumflex femoral artery; O — obturator artery; SG — superior gluteal artery; Um — umbilical artery.

from the inferior epigastric artery, and reached the hip adductors without passing through the obturator foramen. The inferior epigastric artery has a close morphogenetic relationship with the Ob, and the origin of the medial circumflex femoral artery in the foetal pig is similar to "*corona mortis*" which is well-known to surgeons as a prominent and significant anatomic variation of the human Ob [19, 20, 29, 31, 33, 38]. Furthermore, in rats, the origin of the medial circumflex femoral artery is similar to that in a typical human Ob (Fig. 4C). Therefore, a more careful evaluation of the anatomical characteristics of the medial circumflex femoral artery in non-human mammals may help in understanding the variations in the human Ob including the *corona mortis*.

CONCLUSIONS

These findings in the present study can represent an important addition to the anatomical research into variations in the internal iliac artery. These findings will help us to understand the morphogenetic process and will be useful for surgical treatment of domestic animals.

Acknowledgements

This work was performed as a project study of the Faculty of Health and Medical Care, Saitama Medical University, Saitama, Japan. The authors would like to thank Enago (www.enago.jp) for the English language review.

Conflict of interest: None declared

REFERENCES

1. Adachi B. Das arteriensystem der Japaner. Bd. 2. Die Kaiserlich Japanische Universität zu Kyoto, Kyoto 1928.
2. Akibari G, Gilanpour H, Babaei M. The arterial pattern of terminal branch of the abdominal aorta in the male Persian squirrel (sciurus anomalus). Anat Sci. 2016; 13(2): 119–124.

3. Akshara VR, Minnie PA. study on the variations of the branching pattern of the internal iliac artery. Int J Sci Res. 2014; 3(9): 723–725.
4. Anetai H, Tokita K, Kojima R, et al. Variations in the course of the superior gluteal artery in relation to the lumbosacral plexus. Okajimas Folia Anat Jpn. 2017; 94(2): 45–54, doi: 10.2535/ofaj.94.45, indexed in Pubmed: 29249733.
5. Arey L. Developmental Anatomy. WB Saunders, Philadelphia 1956.
6. Blagojevic M, Nesic I, Djelic N, et al. The common iliac artery in the ground squirrel (Citellus citellus). Acta Veterinaria. 2013; 63(4): 463–470, doi: 10.2298/avb1304463b.
7. Blair CB, Nandy K. Persistence of the axis artery of the lower limb. Anat Rec. 1965; 152(2): 161–172, doi: 10.1002/ar.1091520207, indexed in Pubmed: 5842159.
8. Bleich AT, Rahn DD, Wieslander CK, et al. Posterior division of the internal iliac artery: Anatomic variations and clinical applications. Am J Obstet Gynecol. 2007; 197(6): 658.e1–658.e5, doi: 10.1016/j.ajog.2007.08.063, indexed in Pubmed: 18060970.
9. Braithwaite JL. Variations in origin of the parietal branches of the interanl iliac artery. J Anat. 1952; 86: 423–430.
10. Dabydeen DA, Shabashov A, Shaffer K. Congenital absence of the right common iliac artery. Radiol Case Rep. 2008; 3(1): 47–51, doi: 10.2484/rcr.v3i1.47, indexed in Pubmed: 27303500.
11. Elmetwally MA. Uterin blood flow indices in sheep during pregnancy. Qual Prim Care. 2016; 24(4): 197–202.
12. Esaki T, Oka N, Tsurumaru H, et al. A case of a developmental anomaly of the femoral artery: persistent sciatic artery. Jpn J Surg. 1980; 10(1): 72–76, doi: 10.1007/BF02468651, indexed in Pubmed: 7373956.
13. Fujita J. Pelvic arteries in macacus cyclopsis. I. The common iliac artery and the external iliac artery. Okajimas Folia Anat Jpn. 1963; 39: 85–116, doi: 10.2535/ofaj1936.39.3_85, indexed in Pubmed: 14044425.
14. Gegenbaur C. Lehrbuch der Anatomie des Menschen. Wilhelm Engelmann, Leipzig 1883.
15. Gray H. Anatomy of the Human Body. 20th ed. Lea & Febiger, Philadelphia and New York 1918.
16. Graziotti GH, Rodríguez Menéndez JM, Victorica CL, et al. Systematic study of the internal iliac artery in llama (Lama glama). Ann Anat. 2003; 185(5): 461–463, doi: 10.1016/s0940-9602(03)80107-3, indexed in Pubmed: 14575273.
17. Honma S, Aimi Y, Kudo M. Ring formation of the internal iliac artery. Surg Radiol Anat. 2013; 35(2): 169–171, doi: 10.1007/s00276-012-1020-1, indexed in Pubmed: 22968634.
18. Jackson CM. Morris' s treatise on anatomy: A Complete Systematic Treatise by English and American Authors. 5th ed. P. Blakiston's Son, Philadelphia 1914.
19. Jusoh AR, Abd Rahman N, Abd Latiff A, et al. The anomalous origin and branches of the obturator artery with its clinical implications. Rom J Morphol Embryol. 2010; 51(1): 163–166, indexed in Pubmed: 20191138.
20. Kawai K, Honma S, Koizumi M, et al. Inferior epigastric artery arising from the obturator artery as a terminal branch of the internal iliac artery and consideration of its rare occurrence. Ann Anat. 2008; 190(6): 541–548, doi: 10.1016/j.aanat.2008.05.004, indexed in Pubmed: 18706793.
21. Kigata T, Shibata H. Anatomical variations of the arterial branches from the rat iliac arteries. J Vet Med Sci. 2019; 81(1): 1–8, doi: 10.1292/jvms.18-0405, indexed in Pubmed: 30449820.
22. Kochi T, Imai Y, Takeda A, et al. Characterization of the arterial anatomy of the murine hindlimb: functional role in the design and understanding of ischemia models. PLoS One. 2013; 8(12): e84047, doi: 10.1371/journal.pone.0084047, indexed in Pubmed: 24386328.
23. Lipshutz B. A composit study of the hypogastric artery and its branches. Ann Surg. 1918; 67(5): 584–608, doi: 10.1097/00000658-191805000-00012, indexed in Pubmed: 17863918.
24. Mamatha H, Hemalatha B, Vinodini P, et al. Anatomical study on the variations in the branching pattern of internal iliac artery. Indian J Surg. 2015; 77(Suppl 2): 248–252, doi: 10.1007/s12262-012-0785-0, indexed in Pubmed: 26730003.
25. Mansfield AO, Howard JM. Absence of both common iliac arteries. A case report. Anat Rec. 1964; 150: 363–364, doi: 10.1002/ar.1091500404, indexed in Pubmed: 14248306.
26. Merkel FRJ. Henle's grundriss der anatomie des menschen. 1st ed. Friedrich Vieweg und Sohn, Braunschweig 1988.
27. Nayak SB, Shetty SD, Sirasanagandla SR, et al. Multiple variations in the pelvic vasculature - a case report. J Clin Diagn Res. 2015; 9(2): AD01–AD02, doi: 10.7860/JCDR/2015/10775.5526, indexed in Pubmed: 25859441.
28. Nickel R, Schummer A, Seiferle E. The Anatomy of the Domestic Animals. Springer-Verlag, Berlin Heidelberg GmbH 1981.
29. Pai MM, Krishnamurthy A, Prabhu LV, et al. Variability in the origin of the obturator artery. Clinics (Sao Paulo). 2009; 64(9): 897–901, doi: 10.1590/S1807-59322009000900011, indexed in Pubmed: 19759884.
30. Roberts WH, Krishingner GL. Comparative study of human internal iliac artery based on Adachi classification. Anat Rec. 1967; 158(2): 191–196, doi: 10.1002/ar.1091580208, indexed in Pubmed: 6034641.
31. Rusu MC, Cergan R, Motoc AG, et al. Anatomical considerations on the corona mortis. Surg Radiol Anat. 2010; 32(1): 17–24, doi: 10.1007/s00276-009-0534-7, indexed in Pubmed: 19636491.
32. Sakthivelavan S, Aristotle S, Sivanandan A, et al. Variability in the branching pattern of the internal iliac artery in Indian population and its clinical importance. Anat Res Int. 2014; 2014: 597103, doi: 10.1155/2014/597103, indexed in Pubmed: 25580296.
33. Sarikcioglu L, Sindel M, Akyildiz F, et al. Anastomotic vessels in the retropubic region: corona mortis. Folia Morphol. 2003; 62(3): 179–182, indexed in Pubmed: 14507043.
34. Sekiya S, Horiguchi M, Komatsu H, et al. Persistent primitive sciatic artery associated with other various anomalies of vessels. Acta Anat (Basel). 1997; 158(2): 143–149, doi: 10.1159/000147924, indexed in Pubmed: 9311424.
35. Senior HD. The development of the arteries of the human lower extremity. Am J Anat. 1919; 25(1): 54–95, doi: 10.1002/aja.1000250105.
36. Shetty A, Jetti R, Shivaram B, et al. Variant branching pattern of the posterior division of internal iliac artery: a case report. Galle Med J. 2011; 16(2): 37, doi: 10.4038/gmj.v16i2.3753.
37. Shetty S, Kantha L, Sheshgiri C. Bilateral absence of common iliac artery – a cadaveric observation. Int J Anat Vari. 2013; 6: 7–8, doi: 10.2484/rcr.2008v3i1.47.
38. Tajra J, Lima C, Pires F, et al. Variability of the obturator artery with its surgical implications. J Morphol Sci. 2018; 33(02): 096–098, doi: 10.4322/jms.090015.
39. Talalwah WA, Soames R. Internal iliac artery classification and its clinical significance. Rev Arg de Anat Clin. 2014; 6(2): 63–71.
40. Vazquez N, Ríos C, Sorriba V, et al. Arterial distribution to the pelvic cavity and pelvic limb in the pampas deer (Ozotoceros bezoarticus, Linnaeus 1758). Anat Histol Embryol. 2018; 47(2): 133–139, doi: 10.1111/ahe.12331, indexed in Pubmed: 29205895.
41. Vinnakota S, N B. Trifurcation of posterior division of internal iliac artery: A case report. J Evid Based Med Healthc. 2014; 1(1): 1–4, doi: 10.18410/jebmh/1.
42. Yamaki K, Saga T, Doi Y, et al. A statistical study of the branching of the human internal iliac artery. Kurume Med J. 1998; 45(4): 333–340, doi: 10.2739/kurumemedj.45.333, indexed in Pubmed: 9914720.
43. Yazama F, Hatori N, Kudoh H, et al. Bilateral persistent sciatic arteries in a Japanese man. Anat Sci Int. 2002; 77(2): 128–133, doi: 10.1046/j.0022-7722.2002.00003.x, indexed in Pubmed: 12418093.

VIA MEDICA

ORIGINAL ARTICLE

Folia Morphol.
Vol. 80, No. 3, pp. 557–566
DOI: 10.5603/FM.a2020.0094

ISSN 0015–5659
eISSN 1644–3284
journals.viamedica.pl

An analysis of the variations and clinical applications of the lateral circumflex femoral artery

M. Ma, H. Sang, Y. Ye, H. Zhuang, Z. Zhuang, Y. Qiu, X. Li, D. Xu, M.H. Jiang

Department of Human Anatomy Zhongshan School of Medicine, Sun Yat-sen University, Guangzhou, P.R. China

[Received: 28 June 2020; Accepted: 8 July 2020; Early publication date: 14 August 2020]

Background: Identifying the arterial variation of the lateral circumflex femoral artery (LCFA) is a vital step in planning surgical and radiological approach. The aim of the study was to evaluate the variations and discuss the clinical correlates of the LCFA.

Materials and methods: Fifty eight adult cadavers (male 45, female 13) with 115 usable sides were used to assess and classify the origin and branches of the LCFA. Also its external diameter, distance from mid-inguinal ligament to sites of origin from the profunda femoris artery or femoral arteries.

Results: There were seven types of LCFA variations in this sample. We classified them as types A to G, of which type A was normal, that is, the one showing a single LCFA arising from the profunda femoris artery. Nearly 50.43% of the sample had type B–G variations, each having 13, 10, 23, 4, 4, and 3 cases, accounting for 11.30%, 8.70%, 20.00%, 3.48%, 3.48%, and 2.61%, respectively.

Conclusions: There are many variant types in the LCFA. To avoid iatrogenic injuries, clinicians must have a sound understanding of the variation types of this important blood vessel. (Folia Morphol 2021; 80, 3: 557–566)

Key words: lateral circumflex femoral artery, variation, anatomy, clinical significance

INTRODUCTION

The lateral circumflex femoral artery (LCFA) branches from the lateral part of the root of the profunda femoris artery (PFA) and runs horizontally and laterally on the back of the sartorius and rectus femoris muscles. It divides into ascending, transverse, and descending branches [25]. There are several reports of variations of the LCFA and PFA [8, 17, 19] including many case reports in domestic and international literature. Statistically, there is a dearth of published literature analysing the morphometric, types of variations, and clinical significance of the LCFA. With the continued development of vascularised skin flap and vascularised bone reconstruction transplantations as well as the improvement in radiological diagnosis and treatment of peripheral vascular diseases, PFA and its branches have become of important clinical value [13]. In particular, the LCFA and its branches are of great significance in the vascular transplantation and reconstruction surgery [1, 15, 23]. Therefore, this study was designed to provide detailed anatomical data for clinical use by analysing the variations of the LCFA in a sample of 58 cadavers.

Address for correspondence: M.H. Jiang, MD, PhD, Department of Human Anatomy Zhongshan School of Medicine, Sun Yat-sen University, Guangzhou, P.R. China, tel: (86)-20-87330639, e-mail: jiangmh2@mail.sysu.edu.cn; Dr. D. Xu, Department of Human Anatomy Zhongshan School of Medicine, Sun Yat-sen University, Guangzhou, P.R. China, tel: (86)-20-87330639, e-mail: 462695262@qq.com

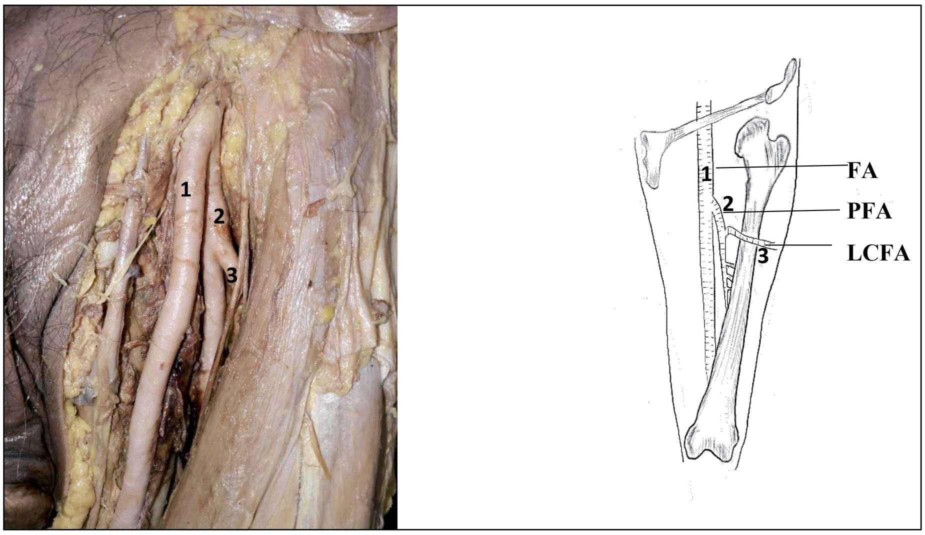

Figure 1. Type A variation in which one single lateral circumflex femoral artery (LCFA) originated from the profunda femoris artery (PFA). A picture: 1 — femoral artery (FA); 2 — PFA; 3 — LCFA.

MATERIALS AND METHODS

Materials

Fifty-eight (male 45, female 13) formalin-fixed adult cadavers from the Department of Human Anatomy, Sun Yat-sen School of Medicine were used in this study resulting in 115 usable LCFAs. Dissection instruments for routine use in gross anatomy such as scalpels, haemostatic forceps, etc. were used. A calibrated Vernier calliper was used for measurement (accuracy 0.01 mm). The specimens were preserved in 10% neutral formalin fixative solution.

Methods

The formalin-fixed and undissected cadavers destined to be used in gross anatomy teaching/dissections (i.e. the skin of the lower abdomen and upper thigh did not have any surgical marks or signs of having been dissected) were selected for meticulous exposure of the femoral artery, its profunda branch as well as the LCFA. The origin of femoral artery (FA) and LCFA and their branches were carefully exposed and observed following a pre-established protocol of lower limb femoral region dissection described previously [11]. Verification of the identities, courses, and branches of the FA, PFA, and LCFA, as well as any variations, were done by two senior anatomists (X.D.Z. and J.M.H., corresponding authors). The external diameters of the FA, PFA and LCFA, the distance between the starting point of the PFA and the midpoint of the inguinal ligament, and the distance between the starting point of the LCFA and the starting point of the PFA were measured with a Vernier calliper and string tracing method. The (Z3i, vivo, China) smartphone was used for recording the images of the *in situ* anatomy and any variations encountered.

RESULTS

Our team conducted an anatomical study on 115 extremities of 58 cadavers. There were seven types of origin variations of the LCFA, namely type A (one single LCFA originated from the PFA, Fig. 1); type B (one single LCFA originated from the FA, Fig. 2); type C (one single LCFA and PFA that arose from a common stem, Fig. 3); type D (two LCFAs both originated from the PFA, Fig. 4); type E (one LCFA originated from the PFA, while the other originated from the FA, Fig. 5); type F (one LCFA originated from the PFA, the other arose from a common stem with the PFA, Fig. 6); type G (one LCFA originated from the FA, the other arose from a common stem with the PFA, Fig. 7).

Type A was the most prevalent variation (58 out of 115, 50.43%) while 13 out of the 115 (11.30%) specimens were type B. The average distances from the midpoint of the inguinal ligament to the origins of the LCFA and the PFA from the FA were 42.65 ± ± 13.87 mm and 33.15 ± 16.37 mm, respectively. The average external diameter of the FA was 9.50 ± 2.53 mm while that of the PFA and the LCFA were 4.79 ± 1.26 mm and 4.37 ± 1.13 mm, respectively (Tables 1 and 2).

Ten out of 115 (8.70%) femoral region specimens had type C variation of the LCFA origin. The average distance between the midpoint of the inguinal lig-

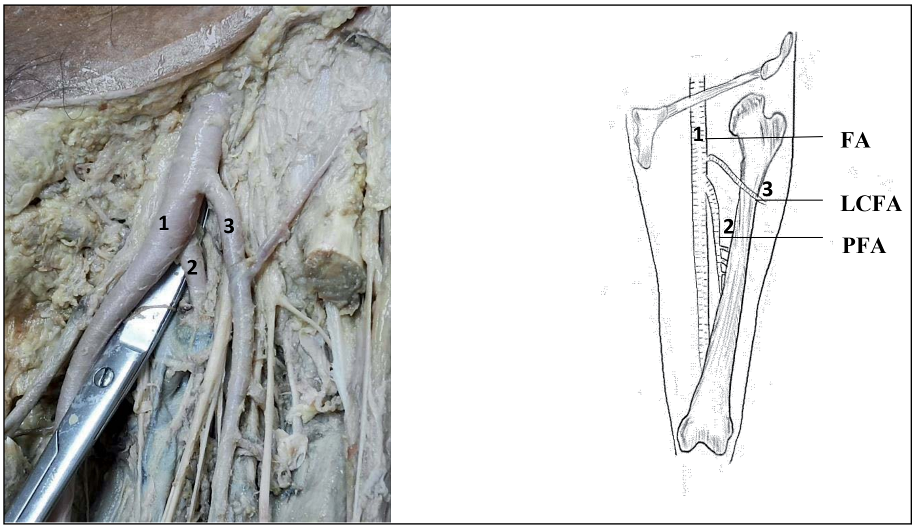

Figure 2. Type B variation in which one single lateral circumflex femoral artery (LCFA) originated from the femoral artery (FA). A picture: 1 — FA; 2 — profunda femoris artery (PFA); 3 — LCFA.

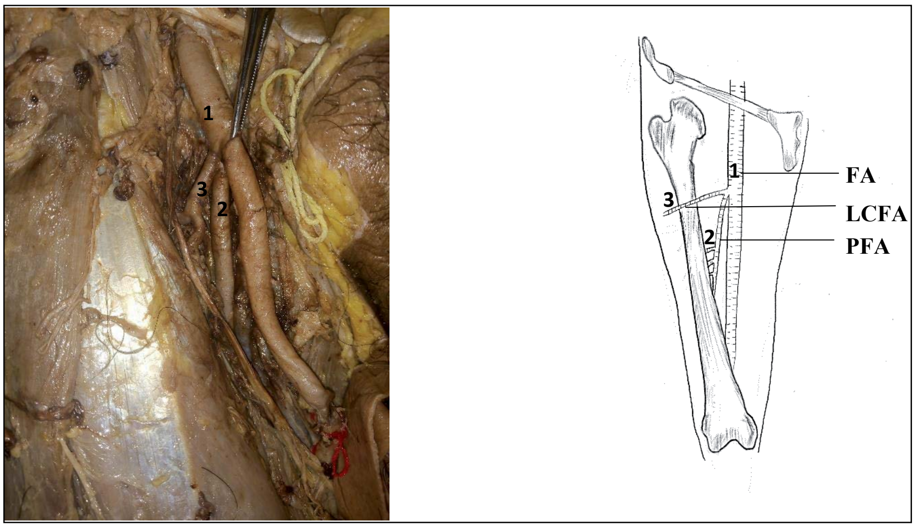

Figure 3. Type C variation in which one single lateral circumflex femoral artery (LCFA) and profunda femoris artery (PFA) that arose from a common stem. A picture: 1 — femoral artery (FA); 2 — PFA; 3 — LCFA.

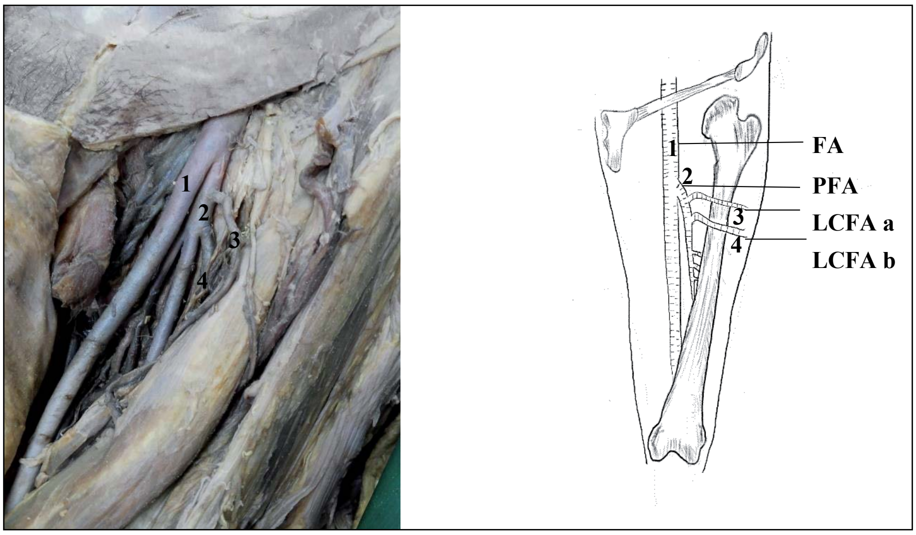

Figure 4. Type D variation in which two lateral circumflex femoral arteries (LCFAs) both originated from the profunda femoris artery (PFA). A picture: 1 — femoral artery (FA); 2 — PFA; 3 — the proximal LCFA (LCFA-a); 4 — the distal LCFA (LCFA-b).

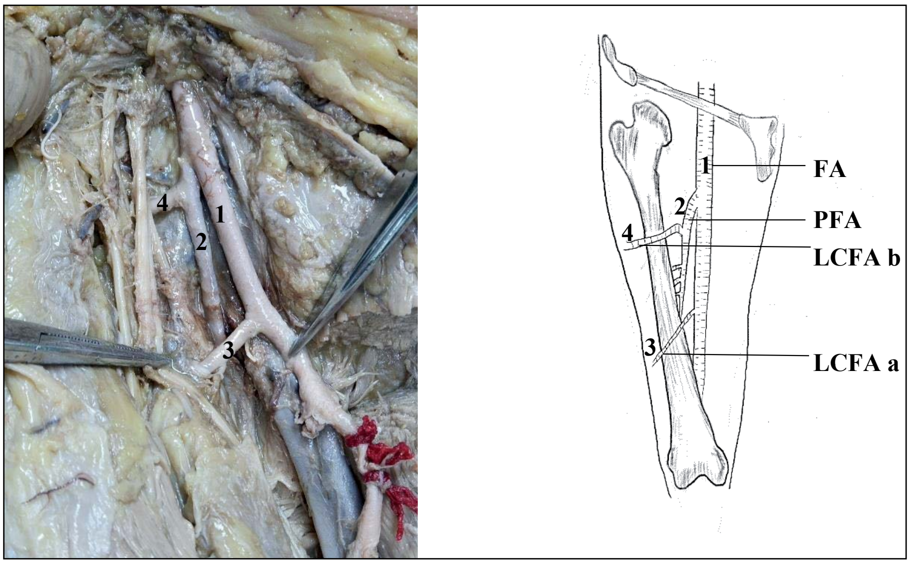

Figure 5. Type E variation in which one lateral circumflex femoral artery (LCFA) originated from the profunda femoris artery (PFA), while the other originated from the femoral artery (FA). A picture: 1 — FA; 2 — PFA; 3 — LCFA originates from FA (LCFA-a); 4 — LCFA originates from PFA (LCFA-b).

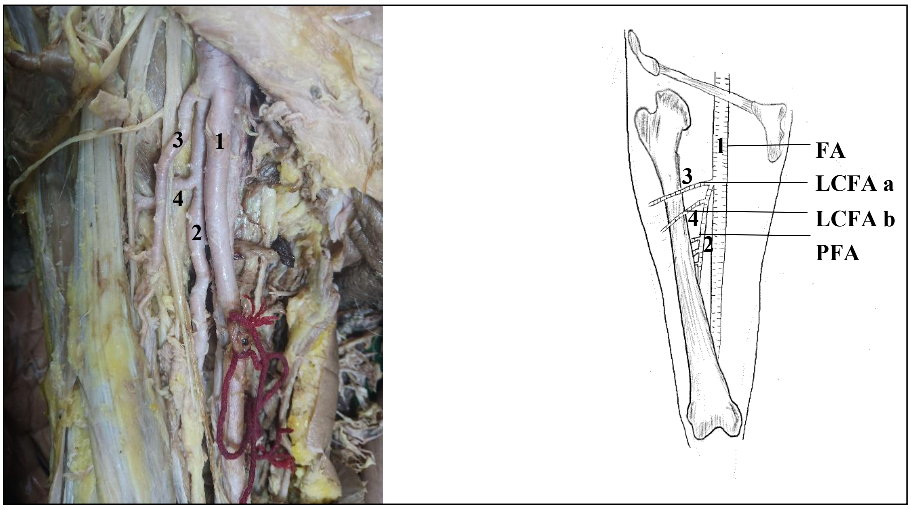

Figure 6. Type F variation in which one lateral circumflex femoral artery (LCFA) originated from the profunda femoris artery (PFA); the other arose from a common stem with the PFA. A picture: 1 — femoral artery (FA); 2 — PFA; 3 — LCFA arises from the common origin with PFA (LCFA-a); 4 — LCFA originates from PFA (LCFA-b).

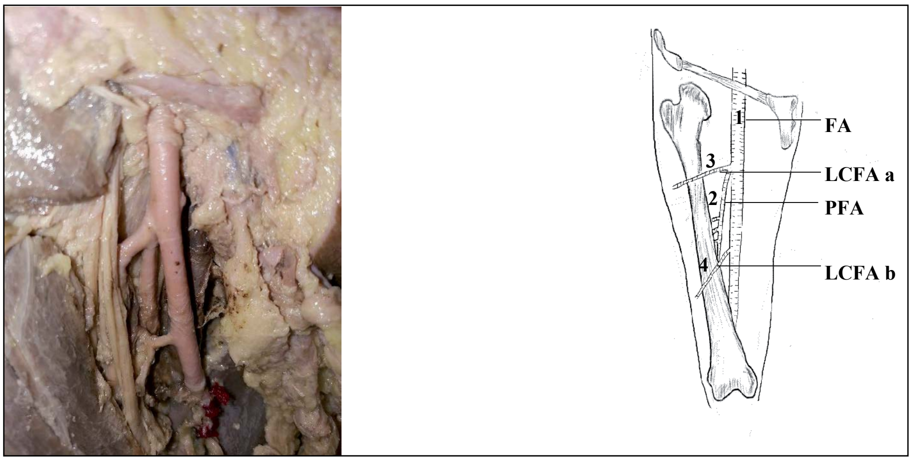

Figure 7. Type G variation in which one lateral circumflex femoral artery (LCFA) originated from the femoral artery (FA); the other arose from a common stem with the profunda femoris artery (PFA). A picture: 1 — FA; 2 — PFA; 3 — LCFA arises from a common origin with PFA (LCFA-a); 4 — LCFA originates from FA (LCFA-b).

ament and the common origin of the PFA and the LCFA from the FA was 34.23 ± 9.96 mm. The average external diameter of the FA was 9.50 ± 2.53 mm while that of the PFA and the LCFA were 4.79 ± 1.26 mm and 4.37 ± 1.13 mm, respectively (Tables 3 and 4).

Twenty-three out of 115 (20.00%) specimens bearing the origin of the LCFA were of type D. In this type, the proximal LCFA was defined as LCFA-a, while the distal one defined as LCFA-b. The average distances from the inguinal ligament midpoint to the origin of the LCFA-a and the LCFA-b from the PFA were 17.26 ± ± 13.26 mm and 30.22 ± 13.84 mm, respectively. The average distance from the midpoint of the inguinal ligament to the exit point of the PFA from the FA was 42.51 ± 14.55 mm. The average external diameters were as follows: the FA was 8.44 ± 2.41 mm, that of the PFA was 5.91 ± 1.89 mm, the LCFA-a was 3.77 ± 1.10 mm and the LCFA-b was 3.17 ± 1.16 mm (Tables 5 and 6).

Four out of 115 (3.48%) specimens were variation type E. In this type, the LCFA that originatced from the FA was designated LCFA-a, while the one coming from the PFA was designated LCFA-b. The average distances from the midpoint of the inguinal ligament to the origins of the PFA and the LCFA-a from the FA were 46.84 ± 4.09 mm and 47.25 ± 26.48 mm, respectively. The LCFA-b sprung from the PFA about 18.55 ± 7.03 mm from where the PFA exited the FA. The average external diameters of the arteries were as follows: the FA 9.14 ± 2.65 mm, the PFA was 5.54 ± 1.36 mm, LCFA-a 3.16 ± 1.28 mm, and the LCFA-b was 4.23 ± 1.28 mm wide (Tables 7 and 8).

The type F variations were also encountered in 4 of the 115 (3.48%) specimens. In this variation type, the LCFA and the PFA shared a common origin defined as LCFA-a, while the other one independently arose from the PFA and was named the LCFA-b. The mean length of the LCFA-a from the midpoint of the inguinal ligament to its FA origin was 49.64 ± 12.40 mm. The LCFA-b exited the PFA about 25.26 ± 6.64 mm down the course of the PFA. The average external diameters of the arteries as follows: FA 10.24 ± 0.78 mm, PFA 6.20 ± 0.77 mm, LCFA-a 4.48 ± 1.91, and LCFA b 3.04 ± 1.43 mm (Tables 9 and 10).

Only 3 (2.61%) out of 115 specimens were type G variations. In this type, the LCFA arising from a common origin with PFA was defined as LCFA-a, while the one arising directly from the FA named LCFA-b. The average distance from the midpoint of the in-

Table 1. Summary of the origin and branches of lateral circumflex femoral artery for type B

Item	N (branch)	$\bar{x} \pm s$ [mm]	Minimum [mm]	Maximum [mm]
PFA-MIL	13	42.65 ± 13.87	16.23	60.64
EDFA	13	9.50 ± 2.53	5.21	13.23
EDPFA	13	4.79 ± 1.26	2.93	6.68
LCFA-MIL	13	33.15 ± 16.37	6.64	66.38
EDLCFA	13	4.37 ± 1.13	2.40	5.52

PFA-MIL — the distance from the midpoint of the inguinal ligament to the origin of the profunda femoris artery; EDFA — the external diameter of the femoral artery; EDPFA — the external diameter of the profunda femoris artery; LCFA-MIL — the distance from the midpoint of the inguinal ligament to the origin of the lateral circumflex femoral artery; EDLCFA — the external diameter of the lateral circumflex femoral artery

Table 2. Details of the origin and branches of lateral circumflex femoral artery for type B

Gender	Age	Side (left or right)	PFA-MIL [mm]	EDFA [mm]	EDPFA [mm]	LCFA-MIL [mm]	EDLCFA [mm]
Male	Old	Right	53.21	6.84	3.73	52.09	3.82
Male	Old	Right	52.76	10.63	6.18	21.32	5.37
Male	Old	Right	31.57	5.30	3.06	9.95	2.40
Male	Old	Left	56.28	9.17	4.70	24.66	3.61
Male	Old	Right	19.88	8.97	5.40	66.38	5.46
Male	Old	Right	54.98	12.71	6.10	33.02	5.14
Male	Old	Right	60.64	12.20	4.23	28.32	5.02
Male	Old	Left	54.09	11.91	5.84	42.78	5.03
		Right	41.43	13.23	6.68	34.96	4.96
Female	Old	Left	44.87	9.90	5.99	6.64	5.16
Female	Old	Left	29.58	8.63	4.08	52.83	5.52
Female	Old	Right	16.23	8.79	2.93	25.26	2.78
Female	Old	Right	38.89	5.21	3.30	32.69	2.53

PFA-MIL — the distance from the midpoint of the inguinal ligament to the origin of the profunda femoris artery; EDFA — the external diameter of the femoral artery; EDPFA — the external diameter of the profunda femoris artery; LCFA-MIL — the distance from the midpoint of the inguinal ligament to the origin of the lateral circumflex femoral; EDLCFA — the external diameter of the lateral circumflex femoral artery

Table 3. Summary of the origin and branches of lateral circumflex femoral artery for type C

Item	N (branch)	$\bar{x} \pm s$ [mm]	Minimum [mm]	Maximum [mm]
CPFALCFA-MIL	10	34.23 ± 9.96	24.22	56.73
EDFA	10	9.37 ± 2.27	5.51	13.4
EDPFA	10	5.50 ± 1.88	3.05	8.92
EDLCFA	10	4.51 ± 1.47	2.07	7.41

CPFALCFA-MIL — the distance from the common origin of the profunda artery and lateral circumflex femoral artery to the midpoint of the inguinal ligament; EDFA — the external diameter of the femoral artery; EDPFA — the external diameter of the profunda femoris artery; EDLCFA — the external diameter of the lateral circumflex femoral artery

guinal ligament to the common origin of the PFA and the LCFA-a from the FA was 92.92 ± 4.40 mm. The average distance from the midpoint of the inguinal ligament to the origin of LCFA-b on the FA was 45.72 ± 6.18 mm. The average external diameters of the arteries were as follows: FA 9.85 ± 0.73 mm, PFA 6.04 ± 0.54 mm, LCFA-a 3.61 ± 1.11, and LCFA-b 5.11 ± 0.76 mm (Tables 11 and 12).

DISCUSSION

The profunda artery and the lateral circumflex femoral artery are prone to having many types of variations. Previously, Shi et al. described the variations of the LCFA and, divided them into four categories namely those originating from the profunda femoris artery and those from the femoral artery as well as the number of roots of origin [21] accounting for 25.00% and 76.56%; 90.62% and 9.38%, respectively. If classified according to this method, the four types of data measured by the author account for 15.15% and 84.84%; 70.43%, and 29.57%, respectively. The frequency with which the LCFA emanated from the

Table 5. Summary of the origin and branches of lateral circumflex femoral artery for type D

Item	N (branch)	$\bar{x} \pm s$ [mm]	Minimum [mm]	Maximum [mm]
PFA-MIL	23	42.51 ± 14.55	24.18	82.25
EDFA	23	8.44 ± 2.41	4.13	13.33
EDPFA	23	5.91 ± 1.89	3.09	10.17
LCFA a-PFA	23	17.26 ± 13.26	4.32	59.55
LCFA b-PFA	23	30.22 ± 13.84	11.14	59.55
EDLCFA a	23	3.77 ± 1.10	2.23	6.56
EDLCFA b	23	3.17 ± 1.16	1.35	5.95

PFA-MIL — the distance from the origin of the profunda femoris artery to the midpoint of the inguinal ligament; EDFA — the external diameter of the femoral artery; EDPFA — the external diameter of the profunda femoris artery; LCFA a-PFA — the distance from the origin of the LCFA a to the origin of the profunda femoris artery; LCFA b-PFA — the distance from the origin of the LCFA b to the origin of the profunda femoris artery; EDLCFA a — the external diameter of the LCFA a; EDLCFA b — the external diameter of the LCFA b

profunda femoris artery was higher than that from the femoral artery, and the number of cases with a single circumflex femoral artery was also more than those with a double. These findings were consistent with the results of Shi et al. [21]. The majority of the LCFAs originated from the profunda femoris artery while a fewer were from the femoral artery or the common stem with the profunda femoris artery [22]. Daksha Dixit et al. [3] studied 114 cases (228 specimens) and found that the LCFA originated from the profunda femoris artery in 171 (75%) specimens, from the femoral artery in 18 (7.89%) specimens and also from a common stem in 31 (13.59%) specimens. Labetowicz et al. [11] found that the LCFA arises from the profunda femoris artery or the femoral artery in 78.75% and 21.25% of cases, respectively. Also, Tomaszewski et al. [26] reported that the lat-

Table 4. Details of the origin and branches of lateral circumflex femoral artery for type C

Gender	Age	Orientation	CPFALCFA-MI [mm]	EDFA [mm]	EDPFA [mm]	EDLCFA [mm]
Male	Old	Right	34.82	10.09	5.90	5.61
Male	Old	Right	29.44	10.70	6.88	4.77
Male	Young	Left	42.55	5.51	3.89	2.07
Male	Old	Left	56.73	11.57	5.07	4.66
Male	Old	Left	24.43	10.64	8.16	7.41
Male	Old	Right	43.42	13.40	8.92	5.81
Female	Old	Left	32.83	8.82	4.93	4.40
		Right	28.28	8.18	4.98	3.65
Female	Old	Right	24.22	7.10	3.21	3.98
Female	Old	Left	25.55	7.69	3.05	2.72

CPFALCFA-MIL — the distance from the common origin of the profunda artery and lateral circumflex femoral artery to the midpoint of the inguinal ligament; EDFA — the external diameter of the femoral artery; EDPFA — the external diameter of the profunda femoris artery; EDLCFA — the external diameter of the lateral circumflex femoral artery

Table 6. Details of the origin and branches of lateral circumflex femoral artery for type D

Gender	Age	Orientation	PFA-MIL [mm]	EDFA [mm]	EDPFA [mm]	LCFA a-PFA [mm]	LCFA b-PFA [mm]	EDLCFA a [mm]	EDLCFA b [mm]
Male	Old	Left	32.69	8.85	5.04	19.18	25.58	2.80	2.29
		Right	82.25	8.65	4.45	4.32	20.42	2.35	2.78
Male	Old	Left	33.31	8.98	6.20	40.54	58.69	2.79	2.35
Male	Old	Left	24.18	7.74	5.42	5.83	23.26	2.69	2.93
Male	Young	Left	28.78	4.13	4.11	7.70	19.39	3.89	3.16
		Right	26.27	5.83	5.39	5.64	15.97	4.10	3.83
Male	Old	Right	47.41	10.23	8.61	15.96	20.55	4.87	5.08
Male	Old	Right	43.44	5.23	3.68	6.93	13.29	3.23	2.60
Male	Young	Right	39.65	4.44	3.09	8.76	31.74	3.15	2.26
Male	Old	Left	48.01	10.02	7.88	14.91	32.85	6.56	1.35
		Right	37.02	9.60	7.21	18.97	35.22	5.76	5.95
Male	Old	Left	36.91	9.65	7.03	4.63	23.63	4.52	2.50
		Right	27.10	9.50	7.07	29.19	53.74	3.69	1.55
Male	Old	Left	52.47	4.90	3.50	27.38	42.14	3.46	2.53
Male	Middle	Right	46.91	6.95	3.99	13.63	11.14	3.12	2.20
Male	Old	Left	47.55	11.05	7.90	22.45	23.98	3.38	4.36
Male	Old	Right	47.23	10.20	5.53	59.55	59.55	2.23	3.06
Male	Old	Right	36.70	9.56	6.88	11.37	40.18	3.19	3.99
Male	Old	Right	29.19	9.69	4.94	9.78	29.28	4.04	3.07
Male	Old	Left	42.26	10.14	8.89	18.62	18.62	5.62	4.78
Male	Old	Right	38.21	13.33	10.17	34.56	47.82	4.68	4.56
Female	Old	Right	80.50	10.67	5.12	10.37	29.90	3.04	1.89
Female	Old	Left	39.86	4.90	3.94	6.70	18.15	3.50	3.87

PFA-MIL — the distance from the origin of the profunda femoris artery to the midpoint of the inguinal ligament; EDFA — the external diameter of the femoral artery; EDPFA — the external diameter of the profunda femoris artery; LCFA a-PFA — the distance from the origin of the LCFA a to the origin of the profunda femoris artery; LCFA b-PFA — the distance from the origin of the LCFA b to the origin of the profunda femoris artery; EDLCFA a — the external diameter of the LCFA a; EDLCFA b — the external diameter of the LCFA b

eral circumflex artery was a branch of the profunda femoris artery and the femoral artery in 76.1% and 19.6%, respectively. Liu et al. [13] divided branches of the profunda artery into four types based on clinical application. In the present sample of 115 cases, the lateral circumflex femoral arteries were classified according to their origin and number of roots giving rise to seven types (six of which were variations). The prevalence of the variations, named herein type A to G, was 50.43%, 11.30%, 8.70%, 20.00%, 3.48%, 3.48%, and 2.61%, respectively.

Based on the variation type, the distance from the mid-point of the inguinal ligament to the origin of the profunda femoris artery was 40.41 ± 13.72 mm (minimum 13.73 mm, maximum 83.64 mm). Nasr et al. found that the mean distance between the mid-point of the inguinal ligament and the origin of PFA and was 51.5 ± 1.9 mm on the right side and 49.7 ± ± 1.9 mm on the left side in males, and 48.5 ± 2.2 mm on the right side and 48.9 ± 2.2 mm on the left side in females [16]. This difference in morphometric data could be the result of individual and racial differences in anthropometric characteristics. Interventions involving cannulation of the femoral artery are being widely used in clinical practice [3]. During the process of puncturing the femoral artery and inserting a cannula, the profunda femoris artery should be avoided as much as possible to prevent the guidewire and catheter straying into it. If the profunda femoris artery is abnormally placed or the origin too high, the guidewire and catheter might easily stray into it [6]. This study provides anatomical data that can help access the femoral artery during clinical intubation, and doctors should pay attention to the unique situation of each patient during femoral artery puncture.

According to the variation type, the diameter of the lateral circumflex femoral artery was 4.30 ± 1.43 mm (minimum 1.01 mm, maximum 7.91 mm) and the average point of origin of the LCFA was 56.98 mm below the inguinal ligament. The deep branch (ascend-

Table 7. Summary of the origin and branches of lateral circumflex femoral artery for type E

Item	N (branch)	x̄ ± s [mm]	Minimum [mm]	Maximum [mm]
PFA-MIL	4	46.84 ± 4.09	42.32	51.44
EDFA	4	9.14 ± 2.65	5.29	11.81
EDPFA	4	5.54 ± 1.36	3.97	7.71
LCFA a-MIL	4	47.25 ± 26.48	18.69	78.49
LCFA b-PFA	4	18.55 ± 7.03	8.59	27.88
EDLCFA a	4	3.16 ± 1.28	1.01	4.26
EDLCFA b	4	4.23 ± 1.28	2.80	6.00

PFA-MIL — the distance from the origin of the profunda femoris artery to the midpoint of the inguinal ligament; EDFA — the external diameter of the femoral artery; EDPFA — the external diameter of the profunda femoris artery; LCFA a-MIL — the distance from the origin of the LCFA a to the midpoint of the inguinal ligament; LCFA b-PFA — the distance from the origin of the LCFA b to the origin of the profunda femoris artery; EDLCFA a — the external diameter of the LCFA a; EDLCFA b — the external diameter of the LCFA b

Table 9. Summary of the origin and branches of lateral circumflex femoral artery for type F

Item	N (branch)	x̄ ± s [mm]	Minimum [mm]	Maximum [mm]
CPFALCFA a-MIL	4	49.64 ± 12.40	37.88	68.55
EDFA	4	10.24 ± 0.78	9.52	11.56
EDPFA	4	6.20 ± 0.77	4.88	6.79
LCFA b- PFA	4	25.26 ± 6.64	17.24	35.70
EDLCFA a	4	4.48 ± 1.91	3.25	7.79
EDLCFA b	4	3.04 ± 1.43	1.31	4.98

CPFALCFA a-MIL — the distance from the common origin of the profunda artery and LCFA a to the midpoint of the inguinal ligament; EDFA — the external diameter of the femoral artery; EDPFA — the external diameter of the profunda femoris artery; LCFA b-PFA — the distance from the origin of the LCFA b to the origin of the profunda femoris artery; EDLCFA a — the external diameter of the LCFA a; EDLCFA b — the external diameter of the LCFA b

Table 8. Details of the origin and branches of lateral circumflex femoral artery for type E

Gender	Age	Orientation	PFA-MIL [mm]	EDFA [mm]	EDPFA [mm]	LCFA a-MIL [mm]	LCFA b-PFA [mm]	EDLCFA a [mm]	EDLCFA b [mm]
Male	Old	Right	43.24	11.39	5.17	68.38	21.21	4.26	6.00
Male	Old	Right	50.37	8.08	5.31	18.69	8.59	3.92	2.80
Male	Old	Right	51.44	11.81	7.71	23.43	27.88	3.47	3.26
Male	Middle	Left	42.32	5.29	3.97	78.49	16.51	1.01	4.86

PFA-MIL — the distance from the origin of the profunda femoris artery to the midpoint of the inguinal ligament; EDFA — the external diameter of the femoral artery; EDPFA — the external diameter of the profunda femoris artery; LCFA a-MIL — the distance from the origin of the LCFA a to the midpoint of the inguinal ligament; LCFA b-PFA — the distance from the origin of the LCFA b to the origin of the profunda femoris artery; EDLCFA a — the external diameter of the LCFA a; EDLCFA b — the external diameter of the LCFA b

Table 10. Details of the origin and branches of lateral circumflex femoral artery (LCFA) for type F

Gender	Age	Orientation	CPFALCFA a-MIL [mm]	EDFA [mm]	EDPFA [mm]	LCFA b-PFA [mm]	EDLCFA a [mm]	EDLCFA b [mm]
Male	Old	Left	52.89	11.56	6.60	23.58	3.60	2.08
Male	Old	Right	37.88	9.52	4.88	35.70	7.79	1.31
Male	Old	Left	68.55	10.01	6.52	17.24	3.29	4.98
Male	Old	Right	39.22	9.85	6.79	24.53	3.25	3.77

CPFALCFA a-MIL — the distance from the common origin of the profunda artery and LCFA a to the midpoint of the inguinal ligament; EDFA — the external diameter of the femoral artery; EDPFA — the external diameter of the profunda femoris artery; LCFA b-PFA — the distance from the origin of the LCFA b to the origin of the profunda femoris artery; EDLCFA a — the external diameter of the LCFA a; EDLCFA b — the external diameter of the LCFA b

ing branch) of the LCFA nourishes the femoral head and neck, and the diameter and position of the vessel should allow for catheter insertion. This feat can easy and safe to treat avascular necrosis of the femoral head [4]. Therefore, data contained in this article provide an anatomical basis for safe endovascular interventions in the treatment of avascular necrosis of the femoral head via the ascending branch of the LCFA.

The applied anatomy of the LCFA, an important branch of the profunda femoris artery, is of great significance in the clinical practice. For instance, it is responsible for vascularisation of the greater trochanter, head, and neck of the femur as well as the vastus lateralis muscle and the knee complex [26]. The lateral circumflex femoral artery is closely associated with the soft tissues around the hip joint and the head and neck of the femur, putting it at risk during traumatic damage to the hip joint and femoral neck [5, 10]. Knowledge of the anatomical variations of the profunda femoris artery and its circumflex branches is vital in angiographic diagnostic procedures and during surgical or radiological interventions involv-

Table 11. Summary of the origin and branches of lateral circumflex femoral artery for type G

Item	N (branch)	x̄ ± s [mm]	Minimum [mm]	Maximum [mm]
CPFALCFA a-MIL	3	92.92 ± 4.40	86.71	96.19
EDFA	3	9.85 ± 0.73	9.12	10.85
EDPFA	3	6.04 ± 0.54	5.55	6.79
LCFA b-MIL	3	45.72 ± 6.18	40.92	54.44
EDLCFA a	3	3.64 ± 1.11	2.23	4.94
EDLCFA b	3	5.11 ± 0.76	4.04	5.65

CPFALCFA a-MIL — the distance from the common origin of the profunda artery and LCFA a to the midpoint of the inguinal ligament; EDFA — the external diameter of the femoral artery; EDPFA — the external diameter of the profunda femoris artery; LCFA b-MIL — the distance from the origin of the LCFA b to the midpoint of the inguinal ligament; EDLCFA a — the external diameter of the LCFA a; EDLCFA b — the external diameter of the LCFA b

ing the femoral region. Orthopaedic surgeons and interventional radiologists must be aware of potential variations of the site of origin and course of the lateral circumflex femoral artery when performing clinical operations such as femoral triangle surgery and hip joint replacement, and vascular radiological intervention such as arterial catheterisation and arteriography [18, 27], as a means to avoid iatrogenic injury and decrease the risks of intra-operative posthaermorrhage, as well as post-operative complications. For instance, the popular anterior approach of hip surgery routinely requires the ligation of the ascending branch of the LCFA. It may jeopardize vascularisation of the proximal femur, especially in conditions of anatomical variations [7].

It is also widely used and of surgical value in thigh flaps [14]. The thigh flap supplied by LCFA and its branches has a great clinical significance in flap plastic surgery, including repairing large soft tissue defect of the extremities [9], head-and-neck region [20] and knee [2], as well as reconstructing defects resulted from perineal and hypogastric tumour resection [24]. For example, the retrograde anterolateral femoral flap with a descending lateral branch of the femoral circumflex artery and the perforating branch of the lateral superior genu artery can better repair soft tissue defects around the knee and middle and upper leg, with sufficient blood supply and satisfactory outcomes [28]. Nevertheless, the anatomical variability of the LCFA complicate the harvest of thigh flaps, thus adequate awareness of these anatomical properties will be conducive to flap refinements and donor-site management [12].

The expanding scope of vascular transplantation and reconstruction has prompted this study on the variations of LCFA and its branches. In patients with iliofemoral artery thrombosis, the LCFA can provide an alternative outflow route for the main artery bypass [23]. Besides, it can be utilized as a high-flow conduit in extracranial–intracranial (EC–IC) bypass surgery in patients with intracranial disease requiring sacrifice of the parent vessel, for example, aneurysm [1]. In recent era, the descending branch of the LCFA has gained popularity in coronary artery bypass grafting. It is worth noting that related clinical trial group encountered an 18% to 20% abandonment rate secondary to anatomical factors [15].

In order to prevent iatrogenic injury and minimise complications, it is of vital importance for radiologists and surgeons to take the variations of LCFA into account during operations in the femoral region and diagnostic interventional procedures, as well as in the field of vascular, plastic and reconstructive surgery. Therefore, a careful examination of blood vessels should be emphasized prior to performing any invasive procedure in femoral region.

CONCLUSIONS

The data of this study provided anatomical variations of the LCFA and recommend that doctors should have a sound understanding of its variations along with those of the profunda artery. This important to prevent iatrogenic injuries and improve clinical outcomes.

Conflict of interest: None declared

Table 12. Details of the origin and branches of lateral circumflex femoral artery for type G

Gender	Age	Orientation	CPFALCFA a-MIL [mm]	EDFA [mm]	EDPFA [mm]	LCFA b-MIL [mm]	EDLCFA a [mm]	EDLCFA b [mm]
Male	Old	Left	86.71	9.57	6.79	40.92	3.75	5.65
Male	Old	Right	95.87	10.85	5.77	41.80	4.94	5.64
Male	Old	Left	96.19	9.12	5.55	54.44	2.23	4.04

CPFALCFA a-MIL — the distance from the common origin of the profunda artery and LCFA a to the midpoint of the inguinal ligament; EDFA — the external diameter of the femoral artery; EDPFA — the external diameter of the profunda femoris artery; LCFA b-MIL — the distance from the origin of the LCFA b to the midpoint of the inguinal ligament; EDLCFA a — the external diameter of the LCFA a; EDLCFA b — the external diameter of the LCFA b

REFERENCES

1. Başkaya MK, Kiehn MW, Ahmed AS, et al. Alternative vascular graft for extracranial-intracranial bypass surgery: descending branch of the lateral circumflex femoral artery. Neurosurg Focus. 2008; 24(2): E8, doi: 10.3171/FOC/2008/24/2/E8, indexed in Pubmed: 18275304.
2. Bhogesha S, Rimal D, Song C. The descending branch of lateral circumflex femoral artery (LCFA) as recipient pedicle for free flap cover of complex defects around the knee. Microsurgery. 2019; 39(6): 573–574, doi: 10.1002/micr.30459, indexed in Pubmed: 30968429.
3. Daksha Dixit DMK, Sureshbhai Rathod P, Mital Pateld M, et al. A study of variations in the origin of profunda femoris artery and its circumflex branches. Int J Biol Med Res. 2011; 2(4): 1084–1089.
4. Dan Z, Zhao L, Wang X. Applied anatomy of avascular necrosis of femoral head treated by interventional treatment of deep branch of medial circumflex femoral artery and ascending branch of lateral circumflex femoral artery. Sichuan J Anat. 2002; 2(02): 73–75.
5. Dewar DC, Lazaro LE, Klinger CE, et al. The relative contribution of the medial and lateral femoral circumflex arteries to the vascularity of the head and neck of the femur: a quantitative MRI-based assessment. Bone Joint J. 2016; 98-B(12): 1582–1588, doi: 10.1302/0301-620X.98B12.BJJ-2016-0251.R1, indexed in Pubmed: 27909118.
6. Fu W. The variation of profunda artery and its management in interventional intubation. J Int Radiol. 1999; 2: 61.
7. Hartog C, Metzler C, Meier C, et al. Anatomy of the lateral circumflex femoral artery: Does the direct anterior approach to the hip jeopardize vascularization of the proximal femur? Orthop Traumatol Surg Res. 2019; 105(7): 1257–1264, doi: 10.1016/j.otsr.2019.07.013, indexed in Pubmed: 31537495.
8. Hyun Kwon J, Hoon Shin Ji. Hypoplastic superficial femoral artery combined with connection of the deep femoral artery to the popliteal artery. Radiology Case Reports. 2018; 13(1): 39–42, doi: 10.1016/j.radcr.2017.10.028.
9. Jin W, Wei Z, Deng C, et al. Clinical application of free descending branch of lateral circumflex femoral artery perforator tissue flap and its impact on donor site. Zhongguo Xiu Fu Chong Jian Wai Ke Za Zhi. 2015; 29(10): 1284–1287, indexed in Pubmed: 26749740.
10. Kalhor M, Beck M, Huff TW, et al. Capsular and pericapsular contributions to acetabular and femoral head perfusion. J Bone Joint Surg Am. 2009; 91(2): 409–418, doi: 10.2106/JBJS.G.01679, indexed in Pubmed: 19181985.
11. Łabętowicz P, Olewnik Ł, Podgórski M, et al. A morphological study of the medial and lateral femoral circumflex arteries: a proposed new classification. Folia Morphol. 2019; 78(4): 738–745, doi: 10.5603/FM.a2019.0033, indexed in Pubmed: 30906974.
12. Lee YC, Chen WC, Chou TM, et al. Anatomical variability of the anterolateral thigh flap perforators: vascular anatomy and its clinical implications. Plast Reconstr Surg. 2015; 135(4): 1097–1107, doi: 10.1097/PRS.0000000000001103, indexed in Pubmed: 25502859.
13. Liu H, Shao D, Guo J, et al. Applied anatomy of the profunda artery and its branches. Sichuan J Anat. 2001(03): 137–140.
14. Liu Y, Ding Q, Zang M, et al. Classification and application of the distally-based thigh flap based on the lateral circumflex femoral artery system. Ann Plast Surg. 2017; 78(5): 497–504, doi: 10.1097/SAP.0000000000000946, indexed in Pubmed: 28118225.
15. Luo XJ, Wang YT, Wang W, et al. Application of the descending branch of the lateral circumflex femoral artery in coronary artery bypass grafting. J Thorac Cardiovasc Surg. 2021; 161(4): 1266–1271, doi: 10.1016/j.jtcvs.2019.09.172, indexed in Pubmed: 31767359.
16. Nasr AY, Badawoud MH, Al-Hayani AA, et al. Origin of profunda femoris artery and its circumflex femoral branches: anatomical variations and clinical significance. Folia Morphol. 2014; 73(1): 58–67, doi: 10.5603/FM.2014.0008, indexed in Pubmed: 24590524.
17. Peng C, Ge S, Zhong H, et al. case of left deep femoral artery with lateral circumflex femoral artery variation. Sichuan J Anat. 2015; 23(03): 62–63.
18. Prough H, Alsayouri K. Anatomy, Bony Pelvis and Lower Limb, Lateral Circumflex Femoral Artery. StatPearls. StatPearls Publishing LLC, Treasure Island (FL) 2020.
19. Shang Y, Li Y, Ning Y, et al. One case of lateral circumflex femoral artery variation. Progress of Anatomical Sciences. 2014; 20(03): 300.
20. Shen Yi, Lu LG, Low DW, et al. Perforator navigation using color Doppler ultrasound and three-dimensional reconstruction for preoperative planning of optimal lateral circumflex femoral artery system perforator flaps in head and neck reconstruction. J Plast Reconstr Aesthet Surg. 2019; 72(6): 990–999, doi: 10.1016/j.bjps.2018.12.025, indexed in Pubmed: 30880047.
21. Shi E, Fang G, Fu Y, et al. Applied anatomical investigation of femoral artery and its branches. J Baotou Med Coll. 2005; 04: 349–350.
22. Sinkeet SR, Ogeng'o JA, Elbusaidy H. Variant origin of the lateral circumflex femoral artery in a black Kenyan population. Folia Morphol. 2012; 71(1): 15–18, indexed in Pubmed: 22532179.
23. Sugawara Y, Sato O, Miyata T, et al. Utilization of the lateral circumflex femoral artery as a midway outflow for aor-to-popliteal grafting: report of a case. Surg Today. 1998; 28(9): 967–970, doi: 10.1007/s005950050264, indexed in Pubmed: 9744412.
24. Tang X, Wei Z, Wang B, et al. Application of the lobulated flap or unilobular flap pedicled with the descending branch of lateral femoral circumflex artery in reconstruction of defects resulted from perineal and hypogastric tumor resection]. Zhonghua Zheng Xing Wai Ke Za Zhi. 2016; 32(2): 111–114, indexed in Pubmed: 30024686.
25. Tanyeli E, Uzel M, Yildirim M, et al. An anatomical study of the origins of the medial circumflex femoral artery in the Turkish population. Folia Morphol. 2006; 65(3): 209–212, indexed in Pubmed: 16988917.
26. Tomaszewski KA, Vikse J, Henry BM, et al. The variable origin of the lateral circumflex femoral artery: a meta-analysis and proposal for a new classification system. Folia Morphol. 2017; 76(2): 157–167, doi: 10.5603/FM.a2016.0056, indexed in Pubmed: 27714726.
27. Vazquez MT, Murillo J, Maranillo E, et al. Patterns of the circumflex femoral arteries revisited. Clin Anat. 2007; 20(2): 180–185, doi: 10.1002/ca.20336, indexed in Pubmed: 16617441.
28. Wang H, Li X, Li S, et al. Clinical application of anterolateral femoral flap with descending branch of circumflex lateral femoral artery and perforating branch of superior lateral genicular artery. Chin J Anat Clin. 2017; 22(6): 515–8, doi: 10.3760/cma.j.issn.2095-7041.2017.06.014.

VIA MEDICA

ORIGINAL ARTICLE

Folia Morphol.
Vol. 80, No. 3, pp. 567–574
DOI: 10.5603/FM.a2020.0079
Copyright © 2021 Via Medica
ISSN 0015–5659
eISSN 1644–3284
journals.viamedica.pl

Types of inferior phrenic arteries: a new point of view based on a cadaveric study

B. Szewczyk[1], P. Karauda[1], Ł. Olewnik[1], M. Podgórski[2], A. Waśniewska[3], R. Haładaj[3], E. Rapacka[3], P. Oszukowski[4], M. Polguj[3]

[1]*Department of Anatomical Dissection and Donation, Medical University of Lodz, Poland*
[2]*Department of Diagnostic Imaging of Polish Mother's Memorial Hospital Research Institute, Lodz, Poland*
[3]*Department of Normal and Clinical Anatomy, Chair of Anatomy and Histology, Medical University of Lodz, Poland*
[4]*Department of Clinical Morphology, Medical University of Lodz, Poland*

[Received: 23 April 2020; Accepted: 22 June 2020; Early publication date: 21 July 2020]

Background: *The diaphragm is supplied by the superior and inferior phrenic arteries. This present study focusses on the latter. The inferior phrenic arteries (IPA) usually originate from the abdominal aorta. The two arteries have different origins, and knowledge of these is important when performing related surgical interventions and interventional radiological procedures. The aim of this study was to identify variations in the origin of the IPA and conduct relevant morphometric analyses.*
Materials and methods: *The anatomical variations in the origins of the left inferior phrenic artery (LIPA) and the right inferior phrenic artery (RIPA) were examined in 48 cadavers fixed in 10% formalin solution. A dissection of the abdominal region of the cadavers was performed according to a pre-established protocol using traditional techniques. Morphometric measurements were then taken twice by two of the researchers.*
Results: *In the cadavers, six types of origin were observed. In type 1, the most common type, the RIPA and LIPA originate from the abdominal aorta (AA) (14 = 29.12%). In type 2, the RIPA and the LIPA originate from the coeliac trunk (CT) (12 = 24.96%). In type 3, the RIPA and the LIPA originate from the left gastric artery, with no CT observed (3 = 6.24%). Type 4 has two subtypes: 4A, in which the LIPA originates from the AA and the RIPA originates from the CT (9 = 18.72%) and 4B, in which the RIPA originates from the AA and the LIPA originates from the CT (6 = 12.48%). In type 5, the LIPA originates from the AA and the RIPA originates from the AA (1 = 2.08%). Type 6 is characterised by the RIPA and LIPA forming a common trunk originating from the CT (3 = 6.24%).*
Conclusions: *Our findings suggest the presence of six different types of LIPA and RIPA origin. The most common form is type 1, characterised by an IPA originating from the abdominal aorta, while the second most common is type 2, in which the IPA originates from the AA by a common trunk. The diversity of other types of origin is associated with the occurrence of coeliac trunk variation (type 3). No significant differences in RIPA diameter could be found, whereas LIPA diameter could vary significantly. No significant differences in RIPA and the LIPA diameter could be found according to sex.* (Folia Morphol 2021; 80, 3: 567–574)

Key words: inferior phrenic arteries, left inferior phrenic artery, right inferior phrenic artery, diaphragm, coeliac trunk

Address for correspondence: Ass. B. Szewczyk, Department of Anatomical Dissection and Donation, Medical University of Lodz, ul. Żeligowskiego 7/9, 90–752 Łódź, Poland, tel: +48 42 630 49 49, +48 42 630 07 49, e-mail: bartlomiej.szewczyk@umed.lodz.pl; Dr. Ł. Olewnik; Department of Normal and Clinical Anatomy University of Łódź, ul. Żeligowskiego 7/9, 90–752 Łódź, Poland, tel: +48 42 630 49 49, +48 42 630 07 49, e-mail: lukasz.olewnik@umed.lodz.pl

INTRODUCTION

The inferior phrenic artery (IPA) usually originates from the abdominal aorta (AA) and consists of two vessels, i.e. the left inferior phrenic artery (LIPA) and the right inferior phrenic artery (RIPA). The two give rise to the ascending (anterior) and the descending (posterior) branches. Although the IPA mainly supplies the diaphragm, it also gives small branches to the liver, stomach, the cardiac part of the oesophagus, the adrenal glands, and retroperitoneum [1, 4, 36].

The anterior branch of the LIPA gives rise to the oesophageal and accessory splenic branches while the RIPA rises along with inferior vena cava [1, 36]. However, the posterior branches of both IPAs run to the lateral crus and can form anastomoses with the musculophrenic artery and the lower posterior intercostal arteries [7, 29, 31].

The LIPA usually runs behind the oesophagus, and goes anteriorly to the left side of the oesophageal hiatus. The ascending branch divides into two trunks: the larger anterior and the smaller posterior. The anterior trunk directly supplies the area of the oesophagogastric junction and the dome of the diaphragm [9]. Additionally, a small number of branches may also attach to the superior pole of the spleen [2, 6, 18, 30].

The RIPA usually passes behind the left hepatic lobe and the inferior vena cava [25, 35]. The ascending branch is usually located cranially and contacts the bare area of the liver [29, 36].

In most cases, the LIPA and RIPA arise separately from the AA above the origin of the coeliac trunk (CT) [25, 30, 36]; however, they may demonstrate various types of origin [13, 20, 23, 35]. Information on the possible position of this artery can be valuable for understanding and treating the source of arterial bleeding at the oesophagogastric junction [9, 39].

The most commonly recognized clinical feature of the RIPA is that it may serve as an extrahepatic collateral arterial supply route to hepatocellular carcinomas [3, 34]. This is important information for surgeons since, in such a case, transcatheter embolisation of RIPA may help in the treatment of unresectable hepatocellular carcinoma [3, 16, 34].

This vessel is one of the main sources of postoperative bleeding in liver transplant recipients. In living donors undergoing right hepatic lobectomy, ligation of the artery is necessary for the donor and for hepatectomy in the recipient [17].

However, previous studies have so far examined each of the arteries separately and none have proposed any classifications. Therefore, the aim of our study was to investigate the anatomy of IPA types by classical anatomical dissection, and to propose a classification based on the origin of both the RIPA and LIPA.

MATERIALS AND METHODS

Anatomical studies

The study was performed on upper abdominal region of 48 adult Caucasian cadavers (29 males and 19 females) that had been fixed in 10% formalin solution before examination. The cadavers were the property of the Department, having been donated to the university anatomy programme. Cadavers with any evidence of surgical intervention in the dissected area were excluded from the study.

Description of the dissection protocol

Firstly, the abdominal cavity was opened by making incisions along the linea alba from the xiphoid process to the pubic symphysis. Next, after making sure there was no evidence of trauma, pathology or prior surgery in the upper abdominal organs, the origin of the RIPA and LIPA was recorded

Upon dissection, the morphological features of the IPA were assessed:
- origin of the LIPA and the RIPA;
- diameter of the LIPA (measurement taken at the origin);
- diameter of the RIPA (measurement taken at the origin).

All measurements were performed using an electronic digital calliper gauge (Mitutoyo Corporation, Kawasaki-shi, Kanagawa, Japan). Each measurement was carried out twice with an accuracy of up to 0.1 mm. The consent for the anatomical studies was obtained from the Local Bioethical Commission RNN/404/19/KE

Statistical analysis

In the statistical analysis, IPA types were compared according to genders and sides with the χ^2 test. The normality of the morphometric data distribution was checked with the Shapiro-Wilk test. As the data was not normally distributed, the Mann-Whitney test and the Wilocoxon sign-rank test were used to compare anthropometric measurements between the sexes and sides, respectively. Differences in morphometric

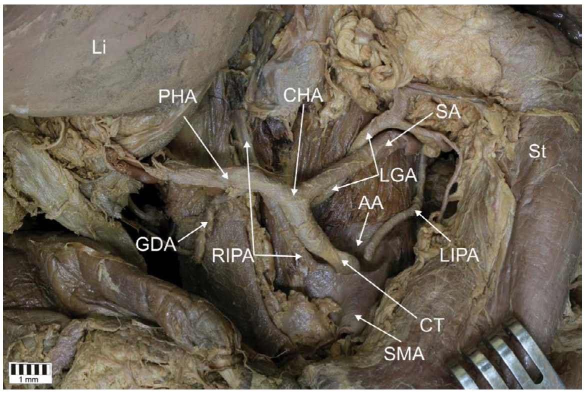

Figure 1. Type 1 — the RIPA and LIPA originate from the abdominal aorta. PHA — proper hepatic artery; GDA — gastro-duodenal artery; RIPA — right inferior phrenic artery; CHA — common hepatic artery; LGA — left gastric artery; SA — splenic artery; LIPA — left inferior phrenic artery; CT — coeliac trunk; SMA — superior mesentery artery; St — stomach; Li — liver; AA — abdominal aorta.

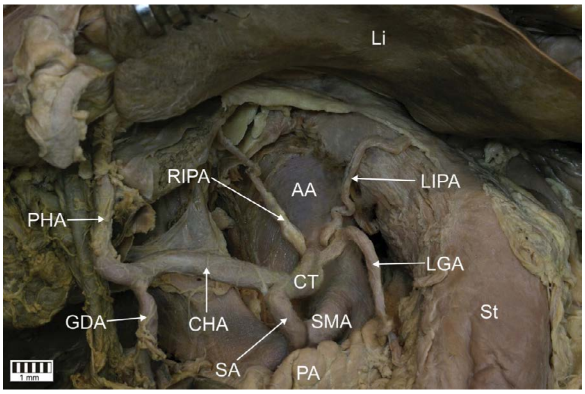

Figure 2. Type 2 — the RIPA and LIPA originate from the coeliac trunk. PHA — proper hepatic artery; GDA — gastro-duodenal artery; RIPA — right inferior phrenic artery; CHA — common hepatic artery; LGA — left gastric artery; SA — splenic artery; LIPA — left inferior phrenic artery; CT — coeliac trunk; SMA — superior mesentery artery; St — stomach; Li — liver; AA — abdominal aorta; PA — pancreas.

measurements between the types were assessed with the Kruskal-Wallis ANOVA with a dedicated *post hoc* test. Statistica 13 software (StatSoft Polska, Krakow, Poland) was used for the analysis and a p-value lower than 0.05 was considered significant. The results are presented as mean and standard deviation unless stated otherwise.

Ethical approval and consent to participate

The cadaver belonged to the Department of Anatomical Dissection and Donation, Medical University of Lodz.

RESULTS

In all the specimens, both IPAs were present. Based on the point of branching, six types of IPA could be identified:

- type 1 — the RIPA and the LIPA originate from the AA (Fig. 1). This type occurred in 14 cadavers;
- type 2 — the RIPA and the LIPA originate from the CT (Fig. 2). This type was observed in 12 cadavers;
- type 3 — the RIPA and the LIPA originate from the left gastric artery (LGA) (Fig. 3). In this type the CT was absent. This type occurred in 3 cadavers;
- type 4 — this type was divided into two subtypes (A, B):
  - A — the LIPA originates from the AA, and the RIPA originates from the CT (Fig. 4). This type occurred in 9 cadavers,
  - B — the RIPA originates from the AA, and the LIPA originates from the CT (Fig. 5). This type occurred in 6 cadavers;

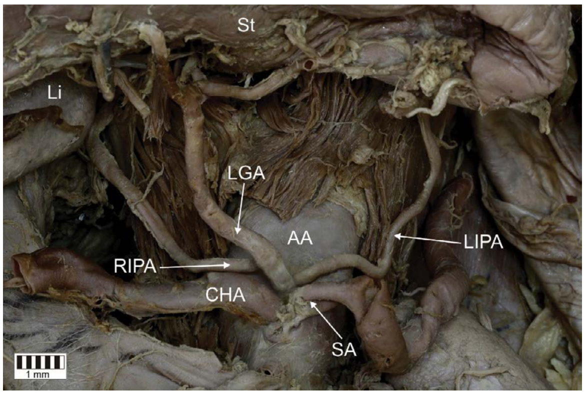

Figure 3. Type 3 — the RIPA and LIPA originate from the left gastric artery. RIPA — right inferior phrenic artery; CHA — common hepatic artery; LGA — left gastric artery; SA — splenic artery; LIPA — left inferior phrenic artery; St — stomach; Li — liver; AA — abdominal aorta.

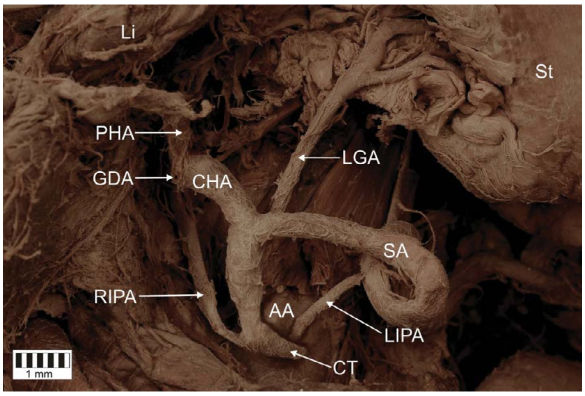

Figure 4. Type 4A — the LIPA originate from the abdominal aorta, and the RIPA originate from the coeliac trunk. PHA — proper hepatic artery; GDA — gastro-duodenal artery; RIPA — right inferior phrenic artery; CHA — common hepatic artery; LGA — left gastric artery; SA — splenic artery; LIPA — left inferior phrenic artery; CT — coeliac trunk; St — stomach; Li — liver; AA — abdominal aorta.

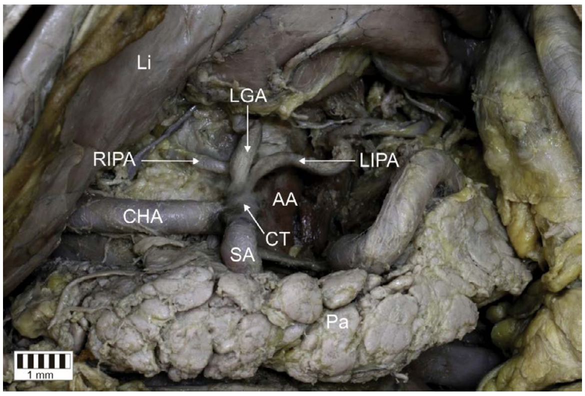

Figure 5. Type 4B — the RIPA originate from the abdominal aorta, and the LIPA originate from the coeliac trunk. RIPA — right inferior phrenic artery; CHA — common hepatic artery; LGA — left gastric artery; SA — splenic artery; LIPA — left inferior phrenic artery; CT — coeliac trunk; Li — liver; AA — abdominal aorta; Pa — pancreas.

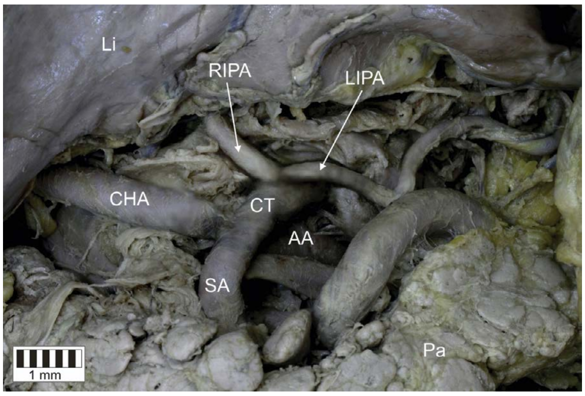

Figure 7. Type 6 — the common trunk for the RIPA and LIPA, which originate from the abdominal aorta. RIPA — right inferior phrenic artery; CHA — common hepatic artery; SA — splenic artery; LIPA — left inferior phrenic artery; Li — liver; AA — abdominal aorta, Pa — pancreas.

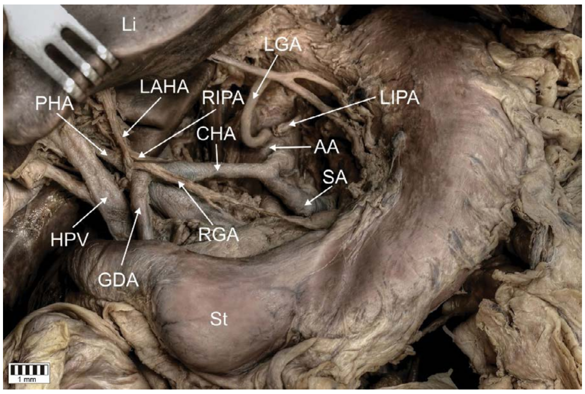

Figure 6. Type 5 — the LIPA originate from the abdominal aorta, and on the right side common trunk for the left accessory hepatic artery and RIPA originate from the abdominal aorta. PHA — proper hepatic artery; GDA — gastro-duodenal artery; RIPA — right inferior phrenic artery; CHA — common hepatic artery; LGA — left gastric artery; SA — splenic artery; LIPA — left inferior phrenic artery; St — stomach; Li — liver; AA — abdominal aorta; LAHA — left accessory hepatic artery; HPV — hepatic portal vein; RGA — right gastric artery.

— type 5 — the LIPA originates from the AA and the RIPA originates from the accessory hepatic artery (Fig. 6). This type occurred in one cadaver;

— type 6 — the RIPA and the LIPA form a common trunk which originates from the AA (Fig. 7). This type occurred in 3 cadavers.

In Figure 8 we have presented all the types we established in the form of diagrams.

Table 1 presents the origin of LIPA and RIPA according to given type. In almost all types, the LIPA and RIPA are single arteries and have different origins. However, both IPAs originate from the CT by a short common trunk in type 6.

Table 1. Comparison of particular types of left inferior phrenic artery (LIPA) and the right inferior phrenic artery (RIPA) origin

	LIPA	RIPA
Type 1	AA	AA
Type2	CT	CT
Type 3	LGA	LGA
Type 4A	AA	CT
Type 4B	CT	AA
Type 5	AA	AHA
Type 6	CT	

AA — abdominal aorta; AHA — accessory hepatic artery; CT — coeliac trunk; LGA — left gastric artery

Table 2. Comparison of types according to sex (number and % for each gender)

	Men	Women
Type 1	5 (35.71)	9 (26.47)
Type 2	5 (35.71)	7 (20.59)
Type 3	1 (7.14)	2 (5.88)
Type 4A	3 (21.43)	6 (17.65)
Type 4B	–	6 (17.65)
Type 5	–	1 (2.94)
Type 6	–	3 (8.82)

Table 2 presents the distribution of IPA types according to sex. Although no significant difference in distribution was observed ($p = 0.4916$), it is important to note that types 4B, 5 and 6 did not occur in men.

Table 3 presents diameters of the LIPA and the RIPA according to sex. In general, no significant difference

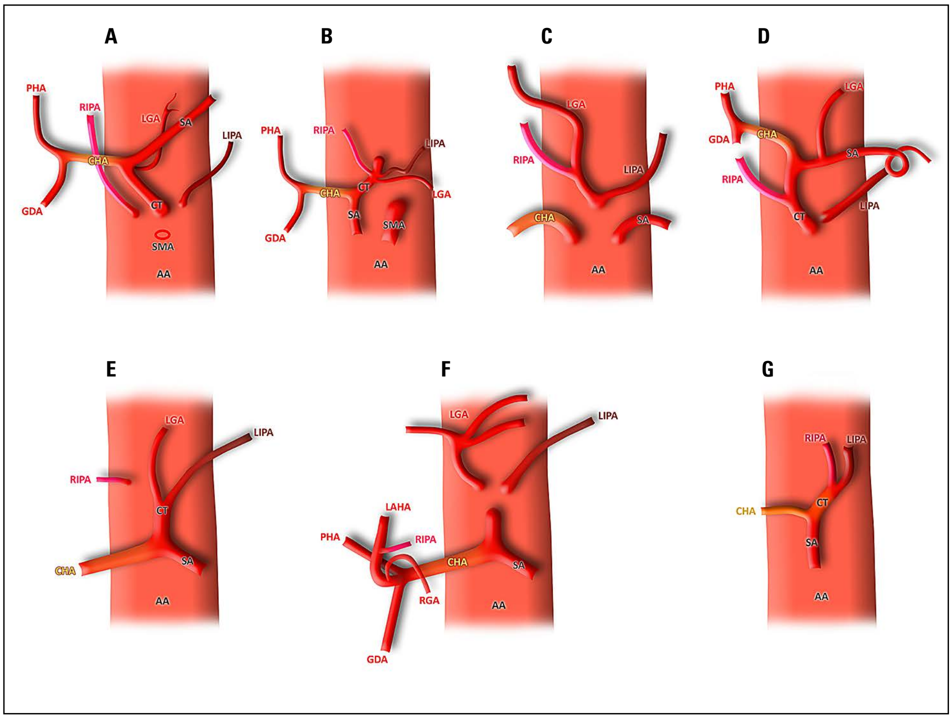

Figure 8. Scheme presents all types of left inferior phrenic artery (LIPA) and the right inferior phrenic artery (RIPA) origins; **A.** Type 1; **B.** Type 2; **C.** Type 3; **D.** Type 4A; **E.** Type 4B; **F.** Type 5; **G.** Type 6.

Table 3. Comparison of left inferior phrenic artery (LIPA) and the right inferior phrenic artery (RIPA) diameter according to type and sex

		LIPA [mm]		RIPA [mm]	
		Men	Women	Men	Women
Type 1	Maximum	3.07	3.19	2.90	3.20
	Minimum	2.54	1.66	2.21	2.01
	Average	2.80	2.45	2.59	2.50
Type 2	Maximum	3.11	2.14	3.57	2.74
	Minimum	1.86	1.88	2.46	1.69
	Average	2.36	2.01	3.04	2.25
Type 3	Maximum	2.61	2.21	3.19	2.41
	Minimum	2.31	2.21	2.85	2.41
	Average	2.46	2.21	3.02	2.41
Type 4A	Maximum	3.55	3.49	4.03	3.11
	Minimum	2.44	2.61	2.74	2.95
	Average	3.02	3.05	3.44	3.01
Type 4B	Maximum	–	2.50	–	2.70
	Minimum	–	1.98	–	2.04
	Average	–	2.24	–	2.55
Type 5	Maximum	–	2.56	–	2.86
	Minimum	–	2.56	–	2.86
	Average	–	2.56	–	2.86
Type 6	Maximum	–	2.28	–	2.28
	Minimum	–	2.02		2.02
	Average	–	2.15		2.15

in mean LIPA or RIPA diameter was observed between sexes: LIPA, 2.46 ± 0.44 mm for women compared to 2.66 ± 0.47 mm for men ($p = 0.1846$); RIPA, 2.59 ± ± 0.46 mm for women compared to 2.73 ± 0.63 mm for men ($p = 0.6830$).

Regarding the types, LIPA diameter was significantly greater in type 4A than in types 1 and 4B ($p = 0.0045$). For the RIPA, the differences were not significant.

DISCUSSION

Vascular abnormalities are very common in the abdomen; the area undergoes many modifications during the formation of the adult vascular system. In addition, it is possible for multiple arterial variants to develop within a single person [14]. The type of IPA varies depending on the occurrence of other abdominal vascular variations; in particular, different origins of both LIPA and RIPA may be observed in the presence of variations of the CT [19, 22, 26, 41].

This correlation can be explained by the embryological development of the CT [4, 10, 11, 24, 27, 32, 37]. The aorta has posterior, lateral and abdominal branches, which form the CT and the longitudinal anastomoses between them. The growth of the longitudinal anastomoses and regression of the abdominal branches affects the formation of various types of the CT division. The IPA primarily arises from the abdominal roots of the aorta and most likely from the same level as the CT [12, 33, 35, 40].

For example, Olewnik et al. proposes that the variant of the CT branching into the common hepatic artery, the LGA, splenic artery and LIPA should be called the coeliacophrenic trunk. This type was observed in 14.5% of a group of 40 cadavers, i.e. the second most common type [2, 23].

We propose the following 6-fold classification of IPA origin based on our findings. In type 1, the lower diaphragmatic arteries are branches of the AA above the CT. Previous studies have found this type to occur in over 50% of preparations [29], while it was observed in about 29.12% of cases in the present study.

Type 2 is characterised by both lower diaphragmatic arteries forming separate branches arising from the CT. It was found to be the most common type by Basile et al. (41% of preparations) [3]; however, it was present in about 24.96% of cadavers in the present study.

In type 3, the RIPA and the LIPA arise from the LGA. It was observed in 6.24% of the cadavers, which was much less common than recorded by other authors, e.g. Loukas et al. [18] note it was present in about 2% of specimens.

In type 4, one IPA originates from the CT and the other from the AA. This type was divided into two subtypes. Subtype 4A, where the LIPA originates from the AA and the RIPA originates from the CT, was observed in about 18.72% of the cadavers. Subtype 4B, in which RIPA originates at the AA and the LIPA at the CT, occurred in 12.48% of the tested specimens. As these subtypes have not been discussed in any previous study, it is not possible to make any comparisons regarding the frequency of occurrence.

In type 5, the LIPA runs directly from the AA, while both RIPA and left accessory hepatic artery originate from the AA. this is a comparatively rare type, occurring in only 2.08% of the examined cadavers. As with type 4, this type has not been discussed in any other previous study.

In our final proposed type, type 6, the LIPA and RIPA form a common trunk arising from the AA. This type was observed in only 6.24% of the studied cadavers; however, Basile et al. [3] reported it in about 21% of specimens.

Table 4. Overview of previous studies which investigated the origin of inferior phrenic artery types and the present study

	Type 1	Type 2	Type 3	Type 4		Type 5	Type 6
				A	B		
Adachi et al. 1928	11	6	1	–	–	–	–
Pick and Anson et al. 1941	37	26	4	–	–	–	–
Greig et al. 1951	77	52	3	–	–	–	–
Kahn et al. 1967	13	–	–	–	–	–	–
Lippert and Pabst et al. 1985	18%	14%	1%	–	–	–	–
Piao et al. 1998	6	4	–	–	–	–	–
Loukas et al. 2005	22	12	–	–	–	–	–
Gwon et al, 2007	–	–	–	–	–	–	–
Basile et al. 2008	42	32	–	–	–	–	–
Ozbulbul et al. 2011	16	18	–	–	–	–	–
Our study	14	12	3	9	6	1	3

Our proposed type 4 (A, B), type 5 and type 6 and their LIPA and the RIPA origins' configurations have not been reported in previous studies (Table 4).

Inferior phrenic arteries are one of the most important collateral arteries that provide blood to hepatocellular carcinoma located in the peripheral segments and bare area of the liver [3, 15].

One of the priorities for successful treatment of hepatocellular carcinoma is the complete embolisation of the blood supply. To ensure this, and prevent complications due to embolisation of the non-targeted branches, computed tomography angiography identification of the arteries supplying the tumour is an important clinical step [8, 21, 25]. In addition to RIPA embolisation, gastroesophageal complications may occur if the ascending branch of the LIPA originates from the RIPA [16, 28]. The same type should also be kept in mind if an IPA embolisation is planned in patients with upper gastroesophageal bleeding [5, 38].

Limitations of the study

The present study does have some limitations. Being based on several morphological details, such as type of the origin, the classification is of quite a heterogeneous nature; as this is only an anatomical study, a spectrum of variation could be presented, and further studies should examine the potential value of angiography or CT for this purpose. Nonetheless, our findings help raise awareness of "what and where" to look for, and offers a uniform classification and terminology which can be used as a foundation for communication with surgeons, particularly those harvesting tendons for transplants. Another limitation is the small research sample (48); however, this group is nevertheless larger than used in similar studies of this type.

CONCLUSIONS

Our work adds a new perspective to our understanding of IPA anatomy by measurements its diameter. Our results indicate that while no significant differences can be found in RIPA diameter, LIPA diameter varies significantly. No significant differences in RIPA or LIPA diameter were found according to sex.

We therefore propose a 6-fold classification created by analysing the departure of the RIPA and LIPA. In contrast to previous studies, we considered the arteries as a pair and not as separate vessels.

Conflict of interest: None declared

REFERENCES

1. Anatomy Atlases Illustrated Encyclopedia of Human Anatomic Variation - Anatomical Variation Radiology Anatomy. https://www.anatomyatlases.org/AnatomicVariants/AnatomyHP.shtml.
2. Aslaner R, Pekcevik Y, Sahin H, et al. Variations in the origin of inferior phrenic arteries and their relationship to celiac axis variations on CT angiography. Korean J Radiol. 2017; 18(2): 336–344, doi: 10.3348/kjr.2017.18.2.336, indexed in Pubmed: 28246513.
3. Basile A, Tsetis D, Montineri A, et al. MDCT anatomic assessment of right inferior phrenic artery origin related to potential supply to hepatocellular carcinoma and its embolization. Cardiovasc Intervent Radiol. 2008; 31(2): 349–358, doi: 10.1007/s00270-007-9236-x, indexed in Pubmed: 18071790.
4. Book — Manual of Human Embryology II - Embryology. https://embryology.med.unsw.edu.au/embryology/index.php/Book_-_Manual_of_Human_Embryology_II#Chapter_XIX._By_W_Felix (Accessed 24 Mar 2020).
5. Dong Il, Ko GYG, Yoon HK, et al. Inferior phrenic artery: anatomy, variations, pathologic conditions, and interventional management. Radiographics. 2007; 27(3): 687–705, doi: 10.1148/rg.273065036, indexed in Pubmed: 17495287.
6. Exhibit E. Inferior Phrenic Artery: Anatomy, Variations, Pathologic Conditions, and Interventional. 2007: 687–706.
7. Goss C. Blood supply and anatomy of the upper abdominal organs with a descriptive atlas. By N. A. Michels. xiv + 581 pages, 172 figures. $24.00. J. B. Lippincott Company, Philadelphia, 1955. The Anatomical Record. 1960; 137(2): 153–154, doi: 10.1002/ar.1091370211.
8. Greig HW, Anson BJ, Coleman SS. The inferior phrenic artery; types of origin in 850 body-halves and diaphragmatic relationship. Q Bull Northwest Univ Med Sch. 1951; 25(4): 345–350, indexed in Pubmed: 14892223.
9. Gürses İA, Gayretli Ö, Kale A, et al. Inferior phrenic arteries and their branches, their anatomy and possible clinical importance: an experimental cadaver study. Balkan Med J. 2015; 32(2): 189–195, doi: 10.5152/balkanmedj.2015.150052, indexed in Pubmed: 26167344.
10. Hemamalini A. Variations in the branching pattern of the celiac trunk and its clinical significance. Anat Cell Biol. 2018; 51(3): 143–149, doi: 10.5115/acb.2018.51.3.143, indexed in Pubmed: 30310705.
11. Huang Y, Mu GC, Qin XG, et al. Study of celiac artery variations and related surgical techniques in gastric cancer. World J Gastroenterol. 2015; 21(22): 6944–6951, doi: 10.3748/wjg.v21.i22.6944, indexed in Pubmed: 26078572.
12. Iezzi R, Cotroneo AR, Giancristofaro D, et al. Multidetector-row CT angiographic imaging of the celiac trunk: anatomy and normal variants. Surg Radiol Anat. 2008; 30(4): 303–310, doi: 10.1007/s00276-008-0324-7, indexed in Pubmed: 18286222.
13. Isogai S, Horiguchi M, Hitomi J. The para-aortic ridge plays a key role in the formation of the renal, adrenal and gonadal vascular systems. J Anat. 2010; 216(6): 656–670, doi: 10.1111/j.1469-7580.2010.01230.x, indexed in Pubmed: 20579173.
14. Kahn C, MacNeil M, Fanola C, et al. Complex arterial patterning in an anatomical donor. Trans Res Anat. 2018; 12: 11–19, doi: 10.1016/j.tria.2018.06.001.
15. Kimura S, Okazaki M, Higashihara H, et al. Analysis of the origin of the right inferior phrenic artery in 178 patients with hepatocellular carcinoma treated by chemoembolization via the right inferior phrenic artery. Acta Radiol. 2007; 48(7): 728–733, doi: 10.1080/02841850701376334, indexed in Pubmed: 17729002.
16. Lee DHo, Chung JW, Kim HC, et al. Development of diaphragmatic weakness after transcatheter arterial chemoembolization of the right inferior phrenic artery: frequency and determinant factors. J Vasc Interv Radiol. 2009; 20(4): 484–489, doi: 10.1016/j.jvir.2008.11.023, indexed in Pubmed: 19157895.
17. Lee JW, Kim S, Kim CW, et al. Massive hemoperitoneum due to ruptured inferior phrenic artery pseudoaneurysm after blunt trauma. Emerg Radiol. 2006; 13(3): 147–149, doi: 10.1007/s10140-006-0524-6, indexed in Pubmed: 17039340.
18. Loukas M, Hullett J, Wagner T. Clinical anatomy of the inferior phrenic artery. Clin Anat. 2005; 18(5): 357–365, doi: 10.1002/ca.20112, indexed in Pubmed: 15971218.
19. Merklin RJ, Michels NA. The variant renal and suprarenal blood supply with data on the inferior phrenic, ureteral and gonadal arteries: a statistical analysis based on 185 dissections and review of the literature. J Int Coll Surg. 1958; 29(1 Pt 1): 41–76, indexed in Pubmed: 13502578.
20. Miclaus GD, Matusz P, Loukas M, et al. Rare case of the trunk of the inferior phrenic arteries originating from a common stem with a superior additional left renal

artery from the abdominal aorta. Clin Anat. 2012; 25(8): 979–982, doi: 10.1002/ca.22161, indexed in Pubmed: 22949218.
21. Miyayama S, Yamashiro M, Yoshie Y, et al. Inferior phrenic arteries: angiographic anatomy, variations, and catheterization techniques for transcatheter arterial chemoembolization. Jpn J Radiol. 2010; 28(7): 502–511, doi: 10.1007/s11604-010-0456-7, indexed in Pubmed: 20799015.
22. Mu GC, Huang Y, Liu ZM, et al. Clinical research in individual information of celiac artery CT imaging and gastric cancer surgery. Clin Transl Oncol. 2013; 15(10): 774–779, doi: 10.1007/s12094-013-1002-8, indexed in Pubmed: 23359186.
23. Olewnik Ł, Wysiadecki G, Polguj M, et al. Types of coeliac trunk branching including accessory hepatic arteries: a new point of view based on cadaveric study. Folia Morphol. 2017; 76(4): 660–667, doi: 10.5603/FM.a2017.0053, indexed in Pubmed: 28612916.
24. Osman A, Abdrabou A. Celiac trunk and hepatic artery variants: A retrospective preliminary MSCT report among Egyptian patients. Egyptian J Radiol Nuclear Med. 2016; 47(4): 1451–1458, doi: 10.1016/j.ejrnm.2016.09.011.
25. Ozbülbül NI, Yurdakul M, Tola M. Does the right inferior phrenic artery have a supplying role in liver cirrhosis without hepatocellular carcinoma? A 64-slice CT study. Diagn Interv Radiol. 2011; 17(3): 239–242, doi: 10.4261/1305-3825.DIR.3395-10.1, indexed in Pubmed: 20690077.
26. Ozbülbül NI. CT angiography of the celiac trunk: anatomy, variants and pathologic findings. Diagn Interv Radiol. 2011; 17(2): 150–157, doi: 10.4261/1305-3825.DIR.3283-10.1, indexed in Pubmed: 20690078.
27. Panagouli E, Venieratos D, Lolis E, et al. Variations in the anatomy of the celiac trunk: A systematic review and clinical implications. Ann Anat. 2013; 195(6): 501–511, doi: 10.1016/j.aanat.2013.06.003, indexed in Pubmed: 23972701.
28. Petrella S, Rodriguez C, Sgrott E, et al. Origin of Inferior Phrenic Arteries in the Celiac Trunk. Int J Morphol. 2006; 24(2), doi: 10.4067/s0717-95022006000300024.
29. Piao DX, Ohtsuka A, Murakami T. Typology of abdominal arteries, with special reference to inferior phrenic arteries and their esophageal branches. Acta Med Okayama. 1998; 52(4): 189–196, doi: 10.18926/AMO/31299, indexed in Pubmed: 9781269.
30. Pick J, Anson B. The inferior phrenic artery: Origin and suprarenal branches. Anat Record. 1940; 78(4): 413–427, doi: 10.1002/ar.1090780402.
31. Pulakunta T, Potu B, Gorantla V, et al. The origin of the inferior phrenic artery: a study in 32 South Indian cadavers with a review of the literature. Jornal Vascular Brasileiro. 2007; 6(3): 225–230, doi: 10.1590/s1677-54492007000300005.
32. Santos PV, Barbosa AB, Targino VA, et al. Anatomical variations of the celiac trunk: a systematic review. Arq Bras Cir Dig. 2018; 31(4): e1403, doi: 10.1590/0102-672020180001e1403, indexed in Pubmed: 30539978.
33. Sheybanifar M. A variation of the inferior phrenic arteries: a case report. Hormozgan Med J. 2019; 23(3), doi: 10.5812/hmj.86605.
34. Shin SW, Do YS, Choo SW, et al. Diaphragmatic weakness after transcatheter arterial chemoembolization of inferior phrenic artery for treatment of hepatocellular carcinoma. Radiology. 2006; 241(2): 581–588, doi: 10.1148/radiol.2412051209, indexed in Pubmed: 17005772.
35. So YH, Chung JW, Yin Y, et al. The right inferior phrenic artery: origin and proximal anatomy on digital subtraction angiography and thin-section helical computed tomography. J Vasc Interv Radiol. 2009; 20(9): 1164–1171, doi: 10.1016/j.jvir.2009.05.036, indexed in Pubmed: 19631560.
36. Standring S, Ellis H, Healy J. et al. Gray's anatomy. The Anatomical Basis of Clinical Medicine. Elsevier Health Sciences, UK 2008.
37. Sureka B, Mittal MK, Mittal A, et al. Variations of celiac axis, common hepatic artery and its branches in 600 patients. Indian J Radiol Imaging. 2013; 23(3): 223–233, doi: 10.4103/0971-3026.120273, indexed in Pubmed: 24347852.
38. Takanami I. Massive haemoptysis due to chronic pancreatitis: control with inferior phrenic artery embolization. Eur J Cardio-Thoracic Surg. 2000; 18(1): 120–122, doi: 10.1016/s1010-7940(00)00468-1.
39. Tanaka R, Ibukuro K, Akita K. The left inferior phrenic artery arising from left hepatic artery or left gastric artery: radiological and anatomical correlation in clinical cases and cadaver dissection. Abdom Imaging. 2008; 33(3): 328–333, doi: 10.1007/s00261-007-9249-6, indexed in Pubmed: 17522754.
40. Winston CB, Lee NA, Jarnagin WR, et al. CT angiography for delineation of celiac and superior mesenteric artery variants in patients undergoing hepatobiliary and pancreatic surgery. Am J Roentgenol. 2007; 189(1): W13–W19, doi: 10.2214/AJR.04.1374, indexed in Pubmed: 17579128.
41. Zeng R, Yao Z, Chen Y, et al. Variant arterial supply to the lesser curvature of the stomach and duodenum from double inferior phrenic arteries. Surg Radiol Anat. 2015; 37(7): 867–869, doi: 10.1007/s00276-014-1392-5, indexed in Pubmed: 25380829.

VIA MEDICA

ORIGINAL ARTICLE

Folia Morphol.
Vol. 80, No. 3, pp. 575–582
DOI: 10.5603/FM.a2020.0098

ISSN 0015–5659
eISSN 1644–3284
journals.viamedica.pl

Morphometry of the aortic arch and its branches. A computed tomography angiography-based study

M. Tapia-Nañez[1], G.A. Landeros-Garcia[1], M.A. Sada-Treviño[2], R. Pinales-Razo[2], A. Quiroga-Garza[1], B.A. Fernandez-Rodarte[1], R.E. Elizondo-Omaña[1], S. Guzman-Lopez[1]

[1]Human Anatomy Department, School of Medicine, Universidad Autónoma de Nuevo León, Mexico
[2]Radiology and Diagnostic Imagining Department, University Hospital "Dr. José Eleuterio González", Universidad Autónoma de Nuevo León, Mexico

[Received: 27 May 2020; Accepted: 14 July 2020; Early publication date: 22 August 2020]

Background: The current study aims to determine the prevalence of variations of the aortic arch using computed tomography angiography (CTA), as well as morphometries and gender correlations.
Materials and methods: A retrospective, transverse, observational and descriptive study of 220 CTA was performed. The branching pattern, most cranial vertebral level of the aortic arch, area of the proximal, middle and distal segments of the arch, area of each branch, and the path of atypical arteries were recorded. Results were analysed and stratified by gender.
Results: The typical aortic arch branching pattern was present in 77.7% without statistical significance between genders. The most common variant was a two-branch pattern with a common trunk and a left subclavian (13.6%), followed by a typical branching pattern with an added left vertebral artery (7.3%). T3 was the most frequent cranial level (32.3%), followed by T2–T3 (26.8%), and T3–T4 (23.2%). The mean areas of the aortic arch were 685.5 ± 183.9, 476.1 ± 124.1, and 445.0 ± 145.1 mm² for the proximal, middle and distal segments, with statistical difference between men and women in the middle and distal segments. Three paths of atypical arteries were identified: bifurcated vertebral artery (0.5%), aberrant right subclavian artery (0.5%), and left subclavian ostium obstruction (0.5%).
Conclusions: Mexican population has one of the highest prevalence of variations in the aortic arch branching pattern. The high probability of finding these should be taken into consideration when assessing patients. A standardised classification method would contemplate future un-reported findings, without causing confusion by the different numbers assigned by each author. (Folia Morphol 2021; 80, 3: 575–582)

Key words: aortic arch, anatomical variants, branching pattern, Mexico

Address for correspondence: Dr. A. Quiroga-Garza, Departamento de Anatomía Humana, Facultad de Medicina, Universidad Autónoma de Nuevo León, Francisco I. Madero S/N, Mitras Centro, 64460 Monterrey, Nuevo León, México, tel: +52 81 8329 4171, e-mail: dr.aquirogag@gmail.com

INTRODUCTION

The aorta is the main arterial trunk in the human body. It originates as the ascending aorta and becomes the aortic arch, which begins anteriorly and ends posteriorly towards the left in the superior mediastinum, at the transverse thoracic plane (an imaginary plane drawn from the angle of Louis [joint between the manubrium and sternal body] to the mid-point between thoracic vertebrae IV–V) [16].

The aortic arch has a classic branching pattern originating from the superior margin, from right to left: brachiocephalic trunk (BT), left common carotid artery (LCC), and left subclavian artery (LS). This pattern is present in 65–80% of individuals [3, 13, 26].

The circulatory system is one of the first systems to be established in the embryo. The primary arterial arches develop from the arterial sac between the 6th and 8th weeks of intrauterine life. The 4th left arch will proceed to become the aortic arch, which will later undergo through exponential growth and join the dorsal aorta. This primary arterial system suffers many changes during its development, and that may constitute one of the causes for the many anatomical variations found in the blood vessels [13, 23].

Variations in the branches of the aortic arch have been described in different populations with a prevalence of up to 35% [16, 26]. These may repercuss during surgical procedures involving the superior mediastinum and neck, as well as in minimally invasive vascular procedures [2, 16, 25]. Some authors suggest a correlation between variations in the aortic arch and other pathologies such as intracranial aneurysms [22] and plates of atheroma at the level of its origin [28]. Patients with congenital heart disease have been linked to higher variability, presenting the normal 3-branch-pattern in only half (50.5%) of the cases [24].

Data regarding aortic arch branch variants are scarce in Latin American [19]. The aim of our study was to determine the prevalence of variants of the aortic arch using computed tomography angiography (CTA), as well as morphometries and gender correlations.

MATERIALS AND METHODS

A retrospective, transverse, comparative, observational study was performed. CTA studies were obtained from the database of the Radiology and Imaging Department at the University Hospital. All images were acquired using a 64-slice tomography (General Electric CT99 Light Speed VCT) Software 2978195VCT, with a rotation of 0.4 s helical acquisition, detector coverage of 20 mm, 400 mAs at 120 kV; thickness of cut of 0.625 mm, pitch of 0.53: 1 mm/rot, field of view of 22 to 33 cm.

Studies were included consecutively from adult patients (≥ 18 years old), without gender distinction, and adequate vascular anatomy visualisation. Those with technical errors that distorted the anatomy, had a history of thoracic surgery or vascular procedures, or alteration of the anatomy due to trauma or other pathologies were excluded.

Measurements were performed by an expert radiologist, with aid of an anatomist. Data obtained was transferred and analysed in a Work Station AW Volume Share2 workstation using multiplanar reformatting with maximum projection intensity and rendering volume. During the measurements, a window range of WW: 4000 and WL: 1000 was used in a standardised manner in all the subjects.

The number of arteries originating within the limits of the aortic arch and the branching pattern were classified according to Natsis et al. [17]. The most cranial vertebral level of the aortic arch was recorded, along with the luminal area of the aorta in the proximal, middle, and distal segments (using the transverse thoracic plane) (Fig. 1). For the proximal and distal segments, a line was drawn from the Louis angle (manubriosternal junction) to the midpoint between the inferior edge of T4 and the superior edge of T5 in a sagittal section of the CTA where the entire aortic arch was seen. The area of these segments was measured at the point where this line crossed respectively using the reconstructed transverse thoracic plane in three-dimensional (3D) for the luminal area (adjusting the plane to visualise a completely transverse view of the aortic arch). The cut-off point for the area in the middle segment was the most cranial vertebral level of the aortic arch where the reconstructed 3D plane was also adjusted to view the real area. The area of each branch (measured at its origin's height) originated in the arch of the aorta and the path of the atypical arteries originating in the arch of the aorta were also evaluated.

Statistical analysis

Sample size was previously calculated based on the variability reported in the literature. This resulted in a sample of 202 individuals with 95% confidence interval. A total of 220 CTA were included. Data were input into a database. The statistical analysis was car-

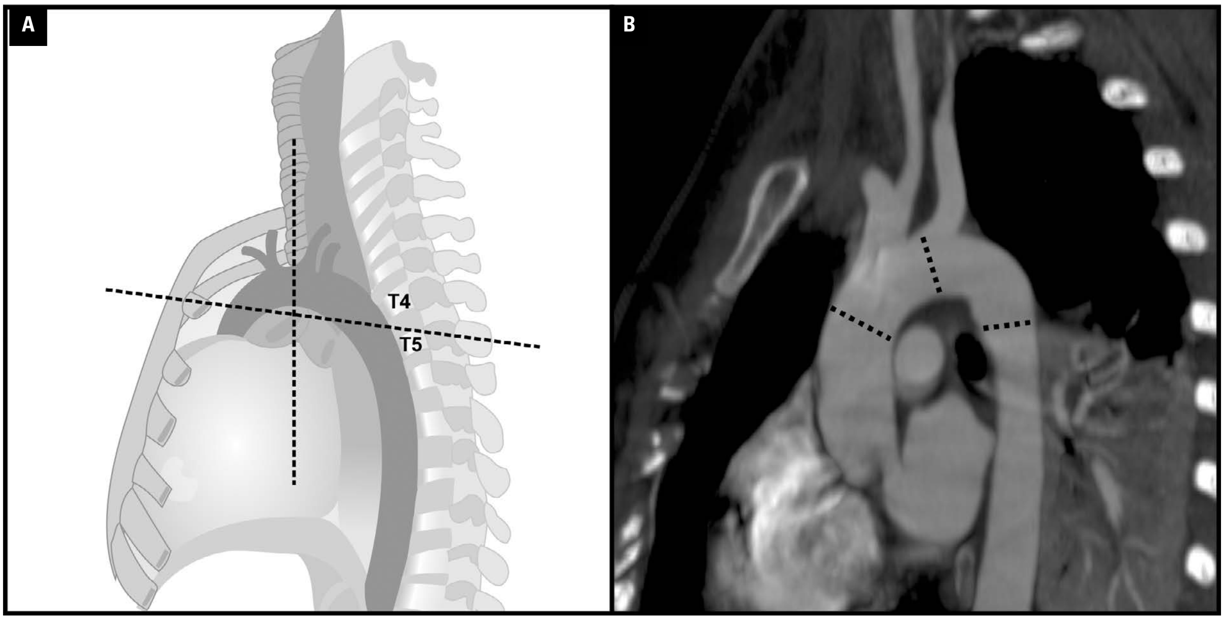

Figure 1. Thorax side view representation; **A.** Graphic representation of the transverse (Louis angle) and longitudinal (most cranial point of the aortic arch) planes used as the reference to mark the segment where the area of the aortic arch will be measured in its proximal, middle and distal segments; **B.** Louis angle plotted from the manubrial-sternal joint to the midpoint between the thoracic vertebrae T4 and T5. Cut lines in the proximal, middle and distal segment of the aortic arch in a computed tomography angiography (the inclination of the lines is due to the study adjustment for a correct visualisation of the vessel area).

ried out using the SPSS software version 20.0 (SPSS Inc., Chicago, IL) for Windows XP. Central tendency tests were performed (mean, standard deviation, frequency). Non-parametric tests with Mann-Whitney U were made to obtain the correlations between genders. Descriptive statistics and measures of central tendency for the prevalence of the evaluated variables were used.

Ethical approval

The study was previously reviewed and approved by the University's ethics and research committees with the registration number AH17-00007. The authors declare no financial or commercial gain for the realisation of this study. Also, the authors declare no conflict of interest. No patient was radiated for the purposes of this study.

RESULTS

A total of 220 CTA were included (114 men, and 106 women), with a mean age of 52.7 ± ± 17.6 years. The classic branching pattern (type 1) was the most prevalent (77.7%, n = 171). Anatomical variations were present in the remaining 22.3% (n = 49); 13.6% (n = 30) with a type 2 (common trunk [CT], left subclavian [LS]) and 7.3% (n = 16) with a type 3 (BT, LCC, left vertebral [LV], and a LS) aortic arch (Fig. 2). Individual cases of type 5 (n = 1, 0.5%) (right common carotid [RCC], LCC, LS, and aberrant right subclavian [ARS]), type 1 inversus (n = 1, 0.5%) (aortic arch to the right: right aortic arch [RAA], BT, LCC, and LS), and an unclassified type or as a proposed type 9 (n = 1, 0.5%) (CT, LS, and LV) were identified (Table 1). The most cranial vertebral level of the aortic arch was obtained using a plane parallel to the transverse thoracic plane (Fig. 1). The majority (82.3%) were between T2–T4 vertebral levels (Fig. 3), with the highest prevalence at T3 (32.3%) (Table 2). The mean areas of the proximal, middle and distal segments of the aortic arch were 685.5 ± 183.9, 476.1 ± 124.1, and 445.0 ± 145.1 mm^2, respectively. Statistical differences between men and women were found in the middle and distal segments (Table 3). There was no statistical difference in the areas according to the branching pattern (p = 0.27, p = 0.30, p = 0.56 for the proximal, middle, and distal segments, respectively). The morphological characteristics of the branches are shown in Table 4. Three paths of atypical arteries were found: bifurcated vertebral artery (n = 1, 0.5%), aberrant right subclavian artery

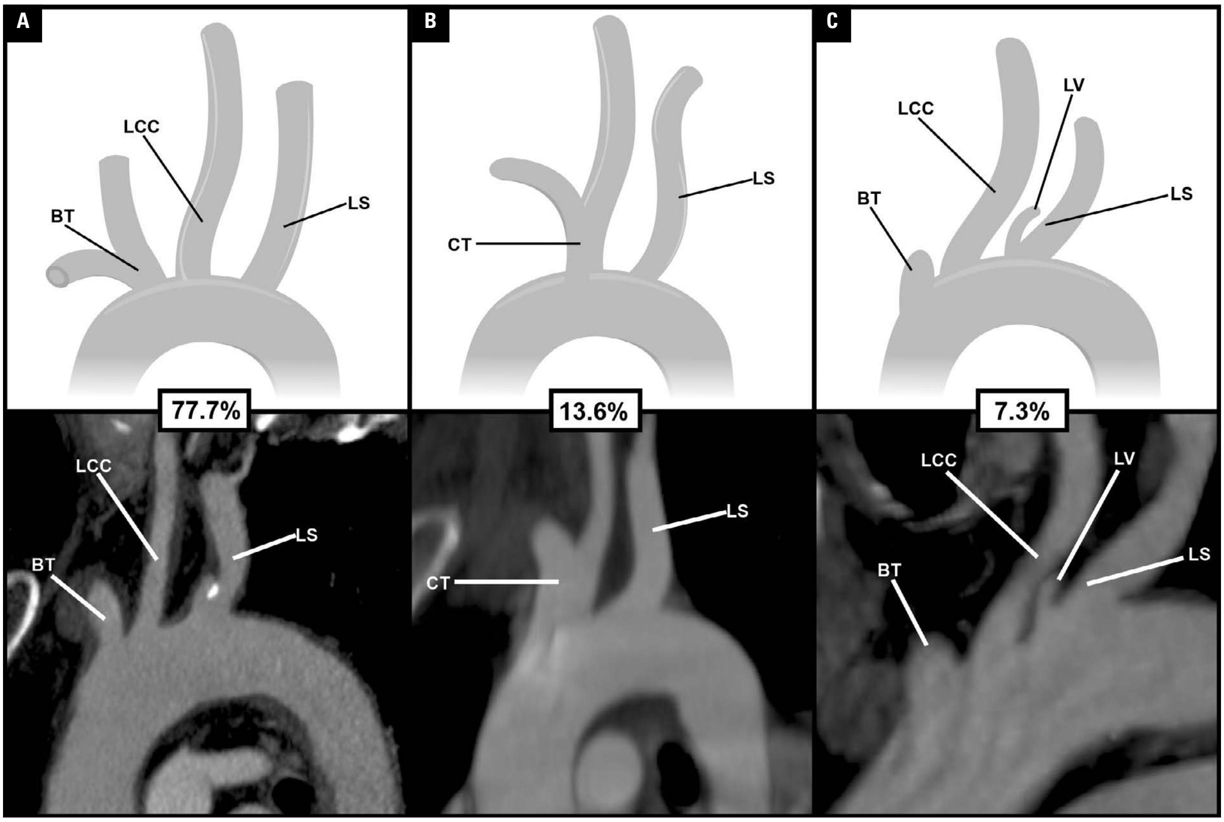

Figure 2. Three most common aortic branching patterns. Upper row demonstrates a graphic representation of the pattern; lower row is a computed tomography angiography slice to demonstrate all branches of the specific pattern; **A.** Classic branching pattern (type 1); **B.** Two--branch pattern (type 2); **C.** Four-branch patter (type 3); BT — brachiocephalic trunk; CT — common trunk; LCC — left common carotid; LS — left subclavian; LV — left vertebral.

Table 1. Branching pattern prevalence

Branching pattern	N (%)
BT, LCC, LS	171 (77.7%)
CT, LS	30 (13.6%)
BT, LCC, LV, LS	16 (7.3%)
RCC, LCC, LS, ARS	1 (0.5%)
RAA, BT, LCC, LS	1 (0.5%)
CT, LS, LV	1 (0.5%)
Total	220 (100%)

BT — brachiocephalic trunk; LCC — left common carotid; LS — left subclavian; CT — common trunk; LV — left vertebral; RCC — right common carotid; LV — left vertebral; ARS — aberrant right subclavian; RAA — right aortic arch; N — sample

(n = 1, 0.5%) and ostium obstruction left subclavian artery (n = 1, 0.5%).

DISCUSSION

The prevalence of classic aortic arch branching pattern in a Mexican population is similar to that reported in the literature, although anatomical variations were higher than most populations (Table 5) [3, 7, 11, 12, 16, 17, 21, 27]. There are only two other studies that include Latin populations, one performed with imaging in a Peruvian population [9] with similar results to our study. A cadaver-based Argentinian study focused on correlating variations to atheroma, concluding a common trunk had a higher incidence of atheroma plaques, therefore a possible increased risk of thromboembolism in clinical scenarios [28]. Three other studies carried out in Colombia, reporting anatomical variations of 25.71%, 28.7%, and 40.1% [8, 20, 21]. The latter with a similar prevalence to ours.

The importance of these variations extends not only to surgical procedures of the superior mediastinum, but also neck, as well as minimally invasive intravascular procedures [18]. For example, right trans-radial coronary angiogram becomes difficult to do satisfactorily with the presence of the right aberrant subclavian artery, increasing the time of the angiogram, increasing manipulation (therefore the risk of intramural hematomas), decreasing the success of the procedure (60%), and the number of catheters

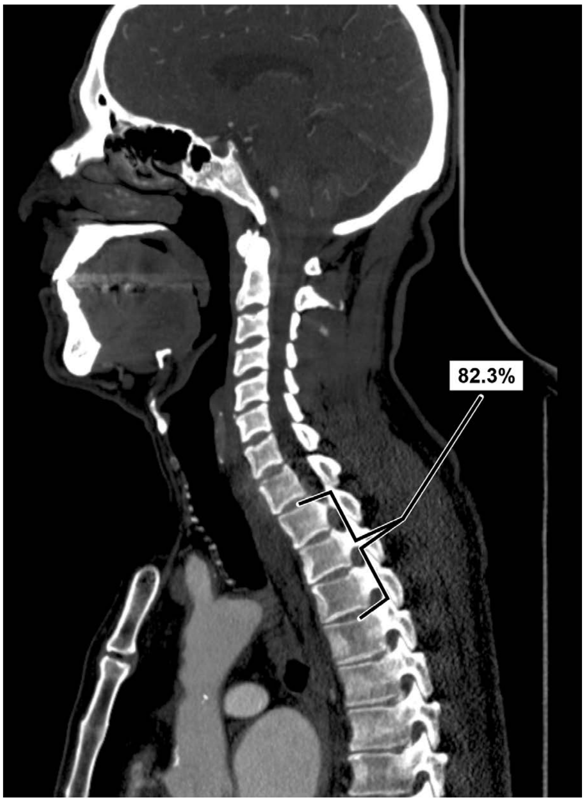

Figure 3. Most cranial level of the aortic arch. The bracket shows that 82.3% of the most cranial level of the aortic arch will be located in that area (T2–T4).

Table 2. Most cranial vertebral level of the superior border of the aortic arch

Vertebral level	Prevalence, n (%)
T1	1 (0.5%)
T1–T2	0 (0.0%)
T2	9 (4.1%)
T2–T3	59 (26.8%)
T3	71 (32.3%)
T3–T4	51 (23.2%)
T4	23 (10.5%)
T4–T5	6 (2.7%)

n — sample

needed [2, 10, 25]. These problems occur especially when the presence of this anatomical variant is unknown [2]. Identification of these may reduce the risk of complications such as haemorrhages [16]. Other studies suggest these anatomical variations may be related to other pathologies such as intracranial aneurysms, higher prevalence of thoracic aortic disease, of bicuspid aortic valve, and aortic arch pathology, although lower risk of arterial hypertension [6, 22]. It has been shown that patients with bovine arch pattern required medical attention at younger ages along with rapid disease progression and an increased need for surgical intervention, along with a higher prevalence of aortic aneurysm and dissections [13].

A two-branch (type 2, CT and LS) variation was the most common variation (13.6%), similar to most, but significantly lower than United States (24.6%), Colombia (27.9%) and Jordan (31.6%) [6, 16, 20]. This was followed by the four-branch pattern (type 3, BT, LCC, LV, and LS), which was one of the highest (7.3%), surpassed by India (8%, 15.3%) [4, 18] and Colombia (8.2%, 8.5%, 9.9%) [8, 20, 21] (Table 5).

A direct relationship between the branch's origin area and the branching pattern was evident in our results. The fewer the branches, the higher the area of origin in each, and vice versa (Table 4).

Using the classification proposed by Natsis et al. [17], types IV–VIII are rarely reported. In our study, one other variant of branching was identified. Great variation according to classification or nomenclature is shown in the literature of the aortic arch branch; each author reports a different classification or classifies the patterns according to their findings, generating confusion when referring to a specific pattern. This is the case with the Natsis type 2 branching pattern (BT, LS); other authors mention it as: type B, pattern C, bovine pattern and type IIA [1, 5, 6, 18]. In the case of the Natsis type 3 (BT, LCC, LS, LV), it has also been referred to as type D, type VI, and type 4 [14, 16, 26]. The Natsis type 5 (RCC, LCC, LS, ARS) has been identified as type F, pattern E, type D, type H, type 6b, and so on with all reported variants [1, 5, 12, 15, 16]. A standardisation of branching pattern classification is necessary to contemplate unclassified findings, easy understanding by the readers without having to memorize the types, and avoid confusion between studies, to better compare results in future evidence-based analysis.

Our study has several strengths. A previous sample size calculation was performed to assure significance of our findings. It includes morphological variations not previously described, such as the most cranial point of the aortic arch and its comparison with the vertebral level, although this was limited by the supine decubitus position of the patient during the study, and not taken in an anatomical position. No other study has reported this data. We also compared the prevalence of variations in Table 5. Due to

Table 3. Aortic arch areas compared between genders

	Mean	Men	Women	P
Proximal	685.5 ± 183.9	708.4 ± 198.4	660.9 ± 164.2	0.05
Middle	476.1 ± 124.1	493.3 ± 127.8	456.6 ± 117.6	0.02*
Distal	445.0 ± 145.1	466.5 ± 151.0	421.9 ± 135.4	0.02*

Values expressed in mm^2 (millimetres squared); *Statistically significant difference. T-test was used for independent samples, compared to gender. Values expressed in squared millimeters ± standard deviation. Statistically significant p value < 0.05.

Table 4. Morphological characteristics of the branches

	Areas, mean ± standard deviation [mm^2]							
	BT	LCC	LS	CT	LV	Aortic arch		
						Proximal	Medial	Distal
Overall (n = 220)	128.3 ± 47.8	58.0 ± 24.9	92.3 ± 27.6	399.5 ± 599.7	14.1 ± 6.7	685.5 ± 183.9	476.1 ± 124.1	445.0 ± 145.1
Type 1 (n = 171)	129.8 ± 48.3	58.6 ± 25.5	92.1 ± 27.4	DNR	DNR	675.1 ± 181.5	470.2 ± 120.2	440.9 (±147.3
Type 2 (n = 30)	DNR	DNR	109.3 ± 45.8	401.6 ± 609.9	DNR	733.8 ± 210.5	507.2 ± 138.0	468.5 ± 136.0
Type 3 (n = 16)	114.2 ± 42.6	50.2 ± 17.7	59.7 ± 28.1	DNR	13.2 ± 5.7	689.9 ± 162.7	463.4 ± 138.2	426.6 ± 143.1

Type 1 — three-branch pattern; Type 2 — two-branch pattern; Type 3 — four-branch pattern; BT — brachiocephalic trunk; LCC — left common carotid; LS — left subclavian; CT — common trunk; LV — left vertebral; DNR — data no reported

Table 5. Prevalence of anatomical variants in different populations

Author (country, year)	Study	Sample (n)	Type 1	Anatomical variations	Two-branch pattern	Four-branch pattern
Grande et al. (Portugal, 1995)	Cad	33	82%	18%	DNR	DNR
Natsis et al. (Greece, 2009)	DSA	633	83%	17%	15%	0.79%
Alsaif et al. (Saudi Arabia, 2010)	Cad	30	75%	25%	16.5%	5.5%
Jakanani et al. (UK, 2010)	CT	861	74%	26%	20%	6%
Müller et al. (Germany, 2011)	CTA	2033	86.7%	13.3%	8%	4.1%
Patil et al. (India, 2012)	Cad	75	77.3%	22.66%	14.66%	8%
Ortiz et al. (Colombia 2012)	Cad	122	71.3%	28.7%	17.2%	8.2%
Budhiraja, et al. (India, 2013)	Cad	52	36.5%	63.5%	19.2%	15.3%
Karacan et al. (Turkey, 2014)	CTA	1000	79.2%	20.8%	14.1%	4.1%
Lale et al. (Turkey, 2014)	CTA	881	87.4%	12.6%	7.2%	2.8%
Huapaya et al. (Peru 2015)	CTA	361	78.1%	21.9%	11.3%	2.2%
Dumfarth et al. (USA, 2015)	CT	556	66.5%	33.5%	24.6%	6.3%
Tapia et al. (China, 2015)	CT	525	76.68%	23.32%	11.8%	4.85%
Jalali et al. (Iran, 2016)	MRA	226	84.9%	15.1%	12.4%	0.9%
Mustafa et al. (Jordan, 2016)	CTA	500	61.2%	38.8%	31.6%	5%
Wang et al. (China, 2016)	CT	2370	83.8%	16.2%	10.24%	4.95%
Prada et al. (Colombia, 2016)	CTA	444	59.9%	40.1%	27.9%	9.9%
Rojas et al. (Colombia, 2017)	Cad	35	74.29%	25.71%	11.43%	8.57%
Tapia-Nañez et al. (Mexico, 2020)	CTA	220	77.7%	22.3%	13.6%	7.3%

Cad — cadaveric; CT — computed tomography; CTA — computed tomography angiography; MRA — magnetic resonance angiography; DSA — digital subtraction angiographies; DNR — data no reported the retrospective design of our study, findings were not correlated to the clinical history of patients. The presence of dyslipidaemia as well as atherosclerotic lesions can significantly affect the area of blood vessels. Measurements were performed by an expert radiologist and anatomist at the same time, without an interobserver index calculation. Although the sample was obtained from a large reference centre for the northeastern part of Mexico, it is not representative of all Mexican populations, due to the ethnical difference between regions in the country. Standardisation of branch classification has not been obtained, with differences between types, making result comparison difficult.

CONCLUSIONS

There is a high prevalence (22.3%) of anatomic variants in the aortic arch. We report a variant unclassified by Natsis et al. [17]. The luminal areas in the proximal, middle, and distal segments of the aortic arch are bigger in men than in women, with statistical difference in the middle and distal segments. Most (82.3%) aortic arches are within T2–T4 vertebral level. These should be taken into consideration when evaluating patients for vascular or mediastinal procedures.

Acknowledgements

Doctor Neri Alejandro Alvarez-Villalobos, Doctor Alejandro Diaz Gonzalez-Colmenero and Doctor Francisco J. Barrera-Flores of the Department of Statistics at the INVEST incubator of the Faculty of Medicine of the Universidad Autonoma de Nuevo Leon for their technical assistance in the realisation of this study.

Conflict of interest: None declared

REFERENCES

1. Acar M, Ulusoy M, Zararsiz I, et al. Anatomical variations in the branching of human aortic arch. Biomed Res India. 2013; 24(4): 531–535.
2. Allen D, Bews H, Vo M, et al. Arteria lusoria: an anomalous finding during right transradial coronary intervention. Case Rep Cardiol. 2016; 2016: 8079856, doi: 10.1155/2016/8079856, indexed in Pubmed: 27478652.
3. Alsaif H, Ramadan W. An anatomical study of the aortic arch variations. JKAU Med Sci. 2010; 17(2): 37–54, doi: 10.4197/med.17-2.4.
4. Budhiraja V, Rastogi R, Jain V, et al. Anatomical variations in the branching pattern of human aortic arch: a cadaveric study from central India. ISRN Anat. 2013; 2013: 828969, doi: 10.5402/2013/828969, indexed in Pubmed: 25938106.
5. De Garis CF, Black IH, Riemenschneider EA. Patterns of the aortic arch in american white and negro stocks, with comparative notes on certain other mammals. J Anat. 1933; 67(Pt 4): 599–619, indexed in Pubmed: 17104452.
6. Dumfarth J, Chou AS, Ziganshin BA, et al. Atypical aortic arch branching variants: A novel marker for thoracic aortic disease. J Thorac Cardiovasc Surg. 2015; 149(6): 1586–1592, doi: 10.1016/j.jtcvs.2015.02.019, indexed in Pubmed: 25802134.
7. Grande NR, Costa eS, Pereira AS, et al. Variations in the anatomical organization of the human aortic arch. A study in a Portuguese population. Bull Assoc Anat (Nancy). 1995; 79(244): 19–22.
8. Herrera Ortiz NE, Ballesteros Acuña LE, Forero Porras PL. Caracterizacion de las Ramas del Arco Aórtico en una Muestra de Poblacion Colombiana: Un Estudio con Material de Autopsia. Int J Morphol. 2012; 30(1): 49–55, doi: 10.4067/s0717-95022012000100008.
9. Huapaya JA, Chávez-Trujillo K, Trelles M, et al. Anatomic variations of the branches of the aortic arch in a Peruvian population. Medwave. 2015; 15(6): e6194, doi: 10.5867/medwave.2015.06.6194, indexed in Pubmed: 26248156.
10. Isser HS, Garg G. Arteria lusoria: A challenge for transradial coronary interventionist. IHJ Cardiovascular Case Reports (CVCR). 2020; 4(1): 7–9, doi: 10.1016/j.ihjccr.2020.04.003.
11. Jakanani GC, Adair W. Frequency of variations in aortic arch anatomy depicted on multidetector CT. Clin Radiol. 2010; 65(6): 481–487, doi: 10.1016/j.crad.2010.02.003, indexed in Pubmed: 20451016.
12. Jalali Kondori B, Asadi MH, Rahimian E, et al. Anatomical variations in aortic arch branching pattern. Arch Iran Med. 2016; 19(1): 72–74, doi: 0161901/AIM.0013, indexed in Pubmed: 26702752.
13. Kahn C, MacNeil M, Fanola C, et al. Complex arterial patterning in an anatomical donor. Transl Res Anat. 2018; 12: 11–19, doi: 10.1016/j.tria.2018.06.001.
14. Makhanya NZ, Mamogale RT, Khan N. Variants of the left aortic arch branches. S Afr J Radiol. 2004; 8(4): 10, doi: 10.4102/sajr.v8i4.102.
15. McDonald J, Anson B. Variations in the origin of arteries derived from the aortic arch, in American whites and negroes. Am J Phys Anthropol. 1940; 27(1): 91–107, doi: 10.1002/ajpa.1330270129.
16. Mustafa AG, Allouh MZ, Ghaida JH, et al. Branching patterns of the aortic arch: a computed tomography angiography-based study. Surg Radiol Anat. 2017; 39(3): 235–242, doi: 10.1007/s00276-016-1720-z, indexed in Pubmed: 27338939.
17. Natsis KI, Tsitouridis IA, Didagelos MV, et al. Anatomical variations in the branches of the human aortic arch in 633 angiographies: clinical significance and literature review. Surg Radiol Anat. 2009; 31(5): 319–323, doi: 10.1007/s00276-008-0442-2, indexed in Pubmed: 19034377.
18. Patil ST, Meshram MM, Kamdi NY, et al. Study on branching pattern of aortic arch in Indian. Anat Cell Biol. 2012; 45(3): 203–206, doi: 10.5115/acb.2012.45.3.203, indexed in Pubmed: 23094209.
19. Popieluszko P, Henry BM, Sanna B, et al. A systematic review and meta-analysis of variations in branching patterns of the adult aortic arch. J Vasc Surg. 2018; 68(1): 298–306.e10, doi: 10.1016/j.jvs.2017.06.097, indexed in Pubmed: 28865978.

20. Prada G, Granados AM, Calle JS, et al. Anatomic variations of the aortic arch depicted on 444 CT angiographies. Eur J Anat. 2016; 20(2): 137–141.
21. Rojas M, Muete W, Quijano Y. Anatomical variations of the aortic arch in a sample of Colombian population. Revista de la Facultad de Medicina. 2017; 65(1): 49–54, doi: 10.15446/revfacmed.v65n1.56046.
22. Shiva Kumar GL, Pamidi N, Somayaji SN, et al. Anomalous branching pattern of the aortic arch and its clinical applications. Singapore Med J. 2010; 51(11): e182–e183, indexed in Pubmed: 21140104.
23. St Gielecki J, Wilk R, Syc B. Digital-image analysis of the aortic arch's development and its variations. Folia Morphol. 2004; 63: 449–454, indexed in Pubmed: 15712142.
24. Tawfik AM, Sobh DM, Ashamallah GA, et al. Prevalence and types of aortic arch variants and anomalies in congenital heart diseases. Acad Radiol. 2019; 26(7): 930–936, doi: 10.1016/j.acra.2018.08.023, indexed in Pubmed: 30266547.
25. Valsecchi O, Vassileva A, Musumeci G, et al. Failure of transradial approach during coronary interventions: anatomic considerations. Catheter Cardiovasc Interv. 2006; 67(6): 870–878, doi: 10.1002/ccd.20732, indexed in Pubmed: 16649233.
26. Vučurević G, Marinković S, Puškaš L, et al. Anatomy and radiology of the variations of aortic arch branches in 1,266 patients. Folia Morphol. 2013; 72(2): 113–122, doi: 10.5603/fm.2013.0019, indexed in Pubmed: 23740497.
27. Wang L, Zhang J, Xin S. Morphologic features of the aortic arch and its branches in the adult Chinese population. J Vasc Surg. 2016; 64(6): 1602–1608.e1, doi: 10.1016/j.jvs.2016.05.092, indexed in Pubmed: 27590535.
28. Yeri L, Gómez J, Fontaneto S, et al. Variation of the origin of aortic arch branches: in relationship with plates of atheroma. Int J Morphol. 2011; 29(1): 182–186, doi: 10.4067/s0717-95022011000100031.

VIA MEDICA

ORIGINAL ARTICLE

Folia Morphol.
Vol. 80, No. 3, pp. 583–589
DOI: 10.5603/FM.a2020.0100
Copyright © 2021 Via Medica
ISSN 0015–5659
eISSN 1644–3284
journals.viamedica.pl

Which morphological abnormalities better define the elongation of transverse aortic arch: a magnetic resonance angiography study

H. Yiğit, E. Ergün, P.N. Koşar

Department of Radiology, University of Health Sciences, Faculty of Medicine, Ankara Health Practice and Research Centre, Ankara, Turkey

[Received: 19 June 2020; Accepted: 13 August 2020; Early publication date: 22 August 2020]

Background: *The aim of the study is to investigate the relation between morphological abnormalities that might indicate elongation of transverse aortic arch (ETA) and various aortic and thoracic measurements, and to determine which morphological criteria define the elongated transverse arch better.*

Materials and methods: *Patients under 40 years of age who underwent contrast enhanced thoracic magnetic resonance angiography were included in the study. Images were evaluated for the presence of morphological arch abnormalities such as late take off (LTO) of left subclavian artery (LSA), flattening of the arch, and kinking at the posterior or anterior contour of the lesser curvature. Various aortic and thoracic measurements, including the distance between the orifices of the left common carotid artery (LCCA) and LSA, were made. Statistical relation between morphological abnormalities and these measurements was analysed. The effect of morphological abnormalities and their combinations on the distance between LCCA and LSA orifices was evaluated by linear regression analysis.*

Results: *Ninety three cases were included in the study. All morphological abnormalities and most of their combinations show statistically significant relation with longer LCCA to LSA distance. The parameters that most affected this distance were combination of flattening with LTO of LSA, anterior kinking and combination of anterior kinking with both flattening and LTO, respectively.*

Conclusions: *Our study showed that the finding which best defines ETA is the combination of LTO and arch flattening. Therefore, we recommend using this combination in the diagnosis of ETA instead of the classical diagnostic criteria including combination of LTO and posterior kinking.* (Folia Morphol 2021; 80, 3: 583–589)

Key words: elongation of transverse aortic arch, cardiovascular abnormalities, anatomy, magnetic resonance angiography

INTRODUCTION

Elongation of transverse aortic arch (ETA) was first defined by Ho et al. [6]. It is the most common aortic abnormality seen in Turner syndrome with the reported frequency of 37–49%, and it is more common in adults than in younger patients [1, 4, 5, 7, 12]. ETA is not specific to Turner syndrome and can be seen in 1.1% of the population without Turner syndrome [3, 11].

Address for correspondence: H. Yiğit, MD, Associate Professor of Radiology Ankara Health Practice and Research Centre, Department of Radiology, Hacettepe Mh. Ulucanlar Cd. No: 89, TR-06280, Altındağ, Ankara, Turkey, tel; +903125953785, fax: +903123626400, e-mail: hasan.yigit@sbu.edu.tr; hayigit@hotmail.com

Ho et al. [6] defined typical characteristics of ETA as the increase in the distance between the origins of left common carotid artery (LCCA) and left subclavian artery (LSA) with flattening of transverse arch and kinking along its lesser curvature. Although their definition emphasis on the increase in the distance between the origins of LCCA and LSA it is not based on a study that directly measures this distance. Their definition of ETA included two morphological criteria: origin of LSA at a level posterior to the trachea on axial images and indentation or convex kinking in the inferior aortic contour along the course of the lesser curvature [6]. In their study and in others related to ETA, the definition of convex kinking points to the angulation in the posterior contour of the aortic arch, also known as aortic isthmus. This anomaly which is also named as "box-shaped" appearance may be associated with angulation in the anterior contour of the arch in addition to the posterior contour; however, kinking in the lesser curvature is defined as posterior kinking in the isthmic region [7]. Although Ho et al. [6] described flattening of the arch as a typical feature of ETA, they didn't add it to the two morphological criteria that they specified for the diagnosis of ETA. Similarly, except Ece et al.'s study [3], it is not clear whether flattening of the arch is used as a criterion of ETA by other studies conducted in the following years.

Mortensen et al. [8] investigated the relation between ETA and the distances between the origins of the arch branches. To the best of our knowledge their study is the only one investigating the relation between ETA and aortic measurements. In the present study we investigated the relation between each aortic morphological abnormality (and combinations of them) that may indicate ETA and various aortic measurements and thoracic diameters and we aimed to determine which morphological criteria define the elongated transverse arch better.

MATERIALS AND METHODS

The study was performed retrospectively and was approved by the institutional review board (approval number 4322). Patients under the age of 40 who underwent contrast enhanced thoracic magnetic resonance (MR) angiography between 2009 and 2019 were retrieved from picture archiving and communication system and reassessed. Informed consent was obtained from all patients prior to MR imaging.

Two 1.5 tesla MR imaging systems (Signa HDi, GE Healthcare, Milwaukee, WI, USA) with 8 channel phased array torso surface coil and (Magnetom Aera, Siemens AG, Erlangen, Germany) 18 channel phased array torso surface coil were used. MR angiography examinations were performed as three-dimensional (3D) contrast enhanced angiography or four-dimensional (4D) high temporal resolution contrast enhanced MR angiography (TRICKS, time-resolved imaging of contrast kinetics or TWIST, time-resolved angiography with interleaved stochastic trajectories). Gadolinium based contrast agent was administered with a 0.1–0.2 mmol/kg dose at a rate of 1.8 mL/s via automatic injector which was followed by 20 mL of saline with the same injection protocol. For optimal scan timing automatic triggering or fluoroscopic triggering was used in 3D contrast enhanced MR angiography. High resolution angiography images were obtained as 10–19 temporal phases.

The inclusion criteria for the study cases were being under 40 years of age and having contrast-enhanced MR angiography examination with diagnostic image quality. Patients under the age of 40 were included to avoid the effect of atherosclerotic changes on the accurate diagnosis of ETA. The main exclusion criterion was having aortic abnormalities such as interrupted aortic arch, double aortic arch etc. that could significantly change the arch morphology and prevent the evaluation of ETA. Data corrected according to body surface area (BSA) were used therefore patients whose BSA could not be calculated due to lack of height and/or weight information were excluded from the study. The cases with insufficient image quality were also excluded.

The image analysis was performed by a radiologist that has 11 years of experience in cardiovascular imaging. In contrast enhanced MR angiography both maximum intensity projection and volume rendering images were evaluated for the presence of morphological abnormalities that might indicate ETA. Origin of LSA at a level posterior to the trachea on axial images (late take off sign: LTO), flattening of the arch (loss of typical upward convexity of the arch), kinking at the posterior or anterior contours of the lesser curvature of the aortic arch were the abnormalities searched for (Fig. 1). Then aortic measurements, including the distance between the orifices of LCCA and LSA, maximum distance between ascending and descending aorta at a level caudal to the aortic arch and ascending and descending aorta diameters at the level of pulmonary trunk, were made. Antero-posterior, right-left and supero-inferior diameters of thoracic cavity were

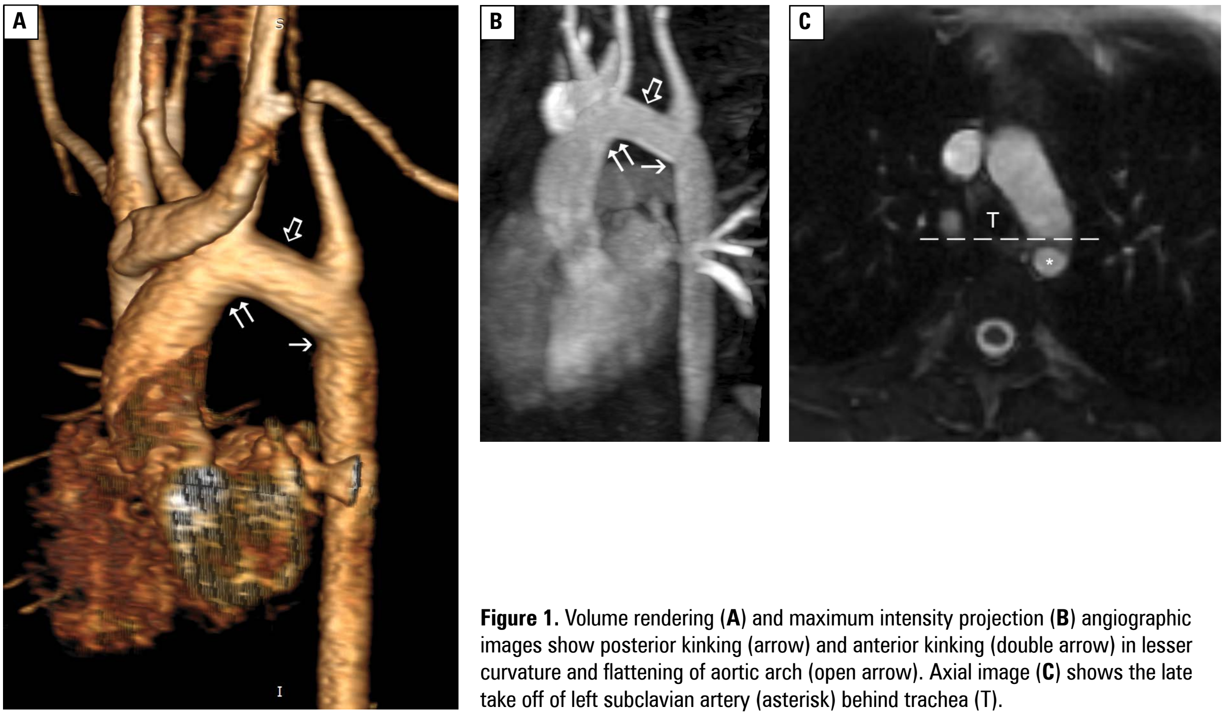

Figure 1. Volume rendering (**A**) and maximum intensity projection (**B**) angiographic images show posterior kinking (arrow) and anterior kinking (double arrow) in lesser curvature and flattening of aortic arch (open arrow). Axial image (**C**) shows the late take off of left subclavian artery (asterisk) behind trachea (T).

measured on three plane localizer images. All measurements were corrected according to BSA and this corrected data was used in statistical analysis. Mosteller formula taking into account the height and weight was used to calculate the BSA [9].

Statistical analysis

Student t test and Mann-Whitney U test were used to evaluate the relation between morphological abnormalities that indicate ETA (and their double, triple, or quadruple combinations) and aortic and thoracic measurements. We used Student t test for normally distributed variables and Mann-Whitney U test for the variables without normal distribution. Linear regression analysis of the morphological abnormalities (or their combinations) that are associated with statistically significant lengthening of the distance between LCCA and LSA orifices was performed to determine the abnormalities that most affected this distance. Statistical analysis was performed with SPSS Statistics for Windows, version 22 (IBM Corp., Armonk, NY, USA).

RESULTS

One hundred forty-nine patients under the age of 40 who underwent thoracic aorta MR angiography were retrieved from picture archiving and communication system. Among them those who didn't have height and weight records and those who had abnormalities that significantly changed the aortic morphology and may prevent its evaluation for ETA were excluded from the study. The abnormalities found in the excluded group was as follows: double outlet right ventricle, aortopulmonary window, transposition of great arteries, coarctation or pseudocoarctation of the aorta, interrupted aortic arch, aortic aneurysm, aberrant right subclavian artery, pulmonary atresia, aortic hypoplasia, double aortic arch, aortic dissection, right sided aortic arch.

Ninety-three cases, 68 (73.1%) female and 25 (26.9%) male, aged 2–39 years were included in the study. Mean age was 17.18 ± 6.88 and median age was 16. Forty-five (48.4%) cases had Turner syndrome and 24 (25.8%) had surgically corrected tetralogy of Fallot. Thirteen (14%) cases had congenital anomalies that wouldn't interfere with the evaluation of ETA. These were situs inversus totalis, pulmonary stenosis, persistent left superior vena cava, partial anomalous pulmonary venous return, hypoplastic right ventricle, Ebstein anomaly and bicuspid aortic valve. Remaining 11 (11.8%) cases didn't have a congenital anomaly or an aortic abnormality.

The frequencies of morphological findings that indicate ETA are shown in Table 1. In Tables 2 and 3, results of the statistical analysis evaluating the relation between morphological findings of ETA with aortic measurements and thoracic diameters are given along with p values. $P < 0.05$ was considered as statistically significant. All measurements that had significant correlation with the morphologic findings were larger in those that had these morphologic findings.

When LTO or flattening or posterior kinking or any combination of them were present, the distance between LCCA and LSA was significantly longer ($p < 0.05$). In addition, there was significant association between each of these findings or any combination of them and ascending and/or descending aorta diameters ($p < 0.05$). Except posterior kinking, these morphological findings or any combination of them had significant association with one or more thoracic measurements. With anterior kinking or its combination with flattening and/or LTO, both the distance between LCCA and LSA and all thoracic diameters were significantly longer ($p < 0.05$). Some of the morphological findings were also significantly associated with the increase in the distance between ascending and descending aorta. They are also shown in Table 2.

According to multivariate linear regression analysis the parameters that most affected the distance between LCCA and LSA were a combination of flattening with LTO, anterior kinking and a combination of anterior kinking with both flattening and LTO, respectively [$F(3, 89) = 21.81$, $p = 0.00$, adjusted $R^2 = 0.40$].

Table 1. Morphological findings sorted according to frequency

Morphologic findings	Total (per cent)
PK	42 (45.2%)
LTO	39 (41.9%)
Flat.	33 (35.5%)
Flat. + LTO	23 (24.7%)
Flat. + PK	23 (24.7%)
PK + LTO	21 (22.6%)
LTO + Flat. + PK	17 (18.3%)
AK	12 (12.9%)
AK + LTO	8 (8.6%)
Flat. + AK	6 (6.5%)
PK + AK	6 (6.5%)
LTO + Flat. + AK	5 (5.4%)
Flat. + PK + AK	4 (4.3%)
LTO + PK + AK	3 (3.2%)
LTO + Flat. + PK + AK	3 (3.2%)

PK — posterior kinking; LTO — late take off; Flat. — flattening; AK — anterior kinking

DISCUSSION

To the best of our knowledge this is the first study that investigates the relation between each component of ETA (and their combinations) and thoracic diameters and various aortic measurements, including the distance between LCCA and LSA. This study also

Table 2. P values for the relation between morphological findings and measurements

Variables	LCCA to LSA distance	AA to DA distance	Thorax AP diameter	Thorax RL diameter	Thorax SI diameter	AA diameter	DA diameter
LTO	0.000*	0.196	0.057	0.029*	0.173	0.034*	0.079
Flat.	0.000*	0.037*	0.005*	0.036*	0.079	0.004*	0.005*
PK	0.025*	0.299	0.218	0.228	0.695	0.051	0.001*
AK	0.008*	0.663	0.035*	0.008*	0.036*	0.701	0.292
Flat. + LTO	0.000*	0.115	0.002*	0.004*	0.025*	0.001*	0.015*
PK + LTO	0.000*	0.009*	0.025*	0.024*	0.147	0.009*	0.012*
Flat. + PK	0.000*	0.029*	0.030*	0.049*	0.328	0.005*	0.007*
Flat. + AK	0.012*	0.373	0.047*	0.006*	0.033*	0.254	0.107
AK + LTO	0.009*	0.373	0.015*	0.002*	0.016*	0.480	0.150
PK + AK	0.133	0.975	0.200	0.122	0.326	0.467	0.164
LTO + Flat. + PK	0.000*	0.029*	0.003*	0.004*	0.037*	0.010*	0.006*
LTO + Flat. + AK	0.023*	0.283	0.046*	0.007*	0.012*	0.201	0.066
LTO + PK + AK	0.215	0232	0.134	0.050	0.263	0.373	0.170
Flat. + PK + AK	0.107	0.353	0.135	0.043*	0.440	0.443	0.256
LTO + Flat. + PK + AK	0.215	0.232	0.134	0.050	0.263	0.355	0.158

*Statistically significant relation; LCCA — left common carotid artery; LSA — left subclavian artery; AP — antero-posterior; RL — right-left; SI — supero-inferior; AA — ascending aorta; DA — descending aorta; PK — posterior kinking; LTO — late take off; Flat. — flattening; AK — anterior kinking

Table 3. Relation between morphological findings and left common carotid artery (LCCA) to left subclavian artery (LSA) distance measurements

Variables	LCCA to LSA distance [mm/m²] (mean ± standard deviation)		
	Positive	Negative	P
LTO	10.83 ± 5.69	6.62 ± 3.27	0.000*
Flat.	11.99 ± 4.88	6.41 ± 3.62	0.000*
PK	9.61 ± 5.39	7.38 ± 4.23	0.025*
AK	11.39 ± 4.06	7.94 ± 4.87	0.008*
Flat. + LTO	13.58 ± 4.90	6.68 ± 3.51	0.000*
PK + LTO	12.24 ± 5.63	7.26 ± 4.05	0.000*
Flat. + PK	11.99 ± 5.38	7.20 ± 4.11	0.000*
Flat. + AK	12.72 ± 3.52	8.09 ± 4.84	0.012*
AK + LTO	12.58 ± 4.26	7.99 ± 4.78	0.009*
PK + AK	10.08 ± 2.93	8.27 ± 4.99	0.133
LTO + Flat. + PK	13.41 ± 5.45	7.26 ± 3.99	0.000*
LTO + Flat. + AK	12.88 ± 3.91	8.13 ± 4.83	0.023*
LTO + PK + AK	10.65 ± 3.40	8.31 ± 4.93	0.215
Flat. + PK + AK	10.97 ± 2.85	8.27 ± 4.94	0.107
LTO + Flat. + PK + AK	10.65 ± 3.40	8.31 ± 4.93	0.215

*Statistically significant relation; PK — posterior kinking; LTO — late take off; Flat. — flattening; AK — anterior kinking

evaluates the anterior kinking of aortic arch which wasn't mentioned in the previous studies.

Ho et al. [6] hypothesized that there may be a disproportion between thoracic cage and great vessel development and this may be the cause of great vessel abnormalities in Turner syndrome; however, contrary to what they expected, they found several thoracic cavity dimensions corrected according to BSA to be higher in these patients when compared to the control group [6]. Their study demonstrated a significant association only between thoracic antero-posterior diameter and ETA; however, in our study we found statistically significant relation between morphological findings that classically define ETA (flattening is included or not) and all thoracic diameters. In addition, we observed a significant association between one or more thoracic diameters and each component of ETA mentioned in its definition by the present study. Anterior kinking, which was first defined by our study, and its combination with flattening and/or LTO were also found to be significantly associated with thoracic diameters. We also found an association between some of the findings of ETA (and their combinations) and the increase in distance between ascending and descending aorta.

Mortensen et al. [8] investigated the relation between ETA and the distance between LCCA and LSA and between innominate artery and LSA in adult Turner syndrome patients. They accepted a combination of posterior kinking and LTO as the diagnostic criteria of ETA. These distances which were not corrected according to BSA were found to be significantly higher in ETA patients when compared to the ones without ETA. Except ours this is the first and the only study which shows that the combination of posterior kinking and LTO indicate a transverse arch that is really elongated. In our study, in which morphological findings were detailed and each morphological finding and their various combinations were investigated separately, each morphological finding that might indicate ETA and most of their double or triple combinations were found to be associated with the increase in the distance between LCCA and LSA. Multiple regression analysis showed that a combination of LTO and flattening had the greatest association with the increase in this distance. Interestingly, posterior kinking and associated combinations which are among the diagnostic criteria of ETA had lesser association with this distance. Instead of posterior kinking, anterior kinking and its combination with flattening and LTO had greater association with the increase in distance between LCCA and LSA. However, in our study group anterior kinking was much less common than the other three main findings, and this may have affected the results of the statistical analysis of anterior kinking and related combinations. Since the combination of LTO and flattening has the greatest association with the increase in the distance between LCCA and LSA, we think that the combination of LTO and flattening should be evaluated instead of the combination of posterior kinking and LTO when investigating ETA.

In the present study we also evaluated the relation between aortic measurements and morphological findings of ETA. Morphological findings and most of their combinations were significantly associated with increased ascending and descending aortic diameters. In the previous studies conducted on patients with Turner syndrome association of ETA with aortic dilatation has been mentioned; however, those studies do not directly evaluate the relation between ETA and aortic diameters [5]. In line with our study, Mortensen et al. [8] reported significant association between the diameter of descending aorta and ETA; however, they didn't use aortic measurements that were corrected according to BSA. They reported that the distance between innominate artery and LSA showed a positive correlation with ascending and descending aorta diameters in adult patients with Turner syndrome, but this correlation was not observed in the control group. In Kim et al.'s study [7] the diameter of aortic sinus and descending aorta were found to be higher in patients with ETA; however, they didn't find a relation between standardised Z-scores of aortic diameters and ETA [7]. Although we did not include patients with aortic aneurysms in our study group, it should be taken into consideration that in our heterogeneous study group there may be different factors affecting aortic diameters which may hinder the evaluation of the relationship between aortic diameters and presence of ETA.

The clinical significance of ETA which is the most frequent aortic abnormality observed in Turner syndrome is controversial. It is thought that the presence of ETA alone does not have a clinical significance but may be an indicator for an abnormal wall structure prone to dilatation and maybe dissection [1, 5]. The studies investigating the effects of aortic abnormalities on blood flow revealed changes in flow characteristics of the arch in patients with ETA [2, 10]. Systolic and diastolic blood pressures in patients with ETA are also reported to be significantly higher when compared to the ones without ETA [6].

Limitations of the study

The present study has some limitations. First, morphological findings, especially flattening of the arch, were determined based on a subjective assessment. Second, evaluation was performed by only one observer; therefore, interobserver variability was not calculated. Third, majority of paediatric and young adult patients who underwent thoracic MR angiography at our centre had Turner syndrome, hence the frequency of morphological abnormalities in the aortic arch cannot be adapted to the general population. However, being frequency of ETA high in the present study population enabled us to evaluate the morphological findings indicating ETA in detail. Although our study group has cases with normal MR angiography findings, it is a limitation that we do not have a control group consisting entirely of healthy volunteers. There may be unpredictable factors that may affect aortic and thoracic diameters in these patients even if they didn't have ETA or morphological findings indicating ETA.

CONCLUSIONS

Although classical diagnostic criteria of ETA include LTO of LSA and kinking at the posterior contour of aortic arch, our study showed that the finding which has the greatest association with ETA is the combination of LTO and arch flattening. Posterior kinking and associated combinations are associated with the increase in distance between LCCA and LSA less than anterior kinking and associated combinations. Therefore, we recommend using the combination of LTO and arch flattening in the diagnosis of ETA instead of the classical diagnostic criteria including the combination of LTO and posterior kinking.

Conflict of interest: None declared

REFERENCES

1. Bondy CA. Turner Syndrome Study Group. Care of girls and women with Turner syndrome: a guideline of the Turner Syndrome Study Group. J Clin Endocrinol Metab. 2007; 92(1): 10–25, doi: 10.1210/jc.2006-1374, indexed in Pubmed: 17047017.
2. Chen J, Gutmark E, Mylavarapu G, et al. Numerical investigation of mass transport through patient-specific deformed aortae. J Biomech. 2014; 47(2): 544–552, doi: 10.1016/j.jbiomech.2013.10.031, indexed in Pubmed: 24210472.
3. Ece B, Yiğit H, Ergün E, et al. Elongated transverse aortic arch in subjects without turner syndrome: A preliminary comput-

ed tomography study. Clin Anat. 2018; 31(6): 887–890, doi: 10.1002/ca.23209, indexed in Pubmed: 29770485.
4. Granger A, Zurada A, Zurada-Zielińska A, et al. Anatomy of turner syndrome. Clin Anat. 2016; 29(5): 638–642, doi: 10.1002/ca.22727, indexed in Pubmed: 27087450.
5. Gutmark-Little I, Backeljauw PF, Gutmark-Little I, et al. Partial anomalous pulmonary venous return is common in Turner syndrome. J Pediatr Endocrinol Metab. 2012; 25(5-6): 435–440, doi: 10.1515/jpem-2012-0046, indexed in Pubmed: 22876535.
6. Ho VB, Bakalov VK, Cooley M, et al. Major vascular anomalies in Turner syndrome: prevalence and magnetic resonance angiographic features. Circulation. 2004; 110(12): 1694–1700, doi: 10.1161/01.CIR.0000142290.35842.B0, indexed in Pubmed: 15353492.
7. Kim HK, Gottliebson W, Hor K, et al. Cardiovascular anomalies in Turner syndrome: spectrum, prevalence, and cardiac MRI findings in a pediatric and young adult population. Am J Roentgenol. 2011; 196(2): 454–460, doi: 10.2214/AJR.10.4973, indexed in Pubmed: 21257900.
8. Mortensen KH, Hjerrild BE, Andersen NH, et al. Abnormalities of the major intrathoracic arteries in Turner syndrome as revealed by magnetic resonance imaging. Cardiol Young. 2010; 20(2): 191–200, doi: 10.1017/S1047951110000041, indexed in Pubmed: 20307329.
9. Mosteller RD. Simplified calculation of body-surface area. N Engl J Med. 1987; 317(17): 1098, doi: 10.1056/NEJM198710223171717, indexed in Pubmed: 3657876.
10. Prahl Wittberg L, van Wyk S, Fuchs L, et al. Effects of aortic irregularities on blood flow. Biomech Model Mechanobiol. 2016; 15(2): 345–360, doi: 10.1007/s10237-015-0692-y, indexed in Pubmed: 26104133.
11. Yiğit H, Ergün E. Elongation of transverse aortic arch; not specific for Turner Syndrome. Clin Anat. 2017; 30(5): 555–556, doi: 10.1002/ca.22816, indexed in Pubmed: 27935115.
12. Yiğit H, Önder A, Özgür S, et al. Cardiac MRI and 3D contrast-enhanced MR angiography in pediatric and young adult patients with Turner syndrome. Turk J Med Sci. 2017; 47(1): 127–133, doi: 10.3906/sag-1511-3, indexed in Pubmed: 28263479.

VIA MEDICA

ORIGINAL ARTICLE

Folia Morphol.
Vol. 80, No. 3, pp. 590–595
DOI: 10.5603/FM.a2020.0080

ISSN 0015–5659
eISSN 1644–3284
journals.viamedica.pl

Relationship of vascular variations with liver remnant volume in living liver transplant donors

B. Yılmaz Çankaya[1], G. Polat[1], N. Aksungur[2], A. Yalçın[3], E. Korkut[2], R. Sade[1], R.B. Pirimoğlu[1], S. Kara[2], M. Ay[1], N. Altuntaş[2], F. Alper[1]

[1]*Department of Radiology, Atatürk University School of Medicine, Erzurum, Turkey*
[2]*Department of General Surgery, Atatürk University School of Medicine, Erzurum, Turkey*
[3]*Department of Radiology, Binali Yıldırım University Mengücek Gazi Training and Research Hospital, Erzincan, Turkey*

[Received: 9 June 2020; Accepted: 19 June 2020; Early publication date: 29 July 2020]

Background: In this study, we investigated the relationship between the portal vein and hepatic artery variations and the remaining liver volume in living donors in liver transplantation.

Materials and methods: In the study, triphasic abdominal computed tomography images of 180 live liver donor candidates were analysed retrospectively. Portal veins were divided into four groups according to the Nakamura classification and seven groups according to the Michels classification. The relationship between vascular variations and remnant liver volume was compared statistically.

Results: According to the Nakamura classification, there were 143 (79.4%) type A, 23 (12.7%) type B, 7 (3.9%) type C and 7 (3.9%) type D cases. Using the Michels classification, 129 (71%) type 1, 12 (6.7%) type 2, 24 (13%) type 3, 2 (2.2%) type 4, 10 (5.6%) type 5, 1 (0.6%) type 6, and 2 (1.1%) type 7 cases were detected. There was no significant difference in the percentage of the remaining volume of the left liver lobe between the groups (p = 0.055, p = 0.207, respectively).

Conclusions: Variations in the hepatic artery and portal vein do not affect the remaining liver volume in liver transplantation donors. (Folia Morphol 2021; 80, 3: 590–595)

Key words: portal vein, hepatic artery, anatomic variations, liver remnant volume, liver transplantation, living donor

INTRODUCTION

An accurate evaluation of potential living donors before liver transplantation is important in preventing postoperative liver failure [19]. There are many factors related to donor safety, such as obesity, age, liver volume, fatty liver, medical problems, anatomical variations, surgical process, and operative procedures [20]. The correct assessment of liver vascularity and volume is very important for both the donor and the recipient [15, 19]. Post-transplantation liver failure has been reported in the right lobe donors at around 10% [15]. On the other hand, the low liver volume of the recipient is an important problem that affects the recovery rate [8, 15]. Triphasic abdominal computed tomography (CT) imaging has minimised errors in vascular and volume assessment [15]. The determination of vascular variations is essential for the operative procedure because they can affect decisions regarding the resection line or the use of grafts [20, 22] A minimum of 30% of liver remnant

Address for correspondence: Dr. B. Yılmaz Çankaya, Atatürk University School of Medicine, Department of Radiology, Erzurum, Turkey, e-mail: dr.bycankaya@gmail.com

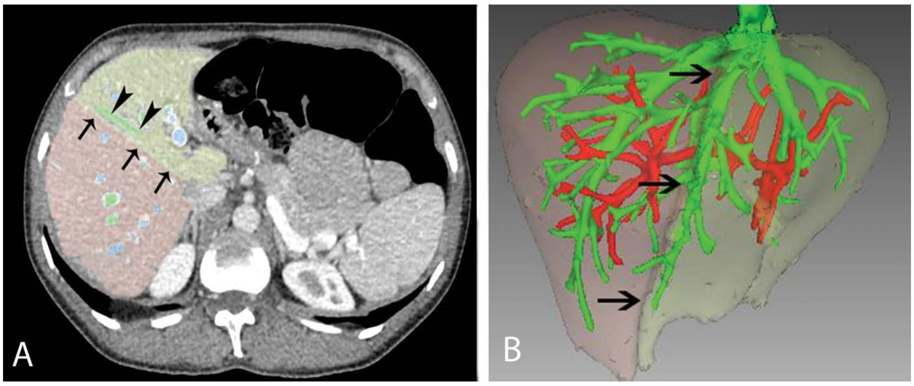

Figure 1. A. The operation resection line (arrows) is made to pass right of the middle hepatic vein (arrowheads); **B.** Liver volume is calculated by distinguishing it from vascular structures through the three-dimensional volume programme.

volume after post-transplantation is considered as the critical limit [8, 19]. Therefore, researchers have explored the relationships between liver volume and vascular structures [3, 9, 12, 18]. Similarly, in this study, we examined the relationship of the portal and hepatic artery variations, which are surgically important parameters before liver transplantation, with the remnant liver volume in liver transplant donors.

MATERIAL AND METHODS

Patient selection

This study was approved by the local ethics committee (number file: B.30.2.ATA.0.01.00/163). All donors were informed about the examination and study procedure, and their written consent was obtained. Of the healthy volunteers who presented to the radiology department of our hospital between July 2018 and January 2020 as potential transplant donors, those aged 18 to 45 years were included in the evaluation. A routine laboratory evaluation, haemogram analysis, liver ultrasonography, and triphasic abdominal CT were performed. After the laboratory and radiological evaluation, 25 patients with fatty liver, 2 with an abdominal aortic aneurysm, and 13 with diffuse atherosclerosis in vascular structures were excluded from the study. The data of the remaining 180 volunteers were evaluated in the study.

CT examination

In this study, a 320-row multi-detector CT device (Aquillion ONE Vision; Toshiba Medical Systems Corporation, Otawara, Japan) was used for liver imaging. All CT scans were performed using the parameters recommended by the manufacturer (slice thickness: 0.5 mm; rotation time: 0.5 s; and scan interval: 240 mm [480 slices, 0.5 mm]). Using a pressure injector, 1.5 mL/kg contrast enhancement (300 mg/mL iohexol) was applied at a rate of 3.5 mL/s. Triphasic images were obtained in the arterial, portal, and hepatic vein phases. The images were evaluated on the radiological workstation (Syngo Via Console, software version 2.1, Siemens AG Medical Solutions, Erlangen, Germany) by a single radiologist (B.Y.C.) with 10 years' experience in the field. The volumetric volume assessment of the liver was undertaken using another workstation (Myrian Pro; Intrasense, Montpellier, France).

Image evaluation

The images were divided into groups according to Nakamura et al.'s [16] anatomic classification of portal veins and Michels et al.'s [5] classification of hepatic arteries. In a three-dimensional (3D) volumetric image processor, the liver parenchymal volume was distinguished from vascular structures (Fig. 1A). Along the Cantlie line used during transplantation (Fig. 1B), the liver was volumetrically divided into two lobes as right and left. The percentage of the remnant left lobe relative to the total liver volume was determined after liver transplantation.

Statistical evaluation

Statistical evaluation was performed using Medcalc statistics (v. 12, Mariagerke, Belgium). The D'Agostino-Pearson test was used to determine whether the data was parametric. The left liver lobe percentages of the four groups formed according to the portal vein classification were compared using the Kruskal-Wallis test. The left liver lobe percentages of the five arterial variation groups formed according to the hepatic artery classification were compared by the

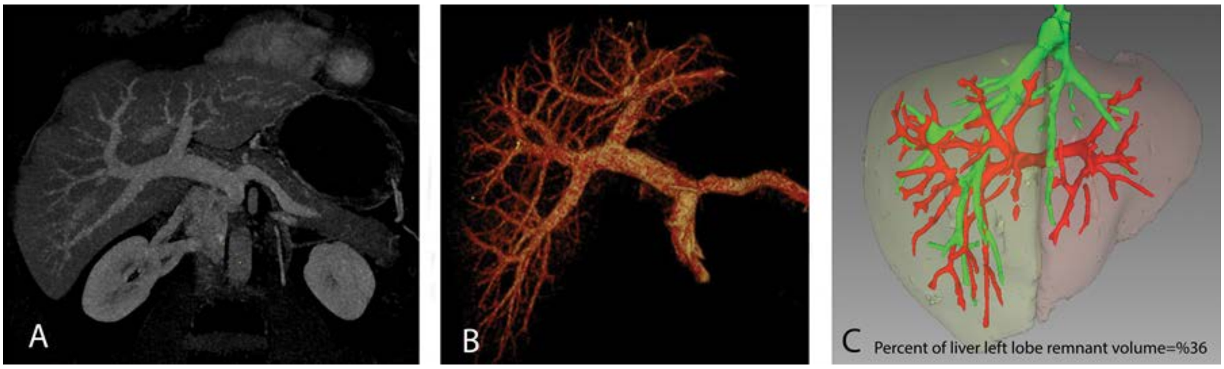

Figure 2. Computed tomography (**A**) and three-dimensional (3D) volume rendering imaging (**B**) show the Nakamura type A portal bifurcation structure. The 3D volumetric programme (**C**) demonstrated liver left lobe volume values in the donor with Nakamura type A.

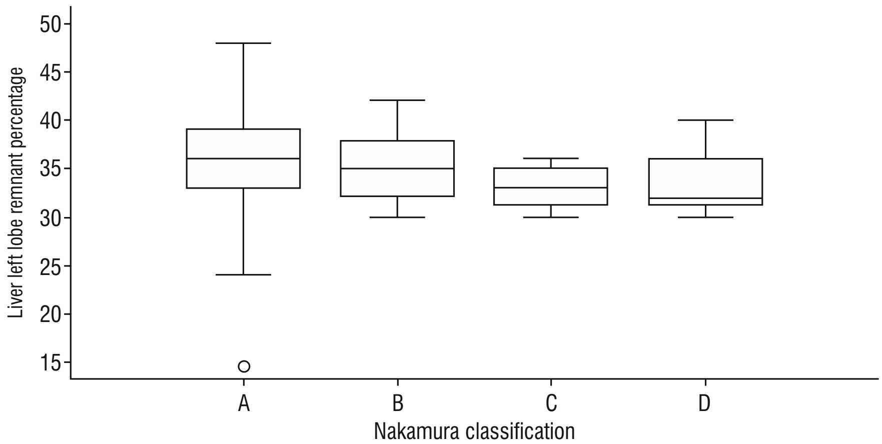

Figure 3. Statistical graph of percentages of left lobe percentage volume according to Nakamura classification.

Kruskal-Wallis test. The demographic data between the groups were comparatively evaluated using the t-test for age and the χ^2 test for gender. P values of < 0.05 were considered as statistically significant.

RESULTS

The mean age of the 180 volunteers evaluated was 28 ± 8.5 years. The number of female volunteers was 76 (41.1%). According to the Nakamura classification, there were 143 (79.4%) type A, 23 (12.7%) type B, 7 (3.9%) type C, and 7 (3.9%) type D patients. There was no statistically significant difference in age and gender distribution between the groups (p = 0.54 and 0.096, respectively). The data of the left liver lobe volume were non-parametric and did not show normal distribution. In the portal vein groups (types A, B, C, and D), the median values (95% confidence interval [CI]) of the left liver lobe volume were found to be 36 (35–37), 35 (33–37), 33 (30.5–35.5), and 32 (30.5–38.5), respectively. There was no significant difference between the Nakamura groups in terms of the left lobe remnant percentage relative to the liver transplantation resection line (p = 0.055; Figs. 2, 3). The related data and statistical results are shown in Table 1.

According to the Michels classification, the following seven groups were observed: type 1 (n = 129; 71%), type 2 (n = 12; 6.7%), type 3 (n = 24; 13%), type 4 (n = 2; 2.2%), type 5 (n = 10; 5.6%), type 6 (n = 1; 0.6%), and type 9 (n = 2; 1.1%). There was no statistical difference in age and gender distribution between these groups (p = 0.341 and 0.132, respectively). In the hepatic artery groups (types 1, 2, 3, 4, 5, 6, and 9), the median values of the left liver lobe volume (95% CI) were found to be 36 (35–37), 34.5 (30.3–38.8), 35 (32–37), 39, 36.5 (33–42), 42, and 30. No significant difference was determined between the Michels groups in relation to the percentage of the left lobe remnant volume relative to the liver transplantation resection line (p = 0.207; Figs. 4, 5). Table 2 presents the related data and statistical results.

Table 1. Nakamura groups, the left lobe remnant percentage relative to the liver transplantation resection line (source: [16])

Portal vein statistics data	Nakamura type A	Nakamura type B	Nakamura type C	Nakamura type D	P
Number of cases	143	23	7	7	
Age [year]	30.4 ± 8.4	30.4 ± 8.7	31.2 ± 10.4	26.1 ± 6.8	0.54
Male gender (%)	85 (59%)	9 (39%)	5 (71%)	5 (71%)	0.096
Left lobe volume percentage, median (95% CI)	36 (35–37)	35 (33–37)	33 (30.5–35.5)	32 (30.5–38.5)	0.055

CI — confidence interval

Table 2. Michels groups, the left lobe remnant percentage relative to the liver transplantation resection line (source: [16])

Hepatic artery statistics data	Michels type 1	Michels type 2	Michels type 3	Michels type 4	Michels type 5	Michels type 6	Michels type 9	P
Number of cases	129 (71%)	12 (6.7%)	24 (13%)	2 (2.2%)	10 (5.6%)	1 (0.6%)	2 (1.1%)	
Age	30.8 ± 8.4	23.5 ± 5.7	30.5 ± 8.8	21 ± 2.8	30.9 ± 9.6	26 ± 0	24 ± 2.8	0.341
Male gender (%)	76 (58.9%)	5 (41.7%)	13 (13.3%)	2 (100%)	6 (60%)	1 (100%)	1 (50%)	0.132
Left lobe volume percentage, median (95% CI)	36 (35–37)	34.5 (30.3–38.8)	35 (32–37)	39 (–)	36.5 (33–42)	42 (–)	30 (–)	0.207

CI — confidence interval

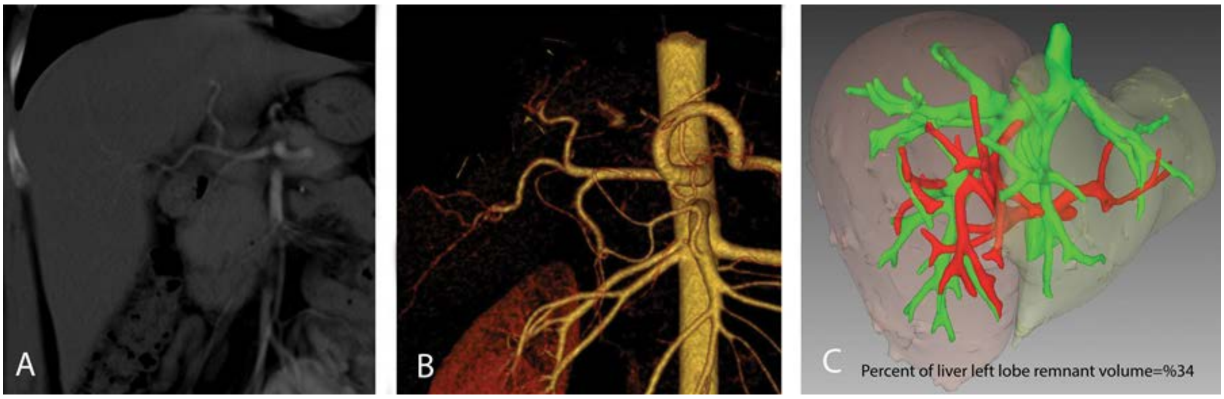

Figure 4. Computed tomography (**A**) and three-dimensional (3D) volume rendering imaging (**B**) show the Michel's type 1 hepatic artery variation. The 3D volumetric programme (**C**) demonstrated liver left lobe volume values in the donor with Michel's type 1 hepatic artery variation.

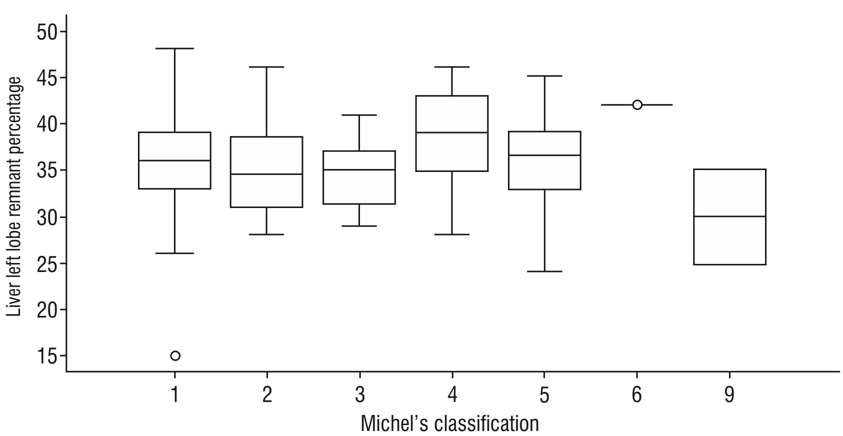

Figure 5. Statistical graph of percentages of left lobe percentage volume according to Michel's classification.

DISCUSSION

In this study, we found that the volume of the left liver lobe was not affected by the portal vein and hepatic artery variations which are important pre-transplantation parameters that determine donor safety and success of the procedure. In the literature, there are some studies that has investigated the effects and relationship of vascular structures concerning liver volume [3, 12, 18]. Since 3D software providing preoperative volumetric evaluation is not available in every centre, researchers have attempted to perform this evaluation using various formulas [14]. In this study, we examined the relationship of the liver remnant volume with the portal vein and hepatic artery anatomical variations, which, to the best of our knowledge, has not been previously evaluated in the literature.

Some external anatomic landmarks can be used to divide the liver into the lobes; however, this approach is not sufficient when planning a liver surgery. Further division of the liver into the segments based on the biliary and vascular trees was introduced previously [4, 7]. On the other hand, various anatomical variations of the liver were reported [17] which can affect the volumetric evaluation. The development of the portal and hepatic venous system is completed at the end of 6th week of development. Embryological origin of the liver veins can conflict with Couinaud's model and segmental anatomy is closely related with an adaptive mechanism of the liver which varies with metabolic demand and perfusion [7].

Abdalla et al. [1] performed the volumetric evaluation of the left lobe and left lobe segmentation and found differences between the patients with a certain standard deviation. It was reported that these differences might be due to anatomical differences [1]. Therefore, they may result from either physical differences or vascular variations between patients. In another study, Altunkaynak et al. [2] showed that the body mass index of the patients was associated with their liver volume. Kokuda et al. [13] detected differences between study groups in terms of liver volume and attributed it to the thoracic width. Such studies demonstrate that liver volume can vary according to the populations examined and their anatomical differences. The current study was conducted in a Turkish population, and no significant difference was observed between the groups in terms of age and gender. Therefore, we focused on the effects of vascular variations on the liver volume in our study.

Vascular variations are important anatomical markers that determine liver segmentation [10]. In particular, portal and hepatic variations are vascular components used in liver segmentation. Therefore, variational changes can affect segmentation (including the right-left lobe separation) [10]. Besides, the proper functioning of the portal vein, hepatic artery, and hepatic vein structures that provide tissue vascularisation allows for the volumetric and functional development of the related tissues [6, 11, 21]. Due to the changes in liver function caused by these functional variations in vascular structures, the differences in anatomical structures and their features may also affect the liver. Similarly, Choi et al. [3] reported that the portal vein flow was related to the volume ratios of the right and left liver lobes; thus, they concluded that vascular drainage might affect the liver volume and functional capacity. However, in the same study, it was shown that the portal vein area was not associated with liver volume [3]. Although no variational assessment was undertaken in this study, the portal vein area was not associated with liver volume which was an important finding revealing that the differences in anatomical structures did not affect the volume. Our results confirmed that the anatomical variations did not result in any changes in the liver volume percentage.

Limitations of the study

Our study had several limitations. First, the number of our patients was not sufficient. Thus, some vascular variations might not be observed, and some were few in statistical terms. The second limitation of our study was that we did not take our patients' body mass indices into account. However, we believe that this parameter would not have had a significant impact on the results as there was no difference in age or gender distribution in the study population.

CONCLUSIONS

In conclusion, variational changes in the hepatic artery and portal vein are important markers that affect decisions concerning the surgical procedure; however, they do not affect the remnant liver volume in liver transplant donors.

Conflict of interest: None declared

REFERENCES

1. Abdalla EK, Denys A, Chevalier P, et al. Total and segmental liver volume variations: implications for liver surgery. Surgery. 2004; 135(4): 404–410, doi: 10.1016/j.surg.2003.08.024, indexed in Pubmed: 15041964.

2. Altunkaynak BZ, Altunkaynak ME. Relationship of body weight and volume of liver. A morphometrical and stereological study. Saudi Med J. 2007; 28(6): 891–895, indexed in Pubmed: 17530105.
3. Choi SH, Kwon JH, Kim KW, et al. Measurement of liver volumes by portal vein flow by Doppler ultrasound in living donor liver transplantation. Clin Transplant. 2017; 31(9), doi: 10.1111/ctr.13050, indexed in Pubmed: 28681460.
4. Couinaud C. Liver anatomy: portal (and suprahepatic) or biliary segmentation. Dig Surg. 1999; 16(6): 459–467, doi: 10.1159/000018770, indexed in Pubmed: 10805544.
5. Covey AM, Brody LA, Maluccio MA, et al. Variant hepatic arterial anatomy revisited: digital subtraction angiography performed in 600 patients. Radiology. 2002; 224(2): 542–547, doi: 10.1148/radiol.2242011283, indexed in Pubmed: 12147854.
6. Cura M, Haskal Z, Lopera J. Diagnostic and interventional radiology for Budd-Chiari syndrome. Radiographics. 2009; 29(3): 669–681, doi: 10.1148/rg.293085056, indexed in Pubmed: 19448109.
7. Hikspoors JP, Peeters MM, Kruepunga N, et al. Human liver segments: role of cryptic liver lobes and vascular physiology in the development of liver veins and left-right asymmetry. Sci Rep. 2017; 7(1): 17109, doi: 10.1038/s41598-017-16840-1, indexed in Pubmed: 29214994.
8. Hiroshige S, Shimada M, Harada N, et al. Accurate preoperative estimation of liver-graft volumetry using three-dimensional computed tomography. Transplantation. 2003; 75(9): 1561–1564, doi: 10.1097/01.TP.0000053755.08825.12, indexed in Pubmed: 12792515.
9. Hwang S, Lee SG, Choi ST, et al. Hepatic vein anatomy of the medial segment for living donor liver transplantation using extended right lobe graft. Liver Transpl. 2005; 11(4): 449–455, doi: 10.1002/lt.20387, indexed in Pubmed: 15776411.
10. Iqbal S, Iqbal R, Iqbal F. Surgical implications of portal vein variations and liver segmentations: a recent update. J Clin Diagn Res. 2017; 11(2): AE01–AE05, doi: 10.7860/JCDR/2017/25028.9453, indexed in Pubmed: 28384848.
11. Jha RC, Khera SS, Kalaria AD. Portal vein thrombosis: imaging the spectrum of disease with an emphasis on MRI features. Am J Roentgenol. 2018; 211(1): 14–24, doi: 10.2214/AJR.18.19548, indexed in Pubmed: 29792748.
12. Kayashima H, Shirabe K, Morita K, et al. Liver regeneration and venous collateral formation in the right lobe living-donor remnant: segmental volumetric analysis and three-dimensional visualization. Transplantation. 2013; 95(2): 353–360, doi: 10.1097/TP.0b013e31827147d8, indexed in Pubmed: 23325006.
13. Kokudo T, Hasegawa K, Uldry E, et al. A new formula for calculating standard liver volume for living donor liver transplantation without using body weight. J Hepatol. 2015; 63(4): 848–854, doi: 10.1016/j.jhep.2015.05.026, indexed in Pubmed: 26057995.
14. Lee WC, Lee CS, Soong RS, et al. Split liver transplantation in adults: preoperative estimation of the weight of right and left hemiliver grafts. Liver Transpl. 2011; 17(1): 93–94, doi: 10.1002/lt.22213, indexed in Pubmed: 21254350.
15. Mohapatra N, Gurumoorthy Subramanya Bharathy K, Kumar Sinha P, et al. Three-dimensional volumetric assessment of graft volume in living donor liver transplantation: does it minimise errors of estimation? J Clin Exp Hepatol. 2020; 10(1): 1–8, doi: 10.1016/j.jceh.2019.03.006, indexed in Pubmed: 32025161.
16. Nakamura T, Tanaka K, Kiuchi T, et al. Anatomical variations and surgical strategies in right lobe living donor liver transplantation: lessons from 120 cases. Transplantation. 2002; 73(12): 1896–1903, doi: 10.1097/00007890-200206270-00008, indexed in Pubmed: 12131684.
17. Singh H, Rabi S. Study of morphological variations of liver in human. Trans Res Anat. 2019; 14: 1–5, doi: 10.1016/j.tria.2018.11.004.
18. Tongyoo A, Pomfret EA, Pomposelli JJ. Accurate estimation of living donor right hemi-liver volume from portal vein diameter measurement and standard liver volume calculation. Am J Transplant. 2012; 12(5): 1229–1239, doi: 10.1111/j.1600-6143.2011.03909.x, indexed in Pubmed: 22221803.
19. Tsang LLC, Chen CL, Huang TL, et al. Preoperative imaging evaluation of potential living liver donors: reasons for exclusion from donation in adult living donor liver transplantation. Transplant Proc. 2008; 40(8): 2460–2462, doi: 10.1016/j.transproceed.2008.07.075, indexed in Pubmed: 18929768.
20. Tung YC, Cheng YF, Huang TL, et al. Impact of different dominant hepatic vein patterns in left-lobe donors of adult living donor liver transplantation. Transplant Proc. 2016; 48(4): 1012–1014, doi: 10.1016/j.transproceed.2015.12.128, indexed in Pubmed: 27320544.
21. Vaidya S, Dighe M, Bhargava P, et al. Chronic hepatic artery occlusion with collateral formation: imaging findings and outcomes. Transplant Proc. 2011; 43(5): 1770–1776, doi: 10.1016/j.transproceed.2011.03.034, indexed in Pubmed: 21693276.
22. Zhijun Z, Wei G, Lin W, et al. Middle hepatic vein allocation in adult right lobe living donor liver transplantation. Clin Transplant. 2014; 28(10): 1194–1201, doi: 10.1111/ctr.12362, indexed in Pubmed: 25328058.

VIA MEDICA

ORIGINAL ARTICLE

Folia Morphol.
Vol. 80, No. 3, pp. 596–604
DOI: 10.5603/FM.a2020.0084

ISSN 0015–5659
eISSN 1644–3284
journals.viamedica.pl

The ameliorative effect of curcumin on cryptorchid and non-cryptorchid testes in induced unilateral cryptorchidism in albino rat: histological evaluation

M.A. Abd-El-Hafez[1], M.D. El-Shafee[1], S.H. Omar[1], A.A. Aburahma[2], S.S. Kamar[1]

[1]*Department of Medical Histology and Cell Biology, Faculty of Medicine, Cairo University, Cairo, Egypt*
[2]*Department of Andrology, Faculty of Medicine, Cairo University, Cairo, Egypt*

[Received: 17 May 2020; Accepted: 30 June 2020; Early publication date: 29 July 2020]

Background: *Cryptorchidism, one or both hidden testes, is the most common abnormality of male sexual development. Subfertility or infertility is associated with both unilateral and bilateral cryptorchidism. In this study, we investigate the possible ameliorative effect of curcumin (Cur) on the induced-unilateral cryptorchidism testicular injury in both cryptorchid (Cryp) and non-cryptorchid (non-Cryp) scrotal testes through histological, immunohistochemical and morphometrics.*

Materials and methods: *Forty adult male albino rats were divided into: control group, Cur control group, Cryp group, and Cryp+Cur group. The rat model was surgically established by fixing the left testis in the abdomen. The treated groups were subjected to surgically induced-unilateral cryptorchidism on the left side then were given Cur (80 mg/kg) orally, for 20 days. Histological analysis using haematoxylin and eosin and periodic acid Schiff's reaction was done. Immunohistochemistry was performed for proliferating cell nuclear antigen (PCNA); to estimate the proliferation in the germinal epithelium, and vimentin; to evaluate Sertoli cells. The results were confirmed by statistical evaluation of the spermatogenic epithelium height, the seminiferous tubules diameter, the basement membrane thickness, the number of PCNA immunostained cells and the area per cent of vimentin immunostaining.*

Results: *Distorted seminiferous tubules, substantial degeneration of the germinal epithelium, thickening of the basement membrane with a significant decrease in PCNA and vimentin immunostaining were observed in Cryp group; mainly in the cryptorchid testis. These structural changes were significantly reversed in Crypt+Cur group.*

Conclusions: *Curcumin proved to be an important and effective medical line for protecting against the unfavourable sequels of cryptorchidism in a rat model.* (Folia Morphol 2021; 80, 3: 596–604)

Key words: testis, unilateral cryptorchidism, curcumin, proliferating cell nuclear antigen (PCNA), vimentin

Address for correspondence: Dr. S.S. Kamar, Department of Medical Histology and Cell Biology, Faculty of Medicine, Cairo University, Cairo, Egypt, tel: +20 01008909069, e-mail: Dr_samaakamar@yahoo.com

The work was conducted in: Faculty of Medicine, Cairo University, Cairo, Egypt.

INTRODUCTION

Cryptorchidism, one or both hidden testes, is the most common abnormality of male sexual development occurring in about 2.4–5% of full-term newborns [14]. The ratio rises to 30% of premature neonates. Related complications of infertility, malignant transformation, depression and trauma have been recorded [15].

Subfertility or infertility is associated with both unilateral and bilateral cryptorchidism. One-third of unilateral undescended testis complained of fertility impairment with incidence of azoospermia in about 13% of cases [11]. The impact of cryptorchidism included not only degeneration of germ cells in response to elevated temperature [17] but also increased intratesticular oxidative stress that produced deleterious testicular changes with reduced spermatogenesis [7]. A previous study has demonstrated that unilateral cryptorchidism was associated with increased number of mast cells in both testes, resulting in fibrosis and deterioration of spermatogenesis [1]. The structural defects of both the retained and scrotal testis have been concluded in other studies [15, 35].

The concept of 'early orchidopexy' has established as the primary treatment for cryptorchidism. However, orchidopexy alone is insufficient to completely restore spermatogenesis and there is a domain for a germinal epithelial protective substance [6]. Human spermatogonial from cryptorchid (Cryp) patients can piecemeally differentiate into haploid spermatids when treated with retinoic acid and stem cell factor [36]. Antioxidants have proved to significantly increase the sperm count and germ cell count in Cryp rats [3].

Curcumin (Cur), the active ingredient of the dietary spice turmeric (*curcuma longa*), is widely used in medical practice. Its efficacy is due to its phenolic group [33]. It is known to be anti-inflammatory, antineoplastic, cardioprotective and renoprotective reagent [36]. Moreover, it has bi-functional antioxidant effects by protecting the cell against the reactive species and stimulating up regulation of cytoprotective proteins [34].

The aim of our study is to evaluate the possible ameliorative effect of Cur on the induced unilateral cryptorchidism in both Cryp and non-Cryp testes.

MATERIALS AND METHODS

Experimental design

This study included 40 adult male albino rats, each of 200–250 g body weight. The animals were bred in the Animal House of Faculty of Medicine, Cairo University. Each group, or subgroup, was kept in separate wire cage at room temperature, fed ad libitum with free water supply. All procedures were held under ethical guidelines of Animal Care and Use Committee of Cairo University. The rats were divided equally into four groups (n = 10).

Control group (GpI): the rats were equally subdivided into two subgroups (n = 5): ***Blank control (GpIa):*** the rats were not exposed to any surgical procedure; and ***Sham (GpIb):*** subjected to sham operation on day 1 of the experiment. Under anaesthesia and complete aseptic conditions, a lower midline abdominal incision was performed. The left testis was displaced into the abdomen then replaced again into the scrotal sac, and then the incision was closed. The rats were administered buprenorphine 0.05 mg/kg by intraperitoneal injection/8 h; as post-operative analgesic for 7 days. Besides, they were given 1 mL dimethyl sulfoxide (DMSO) orally once daily for 20 days.

Curcumin (Cur) control group (GpII): were given Cur at a dose of 80 mg/kg, dissolved in 1 mL DMSO, once daily orally, for 20 days.

Cryptorchid (Cryp) group (GpIII): rats were subjected to surgically induced-unilateral cryptorchidism on the left side. Animals were subjected to the same surgical procedures as GpIb but the left testis was displaced into the abdomen and fixed. The gubernaculum on the left side was separated, the testis was displaced into the abdomen, and the inguinal canal was closed [7]. The incision was sutured and the rats were administered post-operative analgesic. The animals were left for 20 days after surgery without any treatment [22].

Cryptorchid plus curcumin (Cryp+Cur) group (GpIV): rats were subjected to surgically induced-unilateral cryptorchidism on the left side as described in GpIII then were given Cur orally, for 20 days.

All rats were euthanized at the end of the experiment by intraperitoneal injection of thiopental sodium (50 mg/kg). Testis specimens were fixed in Bouin solution and embedded in paraffin. Serial sections of 5 μm thickness were cut and subjected to histological and immunohistochemical studies.

Histological studies

Haematoxylin and eosin stain (HE) to illustrate the morphological change and periodic acid Schiff's (PAS) reaction to demonstrate the basement membrane.

Immunohistochemistry for proliferating cell nuclear antigen, using a mouse monoclonal antibody (Ab)

(Thermo Scientific Laboratories, USA, Cat.# MS106P) as a criterion for the proliferating cells.

Vimentin intermediate filament, using monoclonal antibody (Cell Marque Corporation, Toll-Free North America, Cat.# 347M-18).

Morphometrics

Employing "Leica-Qwin 500 C" image analyser (Cambridge, England), 10 non-overlapping fields/rat testes were examined and the following parameters were estimated:
- height of the spermatogenic epithelium (SEp) and the diameter of the seminiferous tubules in HE sections;
- thickness of the basement membrane in PAS stained sections;
- number of positive (+ve) proliferating cell nuclear antigen (PCNA) immunostained cells;
- area per cent of +ve vimentin immunostaining.

Statistical studies

The estimated measurements were compared and analysed using one-way analysis of variance of SPSS software version-19. Comparison between the different groups was followed by post-hoc Tukey test. Quantitative representative data was obtained and summarised as means ± standard deviations (SD). Probability (p) values < 0.05 were considered statistically significant.

RESULTS

Clinical observation. No mortality was recorded in the experimental rats and no changes were noted in their behaviours in water and food consumption.

HE stain. Testicular sections of control rats and rats from GpII displayed normal architecture of the seminiferous tubules and the interstitial tissue (Fig. 1A, B). The Cryp testes of GpIII revealed severely distorted seminiferous tubules and partial separation of the basement membrane in some areas. In most of the examined fields, there was obvious degeneration of the germinal epithelium with some shed cells in the lumen. The non-Cryp testes from GpIII showed mild disorganisation of the seminiferous tubules. The lining epithelium showed spermatogonia, primary spermatocytes with absence of late stage of germ cells (Fig. 1C, D). The GpIV revealed obvious protection of the abdominal and scrotal testes. There were normal structure of the seminiferous tubules containing spermatozoa in the lumen and the interstitial tissue in both abdominal and scrotal testes. Seminiferous tubule displayed all germinal cell layers with sperm in the lumen (Fig. 1E, F).

PAS stain. Sections from GpIII revealed strong thick +ve PAS reaction in the thick irregular basement membrane in both scrotal and abdominal testes. In GpIV, thin strong + ve PAS reaction in the basement membrane of both abdominal and scrotal testes was illustrated (Fig. 2).

Immunohistochemistry (Fig. 3). Using PCNA immunostaining, the Cryp testes from GpIII showed few +ve PCNA immunostained cells near the basement membrane in severely degenerated SEp. The non-Cryp testes revealed many +ve PCNA immunostained cells in the early stages of the SEp and weak or absent immunostaining in the late stages of the spermatogenic cells. GpIV revealed diffuse +ve PCNA immunostaining in both testes.

In vimentin immunohistochemistry, Cryp testes of GpIII showed +ve vimentin immunostaining in Sertoli cells in the perinuclear region. The right scrotal testes of the same rats revealed +ve vimentin immunostaining mainly in the perinuclear region of Sertoli cells with few +ve apical immunostaining. In GpIV, both testes revealed numerous +ve vimentin immunostaining of Sertoli cells in the perinuclear regions and throughout the cytoplasm extending into the apices.

Statistical analysis (Table 1)

The height of the SEp and seminiferous tubules diameter. GpIII showed a significant decrease in both parameters as compared to GpI, GpII, and GpIV. Meanwhile, both parameters in the Cryp testes of GpIII were significantly decreased as compared to the scrotal testis of GpIII. In GpIV, the mean height of SEp and the mean diameter of seminiferous tubules in the Cryp testes were significantly decreased as compared to GpI, GpII and non-Cryp testes of GpIV.

The thickness of the basement membrane. In both testes of GpIII, the mean thickness of the basement membrane displayed a significant increase as compared with GpI, GpII, and GpIV. In addition, the mean thickness of basement membrane in Cryp testes of GpIII was significantly increased compared to the non-Cryp testes of GpIII. The mean thickness of basement membrane in Cryp and non-Cryp testes of GpIV were comparable.

The mean cell count of +ve PCNA immunostained cells. In both testes of GpIII, the mean cell count of +ve PCNA immunostained cell was significantly decreased as compared to GpI, GpII and

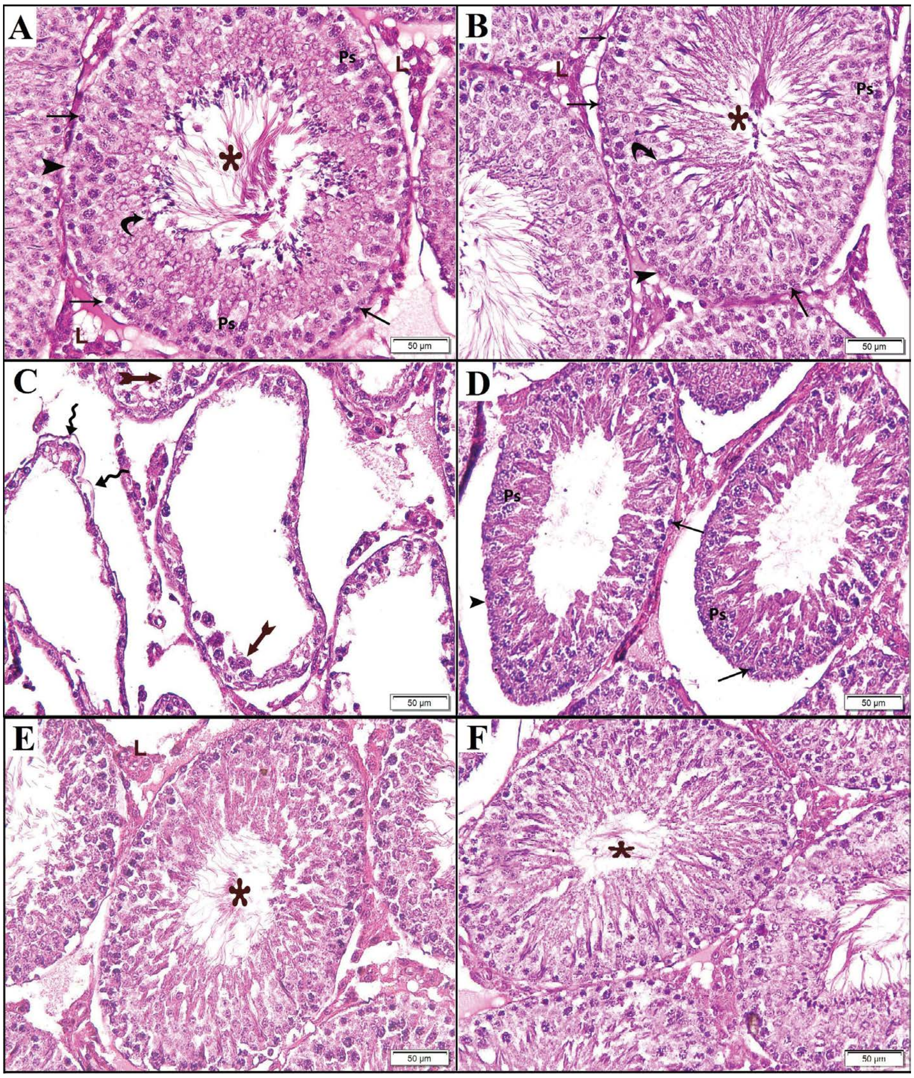

Figure 1. Haematoxylin and eosin (HE)-stained rat testes (×200) showing Group I (GpI; **A**) and Group II (GpII; **B**): the seminiferous tubules containing spermatozoa (star) in the lumen, the interstitial tissue (IS) harbouring clusters of Leydig's cells (L), the spermatogenic epithelium (SEp) resting on basal lamina with Sertoli cells (arrowheads), attached mature spermatids (curved arrows), numerous spermatogonia (arrows) and primary spermatocytes (Ps); **C.** Cryptorchid testis in Group III (GpIII): substantial distortion and collapse of the seminiferous tubules with partial separation of the basement membrane (wavy-arrow), obvious degeneration of the germinal epithelium. Some cells are sloughed in the lumen (bifid-arrow); **D.** Non-cryptorchid testis in GpIII: mild disorganisation of the seminiferous tubules with expansion of interstitial space, the SEp illustrating Sertoli cells (arrowhead), spermatogonia (arrows), Ps, and absence of sperms; Cryptorchid and (**E**) and non-cryptorchid testes (**F**) in Group IV (GpIV): normal structure of the seminiferous tubules with all germinal cell layers, mature spermatids and spermatozoa (star) in the lumen, and IS containing clusters of Leydig's cells (L).

GpIV. Besides, it was significantly decreased in the Cryp testes of GpIII as compared to the non-Cryp testes of GpIII. The mean cell count of +ve PCNA immunostained cell in the Cryp testes of GpIV was significantly decreased as compared with GpI, GpII and non-Cryp testis of GpIV.

The mean area per cent of vimentin immunostaining. Both testis of GpIII showed a significant decrease as compared to GpII and GpIV. In the abdominal testes of GpIV, it was significantly decreased as compared to GpI, GpII and scrotal testes of GpIV.

DISCUSSION

Cryptorchidism is a common congenital malformation in the male reproductive system. It is documented to have long-term sequels such as infertility, depression, and testicular cancer. The impacts included degeneration of germ cells in response to elevated temperature [17] and increased intratesticular oxidative stress [7]. The objectives for cryptorchidism management are to preserve fertility and ameliorate the risk of malignancy [29].

Experimentally induced unilateral cryptorchidism is stellar method to study undescended testis in

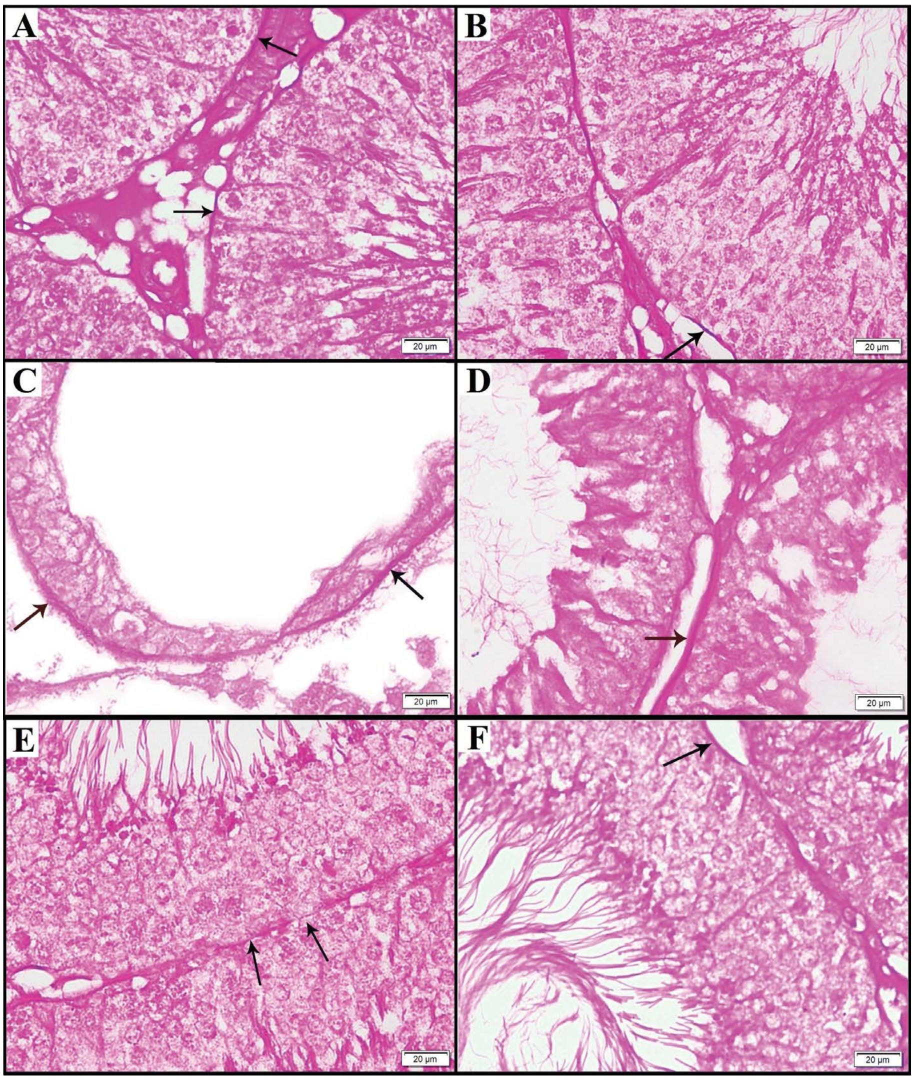

Figure 2. Periodic acid Schiff's (PAS)-stained rat testes (×400) showing: Group I (GpI; **A**) and Group II (GpII; **B**): thin strong +ve PAS reaction in the basement membrane (arrows); Cryptorchid (**C**) and non-cryptorchid (**D**) testes in Group III (GpIII): strong +ve PAS reaction in the thick irregular basement membrane (arrows). Cryptorchid (**E**) and non-cryptorchid (**F**) testes in Group IV (GpIV): thin strong +ve PAS reaction in the basement membrane (arrows).

relevance to spermatogenesis against temperature gradient in both testes [12]. In the present work, cryptorchid testes of GpIII revealed severely distorted seminiferous tubules and SEp. The non-Cryp testes of GpIII displayed mild disorganisation of the seminiferous tubules with absence of sperm in most of fields. However, a significant difference in the height of germinal epithelium and the diameter of seminiferous tubules was noted between the Cryp and the non-Cryp testes of GpIII. These findings were in accordance with previous study of Moon et al. [25]. It was postulated that histological changes associated with cryptorchidism resulted in a significant reduction in the number and the diameter of seminiferous tubules with amelioration of the number and proliferation of spermatogonia. Besides, most of the proliferating cells detected were Sertoli cells suggesting increased risk of Sertoli cell tumours. Also, structural defects of both the retained and scrotal testes were reported [4, 35].

High temperature was suggested to induce disruption of spermatogenesis in cryptorchid testis [12]. Lin et al. [20] found that hyperthermia initiates oxidative stress and apoptosis in spermatogenic cells with subsequent affection of fertility. This was explained by Tekayev et al. [32] that testicular tissues are rich in polyunsaturated fatty acids and poor in antioxidant defence. Thus, they are prone to be attacked by reactive oxygen species (ROS) which are able to oxidize proteins, lipids and deoxyribonucleic acid leading to

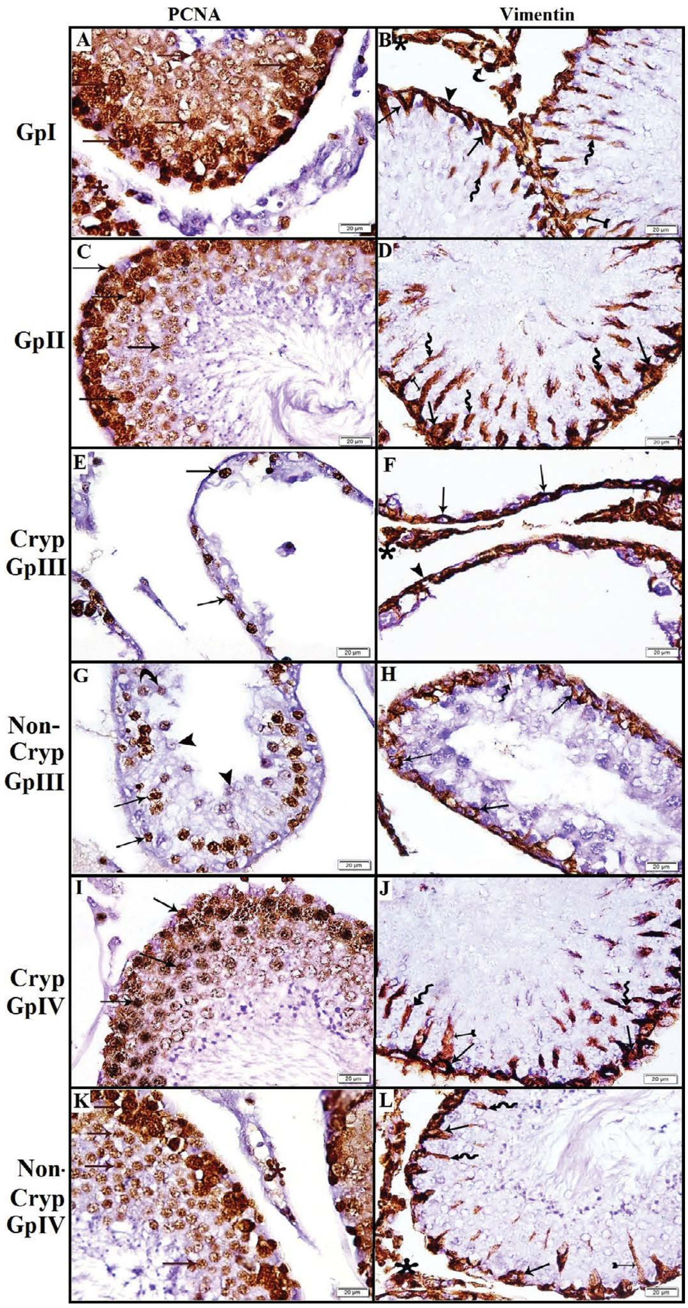

Figure 3. Proliferating cell nuclear antigen (PCNA) and vimentin immunohistochemically stained rat testes (×400). PCNA immunohistochemistry showing: Group I (GpI; **A**) and Group II (GpII; **C**): diffuse +ve PCNA immunostaining in the nuclei of spermatogenic cells (arrow) and in the interstitial tissue (IS) (star); **E.** Cryptorchid testis in Group III (GpIII): few +ve PCNA immunostained cells (arrow) near the basement membrane in severely degenerated spermatogenic epithelium (SEp); **G.** Non-cryptorchid testis in Group III (GpIIII): many PCNA immunostained cells in the early stages of the spermatogenic cells (arrow) with weak (curved-arrow) or absent (arrowhead) immunostaining in the late stages of the spermatogenic cells; Cryptorchid (**I**) and (**K**) non-cryptorchid testes in Group IV (GpIV): diffuse +ve PCNA immunostaining in the nuclei of spermatogenic cells (arrow). Vimentin immunohistochemistry showing: Group I (GpI; **B**) and Group II (GpII; **D**): +ve vimentin immunostaining of Sertoli cells in the perinuclear region (arrows), throughout the cytoplasm (bifid-arrow) and apically from nucleus (wavy-arrows). Positive immunostaining is noted in myoid cells (arrowhead), endothelium (curved--arrow) and IS cells (star); **F.** Cryptorchid testis in GpIII: +ve vimentin immunostaining around the nuclei of Sertoli cells (arrows), in myoid cells (arrowhead) and IS cells (star); **H.** Non-cryptorchid testis in GpIII: +ve vimentin immunostaining mainly in the perinuclear region of Sertoli cells (arrows) with few +ve immunostaining extending through the cytoplasm apically (wavy-arrow); Cryptorchid (**J**) and non-cryptorchid (**L**) testes in GpIV: +ve vimentin immunostaining of Sertoli cells in the perinuclear region (arrows), throughout the cytoplasm (bifid-arrow) and apically from nucleus (wavy-arrows); Cryp — cryptorchid.

Table 1. Curcumin significantly protected the testicular tissue and improved the germinal epithelium proliferation in both cryptorchid (Cryp) and non-cryptorchid testes

Groups	Mean height of spermatogenic epithelium [μm]	Mean diameter of seminiferous tubule [μm]	Mean diameter of the basement membrane thickness [μm]	Mean cell count of PCNA immunostained cells	Mean area per cent of vimentin immunostaining
Group I	97.01 ± 5.64	362.27 ± 16.48	0.85 ± 0.15	36.7 ± 2.93	26.2 ± 3
Group II	97 ± 5.47	357.29 ± 10.13	0.9 ± 0.13	38.1 ± 2.92	26.23 ± 2.66
Cryp; Group III	9.18 ± 2.25*!#	141.94 ± 14.62*!#	5.61 ± 0.61*!#	6.7 ± 1.49*!#	10.89 ± 2.09*#
Non-Cryp; Group III	69.87 ± 7.49*#	202.93 ± 23.96*#	4.67 ± 0.72*#	11.6 ± 2.01*#	11.51 ± 1.76*#
Cryp; Group IV	89.29 ± 2.38*$	297.12 ± 14.99*$	1.13 ± 0.32	32.1 ± 2.08*$	20.28 ± 2.37*$
Non-Cryp; Group IV	95.90 ± 3.89	348.62 ± 14.58	0.84 ± 0.15	36.6 ± 2.07	24.3 ± 2.05

Data presented with means ± standard deviation. *Significant as compared to Group I; ! Significant as compared to Cryp Group III; #Significant as compared to Cryp and non-Cryp group IV; $ Significant as compared to non-Cryp Group IV; PCNA — proliferating cell nuclear antigen cellular damage. The equalisation between production and clearance of ROS provides an important role in the spermatogenesis as physiological level of ROS maintains the body's normal physiological functions, whereas excessive ROS can cause apoptosis.

Interestingly, Acikgoz et al. [1] found that unilateral cryptorchidism was associated with increased number of mast cells in both testes, resulting in deterioration of spermatogenesis. According Aydin et al. [5], the unilateral cryptorchidism causes endocrine dysfunction in the body, influencing the secretion of sex hormone and occurrence of allergic reaction. Recent study has revealed that cryptorchidism leads to hypothalamic-pituitary-gonadal dysfunction, which was assumed to interfere with the contralateral testicular function and morphology [30]. Moreover, it was documented that affection of sensory branch of genito-femoral nerve is a finding in cryptorchidism [17]. The abnormal environment in the Cryp testis has deleterious effects on the genito-femoral nerve that induces changes in blood circulation and the microenvironment in the contralateral non-Cryp testis [26].

Rats from GpIV that received curcumin treatment after induction of unilateral cryptorchidism revealed obvious protection of the abdominal and scrotal testes. They exhibited normal architecture of the seminiferous tubules and SEp. This result was approved by the significant increase in the mean height of germinal epithelium and the mean diameter of the seminiferous tubules as compared to GpIII. However, the means in the non-Cryp testes of GpIV was comparable to GpI and significantly increased as compared to the Cryp testes of GpIV. Thus, indicating substantial protective effect of Cur in the Cryp testis and full protection in the contralateral non-Cryp testis.

In the current study, GpIII displayed significantly thickened irregular basement membrane in both testes as compared to GpI. However, GpIV revealed thin basement membrane of both testes that was comparable to GpI. In the study of Hassanin et al. [16], the thickening of the basement membrane was detected and explained by the harmful effect of oxidative stress on the testis induced by acrylamide. The protective effect of Cur could be referred to its antioxidant effect similar to the antioxidant vitamin E that protected the testis from the oxidative stress.

In PCNA immunohistochemistry, control rats showed diffuse nuclear immunostaining in the spermatogenic cells in addition to the interstitial tissue. Thus, indicating healthy high proliferative capacity of the testicular tissue [28]. In GpIII, significant decrease in PCNA immunostained cells was noted as compared to GpI. If any in the cryptorcid testes, the PCNA immunostained cells were noted near the basement membrane. The scrotal testes showed +ve PCNA immunostained cells, mainly in the early stages of the spermatogenic cells and weak or absent PCNA immunostaining in the late stages. It was reported that the testicular tissues obtained from rats treated with cadmium had a harmful effect on the testis through its oxidative stress activity [27]. This was supported by Dutta et al. [12] who proved that oxidative stress ameliorate the proliferation and induces apoptosis in the highly differentiated spermatogenic cells causing its degeneration in the order of; sperms, spermatids, spermatocytes then spermatogonia.

Testicular sections of rats from GpIV revealed substantial +ve PCNA immunostaining in both abdominal and scrotal testes. However, this significant preservation of the proliferative capacity was still partial in the Cryp testes of GpIV as compared to the scrotal testes of the same group. This is in agreement with Yang et al. [37] who reported that human spermatogonial stem cells from cryptorchid patients can progressively differentiate into haploid spermatids when treated with the antioxidant retinoic acid and stem cell factor. Previous studies proved that antioxidants significantly increase the sperm count and germ cell count in cryptorchid rats [2, 3].

In addition to antioxidant role, it was indicated that curcumin enhances the proliferation, stemness and colony formation in dose dependent manner. In small doses, it increased the expression of marker proteins coupled with the cell growth, telomerase activity and stemness acting signalling pathways [19]. Furthermore, it was reported that curcumin is a favourable anticancer drug due to its beneficial induction of proliferation arrest and cell death in a variety of tumour cells through down-regulation of specific proteins [18]. According to the study of Cao et al. [8] Cur inhibited cancer cell proliferation and augmented apoptosis of osteoclastoma cells via repression of matrix metalloproteinase-9 and nuclear factor kappa beta, and stimulation of c-Jun N-terminal kinases signalling pathways. In addition to the study of Srivastava et al. [31], it synergistically modulated Wnt/beta-catenin signalling pathways and possessed anti-proliferative activity in multiple cancer cell lines. All these findings support the advantageous use of Cur in cryptorchidism, not only to enhance the stemness and proliferation of spermatogonia but also to protect against cancer development.

Vimentin immunohistochemistry in control rats illustrated +ve immunostaining of Sertoli cells basally with characteristic apical projections. Vimentin is an intermediate filament detected in mature Sertoli cells. Its distribution pattern is harmonic with its pivotal role in maintaining tissue integrity and preservation of spermatogenesis. It radiates apically in the cytoplasm to become attached with the specialized membrane junctions, desmosome-like junctions that connect germ cells with Sertoli cells [24].

Cryptorchid testes of GpIII showed substantial reduction in the vimentin immunostaining; mostly detected basally around nuclei of Sertoli cells indicating collapse of the vimentin intermediate filaments and their disorganization in the basal region of the Sertoli cells. The scrotal testes of the same rats revealed few apical vimentin immunostaining besides the perinuclear region denoting partial separation of vimentin away from the plasma membrane [13]. In agreement, Mohammed et al. [23] detected significant decrease of vimentin immunostaining in astaxanthin-induced-testicular damage. The damage was triggered by chronic stress through excessive production of free radicals.

It was reported that cytoskeleton, adherence proteins and cellular adhesion molecules functionally work inter-dependently rather than independently in the homeostasis of spermatogenic cellular junctions [10]. Besides, the disrupted inter-Sertoli germ cell junctions have been demonstrated to cross talk with the defective spermatogenesis in cryptorchidism [9]. On the other hand, the anchoring junction proteins are involved in the regulation of germ cell apoptosis. They can disrupt vimentin filaments at the site of Sertoli germ cell anchoring junction, thus inducing up-regulation surge of the testicular Fas-receptor with subsequent germ cell apoptosis [38].

In GpIV, the mean area per cent of vimentin immunostaining was significantly increased as compared to GpIII. However, the Cryp testes of GpIV displayed significant difference as compared to GpI and scrotal testes of GpIV. These findings signalize that curcumin is capable of preventing disaggregation of Sertoli germ cells contacts and spermatogenic cell apoptosis that was induced by hyperthermia [21].

Limitations of the study

The limitations of this work were the genetic and the hormonal factors that should be included in the estimation of curcumin on the unilateral cryptorchidism for upcoming clinical trials.

CONCLUSIONS

In conclusion, curcumin proved to be an important and effective medical line for protecting against the unfavourable sequels of cryptorchidism parallel to orcheopexy. It is one of the antioxidants that improve the fertility after surgery with potential role to protect against cancer transformation.

Conflict of interest: None declared

REFERENCES

1. Acikgoz A, Asci R, Aydin O, et al. The role of ketotifen in the prevention of testicular damage in rats with experimental unilateral undescended testes. Drug Des Devel Ther. 2014; 8: 2089–2097, doi: 10.2147/DDDT.S67941, indexed in Pubmed: 25364234.
2. Afeefy AA, Salah M, Amina MA. The role of vitamin E in reducing aluminum hydroxide effects on testes of albino rats: a histological and immunohistochemical study. IRJABS. 2016; 10(4): 369–379, doi: 10.7860/JCDR/2017/23927.9886.
3. Asadi N, Bahmani M, Kheradmand A, et al. The Impact of Oxidative Stress on Testicular Function and the Role of Antioxidants in Improving it: A Review. J Clin Diagn Res. 2017; 11(5): IE01–IE05, doi: 10.7860/JCDR/2017/23927.9886, indexed in Pubmed: 28658802.
4. Ateş F, Soydan H, Okçelik S, et al. Clinical and histopathological results of the adult patients with unilateral cryptorchidism. Turk J Urol. 2016; 42(2): 74–79, doi: 10.5152/tud.2016.47886, indexed in Pubmed: 27274891.
5. Aydin S, Baykus Y, Deniz R. Human chorionic gonadotropin levels of pregnant women can be an indicator of boys with cryptorchidism. Med Hypotheses. 2018; 114: 18, doi: 10.1016/j.mehy.2018.02.035, indexed in Pubmed: 29602455.
6. Azari O, Gholipour H, Kheirandish R, et al. Study of the protective effect of vitamin C on testicular tissue following experimental unilateral cryptorchidism in rats. Andrologia. 2014; 46(5): 495–503, doi: 10.1111/and.12106, indexed in Pubmed: 23635089.
7. Bae WJ, Ha US, Choi JB, et al. Protective effect of decursin extracted from angelica gigas in male infertility via Nrf2/HO-1 signaling pathway. Oxid Med Cell Longev. 2016; 2016: 5901098, doi: 10.1155/2016/5901098, indexed in Pubmed: 27034737.
8. Cao F, Liu T, Xu Y, et al. Curcumin inhibits cell proliferation and promotes apoptosis in human osteoclastoma cell through MMP-9, NF-kB and JNK signaling pathways. Int J Clin Exp Pathol. 2015; 8(6): 6037–6045, indexed in Pubmed: 26261481.
9. Chen J, Fok KL, Chen H, et al. Cryptorchidism-induced CFTR down-regulation results in disruption of testicular tight junctions through up-regulation of NF-kB/COX-2/PGE2. Hum Reprod. 2012; 27(9): 2585–2597, doi: 10.1093/humrep/des254, indexed in Pubmed: 22777528.

10. Cheng CY, Mruk DD. The blood-testis barrier and its implications for male contraception. Pharmacol Rev. 2012; 64(1): 16–64, doi: 10.1124/pr.110.002790, indexed in Pubmed: 22039149.
11. Chung E, Brock GB. Cryptorchidism and its impact on male fertility: a state of art review of current literature. Can Urol Assoc J. 2011; 5(3): 210–214, doi: 10.5489/cuaj.10106, indexed in Pubmed: 21672488.
12. Dutta S, Joshi KR, Sengupta P, et al. Unilateral and bilateral cryptorchidism and its effect on the testicular morphology, histology, accessory sex organs, and sperm count in laboratory mice. J Hum Reprod Sci. 2013; 6(2): 106–110, doi: 10.4103/0974-1208.117172, indexed in Pubmed: 24082651.
13. ElGhamrawy TA, Helmy D, Elall HFA. Cadherin and vimentin immunoexpression in the testis of normal and induced infertility models of albino rats. Folia Morphol. 2014; 73(3): 339–346, doi: 10.5603/FM.2014.0050, indexed in Pubmed: 25343410.
14. Fawzy F, Hussein A, Eid MM, et al. Cryptorchidism and Fertility. Clin Med Insights Reprod Health. 2015; 9: 39–43, doi: 10.4137/CMRH.S25056, indexed in Pubmed: 26740750.
15. Goel P, Rawat JD, Wakhlu A, et al. Undescended testicle: An update on fertility in cryptorchid men. Indian J Med Res. 2015; 141(2): 163–171, doi: 10.4103/0971-5916.155544, indexed in Pubmed: 25900951.
16. Hasanin NA, Sayed NM, Ghoneim FM, et al. Histological and Ultrastructure Study of the Testes of Acrylamide Exposed Adult Male Albino Rat and Evaluation of the Possible Protective Effect of Vitamin E Intake. J Microsc Ultrastruct. 2018; 6(1): 23–34, doi: 10.4103/JMAU.JMAU_7_18, indexed in Pubmed: 30023264.
17. Hutson JM, Li R, Southwell BR, et al. Germ cell development in the postnatal testis: the key to prevent malignancy in cryptorchidism? Front Endocrinol (Lausanne). 2012; 3: 176, doi: 10.3389/fendo.2012.00176, indexed in Pubmed: 23316184.
18. Jutooru I, Chadalapaka G, Lei P, et al. Inhibition of NFkappaB and pancreatic cancer cell and tumor growth by curcumin is dependent on specificity protein down-regulation. J Biol Chem. 2010; 285(33): 25332–25344, doi: 10.1074/jbc.M109.095240, indexed in Pubmed: 20538607.
19. Kim JH, Park SH, Nam SW, et al. Curcumin stimulates proliferation, stemness acting signals and migration of 3T3-L1 preadipocytes. Int J Mol Med. 2011; 28(3): 429–435, doi: 10.3892/ijmm.2011.680, indexed in Pubmed: 21519785.
20. Lin C, Choi YS, Park SGi, et al. Enhanced protective effects of combined treatment with beta-carotene and curcumin against hyperthermic spermatogenic disorders in mice. Biomed Res Int. 2016; 2016: 2572073, doi: 10.1155/2016/2572073, indexed in Pubmed: 28050551.
21. Lin C, Shin DG, Park SGi, et al. Curcumin dose-dependently improves spermatogenic disorders induced by scrotal heat stress in mice. Food Funct. 2015; 6(12): 3770–3777, doi: 10.1039/c5fo00726g, indexed in Pubmed: 26412282.
22. Liu F, Huang H, Xu ZL, et al. Germ cell removal after induction of cryptorchidism in adult rats. Tissue Cell. 2012; 44(5): 281–287, doi: 10.1016/j.tice.2012.04.005, indexed in Pubmed: 22832057.
23. Mohammed M, Elfadeel KA, Abdel-Aziz H, et al. The effect of chronic stress on the testis of adult albino Rats and the possible protective effect of astaxanthin supplementation (Histological, immunohistochemical and biochemical studies). J Med Histol. 2019; 2(2): 115–130, doi: 10.21608/jmh.2019.7416.1048.
24. Monleón E, Noya A, Carmen Garza Ma, et al. Effects of an anti-gonadotrophin releasing hormone vaccine on the morphology, structure and function of bull testes. Theriogenology. 2020; 141: 211–218, doi: 10.1016/j.theriogenology.2019.07.019, indexed in Pubmed: 31387698.
25. Moon JH, Yoo DY, Jo YK, et al. Unilateral cryptorchidism induces morphological changes of testes and hyperplasia of Sertoli cells in a dog. Lab Anim Res. 2014; 30(4): 185–189, doi: 10.5625/lar.2014.30.4.185, indexed in Pubmed: 25628730.
26. Morandi G, Cerbone M, Lamback EB, et al. 45,X/46,XY mosaicism presenting with isolated unilateral cryptorchidism and a normal blood karyotype. J Clin Endocrinol Metab. 2018; 103(6): 2079–2082, doi: 10.1210/jc.2017-02671, indexed in Pubmed: 29618062.
27. Morsi AA, Shawky LM, El Bana EA. The potential gonadoprotective effects of grape seed extract against the histopathological alterations elicited in an animal model of cadmium-induced testicular toxicity. Folia Morphol. 2020; 79(4): 767–776, doi: 10.5603/FM.a2020.0003, indexed in Pubmed: 31930466.
28. Portela JMD, Heckmann L, Wistuba J, et al. Development and disease-dependent dynamics of spermatogonial subpopulations in human testicular tissues. J Clin Med. 2020; 9(1): 224, doi: 10.3390/jcm9010224, indexed in Pubmed: 31947706.
29. Radmayr C, Dogan HS, Hoebeke P, et al. Management of undescended testes: European Association of Urology/European Society for Paediatric Urology Guidelines. J Pediatr Urol. 2016; 12(6): 335–343, doi: 10.1016/j.jpurol.2016.07.014, indexed in Pubmed: 27687532.
30. Rodprasert W, Virtanen HE, Mäkelä JA, et al. Hypogonadism and Cryptorchidism. Front Endocrinol (Lausanne). 2019; 10: 906, doi: 10.3389/fendo.2019.00906, indexed in Pubmed: 32010061.
31. Srivastava NS, Srivastava RA. Curcumin and quercetin synergistically inhibit cancer cell proliferation in multiple cancer cells and modulate Wnt/β-catenin signaling and apoptotic pathways in A375 cells. Phytomedicine. 2019; 52: 117–128, doi: 10.1016/j.phymed.2018.09.224, indexed in Pubmed: 30599890.
32. Tekayev M, Bostancieri N, Saadat KA, et al. Effects of Moringa oleifera Lam Extract (MOLE) in the heat shock protein 70 expression and germ cell apoptosis on experimentally induced cryptorchid testes of rats. Gene. 2019; 688: 140–150, doi: 10.1016/j.gene.2018.11.091, indexed in Pubmed: 30529510.
33. Trujillo J, Chirino YI, Molina-Jijón E, et al. Renoprotective effect of the antioxidant curcumin: Recent findings. Redox Biol. 2013; 1: 448–456, doi: 10.1016/j.redox.2013.09.003, indexed in Pubmed: 24191240.
34. Trujillo J, Granados-Castro LF, Zazueta C, et al. Mitochondria as a target in the therapeutic properties of curcumin. Arch Pharm (Weinheim). 2014; 347(12): 873–884, doi: 10.1002/ardp.201400266, indexed in Pubmed: 25243820.
35. Tsounapi P, Honda M, Dimitriadis F, et al. Post-fertilization effect of bilateral primary testicular damage induced by unilateral cryptorchidism in the rat model. Andrology. 2016; 4(2): 297––305, doi: 10.1111/andr.12154, indexed in Pubmed: 26757429.
36. Ueki M, Ueno M, Morishita J, et al. Curcumin ameliorates cisplatin-induced nephrotoxicity by inhibiting renal inflammation in mice. J Biosci Bioeng. 2013; 115(5): 547–551, doi: 10.1016/j.jbiosc.2012.11.007, indexed in Pubmed: 23245727.
37. Yang S, Ping P, Ma M, et al. Generation of haploid spermatids with fertilization and development capacity from human spermatogonial stem cells of cryptorchid patients. Stem Cell Reports. 2014; 3(4): 663–675, doi: 10.1016/j.stemcr.2014.08.004, indexed in Pubmed: 25358793.
38. Zhang S, Zeng Yi, Qu J, et al. Endogenous EGF maintains Sertoli germ cell anchoring junction integrity and is required for early recovery from acute testicular ischemia/reperfusion injury. Reproduction. 2013; 145(2): 177–189, doi: 10.1530/REP-12-0336, indexed in Pubmed: 23241343.

VIA MEDICA

ORIGINAL ARTICLE

Folia Morphol.
Vol. 80, No. 3, pp. 605–617
DOI: 10.5603/FM.a2020.0091

ISSN 0015–5659
eISSN 1644–3284
journals.viamedica.pl

Small intestinal mucosal cells in piglets fed with probiotic and zinc: a qualitative and quantitative microanatomical study

A. Kalita[1], M. Talukdar[2], K. Sarma[2], P.C. Kalita[1], P. Roychoudhury[3], G. Kalita[4], O.P. Choudhary[1], J.K. Chaudhary[5], P.J. Doley[1], S. Debroy[1]

[1]*Department of Veterinary Anatomy and Histology, College of Veterinary Sciences and Animal Husbandry, Central Agricultural University (I), Selesih, Mizoram, India*
[2]*Department of Veterinary Anatomy and Histology, College of Veterinary Science, Assam Agricultural University, Khanapara, Assam, India*
[3]*Department of Veterinary Microbiology, College of Veterinary Sciences and Animal Husbandry, Central Agricultural University (I), Selesih, Mizoram, India*
[4]*Department of Livestock Production and Management, College of Veterinary Sciences and Animal Husbandry, Central Agricultural University (I), Selesih, Mizoram, India*
[5]*Department of Animal Genetics and Breeding, College of Veterinary Sciences and Animal Husbandry, Central Agricultural University (I), Selesih, Mizoram, India*

[Received: 8 July 2020; Accepted: 25 July 2020; Early publication date: 7 August 2020]

Background: *Probiotics and zinc are commonly used and beneficial in pig production. This work aimed to assess the effects of probiotic and zinc on the mucosal cells of the small intestine in respect to digestive capacity and immunity in pre- and post-weaned piglets.*

Materials and methods: *Eighteen Large White Yorkshire piglets were divided equally into control and treatment groups. The piglets were maintained in standard management conditions and were weaned at 28 days of age. The treatment group of piglets fed a mixture of probiotics orally at 1.25×10^9 CFU/day and zinc at 2000 ppm/day from birth to 10 days of age. At three different age-groups viz. day 20 (pre-weaning) and, day 30 and day 60 (post-weaning), the animals were sacrificed. For histomorphology, the tissue samples were processed and stained with Mayer's haematoxylin and eosin for routine study, combined periodic acid-Schiff-Alcian blue for mucopolysaccharides and Masson-Hamperl argentaffin technique for argentaffin cells. The stained slides were observed under the microscope. The samples were processed as per the standard procedure for scanning and transmission electron microscopy. The statistical analysis of the data using the appropriate statistical tests was also conducted.*

Results: *The mucosal epithelium of villi and crypts were lined by enterocytes, goblet cells, argentaffin cells, microfold (M-cell) cells, tuft cells and intraepithelial lymphocytes. The multipotent stem cells were located at the crypt base. The length of the enterocyte microvilli was significantly longer ($p < 0.05$) in the treatment group of piglets. The number of different types of goblet cells and argentaffin cells was more in treated piglets irrespective of segments of intestine and age. The intraepithelial lymphocytes were located in apical, nuclear and basal positions in the lining epithelium of both villus tip and base with their significant increase*

Address for correspondence: Dr. A. Kalita, Department of Veterinary Anatomy and Histology, College of Veterinary Sciences and Animal Husbandry, Central Agricultural University (I), Selesih, Aizawl-796015, Mizoram, India, tel: +91 7002560035, e-mail: arup.kalita@gmail.com

in the treatment group of piglets. The transmission electron microscopy revealed the frequent occurrence of tuft cells in the lining mucosa of the small intestine in treated piglets.

Conclusions: *Dietary supplementation of probiotic and zinc induced the number of different mucosal cells of villi and crypts in the small intestine that might suggest the greater absorptive capacity of nutrients and effective immunity in critical pre and post-weaned piglets.* (Folia Morphol 2021; 80, 3: 605–617)

Key words: probiotic, zinc, lining cells, small intestine, piglets

INTRODUCTION

Piglets during the suckling period, exposed to a variety of stresses. Weaning stress in piglets is the major cause for economic loss to pig farmers [52]. The weaned piglets have limited digestive capacity that might trigger fermentation of undigested protein by opportunistic pathogens residing in the gastrointestinal tract results in diarrhoea [20, 30]. In pig production, diarrhoea has been one of the most frequently encountered clinical signs of disease in neonatal pigs [1]. Enteric diseases in newborn piglets are estimated to account for 5–24% of the overall pre-weaning mortality [51]. The economic impact of such high death rates is huge. The immunology of the porcine intestinal tract is important to resist the piglets from disease, which may lead to retarded growth and death.

There has been considerable interest in using some probiotic microorganisms and antioxidants in feeds. Probiotics are viable microorganisms and supportive substances that, once ingested by animals, produce beneficial physiology effects by assisting in the establishment of an intestinal population, which is beneficial to the host entity and antagonistic to harmful bacteria.

Zinc is an important trace element that is naturally present in the feed and involved in various physiological functions. Feeding supplemental zinc in the form of zinc oxide to nursery pigs has decreased the incidence of nonspecific post-weaning diarrhoea [40]. Zinc is virtually present in all body tissues, but only a small amount is stored in the body. Zinc can immediately be mobilised if the intake of the element is reduced or too low. Therefore, daily consumption of sufficient zinc is necessary, as the body can only compensate for a minimal extent by the use of internal zinc pools for even a short temporary deficiency [6].

There is a paucity of available literature regarding the effects of probiotic and zinc in the cellular structure of intestinal epithelium in pre and post-weaned piglets. Therefore, the present study was undertaken to evaluate and compare the combined effects of probiotic and zinc on different mucosal cells of villi and crypts of the small intestine in the control and treatment group of piglets that are responsible for digestive capacity and immunity in critical pre and post-weaned periods.

MATERIALS AND METHODS

Animals

Eighteen healthy Large White Yorkshire (LWY) piglets, irrespective of sex obtained from three sows, were utilised for the study. Care and management of the animals were provided in Instructional Pig Farm, College of Veterinary Sciences and Animal Husbandry, Central Agricultural University (I), Selesih, Aizawl, Mizoram, India. The Institutional Animal Ethics Committee (IAEC) ethically approved the animals used for the experiment vide Approval No. 770/ac/CPCSEA/ /FVSc/AAU/IAEC/17-18/490 dated 09.08.2017.

Selection, dose and period of treatment

A mixture of probiotic consisted of *Lactobacillus acidophilus* (650 million), *Lactobacillus rhamnosus* (400 million) and *Bifidobacterium longum* (200 million) was orally administered to the treatment group of piglets at 1.25×10^9 CFU/day from birth to 10 days of age [35]. The zinc oxide was given orally to the treatment group of piglets at 2000 ppm/day from birth to 10 days of age [8]. The piglets of the control group were given the same volume of sterilised saline solution.

Experimental design

Each of 6 numbers of piglets was selected from 3 sows at different stages of development as age-group of 20, 30 and 60 days. Out of the 6 piglets, 3 piglets from each litter were used as the control group (C) with basal diet and the other 3 piglets were fed orally with combined probiotic and zinc supplement along with the basal diet and used as treatment group (T). The basal diet used in this experiment was in pellet form and was formulated to provide the nutrient requirements [38]. The piglets were weaned at 28 days of age.

Sample preparation

The experimental animals were first anesthetised using diazepam at 2 mg/kg body weight followed by ketamine at 10 mg/kg body weight intravenously and then exsanguinated the animals. The animals were sacrificed at day 20, 30 and 60 from both the groups. After sacrifice, the abdominal cavity of the animal was opened and parts of the small intestine were observed [24]. Tissue samples were taken immediately after sacrifice from the duodenum (5 cm caudal to the pylorus), jejunum (In the middle of the jejunum) and ileum (5 cm cranial to the ileocaecal valve).

Preparation for light microscopic examination

For histomorphology, the tissue samples (0.5 cm) from each location were fixed in 10% neutral buffered formalin for 24 to 48 hours. All the tissues were dehydrated, cleared and embedded in paraffin wax as per Luna [36]. The paraffin blocks were sectioned at 5 μm thicknesses, dried in room temperature overnight and stained with Mayer's haematoxylin and eosin for routine study [36], combined periodic acid-Schiff-Alcian blue (PAS-AB) for mucopolysaccharides [37] and Masson-Hamperl argentaffin technique for argentaffin cells [47]. The stained slides were visualised in Olympus BX 51 microscope and the images were captured with a ProgRes C5 Cool CCD camera.

Preparation for electron microscopic examination

For transmission electron microscopy (TEM) and scanning electron microscopy (SEM), the tissue samples were cut into small pieces of 1–2 mm size and were fixed in Karnovsky's fixative (2.5% glutaraldehyde in 0.1 M sodium cacodylate buffer at pH 7.2) for 4 hours at 4°C. After washing in 0.1 M buffer (3 changes of 15 min each), the samples were fixed in 0.2 M sodium cacodylate buffer till further use. The processing of samples for SEM was done as per Skrzypek et al. [48]. The viewing of the samples was carried out with a Zeiss SEM operated at 20 kV at the Institute of Advanced Study in Science and Technology (IASST), Guwahati, Assam. The processing of samples for TEM was done at the Sophisticated Analytical Instrument Facility (SAIF), North-Eastern Hill University (NEHU), Shillong as per the standard method [39]. The semi-thin sections were cut with an ultramicrotome at 400 nm thicknesses and stained with toluidine blue before making the ultra-thin sections. Ultra-thin sections were made at 50 nm thicknesses with an ultramicrotome, mounted on copper grids and contrasted with uranyl acetate and lead citrate. The viewing of the sections was carried out with Joel (JEM-2100) TEM operated at 120 kV at SAIF, NEHU, Shillong, Meghalaya.

Statistical analysis

The data obtained were analysed using statistical package SPSS version 20. General Linear Model of two way ANOVA based on Fisher's least significant difference method was used to determine the significant difference among days (20, 30 and 60 days) for control and treatment groups. The significant values in the ANOVA were further tested through the Duncan multiple range test. The obtained results were presented as mean ± SEM and differences were considered significant when $p < 0.05$. An independent sample t-test has been applied between groups (control and treatment) on different days to see the significant changes.

RESULTS

The mucosal epithelium of villi and crypts of the small intestine was covered by lining cells consisting of enterocytes, goblet cells, enteroendocrine (argentaffin) cells, microfold (M-cell) cells, tuft cells and intraepithelial lymphocytes (IEL). In addition, multipotent stem cells were located at the crypt base irrespective of the group of piglets and age.

The enterocytes were simple columnar cells with basally located nuclei in villi (Fig. 1A) and crypts (Fig. 1B). The enterocyte microvilli were significantly higher ($p < 0.05$) in the treated piglets (Fig. 1C) than the control animals (Fig. 1D) in jejunum and ileum at day 30 and day 60. An abundance of mitochondria, Golgi bodies, rough endoplasmic reticulum (ER), and lysosomes were observed in the enterocyte cytoplasm in treated piglets (Fig. 1E) than the control group of animals (Fig. 1F).

The goblet cells were located in the epithelial layer of villi (Fig. 2A) and crypts (Fig. 2B). The apical portion was distended by abundant mucus laden granules (Fig. 2C) and the basal portion shaped like a stem (Fig. 2D). Numerous rough endoplasmic reticulum,

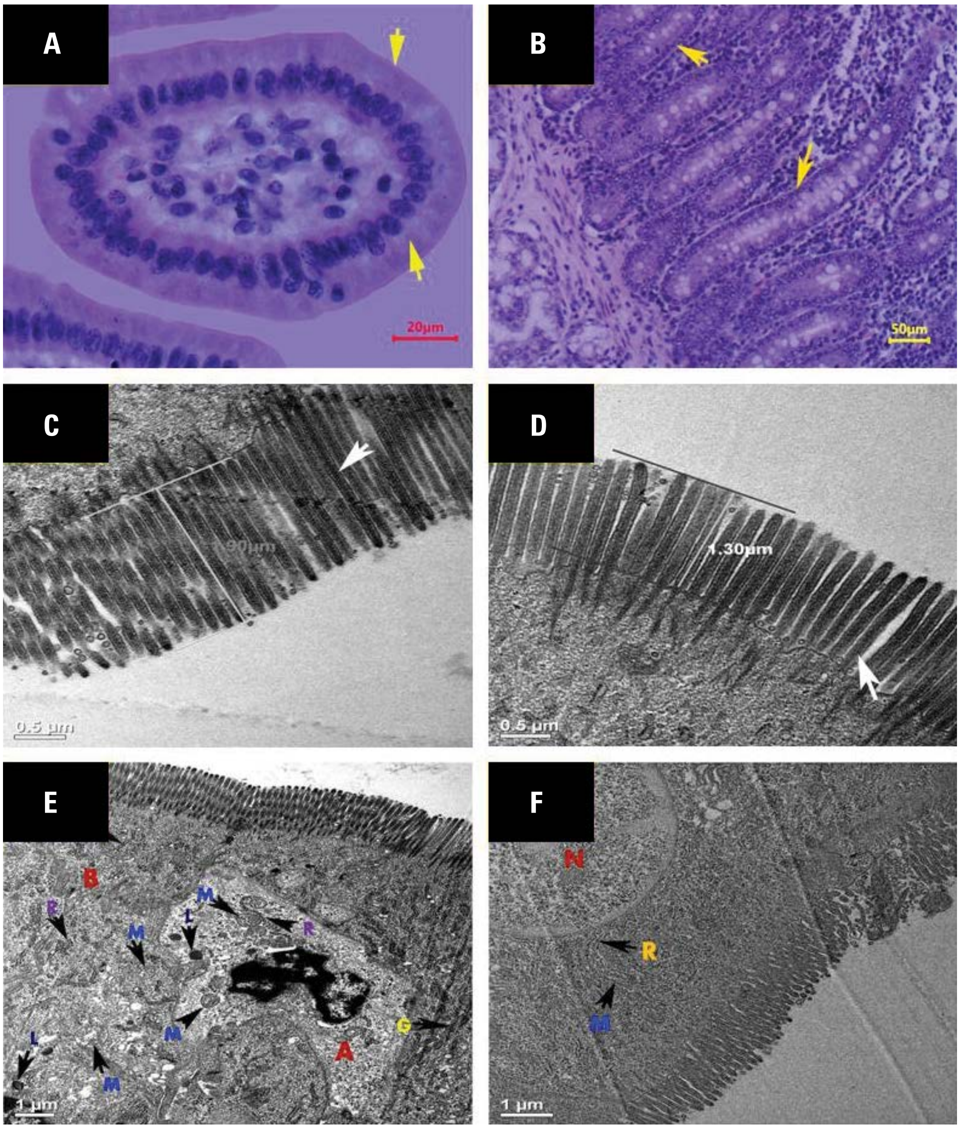

Figure 1. Enterocytes. **A.** Photomicrograph showing basally located nuclei (arrow) in duodenal villi of 20 days old treated piglet (H&E, ×400); **B.** Photomicrograph showing basally located nuclei (arrow) in jejunal crypts of 60 days old treated piglet (H&E, ×100); **C.** Transmission electron microscopy (TEM) micrograph showing longer microvilli (arrow) in the jejunum of 60 days old treated piglet; **D.** TEM micrograph showing shorter microvilli (arrow) in the jejunum of 60 days old control piglet; **E.** TEM micrograph showing macrophage (A) and enterocyte (B) with an abundance of mitochondria (M), rough endoplasmic reticulum (R), lysosomes (L) and Golgi bodies (G) in the jejunum of 60 days old treated piglet; **F.** TEM micrograph showing nucleus (N) and inadequacy of mitochondria (M) and rough endoplasmic reticulum (R) in the jejunum of 60 days old control piglet.

mitochondria and secretory vesicles were recorded in the goblet cells of treated piglets (Fig. 2E). PAS-AB sequential staining showed neutral, acidic and mixed neutral-acidic mucin goblet cells (Fig. 2F), irrespective of group and age. In most segments of the small intestine in treated piglets, the mixed, neutral and acidic mucin goblet cells were significantly higher both in the villi and crypts at different age-groups than the control group of animals (Table 1).

The argentaffin cells were scattered singly in villi (Fig. 3A) and crypts (Fig. 3B) among other cells within the lining epithelium. Their populations were more in the crypts than villi (Fig. 3C) in both the groups of all ages. They had a narrow apex, wide base and contained many small, spheroidal, electron-dense granules (Fig. 3D). In duodenum at day 60, the number of argentaffin cells was significantly higher in villi ($p < 0.05$) and crypts ($p < 0.01$) in the treatment group of piglets (Table 2).

The M-cells were mostly found in the follicle associated epithelium of Peyer's patches in jejunum and ileum. They had less developed brush border with

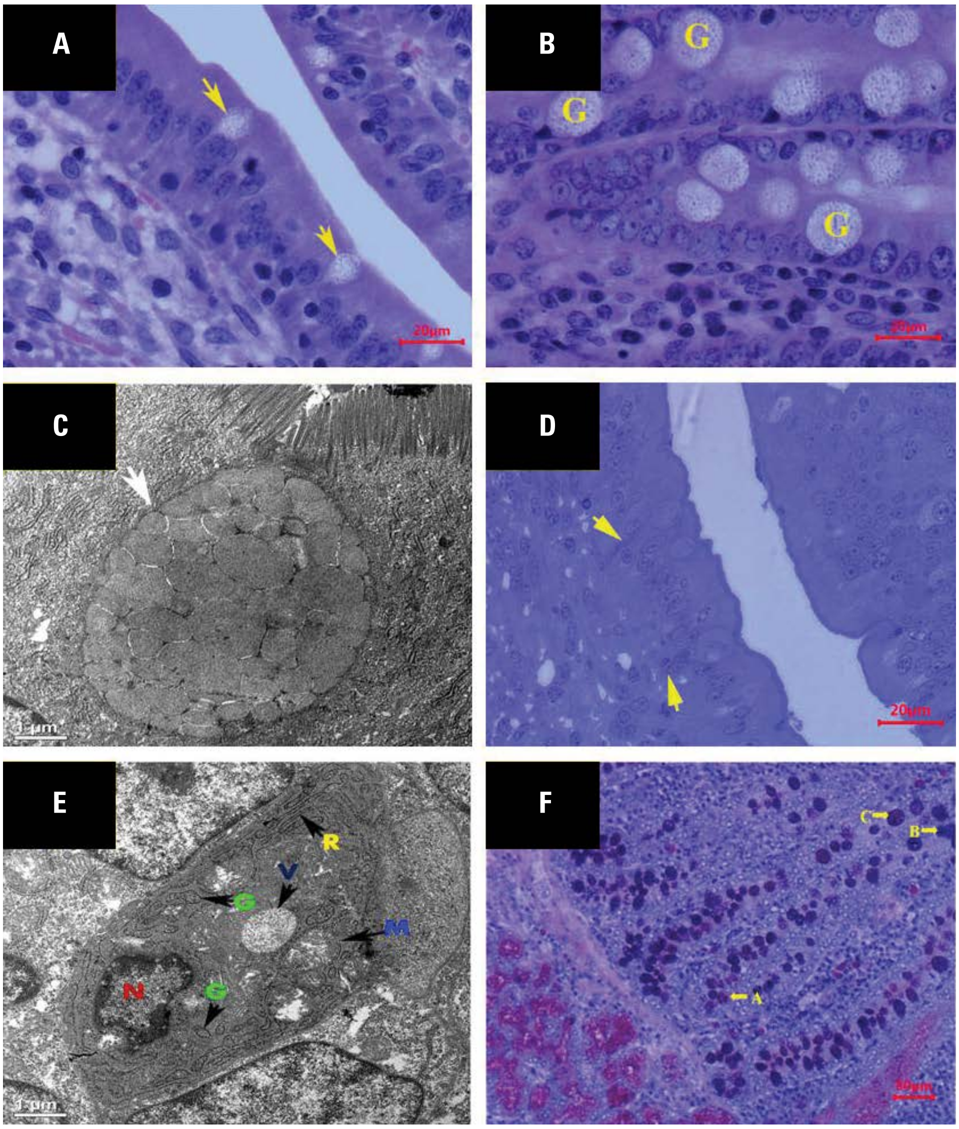

Figure 2. Goblet cells. **A, B.** Photomicrographs showing goblet cells in villus epithelium (arrow) and crypt epithelium (G) in the duodenum of 60 days old treated piglet (H&E, ×400); **C.** Transmission electron microscopy (TEM) micrograph of goblet cell showing abundant mucous laden granules in the ileum of 60 days old treated piglet; **D.** Photomicrograph of the semi-thin section showing goblet cells with distended apical portion and stem-like basal portion (arrow) in the jejunum of 60 days old treated piglet (toluidine-blue, ×400); **E.** TEM micrograph of goblet cell showing mitochondria (M), Golgi bodies (G), rough endoplasmic reticulum (R), nucleus (N) and secretory vesicles (V) in the ileum of 60 days old treated piglet; **F.** Photomicrograph showing neutral (A), acidic (B) and mixed (C) mucins goblet cells in the jejunum of 60 days old treated piglet (AB-PAS, ×100).

irregular microvilli (Fig. 4A) and basolateral indentations or pockets for transportation of antigens and microbes across intestinal epithelium (Fig. 4B). The cytoplasm of villus M-cells was less electron-dense (Fig. 4C) that contained few secretory granules and lysosomes, rich in mitochondria and numerous small vesicles (Fig. 4D).

Under TEM, the mucosal epithelium of the small intestine showed tuft cell in between the enterocytes (Fig. 5). These pear-shaped cells had a broad base, narrow apex, and a "tuft" of microvilli projecting into the lumen. In this study, these cells were encountered more in the duodenum than jejunum and ileum. The frequent occurrences of tuft cells were noted in the treatment group of piglets in comparison to the control group of animals.

The IELs were unevenly distributed at apical, nuclear and basal positions in the lining mucosa of the small intestine (Fig. 6A) in both the groups. In most of the segments of the intestine, the number of IEL population was significantly higher in the treatment group of piglets both in the villus tip and base (Table 3). The treatment group of piglets had a significantly

Table 1. Numbers of Alcian blue-periodic acid Schiff (AB-PAS) positive goblet cells in the small intestine of piglets fed with probiotic and zinc

Parameter	Intestinal segment	Pre-weaning		Post-weaning				P-value	
		Day 20		Day 30		Day 60			
		Control	Treatment	Control	Treatment	Control	Treatment	Control	Treatment
Villus neutral per 200 μm	Duodenum	0.33 ± 0.11^{ap}	0.87 ± 0.13^{q}	0.73 ± 0.19^{ab}	1.03 ± 0.29	0.87 ± 0.21^{b}	1.20 ± 0.19	0.08	0.55
	Jejunum	0.57 ± 0.16^{a}	0.97 ± 0.15^{d}	0.93 ± 0.16^{ab}	1.33 ± 0.13^{de}	1.10 ± 0.15^{b}	1.60 ± 0.28^{e}	0.05	0.08
	Ileum	0.67 ± 0.12^{a}	1.07 ± 0.18^{d}	1.03 ± 0.20^{ab}	1.50 ± 0.18^{de}	1.23 ± 0.23^{br}	1.93 ± 0.26^{es}	0.10	0.02
Villus acidic per 200 μm	Duodenum	0.23 ± 0.09^{ar}	0.73 ± 0.19^{s}	0.70 ± 0.19^{b}	0.93 ± 0.21	0.80 ± 0.17^{b}	1.07 ± 0.25	0.03	0.55
	Jejunum	0.47 ± 0.12	0.87 ± 0.18	0.80 ± 0.24	1.20 ± 0.22	0.93 ± 0.21	1.50 ± 0.26	0.22	0.14
	Ileum	0.47 ± 0.12^{ar}	0.87 ± 0.15^{s}	0.93 ± 0.17^{ab}	1.43 ± 0.29	1.10 ± 0.27^{b}	1.80 ± 0.46	0.07	0.13
Villus mixed per 200 μm	Duodenum	2.83 ± 0.29	2.90 ± 0.28^{D}	2.90 ± 0.27	3.03 ± 0.34^{D}	3.40 ± 0.43^{p}	4.97 ± 0.38^{Eq}	0.44	0.001
	Jejunum	2.97 ± 0.36	3.57 ± 0.34^{D}	3.57 ± 0.42^{r}	4.77 ± 0.30^{Es}	3.73 ± 0.34^{p}	5.17 ± 0.31^{Eq}	0.32	0.002
	Ileum	3.0 ± 0.24	3.70 ± 0.32^{D}	3.77 ± 0.42^{r}	5.03 ± 0.25^{Es}	3.93 ± 0.34^{p}	5.57 ± 0.27^{Eq}	0.12	0.001
Villus total per 200 μm	Duodenum	3.40 ± 0.29^{Ar}	4.50 ± 0.37^{Ds}	4.33 ± 0.35^{AB}	5.0 ± 0.36^{D}	5.07 ± 0.45^{Bp}	7.23 ± 0.49^{Eq}	0.01	0.001
	Jejunum	4.0 ± 0.45^{ar}	5.40 ± 0.41^{Ds}	5.30 ± 0.47^{bp}	7.30 ± 0.36^{Eq}	5.77 ± 0.39^{bp}	8.27 ± 0.47^{Eq}	0.02	0.001
	Ileum	4.13 ± 0.32^{p}	5.63 ± 0.34^{Dq}	5.73 ± 0.54^{p}	7.97 ± 0.39^{Eq}	6.27 ± 0.46^{p}	9.30 ± 0.53^{Fq}	0.003	0.001
Crypt neutral per 200 μm	Duodenum	0.50 ± 0.15^{a}	0.93 ± 0.17^{D}	0.83 ± 0.19^{ab}	1.23 ± 0.22^{D}	1.30 ± 0.25^{b}	2.0 ± 0.32^{E}	0.02	0.009
	Jejunum	0.77 ± 0.17^{ap}	1.43 ± 0.18^{dq}	1.13 ± 0.21^{abr}	1.77 ± 0.15^{des}	1.60 ± 0.28^{b}	2.13 ± 0.32^{e}	0.04	0.11
	Ileum	0.80 ± 0.24^{r}	1.47 ± 0.23^{ds}	1.23 ± 0.20	1.83 ± 0.27^{de}	1.40 ± 0.24^{r}	2.33 ± 0.29^{es}	0.16	0.07
Crypt acidic per 200 μm	Duodenum	0.20 ± 0.12^{Ap}	0.67 ± 0.12^{q}	0.63 ± 0.14^{B}	0.87 ± 0.15	0.77 ± 0.12^{B}	0.93 ± 0.18	0.01	0.44
	Jejunum	0.30 ± 0.09^{Ap}	0.77 ± 0.15^{dq}	0.73 ± 0.14^{B}	1.07 ± 0.17^{de}	0.87 ± 0.12^{Br}	1.47 ± 0.19^{es}	0.003	0.02
	Ileum	0.47 ± 0.10^{ar}	0.83 ± 0.16^{Ds}	0.83 ± 0.20^{ab}	1.37 ± 0.19^{E}	1.0 ± 0.21^{br}	1.63 ± 0.19^{Es}	0.10	0.006
Crypt mixed per 200 μm	Duodenum	4.30 ± 0.34	4.63 ± 0.37^{d}	4.40 ± 0.28	4.77 ± 0.42^{de}	4.73 ± 0.36^{r}	5.90 ± 0.42^{es}	0.62	0.06
	Jejunum	4.43 ± 0.37	4.73 ± 0.34^{d}	4.50 ± 0.48	5.40 ± 0.39^{de}	4.83 ± 0.40^{r}	6.0 ± 0.42^{es}	0.77	0.07
	Ileum	4.73 ± 0.46	5.0 ± 0.38	4.80 ± 0.32	5.60 ± 0.52	5.10 ± 0.44	6.20 ± 0.38	0.80	0.15
Crypt total per 200 μm	Duodenum	5.0 ± 0.37^{Ar}	6.23 ± 0.44^{Ds}	5.87 ± 0.38^{AB}	6.87 ± 0.46^{D}	6.80 ± 0.43^{Bp}	8.83 ± 0.60^{Eq}	0.01	0.001
	Jejunum	5.50 ± 0.32^{ap}	6.93 ± 0.41^{Dq}	6.37 ± 0.57^{abr}	8.23 ± 0.47^{DEs}	7.30 ± 0.57^{bp}	9.60 ± 0.59^{Eq}	0.04	0.001
	Ileum	6.0 ± 0.54	7.30 ± 0.51^{D}	6.87 ± 0.46^{r}	8.80 ± 0.60^{DEs}	7.50 ± 0.56^{p}	10.17 ± 0.49^{Eq}	0.13	0.001

Data are presented as goblet cells/200 μm (mean ± scanning electron microscopy) in different age-groups.
$^{A, B}$Means with different superscripts between control groups significantly differ ($p < 0.01$);
$^{D, E, F}$Means with different superscripts between treatment groups significantly differ ($p < 0.01$);
^{a,b}Means with different superscripts between control groups significantly differ ($p < 0.05$);
^{d,e}Means with different superscripts between treatment groups significantly differ ($p < 0.05$);
^{p,q}Means with different superscripts within groups significantly differ ($p < 0.01$);
^{r,s}Means with different superscripts within groups significantly differ ($p < 0.05$).

higher number of basally located IEL (Fig. 6B) followed by nuclear level both in villus tip and base at different age-groups.

At the bases of the crypts, TEM analysis revealed the presence of crypt base columnar (CBC) stem cells, goblet cells, enteroendocrine cells and absorptive enterocytes in all segments of the small intestine (Fig. 7). The stem cells were irregularly shaped, small, columnar cells with basally located nuclei and scarce cytoplasm. They were found in between the goblet cells, enterocytes or enteroendocrine cells in piglets. The CBC stem cells could be differentiated from the mature absorptive enterocytes with their irregular columnar cells containing uneven elongated nuclei in between the goblet cells (Fig. 7).

DISCUSSION

The results of the current study revealed that treatment with probiotic and zinc significantly increased ($p < 0.05$) the length of microvilli in jejunum and ileum at day 30 and day 60 in post-weaned piglets. This might be showing the greater surface area, which could attribute more absorption of nutrients by the small intestine in piglets fed with probiotic and zinc. The comparison of the present finding could not be discussed with the available literature due to the

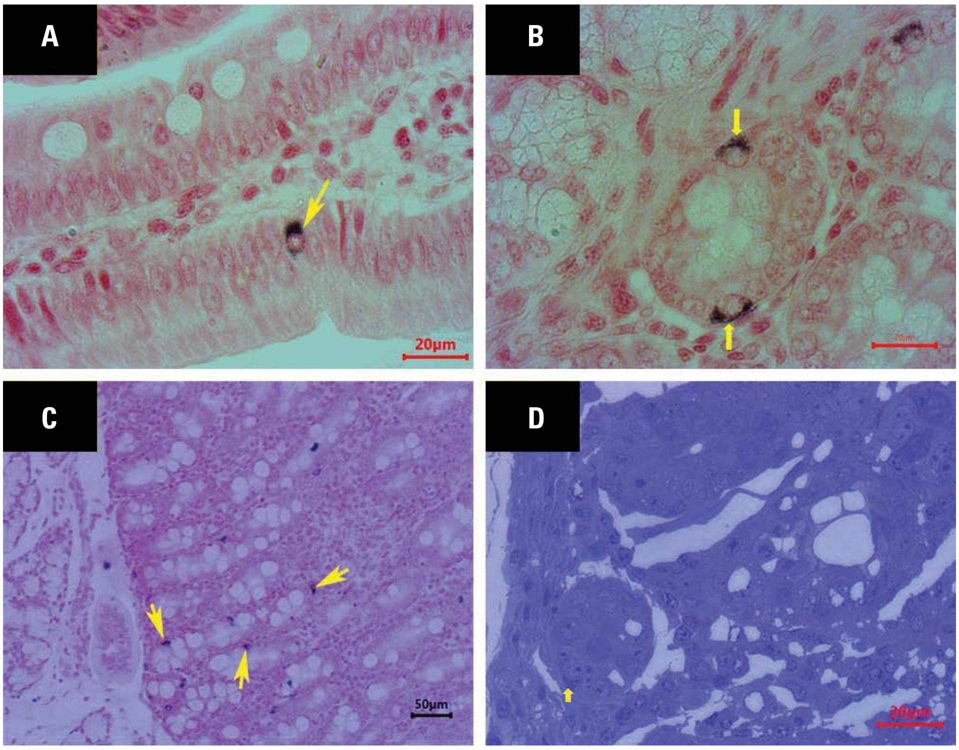

Figure 3. Photomicrographs of argentaffin cells. **A, B.** Argentaffin cells (arrow) in the villus and crypt epithelium of duodenum in 20 days old treated piglet (H&E, ×100); **C.** Abundant numbers of argentaffin cells (arrow) in the crypts of the duodenum of 30 days old treated piglet (H&E, ×100); **D.** Semi-thin section showing argentaffin cells (arrow) in the crypts of jejunum in 30 days old treated piglet (toluidine blue, ×400).

Table 2. Numbers of argentaffin cells in the small intestine of piglets fed with probiotic and zinc

Parameter	Intestinal segment	Pre-weaning		Post-weaning				P-value	
		Day 20		Day 30		Day 60			
		Control	Treatment	Control	Treatment	Control	Treatment	Control	Treatment
Villus argentaffin cell	Duodenum	0.40 ± 0.10	0.47 ± 0.10^{A}	0.43 ± 0.09	0.60 ± 0.10^{A}	0.53 ± 0.13^{r}	1.0 ± 0.16^{Bs}	0.68	0.009
	Jejunum	0.50 ± 0.13	0.77 ± 0.18	0.50 ± 0.12	0.67 ± 0.11	0.53 ± 0.10	0.60 ± 0.14	0.97	0.72
	Ileum	0.33 ± 0.13	0.43 ± 0.09	0.50 ± 0.09	0.63 ± 0.11	0.57 ± 0.11	0.70 ± 0.12	0.33	0.20
Crypt argentaffin cell	Duodenum	1.27 ± 0.10	1.40 ± 0.11^{A}	1.33 ± 0.10	1.53 ± 0.09^{A}	1.43 ± 0.11^{p}	2.03 ± 0.16^{Bq}	0.52	0.002
	Jejunum	1.40 ± 0.13	1.53 ± 0.14	1.40 ± 0.12	1.60 ± 0.17	1.43 ± 0.16	1.67 ± 0.15	0.98	0.83
	Ileum	0.80 ± 0.12	1.07 ± 0.13	0.90 ± 0.12	1.17 ± 0.14	1.0 ± 0.15	1.27 ± 0.14	0.57	0.57

Data are presented as the argentaffin cells/0.24 mm^2 area (mean ± scanning electron microscopy) in different age-groups.
$^{A, B}$Means with different superscripts between treatment groups significantly differ ($p < 0.01$);
^{p,q}Means with different superscripts within groups significantly differ ($p < 0.01$);
^{r,s}Means with different superscripts within groups significantly differ ($p < 0.05$).

dearth of information in this regard. In the current study, the electron microscopy studies confirmed the high activation of enterocytes after dietary inclusion of probiotic and zinc in pre- and post-weaned piglets as compared to the control group. This finding might indicate that probiotic and zinc interacted and activated the intestinal epithelial cells (IECs), which could improve their functions and activate the immune cells present in the small intestine. This fact is in line with previous reports where probiotic strains interact and activate the intestinal epithelial cells [21, 32].

Goblet cells containing different mucins acted as an innate defence mechanism, acting as a diffusion barrier and providing a microecological barrier in the gut [33]. Acid glycoconjugates especially helped the intestinal mucosa to counteract microorganisms and resisted bacterial enzymes [16]. The secretion of mucous from goblet cells was also affected by wean-

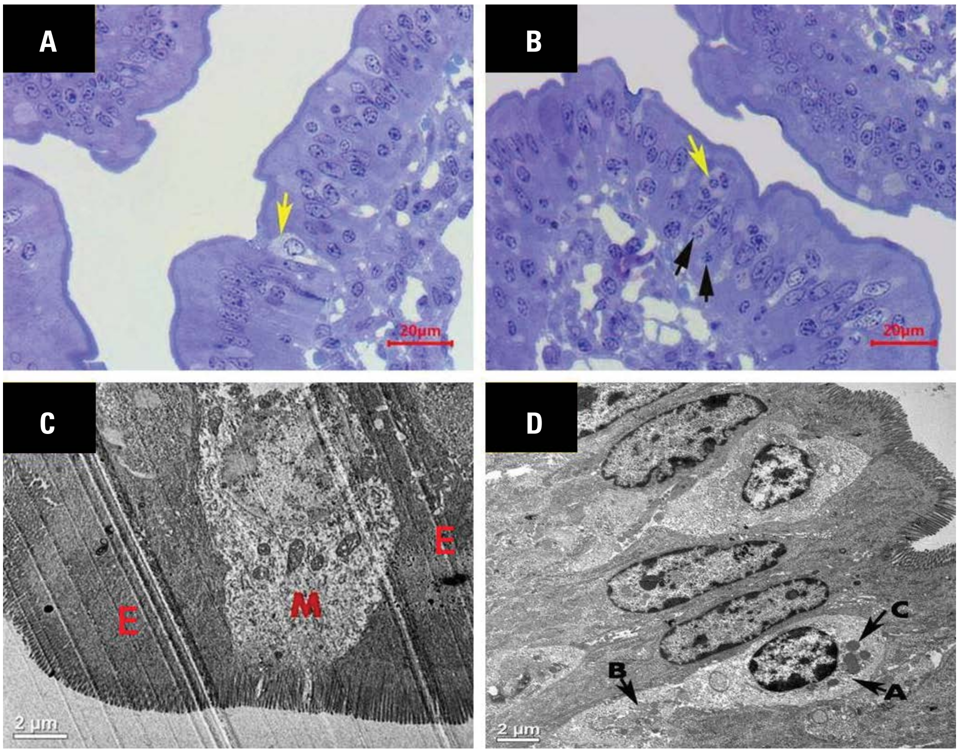

Figure 4. Photomicrographs of M-cells. **A.** Semi-thin section showing M-cell with irregular microvilli (arrow) in 60 days old treated piglet (toluidine-blue, ×400); **B.** Semi-thin section showing M-cell with basolateral pockets (yellow arrow) and trapped antigens (black arrow) in 30 days old treated piglet (toluidine-blue, ×400); **C.** Transmission electron microscopy (TEM) micrograph showing less electron-dense M-cell (M) adjacent to enterocytes (E) in 30 days old treated piglet; **D.** TEM micrograph of M-cell containing small vesicles (A), mitochondria (B) and lysosomes (C) in 30 days old treated piglet.

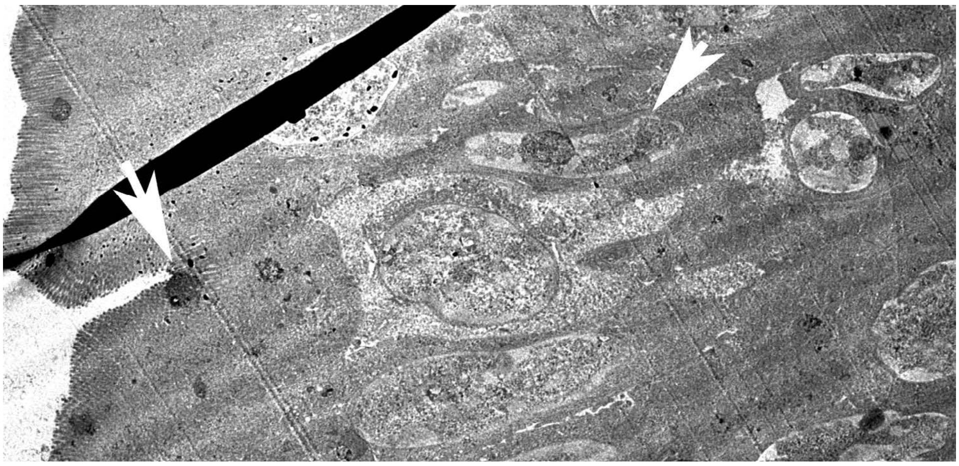

Figure 5. Transmission electron microscopy micrograph showing pear-shaped, wide base and narrow apex tuft cell containing tuft (arrow) in the jejunum of 30 days old treated piglet.

ing and age of the animals [11], the composition of intestinal microbiota [12], and dietary treatment [27]. In our study, the goblet cells were observed both in the villi and crypts of the small intestine as reported by Liu et al. [34] in piglet. These cells appeared as an accumulation of mucous granules with a stem-like basal portion. Similar type of observation was also recorded by Hodges and Dartt [28] in the conjunctiva of eye. In the current study, the number of goblet cells with different mucins increased significantly in most of the segments of the small intestine at different age-groups of treated piglets as compared to the control

Table 3. Numbers of intraepithelial lymphocytes (IEL) in the small intestine in piglets fed with probiotic and zinc

Parameter	Intestinal segment	Pre-weaning		Post-weaning				P-value	
		Day 20		Day 30		Day 60			
		Control	Treatment	Control	Treatment	Control	Treatment	Control	Treatment
Apical IEL villus tip per 100 μm	Duodenum	1.57 ± 0.21	1.63 ± 0.21^{D}	1.90 ± 0.26^{p}	3.17 ± 0.25^{Eq}	2.13 ± 0.26	2.30 ± 0.19^{F}	0.26	0.001
	Jejunum	1.47 ± 0.29^{a}	1.27 ± 0.24^{de}	0.87 ± 0.17^{abp}	1.60 ± 0.19^{dq}	0.73 ± 0.16^{b}	0.90 ± 0.12^{e}	0.04	0.04
	Ileum	0.97 ± 0.19^{a}	0.87 ± 0.17^{d}	0.60 ± 0.13^{ab}	0.73 ± 0.14^{de}	0.47 ± 0.12^{b}	0.37 ± 0.11^{e}	0.05	0.04
Nuclear IEL villus tip per 100 μm	Duodenum	1.27 ± 0.16^{A}	1.37 ± 0.17^{d}	2.30 ± 0.26^{B}	2.07 ± 0.17^{e}	2.17 ± 0.17^{B}	1.90 ± 0.20^{e}	0.001	0.02
	Jejunum	0.97 ± 0.19^{Ap}	3.13 ± 0.26^{dq}	2.10 ± 0.24^{B}	2.07 ± 0.30^{e}	1.17 ± 0.19^{Ap}	2.80 ± 0.34^{deq}	0.001	0.05
	Ileum	1.67 ± 0.21^{ar}	1.0 ± 0.15^{Ds}	1.73 ± 0.21^{a}	1.80 ± 0.20^{E}	1.07 ± 0.17^{b}	1.40 ± 0.19^{DE}	0.04	0.01
Basal IEL villus tip per 100 μm	Duodenum	2.20 ± 0.19^{A}	2.47 ± 0.18^{D}	2.77 ± 0.18^{AB}	3.30 ± 0.32^{E}	3.40 ± 0.29^{Br}	4.30 ± 0.25^{Fs}	0.001	0.001
	Jejunum	1.10 ± 0.18^{A}	1.67 ± 0.23	1.60 ± 0.20^{Ar}	2.30 ± 0.23^{s}	2.73 ± 0.29^{Bp}	1.73 ± 0.19^{q}	0.001	0.08
	Ileum	2.07 ± 0.27^{Ar}	3.27 ± 0.43^{DEs}	2.50 ± 0.19^{A}	2.63 ± 0.18^{D}	3.77 ± 0.24^{B}	3.93 ± 0.21^{E}	0.001	0.01
Total IEL villus tip per 100 μm	Duodenum	5.03 ± 0.32^{A}	5.47 ± 0.29^{D}	6.97 ± 0.40^{Bp}	8.53 ± 0.33^{Eq}	7.70 ± 0.33^{B}	8.50 ± 0.31^{E}	0.001	0.001
	Jejunum	3.53 ± 0.23^{ap}	6.07 ± 0.40^{q}	4.57 ± 0.35^{bp}	5.97 ± 0.33^{q}	4.63 ± 0.36^{b}	5.43 ± 0.27	0.03	0.36
	Ileum	4.70 ± 0.25	5.13 ± 0.49	4.83 ± 0.32	5.23 ± 0.28	5.30 ± 0.34	5.70 ± 0.25	0.35	0.49
Apical IEL villus base per 100 μm	Duodenum	1.63 ± 0.15	1.70 ± 0.15^{d}	2.10 ± 0.28^{r}	1.27 ± 0.28^{des}	2.0 ± 0.21^{p}	1.07 ± 0.17^{eq}	0.30	0.09
	Jejunum	1.10 ± 0.19	0.97 ± 0.20^{d}	0.87 ± 0.16^{p}	1.73 ± 0.20^{eq}	0.73 ± 0.12	1.13 ± 0.17^{d}	0.25	0.014
	Ileum	1.13 ± 0.16^{A}	0.90 ± 0.17^{D}	1.27 ± 0.14^{A}	1.27 ± 0.14^{D}	0.50 ± 0.10^{B}	0.37 ± 0.13^{E}	0.001	0.001
Nuclear IEL villus base per 100 μm	Duodenum	1.37 ± 0.18^{A}	1.47 ± 0.18^{D}	2.43 ± 0.31^{B}	2.60 ± 0.22^{E}	2.40 ± 0.25^{B}	2.73 ± 0.19^{E}	0.004	0.001
	Jejunum	0.90 ± 0.15^{Ap}	1.83 ± 0.14^{q}	1.93 ± 0.20^{B}	2.0 ± 0.19	1.07 ± 0.17^{Ap}	2.23 ± 0.21^{q}	0.001	0.30
	Ileum	0.93 ± 0.14^{a}	0.60 ± 0.14^{D}	1.53 ± 0.15^{b}	1.60 ± 0.15^{E}	1.17 ± 0.15^{abr}	0.73 ± 0.15^{Ds}	0.014	0.001
Basal IEL villus base per 100 μm	Duodenum	1.87 ± 0.20^{A}	2.10 ± 0.18^{D}	2.80 ± 0.23^{Bp}	4.60 ± 0.34^{Eq}	3.70 ± 0.24^{C}	4.40 ± 0.27^{E}	0.001	0.001
	Jejunum	1.47 ± 0.17^{A}	1.97 ± 0.26	2.10 ± 0.22^{A}	2.20 ± 0.26	3.03 ± 0.30^{Bp}	2.03 ± 0.20^{q}	0.001	0.78
	Ileum	1.77 ± 0.20^{ar}	2.60 ± 0.35^{Ds}	2.50 ± 0.24^{b}	2.63 ± 0.23^{D}	2.03 ± 0.24^{abp}	4.10 ± 0.22^{Eq}	0.07	0.001
Total IEL villus base per 100 μm	Duodenum	4.87 ± 0.41^{A}	5.27 ± 0.37^{D}	7.33 ± 0.62^{B}	8.47 ± 0.35^{E}	8.10 ± 0.31^{B}	8.20 ± 0.34^{E}	0.001	0.001
	Jejunum	3.43 ± 0.28^{Ap}	4.77 ± 0.38^{q}	4.90 ± 0.33^{B}	5.83 ± 0.35	4.83 ± 0.35^{B}	5.40 ± 0.39	0.002	0.13
	Ileum	3.83 ± 0.20^{A}	4.10 ± 0.40^{D}	5.30 ± 0.23^{B}	5.50 ± 0.21^{E}	3.70 ± 0.27^{Ap}	5.20 ± 0.27^{Eq}	0.001	0.004

Data are presented as IEL/100 μm (mean ± scanning electron microscopy) in different age-groups.
$^{A, B, C}$Means with different superscripts between control groups significantly differ ($p < 0.01$);
$^{D, E, F}$Means with different superscripts between treatment groups significantly differ ($p < 0.01$);
^{a,b}Means with different superscripts between control groups significantly differ ($p < 0.05$);
^{d,e}Means with different superscripts between treatment groups significantly differ ($p < 0.05$);
^{p,q}Means with different superscripts within groups significantly differ ($p < 0.01$);
^{r,s}Means with different superscripts within groups significantly differ ($p < 0.05$).

group of animals. Many researchers studied goblet cells in piglets after feeding with probiotic and zinc [5, 7, 14, 17, 34, 42]. Most of the results obtained from these researchers were in agreement with the present findings. In the present study, the higher number of different types of goblet cells recorded in the treatment group piglets might be concluded with the better enhancement of epithelial barrier and defence mechanism. This might result in effective immunity and digestibility in this group of piglets.

The distribution of argentaffin cells in the small intestine of control and treated piglets was studied to know the effects of probiotic and zinc on these cells. These cells were concentrated more in the jejunum, followed by duodenum and ileum. However, Sadeghi et al. [45] reported more number of argentaffin cells in the first part of the duodenum in rats. The reports of the present study were not consistent with the above findings, which might be due to variation in species. These argentaffin cells were located as a single cell within the lining epithelium of both villus and crypt in a large population on non-endocrine cells as previously reported by Sadeghi et al. [45] in rats. Under the TEM of this study, these cells had narrow apex, wide base with many small, spheroidal, electron-dense granules in the cytoplasm. The present

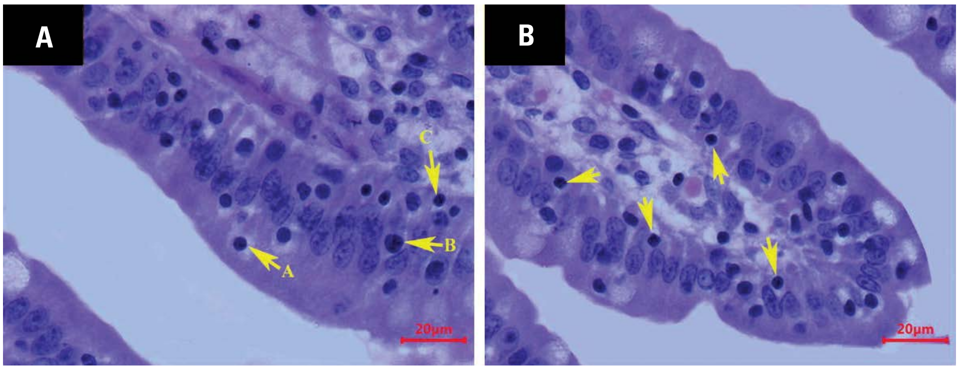

Figure 6. Photomicrographs of jejunum in 30 days old treated piglet (H&E, ×400); **A.** Intraepithelial lymphocytes (IEL) in apical (A), nuclear (B) and basal (C) positions; **B.** IEL located in basal positions (arrow).

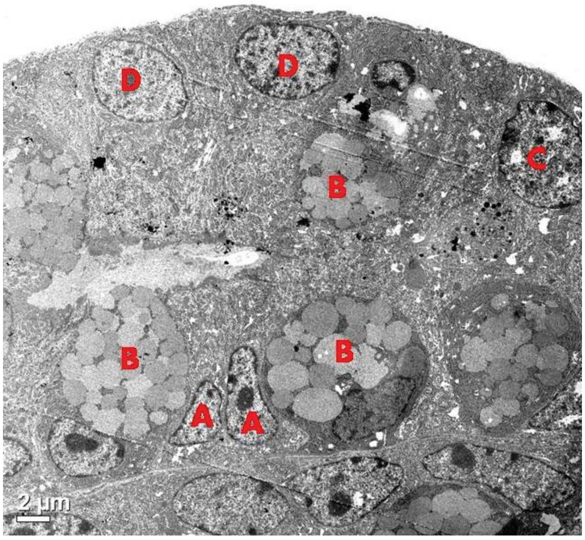

Figure 7. Transmission electron microscopy micrograph of jejunal crypt showing the presence of stem cells (A), goblet cells (B), argentaffin cell (C) and enterocytes (D) in 60 days old treated piglet.

findings were similar to the findings of Gonzalez et al. [23] in pigs. The mean number of argentaffin cells in the current study was significantly higher in villi ($p < 0.05$) and crypts ($p < 0.01$) of the duodenum at day 60 in the treatment group of piglets. More number of these cells revealed in the treatment group of the present study might be correlated with more production of gastrointestinal hormones for better digestion of food [41, 49]. The increase of serotonin secretion by the argentaffin cells created a greater peristaltic movement of the small intestine resulting in effective digestion of food particles [25], which supported the current observation.

The M-cells were specialized epithelial cells of the mucosa-associated lymphoid tissue. They were mostly dispersed in the Peyer's patches of jejunum and ileum. This finding was in consonance to the finding of Hsieh and Lo [29] in mice. In our study, the M-cells showed less developed brush border with irregular microvilli. They transport antigens from the lumen of the intestine to the dome epithelium and neutralise them with a variety of mechanisms. This finding was in agreement with the report of Gebert et al. [22] in pig. The TEM revealed less electron-dense cytoplasm containing abundant mitochondria, lysosomes and small vesicles with few secretory granules. The present findings had a close resemblance to the findings of Renfeng et al. [43] in piglets. In the present study, the differences in M-cells between control and treatment group piglets could not be made due to constraints in enough exposure availability of TEM.

In the present investigation, the mucosal epithelium of the small intestine showed a tuft cell in between the enterocytes. This pear-shaped cell had a broad base, narrow apex, and a "tuft" of microvilli projecting into the lumen as also reported by Ethan [19] in humans. In this study, these cells were encountered more in the duodenum than jejunum and ileum as revealed by Cheng et al. [10] in mouse intestine. The role of tuft cells in epithelial cell survival/self-renewal was reported by Chandrakesan et al. [9], in mucosal healing by Banerjee et al. [3] and possible contacts with nerve fibres relating to endocrine cells by Cheng et al. [10] in mouse intestine. In the present study, the counting of tuft cells in the small intestine of control and treatment group of piglets could not be made as these cells could be identified only with TEM and some special staining. However, frequent occurrences of these cells were noted in the treatment group of piglets in comparison with the control group of animals. This finding might be suggestive of better survival/self-renewal, mucosal healing and digestive ability in the gut of piglets fed with probiotic and zinc compared to control animals.

The intraepithelial lymphocytes were unevenly distributed in the apical, nuclear and basal positions of the lining mucosa of the small intestine in both the groups, as also opined by Deng et al. [15] in hen. In the villus tip of the treatment group of piglets, the number of these IEL was significantly increased ($p < 0.01$) at day 30 in the duodenum and, day 20 and day 30 in the jejunum. Similarly, in the villus base of the treatment group, the total IEL population was significantly higher ($p < 0.01$) at day 20 in jejunum and day 60 in the ileum. In agreement with the present result, several authors had reported an increased number of IEL after probiotic treatments in pig [46] and in chicken [2, 13, 15, 31]. The slight but significant increase in the number of IEL in the treatment group of the present study could be the result of a nonspecific stimulation of the local immune system, possibly by certain antigens of probiotic bacteria. In the present study, most of the IELs were localised at the basement membrane of the epithelium, numerous at the enterocyte nuclear level and relatively few apically in the epithelium. The present findings were in support of the findings of Rieger et al. [44] and Vega-Lopez et al. [50] in the porcine small intestine. In most of the segments of intestine, the number of basally located IEL was significantly increased in the treatment group of piglets as compared to the control group of animals both in villus tip and base. The basal IEL belongs to the "conventional type", i.e., antigen-experienced cells originated from peripheral T cells and homed the gut mucosa, which had immunologic memory function and mounted an adaptive response as reported by Hayday et al. [26] in human. In the present study, the treatment group of piglets had more basally located IEL that might be correlated with effective adaptive immune response in this group of piglets. A significantly higher population of IEL was also recorded at the nuclear level of villus tip and base in the jejunum of treated piglets. The more number of IEL present in the nuclear level of the epithelium was explained by Hayday et al. [26]. According to them, the IEL found at the nuclear level belongs to the "unconventional type". They had functions in between adaptive and innate responses and responsible for the protection of epithelial integrity. Further, Edelblum et al. [18] demonstrated the ability of an IEL population fitting to the "unconventional type" to contact multiple epithelial cells over a short time and thus provide a potential mechanism by which they could prevent epithelial injury and infection. The significantly higher numerical values for nuclear IEL recorded in the present study might conclude with better epithelial cell integrity against injury and infection in the piglets fed with probiotic and zinc compared to control piglets.

The TEM revealed the presence of CBC stem cells along with goblet cells, enteroendocrine cells and absorptive enterocytes, irrespective of segments of intestine and group. These stem cells were irregularly shaped, small, columnar cells with basally located nuclei and scarce cytoplasm. They were found in between the goblet cells, enterocytes or enteroendocrine cells in piglets. The present findings were in agreement with the findings of Gonzalez et al. [23] in pigs. However, Barker et al. [4] reported the presence of stem cells in between Paneth cells on the crypt base in mice. This finding slightly deviated from the present investigation might be due to the absence of Paneth cells in the crypt base of piglets. In the current study, the CBC stem cells could be differentiated from the mature absorptive enterocytes with their irregular columnar cells containing uneven elongated nuclei in between the goblet cells, as described earlier by Gonzalez et al. [23] in pigs. The alterations of CBC stem cells in the present study in between control and treatment group piglets could not be made due to a lack of sufficient view under transmission electron microscopy.

CONCLUSIONS

From the present investigation, it can be concluded that dietary supplementation of probiotic and zinc induced the length of enterocyte microvilli, increased the number of different goblet cells, argentaffin cells, tuft cells and intraepithelial lymphocytes in pre and post-weaned piglets. These alterations might provide better absorption of available nutrients and stimulation of local and adaptive immune responses that resulted in effective digestibility and immunity in the treatment group of piglets as compared to the control group of animals.

Conflict of interest: None declared

REFERENCES

1. Alexander TJL. Neonatal diarrhoea in pigs. CAB International, Wallingford 1994.
2. Bai SP, Wu AM, Ding XM, et al. Effects of probiotic-supplemented diets on growth performance and intestinal immune characteristics of broiler chickens. Poult Sci. 2013; 92(3): 663–670, doi: 10.3382/ps.2012-02813, indexed in Pubmed: 23436517.

3. Banerjee A, McKinley ET, von Moltke J, et al. Interpreting heterogeneity in intestinal tuft cell structure and function. J Clin Invest. 2018; 128(5): 1711–1719, doi: 10.1172/JCI120330, indexed in Pubmed: 29714721.
4. Barker N, van Oudenaarden A, Clevers H. Identifying the stem cell of the intestinal crypt: strategies and pitfalls. Cell Stem Cell. 2012; 11(4): 452–460, doi: 10.1016/j.stem.2012.09.009, indexed in Pubmed: 23040474.
5. Baum B, Liebler-Tenorio EM, Enss ML, et al. Saccharomyces boulardii and bacillus cereus var. Toyoi influence the morphology and the mucins of the intestine of pigs. Z Gastroenterol. 2002; 40(5): 277–284, doi: 10.1055/s-2002-30116, indexed in Pubmed: 12016561.
6. Blaabjerg K, Poulsen HD. The use of zinc and copper in pig production. DCA-Nationalt Center for Jordbrug of Fodevarer. 2017.
7. Bontempo V, Giancamillo ADi, Savoini G, et al. Live yeast dietary supplementation acts upon intestinal morpho-functional aspects and growth in weanling piglets. Anim Feed Sci Tech. 2006; 129(3-4): 224–236, doi: 10.1016/j.anifeedsci.2005.12.015.
8. Case CL, Carlson MS. Effect of feeding organic and inorganic sources of additional zinc on growth performance and zinc balance in nursery pigs. J Anim Sci. 2002; 80(7): 1917–1924, doi: 10.2527/2002.8071917x, indexed in Pubmed: 12162660.
9. Chandrakesan P, May R, Weygant N, et al. Intestinal tuft cells regulate the ATM mediated DNA Damage response via Dclk1 dependent mechanism for crypt restitution following radiation injury. Sci Rep. 2016; 6: 37667, doi: 10.1038/srep37667, indexed in Pubmed: 27876863.
10. Cheng X, Voss U, Ekblad E. Tuft cells: Distribution and connections with nerves and endocrine cells in mouse intestine. Exp Cell Res. 2018; 369(1): 105–111, doi: 10.1016/j.yexcr.2018.05.011, indexed in Pubmed: 29758188.
11. Choi S, Kornegay ET, Eigel W. Characterization of small intestinal mucus glycoproteins from pigs of various ages. Comp Biochem Physiol. 1991; 99(4): 677–680, doi: 10.1016/0300-9629(91)90149-7.
12. Collinder E, Cardona ME, Kozakova H, et al. Biochemical intestinal parameters in pigs reared outdoors and indoors, and in germ-free pigs. J Vet Med A Physiol Pathol Clin Med. 2002; 49(4): 203–209, doi: 10.1046/j.1439-0442.2002.00407.x, indexed in Pubmed: 12069263.
13. Dalloul RA, Lillehoj HS, Shellem TA, et al. Enhanced mucosal immunity against Eimeria acervulina in broilers fed a Lactobacillus-based probiotic. Poult Sci. 2003; 82(1): 62–66, doi: 10.1093/ps/82.1.62, indexed in Pubmed: 12580246.
14. Davis ME, Brown DC, Baker A, et al. Effect of direct-fed microbial and antibiotic supplementation on gastrointestinal microflora, mucin histochemical characterization, and immune populations of weanling pigs. Livestock Sci. 2007; 108(1-3): 249–253, doi: 10.1016/j.livsci.2007.01.063.
15. Deng W, Dong XF, Tong JM, et al. The probiotic Bacillus licheniformis ameliorates heat stress-induced impairment of egg production, gut morphology, and intestinal mucosal immunity in laying hens. Poult Sci. 2012; 91(3): 575–582, doi: 10.3382/ps.2010-01293, indexed in Pubmed: 22334732.
16. Deplancke B, Gaskins HR. Microbial modulation of innate defense: goblet cells and the intestinal mucus layer. Am J Clin Nutr. 2001; 73(6): 1131S–1141S, doi: 10.1093/ajcn/73.6.1131S, indexed in Pubmed: 11393191.
17. Di Giancamillo A, Vitari F, Savoini G, et al. Effects of orally administered probiotic Pediococcus acidilactici on the small and large intestine of weaning piglets. A qualitative and quantitative micro-anatomical study. Histol Histopathol. 2008; 23(6): 651–664, doi: 10.14670/HH-23.651, indexed in Pubmed: 18366003.
18. Edelblum KL, Shen Le, Weber CR, et al. Dynamic migration of $\gamma\delta$ intraepithelial lymphocytes requires occludin. Proc Natl Acad Sci U S A. 2012; 109(18): 7097–7102, doi: 10.1073/pnas.1112519109, indexed in Pubmed: 22511722.
19. Ethan M. 30-anatomy and physiology of the small and large intestine. Pediatric Gastrointestinal and Liver Disease, Elsevier 2016.
20. Fuller R. Probiotics in man and animals. J Appl Microbiol. 1989; 66: 365–378, indexed in Pubmed: 2666378.
21. Galdeano CM, Perdigón G. Role of viability of probiotic strains in their persistence in the gut and in mucosal immune stimulation. J Appl Microbiol. 2004; 97(4): 673–681, doi: 10.1111/j.1365-2672.2004.02353.x, indexed in Pubmed: 15357716.
22. Gebert A, Rothkötter HJ, Pabst R. M Cells in Peyer's Patches of the Intestine. Int Rev Cytol. 1996: 91–159, doi: 10.1016/s0074-7696(08)61346-7.
23. Gonzalez LM, Williamson I, Piedrahita JA, et al. Cell lineage identification and stem cell culture in a porcine model for the study of intestinal epithelial regeneration. PLoS One. 2013; 8(6): e66465, doi: 10.1371/journal.pone.0066465, indexed in Pubmed: 23840480.
24. Habel RE. Guide to the dissection of domestic ruminants. Edwards Brother Inc Ann Arbor, Michigan 1964.
25. Hayat MA. Immunogold-silver staining: principles, methods, and applications. CRC Press, Boca Raton, New York 1995.
26. Hayday A, Theodoridis E, Ramsburg E, et al. Intraepithelial lymphocytes: exploring the Third Way in immunology. Nat Immunol. 2001; 2(11): 997–1003, doi: 10.1038/ni1101-997, indexed in Pubmed: 11685222.
27. Hedemann MS, Jensen BB, Poulsen HD. Influence of dietary zinc and copper on digestive enzyme activity and intestinal morphology in weaned pigs. J Anim Sci. 2006; 84(12): 3310–3320, doi: 10.2527/jas.2005-701, indexed in Pubmed: 17093223.
28. Hodges RR, Dartt DA. Conjunctival goblet cells. Encyclopedia of the Eye. 2010: 369–376, doi: 10.1016/b978-0-12-374203-2.00053-1.
29. Hsieh EH, Lo DD. Jagged1 and Notch1 help edit M cell patterning in Peyer's patch follicle epithelium. Dev Comp Immunol. 2012; 37(2): 306–312, doi: 10.1016/j.dci.2012.04.003, indexed in Pubmed: 22504165.
30. Jensen VB, Harty JT, Jones BD. Interactions of the invasive pathogens Salmonella typhimurium, Listeria monocytogenes, and Shigella flexneri with M cells and murine Peyer's patches. Infect Immun. 1998; 66(8): 3758–3766, doi: 10.1128/IAI.66.8.3758-3766.1998, indexed in Pubmed: 9673259.

31. Lee KW, Lee SH, Lillehoj HS, et al. Effects of direct-fed microbials on growth performance, gut morphometry, and immune characteristics in broiler chickens. Poult Sci. 2010; 89(2): 203–216, doi: 10.3382/ps.2009-00418, indexed in Pubmed: 20075271.
32. Lemme-Dumit JM, Polti MA, Perdigón G, et al. Probiotic bacteria cell walls stimulate the activity of the intestinal epithelial cells and macrophage functionality. Benef Microbes. 2018; 9(1): 153–164, doi: 10.3920/BM2016.0220, indexed in Pubmed: 29124968.
33. Liévin-Le Moal V, Servin AL. The front line of enteric host defense against unwelcome intrusion of harmful microorganisms: mucins, antimicrobial peptides, and microbiota. Clin Microbiol Rev. 2006; 19(2): 315–337, doi: 10.1128/CMR.19.2.315-337.2006, indexed in Pubmed: 16614252.
34. Liu P, Pieper R, Tedin L, et al. Effect of dietary zinc oxide on jejunal morphological and immunological characteristics in weaned piglets. J Anim Sci. 2014; 92(11): 5009–5018, doi: 10.2527/jas.2013-6690, indexed in Pubmed: 25253808.
35. Liu H, Zhang J, Zhang S, et al. Oral administration of Lactobacillus fermentum I5007 favors intestinal development and alters the intestinal microbiota in formula-fed piglets. J Agric Food Chem. 2014; 62(4): 860–866, doi: 10.1021/jf403288r, indexed in Pubmed: 24404892.
36. Luna LG. Manual of histologic staining methods of Armed Forces Institute of Pathology. McGraw Hill Book Company, New York 1968.
37. Mowry RW. Observations on the use of sulphuric ether for the sulphation of hydroxyl groups in tissue sections. J Histochem Cytochem. 1956; 4: 407.
38. NRC Nutrient Requirements of Swine. In: Computer Model Program for Predicting Nutrient Requirements. National Academy of Sciences, Washington, DC, USA 1998.
39. Parsons KR, Bland AP, Hall GA. Follicle associated epithelium of the gut associated lymphoid tissue of cattle. Vet Pathol. 1991; 28(1): 22–29, doi: 10.1177/030098589102800104, indexed in Pubmed: 2017824.
40. Poulsen H. Zinc Oxide for Weanling Piglets. Acta Agric Scand Sect A Anim Sci. 2009; 45(3): 159–167, doi: 10.1080/09064709509415847.
41. Rehfeld JF. The new biology of gastrointestinal hormones. Physiol Rev. 1998; 78(4): 1087–1108, doi: 10.1152/physrev.1998.78.4.1087, indexed in Pubmed: 9790570.
42. Reiter K, Eggebrecht S, Drewes B, et al. Effects of Enterococcus faecium and Bacillus cereus var. toyoi on the morphology of the intestinal mucous membrane in piglets. Biologia. 2006; 61(6): 803–809, doi: 10.2478/s11756-006-0161-2.
43. Renfeng Li, Xiangqin T, Songlin Q, et al. Morphological and Immunohistochemical Identification of Villous M Cells in the Small Intestine of Newborn Piglets. Int J Morphol. 2015; 33(4): 1261–1268, doi: 10.4067/s0717-95022015000400011.
44. Rieger J, Janczyk P, Hünigen H, et al. Intraepithelial lymphocyte numbers and histomorphological parameters in the porcine gut after Enterococcus faecium NCIMB 10415 feeding in a Salmonella Typhimurium challenge. Vet Immunol Immunopathol. 2015; 164(1-2): 40–50, doi: 10.1016/j.vetimm.2014.12.013, indexed in Pubmed: 25669594.
45. Sadeghi M, Hojjati M, Sadeghi F, et al. The Distribution of Enteroendocrine Cells in Small Intestine in Rats. Int J Vet Med Res Rep. 2014: 1–7, doi: 10.5171/2014.818294.
46. Scharek L, Altherr BJ, Tölke C, et al. Influence of the probiotic Bacillus cereus var. toyoi on the intestinal immunity of piglets. Vet Immunol Immunopathol. 2007; 120(3-4): 136–147, doi: 10.1016/j.vetimm.2007.07.015, indexed in Pubmed: 17870185.
47. Singh I. A modification of the Masson-Hamperl method for staining argentaffin cells. Anat Anz. 1964; 115: 81–82, indexed in Pubmed: 14249822.
48. Skrzypek T, Valverde Piedra JL, Skrzypek H, et al. Light and scanning electron microscopy evaluation of the postnatal small intestinal mucosa development in pigs. J Physiol Pharmacol. 2005; 56 Suppl 3: 71–87, indexed in Pubmed: 16077196.
49. Solcia E, Capella C, Buffa R. The diffuse endocrine-paracrine system of the gut in health and disease: ultrastructural features. Scand J Gastroenterol. 1981; 70(Suppl.): 25–36, indexed in Pubmed: 6118945.
50. Vega-López MA, Arenas-Contreras G, Bailey M, et al. Development of intraepithelial cells in the porcine small intestine. Dev Immunol. 2001; 8(2): 147–158, doi: 10.1155/2001/25301, indexed in Pubmed: 11589310.
51. Westin R, Holmgren N, Hultgren J, et al. Post-mortem findings and piglet mortality in relation to strategic use of straw at farrowing. Prev Vet Med. 2015; 119(3-4): 141–152, doi: 10.1016/j.prevetmed.2015.02.023, indexed in Pubmed: 25792335.
52. Wilson AD, Stokes CR, Bourne FJ, et al. Effect of age on absorption and immune responses to weaning or introduction of novel dietary antigens in pigs. Res Vet Sci. 1989; 46(2): 180–186, indexed in Pubmed: 2704882.

VIA MEDICA

ORIGINAL ARTICLE

Folia Morphol.
Vol. 80, No. 3, pp. 618–624
DOI: 10.5603/FM.a2020.0097

ISSN 0015–5659
eISSN 1644–3284
journals.viamedica.pl

Comparison of local rosmarinic acid and topical dexpanthenol applications on wound healing in a rat experimental wound model

M.C. Küba[1], A. Türkoğlu[2], A. Oğuz[3], M.C. Tuncer[4], Ş. Kaya[5], Ö. Başol[3], H. Bilge[3], F. Tatlı[3]

[1]*Department of General Surgery, Batman Regional Public Hospital, Batman, Turkey*
[2]*Gaziantep Medical Park Hospital, Gaziantep, Turkey*
[3]*Department of General Surgery, Faculty of Medicine, University of Dicle, Diyarbakır, Turkey*
[4]*Department of Anatomy, Faculty of Medicine, University of Dicle, Diyarbakır, Turkey*
[5]*Department of Pathology, Diyarbakır Educating and Research Hospital, Diyarbakır, Turkey*

[Received: 8 June 2020; Accepted: 27 July 2020; Early publication date: 22 August 2020]

Background: *The aim of the study was to compare the effects of rosmarinic acid and dexpanthenol in a rat experimental wound model.*
Materials and methods: *Twenty-four Wistar albino rats weighing 200–250 g were randomly divided into three groups. After 2-cm full-thickness skin defects were created, the wounds were washed with sterile 0.9% NaCl solution. After washing, the control group was left untreated, the second group received 5% dexpanthenol cream, and the third group received 10% rosmarinic acid cream. Before excision, the skin was evaluated macroscopically by measuring the reduction in wound size; after excision, histological examination (epithelisation, inflammation, fibrosis, granulation) was performed.*
Results: *Macroscopic comparison of the wound sizes showed that group 3 showed a statistically significant difference in wound size reduction compared to the other two groups. Histopathological examination showed that there was no statistically significant difference between the groups. We found that the rosmarinic acid group had greater wound size reduction than the other two groups. However, epithelialisation was detected in fewer cases.*
Conclusions: *We believe that rosmarinic acid can be used as a topical cream for wound healing, as it leads to significant reduction in wound size, resulting in fewer scars.* (Folia Morphol 2021; 80, 3: 618–624)

Key words: wound healing, rosmarinic acid, dexpanthenol, rat

INTRODUCTION

Wound healing is a serious issue that may be associated with postoperative morbidity. Wound dehiscence and delayed wound healing remain important, serious problems in surgery. The basic principle of wound healing is to maintain adequate tissue perfusion and oxygenation, the anatomical and functional integrity of the affected area, and to ensure proper nutrition and moisture environment [17]. Various pharmacological agents have been studied for accelerating wound healing and preventing necrosis or ischaemia, and extensive efforts are still ongoing.

Address for correspondence: Prof. M.C. Tuncer, PhD, Dicle University, Medical School, Department of Anatomy, 21280, Diyarbakır, Turkey, tel: +90 412 2488001 ext. 4539 (faculty room), fax: +90 412 2488440, mobile phone: +90 532 2744926, e-mail: drcudi@hotmail.com

Sympatholytics, vasodilators, calcium channel blockers, anti-haemorrhagic agents, prostaglandin inhibitors, honey, anticoagulants, glucocorticoids, and free oxygen radical-inhibiting agents have been studied, and achieving various degrees of success. The most important disadvantages of many pharmacological agents are their relatively high doses and systemic use, which means that they have various potential adverse effects and risks. Local application, on the other hand, is more advantageous in terms of these risks [1, 6].

Dexpanthenol is widely used in wound healing in clinical practice. Pantothenate is a stimulant for migration, proliferation, and gene regulation in human dermal fibroblast cultures. Topical dexpanthenol is used both in wound care and for treating dermatological diseases because it stimulates skin regeneration and promotes wound healing [6].

Topical application of antioxidant-containing compounds is beneficial for wound healing and for protecting tissues from oxidative damage [8]. In chemical and cellular systems, rosmarinic acid (RA) and its basic metabolites have antioxidant activity [5]. RA also has anti-bacterial and nematicide effects and important anti-inflammatory properties [5, 7, 10, 21]. As far as we know, the effect of RA on topical wound healing has not been investigated.

Dexpanthenol is widely used for small wounds and abrasions. Although dexpanthenol has been investigated widely for its effects on skin disorders, there has been insufficient evaluation of the effects of both RA and dexpanthenol on wound healing. In the present study, we evaluated the effects of topical RA and dexpanthenol on wound healing in a rat experimental wound model.

MATERIALS AND METHODS

This experimental study was submitted to the Ethics Committee of our University and approved by decision 2016/17 on 13 April, 2016. The experiments were performed in the University's Research and Application Centre Laboratory.

Animals

Twenty-four Wistar albino rats, each weighing an average of 200–250 g, were used. Starting 1 week before the study, the animals were prepared for the experiment, and were kept in a 12-h day/night environment in separate cages and given standard rat feed. The animals were randomly divided into three groups, and fasted 12 hours before the experiment; they were allowed to drink only water.

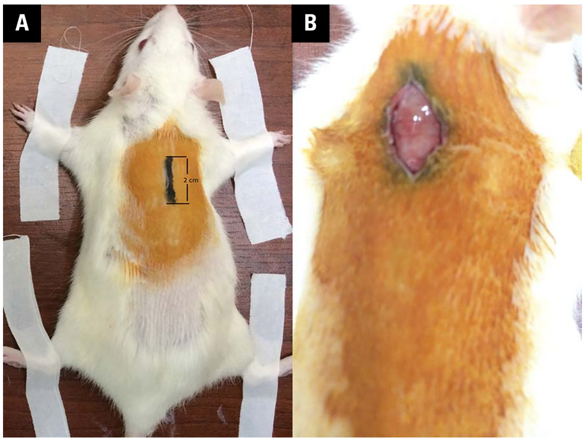

Figure 1. A, B. Incision model created in rats.

Skin defect model

All animals were anesthetised by intramuscular administration of 50 mg/kg ketamine hydrochloride (Ketalar®, Pfizer, Istanbul) and 5 mg/kg xylazine hydrochloride (Rompon®, Bayer, Şişli, Istanbul) under aseptic conditions. The rats were anesthetised in the prone position, shaved, and povidone iodine was administered for antisepsis. A full-thickness skin defect 2 cm in length was created with a #11 scalpel blade (Fig. 1). The wounds of all animals were cleaned with 0.9% NaCl solution, and then the animals were divided into three groups.

Rosmarinic acid (96% ALDRICH Chemistry Product, UK of United Kingdom) and dexpanthenol (Bepanthol®, Bayer Turk Kimya San. Ltd. Sti. Istanbul) were used in the study. We used 18 g cold cream (cera alba, Olei Amygdalanum, Boracis, aqua rosae, oleum rosae) and 2 g powdered RA to prepare 10% RA cream.

Group 1: Control group. After receiving a full-thickness skin incision of approximately 2 cm on the dorsum, the wound was cleaned daily with isotonic saline solution, dressings were performed, and each rat was kept in a separate cage.

Group 2: Dexpanthenol group. After receiving a full-thickness skin incision of approximately 2-cm diameter on the dorsum, the wound was cleaned with isotonic saline solution, and then dexpanthenol (5% cream) was applied daily; each rat was kept in a separate cage.

Group 3: Rosmarinic acid group. After receiving a full-thickness skin incision of approximately 2-cm diameter on the dorsum, the wound was cleaned with isotonic saline solution, and then RA cream (10% cream) was applied daily; each rat was kept in a separate cage.

Wound healing assessment

The wound healing process was evaluated as follows: macroscopically, the reduction in wound size was calculated, and the excised wound tissue was evaluated by histological examination.

Macroscopic evaluation

Following the surgical procedure, the course of healing in all wounds was calculated using Walker's formula [20] after fixation of the rats' drawing on acetate paper on day 0, 3, 5, 7, 10, 14, and 21. In addition, rats whose wound healing was completed were recorded during the daily control.

Walker formula

$$\% \text{ Wound area} = \frac{\text{Wound area on day X}}{\text{Wound area measured on day 1}} \times 100$$

Histological evaluation

On day 21, all animals were sacrificed, and 5 × × 3 cm full-thickness skin, including the incision line, was removed from the dorsum for histological examination. A qualified pathologist evaluated the histopathological examinations. The tissues were fixed in 10% buffered formaldehyde solution for 2 days, and routine follow-up was performed. The tissues were embedded in paraffin blocks after the follow-up phase. Sections (4 μm) obtained from the prepared paraffin blocks were stained with haematoxylin and eosin stain, examined under a light microscope, and photographed by a microscope-mounted camera. Inflammation, granulation tissue formation, and vascularisation were evaluated morphologically. Morphological findings, epithelialisation, cellular content (neutrophils, macrophages, fibroblasts), collagen regeneration, and vascularisation were scored as follows: 0 — no change; 1 — little change; 2 — moderate change; 3 — considerable change.

Statistical analysis

Statistical analysis was performed using SPSS for Windows 13.0 (SPSS Inc., Chicago, IL, USA). Categorical data were evaluated using the χ^2 test. Continuous data were evaluated using the Kruskal-Wallis test, and the Mann-Whitney U test was used for comparison of two groups. $P < 0.05$ was considered statistically significant.

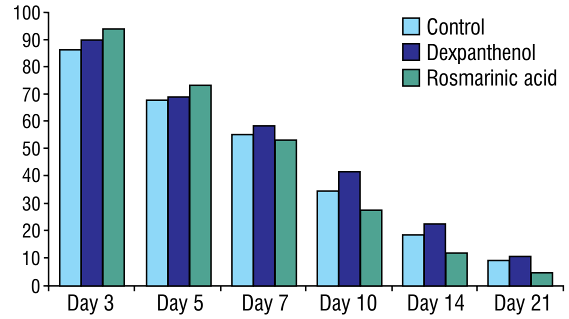

Figure 2. Reduction in wound size according to day.

RESULTS

Evaluation of wound healing scores

The wound healing scores calculated according to Walker's formula in the control, dexpanthenol, and RA groups are given in Figure 2 and Tables 1 and 2. The macroscopic and histopathological evaluations of the groups are as below.

Macroscopic evaluation

In postoperative day 3, the greatest reduction in wound size was observed in the control group, but on day 10 and later, the greatest reduction in the wound size was observed in the RA group. The difference was statistically significant. However, no significant difference was observed in wound sizes between the groups on days 5 and 7.

Histopathological evaluation

When the histopathological examination findings were compared statistically, no statistically significant difference was found between the groups in terms of epithelialisation, inflammation, fibrosis, and granulation (Figs. 3–5, Table 2).

DISCUSSION

Wound dehiscence and delayed wound healing are still important, serious problems in surgery. A proper wound healing process aims to improve the structure and function of the injured tissue. The healing process starts during an injury and can last for years [7, 10, 20]. Various clinicians use many agents topically and systemically for wound healing. Agents that are suggested to be useful in wound healing are reported to have antioxidant, antimicrobial, antibacterial, and anti-inflammatory properties [11, 13, 18]. Topical application of antioxidant-containing compounds for wound healing and for protecting tissues from oxidative damage has been shown to be beneficial [8].

Table 1. Distribution of wound healing score measurements.

Group	Day — median (range)					
	3	5	7	10	14	21
Control	85 (80–95)	68 (51–80)	54.5 (47–75)	34 (32–40)	19.5 (11–23)	9 (6–11)
Dexpanthenol	89.5 (85–93)	70 (65–72)	59 (51–64)	40.5 (37–50)	22 (17–28)	9.5 (7–14)
Rosmarinic acid	94 (89–96)	72.5 (66–83)	52. (44–64)	30 (16–36)	11.5 (9–17)	4.5 (3–7)
P-values (Kruskal-Wallis test)	0.005903	0.397919	0.240973	0.000369	0.000743	0.000712

Table 2. Comparison of histopathological evaluation results between groups

Parameters		Control (%)	Dexpanthenol (%)	Rosmarinic acid (%)	P
Epithelisation	Present	6 (75%)	5 (62.5%)	3 (37.5%)	0.1797
	Absent	2 (25%)	3 (37.5%)	5 (62.5%)	
Inflammation	0	1 (12.5%)	0 (0%)	0 (0%)	0.3302
	1	3(37.5%)	3 (37.5%)	3 (37.5%)	
	2	3 (37,5%)	2 (25%)	5 (62.5%)	
	3	1 (12.5%)	3 (37.5%)	0 (0%)	
Fibrosis	0	0 (0%)	0 (0%)	0 (0%)	0.4932
	1	1 (12.5%)	0 (0%)	0 (0%)	
	2	5 (62.5%)	6 (75%)	4 (50%)	
	3	2 (25%)	2 (25%)	4 (50%)	
Granulation tissue	Present	6 (75%)	4 (50%)	5 (50%)	0.6056
	Absent	2 (25%)	4 (50%)	3 (50%)	

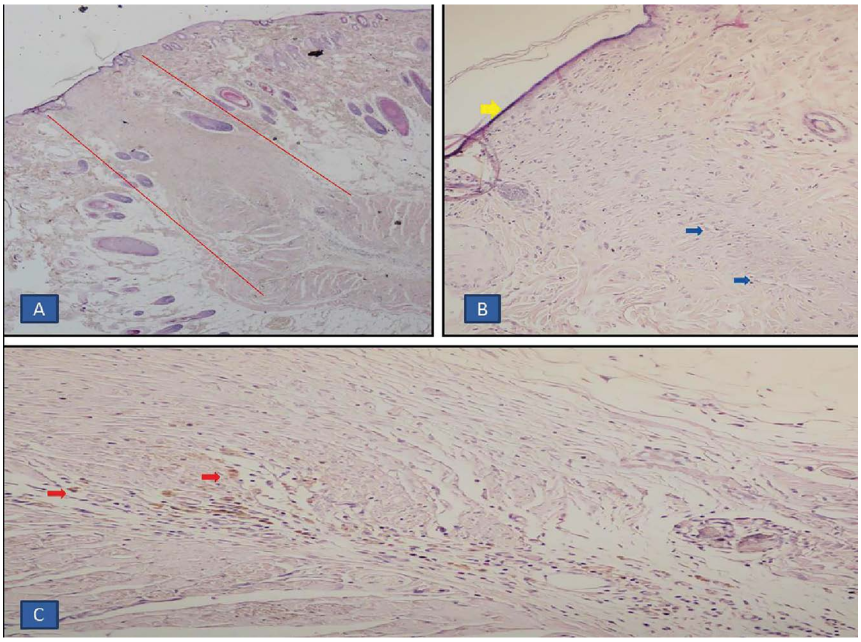

Figure 3. Microscopic view of wound tissues on day (control group). The area between the two red lines in the section belongs to the incision line (haematoxylin-eosin, ×40) (**A**). The yellow arrow indicates epithelialisation on the surface of the incision line; the blue arrows indicate the fibrotic line and vascular structures (haematoxylin-eosin, ×200) (**B**). The red arrows indicate the pigmented macrophages of hemosiderin in brown at the bottom of the incision line (haematoxylin-eosin, ×200) (**C**).

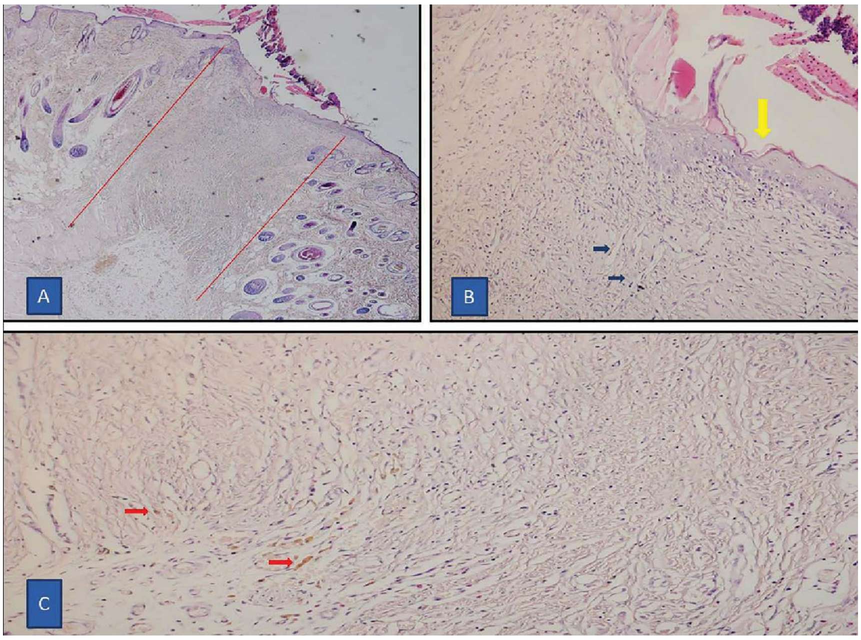

Figure 4. Microscopic view of wound tissues on day (dexpanthenol group). The area between the two red lines in the section belongs to the incision line (haematoxylin-eosin, ×40) (**A**). The yellow arrow indicates epithelialisation on the surface of the incision line; the blue arrows indicate the fibrotic line and vascular structures (haematoxylin-eosin, ×200) (**B**). The red arrows indicate the pigmented macrophages of hemosiderin in brown at the bottom of the incision line (haematoxylin-eosin, ×200) (**C**).

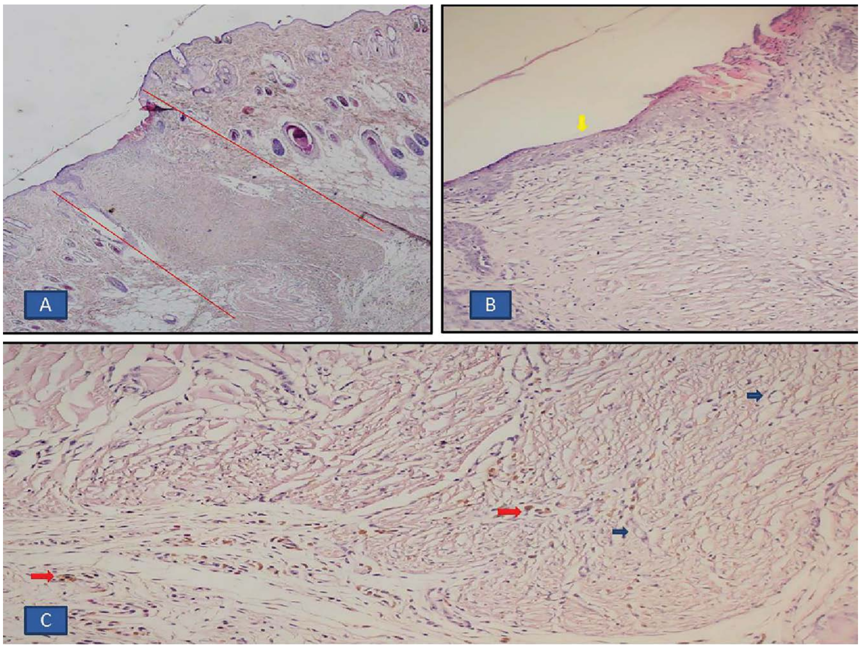

Figure 5. Microscopic view of wound tissues on day (rosmarinic acid group). The area between the two red lines in the section belongs to the incision line (haematoxylin-eosin, ×40) (**A**). The yellow arrow indicates epithelialisation on the surface in the incision line (haematoxylin-eosin, ×200) (**B**). The red arrows indicate the hemosiderin pigmented macrophages, and the blue arrows indicate the vascular structures at the bottom of the incision line (haematoxylin-eosin, ×200) (**C**).

Mushtaq et al. [14] reported that RA has a protective effect against liver and kidney oxidative stress in diabetic rats. RA has an indirect antioxidant effect by affecting the production of cytoprotective genes in the liver, affecting the antioxidant system and nuclear factor-erythroid 2-related factor-2 (NRF2)-dependent phase II enzymes [1, 16]. The antibacterial and anti-inflammatory effects of RA have also been demonstrated previously [5, 10, 21].

In the present study, a significant reduction in wound size was detected in the RA group. On day 3, there was a statistically significant difference between the three groups in the reduction of wound area. This difference is probably due to the anti-inflammatory effect of RA. In early postoperative phase (day 3), the greatest reduction in wound size was observed in the control group, but in late postoperative phase (day 10 and later), the greatest reduction in wound size was observed in the RA group. The difference was statistically significant. However, no significant difference was observed in wound sizes between the groups on days 5 and 7. However, histopathological examination did not reveal a significant difference in epithelisation, inflammation, fibrosis and granulation. Wound healing takes place in a multi-stage, multi-factorial mechanism. The reduction in wound size in favour of RA may be due to the effect of RA on fibroblast cells. Although RA reduced wound size more than dexpanthenol and the control group, the wound healing time was also partially prolonged in this group. This may be due to the blocking of the direct and indirect effects of mediators released from inflammatory cells due to the anti-inflammatory effect of RA. This may explain the inconsistency between the macroscopic findings and histomorphological findings.

Aramwit and Sangcakul [2] applied sericin cream and achieved 90% improvement on day 11 and achieved full recovery on day 15. Kwon et al. [9] observed 90% improvement on day 10 and complete closure on day 14 with 14-day administration of topical recombinant human epidermal growth factor. In the present study, based on the significant statistical findings (approximately 90% on day 14; > 95% improvement on day 21), we concluded that the clinical effect of RA would be seen after day 7 and that RA should be applied for at least 3 weeks for maximum effect. Although the recovery times in our study appear slightly longer than that in the above studies, we believe that this may have been affected by the rat type, wound type, or other environmental factors used, as the recovery time in our control group was longer than that of their control groups.

Dexpanthenol is widely used in wound healing in clinical practice. Pantothenate is a stimulant for migration, proliferation, and gene regulation in human dermal fibroblast cultures. Topical dexpanthenol is used both in wound care and in the treatment of dermatological diseases because it stimulates skin regeneration and promotes wound healing [6]. In a wound healing model, Ulger et al. [19] showed significantly better healing in the dexpanthenol and nebivolol groups than in the control group. Similarly, Oguz et al. [15] observed better recovery in the N-acetylcysteine and dexpanthenol groups than in the control group. In our study, wound healing in the dexpanthenol group was similar to that of the control group, although RA group showed significantly better recovery than the dexpanthenol group. In addition, dexpanthenol caused more epithelialization than RA.

In the RA group, especially on day 7 and later, there was greater reduction in wound size compared to the other two groups. Histomorphological evaluation did not reveal a significant difference, but the evaluation of fibrosis showed that the number of RA rats with grade 3 fibrosis was higher than that of the other two groups. This finding partially supports the above results. Wound contraction is most active in the wound healing process between 7 and 10 days, when fibroblastic cell activation is also high. We believe that RA caused an increase in fibroblastic activity. More comprehensive studies are needed to demonstrate this precisely.

Our histopathological results do not statistically support our macroscopic observations. We did not find any significant difference in terms of inflammation between the groups. However, RA has known anti-inflammatory effects [4]. On the other hand, this effect is usually expressed through the levels of anti-inflammatory molecules. However, we did not analyse the level of pro-inflammatory molecules. Luo et al. [12] reported that RA had an anti-inflammatory effect on acute lung injury by decreasing the levels of pro-inflammatory molecules. Chen et al. [3] showed that RA ameliorated the fibrosis of pterygium epithelial cells by decreasing type I collagen production and downregulating *transforming growth factor* β1/Smad signalling. However, we did not find a statistically significant effect of RA on fibrosis and fibroblast activity. This may indicate a need for new studies on the histopathological and anti-inflammatory effects of RA in a wound healing model. Unlike dexpanthenol, RA also has antibacterial and antiviral effects. These effects may lead RA being more effective than dexpanthenol in wound healing.

CONCLUSIONS

In conclusion, there was greater reduction of wound size in the RA group compared to the dexpanthenol and control groups, but wound healing time was prolonged. In addition, epithelialisation was detected in fewer RA cases than in the other two groups. Significant reduction in wound size will result in less scarring during wound healing. Therefore, we believe that RA can be used in a topical cream for wound healing. However, additional experimental and clinical studies are needed for the duration and amount of use.

Conflict of interest: None declared

REFERENCES

1. Adomako-Bonsu AG, Chan SLf, Pratten M, et al. Antioxidant activity of rosmarinic acid and its principal metabolites in chemical and cellular systems: Importance of physico-chemical characteristics. Toxicol In Vitro. 2017; 40: 248–255, doi: 10.1016/j.tiv.2017.01.016, indexed in Pubmed: 28122265.
2. Aramwit P, Sangcakul A. The effects of sericin cream on wound healing in rats. Biosci Biotechnol Biochem. 2007; 71(10): 2473–2477, doi: 10.1271/bbb.70243, indexed in Pubmed: 17928707.
3. Chen YY, Tsai CF, Tsai MC, et al. Anti-fibrotic effect of rosmarinic acid on inhibition of pterygium epithelial cells. Int J Ophthalmol. 2018; 11(2): 189–195, doi: 10.18240/ijo.2018.02.02, indexed in Pubmed: 29487805.
4. Değer U, Çavuş Y. Investigation of the role of rosmarinic acid treatment in regulating inflammation, cell damage, and angiogenesis in rat ovarian torsion and detorsion models. Acta Cir Bras. 2020; 35(3): e202000304, doi: 10.1590/s0102-865020200030000004, indexed in Pubmed: 32692796.
5. Ekambaram SP, Perumal SS, Balakrishnan A, et al. Antibacterial synergy between rosmarinic acid and antibiotics against methicillin-resistant . J Intercult Ethnopharmacol. 2016; 5(4): 358–363, doi: 10.5455/jice.20160906035020, indexed in Pubmed: 27757265.
6. Heise R, Skazik C, Marquardt Y, et al. Dexpanthenol modulates gene expression in skin wound healing in vivo. Skin Pharmacol Physiol. 2012; 25(5): 241–248, doi: 10.1159/000341144, indexed in Pubmed: 22759998.
7. Jin BR, Chung KS, Cheon SY, et al. Rosmarinic acid suppresses colonic inflammation in dextran sulphate sodium (DSS)-induced mice via dual inhibition of NF-κB and STAT3 activation. Sci Rep. 2017; 7: 46252, doi: 10.1038/srep46252, indexed in Pubmed: 28383063.
8. Kumar B, Vijayakumar M, Govindarajan R, et al. Ethnopharmacological approaches to wound healing--exploring medicinal plants of India. J Ethnopharmacol. 2007; 114(2): 103–113, doi: 10.1016/j.jep.2007.08.010, indexed in Pubmed: 17884316.
9. Kwon YB, Kim HW, Roh DH, et al. Topical application of epidermal growth factor accelerates wound healing by myofibroblast proliferation and collagen synthesis in rat. J Vet Sci. 2006; 7(2): 105–109, doi: 10.4142/jvs.2006.7.2.105, indexed in Pubmed: 16645332.
10. Liu JX, Zhang Y, Hu QP, et al. Anti-inflammatory effects of rosmarinic acid-4-O-β-D-glucoside in reducing acute lung injury in mice infected with influenza virus. Antiviral Res. 2017; 144: 34–43, doi: 10.1016/j.antiviral.2017.04.010, indexed in Pubmed: 28461072.
11. Liu M, Luo G, Wang Y, et al. Nano-silver-decorated microfibrous eggshell membrane: processing, cytotoxicity assessment and optimization, antibacterial activity and wound healing. Sci Rep. 2017; 7(1): 436, doi: 10.1038/s41598-017-00594-x, indexed in Pubmed: 28348388.
12. Luo C, Zou L, Sun H, et al. A review of the anti-inflammatory effects of rosmarinic acid on inflammatory diseases. Front Pharmacol. 2020; 11: 153, doi: 10.3389/fphar.2020.00153, indexed in Pubmed: 32184728.
13. Mulisa E, Asres K, Engidawork E. Evaluation of wound healing and anti-inflammatory activity of the rhizomes of Rumex abyssinicus J. (Polygonaceae) in mice. BMC Complement Altern Med. 2015; 15: 341, doi: 10.1186/s12906-015-0878-y, indexed in Pubmed: 26423525.
14. Mushtaq N, Schmatz R, Ahmed M, et al. Protective effect of rosmarinic acid against oxidative stress biomarkers in liver and kidney of strepotozotocin-induced diabetic rats. J Physiol Biochem. 2015; 71(4): 743–751, doi: 10.1007/s13105-015-0438-4, indexed in Pubmed: 26452500.
15. Oguz A, Uslukaya O, Alabalık U, et al. Topical N-acetylcysteine improves wound healing comparable to dexpanthenol: an experimental study. Int Surg. 2015; 100(4): 656–661, doi: 10.9738/INTSURG-D-14-00227.1, indexed in Pubmed: 25583306.
16. Oğuz A, Böyük A, Ekinci A, et al. Investigation of antioxidant effects of rosmarinic acid on liver, lung and kidney in rats: a biochemical and histopathological study. Folia Morphol. 2020; 79(2): 288–295, doi: 10.5603/FM.a2019.0087, indexed in Pubmed: 31436305.
17. Prisăcaru AI, Andrițoiu CV, Andriescu C, et al. Evaluation of the wound-healing effect of a novel Hypericum perforatum ointment in skin injury. Rom J Morphol Embryol. 2013; 54(4): 1053–1059, indexed in Pubmed: 24399001.
18. Qiu Z, Kwon AH, Kamiyama Y. Effects of plasma fibronectin on the healing of full-thickness skin wounds in streptozotocin-induced diabetic rats. J Surg Res. 2007; 138(1): 64–70, doi: 10.1016/j.jss.2006.06.034, indexed in Pubmed: 17161431.
19. Ulger BV, Kapan M, Uslukaya O, et al. Comparing the effects of nebivolol and dexpanthenol on wound healing: an experimental study. Int Wound J. 2016; 13(3): 367–371, doi: 10.1111/iwj.12314, indexed in Pubmed: 25040679.
20. Walker HL, Mason AD. A standard animal burn. J Trauma. 1968; 8(6): 1049–1051, doi: 10.1097/00005373-196811000-00006, indexed in Pubmed: 5722120.
21. Wang J, Pan X, Han Yi, et al. Rosmarinic acid from eelgrass shows nematicidal and antibacterial activities against pine wood nematode and its carrying bacteria. Mar Drugs. 2012; 10(12): 2729–2740, doi: 10.3390/md10122729, indexed in Pubmed: 23201594.

VIA MEDICA

ORIGINAL ARTICLE

Folia Morphol.
Vol. 80, No. 3, pp. 625–641
DOI: 10.5603/FM.a2020.0149
Copyright © 2021 Via Medica
ISSN 0015–5659
eISSN 1644–3284
journals.viamedica.pl

Unification of frequentist inference and machine learning for pterygomaxillary morphometrics

A. Al-Imam[1, 2], I.T. Abdul-Wahaab[1, 3], V.K. Konuri[4], A. Sahai[5, 6], A.K. Al-Shalchy[7, 8]

[1]*Department of Anatomy and Cellular Biology, College of Medicine, University of Baghdad, Iraq*
[2]*Queen Mary University of London, the United Kingdom*
[3]*Department of Radiology, College of Medicine, University of Baghdad, Iraq*
[4]*Department of Anatomy, All India Institute of Medical Sciences, Raipur, Chhattisgarh, India*
[5]*Dayalbagh Educational Institution, Deemed University, Dayalbagh, Agra, India*
[6]*International Federation of Associations of Anatomists, Seattle, United States of America*
[7]*Neurosurgical Unit, Department of Surgery, College of Medicine, University of Baghdad, Iraq*
[8]*The Royal College of Surgeons, United Kingdom*

[Received: 17 September 2020; Accepted: 24 November 2020; Early publication date: 30 December 2020]

Background: *The base of the skull, particularly the pterygomaxillary region, has a sophisticated topography, the morphometry of which interests pathologists, maxillofacial and plastic surgeons. The aim of the study was to conduct pterygomaxillary morphometrics and test relevant hypotheses on sexual and laterality-based dimorphism, and causality relationships.*

Materials and methods: *We handled 60 dry skulls of adult Asian males (36.7%) and females (63.3%). We calculated the prime distance D [prime] for the imaginary line from the maxillary tuberosity to the midpoint of the pterygoid process between the upper and the lower part of the pterygomaxillary fissure, as well as the parasagittal D [x-y inclin.] and coronal inclination of D [x-z inclin.] of the same line. We also took other morphometrics concerning the reference point, the maxillary tuberosity.*

Results: *Significant sexual as well as laterality-based dimorphism and bivariate correlations existed. The univariate models could not detect any significant effect of the predictors. On the contrary, summative multivariate tests in congruence with neural networks, detected a significant effect of laterality on D [x-y inclin.] (p-value = 0.066, partial eta squared = 0.030), and the interaction of laterality and sex on D [x-z inclin.] (p-value = 0.050, partial eta squared = 0.034). K-means clustering generated three clusters highlighting the significant classifier effect of D [prime] and its three-dimensional inclination.*

Conclusions: *Although the predictors in our analytics had weak-to-moderate effect size underlining the existence of unknown explanatory factors, it provided novel results on the spatial inclination of the pterygoid process, and reconciled machine learning with non-Bayesian models, the application of which belongs to the realm of oral-maxillofacial surgery.* (Folia Morphol 2021; 80, 3: 625–641)

Key words: artificial intelligence, cerebral dominance, laterality, masticatory apparatus, osteology, pterygoid process, pterygopalatine fossa, stomatognathic system

Address for correspondence: Dr. A. Al-Imam, 2601 Chemin de la Canardière, QC G1J 2G3, Quebec, Canada, tel: +1 (581) 700-0110 [Canada], +964 (0) 771 433 8199 [Iraq], e-mail: ahmed.al-imam.1@ulaval.ca; ahmed.mohammed@comed.uobaghdad.edu.iq

INTRODUCTION

The pterygomaxillary region and the maxillary alveolus are unique from the anatomical and clinical standpoint and can be affected by several pathologies [40, 46]. Besides, these regions have peculiar biomechanical properties, blood supply, as well as lymphatic drainage [36]. They neighbour and communicate with some critical areas, including middle cranial fossa, the pterygopalatine fossa, the adjacent part of the base of the skull, the carotid sheath, the nasopharynx and the "danger triangle" of the face [25]. Following a posterior maxillary molar tooth extraction, the management routinely involves dental prostheses and implants. The implant site may require bone grafting techniques that involve the maxillary tuberosity and the pterygoid process of the sphenoid bone, to ensure an implant that closely resembles the normal anatomy and attains biomechanical stability [2]. The clinical applications for studies on morphometry and pathologies affecting the pterygomaxillary junction are valuable for traumatology physicians, oral and maxillofacial surgeons, plastic surgeons and dentists [2, 11].

The configuration of the skull is mainly determined by the development of the brain and the masticatory apparatus and the relationships between the brain capsule and the latter [26]. In mammals, the cranial cavity grows with the enlargement of the brain and approaches the nasal cavity [14]. In humans, the nasal cavity altogether with the facial part of the skull, moves under the braincase, not only because of the evolutionary expansion of cerebral hemispheres but also due to the reduction of the masticatory apparatus [27]. These features distinguish the human skull from the skulls of the lowest mammals as well as anthropoid apes [13]. In animals, the sphenoid bone forms as the result of the fusion of several bones that coexist independently [34]. It, therefore, develops as a mixed bone from several paired and unpaired foci of ossification merging at the time of birth into three parts, which, in turn, fuse to form a single bone by the end of the first year of neonatal life [30].

The primary objective of the current study is to measure several morphometric parameters for the pterygomaxillary region, considering various anatomical landmarks. Morphometry will principally include measuring the distance from the maxillary tuberosity to the midpoint of the pterygoid process located between the upper and the lower part of the pterygomaxillary fissure. We shall also estimate the posterior-superior-medial three-dimensional (3D) inclination, i.e., the parasagittal (x-y plane) and the coronal (x-z plane) inclination, of the line connecting both points. Morphometry will also include other covariables, including the distance from the maxillary tuberosity to the pterygoid hamulus, the greater palatine foramen, the centre of the cruciform suture, foramen ovale, and foramen spinosum. We shall implement non-Bayesian statistical inference and machine learning models to test three hypotheses. The first two will examine the potential sexual dimorphism and laterality-based differences in connection with our morphometry. The third hypothesis will attempt to explore patterns of causations and the interaction effect among different explanatory factors with a particular interest in explaining the variables affecting the 3D inclination of the pterygoid process relative to the maxillary tuberosity. We will also discuss the relevant evolutionary lines of the skull, clinical applications in oral and maxillofacial surgery, as well as reporting anecdotal pathologies of interest. Following a pragmatic review of the literature, we confirm that our study is first of its kind regarding its objective and methodology.

We opine that the present study is novel for five reasons. Firstly, our study is the only one in the literature to address the spatial inclination of the pterygoid process in relation to the maxillary tuberosity within the Asian population. Secondly, we are approaching our research question using an unprecedented methodology, in anatomical sciences, by implementing and contrasting classical non-Bayesian statistics versus machine learning techniques. Thirdly, we implemented several models of regression analytics, multivariate tests, and neural networks to attempt finding the model that best describe and explain the pterygomaxillary morphometrics of interest. Fourthly, we argue that this robust approach in analysing data is externally valid and replicable by other researchers, thereby, serving as a foundation of future research within the discipline of anatomical and morphological sciences. Finally, we are analysing our research question and study objectives not only from an anatomical sciences perspective but also from the viewpoint of evolutionary biology and comparative anatomy, which renders our research genuinely interdisciplinary, combining aspects of human anatomy, vertebrates' evolution, data science, and artificial intelligence.

MATERIALS AND METHODS

Ethics and code of conduct, the osteology sample, morphometry and tools

The study was conducted following the standard protocol of Ethics and Scientific Committee of the College of Medicine (study protocol 155-19 on 29 December 2019), the declaration of Helsinki by World Medical Association, the European Union (EU) protocol on protection of animals used for scientific purposed (EU Directive 210/63/EU), and the ethical principles of Framingham consensus of 1997.

We used a convenience sampling method and calculated the optimal sample size using IBM SPSS version 24. Following the exclusion of defective specimens, we collected 60 normal dry skulls (n = 60) from the Department of Anatomy. These skulls belonged to adults, males (n1 = 22, 36.7%) and females (n2 = 38, 63.3%) (male-to-female ratio 1:1.73), of the Asian ethnicity who had no evident pathologies and had an intact base of the skull. Adulthood was determined by the overall ossification and the status of sutures [49]. We also determined the gender (sex) for each skull using a combination of established criteria from the existing literature on the Asian population, by relying on specific anthropometrics, including the mastoid process measurement [32], features of the temporal bone [29], other craniometric traits and parameters of exocranial surfaces [37, 42], the size and shape of the foramen magnum [48], and the external morphology of the frontal bone and frontal sinuses [20, 24, 32, 37, 42, 48]. We did our measurements after fixing each skull on a rigid manoeuvrable platform, and fine adjusting the 3D axes (x-y-z) to a standard anatomical position in which the Frankfort horizontal plane is parallel to the ground.

We used Neiko 01407A electronic Vernier calliper, which is accurate in measuring the nearest percentile of a millimetre. We measured two-dimensional (2D) morphometric parameters at the base of the skull, including the prime measurement of the distance from the maxillary tuberosity to the midpoint of the pterygoid process located between the upper and the lower part of the pterygomaxillary fissure (D [prime]). We did not choose any other landmark on the pterygoid process to measure the 3D inclination due to the high variation in the shape as well as the spatial orientation of the sphenoid bone as a whole, including the medial and lateral pterygoid plates, pterygoid hamulus, and processus tubarius. We also recorded the distance from the maxillary tuberosity to the pterygoid hamulus (D [hamulus]), the greater palatine foramen (D [greater palatine foramen]), the centre of the cruciform suture (D [cruciform suture]), foramen ovale (D [ovale]), and foramen spinosum (D [spinosum]). We used Neoteck aluminium digital angle finder protractor and a digital protractor application (Toolbox pro v5.4.0), which is accurate to the nearest percentile of a degree. In relation to the vertical line, we measured the parasagittal (x-y) and coronal (x-z) inclination of D [prime] imaginary line. To measure these angles, we approached the skull from the lateral aspect and towards the midsagittal plane of the skull, and took measurements, in millimetres for distances and degrees for inclinations, for each side of the skull, right and left (DR and DL). To avoid measurement errors and biases, we measured the morphometric parameters for each skull twice, and we recorded the average of these for subsequent data analysis.

Data collection and statistical packages, the Bradford Hill criteria, and our hypotheses

We tabulated raw data using Microsoft Excel 2016 with the integrated Analysis ToolPak, an Excel add-in. We imported the data from Excel using the Statistical Package for the Social Sciences (IBM SPSS version 24) to conduct descriptive and inferential statistics as well as to deploy machine learning to our data array. We are using an alpha (α) value of 0.05 as the threshold for significant inferential statistics, and a beta (β) value of 0.20 as the cut-off margin for statistical power.

In 1965, English statistician Austin Bradford Hill proposed criteria to provide evidence for understanding the causality between a predictor and an outcome [45]. Hill mandates the analysis of the strength of association and the effect size, the replicability of the results, the specificity of association, the temporality of causation, the gradient effect relationship, plausibility, coherence and consistency, experimental validation, and analogy [45]. Some authors also add reversibility as an additional element to the criteria [21, 45]. In correspondence with Bradford Hill criteria of causation, we shall test three hypotheses, some of which stem from the general notion of physics and astrophysics that 3D traits represent a derived feature from 2D traits in space [28]. Hence, the 3D topography of the skull, for instance, the inclination of D [prime], are secondary to the basic 2D morphometric parameters that we measured.

For instance, the spatial inclination of D [prime] represents a manifestation of D [prime] itself. On the other hand, D [prime] is also affected by the inclination. Therefore, a bidirectional interaction exists between these two parameters. Our first and second hypotheses will test the effect of laterality and sex, i.e., right versus left and males versus females, respectively, on all the parameters that we measured. In the third hypothesis, we shall test D [prime] and its 3D inclination, D [x-y inclin.] and D [x-z inclin.], as outcome variables while considering sex and laterality as predictors, and controlling for other morphometric parameters as covariates using three models of univariate and multivariate analysis of variance. Using a form of artificial general intelligence, we shall deploy collateral artificial neural networks (supervised machine learning), in addition to clustering analysis (unsupervised machine learning) [4, 35, 39].

Validity and the level-of-evidence

We evaluated the level-of-evidence according to the Oxford Centre for Evidence-based Medicine (OCEBM) [24]. According to the OCEBM, our study represents an amalgam of an observational cross-sectional data analytic of the osteology sample and an internet snapshot for the systematic review of databases of literature [24, 38].

RESULTS

Descriptive statistics

The total sample size was 60 (n = 60) distributed into males and females (n1 = 22 [36.7%], n2 = 38 [63.3%], male-to-female ratio = 1.73). The mean, the standard error, skewness, and kurtossis for D [prime] was 10.76, 0.24, 0.330, and 0.395, D [x-y inclin.] was 13.23, 0.47, 0.120, and 0.058, D [x-z inclin.] was 10.70, 0.43, 0.552, and –0.025), D [hamulus] was 12.32, 0.17, 0.133, and –0.245, D [greater palatine foramen] was 13.59, 0.19, –0.266, and –0.243, D [cruciform suture] was 29.44, 0.23, 0.074, and –0.530, D [ovale] was 33.89, 0.30, –0.674, and 0.618, and D [spinosum] was 34.88, 0.37, –0.117, and –0.024. We also explored descriptive statistics while stratifiing the sample by sex and laterality (Table 1).

Hypothesis 1: Sexual dimorphism

Firstly, when comparing in between males and females, there were no statistically significant differences for all the variables except for D [greater palatine foramen] and in favour of the male group (t = 2.689, df = 118, p-value = 0.008, mean difference = 1.04, 95% confidence interval [CI] = 0.28–1.81, Cohen's d = 0.52). Two variables, D [x-z inclin.] and D [ovale], did not meet the assumptions for running an independent t-test, and therefore, we ran a Mann-Whitney U test. Nevertheless, there was no statistically significant difference between the males and females concerning these two non-normally distributed variables.

Secondly, we stratified the sample based on laterality while comparing males versus females, and we retrieved supplementary results. For the right side of the skull, there was no statistically significant difference between males and females except for D [greater palatine foramen] and in favour of males (t = 2.20, df = 52.53, p-value = 0.032, mean difference = 1.29, 95% CI = 0.12–2.45, Cohen's d = 0.61). For the left side of the skull, there was only a statistically significant difference for D [spinosum] and in favour of males as well (t = 2.69, df = 58, p-value = 0.009, mean difference = 2.60, 95% CI = 0.67–4.53, Cohen's d = 0.73). We infer that the skulls of males and females are sexually dimorphic for a few morphometric parameters, including the distance between the maxillary tuberosity and the greater palatine foramen for both sides of the skull, and the distance from the maxillary tuberosity to foramen spinosum for the left side of the skull only. All sexually dimorphic parameters had a medium effect size and in favour of males. Accordingly, causation may potentially exist between sex and the morphometric parameters of the pterygomaxillary region. Therefore, we are going to incorporate sex as an independent variable, within our three models of univariate and multivariate tests as well as neural networks, for testing the third hypothesis.

Hypothesis 2: Laterality-based dimorphism

Firstly, we compared the right versus the left side of the skull and found no statistically significant difference for all the variables with an exception for D [x-y inclin.] in favour of the left side of the skull (t = –2.54, df = 118, p-value = 0.012, mean difference = –2.35, 95% CI = –4.19 to –0.52, Cohen's d = 0.46), and D [hamulus] in favour of the right side of the skull (t = 3.060, df = 118, p-value = 0.003, mean difference = 1.02, 95% CI = 0.33–1.67, Cohen's d = 0.56). Besides, the variable D [x-z inclin.] and D [ovale] did not satisfy the prerequisites of an inde-

Table 1. Descriptive statistics: Stratification by sex and laterality

Sex	Laterality	Mean		Skewness		Kurtosis	
		Statistic	Standard error	Statistic	Standard error	Statistic	Standard error
Female							
Left							
	D [prime]	11.1642	0.49963	0.487	0.383	0.502	0.750
	D [x-y inclination]	14.4336	0.86614	–0.367	0.383	0.800	0.750
	D [x-z inclination]	11.7788	0.75495	0.639	0.383	–0.337	0.750
	D [hamulus]	11.8062	0.25373	–0.097	0.383	–0.941	0.750
	D [greater palatine foramen]	13.3338	0.32180	–0.362	0.383	0.478	0.750
	D [cruciform suture]	29.0013	0.39891	0.201	0.383	0.610	0.750
	D [ovale]	33.4967	0.68618	–0.502	0.383	–0.123	0.750
	D [spinosum]	34.6055	0.60021	–0.089	0.383	–0.628	0.750
Right							
	D [prime]	10.1075	0.36145	0.180	0.383	–1.032	0.750
	D [x-y inclination]	11.6114	0.72981	0.214	0.383	0.322	0.750
	D [x-z inclination]	9.4439	0.71725	0.969	0.383	0.290	0.750
	D [hamulus]	12.8698	0.35227	0.113	0.383	–0.385	0.750
	D [greater palatine foramen]	13.0736	0.38045	0.082	0.383	–0.637	0.750
	D [cruciform suture]	29.6582	0.42875	–0.017	0.383	–0.966	0.750
	D [ovale]	34.5466	0.34226	–0.104	0.383	–0.970	0.750
	D [spinosum]	34.0616	0.71976	–0.029	0.383	0.222	0.750
Male							
Left							
	D [prime]	11.0308	0.43402	–0.334	0.491	–0.978	0.953
	D [x-y inclination]	14.3481	1.28436	0.408	0.491	–0.815	0.953
	D [x-z inclination]	10.1321	0.85152	–0.315	0.491	0.649	0.953
	D [hamulus]	11.8183	0.34684	0.361	0.491	–1.227	0.953
	D [greater palatine foramen]	14.1356	0.39723	–0.637	0.491	–0.467	0.953
	D [cruciform suture]	29.7637	0.56540	–0.211	0.491	–0.413	0.953
	D [ovale]	32.9981	0.76586	–0.031	0.491	–0.973	0.953
	D [spinosum]	37.2012	0.72911	0.161	0.491	0.595	0.953
Right							
	D [prime]	10.9345	0.63520	–0.038	0.491	0.340	0.953
	D [x-y inclination]	12.8071	0.98168	–0.329	0.491	0.521	0.953
	D [x-z iinclination]	11.5779	1.21917	0.276	0.491	–0.140	0.953
	D [hamulus]	12.7487	0.38554	–0.968	0.491	1.292	0.953
	D [greater palatine foramen]	14.3595	0.39371	–0.163	0.491	0.893	0.953
	D [cruciform suture]	29.4954	0.54688	0.270	0.491	–0.776	0.953
	D [ovale]	34.3200	0.49321	–1.129	0.491	2.521	0.953
	D [spinosum]	34.4622	0.88644	–0.071	0.491	–0.012	0.953

pendent t-test. Hence, we conducted an additional Mann-Whitney U test. Nevertheless, there was no statistically significant difference between the two groups.

Secondly, we made a stratification of the sample based on sex while contrasting the differences of the right versus the left side of the skull, and we acquired auxiliary results. For males, laterality had only a statistically significant differential effect on D [spinosum] and in favour of the left side of the skull (t = –2.386, df = 42, p-value = 0.022, mean difference = –2.74, 95% CI = –5.06 to –0.42, Cohen's d = 0.72). For females, laterality had a significant differential effect on three variables only, including D [x-y inclin.] in favour of the left side of the skull (t = –2.492, df = 74, p-value = 0.015, mean difference = –2.82, 95% CI = –5.08 to –0.57, Cohen's d = 0.57), D [x-z inclin.] in favour of the left side of the skull as well (t = –2.24, df = 74, p-value = 0.028, mean difference = –2.34, 95% CI = –4.41 to –0.26, Cohen's d = 0.51), and D [hamulus] in favour of the right side of the skull (t = 2.45, df = 74, p-value = 0.017, mean difference = 1.06, 95% CI = 0.20–1.93, Cohen's d = 0.56). To summarise, we deduce that there is an evident dimorphism, based on laterality, regarding the parasagittal inclination of D [prime] and for the distance from maxillary tuberosity to the pterygoid hamulus. Further, laterality-based dimorphism exists within males for the distance from maxillary tuberosity to foramen spinosum, and within females for the parasagittal and the coronal inclination of D [prime] as well as for the distance for from the maxillary tuberosity to the pterygoid hamulus. Almost all of these morphometric parameters had a medium effect size.

In contrast to sex-based dimorphism which was fully predominant in males, laterality-based dimorphism was heterogeneous for both sides of the skull, including when stratifying the sample based on sex. Accordingly, causation can exist between laterality and the pterygomaxillary morphometrics. Therefore, we are going to incorporate laterality as another predictor variable within our three models for testing the third hypothesis on causation.

Bivariate correlations and correlation matrices

Bivariate correlations: The whole sample. We used Pearson correlation for all the morphometric parameters with an exception of the non-normally distributed D [x-z inclin.] and D [ovale], for which we used nonparametric tests, including Kendall rank correlation and Spearman correlation. However, we interpreted the results in accordance with the Kendall rank correlation due to its robustness with regard to committing a type-1 statistical error. SPSS computed Pearson's r and Kendall's tau-b correlation coefficients, and the statistical significance for each variable, for one side of the skull versus the contralateral side of it, including D [prime] (Pearson's r = 0.220, p-value = 0.091), D [x-y inclin.] (Pearson's r = –0.064, p-value = 0.627), D [x-z inclin.] (Kendall's tau-b = 0.247, p-value = 0.005), D [hamulus] (Pearson's r = 0.086, p-value = 0.515), D [greater palatine foramen] (Pearson's r = –0.110, p-value = 0.403), D [cruciform suture] (Pearson's r = –0.146, p-value = 0.267), D [ovale] (Kendall's tau-b = 0.017, p-value = 0.848), and D [spinosum] (Pearson's r = 0.088, p-value = 0.504). To summarise, only D [x-z inclin.] had a significant positive correlation but of a weak effect size.

We also made bivariate correlations, as correlation matrices, for each morphometric parameter with the others, i.e., inter-variable correlations. There was only a statistically significant negative correlation between D [prime] and D [hamulus] (Pearson's r = –0.181, p-value = 0.048), and a significant positive correlation between D [ovale] and D [greater palatine foramen] (Kendall's tau-b = 0.127, p-value = 0.040), each had a weak effect size.

Bivariate correlations: Stratification by sex. We stratified the sample by sex and calculated the correlation coefficients and the statistical significance for males and females respectively within each group for D [prime] (males: Pearson's r = –0.050, p-value = 0.825; females: Pearson's r = 0.385, p-value = 0.017), D [x-y inclin.] (Pearson's r = 0.055, p-value = 0.807; Pearson's r = –0.142, p-value = 0.396), D [x-z inclin.] (Kendall's tau-b = 0.229, p-value = 0.135; Kendall's tau-b = 0.245, p-value = 0.031), D [hamulus] (Pearson's r = –0.114, p-value = 0.612; Pearson's r = 0.185, p-value = 0.266), D [greater palatine foramen] (Pearson's r = –0.266, p-value=0.231; Pearson's r = –0.138, p-value = 0.409), D [cruciform suture] (Pearson's r = –0.233, p-value = 0.297; Pearson's r = –0.090, p-value = 0.592), D [ovale] (Kendall's tau-b = –0.048, p-value = 0.756; Kendall's tau-b = 0.031, p-value = 0.782), and D [spinosum] (Pearson's r = 0.159, p-value = 0.479; Pearson's r = 0.037, p-value = 0.825). To summarise, strictly females had a significant positive correlation for two variables only, including D [prime] and D [x-z] inclination, with a weak-to-medium effect size.

Concerning the inter-variable correlations within males, there was only a statistically significant correlation for D [ovale] versus D [greater palatine foramen] of a medium effect size (Kendall's tau-b = 0.338, p-value = 0.001), D [spinosum] versus [greater palatine foramen] of a medium effect size of a medium effect size (Pearson's r = 0.471, p-value = 0.001), D [x-y inclin.] versus D [greater palatine foramen] of a medium effect size (Pearson's r = 0.315, p-value = 0.037), and D [x-z inclin.] versus D [spinosum] of a weak effect size (Kendall's tau-b = –0.236, p-value = 0.024). Concerning the inter-variable correlations within females, there was only a significant negative correlation of a weak effect size for D [prime] versus D [hamulus] (Pearson's r = –0.228, p-value = 0.047). To summarise, significant bivariate correlations exist in between few pterygomaxillary morphometric parameters.

Hypothesis 3: Univariate and multivariate statistics

Model 1A: Univariate analysis of variance without covariates (ANOVA). To test the causality relationship for the third hypothesis via this model, we used a two-factor (two-way) analysis of variance without controlling for any covariates (ANOVA) by feeding the model with D [prime] as the dependent variable, and sex and laterality as the independent variables (model predictors). According to ANOVA corrected model, sex and laterality, as well as the interaction of these two factors, did not have any significant effect on D [prime] (df = 3, F = 1.18, p-value = 0.320, partial eta squared = 0.030, adjusted R^2 = 0.005). Pair-wise comparison, via Post-hoc testing using Bonferroni correction, also failed to detect a significant difference in connection with D [prime] based on sex (mean difference = 0.35, p-value = 0.489) and laterality (mean difference = –0.58, p-value = 0.251). To summarise, model 1A predictors did not have any significant effect on D [prime].

Model 1B: Univariate analysis of variance with covariates (ANCOVA). In this model, we used a two-factor analysis of variance with covariates (ANCOVA). Model 1B has the same architecture of model 1A except that we added seven covariates, including D [x-y inclin.], D [x-z inclin.], D [hamulus], D [greater palatine foramen], D [cruciform suture], D [ovale], and D [spinosum]. Albeit controlling for the covariates, the corrected model also failed to detect any significant effect of sex and laterality on D [prime] (df = 10, F = 1.155, p-value = 0.329, partial eta squared = 0.096, adjusted R^2 = 0.013). Further, subsequent pairwise comparison, using Bonferroni correction, yielded no significant differences in between males versus females (mean difference = 0.20, p-value = 0.700), and the right side of skull versus the left side of the skull (mean difference = –0.58, p-value = 0.298). As with model 1A, the predictors in model 1B did not have a significant effect on the outcome, D [prime].

Model 2A: Multivariate analysis of variance without covariates (MANOVA). In model 2A, we will use a three-way multivariate analysis of variance (MANOVA) without covariates. Here, we will study the effect of three independent variables, including sex, laterality, and D [prime] versus the three-dimensional inclination of D [prime] represented by the two dependent variables D [x-y inclin.] and D [x-z inclin.]. All the prerequisites to run the multivariate model were satisfied, including Box's test for equivalence of covariance matrices (Box's M = 9.626, F = 1.033, df1 = 9, df2 = 65056.903, p-value = 0.410). Hence, we will interpret the results of the multivariate test using Wilks' lambda. Neither D [prime] nor sex had a significant effect on the outcome. Nonetheless, at an alpha value of 0.10, laterality assumed a significant effect on the spatial inclination of D [prime] (Wilks' lambda = 0.952, F = 2.863, hypothesis df = 2, error df = 114, p-value = 0.061, partial eta squared = 0.048), and the interaction of sex and laterality as well (Wilks' lambda = 0.956, F = 2.653, hypothesis df = 2, error df = 114, p-value = 0.075, partial eta squared = 0.044). Tests of between-subjects effects validated the results of the multivariate tests. Laterality had a significant effect on D [x-y inclin.] (df = 1, F = 5.521, p-value = 0.020, partial eta squared = 0.046) but not on D [x-z inclin.]. On the contrary, the interaction of sex and laterality had a significant effect on D [x-z inclin.] (df = 1, F = 4.945, p-value = 0.028, partial eta squared = 0.041) but not on D [x-y inclin.]. To summarise, only two predictors of model 2A had a significant effect on the parasagittal and coronal inclination of D [prime], and each had a weak effect size.

Model 2B: Multivariate analysis of variance with covariates (MANCOVA). In this model, we will run a multivariate analysis of variance while controlling for covariates (MANCOVA) (Box's M = 9.626, F = 1.033, df1 = 9, df2 = 65056.903, p-value = 0.410). The design is similar to model 2A except that we added the rest of the morphometric parameters as covariates. The multivariate model 2B failed to infer any significant effect of the predictors in connection with the outcome variables. However, when considering an alpha value of 0.10 for tests of between-subjects effects, there was a significant effect of laterality on D [x-y inclin.] (df = 1, F = 3.741, p-value = 0.056, partial eta squared = 0.033), and a significant effect of the interaction of sex and laterality on D [x-z inclin.] (df = 1, F = 4.301, p-value

= 0.040, partial eta squared = 0.038). To summarise, the MANCOVA-based model 2B is harmonious with model 2A. However, model 2B is more accurate in terms of predictive power due to the consideration of covariates in multivariate testing.

Model 3A: Multivariate analysis of variance without covariates (MANOVA). Model 3A will run a two-way multivariate analysis of variance without covariates (MANOVA) (Box's M = 24.177, F = 1.274, df1 = 18, df2 = 28191.950, p-value = 0.193). We fed the model with laterality and sex as inputs (predictors), and three outcome variables represented by D [prime], D [x-y inclin.], and D [x-z inclin.]. At an alpha value of 0.10, the multivariate analysis confirmed a significant effect of laterality on D [prime] and its spatial inclination (Wilks' lambda = 0.941, F = 2.366, hypothesis df = 3, error df = 114, p-value = 0.075, partial eta squared = 0.059). Tests of between-subjects effects verified the results of the multivariate tests; it is evident that laterality had a significant effect only on D [x-y inclin.] (df = 1, F = 5.110, p-value = 0.026, partial eta squared = 0.042), while the interaction of sex and laterality also had a significant effect but only on D [x-z inclin.] (df = 1, F = 4.537, p-value = 0.035, partial eta squared = 0.038). The results of model 3A are in line with the previous multivariate models, and each of its predictors had a weak effect size.

Model 3B: Multivariate analysis of variance with covariates (MANCOVA). Model 3B is summative for all the previous three multivariate models. We will use multivariate analysis of variance while controlling for covariates (MANCOVA) (Box's M = 24.177, F = 1.274, df1 = 18, df2 = 28191.950, p-value = 0.193). The model has the same layout of the model 3A, but here, we are also incorporating the rest of the morphometric parameters as covariates. MANCOVA-based multivariate tests of model 3B could not detect any significant effect for the predictors on the outcome variables. However, tests of between-subjects effects at an alpha value of 0.10, detected a significant effect of laterality on D [x-y inclin.] (df = 1, F = 3.443, p-value = 0.066, partial eta squared = 0.030), and another significant effect of the interaction of sex and laterality on D [x-z inclin.] (df = 1, F = 3.926, p-value = 0.050, partial eta squared = 0.034). To recapitulate the multivariate analytics, only laterality, and the interaction of sex and laterality, had a significant effect. The former influenced the parasagittal inclination, while the latter affected the coronal inclination of the imaginary line connecting the maxillary tuberosity to the midpoint of the pterygoid process between the upper and the lower part of the pterygomaxillary fissure. The significant predictor effect persists to be true even when integrating covariates to the multivariate models. However, the effect size remains weak, and none of the predictors had a significant effect on D [prime].

Hypothesis 3: Multiple linear regression

Model A. In all three regression models, we used dummy coding of sex and laterality to fit the linear nature of the analysis, and each model allowed feeding one dependent variable at a time. Here, we designated D [prime] as the dependent variable while all other morphometric parameters, as well as sex and laterality, represented the independent variables. As per the model A summary, the predictors did not have any significant effect on the outcome (R = 0.290, R^2 = 0.084, adjusted R^2 = 0.009, R^2 change = 0.084, F change = 1.121, df1 = 9, df2 = 110, p-value = 0.354).

Model B. In model B, we specified D [x-y inclin.] as the outcome, while other morphometric parameters and the dummy-coded string variables as the model predictors. Similar to the previous model, model B failed to detect any significant effect of the independent variables in connection with the parasagittal inclination of D [prime] (R = 0.290, R^2 = 0.084, adjusted R^2 = 0.018, R^2 change = 0.084, F change = 1.273, df1 = 8, df2 = 111, p-value = 0.265). Nevertheless, "tweaking" the α value for hypothesis testing up to 0.10, it is apparent that laterality had a significant effect on the parasagittal inclination and in favour of the left side of the skull (standardized beta coeffecient = 0.198, t = 1.968, p-value = 0.052).

Model C. The architecture of model C is somewhat similar to the previous model except that we allocated D [x-z inclin.] as the dependent variable. In correspondence with the model C summary, multiple linear regression also failed to infer any significant effect of the predictors on the outcome, the coronal inclination of D [prime] (R = 0.258, R^2 = 0.067, adjusted R^2 = 0.008, R^2 change = 0.067, F change = 1.144, df1 = 7, df2 = 112, p-value = 0.341). Nevertheless, if we "update" the alpha value to 0.10, D [spinosum] will have a significant effect in connection with D [x-z inclin.] (standardized beta coeffecient = –0.185, t = –1.912, p-value = 0.058). We are concluding, based on all three regression models, that only a few predictors, including laterality and D [spinosum], had a significant effect on the spatial inclination of D [prime], and strictly conditioned by manipulating the cut-off margin of the significance level.

Hypothesis 3: Supervised machine learning

Neural networks: Model 1A. We ran a neural network analysis that is complementary to the earlier univariate analysis of variate without covariates (ANOVA) in connection with model 1A for testing the third hypothesis on causality relationship. Here, we used sex and laterality as the input layer (independent variables) and D [prime] as the output layer (dependent variable). Independent variable importance and synaptic weights were superior for laterality (importance = 0.910, normalized importance = 100%) compared to sex (importance = 0.090, normalized importance = 9.9%) in predicting D [prime].

Neural networks: Model 1B. This model is parallel to the univariate analysis of variance while controlling for covariates (ANCOVA) that we implemented to test the third hypothesis using model 1B. For the input layer, we used sex and laterality as independent variables, while considering D [x-y inclin.], D [x-z inclin.], D [hamulus], D [greater palatine foramen], D [cruciform suture], D [ovale], and D [spinosum] as covariates. For the output layer, D [prime] represented the dependent variable. As per the independent variable importance analysis, this model allocated the highest values to D [x-z inclin.] (importance = 0.234, normalized importance = 100.00%), D [x-y inclin.] (0.203, 86.70%), D [hamulus] (0.193, 82.80%), D [greater palatine foramen] (0.132, 56.50%), laterality (0.064, 27.30%), D [ovale] (0.06, 25.70%), D [spinosum] (0.055, 23.40%), D [cruciform suture] (0.038, 16.40%), and sex (0.021, 9.20%). Still, it appears that laterality is more important than sex in predicting D [prime] in aggreement with the nerual network analysis of model 1A. On the other hand, the coronal and the parasagital inclination of D [prime] assumed the highest weights among the covariates.

Neural networks: Model 2A. We implemented neural networks to fulfil the multivariate analysis of variance (MANOVA) for testing the causation in model 2A. We used sex, laterality, and D [prime] as inputs (predictors) versus D [x-y inclin.] and D [x-z inclin.] as outputs (outcome variables). The model's independent variable importance analysis designated the magnitudes for D [prime] (0.483, 100.00%), laterality (0.397, 82.20%), and sex (0.121, 25.00%). According to this model, the spatial orientation of D [prime] is predicted most accurately by D [prime] itself, laterality, and sex as well.

Neural networks: Model 2B. This model is in line with the multivariate analysis of variance with covariates (MANCOVA) that we ran to test the causality relationship of model 2B of the third hypothesis. The input layer included sex and laterality, as well as six covariates, including D [prime], D [hamulus], D [greater palatine foramen], D [cruciform suture], D [ovale], and D [spinosum] as the explanatory variables. Similar, to the neural network of model 2A, the output layer had D [x-y inclin.] and D [x-z inclin.] as the response variable. Independent variable importance analysis quantified the highest values for D [prime] (0.194, 100.00%), D [spinosum] (0.178, 91.50%), D [greater palatine foramen] (0.162, 83.10%), laterality (0.129, 66.30%), D [ovale] (0.127, 65.10%), D [hamulus] (0.120, 61.70%), D [cruciform suture] (0.049, 25.40%), and sex (0.041, 21.10%). In harmony, with the neural network of model 2A, it appears that D [prime], as well as laterality and sex, are important predictors of the parasagittal and coronal inclination of the imaginary line connecting the maxillary tuberosity and midpoint of the pterygoid process located between the upper and the lower part of the pterygomaxillary fissure. However, when controlling for the covariates via this model, it is obvious that the normalized importance of laterality and sex is lower when contrasted with those of model 2A.

Neural networks: Model 3A. We used a neural network that is supportive of the multivariate statistical analysis (MANOVA) in model 3A of the third hypothesis on causation. Here, the inputs had laterality and sex as the only predictors without taking any covariates into account (Fig. 1). The output layer included D [prime], D [x-y inclin.], and D [x-z inclin.] as the dependent variables. The predictor importance analysis showed different results from the neural networks in the previous four models. Here, the neural network assigned more importance for sex (0.597, 100.0%) than laterality (0.403, 67.6%). Nonetheless, this neural network model is still in agreement with our previous results validating that males and females are sexually dimorphic in connection with the morphometry of the pterygomaxillary landmarks.

Neural networks: Model 3B. We are concluding the supervised machine learning analytics with a summative neural network model that is analogous to the multivariate statistical analysis of variance with

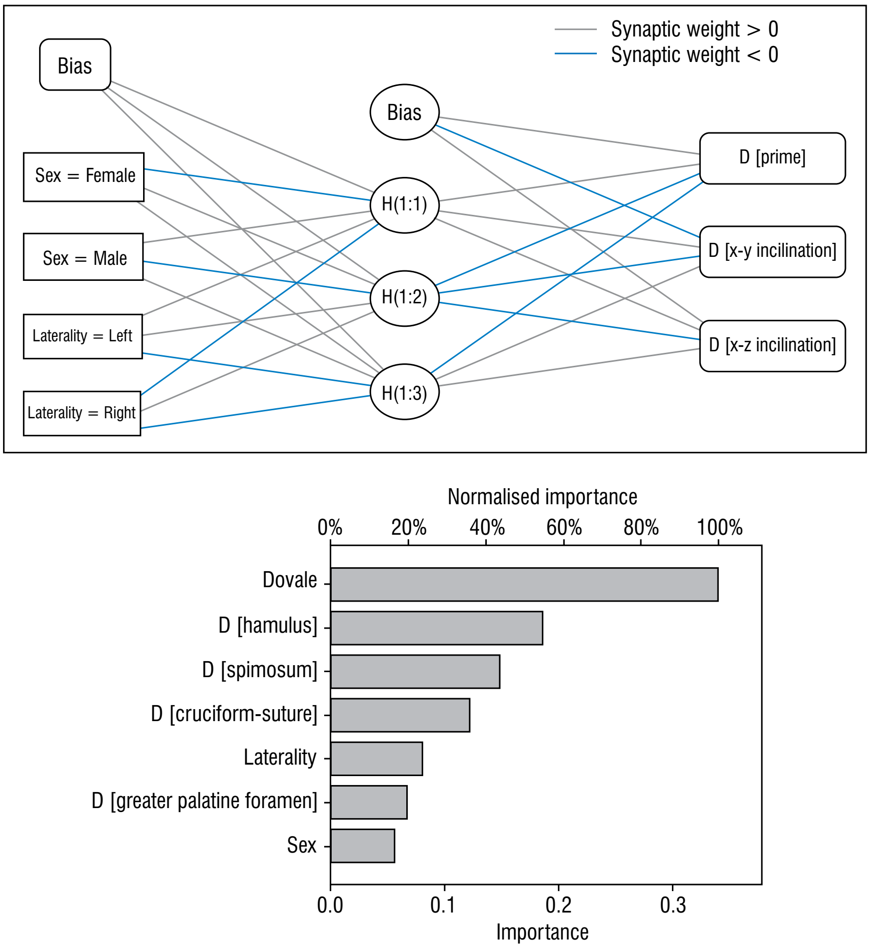

Figure 1. Neural networks with synaptic weights (Model 3a) and independent variable importance analysis (Model 3B).

covariates (MANCOVA) from model 3B of the third hypothesis. Here, the architecture of the network is the same as that of model 3A except that we added five covariates to the input layer including D [hamulus], D [greater palatine foramen], D [cruciform suture], D [ovale], and D [spinosum] (Fig. 1). The independent variable importance analysis assigned the highest importance for D [ovale] (0.34, 100.00%), D [hamulus] (0.185, 54.50%), D [spinosum] (0.149, 43.70%), D [cruciform suture] (0.122, 35.90%), laterality (0.080, 23.60%), D [greater palatine foramen] (0.067, 19.50%), and sex (0.056, 16.50%). Here, the predictor importance analysis departs from that of model 3A by generating a higher weight for laterality when compared to sex, and in harmony with the rest of the neural networks, which is in agreement that laterality-based dimorphism exists among the morphometric parameters. Among all the models, we opine that model 3B neural network is supreme in predicting D [prime] and its spatial inclination by analyzing the interaction between the several predictors, including covariates, on the outcome variables.

Unsupervised machine learning

Two-step cluster analysis. We used two-step clustering by feeding the clustering algorithm with sex and laterality as categorical variables, and the morphometric parameters as continuous variables. For the whole sample, the algorithm generated three clusters of decent quality (Silhouette measure of cohesion and separation = 0.3 out of 1). The largest cluster contributed to 36.7% of the total sample, while each of the other two clusters accounted for 31.7% (largest cluster to smallest cluster ratio = 1.16). Predictor importance analysis assigned the highest importance for sex (predictor importance = 1), laterality (0.63), D [greater palatine foramen] (0.06), D [hamulus] (0.05), D [x-y inclin.] (0.05), D [x-z inclin.] (0.04), D [spinosum] (0.03), D [prime] (0.03), D [ovale] (0.02), and D [cruciform suture] (0.01). The largest cluster included males only (100%), and each of the other two clusters included females only (100%). The predictor importance analysis, cluster comparison, and the cell distribution within each cluster go in line with the earlier results that males and females are sexually dimorphic in addition to the existence of laterality-based dimorphism within skull specimens.

Upon stratifying the sample based on sex, the two-steps cluster analysis generated a total of four clusters, two clusters for each of males and females. For males, the cluster quality was fair (Silhouette measure of cohesion and separation = 0.3), and each cluster had 50% of the total sample size (largest cluster to smallest cluster ratio = 1). Predictor analysis allocated the importance values for laterality (predictor importance = 1), D [spinosum] (0.16), D [hamulus] (0.10), D [ovale] (0.08) D [x-z inclin.] (0.05), D [x-y inclin.] (0.04), D [greater palatine foramen] (0.02), and D [cruciform suture] (0.01). For females, The clustering quality was also similar (average silhouette = 0.3), and each cluster contributed to 50% of the total sample (cluster ratio = 1). The clustering algorithm designated the highest importance to laterality (predictor importance = 1), D [x-y inclin.] (0.10), D [hamulus] (0.10), D [x-z inclin.] (0.09), D [prime] (0.06), D [ovale] (0.04), D [cruciform suture] (0.03), D [spinosum] (0.01), and D [greater palatine foramen] (0.01). The clustering within males and females gave somewhat similar results and corresponded primarily with our earlier results on the existence of a laterality-based dimorphism while assigning relatively higher importance for D [prime] among females.

Stratification of the sample based on laterality also generated four clusters, two for each of the right side of the skull and the left side of the skull, and each cluster was purely made of one of the two sexes, either males or females. For the right side of the skull, the cluster quality was fair (average silhouette = 0.3), and the largest cluster accounted for 63.3% (cluster size ratio = 1.73). The algorithm computed the highest importance for sex (predictor importance = 1), D [greater palatine foramen] (0.11), D [x-z inclin.] (0.07), D [prime] (0.05), D [x-y inclin.] (0.03), D [ovale] (0.01), D [spinosum] (0.01), D [cruciform suture] (0.01), and D [hamulus] (0.01). For the left side of the skull, the clustering parameters were the same as those for the right side. The algorithm calculated the highest importance for sex (predictor importance = 1), D [spinosum] (0.14), D [greater palatine foramen] (0.06), D [x-z inclin.] (0.05),

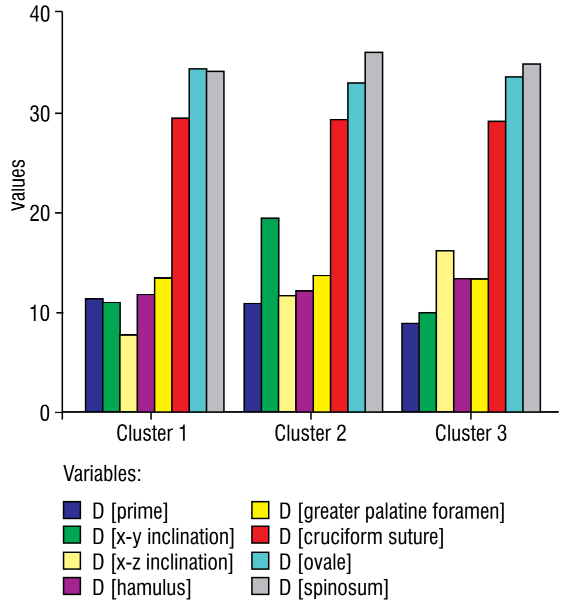

Figure 2. K-means cluster analysis: Final cluster centres.

D [curicform suture] (0.04), and D [ovale] (0.01). Finally, the stratification of the sample based on both sex and laterality together failed to yield any clusters. We conclude that the two-step cluster analysis validates our preexisting results, from independent t-tests and the multivariate models as well as the neural networks, on sex and laterality-based dimorphism in connection with the pterygomaxillary junction morphometrics.

K-means and hierarchical cluster analysis. In SPSS, k-means clustering did not allow to feed string variables to the model, including sex and laterality, and therefore, the results of this algorithm are unique from those of the two-step cluster analysis, as it relied strictly on feeding the model with continuous variables. The k-means clustering yielded three distinguished clusters (Fig. 2), and calculated the final cluster centres for D [prime] (1st cluster = 11.39, 2nd cluster = 10.94, 3rd cluster = 9.01), D [x-y inclin.] (11.05, 19.47, 10.03), D [x-z inclin.] (7.81, 11.82, 16.24), D [hamulus] (11.90, 12.23, 13.46), D [greater palatine foramen] (13.57, 13.72, 13.45), D [cruciform suture] (29.58, 29.38, 29.19), D [ovale] (34.48, 33.03, 33.60), and D [spinosum] (34.17, 36.11, 34.94). ANOVA testing confirmed that only four morphometric parameters significantly differed among the three clusters, including D [prime] (cluster df = 2, error df = 117, F = 8.135, p-value < 0.001), D [x-y inclin.] (cluster df = 2, error df = 117, F = 82.390, p-value < 0.001), D [x-z inclin.] (cluster df = 2, error df = 117, F = 56.875, p-value < 0.001), and D [hamulus] (cluster df = 2, error df = 117, F = 6.827, p-value = 0.002). Compared with the neural network from model 3B, our k-means clustering algorithm conveyed novel results in connection with the importance of D [prime] and its 3D inclination in classifying our sample regardless of sex and laterality for each specimen. We concluded the clustering analysis by conducting a hierarchial clustering which was also successful in creating a dendrogram of multiple levels.

DISCUSSION

Concerning our first hypothesis, significant sexual dimorphism existed in favour of males, and as per our pre-study anticipation. However, these were in connection with two morphometric parameters only, including D [greater palatine foramen] and D [spinosum]. For the second hypothesis, significant laterality-based dimorphism was more diversified as it did not favour one side of skull even when stratifying the sample based on sex, and it involved more morphometric parameters including D [x-y inclin.], D [x-z inclin.], D [hamulus], and D [spinosum]. Each of sexual and laterality-based dimorphism had a medium effect size. Further, significant intra-variable and inter-variable correlations existed for the whole sample and within males and females as well. However, contrary to our expectations, these correlations involved few morphometric parameters and had a weak-to-medium effect size. Testing the third hypothesis using the univariate analysis of variance and multiple linear regression failed to detect any significant predictors. In contrary, multivariate statistical models were triumphant in elucidating the significant effect of laterality, and the interaction of sex and laterality on the parasagittal and coronal inclination of D [prime], respectively. However, the weak effect size for those explanatory variables entails the existence of covert predictors, and perhaps an abundance of them interacting to manifest the full variance within the outcome. Supervised and unsupervised machine learning, using neural networks and clustering analysis, reconciled with the non-Bayesian statistical models, especially the multivariate tests, and across all of our three hypotheses. Besides, k-means cluster analysis highlighted the significant classifier effect of D [prime], its three-dimensional inclination, and D [hamulus].

Concerning the evolutionary lines of the skull, the interrelationship between the brain and the masticatory apparatus determined the overall morphology of the skull [13, 27, 30]. At first, the orbit, the nasal, and the oral cavities were located in front of the cranium [13, 26]. With the enlargement of the brain in mammals, the cranial cavity approached the nasal cavity [19, 34]. In man, the nasal cavity and the facial skeleton moved under the braincase (cranium), not only because the brain is enlarged but also because the masticatory apparatus is minimised [14, 26, 27, 30]. The singularity of the sphenoid bone also emerged because of the fusion of several independent bones that still exist in animals [30]. Therefore, it developed as a mixed bone from several paired and unpaired ossification foci merging at the time of birth into three parts, which, in turn, form a single bone by the end of the first year of life [30]. Throughout evolution, the number of teeth got reduced, and the third molar is still undergoing evolutionary pressure to disappear in humans [13, 14, 26, 30]. Further, the bulging of the forehead and the receding of the snout gave rise to the delicate proportions of the human face [13]. These anatomical features distinguished the human skull from those of lower mammals as well as the nearest anthropoid apes [19, 34]. The evolution of the craniofacial complex took place through natural selection, and yet it is constrained by the interplay of the genotype and phenotype [13, 19, 27]. If "modules" are understood as localised areas of genotypic and phenotypic integration, then we need to define the spatio-temporal boundaries of these modules and enumerate their attributes and testable properties [13, 14]. In 2006, Polanski and Franciscus (2006) [41] pointed out that "evolutionary biology has long maintained that morphological systems go from being more integrated to more modularised throughout evolution" [41]. Hence, intricate anatomical structures like the vertebrate skull become even more modularised [13, 19, 26, 27, 30, 34]. Scholars also refer to "heterochrony" which describes the evolution of ontogeny by modifications in the rate and timing of essential constituents of ontogenetic trajectories, such as the onset, the offset, and the rates of growth and development [51, 52]. Thus, causality can be questionable for craniofacial ontogeny as it is a four-dimensional process encompassing a temporal axis (time), and most evolutionary modifications of development may cause some deviations in the course of events along that axis [30, 34]. Nevertheless, developmental processes others than heterochrony, namely spatial integration, dissociation, and constraints do happen during evolution [14, 51, 52].

The pterygoid plates assume a crucial function from a biomechanical perspective in connection with the stomatognathic system, specifically the masticatory apparatus, palatal muscles, and the pharyngeal constrictors [31]. Several muscles attach to or operate via, the maxillary tuberosity and the pterygoid process of the sphenoid bone, including the buccinator, the pterygoid muscles, levator veli palatini (levator palati), and tensor veli palatine (tensor palati) [31]. Likewise, the pterygoid hamulus mimics Archimedean mechanical systems, having a pulley-like structure for the tensor palati, while the hamulus itself anchors a critical mechanical structure, the pterygomandibular raphe (pterygomandibular ligament) [31, 43]. Besides, several notable neurovascular structures exist in the vicinity of the pterygoid process, primarily the mandibular branch of the trigeminal nerve, the middle meningeal artery, nervus spinosus, the petrosal nerves, as well as the neurovascular elements of the vidian canal [31, 43]. Accordingly, the current study is of prime importance for medicine, surgery, and biomimetics. Implant dentistry specialists also do have interests in the pterygomaxillary junction, which grew exponentially following the introduction of the osseointegration theory by Branemark in the early 1960s [see 1]. Researchers found that rehabilitation of missing teeth in the anterior segment of the maxillary alveolus is far more straightforward than the posterior segment [1]. Reconstruction of the posterior maxilla is a challenge due to several obstacles, some of which relate to the anatomy of the maxillary sinus, and numerous surgical procedures were tried, such as bone augmentation, sinus lift, tilted and short implants, and zygomatic implants [1, 12]. Each of these procedures has restrictions, while the pterygomaxillary region provided an excellent venue for infallible rehabilitation of the posterior maxilla [12]. Balaji et al. [12] described using pterygoid implants for restoring an atrophic posterior maxilla, and they have higher success rates, fewer complications, and better acceptance by patients to manage atrophic posterior maxilla when compared to conventional implants [12]. In 2012, Candel et al. [18] referred to two anatomical sites for retromolar implants, including the pterygoid process and the pterygomaxillary region. According to the systematic review by Bidra and Huynh-Ba (2011) [15], the cumulative survival rate for those implants over ten years, and based on data from one of the studies was 91%.

On the other hand, the maxillary tuberosity is nearby the third molar, and it relates to a critical condition in oral and maxillofacial surgery, alveolar osteitis, which is the most frequent postoperative complication following a tooth extraction, especially for an impacted third molar nearby the maxillary tuberosity [2, 15, 17, 22]. Crawford [22] was the first to describe the condition in 1896. In their meta-analytic study, Bienek and Filliben (2016) [16] declared that the use of oral contraceptives significantly increased the risk of developing alveolar osteitis. Taberner-Vallverdú et al. (2016) [47] wrote on the heterogeneity of therapeutic modalities for alveolar osteitis, including curettage and irrigation, antiseptics, low-level laser therapy, zinc oxide eugenol, and platelet-rich plasma. Marcussen et al. (2016) [33] found that a single preoperative oral dose of amoxicillin or penicillin-V substantially reduced the incidence of alveolar osteitis. From 2012 to 2016, chlorhexidine was the centre of several metareviews. In 2012, Yengopal and Mickenautsch [50] inferred that chlorhexidine had no more adverse reactions compared to a placebo. In the same year, Daly et al. [23] validated that rinsing the alveolar sockets with chlorhexidine (0.12% and 0.2%) or using chlorhexidine gel (0.2%), prevented alveolar osteitis. Sánchez et al. (2017) [44] concluded that chlorhexidine, in any formulation, was also useful for prophylaxis, although the gel was more efficacious. Zhou et al. (2017) [53] deduced the same on the higher efficacy of chlorhexidine gel.

The current study does have limitations, including the sample size, which is relatively small. Other parameters that are unique for the sample cannot be fully known, for example, the exact age, the sub-ethnicities of individuals to whom the skulls belong. Besides, other demographic variables are obscure, including the patterns of cerebral dominance for each individual, the existence of underlying pathologies affecting the skeletal system or other corporeal systems in the premortem. Finally, there are some limitations of statistical analyses. For instance, the immoderate type-1 statistical error that may manifest as a consequence of carrying out multiple data analytics. Some tests, including correlation analytics, were more conservative than others as in the case of Kendall rank correlation versus Spearman correlation, and the same applies to parametric tests when compared to nonparametric tests. Additionally, the interpretation of causality in our hypotheses and different models that we implemented may accept

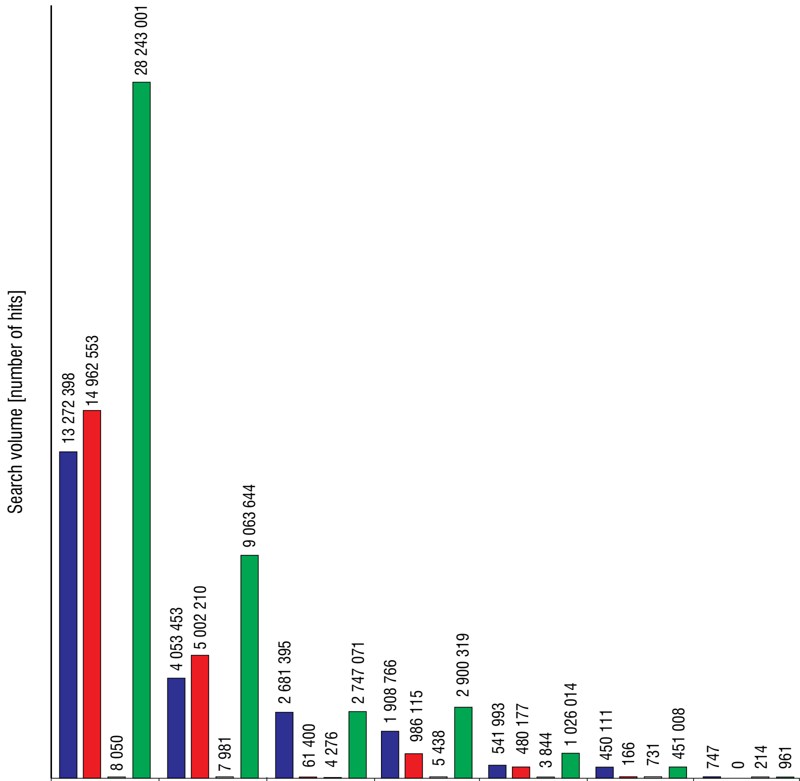

	Population demographic	Morphometry	Non-Bayesian statistics	Artificial intelligence	Applications	Osteology	Combination of themes
PubMed	13 272 398	4 053 453	2 681 395	1 908 766	541 993	450 111	747
Embase	14 962 553	5 002 210	61 400	986 115	480 177	166	0
Cohrane library	8 050	7 981	4 276	5 438	3 844	731	214
Total	28 243 001	9 063 644	2 747 071	2 900 319	1 026 014	451 008	961

Figure 3. Pragmatic review of the literature [Date: 21 August 2020].

different interpretations from a philosophical perspective, including arguing the basis of Hill's criteria when classifying specific variables into independent (predictors) and dependent (outcomes). Furthermore, the multivariate statistical analyses have inherent limitations of their own as per the aphorism of the renowned British statistician George Box, "All models are wrong, but some are useful" [5]. There are also implicit constraints of the statistical packages, SPSS included, when it comes to loading a specific type or a count of variables into a model, including multiple regression, univariate and multivariate analysis of variance, supervised neural networks, and cluster analysis. For example, one may argue that the pterygomaxillary region is of utmost surgical importance to faciomaxillary surgeries, including reconstructive surgeries, and taking all the anthropometric points, lines, and angles into account is mandatory. However, that will render the data analyses too complicated to be executed, especially in connection with the multivariate and neural networks of the third hypothesis. Future research can consider the reciprocation of an abundance of anthropometrics and morphometrics while using advanced statistical packages running on a powerful supercomputer.

Nevertheless, we opine that our study is novel and should be impactful as a base for follow-up research. On 21 August 2020, we scraped the surface web by conducting a systematic review of the medical databases of literature, using Medical Subject Headings (MeSH) and generic keywords, to detect publications of relevance to the present study (Fig. 3). We searched the PubMed (the United States National Library of Medicine), Embase (Elsevier Database), and the Cochrane Library (the Cochrane Database of Systematic Reviews). We deployed a composite of MeSH-based keywords and generic terms, in addition to truncations, and Boolean operators as well. We included keywords related to six main themes, including morphometry, osteology, population demographics, applications in medicine, non-Bayesian statistics, and artificial intelligence. Our systematic review strategy generated a total count of 44,432,018 papers distributed to PubMed (22,908,863, 51.56%), Embase (21,492,621, 48.37%), and the Cochrane Library (30,534, 0.07%). The combination of all themes of keywords retrieved 961 publications, allocated to PubMed (747, 77.73%) and the Cochrane Library (214, 22.27%) (Fig. 3). Hence, most of the publications were indexed in the PubMed database and Embase. However, Embase represented a lot of "noise" with publications that were not relevant to our study, its objectives, and methodology. Using the combination of themes, we filtered the search volume indexed in PubMed (747 publications) down by one-third of the original search volume (518 publications), by limiting the search results to articles written strictly in English, involving human species only, and the adults' age group (19+ years). We retrieved the full-text articles and scanned through the titles and abstracts, and we found very few articles that are relevant to the current study. Nonetheless, we concluded that our study is novel and the first of its kind, given its distinct objectives and pragmatic methodology, using an elaborate array of non-Bayesian statistics in parallel with machine learning.

Future studies should incorporate a larger sample size with a male-to-female ratio that is representative of the underlying population. Researchers can also attempt to use state-of-the-art equipment for the pursuit of exquisite morphometry, including the use of more advanced Vernier calliper and protractor that have fewer measurement errors. Besides, morphometry enthusiasts can record additional parameters, including surface areas and volumetrics, to enhance the accuracy and the predictive power of statistical as well as machine learning models [6]. Overcoming the limitations of data analytics, machine learning algorithms, and the statistical package can also serve as a leverage for reliable subsequent studies in line with the methodology of the present study [3, 7, 9]. Researchers should attempt to study osteology as well as radiology-based samples and compare the results from each to contrast premortem and postmortem specimens. They should also study and compare different ethnicities, age groups, patterns of lateralization of brain functions for the potential modifier effect on the stomatognathic system [8, 10]. Research can involve individuals with pathologies and conditions of interest, for example, those with alveolar osteitis, pterygoid implants, dental prostheses, and ailments that can affect bone density and microstructure. We encourage conducting studies that are not purely observational, studies of quasi-experimental design, randomized case-control trials, aggregate studies, and meta-analytic studies of the supreme level-of-evidence [38].

CONCLUSIONS

Significant sexual, as well as laterality-based dimorphism, and bivariate correlations, existed. For the first hypothesis, significant sexual dimorphism existed favouring males and as per the pre-study anticipation. However, these were in connection with two morphometric parameters only, including D [greater palatine foramen] and D [spinosum]. For the second hypothesis, significant laterality-based dimorphism was more diversified as it did not favour one side of the skull even when stratifying the sample based on sex, and it involved more morphometric parameters including D [x-y inclin.], D [x-z inclin.], D [hamulus], and D [spinosum]. Each of sexual and laterality-based dimorphism had a medium effect size. Significant intra-variable and inter-variable correlations existed for the whole sample. However, contrary to the expectations, these correlations involved few morphometric parameters and had a weak-to-medium effect size. Testing the third hypothesis using the univariate analysis of variance failed to detect any significant predictors. On the contrary, multivariate statistical models were triumphant in elucidating the significant effect of laterality, and the interaction of sex and laterality on the inclination in the parasagittal and coronal planes for D [prime], respectively. These results were consilient with the alternative hypothesis in connection with causality relationships. The weak effect size for those explanatory variables entails covert predictors and perhaps an abundance of them interacting to manifest the total variance within the outcome variables. Supervised and unsupervised machine learning, using neural networks and clustering analysis, reconciled with the non-Bayesian statistical models, especially the multivariate tests, and across all of the three hypotheses. The k-means cluster analysis highlighted the significant classifier effect of D [prime], its 3D inclination, and D [hamulus].

Future studies should incorporate a larger sample size with a male-to-female ratio representing the underlying population. Researchers can also attempt to use state-of-the-art equipment to pursue exquisite morphometry, including the use of Vernier calliper and protractor that have fewer measurement errors. Clinical researchers should explore the relevant morphometry of the maxillary sinus, including its mucosal lining, also known as the Schneiderian membrane, which is of prime importance for maxillofacial surgeons and implant dentists. Morphometry enthusiasts can record additional parameters, including surface areas and volumetrics, to enhance the accuracy, predictive power, and machine learning models. Researchers should attempt to study osteology and radiology-based samples, and compare the results from each to contrast premortem and postmortem specimens. Researchers should also study and compare different ethnicities, age groups, patterns of lateralization of brain functions for the potential modifier effect on the stomatognathic system.

Availability of data

Our data, including the raw dataset, are available upon request from the corresponding author.

Conflict of interest: None declared

REFERENCES

1. Albrektsson T, Zarb G, Worthington P, et al. The long-term efficacy of currently used dental implants: a review and proposed criteria of success. Int J Oral Maxillofac Implants. 1986; 1(1): 11–25, indexed in Pubmed: 3527955.
2. Al-Imam A, Al-Khazraji A. Alveolar osteitis following tooth extraction: systematic review and google trends analysis instigated by the first upper premolar case reported from Iraq. Modern Applied Science. 2019; 13(3): 1, doi: 10.5539/mas.v13n3p1.
3. Al-Imam A, Al-Lami F. Machine learning for potent dermatology research and practice. J Dermatol Dermatol Surg. 2020; 24(1): 1–4, doi: 10.4103/jdds.jdds_54_19.
4. Al-Imam A, Motyka M, Jędrzejko M. Conflicting opinions in connection with digital superintelligence. IAES Int J Artificial Intelligence (IJ-AI). 2020; 9(2): 336–348, doi: 10.11591/ijai.v9.i2.pp336-348.
5. Al-Imam A, Sahai A, Al-Derzi AR, et al. All Models Are Wrong, But Some Are Useful: On the Non-Bayesian Statistical Robustness of Hilton's Law. Eur J Anat. 2020; 24(1): 75–78.
6. Al-Imam A, Sahai A, Al-Nuaimi S, et al. The articular surfaces of the proximal segment of ulna: Morphometry and morphomechanics based on digital image analysis and concepts of fractal geometry. J Anat Soc India. 2018; 67(1): 40–49, doi: 10.1016/j.jasi.2018.04.003.
7. Al-Imam A. A novel method for computationally efficacious linear and polynomial regression analytics of big data in medicine. Modern Applied Science. 2020; 14(5): 1–10, doi: 10.5539/mas.v14n5p1.
8. Al-Imam A. Lateralization of brain functions: a randomized single-blinded observational study. Iran J Psych Behav Sci. 2018; 12(1), doi: 10.5812/ijpbs.8074.
9. Al-Imam A. Optimizing linear models via sinusoidal transformation for boosted machine learning in medicine. J Faculty Med Baghdad. 2019; 61(3/4): 128–136.
10. Al-Imam A. The relation between cerebral dominance and visual analytic skills in Iraqi Medical students, a cross sectional analysis. J Anat Soc India. 2017; 66: S42–S43, doi: 10.1016/j.jasi.2017.08.136.
11. Al-Imam, A. Inferential analysis of big data in real-time: one giant leap for spatiotemporal digital epidemiology in dentistry. Odontostomatol Res Anat Learning a Implantology. 2019; 12(1): 1–14.
12. Balaji VR, Lambodharan R, Manikandan D, et al. Pterygoid implant for atrophic posterior maxilla. J Pharm Bioallied Sci. 2017; 9(Suppl 1): S261–S263, doi: 10.4103/jpbs.JPBS_103_17, indexed in Pubmed: 29284976.
13. Bastir M, Rosas A. Comparative ontogeny in humans and chimpanzees: Similarities, differences and paradoxes in postnatal growth and development of the skull. Ann Anat - Anat Anz. 2004; 186(5-6): 503–509, doi: 10.1016/s0940-9602(04)80096-7.
14. Bastir M, Rosas A. Facial heights: evolutionary relevance of postnatal ontogeny for facial orientation and skull morphology in humans and chimpanzees. J Hum Evol. 2004; 47(5): 359–381, doi: 10.1016/j.jhevol.2004.08.009, indexed in Pubmed: 15530353.
15. Bidra AS, Huynh-Ba G. Implants in the pterygoid region: a systematic review of the literature. Int J Oral Maxillofac Surg. 2011; 40(8): 773–781, doi: 10.1016/j.ijom.2011.04.007, indexed in Pubmed: 21601424.
16. Bienek DR, Filliben JJ. Risk assessment and sensitivity meta-analysis of alveolar osteitis occurrence in oral contraceptive users. J Am Dent Assoc. 2016; 147(6): 394–404, doi: 10.1016/j.adaj.2016.01.011, indexed in Pubmed: 27017181.
17. Blum IR. Contemporary views on dry socket (alveolar osteitis): a clinical appraisal of standardization, aetiopathogenesis and management: a critical review. Int J Oral Maxillofac Surg. 2002; 31(3): 309–317, doi: 10.1054/ijom.2002.0263, indexed in Pubmed: 12190139.
18. Candel E, Peñarrocha D, Peñarrocha M. Rehabilitation of the atrophic posterior maxilla with pterygoid implants: a review. J Oral Implantol. 2012; 38 Spec No: 461–466, doi: 10.1563/AAID-JOI-D-10-00200, indexed in Pubmed: 21568718.
19. Cardini A, Polly PD, Cardini A, et al. Larger mammals have longer faces because of size-related constraints on skull form. Nat Commun. 2013; 4(1): 2458, doi: 10.1038/ncomms3458, indexed in Pubmed: 24045342.
20. Čechová M, Dupej J, Brůžek J, et al. Sex estimation using external morphology of the frontal bone and frontal sinuses in a contemporary Czech population. Int J Legal Med. 2019; 133(4): 1285–1294, doi: 10.1007/s00414-019-02063-8, indexed in Pubmed: 30982130.
21. Cox LA. Modernizing the Bradford Hill criteria for assessing causal relationships in observational data. Crit Rev Toxicol. 2018; 48(8): 682–712, doi: 10.1080/10408444.2018.1518404, indexed in Pubmed: 30433840.
22. Crawford JY. Dry socket. Dent Cosmos. 1896; 38: 929.
23. Daly B, Sharif MO, Newton T, et al. Local interventions for the management of alveolar osteitis (dry socket). Cochrane Database Syst Rev. 2012; 12: CD006968, doi: 10.1002/14651858.CD006968.pub2, indexed in Pubmed: 23235637.
24. Durieux N, Vandenput S, Pasleau F. [OCEBM levels of evidence system]. Rev Med Liege. 2013; 68(12): 644–649, indexed in Pubmed: 24564030.

25. Erdogan N, Unur E, Baykara M. CT anatomy of pterygopalatine fossa and its communications: a pictorial review. Comput Med Imaging Graph. 2003; 27(6): 481–487, doi: 10.1016/s0895-6111(03)00038-7, indexed in Pubmed: 14575781.
26. Hadžiselimović H, Čuš M. The appearance of internal structures of the brain in relation to configuration of the human skull. Cell Tiss Org. 1966; 63(3): 289–299, doi: 10.1159/000142794.
27. Kiliaridis S. Masticatory muscle influence on craniofacial growth. Acta Odontol Scand. 2009; 53(3): 196–202, doi: 10.3109/00016359509005972.
28. Kim SW, Nishimura J, Tsuchiya A. Expanding (3+1)-dimensional universe from a lorentzian matrix model for superstring theory in (9+1) dimensions. Phys Rev Lett. 2012; 108(1): 011601, doi: 10.1103/PhysRevLett.108.011601, indexed in Pubmed: 22304254.
29. Kozerska M, Skrzat J, Szczepanek A. Application of the temporal bone for sex determination from the skeletal remains. Folia Med Cracov. 2015; 55(2): 33–39, indexed in Pubmed: 26839241.
30. Lieberman DE. Sphenoid shortening and the evolution of modern human cranial shape. Nature. 1998; 393(6681): 158–162, doi: 10.1038/30227, indexed in Pubmed: 9603517.
31. Lofgren RH. Surgery of the pterygomaxillary fossa. Arch Otolaryngol. 1971; 94(6): 516–524, doi: 10.1001/archotol.1971.00770070816006, indexed in Pubmed: 5129223.
32. Manoonpol C, Plakornkul V. Sex determination using mastoid process measurement in Thais. J Med Assoc Thai. 2012; 95(3): 423–429, indexed in Pubmed: 22550843.
33. Marcussen KB, Laulund AS, Jørgensen HL, et al. A Systematic Review on Effect of Single-Dose Preoperative Antibiotics at Surgical Osteotomy Extraction of Lower Third Molars. J Oral Maxillofac Surg. 2016; 74(4): 693–703, doi: 10.1016/j.joms.2015.11.017, indexed in Pubmed: 26706491.
34. McBratney-Owen B, Iseki S, Bamforth SD, et al. Development and tissue origins of the mammalian cranial base. Dev Biol. 2008; 322(1): 121–132, doi: 10.1016/j.ydbio.2008.07.016, indexed in Pubmed: 18680740.
35. Møller M. A scaled conjugate gradient algorithm for fast supervised learning. Neural Networks. 1993; 6(4): 525–533, doi: 10.1016/s0893-6080(05)80056-5.
36. Montgomery WW, Katz R, Gamble JF. Anatomy and surgery of the pterygomaxillary fossa. Ann Otol Rhinol Laryngol. 1970; 79(3): 606–618, doi: 10.1177/000348947007900326, indexed in Pubmed: 5426889.
37. Musilová B, Dupej J, Velemínská J, et al. Exocranial surfaces for sex assessment of the human cranium. Forensic Sci Int. 2016; 269: 70–77, doi: 10.1016/j.forsciint.2016.11.006, indexed in Pubmed: 27883982.
38. Oxford Centre for Evidence-Based Medicine. OCEBM Levels of Evidence. https://www.cebm.net/2016/05/ocebm-levels-of-evidence/ (accessed 3 September 2020).
39. Pauler D. The Schwarz criterion and related methods for normal linear models. Biometrika. 1998; 85(1): 13–27, doi: 10.1093/biomet/85.1.13.
40. Pogrel MA, Kaplan MJ. Surgical approach to the pterygomaxillary region. J Oral Maxillofac Surg. 1986; 44(3): 183–187, doi: 10.1016/0278-2391(86)90105-9, indexed in Pubmed: 3456438.
41. Polanski JM, Franciscus RG. Patterns of craniofacial integration in extant Homo, Pan, and Gorilla. Am J Phys Anthropol. 2006; 131(1): 38–49, doi: 10.1002/ajpa.20421, indexed in Pubmed: 16552733.
42. Ramamoorthy B, Pai MM, Prabhu LV, et al. Assessment of craniometric traits in South Indian dry skulls for sex determination. J Forensic Leg Med. 2016; 37: 8–14, doi: 10.1016/j.jflm.2015.10.001, indexed in Pubmed: 26519924.
43. Rodríguez X, Rambla F, De Marcos Lopez L, et al. Anatomical study of the pterygomaxillary area for implant placement: cone beam computed tomographic scanning in 100 patients. Int J Oral Maxillofac Implants. 2014; 29(5): 1049–1052, doi: 10.11607/jomi.3173, indexed in Pubmed: 25216128.
44. Sánchez J, Calvo V, Sánchez A, et al. Sensitization to 10 mites in a tropic area. Der p and Der f are important risk factor for sensitization to other mites from Pyroglyphidae, Acaridae, Chortoglyphidae, and Glyciphagidae families. Rev Alerg Mex. 2017; 64(2): 153–162, doi: 10.29262/ram.v64i2.243, indexed in Pubmed: 28658723.
45. Schünemann H, Hill S, Guyatt G, et al. The GRADE approach and Bradford Hill's criteria for causation. J Epidemiol Community Health. 2011; 65(5): 392–395, doi: 10.1136/jech.2010.119933, indexed in Pubmed: 20947872.
46. Simental AA, Johnson JT, Myers EN. Cervical metastasis from squamous cell carcinoma of the maxillary alveolus and hard palate. Laryngoscope. 2006; 116(9): 1682–1684, doi: 10.1097/01.mlg.0000233607.41540.28, indexed in Pubmed: 16955004.
47. Taberner-Vallverdú M, Sánchez-Garcés MÁ, Gay-Escoda C. Efficacy of different methods used for dry socket prevention and risk factor analysis: A systematic review. Med Oral Patol Oral Cir Bucal. 2017; 22(6): e750–e758, doi: 10.4317/medoral.21705, indexed in Pubmed: 29053647.
48. Toneva D, Nikolova S, Harizanov S, et al. Sex estimation by size and shape of foramen magnum based on CT imaging. Leg Med (Tokyo). 2018; 35: 50–60, doi: 10.1016/j.legalmed.2018.09.009, indexed in Pubmed: 30268691.
49. Urban JE, Weaver AA, Lillie EM, et al. Evaluation of morphological changes in the adult skull with age and sex. J Anat. 2016; 229(6): 838–846, doi: 10.1111/joa.12247, indexed in Pubmed: 25406956.
50. Yengopal V, Mickenautsch S. Chlorhexidine for the prevention of alveolar osteitis. Int J Oral Maxillofac Surg. 2012; 41(10): 1253–1264, doi: 10.1016/j.ijom.2012.04.017, indexed in Pubmed: 22622144.
51. Zelditch M, Fink W. Heterochrony and heterotopy: stability and innovation in the evolution of form. Paleobiology. 2015; 22(2): 241–254, doi: 10.1017/s0094837300016195.
52. Zelditch M, Sheets H, Fink W. The ontogenetic dynamics of shape disparity. Paleobiology. 2016; 29(1): 139–156, doi: 10.1666/0094-8373(2003)029<0139:todosd>2.0.co;2.
53. Zhou S, Zhang T, Peng Bo, et al. Targeted delivery of epirubicin to tumor-associated macrophages by sialic acid-cholesterol conjugate modified liposomes with improved antitumor activity. Int J Pharm. 2017; 523(1): 203–216, doi: 10.1016/j.ijpharm.2017.03.034, indexed in Pubmed: 28336455.

VIA MEDICA

ORIGINAL ARTICLE

Folia Morphol.
Vol. 80, No. 3, pp. 642–649
DOI: 10.5603/FM.a2020.0086
Copyright © 2021 Via Medica
ISSN 0015–5659
eISSN 1644–3284
journals.viamedica.pl

Protrusion of the carotid canal into the sphenoid sinuses: evaluation before endonasal endoscopic sinus surgery

J. Jaworek-Troć[1, 2], J.A. Walocha[1], R. Chrzan[2], P. Żmuda[3], J.J. Zarzecki[4], A. Pękala[1], P. Depukat[1], E. Kucharska[5], M. Lipski[1], A. Curlej-Wądrzyk[6], M.P. Zarzecki[1]

[1]*Department of Anatomy, Jagiellonian University Medical College, Krakow, Poland*
[2]*Department of Radiology, Jagiellonian University Medical College, Krakow, Poland*
[3]*University of Pavia, Italy*
[4]*Medical University of Silesia, Katowice, Poland*
[5]*Departament of Gerontology, Geriatrics and Social Work, Jesuit University Ignatianum, Krakow, Poland*
[6]*Department of Integrated Dentistry, Dental Institute, Jagiellonian University Medical College, Krakow, Poland*

[Received: 31 May 2020; Accepted: 20 July 2020; Early publication date: 7 August 2020]

Background: *Many reports have previously indicated the vast number of anatomical variations of the sphenoid sinuses, e.g. presence of the recesses. Notwithstanding, there are a few crucial neurovascular structures directly neighbouring with the sinuses. The following research aimed to evaluate frequency prevalence of the carotid canal's protrusion into the sphenoid sinuses in adult population.*
Materials and methods: *Computed tomography (CT) scans of the paranasal sinuses of 296 patients (147 females, 149 males) were analysed in this retrospective study. The patients did not present any pathology in the sinuses. Spiral CT scanner Siemens Somatom Sensation 16 was used in the standard procedure in the option Siemens CARE Dose 4D.*
Results: *Protrusion of the carotid canal was found in the majority of the patients — 55.74%, more frequently in males (65.1% of the patients) than in females (46.26% of the patients). The said variant — regardless of gender — was noted more often bilaterally (41.55% of the cases: 29.93% females, 53.02% males) than unilaterally (14.19% of the cases: 16.33% females, 12.08% males). In the unilateral type (regardless of gender), the protrusion was more common for the left sphenoid sinus — 10.81% of the patients (12.24% females, 9.4% males) than for the right — 3.38% of the patients (4.08% females, 2.68% males).*
Conclusions: *Complicated structure of the paranasal sinuses, derived from the high prevalence of their anatomical variations, may perplex routine surgical interventions. Henceforth, referral for a CT scan is imperative in order to abate the risks associated with an invasive procedure in the said region.* (Folia Morphol 2021; 80, 3: 642–649)

Key words: sphenoid sinus, carotid canal, anatomy, radiology, laryngology

Address for correspondence: Dr. M.P. Zarzecki, MD, Department of Anatomy, Jagiellonian University Medical College, ul. Kopernika 12, 31–034 Kraków, Poland, tel/fax: +48 12 422 95 11, e-mail: michal.zarzecki96@gmail.com

INTRODUCTION

Sphenoid sinuses may be found within the diaphysis of the sphenoid bone. Their antrum is lined with the mucous membrane. There is a high prevalence of anatomical variations surrounding them. Size, shape, number of septa present and degree to which they fill in with air are just a few examples of the diversity encountered in the sinuses [15–17].

Vascular and neural structures are located in the proximity of the sphenoid sinuses — they adjoin them through the sinuses' wall. The closeness of these structures and the varied morphological features of the sinuses are crucial factors that have an impact upon a surgery in this region. In order to curtail the surgical risks and potential complications associated with the invasive intervention (including endoscopy), it is advisable for medical professionals to analyse the anatomical parameters of the sinuses [1, 11, 13, 19, 21, 22, 27, 29, 32, 34, 41].

The carotid canal is an osseous structure within the petrous temporal bone that enables the internal carotid artery, the sympathetic nerve plexus and the internal carotid venous plexus to enter the cranium [37]. The internal carotid artery has been divided by Bouthillier et al. [6] into 7 distinct parts, with the petrous segment (C2) and the lacerum segment (C3) related to the carotid canal.

A clear-cut representation of the osseous structures in the paranasal sinuses is the best obtained via a computed tomography (CT) scan, as this method allows separating the diverse anatomical variants of the sinuses.

Functional endoscopic sinus surgery (FESS) is a method that develops quite dynamically these days [4, 5]. The number of the classical extensive surgical interventions carried out on the paranasal sinuses has diminished thanks to the use of the minimally invasive endoscopic procedures.

Since the 1990s, chronic sinusitis has been commonly treated by the FESS that became the method of choice for this type of surgery. Shorter recovery period, smaller number of iatrogenic injuries, as well as excellent insight into the hardly accessible areas, made the endoscopic procedures more preferable to the classical operations [11, 23].

Detailed knowledge of the variant anatomy of the sphenoid sinuses is warranted prior to conducting an invasive procedure e.g. the FESS, the transsphenoidal approach for a pituitary adenoma surgery or closure of the cerebrospinal fluid leakage. Henceforth, the following study aimed to present the prevalence of the protrusion of the carotid canal into the lumen of the sphenoid sinus by retrospectively analysing CT scans of Polish adult population. One of the possible iatrogenic injuries is damaging the carotid canal what might lead to a hard to control bleeding [14, 28]. We hope that by utilising the CT and providing a fresh view onto the carotid canal's protrusion, our study will contribute towards a higher efficacy and safety of the surgeries carried out within the sphenoid sinuses.

MATERIALS AND METHODS

There were 296 patients (147 females, 149 males) referred to the Department of Diagnostic Imaging of the University Hospital in Krakow, that were included in this retrospective analysis. The patients had to be over 18 years old and present no pathologies in the paranasal sinuses. They were excluded if they had a history of: a head trauma or a record of nasal, orbital or cranial basis surgery, and this group comprised of 63 patients.

The medical images were obtained using a spiral CT scanner Siemens Somatom Sensation 16. Standard procedure applied in the option Siemens CARE Dose 4D. Furthermore, no contrast medium was administered to any of the patients. Thanks to the use of the multiplans reconstruction tool, both frontal and sagittal planes were visualised via secondary reconstruction from the transverse planes. Siemens Volume Wizard diagnostic station applied during the data analysis.

The analysis of the medical images involved the presence of the protrusion of the carotid canal into the sphenoid sinuses, including its bilateral and unilateral arrangements. The authors decided that for the protrusion to be noted, it has to modify shape of the wall of the sinus near the carotid canal, so that a part of the carotid canal is convex towards the lumen of the sinus

Statistical analysis

STATISTICA version 13.3 by TIBCO Software Inc.® was used to perform the statistical analysis within this manuscript. Chi^2 test and Fisher's exact test were utilised whilst probing for differences between the various laterality of the protrusion present and gender. A statistically significant value of $p < 0.05$ was chosen for all the results.

RESULTS

The carotid canal's protrusion was prevalent in the majority of the patients — in total this variant was found in 165 patients, more frequently in males (97 patients) than in females (68 patients) (Table 1).

Table 1. The prevalence of the protrusion of the carotid canal in the total research group

PCC	F	F%	M	M%	F + M	F + M%
Present	68	46.26%	97	65.1%	165	55.74%
Absent	79	53.74%	52	34.9%	131	44.26%

PCC — the protrusion of the carotid canal; F — females; F% — the percentage derived from all the females studied; M — males; M% — the percentage derived from all the males studied

Table 2. The prevalence of the protrusion of the carotid canal unilaterally or bilaterally in the total research group

PCC	F	F%	M	M%	F + M	F + M%
Unilaterally	24	16.33%	18	12.08%	42	14.19%
Bilaterally	44	29.93%	79	53.02%	123	41.55%
Absent	79	53.74%	52	34.9%	131	44.26%

PCC — the protrusion of the carotid canal; F — females; F% — the percentage derived from all the females studied; M — males; M% — the percentage derived from all the males studied

Table 3. The prevalence of the unilateral protrusion of the carotid canal in the patients with the unilateral protrusion present

PCC	F	F%	M	M%	F + M	F + M%
RSS	6	4.08%	4	2.68%	10	3.38%
LSS	18	12.24%	14	9.4%	32	10.81%

PCC — the protrusion of the carotid canal; RSS — right sphenoid sinus; LSS — left sphenoid sinus, F — females; F% — the percentage derived from all the females studied; M — males; M% — the percentage derived from all the males studied

The prevalence of the carotid canal's protrusion differed significantly between females and males ($p = 0.001$, χ^2 test). The protrusion was noted more often in males (97/165 of all the cases with the protrusion present, 58.8%), but was absent in the majority of females (79/131 of all the cases with the protrusion absent, 60.3%).

The said variant — regardless of gender — was prevalent more often bilaterally (123 patients: 44 females, 79 males) than unilaterally (42 patients: 24 females, 18 males) (Table 2).

The prevalence of the carotid canal's protrusion unilaterally, bilaterally or its absence differed significantly between females and males ($p < 0.001$, χ^2 test). The unilateral protrusion was found more often in females (24/42 cases of the total unilateral protrusion, 57.1%), similarly to the protrusion's absence — also more common in females (79/131 cases with the protrusion absent, 60.3%), but the bilateral protrusion was prevalent more frequently in males (79/123 cases of the total bilateral protrusion, 64.2%).

In case of the unilateral arrangement (42 cases), regardless of gender, the protrusion was found more frequently in the left sphenoid sinus — 32 patients (18 females, 14 males) than in the right sphenoid sinus — 10 patients (6 females, 4 males) (Table 3).

Notwithstanding, gender was not a significant factor determining the side of the presence of the unilateral protrusion ($p = 0.999$, Fisher's exact test). In both female and male groups, the protrusion on the left side predominated in the majority of cases (approximately 75% of the patients of the respective gender with a unilateral protrusion) (Fig. 1).

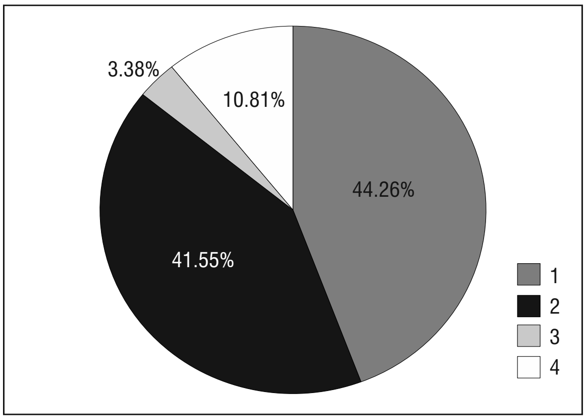

Figure 1. The prevalence of the protrusion of the carotid canal in the total research group (including its location) — cumulative data; 1 — absent; 2 — bilaterally present; 3 — present on the right side; 4 — present on the left side.

Protrusion of the carotid canal was found in total of almost half of the sinuses studied — in 288 sinuses out of the 592 sinuses researched (294 female sinuses, 298 males sinuses), slightly more common on the left side — 155 sinuses (62 in females, 93 in males), than on the right side — 133 sinuses (50 in females, 83 in males).

Table 4. The prevalence of the protrusion of the carotid canal in the total number of the sphenoid sinuses studied

PCC altogether	F	F%	M	M%	F + M	F + M%
Present	112	38.1%	176	59.06%	288	48.65%
Absent	182	61.9%	122	40.94%	304	51.35%

PCC — the protrusion of the carotid canal; F — female sinuses; F% — the percentage derived from all the female sinuses studied; M — male sinuses; M% — the percentage derived from all the male sinuses studied

Table 5. The prevalence of the unilateral protrusion of the carotid canal in the total number of the sphenoid sinuses studied

PCC altogether	F	F%	M	M%	F + M	F + M%
RSS	50	17.01%	83	27.85%	133	22.47%
LSS	62	21.09%	93	31.21%	155	26.18%

PCC — the protrusion of the carotid canal; RSS — right sphenoid sinus; LSS — left sphenoid sinus; F — female sinuses; F% — the percentage derived from all the female sinuses studied; M — male sinuses; M% — the percentage derived from all the male sinuses studied

Figure 2. Axial computed tomography scan of the paranasal sinuses showing absence of the protrusions of the carotid canals.

Figure 3. Axial computed tomography scan of the paranasal sinuses showing unilateral protrusion of the carotid canal into the left sphenoid sinus.

The proportion of the present and absent protrusions differed significantly between female and male groups ($p < 0.001$, χ^2 test). In females, it was not noted in approximately 62%, whereas in males it was prevalent in approximately 60% (Tables 4, 5).

The proportion of the presence of the unilateral protrusion of the carotid canal on the right and left sides did not differ significantly between females and males ($p = 0.676$, χ^2 test). In both female and male groups, the unilateral protrusion of the carotid canal on the left side was slightly more common (it comprised approximately 55% of the sinuses of the respective gender with a unilateral protrusion) than on the right.

Figures 2–5 present examples of the carotid canal's protrusion into the sphenoid sinuses, evaluated during this research.

DISCUSSION

Protrusion of the carotid canal was prevalent in the majority of the patients — in total this variant was noted in 55.74% of the patients, more frequently in males (65.1%) than in females (46.26%). The said variant — regardless of gender — was present bilaterally more often (41.55% of the patients: 29.93% females, 53.02% males) than unilaterally (14.19% of the patients: 16.33% females, 12.08% males). In case of the unilateral variant, regardless of gender,

Figure 4. Axial computed tomography scan of the paranasal sinuses showing unilateral protrusion of the carotid canal into the right sphenoid sinus.

Figure 5. Axial computed tomography scan of the paranasal sinuses showing bilateral protrusions of the carotid canals into the sphenoid sinuses.

the protrusion was found more frequently in the left sphenoid sinus (10.81% of the cases: 12.24% females, 9.4% males) than in the right sphenoid sinus (3.38% of the cases: 4.08% females, 2.68% males). To the best knowledge of the authors, it is so far the first study that has comprehensively taken into the consideration the possible correlation between the carotid canal's protrusion and gender, probing for its statistical significance in all presented here variants amongst the Polish population. Most notably, we have found that the protrusion was absent in 62% of the females studied, whereas in males it was present in approximately 60% of the patients, a statistically significant result ($p < 0.001$, χ^2 test).

The results presented in this work are in accordance with the data provided by other scientists. Mamatha et al. [28] stated the total prevalence of the carotid canal's protrusion as 50% (their research material: 20 CT scans), where it was bilaterally present in 15% and unilaterally in 35% (on the right side in 5%, on the left side in 30%).

On the other side, Lupascu et al. [26] provided the prevalence of the protrusion of the carotid canal as 55% (in case of the C3 segment of the artery) and as 57% (in case of the C4 segment of the artery). Moreover, Ozturan et al. [31] also noted this variant very often — in 64.5%, as well as Tan and Chong [40] — 65–72%, and Tan and Ong [39] — 67.7%.

Slightly lower prevalence was given by Hewaidi and Omami [14] — 41% (11.3% on the right side, 7% on the left side, 22.6% bilaterally). They researched 300 CT scans of people of Lebanese origins.

Elwany et al. [10], stated the prevalence of the protrusion of the carotid canal basing on the division into three types relative to the segments of the carotid canal: the presellar segment (42.7%), the subsellar segment (29.5%) and the postsellar segment (17.7%), noting that the protrusion may involve the carotid canal as a whole (18.2%), but they did not provide the criteria of the evaluation of the protrusion.

Kantarci et al. [19] evaluated the presence of this variant as 16% (bilaterally) and 7% (unilaterally). The study was conducted on the Turkish population (512 CT scans), but the age of the patients was not provided. Similar results were given by Kajoak et al. [18] — 25.4%, Tomovic et al. [42] — 28.2%, Chinese researchers — Li et al. [25] — 29.25% (8.68% unilaterally, 20.57% bilaterally), Turkish scientists — Bademci and Unal [3] — 31.1%, and Thai researchers — Nitinavakarn et al. [30] — 32.4% (17% unilaterally, 24% bilaterally).

Definitely lower prevalence of this variant was found by Anusha et al. [2] — 10% (36.7% on the right side, 53.3% on the left side and 10% bilaterally) in their study of 300 CT scans of the adult Malaysians. Even lower prevalence was provided

Table 6. The prevalence of the protrusion of the carotid canal

Author (materials and methods)	Present	Unilateral	On the right side	On the left side	Bilateral
Mamatha et al. (20 CT scans)	50%	35%	5%	30%	15%
Lupascu et al. (200 CT scans)	55%/57%	–	–	–	–
Ozturan et al. (999 CT scans)	64.5%	–	–	–	–
Tan and Chong (–)	65–72%	–	–	–	–
Tan and Ong (48 skulls, dissection and endoscopic study)	67.7%	–	–	–	–
Hewaidi and Omami (300 CT scans)	41%	18.3%	11.3%	7%	22.6%
Elwany et al. 1999 (93 skulls, dissection and endoscopic study)	89.9%	–	–	–	–
Kantarci et al. (512 CT scans)	23%	7%	–	–	16%
Kajoak et al. (201 CT scans)	25.4%	–	–	–	–
Tomovic et al. (170 HRCT)	28.2%	–	–	–	–
Li et al. (350 CT scans)	29.25%	8.68%	–	–	20.57%
Bademci and Unal et al. (45 CT scans)	31.1%	–	–	–	–
Nitinavakarn et al. (88 CT scans)	32.4%	17%	–	–	24%
Anusha et al. (300 CT scans)	10%	90%	36.7%	53.3%	10%
Kazkayasi et al. (267 CT scans)	5.2%	2.6%	–	–	2.6%
Cope (–)	?	–	–	–	–
Priyadarshini et al. (100 CT scans)	0%	–	–	–	–
Jaworek-Troć et al. (296 CT scans)	55.74%	14.19%	3.38%	10.81%	41.55%

CT — computed tomography; ? — the authors were aware of this variant but did not provide numerical values

by Kazkayasi et al. [21] — 5.2% (2.6% unilaterally, 2.6% bilaterally) — study of 267 CT scans of Turkish population.

Cope noted that the protrusion of the carotid canal may happen, but did not provide the frequency and location of the said variant [8].

Priyadarshini et al. [33] stated completely different results in their research of 100 CT scans of the patients, as they did not find even one case of the protrusion of the carotid canal. The research material studied (people of the Indian origins) and/or the evaluation criteria of the presence of the protrusion (not provided in the work) might have influenced the data (Table 6).

Precise and current anatomy of the sphenoid sinuses is of immense importance, especially whilst trying to gain access to the sella turcica using endoscopic or microscopic approaches [28]. One of the possible iatrogenic injuries caused during a transsphenoidal intervention is damaging the internal carotid artery or the optic nerve. Ciric et al. [7] have found that for the transsphenoidal approach to the pituitary surgery, the risk of injuring the internal carotid artery was 1.1%. Notwithstanding, the rate of iatrogenic vascular damage during expanded endoscopic endonasal resection of suprasellar craniopharyngomas was noted in 5% by Gardner et al. [12]. Interestingly, patients with acromegaly were found to have the protrusion of the carotid canal into the sphenoid sinuses present more often than the control group (33.5% vs. 13.3%) [35], although the limited number of patients studied (45 with acromegaly and 45 controls) might diminish the significance of the research, as also noted by the authors.

Henceforth, it is crucial for surgeons to become acquainted with the various anatomies of the sphenoid sinuses, particularly with the protrusion of the carotid canal into the sphenoid sinuses. Its unawareness might lead to fatal complications due to the arterial bleeding from the internal carotid artery that would not be easy to repair within the closed and narrow space of the sphenoid sinus [14, 28]. Lastly, it might also be a case that an infectious disease of the sphenoid sinuses may make the protruded internal carotid artery more prone to injuries [36].

In furtherance of avoiding the injury to the internal carotid artery, it is possible to utilise three-dimensional CT angiography or micro-Doppler probe to help localise the vessel [9, 24]. Notwithstanding, even when the micro-Doppler probe was applied, there were mistakes with proper identification of the artery [9]. Stecco et al. [38] have found the use of virtual dissection tables very helpful whilst diagnosing perplexing Le Fort fractures (all of them involve the pterygoid process of the sphenoid bone) that were noted as doubtful on the standard Picture Archiving and Communication System, and hence allowed for a more confident diagnosis. It might be possible that the virtual dissection tables will also prove useful in preoperational planning involving the sphenoid sinus, which is well known to be the least accessible of the paranasal sinuses. Yet another novel technology is the use of virtual endoscopy, which in the study led by Kapakin [20] allowed presence of transmural lesions to be visualised in addition to expected visualisation of the inner surface of the paranasal sinuses. It is undoubtedly prudent to know as much about the location of the internal carotid artery prior to surgery as possible. Furthermore, we would like to acknowledge Sasagawa et al. [35] and emphasise that there is still need to correlate and report the intraoperative findings with preoperative imaging investigations (i.e. the CT).

CONCLUSIONS

As shown in our study, the protrusion of the carotid canal was found in the majority of the patients and the said variant was bilateral more frequently than unilateral. In case of the unilateral arrangement, the protrusion into the left sphenoid sinus was noted more commonly. In order to conduct a safe procedure in the paranasal sinuses, it is advisable for medical professionals to refer their patients for a CT scan before the planned operation, so as to become acquainted with the anatomical variations that may be present in the sinuses.

Ethical approval

All procedures performed in studies involving human participants were in accordance with the ethical standards of the institutional and/or national research committee and with the 1964 Helsinki declaration and its later amendments or comparable ethical standards. For this type of study formal consent is not required.

Acknowledgements

The authors would like to express their sincere gratitude to Mr Jacenty Urbaniak for the technical support.

Conflict of interest: None declared

REFERENCES

1. Abdullah BJ, Arasaratnam A, Kumar G, et al. The sphenoid sinuses: computed tomographic assessment of septation, relationship to the internal carotid arteries and sidewall thickness in the Malaysian population. J HK Coll Radiol. 2001; 4: 185–188.
2. Anusha B, Baharudin A, Philip R, et al. Anatomical variants of surgically important landmarks in the sphenoid sinus: a radiologic study in Southeast Asian patients. Surg Radiol Anat. 2015; 37(10): 1183–1190, doi: 10.1007/s00276-015-1494-8, indexed in Pubmed: 25990686.
3. Bademci G, Unal B. Surgical importance of neurovascular relationships of paranasal sinus region. Turkish Neurosurgery. 2005; 15(2): 93–96.
4. Becker DG. The minimally invasive, endoscopic approach to sinus surgery. J Long Term Eff Med Implants. 2003; 13(3): 207–221, doi: 10.1615/jlongtermeffmedimplants.v13.i3.70, indexed in Pubmed: 14516186.
5. Bogusławska R. Badanie zatok przynosowych metoda tomografii komputerowej dla celów chirurgii endoskopowej. Warszawa 1995.
6. Bouthillier A, van Loveren HR, Keller JT. Segments of the internal carotid artery: a new classification. Neurosurgery. 1996; 38(3): 425–32; discussion 432, doi: 10.1097/00006123-199603000-00001, indexed in Pubmed: 8837792.
7. Ciric I, Ragin A, Baumgartner C, et al. Complications of transsphenoidal surgery: results of a national survey, review of the literature, and personal experience. Neurosurgery. 1997; 40(2): 225–236, doi: 10.1097/00006123-199702000-00001, indexed in Pubmed: 9007854.
8. Cope VZ. The Internal Structure of the Sphenoidal Sinus. J Anat. 1917; 51(Pt 2): 127–136, indexed in Pubmed: 17103809.
9. Dusick JR, Esposito F, Malkasian D, et al. Avoidance of carotid artery injuries in transsphenoidal surgery with the Doppler probe and micro-hook blades. Neurosurgery. 2007; 60(4 Suppl 2): 322–328, doi: 10.1227/01.NEU.0000255408.84269.A8, indexed in Pubmed: 17415170.
10. Elwany S, Elsaeid I, Thabet H. Endoscopic anatomy of the sphenoid sinus. J Laryngol Otol. 1999; 113(2): 122–126, doi: 10.1017/s0022215100143361, indexed in Pubmed: 10396560.
11. Eryilmaz A, Ozeri C, Bayiz U, et al. Functional endoscopic sinus surgery (FESS). Turk J Med Res. 1993; 11(5): 221–223.
12. Gardner PA, Kassam AB, Snyderman CH, et al. Outcomes following endoscopic, expanded endonasal resection of suprasellar craniopharyngiomas: a case series. J Neurosurg. 2008; 109(1): 6–16, doi: 10.3171/JNS/2008/109/7/0006, indexed in Pubmed: 18590427.
13. Haetinger RG, Navarro JAC, Liberti EA. Basilar expansion of the human sphenoidal sinus: an integrated anatomical and computerized tomography study. Eur Radiol. 2006; 16(9): 2092–2099, doi: 10.1007/s00330-006-0208-3, indexed in Pubmed: 16642328.
14. Hewaidi GH, Omami G. Anatomic variation of sphenoid sinus and related structures in libyan population: CT scan study. Libyan J Med. 2008; 3(3): 128–133, doi: 10.4176/080307, indexed in Pubmed: 21499453.

15. Jaworek-Troć J, Iwanaga J, Chrzan R, et al. Anatomical variations of the main septum of the sphenoidal sinus and its importance during transsphenoidal approaches to the sella turcica. Trans Res Anat. 2020; 21: 100079, doi: 10.1016/j.tria.2020.100079.
16. Jaworek-Troć J, Zarzecki M, Bonczar A, et al. Sphenoid bone and its sinus - anatomo-clinical review of the literature including application to FESS. Folia Med Cracov. 2019; 59(2): 45–59, indexed in Pubmed: 31659348.
17. Jaworek-Troć J, Zarzecki M, Zamojska I, et al. The dimensions of the sphenoid sinuses: evaluation before the functional endoscopic sinus surgery. Folia Morphol. 2021; 80(2): 275–282, doi: 10.5603/FM.a2020.0059, indexed in Pubmed: 32488857.
18. Kajoak SA, Ayad CE. Najmeldeen M, Abdalla EA. Computerized tomography morphometric analysis of the sphenoid sinus and related structures in Sudanese population. Glo/Adv Res J Med Med Sci. 2014; 3(7): 160–167.
19. Kantarci M, Karasen RM, Alper F, et al. Remarkable anatomic variations in paranasal sinus region and their clinical importance. Eur J Radiol. 2004; 50(3): 296–302, doi: 10.1016/j.ejrad.2003.08.012, indexed in Pubmed: 15145491.
20. Kapakin S. The paranasal sinuses: three-dimensional reconstruction, photo-realistic imaging, and virtual endoscopy. Folia Morphol. 2016; 75(3): 326–333, doi: 10.5603/FM.a2016.0006, indexed in Pubmed: 26916200.
21. Kazkayasi M, Karadeniz Y, Arikan OK. Anatomic variations of the sphenoid sinus on computed tomography. Rhinology. 2005; 43(2): 109–114, indexed in Pubmed: 16008065.
22. Keast A, Yelavich S, Dawes P, et al. Anatomical variations of the paranasal sinuses in Polynesian and New Zealand European computerized tomography scans. Otolaryngol Head Neck Surg. 2008; 139(2): 216–221, doi: 10.1016/j.otohns.2008.05.014, indexed in Pubmed: 18656718.
23. Krzeski A, Osuch-Wójcikiewicz E, Szwedowicz P, et al. Chirurgia endoskopowa w leczeniu guzów jam nosa i zatok przynosowych. Mag ORL. 2004; 3(3): 79–84.
24. Leong JL, Batra PS, Citardi MJ. Three-dimensional computed tomography angiography of the internal carotid artery for preoperative evaluation of sinonasal lesions and intraoperative surgical navigation. Laryngoscope. 2005; 115(9): 1618–1623, doi: 10.1097/01.mlg.0000173156.26930.15, indexed in Pubmed: 16148705.
25. Li Y, Sun J, Zhu X, et al. Study of the relationship between sphenoid sinus volume and protrusions in the sphenoid sinus. Forensic Med Anat Res. 2014; 02(01): 2–7, doi: 10.4236/fmar.2014.21002.
26. Lupascu M, Comsa G, Zainea V. Anatomical variations of the sphenoid sinus — a study of 200 cases. ARS Medica Tomitana. 2014; 20(2): 57–62, doi: 10.2478/arsm-2014-0011.
27. Mafee MF, Chow JM, Meyers R. Functional endoscopic sinus surgery: anatomy, CT screening, indications, and complications. Am J Roentgenol. 1993; 160(4): 735–744, doi: 10.2214/ajr.160.4.8456654, indexed in Pubmed: 8456654.
28. Mamatha H, Saraswathi G, Prasanna LC. Variations of sphenoid sinus and their impact on related neurovascular structures. Curr Neurobiol. 2010; 1(2): 121–124.
29. Mutlu C, Unlu HH, Goktan C, et al. Radiologic anatomy of the sphenoid sinus for intranasal surgery. Rhinology. 2001; 39(3): 128–132, indexed in Pubmed: 11721501.
30. Nitinavakarn B, Thanaviratananich S, Sangsilp N. Anatomical variation of the lateral nasal wall and paranasal sinuses: a CT study for endoscopic sinus surgery (ESS) in Thai patients. J Med Assoc Thai. 2005; 88(6): 763–768.
31. Ozturan O, Yenigun A, Degirmenci N, et al. Co-existence of the Onodi cell with the variation of perisphenoidal structures. Eur Arch Otorhinolaryngol. 2013; 270(7): 2057–2063, doi: 10.1007/s00405-012-2325-8, indexed in Pubmed: 23274877.
32. Perez-Pinas I, Sabate J, Carmona A, et al. Anatomical variations in the human paranasal sinus region studied by CT. J Anat. 2000; 197(2): 221–227, doi: 10.1046/j.1469-7580.2000.19720221.x.
33. Priyadarshini D, Latha PV, Ashvini K, et al. The anatomical variations in the neurovascular relations of the sphenoid sinus: an evaluation by coronal computed tomography. Turk Neurosurg. 2015; 25(2): 289–293, doi: 10.5137/1019-5149.JTN.10638-14.0, indexed in Pubmed: 26014015.
34. Sareen D, Agarwal AK, Kaul JM, et al. Study of Sphenoid Sinus Anatomy in Relation to Endoscopic Surgery. Int J Morphol. 2005; 23(3): 261–266, doi: 10.4067/s0717-95022005000300012.
35. Sasagawa Y, Tachibana O, Doai M, et al. Carotid artery protrusion and dehiscence in patients with acromegaly. Pituitary. 2016; 19(5): 482–487, doi: 10.1007/s11102-016-0728-z, indexed in Pubmed: 27207439.
36. Sirikci A, Bayazit YA, Bayram M, et al. Variations of sphenoid and related structures. Eur Radiol. 2000; 10(5): 844–848, doi: 10.1007/s003300051016, indexed in Pubmed: 10823645.
37. Standring S. Gray's Anatomy: The Anatomical Basis of Clinical Practice. Elsevier Ltd, Spain 2008: 830–845.
38. Stecco A, Boccafoschi F, Falaschi Z, et al. Virtual dissection table in diagnosis and classification of Le Fort fractures: A retrospective study of feasibility. Trans Res Anat. 2020; 18: 100060, doi: 10.1016/j.tria.2019.100060.
39. Tan HKK, Ong YK. Sphenoid sinus: an anatomic and endoscopic study in Asian cadavers. Clin Anat. 2007; 20(7): 745––750, doi: 10.1002/ca.20507, indexed in Pubmed: 17583590.
40. Tan HM, Chong VF. CT of the paranasal sinuses: normal anatomy, variations and pathology. CME Radiology. 2001; 2(3): 120–125.
41. Terra ER, Guedes FR, Manzi FR, et al. Pneumatization of the sphenoid sinus. Dentomaxillofac Radiol. 2006; 35(1): 47–49, doi: 10.1259/dmfr/55048928, indexed in Pubmed: 16421265.
42. Tomovic S, Esmaeili A, Chan NJ, et al. High-resolution computed tomography analysis of variations of the sphenoid sinus. J Neurol Surg B Skull Base. 2013; 74(2): 82–90, doi: 10.1055/s-0033-1333619, indexed in Pubmed: 24436893.

VIA MEDICA

ORIGINAL ARTICLE

Folia Morphol.
Vol. 80, No. 3, pp. 650–656
DOI: 10.5603/FM.a2020.0104
Copyright © 2021 Via Medica
ISSN 0015–5659
eISSN 1644–3284
journals.viamedica.pl

Three-dimensional verification of volumetric measurements and relationships between the condyle and the rest of the mandible; a novel approach

H.Y.A. Marghalani[1], M.A. Barayan[2], K.H. Zawawi[1], A.R. Afify[3], R.A. Alansari[1], F.F. Alsulaimani[1]

[1]*Orthodontic Department, Faculty of Dentistry, King Abdulaziz University, Jeddah, Saudi Arabia*
[2]*Oral Basic Science, Oral and Maxillofacial Radiology Department, Faculty of Dentistry, King Abdulaziz University, Jeddah, Saudi Arabia*
[3]*Orthodontic Department, Faculty of Dentistry, Mansoura University, Mansoura, Egypt*

[Received: 29 June 2020; Accepted: 21 August 2020; Early publication date: 2 September 2020]

Background: Few studies have investigated the volumetric relationship between the condyles and the mandible bilaterally.
Materials and methods: Condylar and mandibular segmentations from a sample of cone-beam computed tomography for 37 individuals were selected. T-test, correlation and linear regression analyses were performed to assess the relationships between the volumes of the condyles and mandible.
Results: The volume of the condyles and the mandible was significantly different between genders ($p < 0.05$). There was a significant but moderate correlation between the volumes of the condyle and the rest of the mandible on the same side ($p < 0.01$). A regression analysis model demonstrated that condylar volume is related to the volume of the mandible.
Conclusions: The relationship between the condylar volume and the rest of the mandible was found to be moderate. The relation between the condylar volume and mandibular volume is described by the regression equations for each side of the jaw. Sexual dimorphism exists in condylar and mandibular volumes. (Folia Morphol 2021; 80, 3: 650–656)

Key words: cone-beam computed tomography, volume, condyle, mandible, segmentation

INTRODUCTION

The mandible has many vital roles for humans, such as mastication, and facial aesthetics [1]. Moreover, the relationship between the mandible and the condyle has been the focus of some studies [4, 16]. Most of the researches that studied the mandible utilised two-dimensional imaging such as cephalometric radiographs which have limitations in accuracy and reliability [10, 11, 20].

Condylar growth was suggested to be regulated by the function of the temporomandibular joint [23]. An example of the effect of function on growth is the presence of structural asymmetry due to functional shift causing more growth on the protruded side [23]. Also, mandibular asymmetry was found in patients suffering from unilateral anterior disc displacement that caused the condylar height to be shorter on the affected side [25].

Address for correspondence: Dr. H.Y.A. Marghalani, Orthodontic Department, Faculty of Dentistry, King Abdulaziz University, P.O. Box 80209, Jeddah 21589, Saudi Arabia, e-mails: hymarghalani@kau.edu.sa

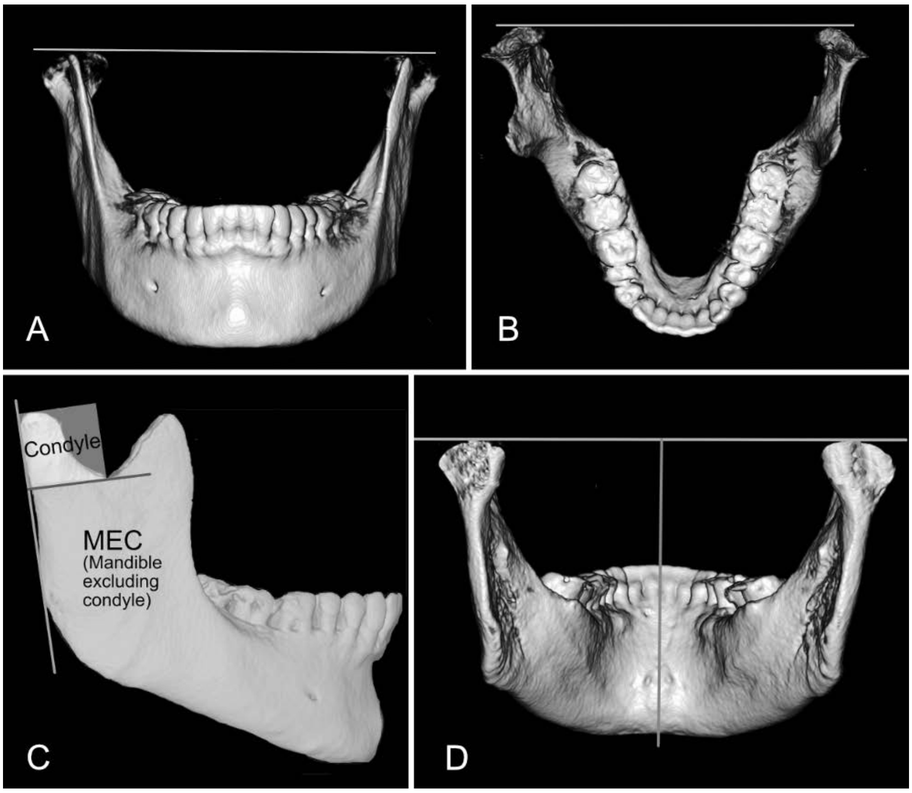

Figure 1. A. Orientation of the mandible in the coronal plane; **B.** Orientation of the mandible in the transverse plane; **C.** Segments of mandible used for volumetric measurement. The condyle is segmented out of mandible using landmarks shown; **D.** Identification of mandibular midline using line passing above condyles and perpendicular line to lingual foramen between genial tubercles.

Three-dimensional imaging using cone-beam computed tomography (CBCT) has become an integral part of dentistry [9]. High-resolution images of the craniofacial structures enable accurate volumetric and linear measurements [5, 21]. In dentistry, CBCT is commonly used before the placement of dental implants, assessment of impacted teeth and temporomandibular joint [2]. CBCT is also used to measure the volume of craniofacial structures [5, 7, 21].

To the best of our knowledge, few studies, have investigated the volumetric relationship between the condyles and the mandible bilaterally. The main objective of this study was to assess the relationship between the volume condyle and the mandible, using the CBCT segmentation method. A secondary objective was to evaluate if the mandibular volume can be predicted by the volume of the ipsilateral condyle.

MATERIALS AND METHODS

This study was approved by the Research Ethics Committee (No. 084-09-18). The sample consisted of consecutive patients who had CBCT imaging at the Radiology Department at the Faculty of Dentistry with the following inclusion criteria: 1) patients 17 years or older, 2) adequate resolution of the CBCT images of all the mandible and condyles, 3) no craniofacial deformity, pathology, fractures or jaw surgery, and 4) no dental anomalies such as supernumerary, fusion or impacted teeth.

Using the G*Power software (Heinrich Heine Universitat Dusseldorf, Germany), a priori power analysis was performed to calculate the appropriate sample size. For the correlation analysis (2-tailed) with alpha set as 0.05 and power of 0.80, the required total sample size was 13 individuals. While, with alpha set as 0.01 and power of 0.95, the required total sample size was 26 individuals.

Cone-beam computed tomography images were taken using iCAT (Imaging Sciences International, Hatfield, PA, USA) with settings of 120 Kvp and 5 mA, and segmented separating the mandible from the skull using OnDemand software (build 1.0.10.7462 by cybermed, Seoul, Korea). The mandible was oriented using intercondylar line tangent to the most superior and posterior aspect of condyles and was parallel to a horizontal line in the coronal and transverse planes (Fig. 1A, B).

Table 1. Comparison of total condyle and mandible excluding condyle (MEC) volumes between males and females

	Males (n = 13)	Females (n = 24)	P
Total condyle volume	5,757.7 (1441.6)	4,671.9 (1205.1)	0.02
Total MEC volume	75,177.4 (10976.8)	61,226.0 (10905.4)	0.001

Data are presented as mean (standard deviation) in mm^3

Table 2. Comparisons between right and left condyle and mandible excluding condyle (MEC) volumes for the total sample

	Volume [mm^3]		P
	Right (n = 37)	Left (n = 37)	
Condyle	2496.5 (708.7)	2556.7 (719.5)	0.718
MEC	33201.3 (6687.2)	32926.51 (6120.6)	0.854

Data are presented as mean (standard deviation)

Digital segmentation of the condyle was done using landmarks that were derived from the guidelines of the AOCMF classification system [17]. A tangent line to the most posterior part of the mandible touching both the condylar and gonial regions was drawn. From this line, another perpendicular line passing the most inferior point of the sigmoid notch was formed. The volume above the sigmoid notch line was the condylar volume; while the remaining volume was the mandible and was referred to as "mandible excluding condyle" (MEC) (Fig. 1C). To segment the mandible into two halves, a line perpendicular to the intercondylar line and passing through lingual foramen between the two genial tubercles in the anterior lingual aspect of the mandible (Fig. 1D). This perpendicular line was found to be a stable midline structure for the mandible [12].

All measurements were performed using OnDemand software by one investigator with more than 5 years of experience from the Maxillofacial Radiology Department. The measurements were performed twice with at least 2 weeks interval to test the intra-examiner reliability. The interclass correlation coefficient showed that the intra-examiner reliability ranged from 0.967 to 0.994.

Statistical analysis

Data on the condylar and MEC volumes were collected and analysed using Statistical Package for Social Sciences (SPSS Version 25, Armonk, NY: IBM Corp., USA). The Shapiro-Wilk test showed a normal distribution of the data. Comparisons between variables were performed using the t-test. Pearson correlation coefficient and linear regression analysis were performed. A significant level was set at $p < 0.05$.

RESULTS

The sample included 74 segmentations for 37 patients, 13 (35.1%) males and 24 (64.9%) females. The mean age was 29 ± 13 years for males and 40 ± ± 14 years for females. There was a significant difference in age between sexes ($p = 0.031$).

Table 1 shows comparisons of the total condyle and MEC volumes between males and females. The total condylar volume and MEC were significantly larger in males than in females ($p = 0.02$ and 0.001, respectively).

Table 2 shows comparisons between right and left condylar and MEC volumes for the total sample (combined males and females). The volume of the left condyles was larger (mean = 2556.7 mm^3) than the right condyle (mean = 2496.5 mm^3); however, the difference was not statistically significant ($p = 0.718$). Interestingly, the right MEC volume (mean = 33201.3 mm^3) was larger than the left MEC (mean = 32926.5 mm^3), but this difference was also not statistically significant ($p = 0.854$).

Table 3 shows in detail the comparisons between gender and sides of the condyle and MEC volumes. There were no significant differences between the right and left volumes of the condyles in males or females ($p > 0.05$). However, the right and left condyles were statistically significantly different between males and females, $p = 0.024$ and 0.026, respectively. MEC volume was not different between the right and left in both males and females, $p > 0.05$. However, males had a significantly larger right and left MEC compared to females, $p = 0.001$.

There was a strong correlation between the volumes of the right and left condyles and the right and left MEC ($r = 0.859$ and 0.972, respectively). The cor-

Table 3. Comparisons between gender and sides of condyle and mandible excluding condyle (MEC) volumes.

	Males (n = 13)	Females (n = 24)	Difference	P
Condyle				
Right	2,848.6 (649.1)	2,305.8 (676.9)	542.8	0.024
Left	2,908.55 (827.4)	2,366.18 (587.6)	542.4	0.026
Difference	59.9	60.4		
P	0.84	0.74		
MEC				
Right	37,972.7 (5,917.3)	30,616.9 (5,646.9)	7355.8	0.001
Left	37,204.7 (5,164.0)	30,609.2 (5,364.2)	6595.6	0.001
Difference	767.9	7.7		
P	0.73	0.996		
Total (Condyle + MEC)				
Right	40,821.3 (6361.8)	32,922.7 (5884.1)	7898.6	0.001
Left	40,113.3 (5,671.4)	32,975.3 (5,587.7)	7137.9	0.001
Difference	708.0	52.7		
P	0.77	0.975		

Data are presented as mean (standard deviation) in mm^3

Table 4. Correlations analysis of condylar and mandible excluding condyle (MEC) volumes

	Condyle Right	Condyle Left	MEC Right	MEC Left
Condyle Right				
Condyle Left	0.859**			
MEC Right	0.528*	0.535*		
MEC Left	0.535*	0.525*	0.972**	

*p = 0.001, **p < 0.001

relations between the right condyle and right MEC as well as the left condyle and left MEC were moderate (r = 0.528 and 0.525, respectively) (Table 4).

Linear regression analysis showed that there was a significant linear relationship between condyle volume and the rest of the MEC on each side (p < 0.001) (Figs. 2–4). The equation to predict the volume of the right MEC from the right condyle (Condyle Rt) is: **Volume of right MEC = 20764.1 + 4.98 (Condyle Rt)**. For the prediction of left MEC from the left condyle (Condyle Lt) the equation is: **Volume of left MEC = = 21508.1 + 4.47 (Condyle Lt)**.

DISCUSSION

In this study, a volumetric comparison was made between the right and left condyles and the rest of mandible in males and females. There was a significant difference in the total volumes of condyles and MEC between males and females with higher means in males. In the current study, the mean age of females was larger than males. This difference might be due to the larger number of females visiting orthodontics clinics than males in the sample. This study may suggest that sexual dimorphism exists in the volume of the condyles and rest of the mandible in each side in individuals who completed their growth, with males having larger volumes than females. Other studies also confirmed sexual dimorphism in the mandible [3, 24]. The mean maximum bite force in males was shown to be significantly higher than in females [8], which could explain the difference in volume between males and females.

Perfect facial symmetry is usually found in high quality individuals who maintain symmetric facial development even during genetic and environmental stressors [18]. In our study, when comparing the volume of the condyles and MEC between the right and left sides, no differences were found when comparing the total sample or dividing it based on gender (Table 3). This could be attributed to the fact that our sample

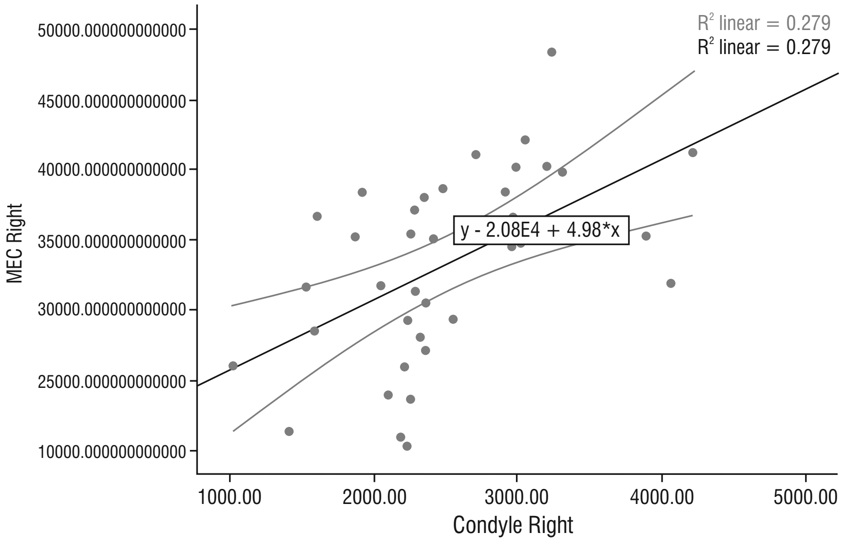

Figure 2. Correlation between right condylar volume and right mandible excluding condyle volume; MEC — mandible exluding condyle.

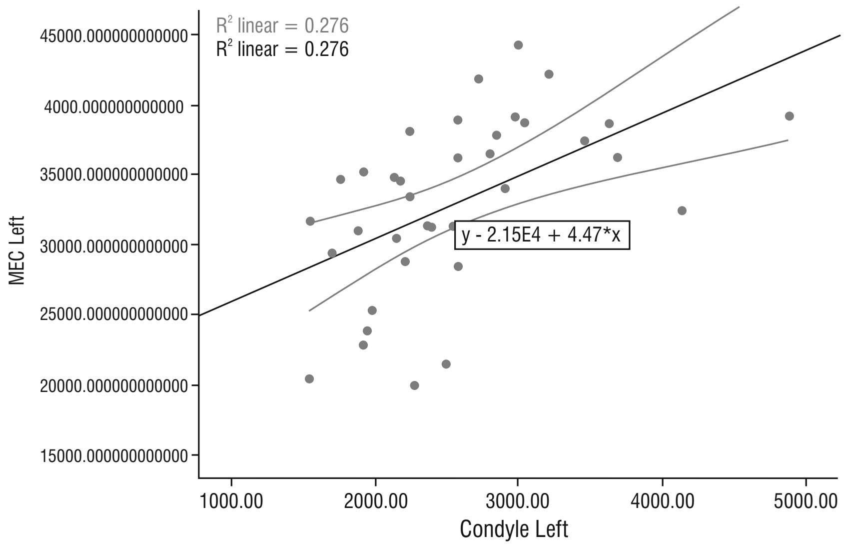

Figure 3. Correlation between left condylar volume and left mandible excluding condyle volume; MEC — mandible exluding condyle.

did not present with significant facial or mandibular asymmetry.

Sella-Tunis et al. [19] found that the function of muscles of mastication, especially the temporalis muscle, in addition to condyles, has a contributing factor to the volume of MEC. This finding might be the cause of larger mean volume in the right MEC but smaller volume in the right condyle than the other side. This finding could be attributed to the fact that most of the patients might be chewing on the right side [22]. Another study was demonstrated by Miyazaki et al. [14] who investigated the effect of muscle activity on the condyle, found that the difference in the lateral activity of the masseter muscle affects the chondrogenesis of the condyle for growing patients. Also, the function of both the masseter and temporalis muscles were found to contribute to the shape of the mandible [19].

In this study, the positive correlation between condyle and mandible is supported by other studies. For example, it was found that the growth of the condyle by itself is related to the vertical and horizontal growth of the ramus [13]. Mandibular growth has been postulated to be affected by the condylar cartilage. According to the functional matrix theory, the mandible grows in response to the soft tissue matrix surrounding it [15]. Moreover, if the condyle was fractured on one side, asymmetry will be caused

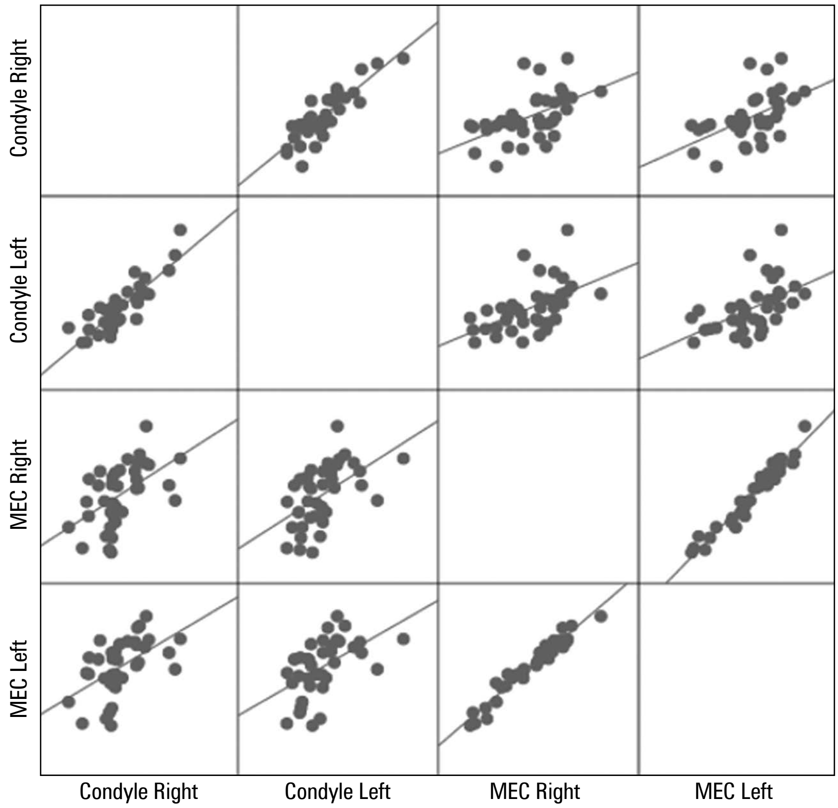

Figure 4. Matrix showing various relationships between condylar and mandible excluding condyle volumes; MEC — mandible exluding condyle.

by the decrease of both the condylar process and the associated side of the mandible [6]. These studies show that there is a relationship between condyle and mandible. Our study analysed this relationship in further detail.

In the current study, the volume of each condyle was found to be related to the volume of the rest of the mandible (MEC) where we found a moderate to strong positive correlation between the condyles and the MEC on each side. Our results are in agreement with Meikle [13].

The linear regression model between the volume of MEC and the condyles demonstrate that condylar volume has an influence on the MEC volume. So, as the condylar volume increases, the MEC volume increases.

The current study has some limitations such as gender and age distribution were not equal. This could be attributed to the stringent inclusion criteria. Future prospective longitudinal multicentre studies with a larger sample size are needed.

CONCLUSIONS

Within the limitations of this study, we found that sexual dimorphism exists in the volume of the condyles and rest of the mandible in each side in individuals who completed their growth, with males having larger volumes than females. It also confirms using CBCT segmentation that the condyle, at a specific time point, is related to the volume of the rest of the mandible on each side. Also, this study shows that the condylar volume can predict the volume of MEC.

Conflict of interest: None declared

REFERENCES

1. Choi AH, Conway RC, Taraschi V, et al. Biomechanics and functional distortion of the human mandible. J Investig Clin Dent. 2015; 6(4): 241–251, doi: 10.1111/jicd.12112, indexed in Pubmed: 25044432.
2. De Vos W, Casselman J, Swennen GRJ. Cone-beam computerized tomography (CBCT) imaging of the oral and maxillofacial region: a systematic review of the literature. Int Oral Maxillofac Surg. 2009; 38(6): 609–625, doi: 10.1016/j.ijom.2009.02.028, indexed in Pubmed: 19464146.
3. Fan Yi, Penington A, Kilpatrick N, et al. Quantification of mandibular sexual dimorphism during adolescence. J Anat. 2019; 234(5): 709–717, doi: 10.1111/joa.12949, indexed in Pubmed: 30834524.
4. Farronato M, Cavagnetto D, Abate A, et al. Assessment of condylar volume and ramus height in JIA patients with unilateral and bilateral TMJ involvement: retrospective case-control study. Clin Oral Investig. 2020; 24(8): 2635–2643, doi: 10.1007/s00784-019-03122-5, indexed in Pubmed: 31760476.

5. García-Sanz V, Bellot-Arcís C, Hernández V, et al. Accuracy and reliability of cone-beam computed tomography for linear and volumetric mandibular condyle measurements. A human cadaver study. Sci Rep. 2017; 7(1): 11993, doi: 10.1038/s41598-017-12100-4, indexed in Pubmed: 28931867.
6. Hu Y, Yang Hf, Li S, et al. Condyle and mandibular bone change after unilateral condylar neck fracture in growing rats. Int J Oral Maxillofac Surg. 2012; 41(8): 912–921, doi: 10.1016/j.ijom.2011.12.036, indexed in Pubmed: 22429642.
7. Huntjens E, Kiss G, Wouters C, et al. Condylar asymmetry in children with juvenile idiopathic arthritis assessed by cone-beam computed tomography. Eur J Orthod. 2008; 30(6): 545–551, doi: 10.1093/ejo/cjn056, indexed in Pubmed: 19054811.
8. Jain V, Mathur VP, Pillai RS, et al. A preliminary study to find out maximum occlusal bite force in Indian individuals. Indian J Dent Res. 2014; 25(3): 325–330, doi: 10.4103/0970-9290.138330, indexed in Pubmed: 25098989.
9. Jiang YY, Sun L, Wang H, et al. Three-dimensional cone beam computed tomography analysis of temporomandibular joint response to the Twin-block functional appliance. Korean J Orthod. 2020; 50(2): 86–97, doi: 10.4041/kjod.2020.50.2.86, indexed in Pubmed: 32257934.
10. Kilic N, Kiki A, Oktay H. Condylar asymmetry in unilateral posterior crossbite patients. Am J Orthod Dentofacial Orthop. 2008; 133(3): 382–387, doi: 10.1016/j.ajodo.2006.04.041, indexed in Pubmed: 18331937.
11. Lippold C, Kruse-Losler B, Danesh G, et al. Treatment of hemimandibular hyperplasia: the biological basis of condylectomy. Br J Oral Maxillofac Surg. 2007; 45(5): 353–360, doi: 10.1016/j.bjoms.2006.10.011, indexed in Pubmed: 17145124.
12. McDonnell D, Reza Nouri M, Todd ME. The mandibular lingual foramen: a consistent arterial foramen in the middle of the mandible. J Anat. 1994; 184 (Pt 2): 363–369, indexed in Pubmed: 8014127.
13. Meikle MC. The role of the condyle in the postnatal growth of the mandible. Am J Orthod. 1973; 64(1): 50–62, doi: 10.1016/0002-9416(73)90280-7, indexed in Pubmed: 4577167.
14. Miyazaki M, Yonemitsu I, Takei M, et al. The imbalance of masticatory muscle activity affects the asymmetric growth of condylar cartilage and subchondral bone in rats. Arch Oral Biol. 2016; 63: 22–31, doi: 10.1016/j.archoralbio.2015.11.020, indexed in Pubmed: 26669214.
15. Moss ML, Rankow RM. The role of the functional matrix in mandibular growth. Angle Orthod. 1968; 38(2): 95–103, doi: 10.1043/0003-3219(1968)038<0095:TROTFM>2.0.CO;2, indexed in Pubmed: 5239131.
16. Nakano H, Maki K, Shibasaki Y, et al. Three-dimensional changes in the condyle during development of an asymmetrical mandible in a rat: a microcomputed tomography study. Am J Orthod Dentofacial Orthop. 2004; 126(4): 410–420, doi: 10.1016/j.ajodo.2004.04.016, indexed in Pubmed: 15470344.
17. Neff A, Cornelius CP, Rasse M, et al. The Comprehensive AOCMF Classification System: Condylar Process Fractures — Level 3 Tutorial. Craniomaxillofac Trauma Reconstr. 2014; 7(Suppl 1): S044–S058, doi: 10.1055/s-0034-1389559, indexed in Pubmed: 25489390.
18. Rhodes G, Proffitt F, Grady J, et al. Facial symmetry and the perception of beauty. Psychon Bull Rev. 1998; 5(4): 659–669, doi: 10.3758/bf03208842.
19. Sella-Tunis T, Pokhojaev A, Sarig R, et al. Human mandibular shape is associated with masticatory muscle force. Sci Rep. 2018; 8(1): 6042, doi: 10.1038/s41598-018-24293-3, indexed in Pubmed: 29662127.
20. Taneja VK, Kumar GA, Farishta S, et al. An assessment of skeletal craniofacial asymmetry in South Indian population. J Contemp Dent Pract. 2012; 13(1): 80–84, doi: 10.5005/jp-journals-10024-1100, indexed in Pubmed: 22430699.
21. Tecco S, Saccucci M, Nucera R, et al. Condylar volume and surface in Caucasian young adult subjects. BMC Medical Imaging. 2010; 10(1): 28, doi: 10.1186/1471-2342-10-28.
22. Tiwari S, Nambiar S, Unnikrishnan B. Chewing side preference - Impact on facial symmetry, dentition and temporomandibular joint and its correlation with handedness. J Orofacial Sci. 2017; 9(1): 22, doi: 10.4103/jofs.jofs_74_16.
23. Von den Hoff JW, Delatte M. Interplay of mechanical loading and growth factors in the mandibular condyle. Arch Oral Biol. 2008; 53(8): 709–715, doi: 10.1016/j.archoralbio.2008.03.002, indexed in Pubmed: 18395696.
24. Watanabe H, Mohammad Abdul M, Kurabayashi T, et al. Mandible size and morphology determined with CT on a premise of dental implant operation. Surg Radiol Anat. 2010; 32(4): 343–349, doi: 10.1007/s00276-009-0570-3, indexed in Pubmed: 19812884.
25. Xie Q, Yang C, He D, et al. Will unilateral temporomandibular joint anterior disc displacement in teenagers lead to asymmetry of condyle and mandible? A longitudinal study. J Craniomaxillofac Surg. 2016; 44(5): 590–596, doi: 10.1016/j.jcms.2016.01.019, indexed in Pubmed: 27021265.

VIA MEDICA

ORIGINAL ARTICLE

Folia Morphol.
Vol. 80, No. 3, pp. 657–664
DOI: 10.5603/FM.a2020.0087

ISSN 0015–5659
eISSN 1644–3284
journals.viamedica.pl

The influence of antero-posterior dentoskeletal pattern on the value of nasal soft tissue angles: a cephalometric study

T. Perović[1], Z. Blažej[1], I. Jovanović[2]

[1]*Department for Orthodontics and Dentofacial Orthopaedics, Dental Clinic, Niš, Serbia*
[2]*Department for Anatomy, Faculty of Medicine, University of Niš, Serbia*

[Received: 1 June 2020; Accepted: 25 July 2020; Early publication date: 7 August 2020]

Background: *The aim of this study was to examine the influence of sagittal dentoskeletal pattern on the value of profile nasal soft tissue angles and estimate the significance of examined differences for each angle.*

Materials and methods: *Lateral cephalograms were used to examine the nasofrontal angle, nasofacial angle, nasal tip angle, and nasolabial angle of 120 adult Caucasian subjects (60 male and 60 female) from the central Balkan area. Subjects were divided into four groups according to the ANB angle and incisors inclination: class I as the control group, class II division 1, class II division 2 and class III.*

Results: *By evaluating the influence of sagittal dentoskeletal relationships on the values of examined angles, significant differences were found among subjects with class I and class II/2 (p = 0.028), so as class III (p = 0.002) for nasal tip angle. The nasofacial angle was found to differ among subjects with class I and class II/1 (p = 0.002), so as class III (p = 0.001).*

Conclusions: *Different dentoskeletal patterns have significant influence on values of the nasal tip angle and nasofacial angle, and don't have influence on the values of the nasofrontal and nasolabial angle.* (Folia Morphol 2021; 80, 3: 657–664)

Key words: cephalometry, nose, dentoskeletal pattern

INTRODUCTION

The nose is central and most prominent part of the middle segment of the face, which is crucial for assessing facial harmony and attractiveness. The nasal pyramid plays a notable cosmetic role in the appearance of the whole face; providing harmony and balance to the face [22]. This segment as well as shape of the nose represents a "signature" indicating ethnicity, race, age, and gender [18, 19, 22, 23, 31, 32]. Farkash was the first who began to apply selective anthropometric parameters that later researchers standardised and created "ideal nose" (cited by Lazovic [15]). Some of the shapes are purely racial-specific [22], so as angles that nose create with the nearby profile contours [33].

Are changes in the nasal profile angles correlated with different antero-posterior dentofacial pattern and to what extent? Since the midfacial segment and nose form the nasomaxillary complex, each antero-posterior jaw discrepancy is expected to influence the profile angles of this facial segment. Contours of the facial soft tissue differ from the contours of basic skeletal structures in certain areas, especially in the nasal third of the profile [12, 24, 28, 29]. Therefore,

Address for correspondence: Dr. T. Perović, Sestre Baković 16/22, 18000 Niš, Serbia, tel: +381 18 520 763, fax: +381 18 453 67 36, e-mail: tatjana.tanic@gmail.com

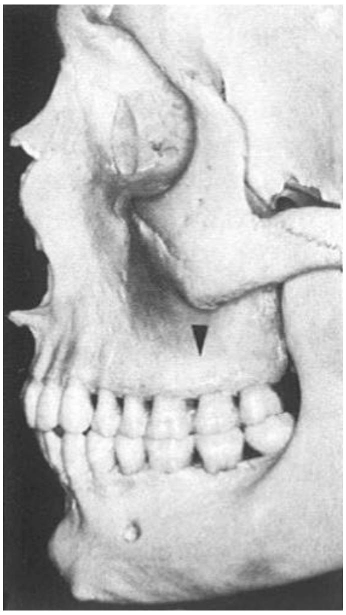

Figure 1. Skull with class I dentoskeletal pattern (source [26]).

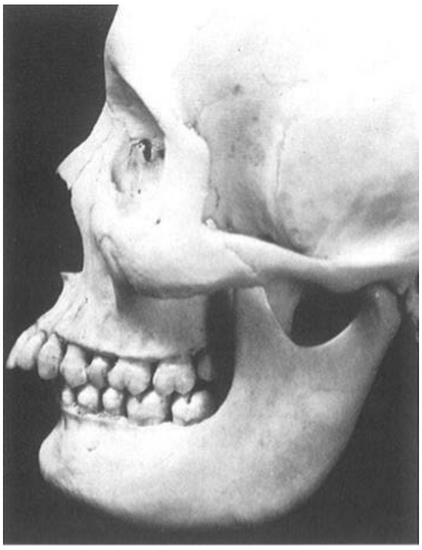

Figure 2. Skull with class II division 1 dentoskeletal pattern (source [26]).

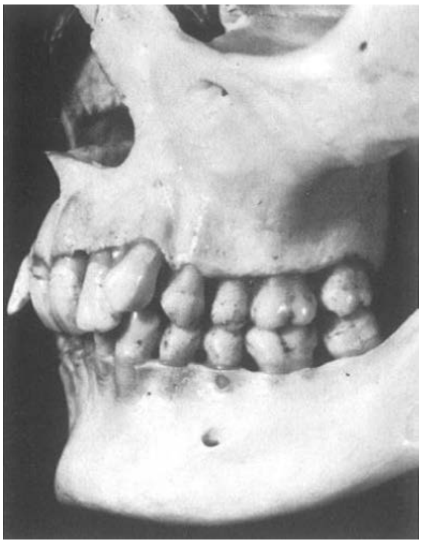

Figure 3. Skull with class II division 2 dentoskeletal pattern (source [26]).

facial profile angles are influenced by composite effect of skeletal and soft tissue profile. This fact indicates a possibility of difficult facial reconstruction based on the skull, because nose can have any shape. Likewise, angles that nose makes with nearby facial components can have any value inside the range of variations (racial, age and gender).

Dentoskeletal patterns highly influence the facial profile and facial aesthetics [24], especially the lower part of the face profile. However, some of the dentoskeletal patterns can imply a certain shape of the nose [23].

According to angle, class I dentoskeletal pattern is usually related to normal anteroposterior jaw relationship (Fig. 1), the straight profile and pleasant face.

Class II division 1 pattern present retroposition of the lower jaw in relation to the upper jaw (Fig. 2) and indicates a convex profile with the chin set posterior, therefore the dominant nose.

Class II division 2 pattern indicates a convex profile with characteristically emphasized tip of the nose and chin, having the tendency of mutual convergency (Fig. 3) [23]. This specific facial profile morphotype exists due to retropositioned dentoalveolar segment.

Class III pattern indicates overdeveloped lower jaw (Fig. 4) that is dominant in relation to other facial features (nose, forehead, lips). Persons with class III have a concave profile. This pattern is considered the least aesthetic [2, 24].

The aim of this study is to determine the values of facial profile angles of the midfacial (nasal) segment in subjects with class I, class II division 1, class II division 2, and class III, in order to, examine, in this way, the influence of dentoskeletal pattern on the value of angular profile parameters of the nose region, as well as to examine the significance of the established variations for each angle individually.

MATERIALS AND METHODS

The study was conducted at the Faculty of Medicine, Niš, Serbia. Before the commencement of the study, each volunteer gave an informed consent as to the purpose and nature of the study. All work was per-

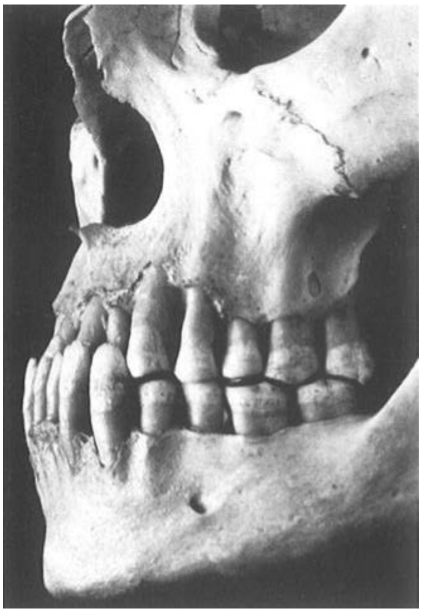

Figure 4. Skull with class III dentoskeletal pattern (source [26]).

Figure 5. The cephalometric ANB angle and the angle of inclination of upper incisors.

formed in accordance with the Declaration of Helsinki and was approved by the Faculty's Ethics Committee (General project title of Clinical and Experimental Examination of the Stomatognathic System and Modern Therapeutic Procedures, Project Number 11, March 8th, 2017, Niš, Republic of Serbia).

This study included the examination and the analyses of cephalometric radiography data (lateral cephalograms) obtained from the profile angles of 120 adult Caucasian subjects (60 male and 60 female) from the central Balkan area (Serbia). The cephalograms were taken from the archives of the subjects. Lateral cephalograms were recorded during the routine diagnostic procedures for subjects who were examined at the Department of Dentofacial Orthopaedics at the Clinic of Dentistry in Niš, aged 18–30 years, and who underwent orthodontic therapy for the first time. The subjects with a history of trauma, craniofacial anomalies, cleft lip and palate, and previous orthodontic, prosthetic or orthognathic treatment were excluded from the study. Cephalometric radiographs of the head were done using a cephalostat (head-holding device). All subjects included in the study underwent a detailed clinical assessment and analyses of their dental and skeletal profiles, as well as soft tissue profiles on cephalometric radiography. The equipment used for the imaging analyses was the Rotograf Plus (20090 Buccinasco MI Italy) (Number and series: 00036045), and the CEI-OPX/105 X-ray tube (CEI, Bologna) with a protective filter (2.5 mm aluminium-equivalent). Lateral cephalometric films were taken from a distance of 165 cm away from the tube, using a cephalostat to ensure rigid head fixation. The subjects were placed in the cephalostat in such a way that the sagittal plane of the head was at a 90° angle to the path of the X-rays. The Frankfort horizontal plane (from the lower edge of foramen orbitale and upper rim of the external auditory canal) was parallel to the ground, the teeth were in the central occlusion position, and the lips were in relaxed position. No corrections of the magnification factors were required, since all the radiographs were taken with the same equipment and the same proportions. Each cephalogram was fixed on the viewing box with the profile to the right, and the acetate tracing paper was fixed by a tape at the top. The soft tissue and skeletal features were traced manually in a darkened room, using a 0.5 mm lead pencil. All the image tracing was done by the main investigator. Subjects were divided into four groups. The size of the ANB angle according to Steiner and the angle inclination of the upper incisors were the criteria used to categorise the subjects in this study. The cephalometric ANB angle was the parameter that defined the sagittal relationship between the upper and lower jaw as orthognathic, distal, or mesial (Fig. 5).

The points that determined the ANB angle included, point N, the nasion, located on the suture between the frontal and nasal bones; point A, the deepest point on the line between the anterior nasal spine and the prosthion (alveolar point); and point B,

Table 1. Facial landmarks (with abbreviations) used for the determination of angular parameters

Glabella (G)	The most anterior point of the middle line of the forehead
Nasion (N)	The point in the middle line located at the nasal root
Nasal dorsum (Nd)	The middle point the external ridge of the nose
Pronasale (Prn)	The most prominent point of the tip of the nose
Columella (Cm)	The most inferior and anterior point of the nose
Subnasale (Sn)	The point where the upper lip joins the columella
Labiale superior (Ls)	The point that indicates the mucocutaneous border of the upper lip
Pogonion (Pg)	The most anterior point of the chin

the deepest point from the line between the infradentale and the pogonion (midline of the chin).

The first group was with a eugnathic dentoskeletal relationship (class I) and the ANB angle between 2° and 4°. The second group was with a distal dentoskeletal pattern, an ANB angle > 4°, and the inclination angle of the upper incisor > 22° (class II, division I, or class II/1). The third group was with a distal pattern, an ANB angle > 4° and the inclination angle of the upper incisors inclination < 22° (class II, division 2, or class II/2). The fourth group was with a mesial pattern and an ANB angle < 1° (class III). Each group consisted of 30 subjects (15 males, 15 females). Since subjects with class I generally had a harmonic facial profile due to the eugnathic jaw relationship, this group was taken as the control and then compared to the other three groups.

Then, on the radiograph of each patient, the following anthropometric soft tissue points were determined (Table 1, Fig. 6).

By pulling the lines from these points, the following profile angles were formed (Fig. 7):

— nasofrontal angle (G-N-Nd) — angle between glabella (G) to nasion (N) line and nasion to nasal dorsum (Nd) line;

— nasofacial angle or nasal projection angle (Prn-N-Pg) — angle between nasion (N) to pogonion line (Pg) and nasion to tip (Prn) line;

— nasal tip angle (N-Prn-Cm) — angle between nasion (N) to tip/pronasale line (Prn) and tip to columella (Cm) line;

— nasolabial angle (Cm-Sn-Ls) — angle between columella point (Cm) to subnasale (Sn) line and subnasale to labiale superior (Ls) line.

Since these were angular measures, all results were expressed in degrees (°).

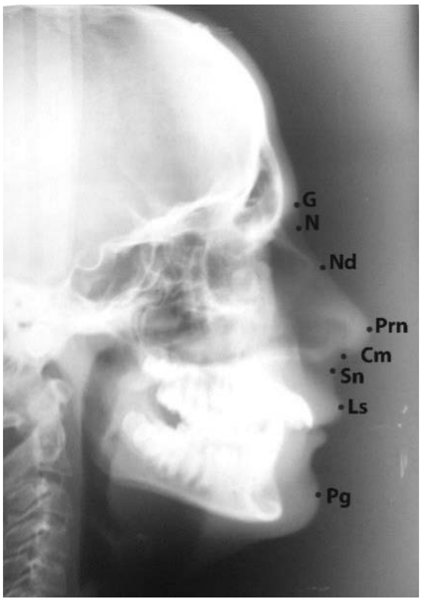

Figure 6. The landmarks used in this investigation: glabella (G), nasion (N), nasal dorsum (Nd), pronasale (Prn), columella (Cm), subnasale (Sn), labiale superior (Ls), pogonion (Pg).

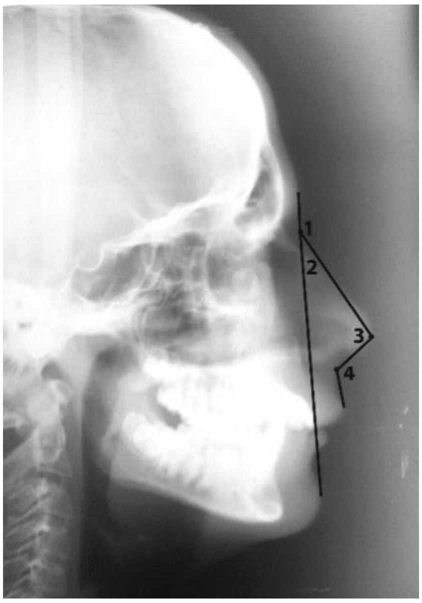

Figure 7. Angular parameters: 1 — nasofrontal angle (G-N-Nd); 2 — nasofacial angle (Prn-N-Pg); 3 — nasal tip angle (N-Prn-Cm); 4 — nasolabial angle (Cm-Sn-Ls).

Statistical analysis

Statistical analysis of obtained morphometric data was performed by IBM SPSS Statistics (version 25). Results of the Kolmogorov-Smirnov test showed that majority of the morphometric parameters were not normally distributed. Consequently, significance of detected differences was evaluated by non-parametric Mann-Whitney U test.

Table 2. Descriptive statistics for class I, class II division 1, class II division 2 and class III

	Class I	Class II/1	Class II/2	Class III
G-N-Nd	138.80 ± 9.39 117.0–153.0	138.50 ± 9.91 111.0–152.0	138.70 ± 6.63 121.0–148.0	134.23 ± 12.58 110.0–160.0
Prn-N-Pg	29.63 ± 3.61 25.0–39.0	33.13 ± 4.61 26.0–47.0	31.00 ± 4.16 23.0–38.0	26.07 ± 4.08 20.0–35.0
N-Prn-Cm	91.00 ± 5.39 79.0–98.0	88.87 ± 6.28 75.0–102.0	86.57 ± 11.15 60.0–108.0	86.20 ± 8.21 72.0–114.0
Cm-Sn-Ls	111.67 ± 10.76 90.0–130.0	114.30 ± 8.56 92.0–133.0	111.37 ± 14.3 80.0–135.0	106.47 ± 10.94 86.0–132.0

Data are shown as mean value ± standard deviation and minimum–maximum.

Table 3. Statistical differences between class I and other groups

Z value; P — probability value	I–II/1	I–II/2	I–III
G-N-Nd — Z; P	–0.044; 0.965	–0.333; 0.739	–1.480; 0.139
Prn-N-Pg — Z; P	–3.162; 0.002**	–1.577; 0.115	–3.401; 0.001***
N-Prn-Cm — Z; P	–1.704; 0.088	–2.201; 0.028**	–3.132; 0.002**
Cm-Sn-Ls — Z; P	–1.030; 0.303	–0.163; 0.871	–1.701; 0.089

**Highly significant $0.01 \geq p > 0.001$; ***Very highly significant $p \leq 0.001$

In the statistical assessment, the following levels of significance were used: not significant $p > 0.05$; significant $0.05 \geq p > 0.01$ (*); highly significant $0.01 \geq p > 0.001$ (**); very highly significant $p \leq 0.001$ (***); p = probability value.

RESULTS

Descriptive statistics of average angular values for different parameters in four groups with different dentoskeletal pattern (class I, class II/1, class II/2, class III) were shown in Table 2. The statistical differences of average values of the examined angles between the group with class I and the other three groups were shown in Table 3:

— nasofrontal angle: the average value for subjects in current study with class I was 138.80 ± 9.39°, that was similar to other groups without significant differences;
— nasofacial angle: the average value for subjects with class I was 29.63 ± 3.61°, and for the group with class II/1 (33.13 ± 4.61°) that's significantly higher. Average value in the group with class III (26.07 ± 4.08°) that's significantly lower related to the control group;
— nasal tip angle: the average value for subjects with class I was 91 ± 5.39°. Significant differences were established by comparing class I and class II/2, so as class I and III subjects;
— nasolabial angle: the average value of this angle in subjects with class I was 111.67 ± 10.76°. There were no significant differences between the subjects with class I and other patterns.

DISCUSSION

Protrusion or retrusion of midfacial (nasal) segment influences the facial aesthetics and can be objectively determined by measuring the facial angles of this segment. Protrusion of this segment is racially characteristic for Africans, retrusion for Asians [6, 11, 17]. In Caucasians, retrusion of nasal third is rarely connected to normal racial anthropological variations. It is the consequence of dentofacial deformity or existence of adenoid face. In case of adenoid face, middle third of the face is short and depressed with nose that undeveloped in all three dimensions. External physiognomy of the nose is divided into its component, aesthetic parts.

The nasofrontal angle is more open in females than in males, revealing a less convex nasal radix [16]. It demonstrates a higher nasal tip rotation in females, which is considered aesthetically favourable [4, 7, 8, 20]. According to various authors, in Caucasian eugnathic subjects, it has a value of 132.39 ± 8.015° [1], 133.16 ± 8.88° [32], 137.13 ± 7.98° [5], to 139.1 ± ± 6.35° [3], that's similar to mean values in the current study (Table 2). The nasofrontal angle is independent of the sagittal dentoskeletal pattern as indicated by these results. Based on reported results, among members of different races, there are higher differences in values of nasofrontal angle than among subjects with different pattern. Results indicate large standard deviations and a large degree of individual variability. Accordingly, comparisons should be performed with the range of normal values not mean values.

The nasofacial angle indicates its prominence in relation to the entire facial massif [6]. The average values for eugnathic subjects range, according to various authors, from 30° to 40.5° [3, 8, 20]. In the current study, for subjects with class I it is 29.63 ± ± 3.61°, being lower than values published by other authors. This value is significantly lower than average in the group with class II/1 and higher than average in the group with class III (Tables 2, 3). The result was the effect of the pogonion point position. The pogonion has an anterior position in subjects with class III, thus reducing the nose projection in relation to the N-Pg line. On the other hand, in subjects with class II/1, the distal pogonion projection, due to posterior mandible position, leads to a larger projection of the nose tip in relation to the N-Pg line. Because of this finding, it would be better if this angle was reduced at class II division 1, so distal position of mandible can be camouflaged. On the other hand, it would be better if that angle was increased at class III, so domination of mandible is camouflaged. Insignificant differences were found in values of this angle between the group with class I and class II/2, since the pogonion position of both groups, due to the specific skeletal pattern of this class, is similar to the one with class I. Fortes et al. [10] by comparing this angle to Caucasian subjects with pleasant and unpleasant facial profiles, found the values of 32.73 ± 2.77° for pleasant facial profiles and the values of 33.43 ± 3.01° for unpleasant facial profiles. The difference is statistically insignificant. Accordingly, the aesthetic impression is not affected by the value of the nasal projection angle [10].

The average value of **the nasal tip angle** in the Caucasian eugnathic subjects is 70.1° to 84.3° [1, 3, 5, 20, 31, 32], in the current study 91 ± 5.39°, indicating higher values compared to subjects from other reference studies. Significant differences were established by comparing class I and class II/2, so as class I and III (Table 3). Mentioned differences in the nose tip angle between class I and class II/2 may be explained by a specific nose tip in subjects with this dentoskeletal pattern. A smaller nose tip angle characterizes these subjects, therefore the tip of the nose has a tendency of convergence with the chin, being a frequent characteristic class II/2 [23]. Subjects with class III are found to have a significantly smaller nose tip angle thus indicating a compensatory tendency of the nose tip to mask the skeletal discrepancy. Consequently the nasomaxillary complex is positioned more posterior in relation to the lower jaw. The sharper nasal tip (reduced nose tip angle) is responsible for the reduced nasolabial angle [4, 5, 21].

The nasolabial angle is important in the assessment of the relationship between the nasal base and the upper lip. It is a strategic part of the facial profile. Burstone defines the nasolabial angle as a representation of the maxilla inclination — when increased, this angle represents the maxillary retroclination, and when decreased, it represents the maxillary proclination [9]. Some authors consider this angle to be of great clinical importance with its size depending on the anteroposterior position and the inclination of the upper incisors respectively [21]. Other authors believe that analyses of this angle can’t provide the answer which segment of the nasomaxillary complex causes the problem. Therefore identification of the exact cause of decreasing the nasolabial angle is difficult to achieve. This angle is formed of two lines, one from the base of the nose, and the other from the upper lip. They are independent as the measurement of this angle does not reveal the component responsible for its variability. It could be either a nose or a lip, or both [9, 10]. It is believed that the larger angle is aesthetically more favourable for women, whereas the sharper one for men [13, 19, 25, 27]. The average value of this angle in subjects of current study with class I is 111.67 ± 10.76°. In other studies performed on the Caucasian eugnathic subjects, slightly lower values were obtained: Ballin et al. [5] in Brazilian Caucasian 105.41 ± 10.66° [5], Anić-Milošević et al. [3] for males 105.49° and for females 109.78°, Lapter-Varga et al. [14] 106.39°, Uysal et al. [30] for males 102.9 ± 10.5°, for females 107.7 ± 8.6° in Turkey and for Caucasian North American 112.6 ± ± 10.6° for males and 111.1 ± 9.7° for females, being close to the average values of nasolabial angle in our sample. Fortes et al. [10] when comparing this angle with Caucasian subjects, found the following average values: 104.37 ± 7.25° for pleasant facial profiles and 104.53 ± 12.91° for unpleasant facial profiles. The difference is statistically insignificant.

In the current study the values of the nasolabial angle in subjects with different patterns are approximate, with insignificant differences (Table 3). The result is unexpected since different dentoskeletal patterns indicate different projections of the nasomaxillary complex. Consequently, thickness of the upper lip compensates the development of the nasomaxillary complex, which most likely masks skeletal discrepancy and maintains an angle relationship with columella [25, 27], making insignificant the established differences on our sample.

During forensic facial reconstruction based on the skull, as the most defined angles were determined nasofrontal and nasolabial angle. These angles, with knowing average thickness of the soft tissues on specific places, are possible to determine with a lot of accuracy. However, when it comes to the nose tip angle and the nasofacial angle we need to take into consideration dentoskeletal pattern because the values of these angles are conditioned with the dentoskeletal class, which is established in the current study.

CONCLUSIONS

By comparing the average values of the profile angles of the midfacial segment, it was established that the nasal tip angle is significantly lower in subjects with class II division 2 as well as class III. The nasofacial angle was significantly higher in subjects with class II division 1 and significantly lower with class III. The frontonasal and nasolabial angle were independent of the sagittal dentoskeletal pattern.

Conflict of interest: None declared

REFERENCES

1. Akter L, Hossain M. Angular photogrammetric soft tissue facial profile analysis of Bangladeshi young adults. APOS Trends Orthod. 2017; 7: 279–286, doi: 10.4103/2321-1407.219434.
2. Al Taki A, Guidoum A. Facial profile preferences, self-awareness and perception among groups of people in the United Arab Emirates. J Orthod Sci. 2014; 3(2): 55–61, doi: 10.4103/2278-0203.132921, indexed in Pubmed: 24987664.
3. Anić-Milosević S, Lapter-Varga M, Slaj M. Analysis of the soft tissue facial profile by means of angular measurements. Eur J Orthod. 2008; 30(2): 135–140, doi: 10.1093/ejo/cjm116, indexed in Pubmed: 18263886.
4. Armijo BS, Brown M, Guyuron B. Defining the ideal nasolabial angle. Plast Reconstr Surg. 2012; 129(3): 759–764, doi: 10.1097/PRS.0b013e3182402e12, indexed in Pubmed: 22090249.
5. Ballin AC, Carvalho B, Dolci JE, et al. Anthropometric study of the caucasian nose in the city of Curitiba: relevance of population evaluation. Braz J Otorhinolaryngol. 2018; 84(4): 486–493, doi: 10.1016/j.bjorl.2017.06.004, indexed in Pubmed: 28728950.
6. Diomande M, Beugre JB, Koueita MK, et al. Relationship between Angular Measurements and Facial Shape of Young Ivorians with Normal Dental Occlusion. Sci World J. 2018; 2018: 6395910, doi: 10.1155/2018/6395910, indexed in Pubmed: 29681778.
7. El-Hadidy M, El-Din AB, El-Bassioni L, et al. Cephalometric analysis for evaluating the profile nasal morphology in egyptian adults. J Plast Reconstr Surg. 2007; 31(2): 243–249.
8. Ezeuko V, Eboigbe P. Angular photogrammetric analysis of the facial profile of the adults of Bini ethnicity of Nigeria. Ann Bioanthropol. 2015; 3(1): 14–17, doi: 10.4103/2315-7992.160737.
9. Fitzgerald J, Nanda R, Currier G. An evaluation of the nasolabial angle and the relative inclinations of the nose and upper lip. Am J Orthod Dentofac Orthop. 1992; 102(4): 328–334, doi: 10.1016/0889-5406(92)70048-f.
10. Fortes HN, Guimarães TC, Belo IM, et al. Photometric analysis of esthetically pleasant and unpleasant facial profile. Dental Press J Orthod. 2014; 19(2): 66–75, doi: 10.1590/2176-9451.19.2.066-075.oar, indexed in Pubmed: 24945516.
11. Darkwah W, Kadri A, Adormaa B, et al. Cephalometric study of the relationship between facial morphology and ethnicity: Review article. Trans Res Anat. 2018; 12: 20–24, doi: 10.1016/j.tria.2018.07.001.
12. Hamid S, Abuaffan AH. Facial soft tissue thickness in a sample of Sudanese adults with different occlusions. Forensic Sci Int. 2016; 266: 209–214, doi: 10.1016/j.forsciint.2016.05.018, indexed in Pubmed: 27314547.
13. Kim SY, Bayome M, Park JH, et al. Evaluation of the facial dimensions of young adult women with a preferred facial appearance. Korean J Orthod. 2015; 45(5): 253–260, doi: 10.4041/kjod.2015.45.5.253, indexed in Pubmed: 26445720.
14. Lapter-Varga M, Anić Milosević S, Vusić A, et al. Soft tissue facial profile of normal dental and skeletal subjects in Croatian population aged 12 to 15 years. Coll Antropol. 2008; 32(2): 523–528, indexed in Pubmed: 18756905.
15. Lazović DG. Analysis of anatomical and morphological characteristics of the nasal pyramid as a criterion for approach selection in rhinoplasty. Dissertation. University of Belgrade, 2016.
16. Letort-Mena JJ, Astudillo-Molina JM, Pedroza-Campo F, et al. Anthropometric measures of nasal pyramid in young people Ecuadorians and their cosmetic preferences. Acta otorrinolaringologica cir. Cabezacuello. 2018; 46(1): 39–45, doi: 10.37076/acorl.v46i1.98.
17. Müller G. Kiefer-Gebiß-Anomalien und Rasse. Fortschritte der Kieferorthopädie. 1965; 26(2): 101–145, doi: 10.1007/bf02163502.
18. Nondumiso YHM. Soft tissue facial profile assessment of 15-20 year old Tswana subjects. MSD thesis, University of Pretoria, 2009.
19. Pandian KS, Krishnan S, Kumar SA. Angular photogrammetric analysis of the soft-tissue facial profile of Indian adults. Indian J Dent Res. 2018; 29(2): 137–143, doi: 10.4103/ijdr.IJDR_496_16, indexed in Pubmed: 29652003.
20. Peck G, Michelson L. Anatomy of aesthetic surgery of the nose. Clin Plastic Surg. 1987; 14(4): 737–748, doi: 10.1016/s0094-1298(20)31499-1.

21. Perkins K, Shah A, Patel A, et al. The effect of nasal tip rotation on upper lip length. Aesthet Surg J. 2017; 37(5): 504–510, doi: 10.1093/asj/sjw234, indexed in Pubmed: 28034843.
22. Perovic T. Facial Profile - Harmony and Aesthetic. LAP LAMBERT Academic Publishing. Saarbrücken, Germany 2019.
23. Perović T. Class II/2 malocclusions and the face profile harmony. Med Sci Monit. 2017; 23: 5589–5598, doi: 10.12659/msm.905453.
24. Reis S, Abrão J, Filho LC, et al. Estudo comparativo do perfil facial de indivíduos Padrões I, II e III portadores de selamento labial passivo. Revista Dental Press de Ortodontia e Ortopedia Facial. 2006; 11(4): 36–45, doi: 10.1590/s1415-54192006000400005.
25. Santos R, Ruellas A. Dentofacial characteristics of patients with Angle Class I and Class II malocclusions. Dental Press J Orthod. 2012; 17(2): 46.e1–46.e7, doi: 10.1590/s2176-94512012000200010.
26. Schulze Ch. Lehrbuch fűr Kieferorthopadie. Buch- und Zeitschriftenverl [in Germany]. Die Quintessenz Bibliothek, Berlin 1993.
27. Tanić T, Blažej Z, Mitić V. [Soft tissue thickness of face profile conditioning by dento-skeletal anomalies]. Srp Arh Celok Lek. 2011; 139(7-8): 439–445, doi: 10.2298/sarh1108439t, indexed in Pubmed: 21980651.
28. Traldi A, Valdrighi HC, de Souza LZ, et al. Evaluation of facial morphology and sagittal relationship between dental arches in primary and mixed dentition. Dental Press J Orthod. 2015; 20(4): 63–67, doi: 10.1590/2176-9451.20.4.063-067.oar, indexed in Pubmed: 26352847.
29. Umale W, Singh K, Azam A, et al. Evaluation of horizontal lip position in adults with different skeletal patterns: a cephalometric study. J Oral Health Craniofac Sci. 2017; 2(1): 009–016, doi: 10.29328/journal.johcs.1001005.
30. Uysal T, Baysal A, Yagci A, et al. Ethnic differences in the soft tissue profiles of Turkish and European-American young adults with normal occlusions and well-balanced faces. Eur J Orthod. 2012; 34(3): 296–301, doi: 10.1093/ejo/cjq165, indexed in Pubmed: 21273287.
31. Uzun A, Akbas H, Bilgic S, et al. The average values of the nasal anthropometric measurements in 108 young Turkish males. Auris Nasus Larynx. 2006; 33(1): 31–35, doi: 10.1016/j.anl.2005.05.004, indexed in Pubmed: 16039817.
32. Uzun A, Ozdemir F. [Morphometric analysis of nasal shapes and angles in young adults]. Braz J Otorhinolaryngol. 2014; 80(5): 397–402, doi: 10.1016/j.bjorl.2014.07.010, indexed in Pubmed: 25303814.
33. Wen YiF, Wong HM, Lin R, et al. Inter-Ethnic/Racial facial variations: a systematic review and Bayesian meta-analysis of photogrammetric studies. PLoS One. 2015; 10(8): e0134525, doi: 10.1371/journal.pone.0134525, indexed in Pubmed: 26247212.

VIA MEDICA

ORIGINAL ARTICLE

Folia Morphol.
Vol. 80, No. 3, pp. 665–674
DOI: 10.5603/FM.a2020.0102

ISSN 0015–5659
eISSN 1644–3284
journals.viamedica.pl

A morphometric study of the thoracolumbar spine spinous process and lamina space in the Chinese

L.N. Leng[1, 2], H.J. Ma[3, 4]*, D.W. Si[5]*

[1]Graduate School, HeBei North University, Zhangjiakou, Hebei Province, China
[2]Hebei General Hospital, Shijiazhuang, Hebei, China
[3]HeBei North University, Zhangjiakou, Hebei Province, China
[4]Hebei Key Laboratory of Metabolic Diseases, Hebei General Hospital, Shijiazhuang, Hebei, China
[5]Department of Anatomy of College of Basic Medical Sciences, North China University of Science and Technology, Tangshan, Hebei Province, China

[Received: 27 April 2020; Accepted: 22 July 2020; Early publication date: 24 August 2020]

Background: *The aim of the study was to analyse the anatomical parameters of the thoracolumbar spine spinous process and lamina space for Chinese anatomic study, and provide an anatomical reference for its clinical operation.*

Materials and methods: *Samples from 24 adult autopsy subjects were obtained from the thoracolumbar spine spinous process and lamina space at levels T1 through L5. Direct measurements were made for the spinous process spacing distance, spinous process length, width, thickness and inclination angle, and the lamina space width and height.*

Results: *1. Distance of the spine spinous process spacing: Thoracic part: The maximum tip distance was observed at T4~T5 level, and the minimum tip distance was observed at T9~T10 level. The maximum centre distance and root distance were observed at T11~T12 level, and the minimum were observed at T5~T6 level separately. Lumbar part: distance of spinous process spacing in lumbar part showed a decreasing pattern from L1~L2 to L5~S1. 2. Length, width, thickness of the spine spinous process: 1) The length of the spinous process: The upper border gradually increased from T1 to T6 and then decreased till T12 region. The centre region is T8 maximum, T11 minimum. The lower border length showed a decreasing trend from T1 to T12. Lumbar part: The length increased from L1 and reached maximum value at L3. Then, the length decreased gradually to reach minimum value at L5. 2) The width of the spinous process: The width showed an increasing trend from T1 to T12. Lumbar part: Maximum width was seen at L3 and a minimum L5. 3) The thickness of the spinous process: Tip thickness > Centre thickness > Root thickness in each thoracic and lumbar vertebra. Thoracic part: the maximum tip thickness is T1, T7 minimum, The maximum centre thickness is T12, T7 minimum. The maximum root height is T6, T9 minimum. Lumbar part: Maximum tip thickness was seen at L1, and a minimum L3. Maximum centre thickness was seen at L5, and a minimum L2. Maximum root thickness was seen at L2, and a minimum L1. 3. Inclination angle of the spine spinous process: The*

Address for correspondence: Dr. H.J. Ma, HeBei North University, Zhangjiakou 075000, Hebei Province, China; Hebei Key Laboratory of Metabolic Diseases, Hebei General Hospital, 348 Heping West Road, Xinhua District, Shijiazhuang 050051, Hebei, China, e-mail: huijuanma76@163.com

*Huijuan Ma and Daowen Si contributed equally to this paper.

inclination angle gradually decreased from T1 to T7 to minimum value at T7 and then increased till T12 region. 4. Width and height of lamina space: 1) The width of lamina space: For thoracic part, the data became shorter gradually from T1~T2 to T5~T6, and then increased till to T11~T12. For lumbar part, the width of lamina space increased from T12~L1 to L5~S1. 2) The height of lamina space: In the thoracic vertebrae, the maximum height of centre region was observed at T11~T12 and the minimum mean value was observed at T3~T4. In the lumbar vertebrae, the height of the lamina space was gradually increased from T12~L1 to L5~S1.

Conclusions: *This study reports morphometric data of the thoracolumbar spine spinous process and lamina space in the Chinese population, which provides an anatomic basis for thoracolumbar spine design of internal fixation, posterior surgery, puncture and epidural anaesthesia.* (Folia Morphol 2021; 80, 3: 665–674)

Key words: thoracolumbar spinous process, lamina space, anatomy, morphology

INTRODUCTION

Lumbar spinous processes (SPs) are an appealing target for applications in spine surgery, which are relatively superficial and easy to access anatomically. Currently, a number of devices and techniques use lumbar SPs or the lamina space for instrumentation [2, 11, 16–18, 30, 39]. Thoracic part of vertebral column is even more complex [8, 9, 29, 33]. Knowledge of morphology of the thoracic spine is essential for the anaesthetic and surgical procedures carried out in this part of the vertebral column, to achieve desired results and to avoid complications. Thoracic epidural anaesthesia and pedicle screw fixation of thoracic spine have made the morphometric analysis of the thoracic pedicle a clinical necessity for all the surgeons practicing this procedure [28, 34]. Recently, the anatomical parameters of lumbar spine process have been well described [4, 27, 31], and previously studies have provided information regarding thoracic SP [13, 15, 26, 35, 38]. There are only few reports on the measurement of lamina space. However, a comprehensive description of the related parameters of the thoracolumbar SP and lamina space has not been reported. Meanwhile, to our knowledge, spine morphology varies across different races [19]. There have been few reports of SP morphometry in the Chinese population.

Therefore, it is essential to understand the precise anatomy of the SP and lamina space. The purpose of this study was to determine the morphometric parameters of the thoracolumbar SP and lamina space, and to provide an anatomic basis for lamina space stabilisation devices, other posterior surgery, puncture and epidural anaesthesia for the Chinese population.

MATERIALS AND METHODS

Materials

Twenty-four formalin-fixed intact adult male cadavers from the Department of Anatomy of North China University of Science and Technology ages ranged from 35 to 69 years, with a mean of 47 years. And height ranged from 160 to 175 cm, with a mean of 168 cm. There were no malformations and local pathological changes of the spine. Measurement instruments consist of electronic vernier calliper and compass.

Measuring parameters

The cadavers were placed in a prone position for numbering the vertebra. The posterior lumbar spine (T1–T12) (S1–S5) was exposed, and the SP, vertebral plate, and articular process were revealed (Fig. 1). Symmetric structures were measured bilaterally. Measurements were made using an electronic vernier calliper accurate to 0.01 mm and a compass. After each measurement, compass and electronic vernier calliper were restored the initial state of zero. All data were measured 3 times to take its average value. Statistical analysis was used to determine the average (mean), standard deviation and minimum and maximum values. The main measuring parameters were as follows:

Distance of the spine spinous process spacing, which is between the lower border of the upper adjacent SP and the upper border of the lower adjacent SP.

Figure 1. The thoracic and lumbar vertebral lamina and articular process after removed all muscles and ligaments.

Figure 3. The distance, length, height of the spine spinous process in the lumbar part.

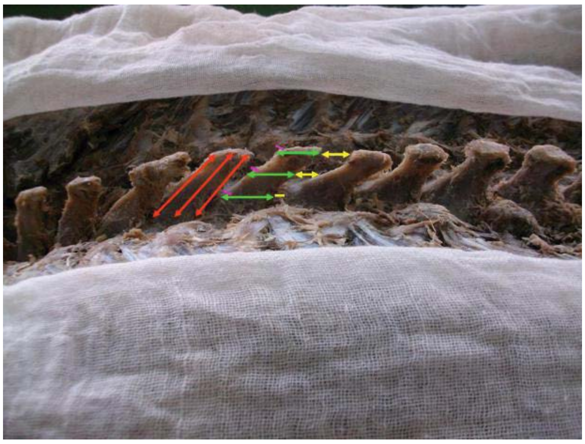

Figure 2. The distance, length, width, height of the spine spinous process in the thoracic part.

Figure 4. The lamina space after removed all the spinous process and the surrounding connective tissue.

The tip distance (TD), centre distance (CD) and root distance (RD) between the adjacent SPs were measured respectively (Figs. 2, 3). The TD in this article has the same meaning as distance between the two adjacent spinous processes (DB) in other articles [4, 27].

Length, width, thickness of the spine spinous process: 1) The length of the SP was evaluated in the upper border (UL), centre region (CL) and lower border (LL) (Figs. 2, 3). 2). The width of the SP was measured in the tip border (TW), centre region (CW) and root border (RW). 3) The thickness of the SP was evaluated in the tip border (TT), centre region (CT) and root border (RT).

Inclination angle of the spine spinous process: The inclination angle of SP was measured by measuring the angles between the straight line of the upper edge (UI), the centre (CI) and the lower edge (LI) of spinous process and the tangent line of the spines, which is in the state of natural bending.

Width and height of lamina space: After removed all the SP and the surrounding connective tissue, the lamina space were fully exposed (Fig. 4). Two feet of a compass were put into the lamina space to measure the width of lamina space (WI), and the height between the upper and lower lamina from the left side (LHI), centre region (CHI) and right side (RHI) (Fig. 5).

Collected data were analysed and compared with other studies. The schematic diagram of relevant anatomical indicators of SP was shown at Figure 6.

Ethics statement

This study was conducted in accordance with the Declaration of Helsinki (Edinburgh 2000 revised). The Institutional Review Board of North China University of Sci-

Figure 5. The height of the centre region of lamina space measured with compasses.

ence and Technology approved this study, confirm that the study was performed in accordance with relevant guidelines/regulations and informed consent was obtained from family members or their legal guardian(s).

RESULTS

Distance of the spine spinous process spacing (Table 1)

The TD > the CD > the RD in each thoracic vertebra. The TD: The maximum was observed at T4~T5 (16.80 ± 2.34 mm) level, and the minimum was observed at T9~T10 (9.82 ± 1.93 mm) level. The CD: The maximum was observed at T11~T12 (10.98 ± ± 1.91 mm) level, and the minimum was observed at T5~T6 (7.56 ± 2.44 mm) level. The RD: The maximum was observed at T11~T12 (9.14 ± 2.80 mm) level, and the minimum was observed at T5~T6 (4.94 ± ± 1.92 mm) level.

The CD > the TD > the RD in L1~L2 and L2~L3 levels. The CD > the RD > the TD in L3~L4, L4~L5 and L5~S1 levels. The TD is L2~L3 maximum (11.94 ± 2.01 mm), L5~S1 minimum (6.51 ± ± 1.47 mm). The CD is L1~L2 maximum (12.48 ± ± 1.21 mm), L5~S1 minimum (7.74 ± 1.82 mm). The RD is L2~L3 maximum (10.69 ± 2.02 mm), L4~L5 minimum (7.46 ± 2.26 mm). Distance of spinous process spacing in lumbar part showed an decreasing pattern from L1~L2 to L5~S1.

Length, width, thickness of the spine spinous process (Table 2)

The length of the spinous process

Thoracic part: the UL > the CL > the LL in each thoracic SP. The UL gradually increased from T1 to

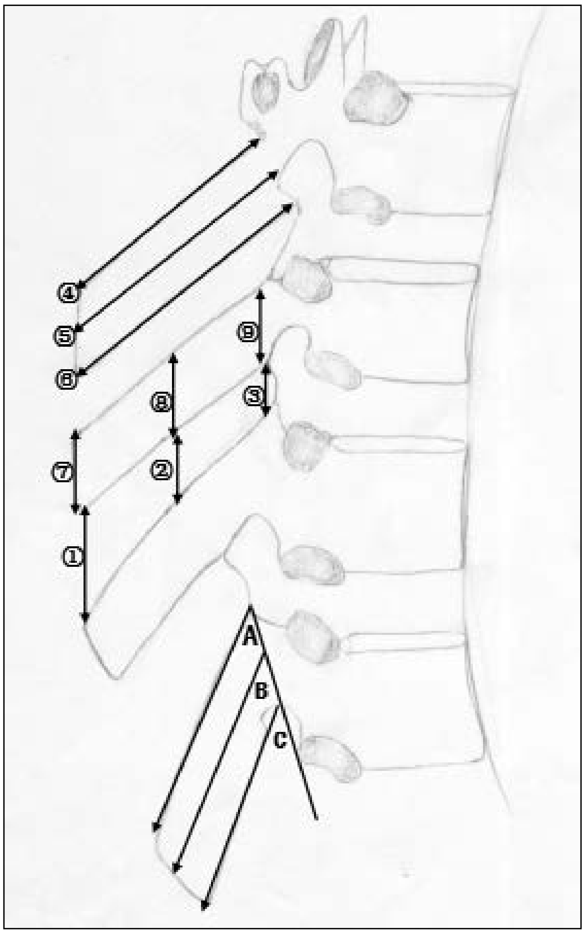

Figure 6. The schematic diagram of relevant anatomical indicators of spinous process. 1 — the tip distance (TD) of the spine spinous process spacing; 2 — the centre distance (CD) of the spine spinous process spacing; 3 — the root distance (RD) of the spine spinous process spacing; 4 — the upper length (UL) of the spine spinous process; 5 — the centre length (CL) of the spine spinous process; 6 — the lower length (LL) of the spine spinous process; 7 — the tip width (TW) of the spinous process; 8 — the centre width (CW) of the spinous process; 9 — the root width (RW) of the spinous process; A — the inclination angle of spinous process upper edge (UI); B— the inclination angle of spinous process centre edge (CI); C — the inclination angle of spinous process lower edge (LI).

T6 to maximum value at T6 with mean of 33.38 ± ± 2.94 mm and then decreased till T12 region with mean of 25.25 ± 2.36 mm. The CL is T8 (30.75 ± 2.59 mm) maximum, T11 (22.52 ± 2.12 mm) minimum. The LL length showed a decreasing trend from T1 to T12. Maximum LL was seen at T1 (29.82 ± 2.54 mm) and a minimum T12 (20.35 ± 1.57 mm). Lumbar part: the UL > the CL > the LL in each lumbar SP. The length increased from L1 and reached maximum value at L3 with mean of 29.17 ± 2.35 mm (UL), 27.23 ± ± 2.23 mm (CL), 24.89 ± 2.04 mm (LL). Then, the length decreased gradually to reach minimum value at L5 with the mean of 25.12 ± 2.37 mm (UL),

Table 1. Distance of the spine spinous process spacing (mean ± standard deviation, mm)

Spinous process spacing	Tip distance (TD)	Centre distance (CD)	Root distance (RD)
T1~T2	10.54 ± 1.91	9.18 ± 1.71	5.82 ± 1.29
T2~T3	12.66 ± 1.97	9.38 ± 2.51	5.54 ± 1.40
T3~T4	14.56 ± 1.91	9.85 ± 2.03	5.67 ± 1.62
T4~T5	16.80 ± 2.34	9.91 ± 2.24	5.44 ± 1.94
T5~T6	12.10 ± 1.82	7.56 ± 2.44	4.94 ± 1.92
T6~T7	12.21 ± 2.73	8.71 ± 2.44	5.99 ± 2.53
T7~T8	10.82 ± 2.04	8.52 ± 1.73	6.13 ± 2.02
T8~T9	10.28 ± 2.17	8.03 ± 1.69	5.68 ± 1.82
T9~T10	9.82 ± 1.93	7.59 ± 1.32	5.65 ± 1.61
T11~T12	11.99 ± 1.90	10.98 ± 1.91	9.14 ± 2.80
L1~L2	11.70 ± 1.30	12.48 ± 1.21	10.23 ± 1.44
L2~L3	11.94 ± 2.01	12.38 ± 1.61	10.69 ± 2.02
L3~L4	9.29 ± 1.47	10.27 ± 2.32	9.72 ± 2.42
L4~L5	6.76 ± 1.63	7.77 ± 1.12	7.46 ± 2.26
L5~S1	6.51 ± 1.47	7.74 ± 1.82	7.51 ± 2.28

Table 2. Length, width and thickness of spine spinous process (mean ± standard deviation, mm)

T1~L5	Length			Width			Thickness		
	Upper (UL)	Centre (CL)	Lower (LL)	Tip (TW)	Centre (CW)	Root (RW)	Tip (TT)	Centre (CT)	Root (RT)
T1	32.48 ± 3.28	29.69 ± 2.61	29.82 ± 2.54	11.38 ± 0.99	10.99 ± 0.80	15.82 ± 1.42	7.57 ± 1.03	7.68 ± 1.00	9.76 ± 1.33
T2	31.53 ± 2.96	29.86 ± 2.60	28.67 ± 2.50	11.72 ± 1.10	12.95 ± 1.38	16.12 ± 1.53	6.52 ± 0.94	7.38 ± 0.97	12.14 ± 1.00
T3	33.03 ± 3.74	30.35 ± 2.68	28.47 ± 2.38	13.30 ± 0.84	14.11 ± 1.42	17.92 ± 1.55	5.47 ± 0.77	6.88 ± 0.93	12.77 ± 1.22
T4	31.43 ± 3.21	29.51 ± 2.75	27.55 ± 2.40	13.83 ± 0.91	15.05 ± 0.86	18.52 ± 1.28	5.18 ± 0.73	6.41 ± 0.92	12.69 ± 1.58
T5	32.98 ± 2.44	27.50 ± 2.46	28.39 ± 2.53	28.39 ± 2.53	15.73 ± 0.80	19.80 ± 1.64	5.07 ± 0.62	6.79 ± 1.01	12.05 ± 1.42
T6	33.38 ± 2.94	29.94 ± 2.86	28.24 ± 2.40	28.24 ± 2.40	16.07 ± 1.09	20.14 ± 1.60	4.76 ± 0.80	6.36 ± 1.01	13.67 ± 1.52
T7	31.55 ± 2.77	29.64 ± 2.42	27.80 ± 3.08	27.80 ± 3.08	15.39 ± 1.79	20.36 ± 1.54	4.41 ± 0.77	5.73 ± 0.99	10.13 ± 2.05
T8	32.65 ± 2.74	30.75 ± 2.59	25.15 ± 2.60	25.15 ± 2.60	15.62 ± 1.21	20.42 ± 1.56	4.89 ± 0.67	5.95 ± 0.84	8.43 ± 0.78
T9	31.50 ± 2.92	23.07 ± 2.33	22.90 ± 2.69	22.90 ± 2.69	16.93 ± 0.91	22.18 ± 1.52	5.26 ± 0.74	6.22 ± 0.73	7.87 ± 1.69
T10	29.62 ± 2.80	23.09 ± 2.52	21.53 ± 2.87	21.53 ± 2.87	17.37 ± 0.84	22.56 ± 1.50	6.03 ± 1.10	6.93 ± 0.85	10.27 ± 1.70
T11	25.49 ± 2.90	22.51 ± 2.12	20.77 ± 2.15	20.77 ± 2.15	18.56 ± 0.90	22.60 ± 1.30	6.50 ± 0.80	7.87 ± 0.86	10.98 ± 1.28
T12	25.25 ± 2.36	23.13 ± 2.44	20.35 ± 1.57	20.35 ± 1.57	19.88 ± 1.53	23.80 ± 0.81	7.03 ± 1.11	8.50 ± 0.98	12.14 ± 1.45
L1	25.59 ± 2.13	25.52 ± 2.85	21.66 ± 2.34	22.68 ± 2.17	21.99 ± 1.10	24.94 ± 1.48	7.70 ± 1.26	7.75 ± 0.74	9.74 ± 1.51
L2	27.09 ± 2.10	25.78 ± 2.52	24.05 ± 2.22	22.23 ± 0.72	22.48 ± 1.49	25.19 ± 1.30	7.16 ± 1.32	7.28 ± 0.95	11.43 ± 1.76
L3	29.17 ± 2.35	27.23 ± 2.23	24.89 ± 2.04	23.68 ± 1.41	23.56 ± 1.36	25.83 ± 0.96	7.12 ± 1.14	7.47 ± 0.51	9.93 ± 1.51
L4	27.88 ± 2.44	26.33 ± 2.32	22.68 ± 2.84	23.59 ± 1.44	21.26 ± 0.91	23.35 ± 1.71	7.63 ± 1.19	7.39 ± 0.67	11.43 ± 0.89
L5	25.12 ± 2.37	23.76 ± 2.82	20.80 ± 2.75	19.54 ± 0.78	17.91 ± 1.85	17.20 ± 1.72	7.25 ± 0.92	8.11 ± 0.83	10.69 ± 1.80

23.76 ± 2.82 mm (CL), 20.80 ± 2.75 mm (LL). Upper border length of the lower spine > lower border length of the upper adjacent spine.

The width of the spinous process

Thoracic part: RW > CW > TW in each thoracic vertebra approximately, and the width mentioned showed an increasing trend from T1 with the mean of 11.38 ± 0.99 mm (TW), 10.99 ± 0.80 mm (CW), 15.81 ± 1.42 mm (RW) to T12 with the mean of 20.28 ± 1.57 mm (TW), 19.88 ± 1.53 mm (CW), 23.80 ± 0.81 mm (RW). Lumbar part: Maximum width was seen at L3 with the mean of 23.68 ± 1.41 mm (TW), 23.56 ± 1.36 mm (CW), 25.83 ± 0.96 mm (RW) and

Table 3. The inclination angle of spinous process (mean ± standard deviation, °)

T1~T12	Upper edge inclination angle (UI)	Centre edge inclination angle (CI)	Lower edge inclination angle (LI)
T1	61.20 ± 2.17	62.63 ± 3.38	67.70 ± 3.50
T2	58.33 ± 3.50	60.50 ± 3.12	64.80 ± 3.77
T3	54.30 ± 4.14	57.38 ± 3.46	59.20 ± 3.03
T4	49.40 ± 1.95	52.50 ± 3.78	55.00 ± 3.16
T5	40.57 ± 3.74	45.83 ± 3.66	48.40 ± 2.70
T6	38.29 ± 3.25	41.50 ± 3.82	43.67 ± 3.43
T7	37.25 ± 3.15	38.14 ± 2.48	39.50 ± 3.70
T8	40.89 ± 2.57	41.44 ± 3.28	42.14 ± 3.34
T9	42.63 ± 3.89	45.38 ± 3.93	52.88 ± 1.96
T10	51.67 ± 3.93	57.44 ± 2.46	61.11 ± 2.67
T11	59.50 ± 2.33	71.38 ± 3.50	78.00 ± 2.65
T12	74.29 ± 3.50	78.20 ± 3.70	86.50 ± 2.38

a minimum L5 with the mean of 19.54 ± 0.78 mm (TW), 17.91 ± 1.85 mm (CW), 17.20 ± 1.72 mm (RW).

The thickness of the spinous process

Tip thickness (TT) > centre thickness (CT) > root thickness (RT) in each thoracic and lumbar vertebra. Thoracic part: the maximum TT is T1 (7.57 ± 1.03 mm), T7 minimum (4.41 ± 0.77 mm), The maximum CT is T12 (8.50 ± 0.98 mm), T7 minimum (5.73 ± 0.99 mm). The maximum RT is T6 (13.67 ± 1.52 mm), T9 minimum (7.87 ± 1.69 mm). Lumbar part: Maximum TT was seen at L1 with the mean of 7.70 ± 1.26 mm, and a minimum L3 with the mean of 7.12 ± 1.14 mm. Maximum CT was seen at L5 with the mean of 8.11 ± ± 0.83 mm, and a minimum L2 with the mean of 7.28 ± 0.95 mm. Maximum RT was seen at L2 with the mean of 11.43 ± 1.76 mm, and a minimum L1 with the mean of 9.74 ± 1.51 mm.

Inclination angle of the spine spinous process (Table 3)

The inclination angle gradually decreased from T1 to T7 to minimum value at T7 with mean of 37.25 ± ± 3.15° (UI), 38.14 ± 2.48° (CI) and 86.50 ± 2.38° (LI) and then increased till T12 region with mean of 74.29 ± 3.50° (UI), 78.20 ± 3.70° (CI) and 39.50 ± ± 3.70° (LI). And the lower edge inclination angle (LI) > the centre edge inclination angle (CI) > the upper edge inclination angle (UI) in each thoracic vertebra. Generally, the inclination angle of lumbar spine is basic 90 degrees, which is of little significance. Thus we did not measure the inclination angle of lumbar spine.

Width and height of lamina space (Table 4)

The width of lamina space: For thoracic part, the data became shorter gradually from T1~T2 (11.73 ± ± 2.51 mm) to T5~T6 (9.63 ± 3.63 mm), and then increased till to T11~T12 (10.70 ± 4.67 mm). For lumbar part, the width of lamina space increased from T12~L1 (12.18 ± 1.43 mm) to L5~S1 (15.64 ± ± 1.73 mm). Among them, the increment of L5~S1 width was the largest, and larger about 2 mm than L4~L5 width.

The height of lamina space: In the thoracic vertebrae, the maximum height of centre region was observed at T11~T12 (7.47 ± 2.78 mm) and the minimum mean value was observed at T3~T4 (5.20 ± ± 1.77 mm). Since the thoracic space height is small, the left and right sides are difficult to measure, so this study did not measure this two indicators. In the lumbar vertebrae, the height of the lamina space was gradually increased from T12~L1 to L5~S1. The height of the centre region was greater than the height of the left and right sides, and there was no significant difference between the heights of the left and right sides. The centre height increased from 9.68 ± 1.76 mm to 11.88 ± 1.78 mm, the left height increased from 6.91 ± 1.16 mm to 7.79 ± 1.19 mm, and the right height increased from 7.04 ± 0.92 mm to 7.79 ± 1.06 mm.

DISCUSSION

At present, lumbar spine process-related indicators have been reported [4, 27, 31], and there are a few reports on the measurement of thoracic SPs [13, 15, 26, 35, 38]. There are also some studies

Table 4. The width and height of lamina space (mean ± standard deviation, mm)

Lamina space	Width (WI)	Height		
		Centre region (CHI)	Left side (LHI)	Right side (RHI)
T1~T2	11.73 ± 2.51	6.20 ± 2.49	—	—
T2~T3	11.53 ± 2.87	6.01 ± 2.25	—	—
T3~T4	10.20 ± 3.44	5.20 ± 1.77	—	—
T4~T5	10.62 ± 3.84	5.49 ± 2.10	—	—
T5~T6	9.63 ± 3.63	5.65 ± 2.03	—	—
T6~T7	10.92 ± 4.95	5.32 ± 2.14	—	—
T7~T8	10.80 ± 4.94	5.91 ± 2.67	—	—
T8~T9	10.33 ± 4.28	5.52 ± 2.17	—	—
T9~T10	10.20 ± 4.54	6.00 ± 2.57	—	—
T10~T11	9.72 ± 5.12	6.92 ± 4.28	—	—
T11~T12	10.70 ± 4.67	7.47 ± 2.78	—	—
T12~L1	12.18 ± 1.43	9.68 ± 1.76	6.91 ± 1.16	7.04 ± 0.92
L1~L2	12.81 ± 2.12	10.24 ± 0.91	7.06 ± 0.66	7.18 ± 0.66
L2~L3	12.92 ± 1.80	11.19 ± 0.83	7.30 ± 0.77	7.29 ± 0.56
L3~L4	13.10 ± 1.91	11.20 ± 1.37	7.43 ± 0.57	7.44 ± 0.84
L4~L5	13.71 ± 1.37	11.32 ± 0.77	7.60 ± 0.87	7.56 ± 0.88
L5~S1	15.64 ± 1.73	11.88 ± 1.78	7.79 ± 1.19	7.79 ± 1.06

that report measurements of thoracic and lumbar spine-related indicators separately, which are not comprehensive enough. In the morphology of lumbar spine processes studied by Cai et al. [4], only the distance, height, thickness of the upper, middle and lower borders of the lumbar spine were studied. Bo Ran et al. [27] performed lumbar spine morphology in Chinese population by three-dimensional computed tomography reconstruction. Kiranpreet Kaur et al. [15] only reported the inclination angle of the thoracic spine. Jeremy D. Shaw et al. [31] analysed the length, width, height, slope and tail morphology of lumbar spine, but did not measure the distance between SPs spacing. In our study, more relevant indicators of thoracolumbar spine and lamina space were measured based on intact corpses, which include distance of SPs spacing, SP length, width, thickness, and inclination angle of the SP, and width, height (centre, left and right) of the lamina space.

The experimental results of the SP spacing distance in each thoracic vertebra show that the tip distance > the centre distance > the root distance. The maximum of the tip distance was observed at T4~T5, and the minimum was T9~T10. The maximum of the centre distance was observed at T11~T12, and the minimum was T5~T6. The maximum of the root distance was observed at T11~T12, and the minimum was T5~T6. Thus, the thoracic SP spacing distance is wedge-shaped. In the sagittal plane, the front is high and the back is low. To avoid damage caused by stress concentration of the implant, the internal fixation device should have a wedge-shaped structure, which is high in front and low in back. The maximum tip distance of lumbar SP spacing was noted at L2~L3, while the minimum tip distance was L5~S1. The maximum centre distance of lumbar SP spacing was noted at L1~L2, then it gradually decreased to the minimum root distance (L5~S1). The maximum root distance of lumbar SP spacing was noted at L2~L3, while the minimum root distance was L4~L5. The above results are different from the data of Cai et al. [4], which considered that distance between lumbar spines was gradually decreased from L1~L2 to L5~S1. And our results differ from Bo Ran [27] and others' opinion, which hold that the distance between lumbar spines was gradually decreased from L1~L2 to L4~L5, and then increased from L4~L5 to L5~S1. Cai et al. [4] and Bo Ran et al. [27] measured the above parameter at only one point, while our study performed it at three points (tip, centre and root), which is more comprehensive and detailed. Recently, numerous lamina space implants have been introduced and have shown favourable outcomes in the treatment of degenerative disc disease, herniated nucleus pulposus, lumbar spinal stenosis, lumbar instability, and degenerative lumbar spondylolisthesis [2, 7, 23, 32, 37]. Nevertheless, there are still complications with lamina space implants. Therefore, choosing optimal sizes of implants is important to avoid unnecessary complications and the size of the device should be carefully evaluated [3, 14]. The data in this study can help clinicians grasp the optimal size of the implant, which is one way to reduce complications.

By measuring the length of the spine SP, we can learn that the upper border > the centre region > the lower border in each thoracic and lumbar SP. In the lumbar part, L3 is the maximum and L5 is the minimum, which is consistent with the conclusions drawn by Cai et al. [4] and Bo Ran et al. [27]. Usually, spinal lesions are treated with a posterior approach, where surgeons can remove the posterior part of the spine in order to expand the field of vision. In this process, the knowledge of the length, width and thickness of the spine SPs provides a comprehensive reference for the type of instrument chosen and the location of the occlusal site. With known length, width, and thickness, we can estimate the size of the SPs of the spine, which is important for lumbar interbody fusion [12]. In addition, the designing of SP internal fixation provides an equivalent pain/function improvement compared to conventional posterior-lumbar-interbody-fusion pedicle screw fixation, reducing the number of hospitalisations and operations [5]. So, the above indicators are also important reference indicators for the design of SP internal fixation devices.

The SP of the thoracic spine is obliquely posteriorly downward, but the specific values of the inclination angle are rare. Kiranpreet Kaur et al. [15] used the scanner software to measure the SP angle of volunteers, showing that the SP angle increased from T1 and reached maximum value at T6 level, then decreased gradually and reached minimum value at T12 level. In our study, the intact cadaver specimens were used to expose the SPs of the thoracic spine. The inclination angle of SP was measured by measuring the angles between the straight line of the upper edge, the centre and the lower edge of SP and the tangent line of the spines, which is in the state of natural bending. The inclination angle gradually decreased from T1 to T7 to minimum value and then increased till T12 region, which is slightly different from result of the above document. In clinical application, the setting of the inclination angle of the upper and lower edges of the SP internal fixation needs to refer to the inclination angle of the SP to be inserted into the internal fixation.

Laminar space plays an important role in spinal surgery. Clinically, most of the procedures such as disc herniation, spinal stenosis, and intraspinal schwannomas need to be taken from the lamina space. Therefore, the study of anatomical parameters of the laminar space can provide a basis for relevant clinical operations. For example, in the treatment of disc herniation, percutaneous endoscopic laser-assisted discectomy (PELD) has been widely used in clinical practice in recent years [1, 20, 22]. The outer diameter of the required endoscope is 7.5 mm, and the working channel is at the centre of the lamina space. According to the data obtained in this experiment, it is not difficult to implement PELD in L4~L5 and L5~S1. For another example, spinal stenosis is also a common disease in the spinal region, which is due to a cascade of degenerative processes starting with degeneration of posterior annulus to disc herniation and dehydration, then to loss of disc height, overriding of the facets, and/or infolding of ligamentum flavum, and ultimately stenosis. This condition occurs as a result of age-related spinal degeneration, particularly in the lamina space disc and ligamentum flavum. Common symptoms include radicular pain and neurogenic claudication, which is mainly treated by surgical intervention [6, 24, 36]. This requires some anatomical parameters of the lamina space to guide the operation. In addition, the removal of schwannomas in the spinal canal also requires from lamina space [21, 25], whose anatomical parameters are particularly important. In addition to the surgical approach, the measurement of the width and height of the lamina space provides an anatomical basis for the intraspinal puncture approach. According to reports in the literature, emergency doctors can quickly obtain lumbar anatomical markers by ultrasound [10], These data can also provide reference and experience for clinicians to help clinical first aid and other treatments.

CONCLUSIONS

More related indicators of the thoracolumbar spine spinous process and intervertebral space were measured based on intact cadavers in our study, including the distance, length, width, thickness, inclination angle of the spinous process and the width, height of the intervertebral space, to provide comprehensive anatomic basis for thoracolumbar spine design of internal fixation, posterior surgery, puncture and epidural anaesthesia for the Chinese population.

Acknowledgements

We thank Dr. Guangyao Song for his careful reading of the manuscript and helpful suggestions.

Conflict of interest: None declared

REFERENCES

1. Ahn Y, Lee SH, Park WM, et al. Percutaneous endoscopic lumbar discectomy for recurrent disc herniation: surgical technique, outcome, and prognostic factors of 43 consecutive cases. Spine (Phila Pa 1976). 2004; 29(16): E326–E332, doi: 10.1097/01.brs.0000134591.32462.98, indexed in Pubmed: 15303041.
2. Bono CM, Vaccaro AR. Lamina space process devices in the lumbar spine. J Spinal Disord Tech. 2007; 20: 255–261.
3. Bowers C, Amini A, Dailey AT, et al. Dynamic interspinous process stabilization: review of complications associated with the X-Stop device. Neurosurg Focus. 2010; 28(6): E8, doi: 10.3171/2010.3.FOCUS1047, indexed in Pubmed: 20568923.
4. Cai B, Ran B, Li Q, et al. A morphometric study of the lumbar spinous process in the Chinese population. Braz J Med Biol Res. 2015; 48(1): 91–95, doi: 10.1590/1414-431x20144164, indexed in Pubmed: 25493388.
5. Castilleja A, Broomall PA. Pedicle screws vs minimally invasive posterior-lumbar-interbody-fusion with spinous process fixation in the workers compensation population: early outcomes with minimum one year follow up. Orthopaedic Surg. 2014: E123–E124.
6. Chen PGC, Daubs MD, Berven S, et al. Surgery for degenerative lumbar scoliosis: the development of appropriateness criteria. Spine (Phila Pa 1976). 2016; 41(10): 910–918, doi: 10.1097/BRS.0000000000001392, indexed in Pubmed: 26679874.
7. Chiu JC. lamina space process decompression (IPD) system (X-STOP) for the treatment of lumbar spinal stenosis. Surg Technol Int. 2006; 15: 265–275.
8. Dommisse GF. The blood supply of the spinal cord. J Bone Joint Surg. 1974; 56-B(2): 225–235, doi: 10.1302/0301-620x.56b2.225.
9. Drake RL. ed. In: Textbook of Gray's Anatomy for Students 1st ed. Churchill Livingstone Publications, Philadelphia 2005: 33–63.
10. Ferre RM, Sweeney TW. Emergency physicians can easily obtain ultrasound images of anatomical landmarks relevant to lumbar puncture. Am J Emerg Med. 2007; 25(3): 291–296, doi: 10.1016/j.ajem.2006.08.013, indexed in Pubmed: 17349903.
11. Gazzeri R, Galarza M, Alfieri A. Controversies about interspinous process devices in the treatment of degenerative lumbar spine diseases: past, present, and future. Biomed Res Int. 2014; 2014: 975052, doi: 10.1155/2014/975052, indexed in Pubmed: 24822224.
12. Hu MW, Liu ZL, Zhou Y, et al. Posterior lumbar interbody fusion using spinous process and laminae. J Bone Joint Surg Br. 2012; 94(3): 373–377, doi: 10.1302/0301-620X.94B3.27629, indexed in Pubmed: 22371546.
13. Husted DS, Haims AH, Fairchild TA, et al. Morphometric comparison of the pedicle rib unit to pedicles in the thoracic spine. Spine (Phila Pa 1976). 2004; 29(2): 139–146, doi: 10.1097/01.BRS.0000105537.49674.A3, indexed in Pubmed: 14722404.
14. Ihm EH, Han InBo, Shin DAh, et al. Spinous process morphometry for interspinous device implantation in Korean patients. World Neurosurg. 2013; 79(1): 172–176, doi: 10.1016/j.wneu.2011.04.027, indexed in Pubmed: 22120390.
15. Kaur K, Singh R, Prasath V, et al. Computed tomographic-based morphometric study of thoracic spine and its relevance to anaesthetic and spinal surgical procedures. J Clin Orthop Trauma. 2016; 7(2): 101–108, doi: 10.1016/j.jcot.2015.12.002, indexed in Pubmed: 27182147.
16. Kim D, Albert T. Interspinous process spacers. J Am Acad Orthop Surg. 2007; 15(4): 200–207, doi: 10.5435/00124635-200704000-00003.
17. Kim HoJ, Bak KH, Chun HJ, et al. Posterior interspinous fusion device for one-level fusion in degenerative lumbar spine disease : comparison with pedicle screw fixation: preliminary report of at least one year follow up. J Korean Neurosurg Soc. 2012; 52(4): 359–364, doi: 10.3340/jkns.2012.52.4.359, indexed in Pubmed: 23133725.
18. Leahy JC, Mathias KJ, Hukins DW, et al. Design of spinous process hooks for flexible fixation of the lumbar spine. Proc Inst Mech Eng H. 2000; 214(5): 479–487, doi: 10.1243/0954411001535507, indexed in Pubmed: 11109855.
19. Lee HM, Kim NH, Kim HJ, et al. Morphometric study of the lumbar spinal canal in the Korean population. Spine (Phila Pa 1976). 1995; 20(15): 1679–1684, doi: 10.1097/00007632-199508000-00006, indexed in Pubmed: 7482017.
20. Lee SH, Kang HS. Percutaneous endoscopic laser annuloplasty for discogenic low back pain. World Neurosurg. 2010; 73(3): 198–206; discussion e33, doi: 10.1016/j.surneu.2009.01.023, indexed in Pubmed: 20860958.
21. Lee SE, Jahng TA, Kim HJ. Different surgical approaches for spinal schwannoma: a single surgeon's experience with 49 consecutive cases. World Neurosurg. 2015; 84(6): 1894–1902, doi: 10.1016/j.wneu.2015.08.027, indexed in Pubmed: 26325210.
22. Lühmann D, Burkhardt-Hammer T, Borowski C, et al. Minimally invasive surgical procedures for the treatment of lumbar disc herniation. GMS Health Technol Assess. 2005; 1: Doc07, indexed in Pubmed: 21289928.
23. Mariottini A, Pieri S, Giachi S, et al. Preliminary results of a soft novel lumbar intervertebral prothesis (DIAM) in the degenerative spinal pathology. Acta Neurochir Suppl. 2005; 92: 129–131, doi: 10.1007/3-211-27458-8_28, indexed in Pubmed: 15830984.
24. Miscusi M, Trungu S, Forcato S, et al. Long-term clinical outcomes and quality of life in elderly patients treated with interspinous devices for lumbar spinal stenosis. J Neurol Surg A Cent Eur Neurosurg. 2018; 79(2): 139–144, doi: 10.1055/s-0037-1604280, indexed in Pubmed: 28750451.
25. Onen MR, Simsek M, Naderi S. Alternatives to surgical approach for giant spinal schwannomas. Neuro-

sciences (Riyadh). 2016; 21(1): 30–36, doi: 10.17712/nsj.2016.1.20150242, indexed in Pubmed: 26818164.
26. Panjabi MM, O'Holleran JD, Crisco JJ, et al. Complexity of the thoracic spine pedicle anatomy. Eur Spine J. 1997; 6(1): 19–24, doi: 10.1007/BF01676570, indexed in Pubmed: 9093823.
27. Ran B, Li Q, Yu B, et al. Morphometry of lumbar spinous process via three dimensional CT reconstruction in a Chinese population. Int J Clin Exp Med. 2015; 8(1): 1129–1136, indexed in Pubmed: 25785103.
28. Richardson J, Groen G. Applied epidural anatomy. Continuing Education Anaesthesia Critical Care Pain. 2005; 5(3): 98–100, doi: 10.1093/bjaceaccp/mki026.
29. Romanes GJ. ed. 15th ed. Cunninghams Manual of Practical Anatomy. vol. II. Oxford University Press, New York 1996: 3–82.
30. Sénégas J. Mechanical supplementation by non-rigid fixation in degenerative intervertebral lumbar segments: the Wallis system. Eur Spine J. 2002; 11 Suppl 2: S164–S169, doi: 10.1007/s00586-002-0423-9, indexed in Pubmed: 12384740.
31. Shaw JD, Shaw DL, Cooperman DR, et al. Characterization of lumbar spinous process morphology: a cadaveric study of 2,955 human lumbar vertebrae. Spine J. 2015; 15(7): 1645–1652, doi: 10.1016/j.spinee.2015.03.007, indexed in Pubmed: 25777742.
32. Shim C, Park S, Lee SH, et al. Biomechanical evaluation of an interspinous stabilizing device, locker. Spine. 2008; 33(22): E820–E827, doi: 10.1097/brs.0b013e3181894fb1.
33. Singh R, Srivastva SK, Prasath CS, et al. Morphometric measurements of cadaveric thoracic spine in Indian population and its clinical applications. Asian Spine J. 2011; 5(1): 20–34, doi: 10.4184/asj.2011.5.1.20, indexed in Pubmed: 21386943.
34. Suk SI, Kim WJ, Lee SM, et al. Thoracic pedicle screw fixation in spinal deformities: are they really safe? Spine (Phila Pa 1976). 2001; 26(18): 2049–2057, doi: 10.1097/00007632-200109150-00022, indexed in Pubmed: 11547207.
35. Ugur HC, Attar A, Uz A, et al. Thoracic pedicle: surgical anatomic evaluation and relations. J Spinal Disord. 2001; 14(1): 39–45, doi: 10.1097/00002517-200102000-00007, indexed in Pubmed: 11242273.
36. Weinstein JN, Tosteson TD, Lurie JD, et al. Surgical versus nonoperative treatment for lumbar spinal stenosis four-year results of the Spine Patient Outcomes Research Trial. Spine (Phila Pa 1976). 2010; 35(14): 1329–1338, doi: 10.1097/BRS.0b013e3181e0f04d, indexed in Pubmed: 20453723.
37. Yano S, Hida K, Seki T, et al. A new ceramic interspinous process spacer for lumbar spinal canal stenosis. Operative Neurosurgery. 2008; 63(suppl_1): ONS108–ONS114, doi: 10.1227/01.neu.0000310693.86660.d3.
38. Zindrick MR, Knight GW, Sartori MJ, et al. Pedicle morphology of the immature thoracolumbar spine. Spine (Phila Pa 1976). 2000; 25(21): 2726–2735, doi: 10.1097/00007632-200011010-00003, indexed in Pubmed: 11064516.
39. Zucherman JF, Hsu KY, Hartjen CA, et al. A prospective randomized multi-center study for the treatment of lumbar spinal stenosis with the X STOP interspinous implant: 1-year results. Eur Spine J. 2004; 13(1): 22–31, doi: 10.1007/s00586-003-0581-4, indexed in Pubmed: 14685830.

VIA MEDICA

ORIGINAL ARTICLE

Folia Morphol.
Vol. 80, No. 3, pp. 675–682
DOI: 10.5603/FM.a2020.0107
Copyright © 2021 Via Medica
ISSN 0015–5659
eISSN 1644–3284
journals.viamedica.pl

Anatomic morphological study of thoracolumbar foramen in normal adults

Y. Wang[1], Y. Cai[2, 3], Y. Xu[1], H. Guan[1], M. Gao[2], Y. He[2], L. Wang[4], H. Wang[2], X. Li[2], Z. Li[2], J. Yu[5], Y. Fu[5], Y. Zhang[5], Y. Zhao[5], D. Xin[5]

[1]*School of Postgraduates of Inner Mongolia Medical University, Hohhot, China*
[2]*Human Anatomy of Inner Mongolia Medical University, Hohhot, China*
[3]*Digital Medical Centre, School of Basic Medical Sciences, Inner Mongolia Medical University, Hohhot, China*
[4]*Inner Mongolia International Mongolian Medical Hospital, Hohhot, China*
[5]*The Second Affiliated Hospital of Inner Mongolia Medical University, China*

[Received: 25 July 2020; Accepted: 19 August 2020; Early publication date: 2 September 2020]

Background: *Based on computed tomography images of the thoracolumbar intervertebral foramen and its surrounding parameters, and analysing the intervertebral foramen morphology and the correlation between the measured parameters, to provide an anatomical basis for clinical minimally invasive transvertebral surgery.*
Materials and methods: *Ten fresh adult cadaveric specimens (32–50 years old) with bilateral (T_1–S_1) spinal segments were selected for a total of 20 sides, a total of 340 intervertebral foramens and were measured with vernier callipers in the Department of Anatomy, Inner Mongolia Medical University. The intervertebral foramen height, the minimum sagittal diameter of the foramen, the width of the spinal ganglion, the sagittal diameter of the spinal ganglion and the sagittal diameter of the intervertebral foramen were measured. This study was reviewed and approved by the local Ethics Committee.*
Results: *The results of the minimum sagittal diameter of the $T_{9–10}$~L_5/S_1 intervertebral foramen were (6.93 ± 1.99) mm, (7.33 ± 1.44) mm, (7.41 ± 0.63) mm, (6.85 ± ± 1.08) mm, (6.79 ± 1.86) mm, (7.82 ± 3.25) mm, (8.23 ± 2.27) mm, (9.17 ± 2.33) mm, (8.38 ± 1.63) mm; the average height of the T2/3 to L5/S1 intervertebral space was (4.82 ± 1.88) mm, (3.95 ± 0.80) mm, (4.04 ± 0.52) mm, (4.26 ± 0.78) mm, (4.39 ± ± 1.16) mm, (5.15 ± 1.59) mm, (5.51 ± 1.49) mm, (5.97 ± 2.60) mm, (7.13 ± 2.07) mm, (8.94 ± 1.37) mm, (9.01 ± 1.47) mm, (11.63 ± 1.63) mm, (14.20 ± 1.37) mm, (14.22 ± 2.33) mm, (14.22 ± 2.33) mm, (13.32 ± 1.37) mm intervertebral foramen height, intervertebral foramen minimum sagittal diameter, spinal ganglion width, spinal ganglion sagittal diameter. $P > 0.05$ for comparison of the left and right sides of the intervertebral space, with no statistically significant difference. $L_{4/5}$, L_5/S_1 segment left and right bilateral contrast with the middle height of the vertebral space $p < 0.05$, the difference is statistically significant. The remaining segments left and right bilaterally contrasted $p > 0.05$, and the difference was not statistically significant.*
Conclusions: *The minimum height of intervertebral foramen in the thoracolumbar segment was $T_{6/7}$, and $L_{1/2}$ was the minimum height in the lumbar segment. When placing a spinal endoscopic working channel safely into intervertebral foramen, it is necessary to perform an enlarging foraminoplasty to reduce the risk of injury to the exiting nerve root.* (Folia Morphol 2021; 80, 3: 675–682)

Key words: adult, thoracic spine, lumbar spine, intervertebral foramen, anatomical measurements

Address for correspondence: Dr. H. Wang; Dr. X. Li, Human Anatomy Inner Mongolia Medical University Basic Medical College, Hohhot, 10110, China, tel: +86 471 6657009, fax: +86 471 6657562, e-mail: 18647398868@163.com; 798242742@qq.com

INTRODUCTION

The nucleus pulposus of the intervertebral disc decreases with age, leading to disc degeneration, which is the major cause of herniated discs. Thoracic disc herniation (TDH) has a low incidence of TDH, which has been reported to account for 0.25–0.75% of spinal disc herniation, compared to 0.1–0.0001% in the general population [9]. It mainly occurs between T_8–L_1, most often in patients aged 30–50 years, with an equal proportion of men and women, with complex and varied clinical manifestations, diagnostic difficulties and surgical difficulties [3]. Lumbar disc herniation is a common orthopaedic condition. The prevalence of lower back pain is estimated at 4.8% in men aged 35 years, and 2.5% in women of that age. Spinal nerve entrapment due to intervertebral foramen stenosis, or spinal space herniation is more common [2]. For patients who have failed to respond to conservative treatment, surgery is often used, and minimally invasive surgery is used to treat herniated discs through lumbar intervertebral spondylolisthesis. The results are significant, and there is a large body of literature confirming the clinical superiority of the transforaminal path for lumbar disc herniation over traditional surgical approaches [1, 6]. Treatment of herniated discs using intervertebral endoscopic techniques can reduce peri-spinal muscle and soft tissue injury, increase spinal stability, and is associated with a small trauma, rapid recovery and short hospital stay [8]. With the increasing development of a large number of intervertebral foramen techniques, there is a need for clinicians to further improve their understanding of intervertebral foramen anatomy. In this paper, we use adult cadaveric specimens to study the anatomical and morphological changes of intervertebral foramen in the thoracolumbar spine and to investigate the normal intervertebral foramen, spinal nerves and intervertebral space morphology, measurement of its diameter line, and correlation analysis of the spinal ganglion with the size of the intervertebral foramen. It provides anatomical basis for selection of position and angle for minimally invasive clinical transvertebral foramen path surgery.

MATERIALS AND METHODS

Ten fresh cadaver specimens were collected, ranging in age from 32 to 50 years, with an average age of 43.2 years, on the intact spine of a normal fresh adult cadavers (T_1 to S_1), bilaterally on 20 sides with a total of 340 intervertebral foramen. This study was reviewed and approved by the local Ethics Committee. The data in the literature are varied, mainly because of individual variations and the different degrees of degenerative change in the spine. In this study, none of the subjects had symptoms or any degenerative changes of the spine. Therefore, our results provide the normal morphometric anatomy for the nerve roots and dorsal root ganglion.

Observational indicators

Use of vernier callipers (Japan Mitutoyo, accuracy 0.02 mm), compasses, stainless steel rulers (accuracy 1 mm), medical power saws. Drill (Shanghai Bojin Medical Instrument Co., Ltd., BYJ-1) tools, surgical instruments: scalpels, surgical scissors, haemostatic forceps, dissecting instruments, etc. forceps, hacksaw. Measure the height (vertical diameter) of the intervertebral foramen bilaterally at each spinal segment with reference to Wu Bo (2017) [13] defining the intervertebral level at the upper margin of the intervertebral space The distance from the anterior boundary of the foramen to the posterior boundary of the intervertebral foramen is the minimum sagittal diameter of the intervertebral foramen, the wide spinal ganglion, the sagittal diameter of the spinal ganglion, and the intervertebral space. Left, middle, and right heights' measurements were taken by the same measurer familiar with the anatomical landmarks for which the relevant indexes were collected, and the recording length/mm (d/mm) was Unit.

Specimen production dissect the thoracic and lumbar segments of 10 adult cadaveric specimens, remove internal organs, and use a hacksaw to saw the upper end of the spinal specimen from the bulge. Horizontal dissociation, marking the 12th rib, identifying the lumbar segment, inferiorly dissociating horizontally from the hip joint, followed by local dissociative manoeuvres, removing the skin The lumbaris major muscle is carefully resected to expose the entire thoracic spine, lumbar spine, intervertebral space, intervertebral foramen, and the muscles and surrounding soft tissue structures. Nerve root structures, keeping the position of nerve roots within the intervertebral foramen intact, and making morphological observations of the intervertebral foramen, nerve roots, and intervertebral spaces (Fig. 1). The upper end of the scalpel was detached from the vertebral space at the C_7/T_1 segment with a scalpel, and the lower end of the scalpel was used to divide the ribs one by one along the rib joint with a medical electric saw drill and the thoracic vertebrae (Fig. 2). The intervertebral foramen height was measured, i.e., the distance from the superior to the inferior margin of the foramen; the minimum sagittal diameter of

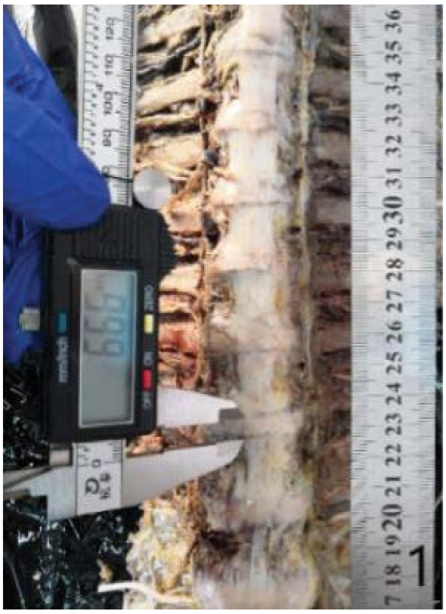

Figure 1. Lumbar intervertebral foramen of the thoracic vertebrae, measuring the height of the intervertebral disc.

Figure 2. Posterior view of the spinal canal.

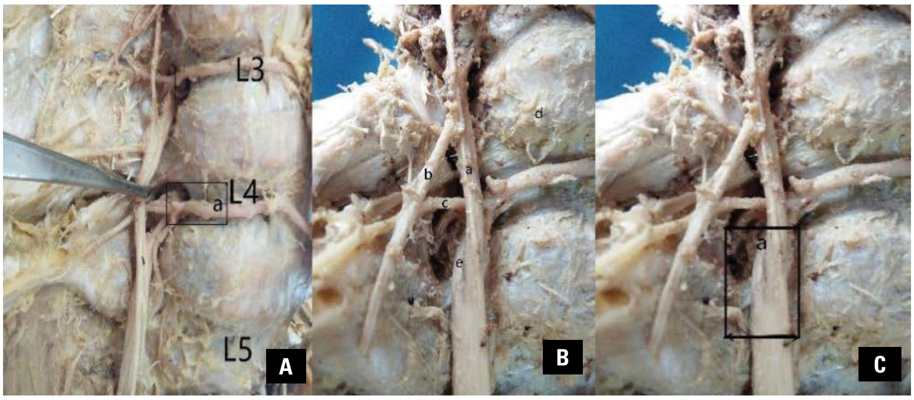

Figure 3. A. Sympathetic dry; **B.** Grey white traffic branch; **C.** Lumbar artery; **D.** Vertebral; **E.** Pedicle anterior branch.

the foramen, i.e., the distance between the posterior margin of the intervertebral space and the distance; observation of the intervertebral foramen walking nerves (Fig. 3A–C); measurement of the intervertebral space height, i.e., the superior and inferior endplate levels distance between them (Fig. 4); the spinal sagittal diameter, which is the maximum distance between the axial edges of the spinal ganglia; the spinal width, which is the distance perpendicular to the maximum distance between spinal ganglion edges (Fig. 5).

Statistical methods

GraphPad Prism 8.0 was used and the measures were expressed as mean ± standard deviation ($\bar{x} \pm s$). Paired t-tests were used between left and right lateral comparisons and between ipsilateral comparisons; one-way ANOVA was used between comparisons of different segments; determination of intervertebral foramen index and spinal ganglion index by bivariate correlation Pearson's correlation coefficient test the correlation between. Using Pearson's correlation coefficient test, the correlation coefficient (r) is interpreted as follows: < 0.2 indicates a weak correlation. 0.2–0.4 indicates weak correlation, 0.4–0.7 moderate correlation, 0.7–0.9 high correlation, > 0.9 indicates almost perfect correlation. The test level was alpha = 0.05; $p < 0.05$ was statistically significant.

RESULTS

Left and right bilateral comparison $p > 0.05$ for the left and right sides of each measure, the differences are not statistically significant, and the statistical data are combined.$T_{1/2}$~L_5/S_1 segment intervertebral foramen height comparison $p < 0.0001$, the difference is statistically significant.$T_{9/10}$~L_5/S_1 segment. The minimum sagittal diameter of intervertebral foramen was $p > 0.05$, and the difference was not statistically significant.$T_{6/7}$~L_5/S_1 segment interspinal nerve ($p < 0.05$), statistically significant difference. $P < 0.05$ for $T_{7/8}$~L_5/S_1 intersegmental chiropractic width. The differences were statistically significant (Tables 1, 2).

Measurement of anatomical parameters of the intervertebral space $p > 0.05$ for comparison of the left and right heights of the intervertebral space,

Figure 4. Measuring the right side of the intervertebral disc; a — vertebral body; b — intervertebral disc.

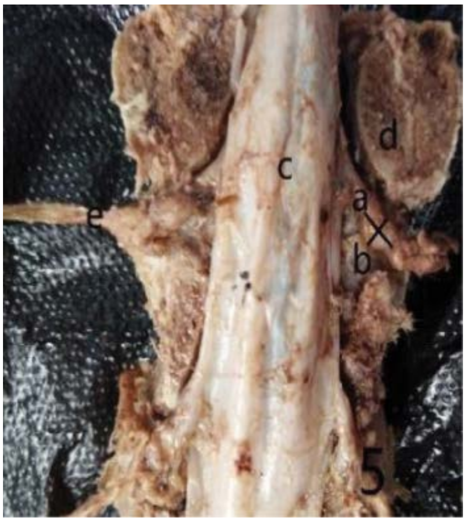

Figure 5. Measurement of spinal ganglion; a — spinal ganglion wide; b — spinal ganglion sagittal diameter; c — dural sac; d — pedicle; e — spinal nerve posterior root.

Table 1. Measurements of the high of intervertebral foramens, minimal sagittal diameter of intervertebral foramen (mean ± standard deviation)

	The high of intervertebral foramens [mm] (n = 340)				Minimal sagittal diameter of intervertebral foramen [mm] (n = 180)			
	Left	Right	Bilateral	P	Left	Right	Bilateral	P
$T_{1/2}$	9.38 ± 0.70	9.03 ± 1.10	9.20 ± 0.91	0.516	–	–	–	–
$T_{2/3}$	9.44 ± 0.83	9.52 ± 1.39	9.48 ± 1.06	0.909	–	–	–	–
$T_{3/4}$	9.43 ± 1.55	8.95 ± 1.73	9.19 ± 1.55	0.359	–	–	–	–
$T_{4/5}$	7.29 ± 1.24	7.51 ± 1.29	7.40 ± 1.14	0.799	–	–	–	–
$T_{5/6}$	6.26 ± 1.07	6.09 ± 1.26	6.17 ± 1.09	0.754	–	–	–	–
$T_{6/7}$	5.49 ± 1.25	6.35 ± 1.52	5.92 ± 1.20	0.471	–	–	–	–
$T_{7/8}$	7.28 ± 3.68	7.69 ± 3.40	7.48 ± 3.34	0.504	–	–	–	–
$T_{8/9}$	10.01 ± 5.97	9.00 ± 6.14	9.46 ± 5.75	0.006	–	–	–	–
$T_{9/10}$	9.31 ± 5.09	9.10 ± 4.74	9.21 ± 4.64	0.626	6.63 ± 0.52	7.23 ± 3.36	6.93 ± 1.99	0.815
$T_{10/11}$	9.84 ± 3.41	9.85 ± 3.41	9.71 ± 3.03	0.071	7.22 ± 1.00	7.44 ± 0.85	7.33 ± 1.44	0.792
$T_{11/12}$	10.44 ± 1.68	10.57 ± 1.74	10.51 ± 1.73	0.842	7.40 ± 0.56	7.42 ± 0.82	7.41 ± 0.63	0.976
T_{12}/L_1	9.00 ± 1.07	10.23 ± 1.68	9.50 ± 1.41	0.371	7.38 ± 1.01	6.32 ± 0.83	6.85 ± 1.08	0.104
$L_{1/2}$	12.22 ± 2.10	12.32 ± 1.52	12.27 ± 1.34	0.854	7.48 ± 2.35	6.00 ± 1.29	6.79 ± 1.86	0.218
$L_{2/3}$	14.71 ± 2.29	15.01 ± 1.26	14.86 ± 2.36	0.799	8.70 ± 3.90	6.94 ± 2.56	7.82 ± 3.25	0.468
$L_{3/4}$	16.68 ± 2.27	15.21 ± 2.53	15.94 ± 2.43	0.435	8.83 ± 2.93	7.62 ± 1.241	8.23 ± 2.27	0.317
$L_{4/5}$	15.44 ± 2.23	15.40 ± 2.75	15.42 ± 2.34	0.964	9.02 ± 2.61	9.30 ± 2.22	9.17 ± 2.33	0.789
L_5/S_1	13.37 ± 2.02	12.40 ± 2.06	12.88 ± 2.13	0.194	8.85 ± 2.07	7.92 ± 1.78	8.38 ± 1.63	0.128
F-value	11.27		$P < 0.0001$		1.91		$P > 0.05$	

Table 2. The transverse diameter of the dorsal root ganglion (n = 240) and longitudinal diameter of the dorsal root ganglion (n = 220) (mean ± standard deviation)

	The transverse diameter of the dorsal root ganglion [mm]				Longitudinal diameter of the dorsal root ganglion [mm]			
	Left	Right	Bilateral	P	Left	Right	Bilateral	P
$T_{6/7}$	5.03 ± 1.80	4.79 ± 1.49	4.91 ± 1.48	0.556	–	–	–	–
$T_{7/8}$	4.38 ± 0.85	4.39 ± 1.18	4.38 ± 0.92	0.984	6.22 ± 0.35	7.33 ± 1.00	6.95 ± 0.95	0.251
$T_{8/9}$	4.94 ± 1.90	5.10 ± 2.00	5.02 ± 1.75	0.216	7.35 ± 1.42	6.56 ± 0.22	6.96 ± 1.03	0.283
$T_{9/10}$	5.05 ± 1.52	4.74 ± 1.67	4.90 ± 1.51	0.068	7.13 ± 0.93	6.10 ± 1.21	6.71 ± 1.05	0.467
$T_{10/11}$	5.87 ± 1.38	5.46 ± 1.65	5.66 ± 1.42	0.433	8.37 ± 2.53	7.01 ± 1.07	7.69 ± 1.94	0.384
$T_{11/12}$	5.77 ± 1.13	5.46 ± 0.81	5.61 ± 1.41	0.647	7.61 ± 1.24	7.03 ± 1.14	7.31 ± 1.07	0.675
T_{12}/L_1	5.96 ± 1.38	7.66 ± 1.65	6.64 ± 2.18	0.433	8.37 ± 1.53	7.01 ± 1.07	6.52 ± 1.24	0.384
$L_{1/2}$	6.65 ± 2.10	6.37 ± 2.56	6.51 ± 1.24	0.602	6.50 ± 1.55	6.29 ± 1.51	7.67 ± 1.80	0.806
$L_{2/3}$	6.42 ± 2.26	6.80 ± 2.47	6.61 ± 2.70	0.472	9.31 ± 1.21	7.80 ± 1.41	8.55 ± 1.64	0.499
$L_{3/4}$	8.15 ± 4.11	7.77 ± 4.72	7.96 ± 4.18	0.681	12.01 ± 2.20	10.37 ± 1.70	11.19 ± 1.14	0.207
$L_{4/5}$	8.99 ± 4.41	9.20 ± 6.10	9.08 ± 4.71	0.632	11.46 ± 1.54	9.43 ± 1.36	10.82 ± 1.09	0.343
$L_{5/S1}$	4.65 ± 0.46	4.24 ± 0.86	4.44 ± 0.70	0.198	10.41 ± 1.61	11.1 ± 1.81	10.46 ± 1.49	0.144
F-value	3.494		P < 0.05		3.068		P < 0.05	

Table 3. Intervertebral disc height [mm] (n = 320) (mean ± standard deviation)

	Left	Right	P1	Middle	Bilateral	P2
$T_{2/3}$	3.80 ± 1.37	3.67 ± 0.58	0.851	5.78 ± 2.11	4.82 ± 1.88	0.256
$T_{3/4}$	3.90 ± 0.62	3.62 ± 0.60	0.724	4.41 ± 1.05	3.95 ± 0.8	0.388
$T_{4/5}$	3.92 ± 0.38	3.71 ± 0.49	0.657	4.49 ± 0.38	3.99 ± 0.51	0.1
$T_{5/6}$	4.01 ± 0.50	4.00 ± 0.84	0.974	4.79 ± 0.84	4.26 ± 0.78	0.268
$T_{6/7}$	4.03 ± 0.91	4.86 ± 1.30	0.072	4.27 ± 1.39	4.39 ± 1.16	0.868
$T_{7/8}$	5.48 ± 2.07	5.28 ± 0.73	0.88	4.82 ± 1.15	5.21 ± 1.5	0.651
$T_{8/9}$	5.25 ± 2.21	5.92 ± 1.08	0.634	4.93 ± 1.23	5.51 ± 1.49	0.497
$T_{9/10}$	6.40 ± 4.05	6.17 ± 2.47	0.824	4.84 ± 1.82	6.61 ± 2.87	0.3
$T_{10/11}$	6.34 ± 1.83	8.66 ± 1.65	0.148	6.42 ± 2.55	7.53 ± 1.84	0.421
$T_{11/12}$	9.70 ± 0.61	8.83 ± 0.81	0.003*	8.62 ± 1.02	8.94 ± 1.37	0.674
T_{12}/L_1	9.29 ± 1.54	8.94 ± 1.12	0.551	8.81 ± 1.89	9.01 ± 1.47	0.787
$L_{1/2}$	13.39 ± 3.00	10.06 ± 2.32	0.229	11.45 ± 1.67	11.63 ± 1.63	0.888
$L_{2/3}$	15.27 ± 2.53	13.13 ± 2.38	0.059	14.19 ± 2.37	14.18 ± 2.15	0.993
$L_{3/4}$	14.56 ± 2.73	12.83 ± 1.85	0.236	15.26 ± 2.21	13.69 ± 2.35	0.293
$L_{4/5}$	13.72 ± 2.06	14.40 ± 0.70	0.558	18.22 ± 2.21	14.06 ± 1.47	0.002*
$L_{5/S1}$	13.47 ± 1.54	13.16 ± 1.34	0.631	20.00 ± 0.82	13.32 ± 1.37	0.000*

*P < 0.05 — the difference is statistically significant; P1 — for left-right side comparison; P2 — for middle and bilateral comparison

the difference was not statistically significant, and statistical data were combined. $L_{4/5}$, L_5/S_1 $p < 0.05$ for the comparison between the left and right sides of the S_1 segment and the middle height of the intervertebral space, the difference was statistically significant. The remaining segments left and right bilateral and vertebral space intermediate height contrast $p > 0.05$, the difference was not statistically significant (Table 3).

Correlation analysis of spinal ganglion width and spinal ganglion sagittal diameter with intervertebral foramen height and intervertebral foramen

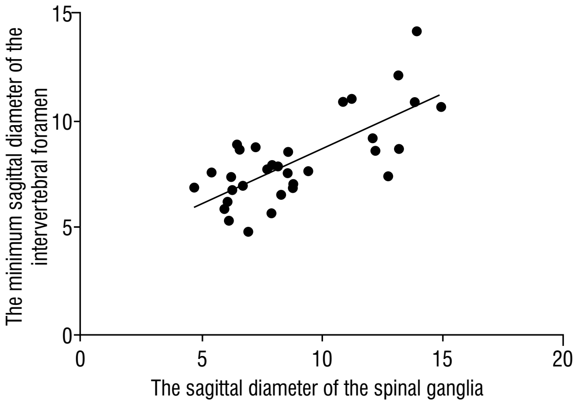

Figure 6. The minimum sagittal diameter of the intervertebral foramen is positively correlated with the sagittal diameter of the spinal ganglia.

minimum sagittal diameter, spinal ganglion sagittal diameter. The minimum sagittal diameter of the intervertebral foramen (r = 0.728), with r between 0.7 and 0.9, positively correlated and highly correlated (Fig. 6).

Analysis of the correlation between intervertebral foramen height and the left, right, and median height of the intervertebral space (Fig. 7). The intervertebral foramen height is positively correlated with the left and right bilateral height of the intervertebral space (r = 0.917), with r between 0.7 and 0.9, and height correlation. The intervertebral foramen height is positively and highly correlated with the median height of the intervertebral space (r = 0.877), with r ranging from 0.7 to 0.9.

DISCUSSION

There are broadly two methods for measuring intervertebral foramen morphology in China: one is direct measurement and the other is indirect measurement. The direct measurement tool is used to collect data from cadaveric specimens, while the indirect measurement mainly uses X-ray technique, three-dimensional computed tomography imaging and magnetic resonance imaging measurement [4]. In addition, after software post-processing to reconstruct the intervertebral foramen image, the measurement is performed, while the presence of soft tissue shadowing affects the experiment using X-ray and magnetic resonance imaging. In this paper, we collected 10 fresh cadaveric specimens and directly measured the morphology of the intervertebral foramen, which enabled direct, realistic and accurate observation of the intervertebral foramen. Zi-xuan et al. [16] measured cadavers under the X-ray technique similar to the measurements in this paper. The resultant anterior disc heights were (11.8 ± 1.2) mm, (13.0 ± ± 1.6) mm, (13.6 ± 1.9)mm, (14.3 ± 2.0) mm, (14.7 ± ± 2.5)mm. This the study is consistent with previous literature and the results are reliable and accurate. Rühli et al. [10] measured cadaveric specimens using vernier callipers. Comparing men and women revealed that the width of the intervertebral foramen was larger in women than in men at the lumbar segment. All specimens in this study were male, and the difference between the left and right sides of each measurement comparing the same individual was not statistically significant.

The bony border morphology of the intervertebral foramen has been described in the literature as an inverted teardrop, inverted pear shape, or oval shape, affecting the intervertebral foramen. There are many factors that contribute to size, such as degenerative changes in the bony borders of the intervertebral foramen, herniated discs, subluxation of the small joints, and hypertrophy of the ligamentum flavum [10]. Zhu et al. [15] retrospectively analysed the changes in intervertebral foramen morphology before and after unilateral transverse lumbar interbody fusion. Compared to the oblique or transverse cage approach, the transverse approach is preferred to reduce lumbar lordosis without affecting the contralateral side. The size of intervertebral foramen is good for decompression of lumbar spinal stenosis, and it is easy to determine the normal size of intervertebral foramen stenosis. The study observed that

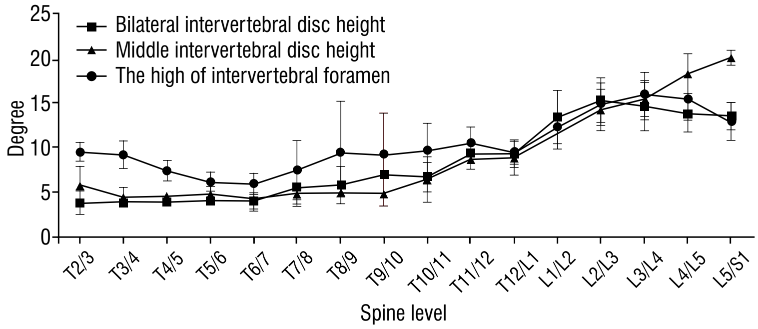

Figure 7. High correlation analysis between the height of intervertebral foramen and the left and right sides and the middle of intervertebral space.

the transverse section of the spinal nerve root was oval in shape, the transverse section of the thoracic spinal nerve was smaller, and the intervertebral foramen went outward and backward, and the lumbar section was smaller. The spinal nerve cross-section is large and goes obliquely outward and downward after exiting the intervertebral foramen. The wide thoracic segment of the spinal ganglion, T_6–T_{12}, has a gradually increasing trend; the lumbar segment, L_1–S_1, has an essentially unchanged trend of $L_{1/2}$; $L_{3/4}$ maximal, L_5/S_1 minimal. The trend of the sagittal diameter of spinal ganglion was not obvious in the thoracic segment from T_7 to T_{12}, but in the lumbar segment from L_1 to S_1, $l_{4/5}$ maximal, L_5/S_1 minimal. The height of the intervertebral gap was larger in the middle and smaller in the left and right sides of the L_5/S_1 and $L_{4/5}$ segments compared to the right and left sides of the L_5/S_1 and $L_{4/5}$ segments. Because the intervertebral space morphology dictates that artificial intervertebral space designs cannot be designed to be directly rectangular [11], this study also found that the intervertebral gap height median height in the L_5/S_1 and $L_{4/5}$ segments compared to the right and left sides of the spine. Large in the middle and small on the left and right side need to be designed to have a large middle height of the vertebral space and a small height of the vertebral space on both sides, which can improve the biomechanics of the spine.

There are now five types of surgical access for the treatment of TDH, including anterior access, lateral access, pedicle access, intervertebral access, thoracoscopic access. According to the literature, anterior surgical access is more difficult to learn and has a higher incidence of complications [9]. When encountering large disc size, disc calcification and central TDH, the intervertebral approach is not applicable, and there is a lack of treatment in the current literature. Evidence for the safety of surgical access for TDH is attributed to, among other reasons, the low incidence of TDH. Currently, percutaneous endoscopic lumbar discectomy has become the most promising treatment of lumbar intervertebral disc protrusion and minimally invasive spinal surgery. Percutaneous endoscopic lumbar discectomy is widely used in clinical practice with its advantages of less trauma, quicker recovery, shorter operation time, less pain, and improved lumbar spinal cord function [5]. Hoyland et al. [7] found that neural tissue accounted for less than 35% of the total intervertebral foramen. Other studies found the largest at L_5/S_1 and the smallest at $L_{1/2}$. On the contrary, the L_5/S_1 intervertebral foramen was the smallest. In the study of Rühli et al. [10], osseous intervertebral foramen at the L_5 level was found to be the largest. The value of the intervertebral foramen sagittal diameter is less than the L_1 level. The size of the working trocar used for minimally invasive interbody surgery is chosen to be less than the height of the intervertebral space measured in this paper, and the outer diameter of the annular saw is often chosen to be 7.5 mm [14], without articular projection enlargement, in intervertebral foraminoscopy. The operative space is small, and the lower intervertebral foramen is relatively safe compared to the upper, due to the small number of vital structures. The YESS technique requires Kambin triangle entry, this paper found that the spinal ganglion sagittal diameter is positively correlated with the minimum sagittal diameter of the intervertebral foramen, and careful attention should be paid during surgery. Identify the structures surrounding the intervertebral foramen to avoid damage to the surrounding spinal nerves. The TEYESS requires clipping of the supra-articular foramina to enlarge the intervertebral foramen without entering the intervertebral space through Kambin's triangle. The trocar is more easily accessed by the enlarged intervertebral foramen.

In addition, $T_{1/2}$ to L_5/S_1 intervertebral foramen height observes that the thoracic intervertebral foramen height changes in T_2 to T_{12} with a trend of decreasing first. The trend of change from $T_{2/3}$ to L_5/S_1 in the thoracic and lumbar segments is that the first one gradually increases, the second one increases after $T_{6/7}$, and the third one is the smallest in $T_{11/12}$. Decreasing to $T_{6/7}$ minimum, then increasing to $T_{7/8}$ greater, then decreasing, $T_{9/10}$ smaller, then increasing, reaching larger at $L_{3/4}$. Lumbar intervertebral foramen height is greater at $L_{3/4,}$ $L_{4/5}$, smallest at $L_{1/2}$, smaller at L_5/S_1; lumbar L_1–S_1 the minimum sagittal diameter of the intervertebral foramen tends to increase and then decrease, being smallest at $L_{1/2}$ and largest at $L_{4/5}$. Vialle et al. [12] measured the lumbar segments of eight male adult specimens. The mean value of the maximum longitudinal diameter of the spinal ganglion was 13.25 mm and the mean value of the minimum sagittal diameter of the spinal ganglion was 7.05 mm, which is similar to that of this paper. The findings were consistent. The intervertebral foramen height in the same segment was greater than the minimum sagittal diameter of the intervertebral foramen. The minimum sagittal diameter of intervertebral foramen in different segments is not statistically significant, and the influence of different vertebral sequence changes can be ignored when designing. Knowing the change of intervertebral foramen in different segments of the thoracolumbar spine and choosing the correct intervertebral perforator trocar will help to improve the success rate of surgery and reduce the number of cases.

CONCLUSIONS

The minimum height of intervertebral foramen in the thoracolumbar segment was $T_{6/7}$, and $L_{1/2}$ was the minimum height in the lumbar segment. When placing a spinal endoscopic working channel safely into intervertebral foramen, it is necessary to perform an enlarging foraminoplasty to reduce the risk of injury to the exiting nerve root.

Acknowledgements

This study was supported by Study on the National Natural Science Foundation of China (81860383, 81560348, 81460330); Natural Science Foundation of Inner Mongolia Autonomous Region (2020MS08124); Young Science and Technology Talents Project of Inner Mongolia Education Department (njyt-15-b05); Science and Technology Plan Project of Inner Mongolia Autonomous Region (2016,2019GG115); Science and Technology Innovation Guidance Project of Inner Mongolia Autonomous Region (2017); Natural Science Foundation of Inner Mongolia Autonomous Region (2016ms08131,2020MS08124); Inner Mongolia Scholarship Fund, Department of Human Resources and Social Services (TDK2017KJBW012); Inner Mongolia Autonomous Region "Grassland Talent" project youth innovation and entrepreneurship talent project (2020); Transformation Project of Scientific and Technological Achievements of Inner Mongolia Medical University (201903); Inner Mongolia Mongolian Medicine Collaborative Innovation Centre (2021, No.MyyxTYB202104).

Conflict of interest: None declared

REFERENCES

1. Ahn SS, Kim SH, Kim DW, et al. Comparison of outcomes of percutaneous endoscopic lumbar discectomy and open lumbar microdiscectomy for young adults: a retrospective matched cohort study. World Neurosurg. 2016; 86: 250–258, doi: 10.1016/j.wneu.2015.09.047, indexed in Pubmed: 26409086.
2. Bono C. Lumbar disc herniation and radiculopathy. Principles Orthopedic Practice Primary Care Providers. 2017: 37–46, doi: 10.1007/978-3-319-68661-5_3.
3. Court C, Mansour E, Bouthors C. Thoracic disc herniation: Surgical treatment. Orthop Traumatol Surg Res. 2018; 104(1S): S31–S40, doi: 10.1016/j.otsr.2017.04.022, indexed in Pubmed: 29225115.
4. Cramer GD, Cantu JA, Dorsett RD, et al. Dimensions of the lumbar intervertebral foramina as determined from the sagittal plane magnetic resonance imaging scans of 95 normal subjects. J Manipulative Physiol Ther. 2003; 26(3): 160–170, doi: 10.1016/S0161-4754(02)54109-9, indexed in Pubmed: 12704308.
5. Dalbayrak S, Yaman O, Yilmaz M, et al. Transforaminal approach in lumbar disc herniations: transforaminal microdiscectomy (TFMD) technique. Turk Neurosurg. 2015; 25(1): 29–35, doi: 10.5137/1019-5149.JTN.8197-13.1, indexed in Pubmed: 25640542.
6. He S, Sun Z, Wang Y, et al. Combining YESS and TESSYS techniques during percutaneous transforaminal endoscopic discectomy for multilevel lumbar disc herniation. Medicine (Baltimore). 2018; 97(28): e11240, doi: 10.1097/MD.0000000000011240, indexed in Pubmed: 29995758.
7. Hoyland JA, Freemont AJ, Jayson MI. Intervertebral foramen venous obstruction. A cause of periradicular fibrosis? Spine (Phila Pa 1976). 1989; 14(6): 558–568, doi: 10.1097/00007632-198906000-00002, indexed in Pubmed: 2749370.
8. Kanno H, Aizawa T, Hahimoto Ko, et al. Minimally invasive discectomy for lumbar disc herniation: current concepts, surgical techniques, and outcomes. Int Orthop. 2019; 43(4): 917–922, doi: 10.1007/s00264-018-4256-5, indexed in Pubmed: 30607499.
9. Kerezoudis P, Rajjoub KR, Goncalves S, et al. Anterior versus posterior approaches for thoracic disc herniation: Association with postoperative complications. Clin Neurol Neurosurg. 2018; 167: 17–23, doi: 10.1016/j.clineuro.2018.02.009, indexed in Pubmed: 29428625.
10. Rühli FJ, Müntener M, Henneberg M. Human osseous intervertebral foramen width. Am J Phys Anthropol. 2006; 129(2): 177–188, doi: 10.1002/ajpa.20263, indexed in Pubmed: 16323199.
11. Tang R, Gungor C, Sesek RF, et al. Morphometry of the lower lumbar intervertebral discs and endplates: comparative analyses of new MRI data with previous findings. Eur Spine J. 2016; 25(12): 4116–4131, doi: 10.1007/s00586-016-4405-8, indexed in Pubmed: 26873104.
12. Vialle E, Vialle LR, Contreras W, et al. Anatomical study on the relationship between the dorsal root ganglion and the intervertebral disc in the lumbar spine. Rev Bras Ortop. 2015; 50(4): 450–454, doi: 10.1016/j.rboe.2015.06.013, indexed in Pubmed: 26401504.
13. Wu Bo, Zhao qing-hao, Zhou Xiao-qi, et al. Applied anatomy of lumbar intervertebral foramen mirror. Chinese J Clin Anat. 35.01; 2017; 5-8, doi: 10.13418/j.issn.1001-165x.2017.01.002
14. Zhen-zhou L, Wen-wen W, Shu-xun H. Design and clinical application of the instrument for percutaneous posterolateral lumbar foraminoplasty. Chinese J Orthopaedics. 2011; 10: 1026–1032, doi: CNKI:SUN:ZHGK.0.2011-10-011.
15. Zhu K, Yan S, Guo S, et al. Morphological changes of contralateral intervertebral foramen induced by cage insertion orientation after unilateral transforaminal lumbar interbody fusion. J Orthop Surg Res. 2019; 14(1): 79, doi: 10.1186/s13018-019-1121-1, indexed in Pubmed: 30866988.
16. Zi-xuan W, Tao S. Parameter measurement of lumbar disc related to artificial disc replacement in Chinese. J Clin Rehab Tissue Engineering Res. 2011; 15(48): 8973–8976, doi: CNKI:SUN:XDKF.0.2011-48-022.

VIA MEDICA

ORIGINAL ARTICLE

Folia Morphol.
Vol. 80, No. 3, pp. 683–690
DOI: 10.5603/FM.a2020.0127

ISSN 0015–5659
eISSN 1644–3284
journals.viamedica.pl

Menisco-fibular ligament — an overview: cadaveric dissection, clinical and magnetic resonance imaging diagnosis, arthroscopic visualisation and treatment

U.E. Zdanowicz[1, 2], B. Ciszkowska-Łysoń[1], P. Krajewski[3], B. Ciszek[4], S.F. Badylak[1]

[1]*Carolina Medical Center, Warsaw, Poland*
[2]*McGowan Institute for Regenerative Medicine University of Pittsburgh, PA, United States*
[3]*Department of Forensic Medicine, Medical University of Warsaw, Poland*
[4]*Department of Descriptive and Clinical Anatomy, Medical University of Warsaw, Poland*

[Received: 24 May 2020; Accepted: 28 September 2020; Early publication date: 15 October 2020]

Background: *Injury to the menisco-fibular ligament (MFiL) is not commonly recognised. The anatomy of the lateral meniscus is complex and structure-function relationships are only partly understood. The purpose of the present study was to evaluate the MFiL, an anatomic structure rarely discussed that stabilises the lateral meniscus at the level of the hiatus popliteus and may have a crucial role in pathology of lateral meniscus injury.*

Materials and methods: *The MFiL was dissected from its attachment at the lateral meniscus to its insertion on fibular head in 12 human normal cadaver knees. The dimensions were determined and its anatomic position visualised throughout a 90° range of motion. Findings were documented on digital photographs and on video. Results were compared against the magnetic resonance imaging (MRI) appearance of the injured MFiL in 20 patients. Concomitant knee injuries in those patients were also analysed to determine the most frequent pattern of injuries.*

Results: *The normal MFiL showed an inverted trapezoid-shape with a mean width proximally of 13 mm, mean width distally of 8.5 mm and a mean length of 18.4 mm. MRI visualisation of the ligament was possible even in regular sequences; however, additional radial plane sequences were also used. Arthroscopic visualisation and manipulation was optimal when the camera was inserted into the postero-lateral gutter with full knee extension.*

Conclusions: *The MFiL stabilises the postero-lateral knee in concert with the menisco-femoral ligaments. Injury to the MFiL can be a cause of chronic postero-lateral pain syndrome with associated instability. Further anatomical and biomechanical studies are needed in order to fully evaluate its importance.* (Folia Morphol 2021; 80, 3: 683–690)

Key words: menisco-fibular ligament, lateral meniscus, anatomy, knee, arthroscopy, postero-lateral corner

Address for correspondence: Dr. U.E. Zdanowicz, Carolina Medical Center, ul. Pory 78, 02–757 Warszawa, Poland, e-mail: u.zdanowicz@icloud.com

INTRODUCTION

A thorough understanding of anatomic structure-function relationships is necessary for optimal surgical repair following injury. The purpose of the present study was to evaluate the menisco-fibular ligament (MFiL) — a stabilising structure that maintains the lateral meniscus at the level of hiatus popliteus. This ligament is a relatively unknown ligament and there are only a few studies describing it. On the other hand injuries to lateral meniscus at the level of hiatus popliteus are common, but also hard to handle. Results of suturing lateral meniscus in that area are not always favourable. And failing to save lateral meniscus inevitably leads to early osteoarthrosis [6].

Comparative anatomy in mammals offers insight into structure-function relationships in the human knee. The fruit bat (Pteropus), for example, which has only flexion and extension capability with no rotational movement of the knee joint, has no menisci. On the other hand, lower monkeys (ex. Rhesus, Capuchin), have greater rotational movement in the knee than man, and has a medial meniscus that is similar to man. However, the lateral meniscus is not attached to tibia, but continues obliquely, posterior to posterior cruciate ligament and finds its insertion on femur (similarly to posterior menisco-femoral ligament, Wrisberg's ligament in humans) [10]. Therefore, logically the human lateral meniscus (Fig. 1) anatomy and biomechanics are somewhere between the fruit bat and the monkey and is characterised by both medial and lateral menisci and rather rigid fixation with its posterior root attachment to tibia.

Development of menisco-fibular ligament

In lower vertebrates, as well as during human embryonic development, both the tibia and fibula (with attached popliteus tendon) articulate with the femur. However, at 7–8 weeks gestation, the fibula moves distally and the popliteus tendon forms a new attachment to the femur, concomitantly retaining its original insertion to fibula, which later is called the popliteo-fibular ligament. As a result, humans have an intra-articular popliteus tendon and a hiatus popliteus [3, 5]. At 11 weeks of embryonic development, a direct connection between fibula and lateral meniscus is formed: the MFiL (Fig. 2) [1]. The MFiL is a thick fibrous band connecting inferior edge of posterior part of lateral meniscus with the head of fibula, and to a limited extent, provides reinforcement of the coronary ligament (menisco-tibial ligament). According to Bozkurt et al. [1] the mean thickness of MFiL is 3.84 mm (including the capsule to which it adheres).

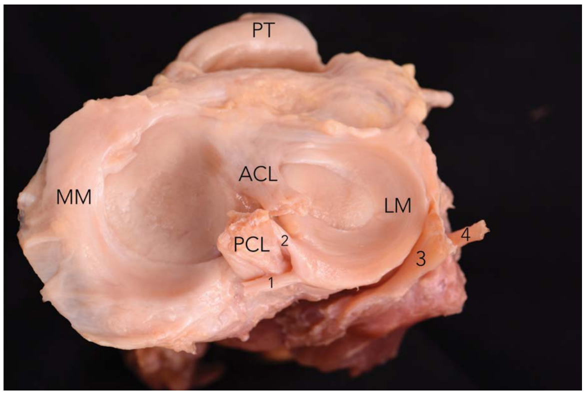

Figure 1. Cadaveric dissection of human right knee; MM — medial meniscus; LM — lateral meniscus; ACL — anterior cruciate ligament; PCL — posterior cruciate ligament; PT — patellar tendon; 1 — posterior menisco-femoral ligament (Wrisberg ligament); 2 — anterior menisco-femoral ligament (Humphrey ligament); 3 — popliteus tendon; 4 — lateral collateral ligament.

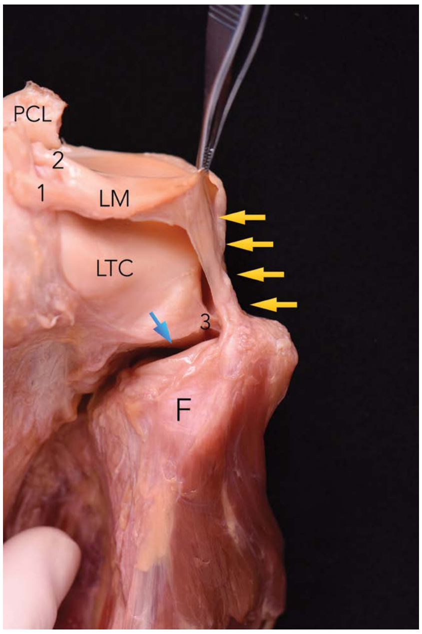

Figure 2. Cadaveric dissection of human right knee; posterior view; LM — lateral meniscus; PCL — posterior cruciate ligament; LTC — lateral tibial condyle; 1 — posterior menisco-femoral ligament; 2 — anterior menisco-femoral ligament; 3 — superior joint capsule of proximal tibio-fibular joint (marked with blue arrow). Menisco-fibular ligament is marked with yellow arrows.

The coronary ligament attaches just below articular margin of proximal lateral tibial condyle, while the distal attachment of MFiL is on fibular head [8]. This relatively large ligament is believed to stabilise the lateral meniscus and thus have a significant impact on the biomechanics of the lateral meniscus and play a role in lateral meniscal tears. The presence of the MFiL may biomechanically explain lateral meniscus longitudinal tears at the level of hiatus popliteus. While the knee moves from flexion to extension and the lateral meniscus moves anteriorly following the femoral condyles and being pulled by menisco-femoral ligaments, the MFiL, together with menisco-popliteal fascicles acts to limit that movement (Fig. 3). If that balance gets interrupted by an external force for example, meniscal injury can occur.

In this study we are investigating anatomy and pathology of this unknown MFiL from three different perspectives: anatomical dissection, magnetic resonance imaging (MRI) and arthroscopic appearance.

MATERIALS AND METHODS

Twelve cadaver knees, 9 right and 3 left, were dissected. Ten of the knees were in males and two in females. The mean age was 67 years with a range of 52 to 74 years. Knees with severe osteoarthritic changes (grade IV according to Outerbridge classification of osteochondral injuries) were excluded from the study. Classical anatomical dissection was conducted with careful layer by layer removal of tissue within the postero-lateral corner until the MFiL was clearly identified in all specimens. The length and the width of the ligament was measured and the anatomical findings were documented with digital photographs and video recordings.

The present study also included retrospective evaluation of the MRI of an injured MFiL in 20 patients. These patients included 13 males and 7 females, with a mean age of 37 years and a range of 18 to 53 years. These MRI included 12 left and 8 right knees. All MRI were performed in 1.5 T Signa HDxt 1.5T, GE Medical Systems, in 8chHD Knee Array Coil. The following sequences were performed: sagittal PD FSE, sagittal PD FSE Fat Sat (slice thickness 2.0 mm); coronal PD FSE (slice thickness 3.0 mm) and axial STIR (slice thickness 3.5 mm).

RESULTS

Anatomic dissection

The MFiL in 12 cadaveric knees was an inverted trapezoid-shaped structure, with a mean width proximally of 13 mm (range: 9–17 mm), a mean width distally of 8.5 mm (range: 4.3–12 mm) and a mean length of 18.4 mm (range: 14–26 mm) (Fig. 4). The proximal attachment of the MFiL began at the inferior edge of posterior part of lateral meniscus. At the level of the articular surface of lateral tibial condyle: the medial, vertical edge of ligament began at about the level where popliteus tendon crosses the lateral meniscus, however its lateral

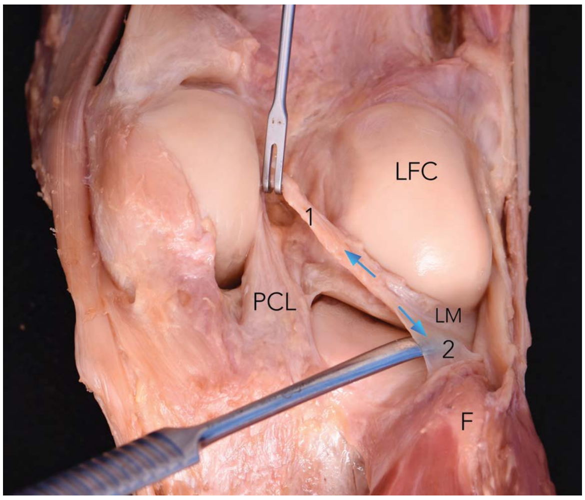

Figure 3. Cadaveric dissection of human right knee; posterior view; LM — lateral meniscus; LFC — lateral femoral condyle; PCL — posterior cruciate ligament; F — fibula; 1 — posterior menisco-femoral ligament (Wrisberg ligament); 2 — menisco-fibular ligament. Notice the way in which menisco-femoral ligament works against menisco-fibular ligament — marked with blue arrows.

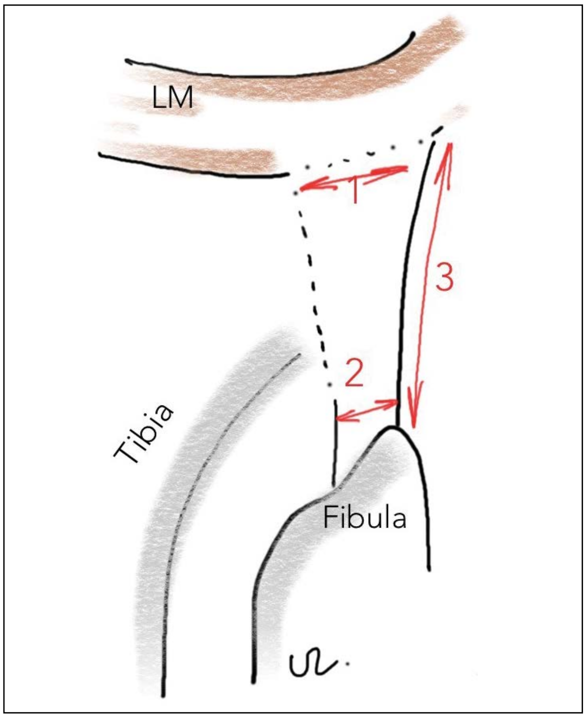

Figure 4. Schematic drawing of measurements taken of menisco-fibular ligament; 1 — proximal width; 2 — distal width; 3 — length; LM — lateral meniscus.

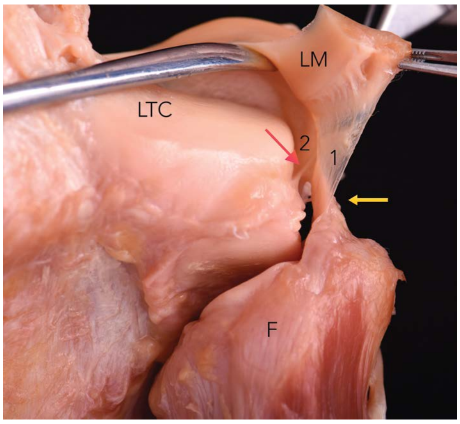

Figure 5. Cadaveric dissection of human right knee; posterior view; LTC — lateral tibial condyle; LM — lateral meniscus, being elevated from tibial plateau; F — fibula; 1 — menisco-fibular ligament, notice its distal, fibular attachment (marked with yellow arrow); 2 — menisco-tibial (coronary) ligament, notice its distal (tibial) attachment (marked with red arrow). Menisco-fibular ligament on its lateral margin becomes menisco-tibial ligament, and only way to distinguish those two, is by observing its distal attachment.

edge could be distinguished from the coronary ligament only by observing its distal attachment (coronary ligament attached to tibia, while MFiL to fibula) (Fig. 5). Stated differently, the ligaments are confluent proximally and are separate and distinct structures distally.

The distal attachment of the MFiL on fibular head is deeper than the distal attachment of fibular collateral ligament. The MFiL attaches just behind the cartilage margin of articular surface of fibular head at the proximal tibio-fibular joint.

In 4 of the 12 knees the MFiL was positioned superficial to the coronary ligament. While flexing the knee, the posterior margin of MFiL is positioned more horizontal, while extension of the knee results in more vertical and tense positioning of the ligament.

Magnetic resonance (MR) evaluation

We retrospectively evaluated 20 patients with injury to MFiL. We also analysed other concomitant knee injuries in those patients.

The 12 patients with MFiL injury showed a variety of different injury patterns: oedema, partial and complete tears. There was only 1 of the 20 patients with isolated MFiL injury. All remaining patients had complex, multiligament injuries (Table 1). The most common knee injury associated with MFiL injury was a complete anterior cruciate ligament tear.

The ligament may be best visualised in sagittal PD FSE sequence, especially if there is contrast or haemarthrosis (Fig. 6). In acute cases, local oedema may be the only indicator of MFiL injury. Radial plane images (often used in hip, but also knee MRs [11]) (Fig. 7A, B) can facilitate visualisation of MFiL injury. Proton density weighted radial sequences are planned on the axial image of the knee. The centre of the radial plane is set at the middle of the joint on the tibial eminence. Three-dimensional volumetric reconstruction in the plane of the ligament may also give excellent visualisation.

Arthroscopic evaluation

Findings of the present study were used to develop a protocol for arthroscopic visualisation and treatment of the MFiL. The knee is positioned in full extension and the camera is placed in the postero-lateral gutter of the knee joint, anteriorly to intraarticular part of popliteus tendon, through superior-lateral portal. The "working portal" is standard antero-lateral portal (Fig. 8A–C). In this position the MFiL may be easily evaluated and treated (Fig. 9A, B). The MFiL maybe also visible from anterior, beneath the lateral meniscus (Fig. 10). Suturing of the ligament is best performed with a small pig-tail device.

DISCUSSION

The anatomy of the lateral meniscus is complex and structure-function relationships are only partly understood. Injury to the MFiL is not commonly recognised. The purpose of the present study was to evaluate the MFiL, an anatomic structure rarely discussed that stabilises the lateral meniscus at the level of the hiatus popliteus and may have a crucial role in pathology of lateral meniscus injury.

According to Seebacher et al. [12] and Davies et al. [4], the lateral compartment of the knee joint consists of three layers:
- I — superficial layer is formed by iliotibial band and biceps femoris tendon;
- II — middle layer consists of fibres to lateral patellar retinaculum (patello-femoral ligament and patello-meniscal ligament);
- III — deep layer, being the most complex one, which may be further divided into superficial (with lateral collateral ligament and fabello-fibular ligament) and deep (with coronary ligament and arcuate ligament) lamina.

Although not described in above mentioned studies: the MFiL would be a part of the deep lamina of the third layer of the lateral compartment.

Obaid et al. [9] evaluated the MFiL in 160 MRI studies of 152 patients. He described the MFiL as a curvilinear or straight hypointense structure, an-

Table 1. Patients with menisco-fibular ligament (MFiL) injuries confirmed in magnetic resonance. Different concomitant injuries are presented in the table

Patient	Sex	Age	Side	MFiL	MM	LM	ACL	PCL	MCL	FCL	HL	WL	MPF	PFL	AL	PT	FPML
1	Male	43	Left	Partial injury	B	B	+		PI		PI					O	+
2	Male	53	Left	Partial injury and oedema	BuH	B	+		PI		PI	PI		PI		PI	+
3	Female	23	Right	Partial injury and oedema	B	B	+		+		PI	PI	B				+
4	Female	32	Left	Oedema	B	B	PI		PI			PI					
5	Female	46	Right	Partial injury and oedema	B	B	+	PI		PI				PI	PI	O/PI	
6	Male	18	Right	Partial injury and oedema	B	PI	+					PI	PI				+
7	Male	34	Left	Partial injury	PostM	+	+			PI				PI		PI	
8	Male	37	Left	Partial injury and oedema	B	+	+				PI						+
9	Female	21	Left	Partial injury and oedema			+		PI		PI	PI					+
10	Male	19	Right	Partial injury			+						PI	PI			
11	Male	42	Right	Complete injury		D											
12	Male	39	Left	Scar			+					Sc					
13	Male	31	Right	Partial injury and oedema	PostM	D	PI		PI	PI		PI	O	O		O	+
14	Female	34	Right	Partial injury and oedema	PostM	Rad	ACLr+		PI	PI	O					Sc	
15	Male	53	Right	Complete injury	D	PostM+						+	+				
16	Male	47	Right	Partial injury	PI		ACLr/PI		PI	PI			PI		PI	PI	
17	Male	34	Right	Partial injury	O / +		+		PI	PI		PI	PI	PI		PI	
18	Female	48	Left	Complete injury	O	+	PI		+	PI	PI		PI			PI	
19	Male	48	Right	Complete injury	+	+	PI		PI	PI				PI	PI		
20	Female	43	Right	Partial injury	PI	+	PI		PI	PI	PI					O	

+ — complete injury; ACL — anterior cruciate ligament; ACLr — anterior cruciate ligament reconstruction; AL — arcuate ligament; B — bruising; BuH — bucket handle tear; D — degenerative changes; FCL — fibular collateral ligament; FPML — fracture of posterior margin of lateral tibial condyle; HL — Humphrey ligament; LM — lateral meniscus; MCL — medial collateral ligament; MM — medial meniscus; MPF — menisco-popliteal fascicles; O — oedema; PCL — posterior cruciate ligament; PFL — popliteo-fibular ligament; PI — partial injury; PostM — postmeniscectomy; PT — popliteus tendon; Ra — radial tear; Sc — scar; WL — Wrisberg ligament

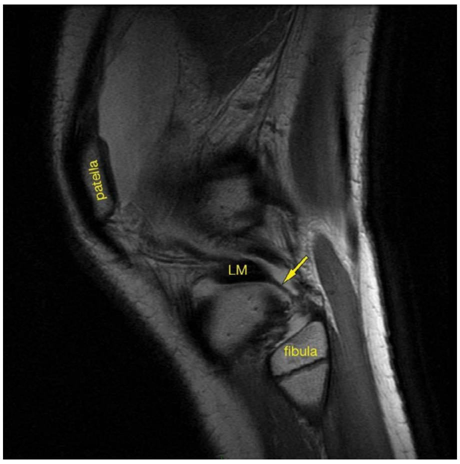

Figure 6. Magnetic resonance imaging scan in sagittal plane: intact menisco-fibular ligament (marked with yellow arrow); LM — lateral meniscus.

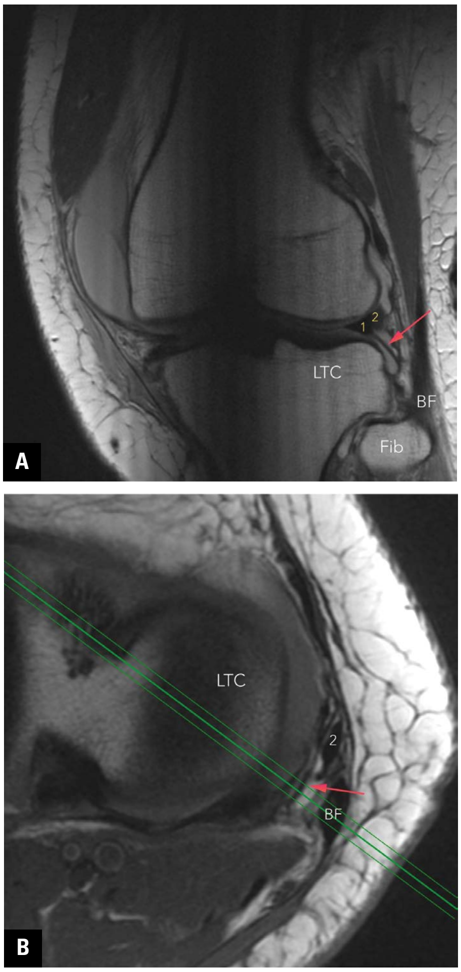

Figure 7. Magnetic resonance imaging scan in special radial plane; **A.** Intact menisco-fibular ligament (marked with red arrow); 1 — lateral meniscus; 2— popliteus tendon; LTC — lateral tibial condyle; BF — biceps femoris tendon; Fib. — Fibula; **B.** Magnetic resonance imaging axial image showing the way in which radial plane was planned, perpendicular to the plane of menisco-fibular ligament (also marked with red arrow).

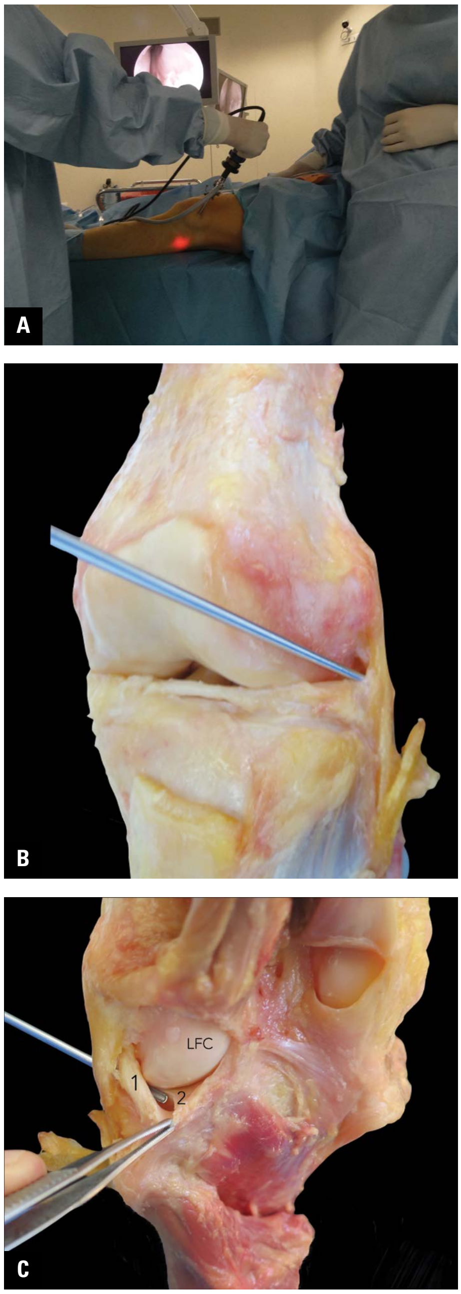

Figure 8. A. Arthroscopic visualisation of menisco-fibular ligament. The knee is in full extension. Camera is placed in the postero-lateral gutter of the knee joint, anteriorly to intraarticular part of popliteus tendon, through superior-lateral portal; Panels **B** and **C** demonstration of camera's positioning on cadaver specimen; LFC — lateral femoral ligament; 1 — popliteus tendon; 2 — menisco-popliteral superior fascicles.

terior and lateral to popliteus tendon, running from inferior margin of lateral meniscus to the apex of fibular head. The visualisation of the ligament was determined by the presence or absence of joint fluid. In his study the presence of the MFiL was confirmed in approximately half of the cases. Lee et al. [7] performed MR arthrography with 70 degrees of knee

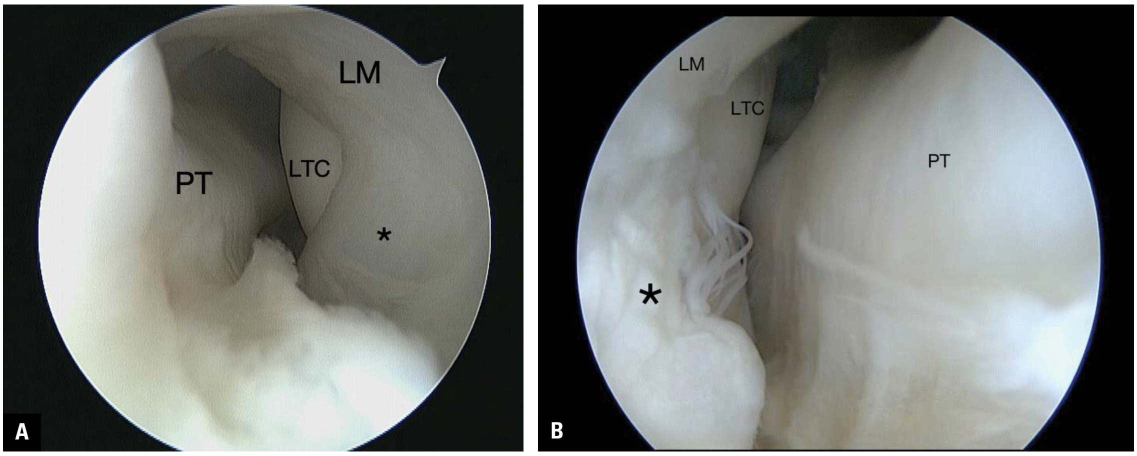

Figure 9. Arthroscopic view of postero-lateral gutter. The knee is in full extension. Camera is placed in the postero-lateral gutter of the knee joint, anteriorly to intraarticular part of popliteus tendon, through superior-lateral portal — see details on Figure 8. **A.** (*) — intact menisco--fibular ligament of the right knee; **B.** (*) — complete rupture of menisco-fibular ligament of the left knee; LM — lateral meniscus; PT — popliteus tendon; LTC — lateral tibial condyle.

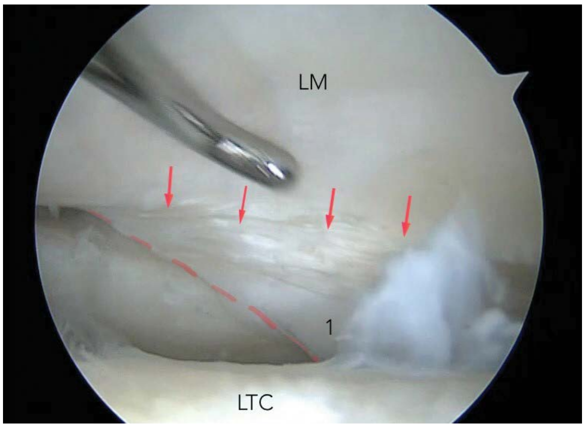

Figure 10. Arthroscopic appearance of torn menisco-fibular ligament (marked with red arrows) in the left knee joint. Camera is placed through standard antero-lateral portal, arthroscopic hook through standard antero-medial portal. Arthroscopic hook is elevating lateral meniscus (LM); LTC — lateral tibial condyle; 1 — menisco-fibular ligament.

flexion in 19 patients. Adding intraarticular contrast and knee flexion increased detectability of the MFiL up to almost 90% of cases. Aforementioned study by Ciszkowska et al. [2] correlated MRI images with gross anatomic dissection of MFiL in 25 cadaver knees. The presence of the MFiL was confirmed in both MRI and gross anatomic dissections of knees. With MRI, the linear, hypointense line of thin ligament extending between the posterior third of the lateral meniscus and the apex of the fibula was best defined on sagittal images. The ligament could be also visualised on axial and coronal images. The mean thickness of the ligament in the midsubstance was 1.37 mm (min 0.71 mm; max 2.15 mm). The length and width were difficult to define in MRI because of the small size and spatial shape of the ligament. The gross anatomic dissections confirmed the trapezoid shape of flat ligament. The mean length of the ligament was 19 mm, proximal width 12 mm, distal width 7.5 mm. There are different ways to visualise the MFiL in MR examination. MRI radial planes were described by Quinn et al. [11]. These planes, when evaluated in correlation with regular planes (especially sagittal) may further improve accurate interpretation of the MFiL integrity.

To the best of our knowledge, there are no other studies describing arthroscopic visualisation and treatment of the MFiL. The protocol proposed herein is minimally invasive and does not require an excessive surgical approach. Based upon the frequency of injury and association with anterior cruciate ligament injuries, it is advisable to routinely evaluate the MFiL, especially in cases of lateral meniscus injury or chronic pain in the postero-lateral knee corner.

CONCLUSIONS

The MFiL is a rarely discussed anatomic structure that is important for stabilisation of the lateral meniscus. Further anatomical and biomechanical studies are needed to fully evaluate its clinical importance. In cases of chronic postero-lateral pain syndrome it may be helpful to evaluate postero-lateral corner structures, as well as the MFiL as a possible cause of pain and instability. The reconstruction of this ligament during lateral meniscus allograft implantation may also be considered.

Acknowledgements

The authors gratefully acknowledge Maciej Śmiarowski (maciej.smiarowski@gmail.com) for taking cadaveric specimens photographs; Marek Tramś for his enormous help with cadaveric dissection; Karolina Popek-Pułczyńska, Sławomir Karpiński and the whole team of Medical Training Centre (www.cem-med.pl) for their support in the research; Izabela Murawska and Carolina Medical Centre (www.carolina.pl) for their support.

Conflict of interest: None declared

REFERENCES

1. Bozkurt M, Elhan A, Tekdemir I, et al. An anatomical study of the meniscofibular ligament. Knee Surg Sports Traumatol Arthrosc. 2004; 12(5): 429–433, doi: 10.1007/s00167-003-0450-z, indexed in Pubmed: 14634721.
2. Ciszkowska-Łysoń B, Zdanowicz U, Śmigielski R, et al. Underestimated Meniscofibular Ligament: Cadaveric Investigation of Anatomy with Mri Correlation. In: Abstract book 41st Congress of the Polish Medical Society of Radiology, 2 - 4 June 2016, Kraków. p. 145–146.
3. Covey DC. Injuries of the posterolateral corner of the knee. J Bone Joint Surg Am. 2001; 83(1): 106–118, doi: 10.2106/00004623-200101000-00015, indexed in Pubmed: 11205847.
4. Davies H, Unwin A, Aichroth P. The posterolateral corner of the knee. Injury. 2004; 35(1): 68–75, doi: 10.1016/s0020-1383(03)00094-9.
5. Haines RW. The tetrapod knee joint. J Anat. 1942; 76(3): 270–301, indexed in Pubmed: 17104897.
6. Jørgensen U, Sonne-Holm S, Lauridsen F, et al. Long-term follow-up of meniscectomy in athletes. A prospective longitudinal study. J Bone Joint Surg Br. 1987; 69(1): 80–83, doi: 10.1302/0301-620X.69B1.3818740, indexed in Pubmed: 3818740.
7. Lee YH, Song HT, Kim S, et al. Magnetic resonance arthrographic dissection of posterolateral corner of the knee: revealing the meniscofibular ligament. Yonsei Med J. 2012; 53(4): 820–824, doi: 10.3349/ymj.2012.53.4.820, indexed in Pubmed: 22665352.
8. Natsis K, Paraskevas G, Anastasopoulos N, et al. Meniscofibular ligament: morphology and functional significance of a relatively unknown anatomical structure. Anat Res Int. 2012; 2012: 214784, doi: 10.1155/2012/214784, indexed in Pubmed: 22811916.
9. Obaid H, Gartner L, Haydar AA, et al. The meniscofibular ligament: an MRI study. Eur J Radiol. 2010; 73(1): 159–161, doi: 10.1016/j.ejrad.2008.09.026, indexed in Pubmed: 18995979.
10. Parsons FG. The Joints of Mammals compared with those of Man: A Course of Lectures delivered at the Royal College of Surgeons of England. J Anat Physiol. 1899; 34(Pt 1): 41–68.
11. Quinn SF, Brown TR, Szumowski J. Menisci of the knee: radial MR imaging correlated with arthroscopy in 259 patients. Radiology. 1992; 185(2): 577–580, doi: 10.1148/radiology.185.2.1410376, indexed in Pubmed: 1410376.
12. Seebacher JR, Inglis AE, Marshall JL, et al. The structure of the posterolateral aspect of the knee. J Bone Joint Surg. 1982; 64(4): 536–541, doi: 10.2106/00004623-198264040-00008.

VIA MEDICA

ORIGINAL ARTICLE

Folia Morphol.
Vol. 80, No. 3, pp. 691–698
DOI: 10.5603/FM.a2020.0105

ISSN 0015–5659
eISSN 1644–3284
journals.viamedica.pl

A cadaveric analysis of anatomical variations of the anterior belly of the digastric muscle

H. Anderson, R.P. Tucker

Department of Cell Biology and Human Anatomy, University of California, Davis, United States

[Received: 2 June 2020; Accepted: 20 July 2020; Early publication date: 2 September 2020]

Background: *The anterior belly of the digastric muscle (ABDM) presents highly variable and frequent anatomical variations. Since the ABDM functions as a landmark for clinical procedures involving the submental region, it is important to have a comprehensive understanding of its variations. In this study, we sought to improve our knowledge of ABDM variations in the ethnically diverse whole-body donor population in Northern California. Specific aims were: (1) to determine the frequency of ABDM and anterior belly (AB) accessory muscle variations in cadavers donated to the UC Davis Body Donation Programme, (2) to classify these variations identified in this population using the previously proposed nomenclatures by Yamada (1935) and Zlabek (1933), and (3) to investigate the innervation and arterial supply to the representative ABDM and AB accessory muscle variations.*
Materials and methods: *During the 2018 and 2019 gross anatomy dissection laboratories at the UC Davis School of Medicine, the submental regions of 48 cadavers were examined and classified.*
Results: *Fifteen (31.2%) cadavers presented ABDM and AB accessory muscle variations. These variations were clearly categorised using the morphology of the ABDMs and attachments of the AB accessory muscles. We also identified three previously unreported types of variations, two of which presented the fusion of right and left ABDMs and one presenting an ectopic tubercle beneath the mandibular symphysis to which a pair of AB accessory muscles were attached.*
Conclusions: *Anterior belly of the digastric muscle variations were found in 1 in 3 individuals in the local Northern California population. Knowledge of the prevalence and common patterns of ABDM variations in the general population would be valuable information when an operation or examination is performed in the submental region.* (Folia Morphol 2021; 80, 3: 691–698)

Key words: anatomical variation, submental region, suprahyoid muscle, cadaver, gross anatomy laboratory

INTRODUCTION

The anterior belly of the digastric muscle (ABDM) typically originates from the digastric fossa of the mandible and inserts onto the body and greater horn of the hyoid bone and the intermediate tendon that it shares with the posterior belly of the digastric muscle. Variations in this arrangement were reported as early as in the 18th century [25], in the 19th century (e.g. [11]), and a broad range of variations were classified by Zlabek [28] and Yamada [25]. The frequency of ABDM

Address for correspondence: Ass. Prof. H. Anderson, Department of Cell Biology and Human Anatomy, University of California, 1 Shields Avenue, Davis, CA 95616, USA, tel: +1 530 752 0389, e-mail: hnanderson@ucdavis.edu

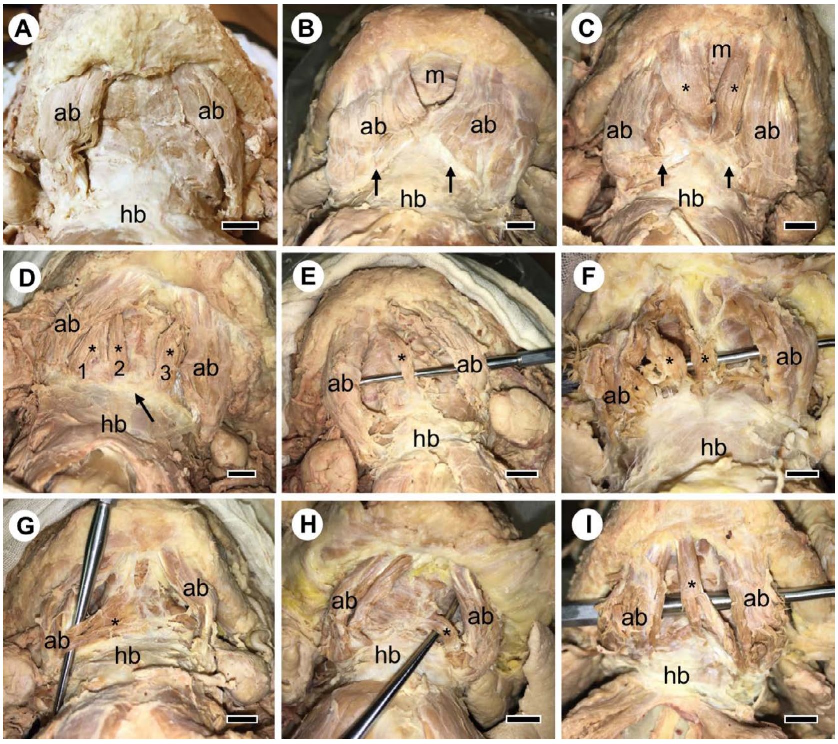

Figure 1. Summary of 1 standard and 8 variations of anterior belly of the digastric muscle (ABDM) observed in the 2018 gross anatomy laboratory. The age of each cadaver and brief description of the observed variations are summarised; **A.** 76-year-old male presenting a standard pattern of the ABDM and the mylohyoid muscle; **B.** 62-year-old male with fused sheet-like ABDMs. Atavistic type; **C.** 55-year-old male with a pair of anterior belly (AB) accessory muscles. Bilateral origin (anterior) type; **D.** 60-year-old male with three AB accessory muscles (1–3). All three accessory muscles insert into the fibrous tendinous arch. Bilateral origin (anterior) type; **E.** 63-year-old male with an AB accessory muscle on the right side. Unilateral origin (anterior) type; **F.** 85-year-old male with two AB accessory muscles on the right side. Unilateral origin (anterior) type; **G.** 90-year-old female with an AB accessory muscle on the right side. Unilateral insertion (posterior) type; **H.** 70-year-old male with an AB accessory muscle on the left side. Unilateral insertion (posterior) type; **I.** 57-year-old female with an AB accessory muscle traversing across the midline. The insertion side of the accessory muscle is bifurcated. Mixed type with variation of bifurcation; ab — anterior belly of the digastric muscle; hb — hyoid bone; asterisk — accessory anterior belly muscles; arrows — fibrous tendinous arch. The scale bar corresponds to 1 cm.

anatomical variations in dissected cadavers reported in the literature differs significantly, ranging from 5% to 70% [8, 13, 17, 25, 28]. These differences could be attributed to the small sample size in some studies as well as characteristics stemming from the common ancestry of the sample population. Types of structural variations reported for the ABDM and its accessory muscles also demonstrate significant diversity, including non-standard morphology of the ABDM itself, the location and number of anterior belly (AB) accessory muscles, and relationships of AB accessory muscles with the mylohyoid muscle [3, 8, 25, 28]. These complexities present a challenge in categorising ABDM variations.

In the current study we examined 48 cadavers for the incidence and types of variations in the ABDM and AB accessory muscles. These variations were classified according to the schema proposed by Yamada (1935) [25] and Zlabek (1933) [28]. During the course of this investigation three previously undescribed variations were found, and the blood supply and innervation of the representative variants were investigated. Our study confirms that variations in the ABDM are common, and that many novel variations may remain to be described. These variations may be of interest to developmental biologists studying the origins of the suprahyoid muscles as well as to clinicians who perform examination and surgeries in the submental and digastric triangles of the neck.

MATERIALS AND METHODS

Forty-eight cadavers (male 23, female 25, average age 75) dissected by first year medical students in the gross anatomy laboratory over a 2-year period (2018 and 2019) at the UC Davis School of Medicine were included in this study. Bodies were originally donated to the UC Davis Body Donation Programme. During the dissection of the submental region in the laboratory, an atypical arrangement of the ABDM, being accompanied with bilateral accessory muscle bundles, was identified in 1 cadaver (Fig. 1C). This finding prompted

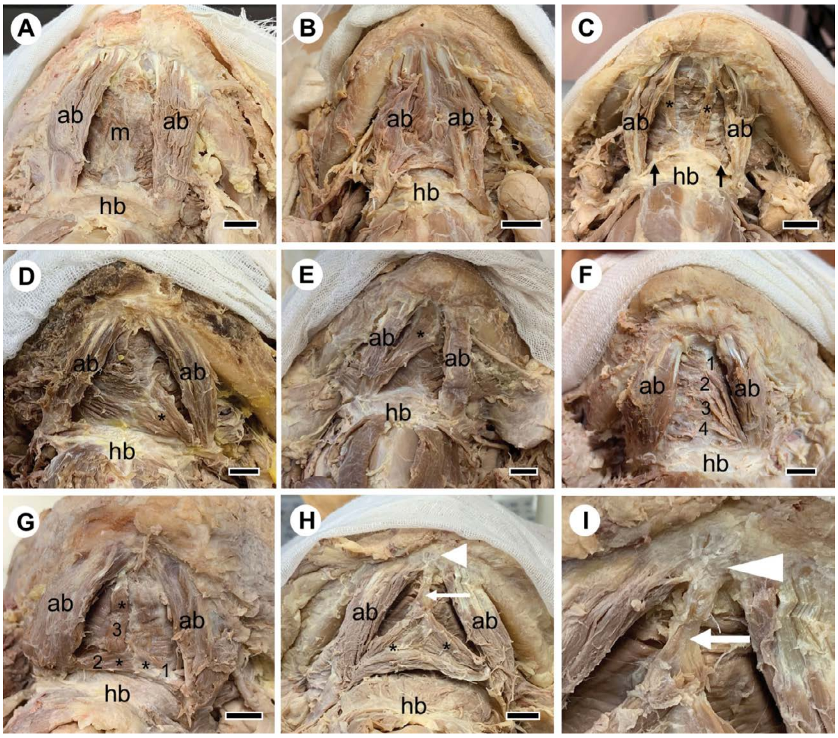

Figure 2. Summary of 1 standard and 8 variations of anterior belly of the digastric muscle (ABDM) observed in the 2019 gross anatomy laboratory. The age of each cadaver and brief description of the observed variations are summarised; **A.** 95-year-old female presenting a standard pattern of the ABDM and the mylohyoid muscle; **B.** 70-year-old female with fused sheet-like ABDMs. Atavistic type; **C.** 87-year-old female with a pair of thin anterior belly (AB) accessory muscle strips. Bilateral origin (anterior) type; **D.** 88-year-old female with an AB accessory muscle on the left side. Unilateral insertion (posterior) type; **E.** 66-year-old female with an AB accessory muscle on the right side. Unilateral insertion (posterior) type; **F.** 94-year-old female with 4 sprigs of AB accessory muscles on the left side. Unilateral insertion (posterior) type; **G.** 83-year-old male with 3 AB accessory muscles, origin and insertion types on the right and insertion type on the left. Complex type; **H.** 81-year-old male with bilateral AB accessory muscles. Complex type. Arrow head indicates the ectopic tubercle and arrow indicates the fibrous bundle (origin type variation) connecting the tubercle and the two-insertion type AB accessory muscles; **I.** A magnified view of the tubercle and fibrous bundle shown in panel H; ab — anterior belly of the digastric muscle; hb — hyoid bone; asterisk — accessory anterior belly muscles; arrows — fibrous tendinous arch. The scale bar corresponds to 1 cm.

examinations of anatomical variations in the submental region, leading to identifying 15 cadavers with non-standard muscle arrangements in the submental region involving the ABDM and the mylohyoid muscle (Figs. 1, 2). Two cadavers (Fig. 1B, C) were also examined further for the innervation and blood supply to the ABDM and its accessory muscle (Fig. 3).

RESULTS

Structural variations of the submental region muscles

We have identified anatomical variations comprising atypical arrangements of the ABDM with or without the involvement of the mylohyoid muscle. From 48 cadavers, 15 exhibited submental muscle variations (8 out of 24 cadavers in the year of 2018 and 7 out of 24 cadavers in the year of 2019). Of these 15 cadavers, 8 were male and 7 were female. The average frequency of the bodies with ABDM variations in the 2 years was 31.2%, and year-to-year frequency was comparable (2018, 33.3% and 2019, 29.2%).

In the current study, in an attempt to provide consistency for organizing ABDM variations, we applied the classifications proposed by Yamada (1935) [25] and Zlabek (1933) [28]. Their classification system of non-standard ABDM comprises six types, primarily based on the position(s) of the AB accessory muscles. They are: 1) atavistic type, 2) origin (anterior) type, 3) insertion (posterior) type, 4) mixed type, 5) complex (composite) type, and 6) deletion type. In our study, the deletion type, which is characterised by the lack of the ABDM, was not observed. Below, the 5 types of AB variations identified in 15 cadavers in our gross anatomy laboratory sessions are described.

Atavistic type

The atavistic type ABDM is characterised by its broad attachment at the origin site (mandibular side)

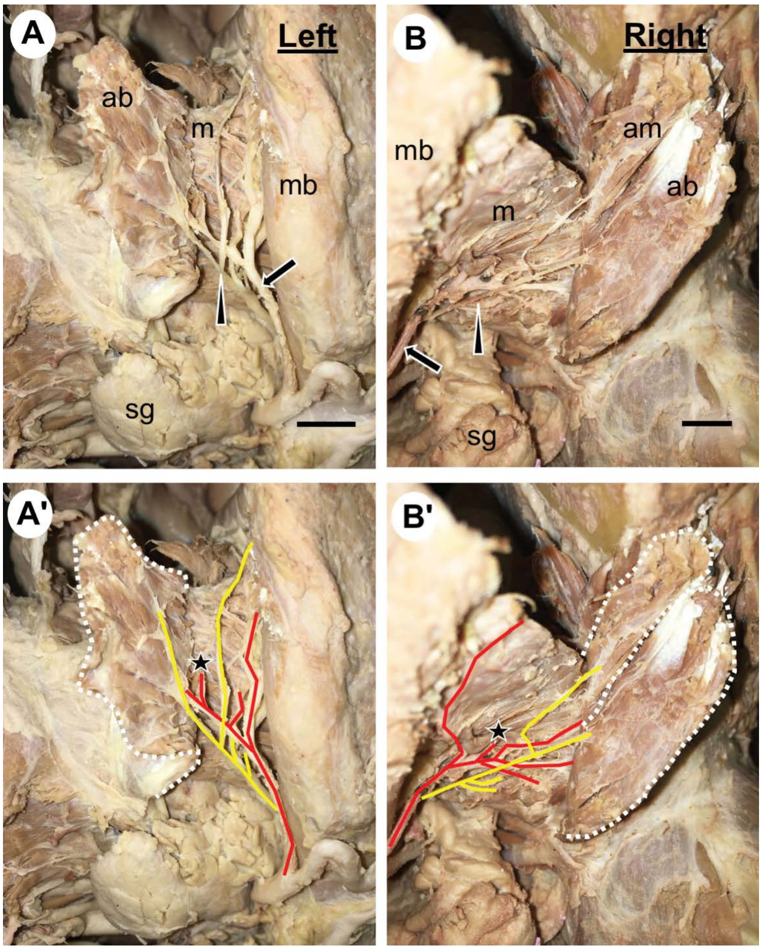

Figure 3. Arterial blood supply and innervation to the anterior belly of the digastric muscle (ABDM) and anterior belly (AB) accessory muscle of the atavistic and origin variations. The submental regions of the atavistic type variation (Fig. 1B) and origin type variation (Fig. 1C) were further dissected to follow the paths of the submental artery and the nerve to mylohyoid. The ABDM and AB accessory muscle were detached from the mandible and reflected to show the arterial supply and innervation; **A, A'.** The dissection of the left side of the submental region of the cadaver shown in Figure 1B; **B, B'.** The dissection of the right side of the submental region of the cadaver shown in Figure 1C. In panels A and B, black arrow indicates the submental artery and arrowhead indicates the nerve to mylohyoid. In panels A' and B' the paths of the submental artery and the nerve to mylohyoid are indicated in red and yellow, respectively. The asterisk indicates the location where a branch of the submental artery penetrates the mylohyoid muscle to enter the oral cavity. The white broken line indicates the border of the ABDM and AB accessory muscle; ab — the anterior belly of the digastric muscle; am — the anterior belly accessory muscle; m — mylohyoid; mb — mandible. The scale bar corresponds to 1 cm.

as well as the insertion site (hyoid side). The medial borders of the right and left AB muscles touch at the midline to cover the surface of the mylohyoid [25, 28]. The term "atavistic" was proposed because this type of ABDM arrangement has been reported as a standard form in certain non-human primates [4, 22, 25]. In the current study, 2 cadavers exhibited symmetric atavistic type variations (Figs. 1B, 2B). Both of them presented a sheet of ABDM, formed by fusion of the right and left anterior bellies. The ABDM sheet and the mylohyoid muscle below were physically separate.

In the atavistic variation shown in Figure 1B, the muscle width at the origin and insertion sites were equally broad and each ABDM presented as a rectangular muscle. Over the mylohyoid raphe the two lower angles of the right and left ABDM rectangular sheets merged, creating a small reverse triangular window below the mandibular symphysis (Fig. 1B). The ABDM attachment on the mandible extended laterally from the digastric fossa and the muscle attachment on the hyoid side extended from the midline on the fibrous tendinous arch towards the intermediate tendon of the digastric muscle. The right and left tendinous arches angled upward and fused at the midline (Fig. 1B). This type of fibrous tendinous arch was initially described by Reid (1886) [16] as "aponeurotic-like tendon" and described also in more recent reports [18, 24]. In the atavistic variation shown in Figure 2B, the medial borders of the right and left ABDMs met at the mandibular symphysis. This positional shift of the attachments resulted in a fully fused ABDM sheet at the midline, forming a symmetric trapezoid muscle sheet overlaying the mylohyoid muscle. In these two atavistic variations (Figs. 1B, 2B), there was no recognizable accessory muscle and the ABDM itself appeared to have broadened to develop a muscle sheet. To the best of our knowledge, these atavistic type variations, in which right and left ABDMs are fused to form a symmetric muscle sheet, have not been reported in the literature.

Origin (anterior) type

The origin type is characterised by an AB accessory muscle conjoined to an ABDM at the origin (anterior) side that inserts into the fibrous tendinous arch attached to the hyoid bone [25, 28]. This variation may be presented bilaterally or unilaterally. The origin type is further subdivided into the continuous origin type, in which the AB accessory muscle overlaps with the ABDM with no space in-between, and the muscle-bundle origin type, in which the AB accessory muscle is visibly separated from the ABDM [25]. In the current study, we observed 5 muscle-bundle origin type variations; 3 were bilateral (Figs. 1C, D, 2C) and 2 were unilateral (Fig. 1E, F). In the bilateral origin type variations, 2 cadavers presented 2 AB accessory muscles (Figs. 1C, 2C) and 1 cadaver presented 3 accessory muscles (Fig. 1D). In the variation shown in Figure 1C, a robust pair of AB accessory muscles traversed from the mandible to the fibrous tendinous arch. This specific variation likely resembles the variation type previously described as "mento-hyoid" or "m. mentohyoideus" [11, 22] and in a more recent report, as bilateral AB accessory muscles inserting on the fibrous band [24]. The AB accessory muscles observed in the rest of origin type variations were much smaller and thinner. In the bilateral origin type variation shown in Figure 1D, all three accessory muscle strips originated from the medial border of the ABDMs and inserted into the fibrous tendinous arch. In the third bilateral origin type variation (Fig. 2C), the left accessory muscle strip originated from the mandible and inserted into the tendinous arch near the midline, while the right accessory strip originated from the anterior medial border of the ABDM and merged into the mylohyoid muscle. In the two unilateral origin type variations (Fig. 1E, F), accessory muscle strips were found on the right. In the variation shown in Figure 1E, the accessory muscle strip originated from the mandible medial to the digastric fossa and merged with the mylohyoid muscle near the hyoid bone. In the variation shown in Figure 1F, one accessory muscle strip originated from the medial border of the ABDM and the other originated from the mandible medial to the ABDM. Both AB accessory muscles inserted on the hyoid bone.

Insertion (posterior) type

The insertion type is characterised by the presence of an AB accessory muscle emerging from the intermediate tendon of the digastric muscle medial to the ABDM [25, 28]. The AB accessory muscle then extends anteromedially to the inter-digastric area. In the majority of cases, an insertion type AB accessory muscle merges with the mylohyoid muscle, most often at the mylohyoid raphe. When there is a space physically separating the AB accessory from the ABDM, the variation is classified as a muscle-bundle insertion type. Alternatively, when the AB accessory muscle overlaps with the ABDM and extends to the mandible, it is classified as the continuous insertion type [25]. In the current study, we observed 5 cadavers presenting unilateral muscle-bundle insertion type variation (Figs. 1G, H, 2D–F). A single AB accessory muscle fanned out from the intermediate tendon medially to merge into the mylohyoid at the posterior half of the raphe (Figs. 1G, H, 2D) or at the anterior half of the raphe (Fig. 2E). In one of the insertion type variations, four very delicate sprigs of AB accessory muscles emerged from the intermediate tendon, all of which merged into the mylohyoid muscle at the raphe (Fig. 2F).

Mixed type

The mixed type is characterised by an AB accessory muscle traversing across the midline in the submental region [25, 28]. In the current study, we identified 1 cadaver presenting this variation (Fig. 1I). This AB accessory muscle originated from the right side on the mandible and divided into 2 muscle segments on the hyoid side, with the lateral segment inserting on the left digastric intermediate tendon and the medial segment inserting into the mylohyoid muscle at the raphe.

Complex (composite) type

The complex type is characterised by the coexistence of multiple variations described above, the origin (anterior), insertion (posterior), and mixed types, in one individual [25, 28]. We identified 2 cadavers presenting bilateral complex type variations (Fig. 2G, H). The complex variation shown in Figure 2G contained two insertion type AB accessory muscles and one origin type AB accessory muscle. The two insertion type AB accessory muscles were fan shaped, emerging from the right and left intermediate tendons (muscles 1 and 2) and merged with the mylohyoid muscle and with each other at the raphe. The origin type AB accessory muscle (muscle 3) emerged from the upper medial border of the ABDM and inserted into the mylohyoid muscle at the superior border of the AB accessory muscle 2 (Fig. 2G). The arrangement of these three AB accessory muscles is similar to the variation reported by Zdilla et al. (2018) [27]. The second complex type variation, shown in Figure 2H, consisted of insertion and origin type variations. However, it was unique in the sense that there was an ectopic bony tubercle directly beneath the mandibular symphysis. The presence of this type of ectopic tubercle has not been reported previously. Bundles of tendinous fibres connected the superior angle of the pair of insertion type accessory muscles to this ectopic tubercle (Fig. 2H, I). These fan-shaped AB accessory muscles emerged from the right and left intermediate tendons and merged at the midline with each other and with the mylohyoid muscle at the raphe (Fig. 2H).

Arterial blood supply and innervation to the ABDMs and AB accessory muscles

Arterial blood to the submental region is typically supplied by the submental artery, a branch of the facial artery [6]. Innervation to the anterior belly of the digastric muscle and mylohyoid muscle is typically provided by the nerve to the mylohyoid, a branch of the mandibular division of the trigeminal nerve [12]. To examine whether the arterial blood supply pattern may be altered by the presence of ABDM variations, we dissected the submental region of the 8 cadavers shown in Figure 1B–I and confirmed that the submental artery was the source of the blood supply in all of these cadavers. Innervation to the submental region was also examined in the atavistic type and origin type variations (Fig. 1B, C, respectively). Figure 3 summarises the passages of the submental artery and the nerve to mylohyoid in the submental regions of these cadavers. In the atavistic type ABDM variation (Fig. 3A, A'), the nerve to mylohyoid (indicated by the arrowhead) travelled between the mylohyoid muscle and the ABDM sheet to provide innervation to the both muscles. The submental artery (indicated by the arrow) travelled in parallel with the nerve to mylohyoid and then penetrated the mylohyoid muscle (indicated by the asterisk in Fig. 3A'), entering the oral cavity to supply the sublingual gland. This pattern of the submental artery supplying the sublingual gland is relatively common [7] and it is not associated with particular structural variations of the submental triangle muscles. In the bilateral origin type variation (Fig. 3B, B'), the nerve to mylohyoid also travelled in parallel with the submental artery to pass between the external surface of the mylohyoid muscle and the inner surface of the ABDM, and then continued to innervate the AB accessory muscle. Also, in this cadaver, a branch of the submental artery penetrated the mylohyoid muscle to enter the oral cavity to supply the sublingual gland (indicated by the asterisk in Fig. 3B').

DISCUSSION

The digastric muscle is a suprahyoid muscle that depresses the mandible to assist chewing and speech, and also to stabilise the hyoid bone during swallowing and speaking [2, 20]. Reflecting the digastric muscle's contribution to these vital human activities, it has been reported that declined volume of the digastric muscle is correlated with the severity of dysphagia in stroke patients [21].

Developmentally, the digastric muscle is a hybrid muscle consisting of two muscle bellies derived from separate embryological origins; the anterior belly originates from the first pharyngeal arch, whereas the posterior belly originates from the second pharyngeal arch. The mylohyoid muscle, located adjacent to the anterior belly muscle, shares a common embryological origin with the ABDM. Accordingly, innervation and blood supply are typically shared between these two muscles, i.e., both are innervated by the nerve to the mylohyoid and supplied by the submental artery, respectively [14, 19].

Schematic representations of the types of variations identified in this report, "atavistic, origin, insertion, mixed, complex" are summarised in Figure 4. In the origin type variations, two AB accessory muscles had their distal end fused with the mylohyoid muscle (Figs. 1E, 2C). All of the insertion type AB accessory muscles found in the insertion type only variations (Figs. 1G, H, 2D–F) and in the complex type variations (Fig. 2G, H) consistently had their proximal ends fused with the mylohyoid muscle at the raphe. In the literature, fusion of AB accessory muscle and the mylohyoid has also been repeatedly reported [8, 25, 28]. The frequent fusion of the AB accessory muscle and the mylohyoid muscle may indicate that these two muscles develop from a common embryonic primordium during embryogenesis.

In this study, we observed three variations that have not been previously reported in literature. Two are the atavistic type variations (Figs. 1B, 2B) in which right and left ABDMs are fused to form a symmetric muscle sheet. No AB accessory muscles were observed in these variations. The closest variation to these atavistic variations we could find in the literature was a variation in which right and left AB accessory muscles fused at the midline of the submental triangle. In this case, the ABDMs and the accessory muscles were still visibly discernible by distinct striations of the muscle fibres [1]. Another is the complex type variation with an ectopic tubercle elongated from the mandible at

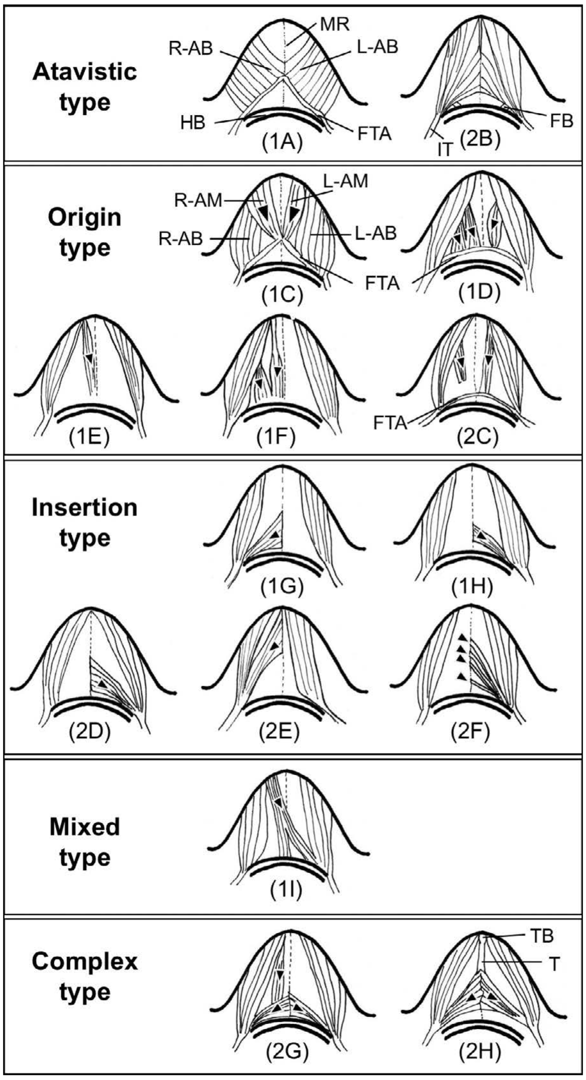

Figure 4. Schematic representations of the anterior belly of the digastric muscle (ABDM) and anterior belly (AB) accessory muscle variations identified in this report. Sketches highlighting the arrangements of the ABDM and AB accessory muscle variations are shown. Among the 15 variations we have identified, 2 were atavistic type, 5 were origin type, 5 were insertion type, 1 was mixed type and 2 were complex type. Letters in parenthesis shown below the drawings correspond to the listings in Figures 1 and 2. An arrowhead indicates an AB accessory muscle; FTA — fibrous tendinous arch; FB — fibrous band; HB — hyoid bone; IT — intermediate tendon; R-AB, L-AB — right or left anterior belly of the digastric muscle; R-AM, L-AM — right or left AB accessory muscle; MR — mylohyoid raphe; TB — tubercle; T — tendon.

the symphysis, to which a pair of insertion type AB accessory muscles are attached via a tendinous fibre (Fig. 2H). These three newly identified variations suggest the fluidity of muscle development in the submental region.

Utilising three-dimensional reconstructions of human embryos, it has been reported that the developing mylohyoid and ABDM initially establish an anterior attachment with Meckel's cartilage at the late embryonic stages. While Meckel's cartilage is being encased by the mandibular bone during the late embryonic and early foetal stages, the attachment of these muscles shifts from Meckel's cartilage to the mandibular bone that is extending over the cartilage [15]. Such transitions could lead to erroneous muscle reattachment, possibly causing fragmentation of developing muscles as well as ectopic insertion, which may result in the formation of AB accessory muscles as well as their fusion with the mylohyoid muscle (as described in numerous previous reports) and the AB accessory muscle variations (in the current report). Radlanski et al. (2001) [15] also described that during the early stage of mylohyoid muscle development, some of the muscle fibres gained the direction of striation corresponding to that of developing digastric muscle nearby. This observation may imply a possible developmental process for the origin type AB accessory muscles that are presented in Figure 1C in this report and also the "mento-hyoid muscle" and "m. mentohyoideus" described by Macalister (1875) [11] and Stracker (1908) [22], respectively.

It has been proposed that the relative spatial relationship of an AB accessory muscle with the nerve to mylohyoid, superficial or deep, indicates the origin of muscular primordium from which the AB accessory muscle developed [18]. These authors suggest that the nerve to the mylohyoid penetrates into the middle of the common muscular primordium of the mylohyoid and ABDM during embryogenesis. Consequently, the ABDM develops superficial to, and the mylohyoid muscle develops deep to, the nerve to the mylohyoid. According to this classification system, the sheet-like atavistic type ABDM variation (Fig. 1B) originated from the primordium of the ABDM, not from the primordium of the mylohyoid muscle, since it is positioned superficial to the nerve to the mylohyoid (Fig. 3A'). Similarly, the origin type AB accessory muscle shown in Figure 1C originated from the primordium of the ABDM, since it is located superior to the nerve to the mylohyoid (Fig. 3B'). Although it is often challenging to dissect intact innervation to small AB accessory muscles, this classification system would be useful to ascertain their embryological origin in relation to the mylohyoid muscle.

Clinically, structural variations of the ABDM have implications in surgeries involving the muscles of the submental region such as correction of facial paralysis and an array of cosmetic surgeries for improving the frontal neck contour [5, 9, 10, 23, 26]. The ABDM variations, especially those with atavistic type variation and robust AB accessory muscles, could cause misidentification of the suprahyoid muscle groups which affects diagnosis involving the submandibular region [1, 26, 27]. Therefore, attracting attention to the frequent occurrence and morphological complexity of ABDM variations in the general population has significant clinical importance.

CONCLUSIONS

In our current report, we examined 48 cadavers and found that 15 cadavers presented ABDM variations (31.2%) in the ethnically diverse donor population in Northern California. Since the ABDM is an important landmark for procedures involving the submental region, the high prevalence of non-standard arrangements calls for close attention.

Acknowledgements

The authors are grateful to the staff of the UC Davis Body Donation Programme for their support and wish to express gratitude to the individuals who donated the bodies for the advancement of medical education and research. The authors declare that they have no conflict of interest to report.

Conflict of interest: None declared

REFERENCES

1. Buffoli B, Lancini D, Ferrari M, et al. Symmetrical anatomical variant of the anterior belly of the digastric muscle: clinical implicat. Folia Morphol. 2016; 75(1): 112–116, doi: 10.5603/FM.a2015.0077, indexed in Pubmed: 26365851.
2. Coquerelle M, Prados-Frutos J, Rojo R, et al. The fetal origin of the human chin. Evol Biol. 2017; 44(3): 295–311, doi: 10.1007/s11692-017-9408-9.
3. De-Ary-Pires B, Ary-Pires R, Pires-Neto MA. The human digastric muscle: patterns and variations with clinical and surgical correlations. Ann Anat. 2003; 185(5): 471–479, doi: 10.1016/S0940-9602(03)80110-3, indexed in Pubmed: 14575275.
4. Diogo R, Wood B. Soft-tissue anatomy of the primates: phylogenetic analyses based on the muscles of the head, neck, pectoral region and upper limb, with notes on the evolution of these muscles. J Anat. 2011; 219(3): 273–359, doi: 10.1111/j.1469-7580.2011.01403.x, indexed in Pubmed: 21689100.
5. Edgerton MT. Surgical correction of facial paralysis: a plea for better reconstructions. Ann Surg. 1967; 165(6): 985–998, doi: 10.1097/00000658-196706000-00014, indexed in Pubmed: 6026317.
6. Hamparian AM. Blood supply of the human fetal mandible. Am J Anat. 1973; 136(1): 67–75, doi: 10.1002/aja.1001360106, indexed in Pubmed: 4682141.
7. Katsumi Y, Tanaka R, Hayashi T, et al. Variation in arterial supply to the floor of the mouth and assessment of relative hemorrhage risk in implant surgery. Clin Oral Implants Res. 2013; 24(4): 434–440, doi: 10.1111/j.1600-0501.2011.02348.x, indexed in Pubmed: 22092873.
8. Kim SD, Loukas M. Anatomy and variations of digastric muscle. Anat Cell Biol. 2019; 52(1): 1–11, doi: 10.5115/acb.2019.52.1.1, indexed in Pubmed: 30984445.
9. Labbé D, Giot JP, Kaluzinski E. Submental area rejuvenation by digastric corset: anatomical study and clinical application in 20 cases. Aesthetic Plast Surg. 2013; 37(2): 222–231, doi: 10.1007/s00266-013-0083-7, indexed in Pubmed: 23435506.
10. Langsdon PR, Velargo PA, Rodwell DW, et al. Submental muscular medialization and suspension. Aesthet Surg J. 2013; 33(7): 953–966, doi: 10.1177/1090820X13502220, indexed in Pubmed: 23986490.
11. Macalister A. Additional observations on muscular anomalies in human anatomy. (Third series) With a catalogue of the principal muscular variations hitherto published. Trans Roy Irish Acad Sci. 1875; 25: 1–134.
12. Moore KL, Dalley AF, Agur AMR. Clinically oriented anatomy. 8th ed. Wolters Kluwer, 2018: 1010–1011.
13. Ozgur Z, Govsa F, Celik S, et al. An unreported anatomical finding: unusual insertions of the stylohyoid and digastric muscles. Surg Radiol Anat. 2010; 32(5): 513–517, doi: 10.1007/s00276-009-0553-4, indexed in Pubmed: 19763380.
14. Pinar YA, Govsa F, Bilge O. The anatomical features and surgical usage of the submental artery. Surg Radiol Anat. 2005; 27(3): 201–205, doi: 10.1007/s00276-005-0317-8, indexed in Pubmed: 16003485.
15. Radlanski RJ, Renz H, Tabatabai A. Prenatal development of the muscles in the floor of the mouth in human embryos and fetuses from 6.9 to 76 mm CRL. Ann Anat. 2001; 183(6): 511–518, doi: 10.1016/S0940-9602(01)80057-1, indexed in Pubmed: 11766522.
16. Reid RW. Anterior belly of the digastric muscle of both sides, arising from the lower border of the horizontal ramus of the inferior maxillary bone. J Anat Physiol. 1886; 21(Pt 1): 78, indexed in Pubmed: 17231671.
17. Sargon MF, Onderoğlu S, Sürücü HS, et al. Anatomic study of complex anomalies of the digastric muscle and review of the literature. Okajimas Folia Anat Jpn. 1999; 75(6): 305–313, doi: 10.2535/ofaj1936.75.6_305, indexed in Pubmed: 10217948.
18. Sakamoto Y, Akita K. Supernumerary muscle bundles in the submental triangle: their positional relationships according to innervation. Surg Radiol Anat. 2004; 26(3): 245–253, doi: 10.1007/s00276-004-0227-1, indexed in Pubmed: 14872289.
19. Som PM, Laitman JT. Embryology, Variations, and Innervations of the Human Neck Muscles. Neurographics. 2017; 7(3): 215–242, doi: 10.3174/ng.3170206.
20. Sowman PF, Flavel SC, McShane CL, et al. Asymmetric activation of motor cortex controlling human anterior digastric muscles during speech and target-directed jaw movements. J Neurophysiol. 2009; 102(1): 159–166, doi: 10.1152/jn.90894.2008, indexed in Pubmed: 19420123.
21. Sporns PB, Muhle P, Hanning U, et al. Atrophy of swallowing muscles is associated with severity of dysphagia and age in patients with acute stroke. J Am Med Dir Assoc. 2017; 18(7): 635.e1–635.e7, doi: 10.1016/j.jamda.2017.02.002, indexed in Pubmed: 28363443.
22. Stracker O. Die Häufigkeit interponierter Muskelkörper zwischen den vorderen Bäuchen des M. digastricus Anat Anz. 1908; 33: 117–236.
23. Tan ST. Anterior belly of digastric muscle transfer: a useful technique in head and neck surgery. Head Neck. 2002; 24(10): 947–954, doi: 10.1002/hed.10150, indexed in Pubmed: 12369074.
24. Uzun A, Aluclu A, Kavakli A. Bilateral accessory anterior bellies of the digastric muscle and review of the literature. Auris Nasus Larynx. 2001; 28(2): 181–183, doi: 10.1016/s0385-8146(00)00100-0, indexed in Pubmed: 11240328.
25. Yamada S. Beobachtungen über den Venter anterior des Musculus digastricus mandibulae bei japanishen Erwachsenen und Foeten. Acta Anat Nippon. 1935; 8: 303–347.
26. Zdilla MJ, Pancake AR, Lambert HW. Morphometrics of the anterior belly and intermediate tendon of the digastric muscle: sexual dimorphism and implications for surgery. J Craniofac Surg. 2016; 27(5): 1321–1326, doi: 10.1097/SCS.0000000000002708, indexed in Pubmed: 27258716.
27. Zdilla MJ, Mangus KR, Swearingen JV, et al. The submental arrowhead variation of the mylohyoid and anterior belly of the digastric muscles. Surg Radiol Anat. 2018; 40(12): 1429–1436, doi: 10.1007/s00276-018-2110-5, indexed in Pubmed: 30306209.
28. Zlabek K. Contribution a la connaissance des anomalies du ventre anterieur du digastrique de l'Homme. Arch Anat Histol Embryol. 1933; 16: 357–406.

VIA MEDICA

CASE REPORT

Folia Morphol.
Vol. 80, No. 3, pp. 699–706
DOI: 10.5603/FM.a2020.0078

ISSN 0015–5659
eISSN 1644–3284
journals.viamedica.pl

Carotid paragangliomas: case report and imaging review

R.A. Baz[1], C. Scheau[2], N. Sârbu[3], D.O. Costea[4], A. Dijmărescu[5], P. Bordei[6]

[1]*Department of Radiology, "Sf. Apostol Andrei" County Hospital, Constanta, Romania*
[2]*Department of Physiology, Carol Davila University of Medicine and Pharmacy, Bucharest, Romania*
[3]*Department of Radiology, Faculty of Medicine and Pharmacy "Dunărea de Jos" Galati, Romania*
[4]*Department of Surgery, "Sf. Apostol Andrei" County Hospital, Constanta, Romania*
[5]*Department of Radiology, Fundeni Clinical Institute, Bucharest, Romania*
[6]*Department of Anatomy, Faculty of Medicine, Constanta, Romania*

[Received: 4 June 2020; Accepted: 29 June 2020; Early publication date: 21 July 2020]

Background: *Presentation of case reviews depicting the imaging characteristics of carotid paragangliomas, associated with a thorough analysis of the anatomical morphological features and the current therapeutic strategies.*

Materials and methods: *We present the cases of 3 patients diagnosed with carotid paragangliomas in our clinic, illustrating diagnostic imaging elements by computer tomography (CT) and magnetic resonance imaging (MRI), but also the postoperative aspect of the carotid system, with respective anatomical, clinical and surgical considerations.*

Results: *The imaging aspect of the carotid paragangliomas is characterised by a mass of soft tissue with intense contrast enhancement and with "salt and pepper" MRI appearance on conventional spin-echo sequences. The postoperative evolution of the patients included in the article was favourable, without any perioperative complications or signs of local tumour recurrence.*

Conclusions: *Carotid paragangliomas are rare, often asymptomatic tumours, but with potential for increased malignancy, which raises the need for good knowledge of the cervical region pathology as well as the features of neuroendocrine tumours. CT and MRI examinations are essential for diagnosis, staging and, implicitly, for establishing the therapeutic strategy.* (Folia Morphol 2021; 80, 3: 699–706)

Key words: paraganglioma, carotid body tumour, carotid arteries, diagnostic tools, imaging, therapeutic strategy

INTRODUCTION

Carotid paragangliomas (CPs), also known as carotid body tumours, are neuroendocrine tumours originating in the parenchymal cells of the neuroectoderm and neural crests, but also in the mesodermal elements of the third branchial arch [1, 17, 19, 28, 30]. Thus, the cells that make up paragangliomas are similar to the cells in the amine precursor uptake and decarboxylation system and can release catecholamines, cholecystokinin, serotonin, somatostatin, and vasoactive intestinal peptide [20].

Paragangliomas have variable localisation and may develop in the head, neck, thorax, or abdomen. Head and neck paragangliomas can show the follow-

Address for correspondence: C. Scheau, MD, PhD, 8 Eroii Sanitari Blvd., 5th district, 050474, Bucharest, Romania, tel: +40213103722, e-mail: cristian.scheau@umfcd.ro

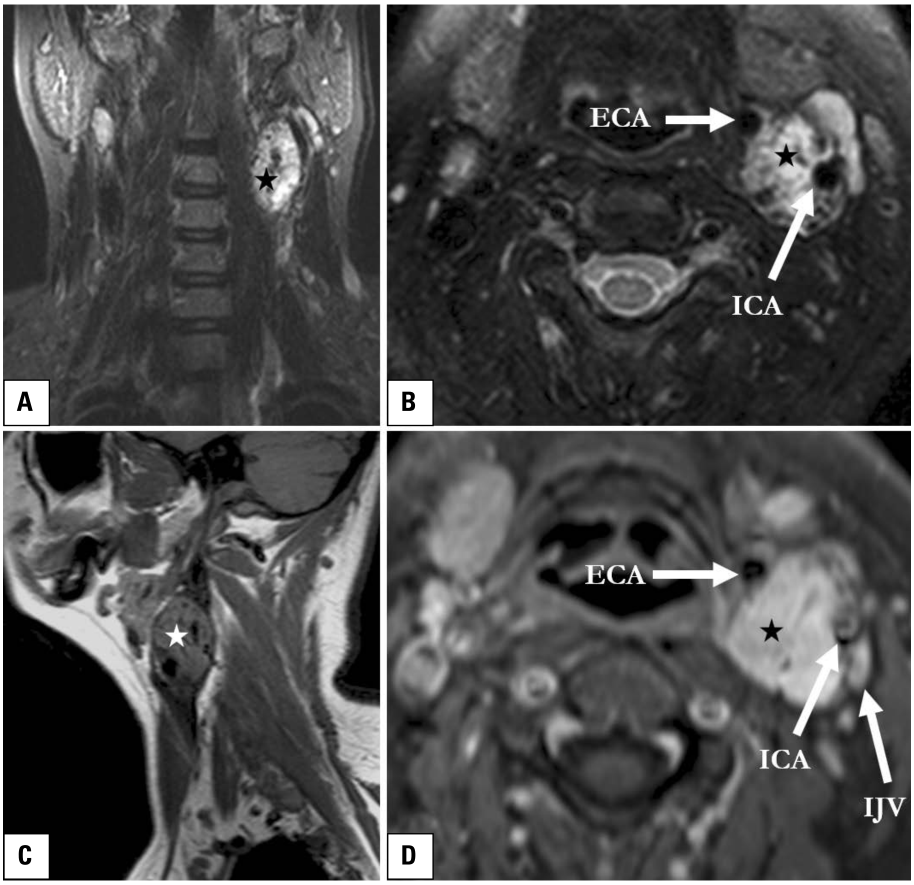

Figure 1. Magnetic resonance imaging investigation consisting of coronal short tau inversion recovery (STIR) (**A**), axial T2 fat-saturated WI (**B**), sagittal T1 WI (**C**), and gadolinium-enhanced axial T1 fat-saturated images depicting a inhomogeneous oval solid mass (star) with intermediate signal on T1 WI and high signal on T2 WI, intralesional foci in signal void that create an overall "salt and pepper" appearance, developed at the level of left carotid bifurcation (**D**); the lesion shows intense early enhancement, widens the angle of bifurcation of the common carotid artery and spreads the left external carotid artery (ECA) and internal carotid artery (ICA), without altering their permeability and rapid blood flow signal; IJV — internal jugular vein.

ing topography: carotid (carotid glomus), tympanic (glomus tympani), jugular (glomus jugulare) or vagal (glomus vagale) [22]. These tumours are rare [1, 26, 30], can be single or multifocal tumours, and are considered benign but with malignant potential in 6–12% of cases [14, 19, 28, 34]. CPs represent 0.6% of head and neck neoplasms, accounting for 60–70% of paragangliomas of the head and neck region, and make up 0.5% of tumours affecting the entire body [1, 14, 34].

The majority of paragangliomas are sporadic; however, in about 40% of cases, family history is demonstrated [5]. Hereditary tumours are more often multicentric and tend to occur earlier than sporadic forms, with a peak incidence at 30–35 years of age [18]. Familial paragangliomas exhibit autosomal dominant transmission and are commonly seen in patients with von Hippel-Lindau disease, type I neurofibromatosis, and type II multiple endocrine neoplasias [23].

The scope of this paper is to mark the essential diagnostic elements of CPs useful to the clinicians and surgeons in planning the therapeutic strategy. Starting from the presentation of 3 illustrative cases investigated in our clinic, we analysed the specific literature data and detailed the most important elements involved in the management of these tumour types.

CASE REPORTS

Case 1

A 42-year-old woman was admitted to the hospital for a painless left cervical tumour measuring close to 3 cm, with a soft consistency, and mobile in the transverse plane. The ultrasound showed a submandibular hypoechogenic mass that displaced the internal carotid artery. The magnetic resonance imaging (MRI) examination revealed a hypervascular lesion with a "salt and pepper" appearance located in the left carotid space, at the terminal bifurcation of the common carotid artery, with suggestive characteristics for CP (Fig. 1). The patient refused surgery, but 90 days later she returned determined to receive

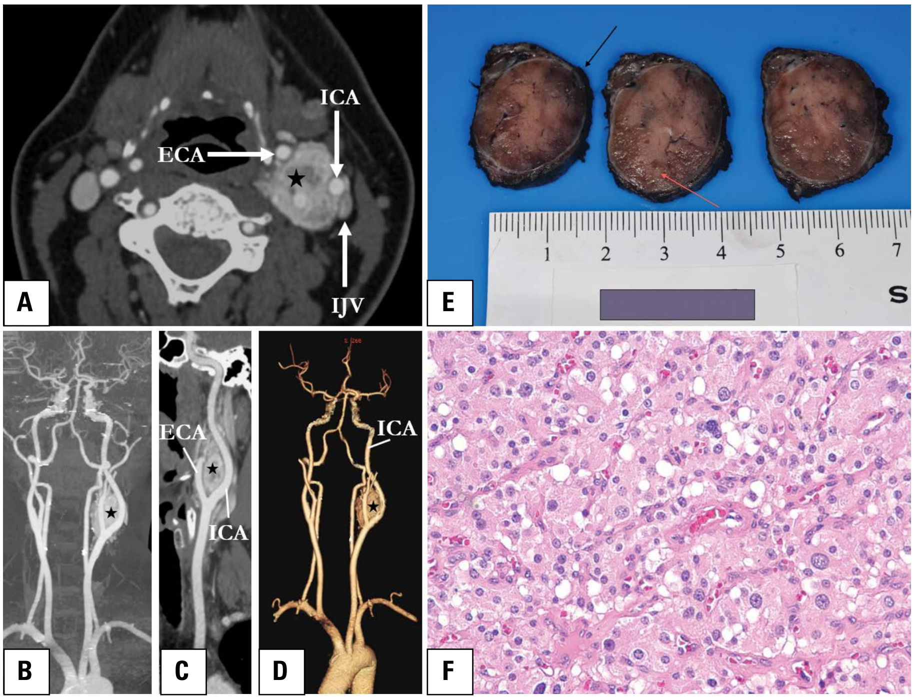

Figure 2. Computed tomography (CT) examination: axial CT angiography (**A**), coronal-oblique maximum-intensity-projection reformatted image (**B**), curved-planar reformatted image of the left internal carotid artery (ICA) (**C**), and three-dimensional volume-rendered reformatted image (**D**). Large solid mass (star), with intense and slightly inhomogeneous enhancement, located at the level of the left carotid bifurcation, separating the external carotid artery (ECA) and ICA. The described lesion encases about 50% of the circumference of the ICA, without modifying its lumen (type II Shamblin) and is adjacent to the internal jugular vein (IJV). Macroscopic appearance (**E**) of the carotid body tumour after complete excision with a pseudo capsule (black arrow) and multiple feeding vessels (orange arrow). Microscopic specimen (**F**): uniform polygonal cells with abundant eosinophilic granular cytoplasm and large, regular, central nuclei.

treatment. Computed tomography (CT) angiography confirmed a bright and rapidly enhancing mass located at the level of the left carotid bifurcation compatible with a diagnosis of a type II Shamblin CP (Fig. 2). The chosen treatment course implied the surgical cure of the tumour with a favourable postoperative evolution, without incidents, and with no detectable tumour recurrence on imaging follow-up at 3 months and, subsequently, at 6 and 12 months.

Case 2

A 55-year-old woman with no particular pathological background was admitted with a right cervical mass showing slow dimensional progression within a year, with no other associated symptoms. The clinical examination and ultrasound confirmed the presence of a tumour with soft consistency adjacent to the right internal carotid artery. The MRI and CT examinations revealed a type IIIa Shamblin CP, with a characteristic "salt and pepper" appearance at the level of the right carotid bifurcation, with a small extension to the submandibular space and the right postero-lateral wall of the pharynx (Fig. 3). The patient showed favourable postoperative outcome with a good evolution and is periodically evaluated in our clinic, without complications or tumour recurrence at 3.5 years after surgery.

Case 3

A diabetic 46-year-old woman presented with a left-cervical mass manifested in the last 2 years, with a gradual increase in size and associating dysphonia at the time of hospitalisation. The ultrasound examination suspected a CP by highlighting a hypoechogenic mass at the carotid bifurcation, which splayed the external and internal carotid arteries, extending medially to the retropharyngeal space, anteriorly to the submandibular branch, and posteriorly through the soft prevertebral tissues. CT angiography established the diagnosis of a type IIIb Shamblin CP (Fig. 4). No incidents occurred during the surgical procedure and intraoperative observations confirmed the inclusion and infiltration of the internal carotid artery. The follow-up examinations performed at 3 and 12 months did not reveal any complications or local tumour recurrence.

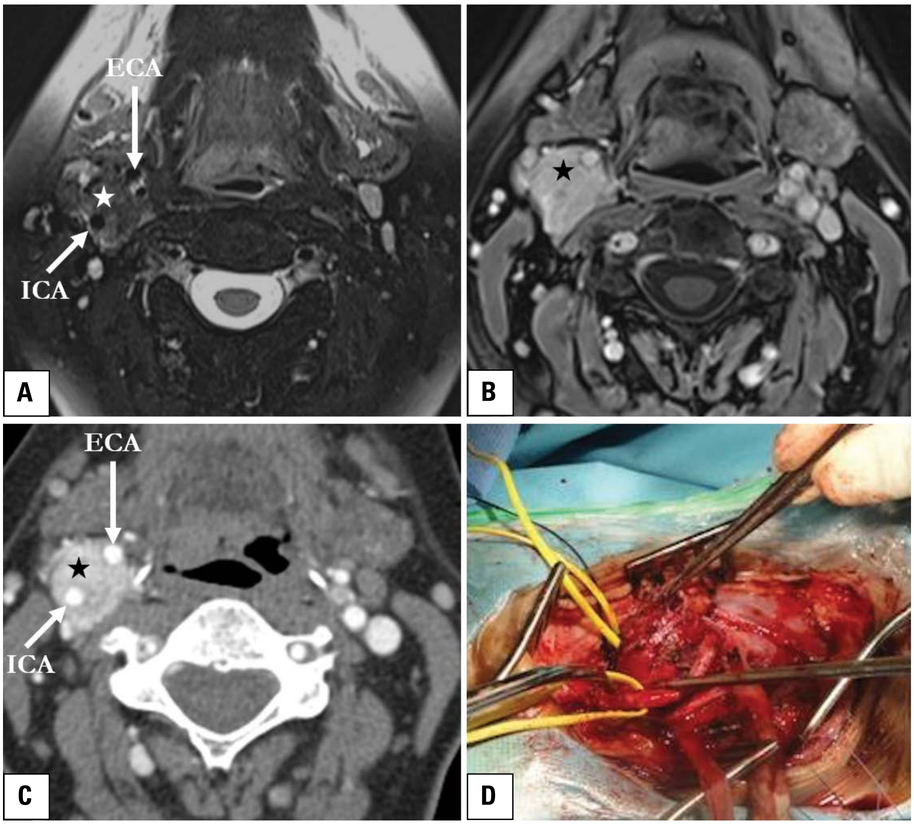

Figure 3. Magnetic resonance imaging saturated T2 axial fat image (**A**) and gadolinium-enhanced T1 fat axial image (**B**), and axial computed tomography postcontrast-arterial phase (**C**) showing a solid mass (star) with well-defined contour, inhomogeneous signal, "salt and pepper" aspect, and intense early contrast enhancement, located at the level of the right carotid bifurcation, separating the right internal carotid artery (ICA) and external carotid artery (ECA). The lesion splays the carotid arteries, encloses the ICA and ECA without infiltrating them. Intraoperative view of the carotid body tumour before complete excision (**D**).

Imaging review of paragangliomas

Imaging is an essential part of the diagnostic protocol in the management of carotid glomus tumours. CT and MRI examinations using contrast mediums are useful in lesion detection, thus obtaining valuable information regarding the lesion size, the relationship with the adjacent anatomical structures, and the degree of vascularisation. Additionally, blood flow downstream of the lesion can be ascertained, and the presence of collateral circulation, anatomic variants, and other synchronous paragangliomas in other regions of the body can also be demonstrated [33].

Ultrasonography is a first-line imaging method for determining the location and features of lateral-cervical masses. CP appears as a well-delimited round-oval hypoechogenic mass located at the level of the carotid sinus, causing the carotid bifurcation to flare. Colour Doppler or Doppler duplex highlights the hypervascular character of the lesion and allows differentiation from other tumours, but with limited possibilities in detecting local invasion [15].

Computed tomography shows CP as a soft tissue mass located in the carotid space, with intense and homogeneous early enhancement due to its highly vascular nature. Large tumours may exhibit a heterogeneous structure due to the presence of thrombi or focal haemorrhages. Flaring (splaying) of the external and internal carotid arteries, a hallmark of CP, can also be easily visualised on CT (Fig. 5). Irradiation and the allergic risk to the iodinated contrast substance are the main disadvantages of CT [32].

Magnetic resonance imaging has proven its superiority to other imaging techniques in offering a more accurate appreciation of lesion margins and invasion of adjacent structures [24]. Using native and contrast-enhanced spin-echo sequences with fat suppression, MRI examination can determine vascular invasion more accurately compared to CT, and can also provide more detailed vascular morphometry measurements [9]; additionally, MRI can reveal lesions smaller than 5 mm, while CT usually depicts lesions larger than 8 mm [31]. The typical MRI aspect of CP is given by the presence of multiple punctiform or serpentine shaped intralesional

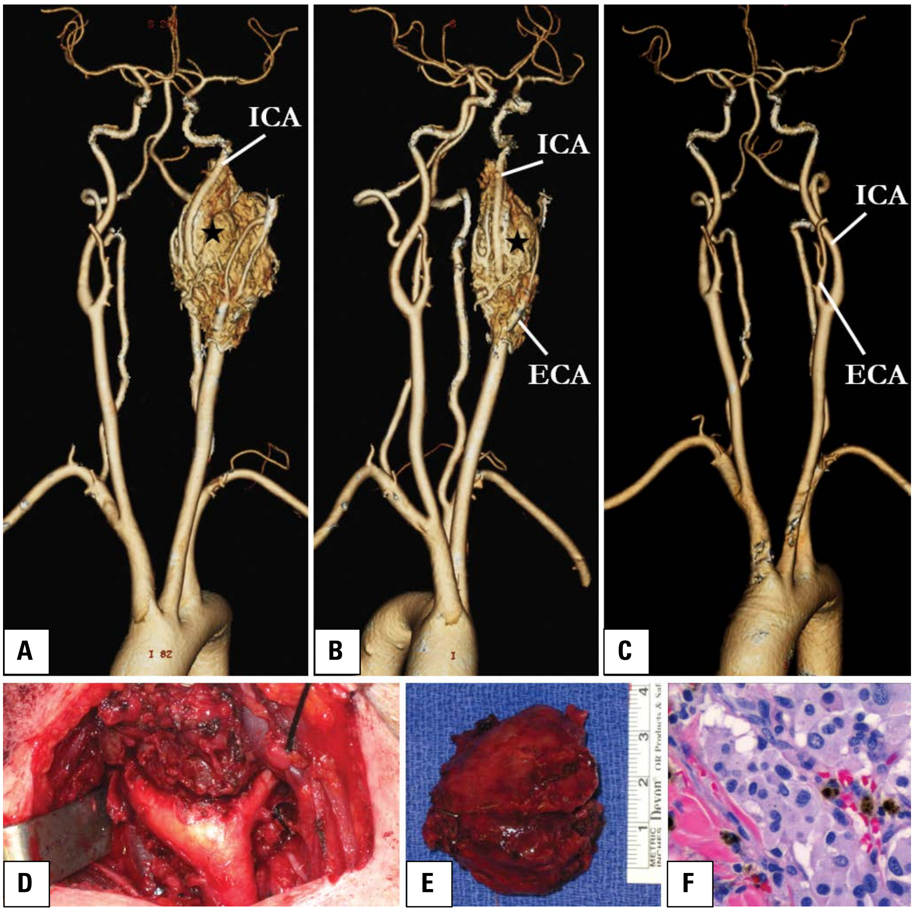

Figure 4. Computed tomography angiography coronal-oblique volume-rendered images pre- (**A, B**) and postoperatively (**C**) highlighting a large hypervascular mass (star) at the level of the left carotid bifurcation that splays the carotid arteries and infiltrates the internal carotid wall, correspondingly to a type IIIb Shamblin tumour. Imaging performed 1 year after surgery demonstrates the absence of recurrence and normal appearance of the left carotid arteries. Intraoperative appearance of the carotid body tumour (**D**). Gross pathology specimen with a meaty appearance with a bulging surface (**E**). Photomicrograph of the histologic specimen (haematoxylin and eosin, ×400) showing highly vascularised fibrous septa surrounding the chief neoplastic cells (**F**); ICA — internal carotid artery; ECA — external carotid artery.

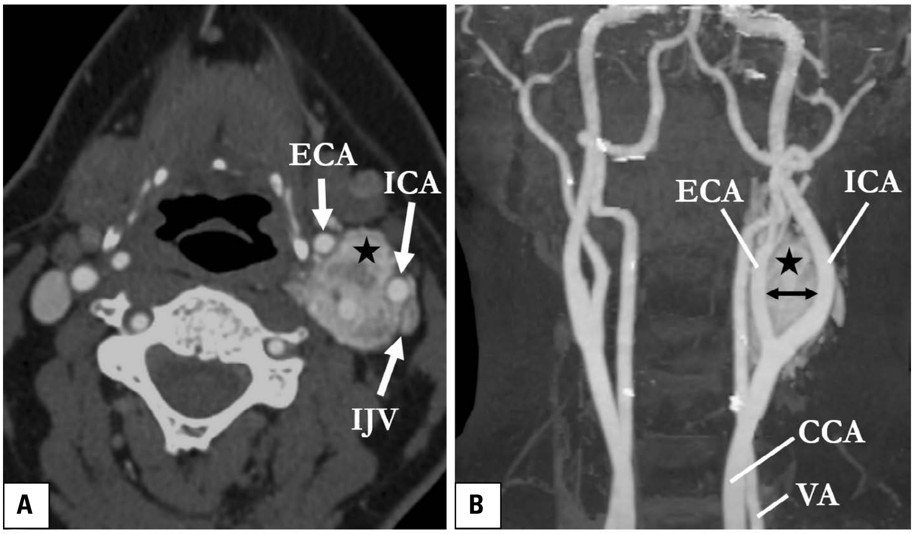

Figure 5. Contrast-enhanced computed tomography: axial images (**A**) and coronal-oblique maximum-intensity-projection (**B**) showing a widening of the distance between the left carotid arteries (black arrow) as a result of the development of a carotid body tumour (star). Left side vessels are marked: vertebral (VA), common carotid (CCA), internal carotid (ICA) and external carotid (ECA) arteries.

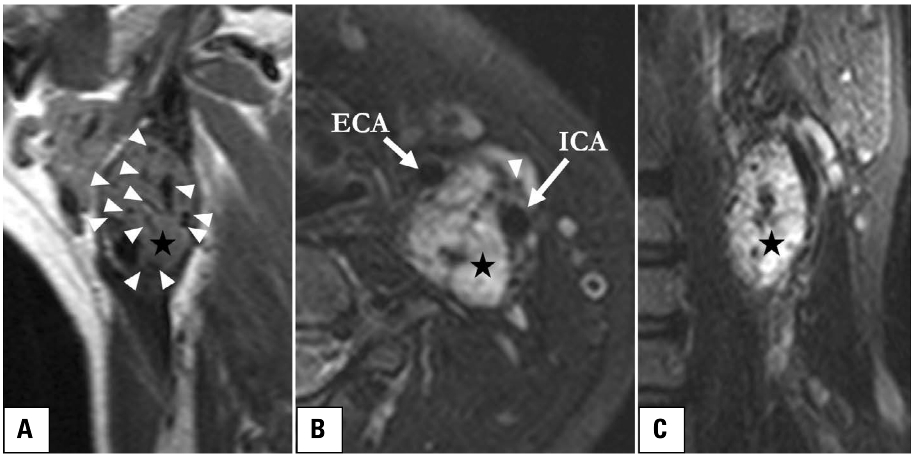

Figure 6. Magnetic resonance imaging aspect of a carotid body tumour with "salt and pepper" sign generated by signal void areas due to numerous intratumoural vessels (arrowheads); **A.** T1 WI; **B.** T2 FS WI; **C.** Short tau inversion recovery (STIR) images; ICA — internal carotid artery; ECA — external carotid artery.

foci with signal void. These are caused by the higher flow velocity in the intratumoural vessels and give the whole lesion a "salt and pepper" appearance (Fig. 6). The "salt" represents areas of hyperintensities due to slow vascular flow or microhaemorrhages, while the "pepper" corresponds to the above-mentioned areas with markedly decreased T1 and T2 signals (signal void) [15]. This imaging pattern is rarely found in lesions smaller than 1 cm, and can also be observed in other hypervascular tumours such as renal cell carcinoma metastases and thyroid carcinoma metastases [12].

Conventional digital subtraction angiography is the gold standard for evaluating the vascular architecture of these tumours. The typical angiographic aspect of paragangliomas is that of a hypervascular mass which splays the internal and external carotid arteries and presents large feeding arteries, intense arterial flash, and quick contrast washout. The tributary arteries of CPs are the ascending pharyngeal artery and the ascending cervical artery. As the tumour increases in size, contributions from other arterial sources such as the facial, lingual, or thyroid arteries may add up. It is mandatory to note the patency of the internal jugular vein, which may be thrombosed in large CPs [6].

Differential imaging diagnosis of paragangliomas should include nerve sheath tumours that displace the carotid arteries medially and anteriorly while the internal jugular vein is pushed posteriorly, as compared to CPs that splay the carotids; other diagnoses include vagal glomus tumours which display similar morphological characteristics but are more rostrally located, and also hypervascular metastatic adenopathies from renal or thyroid malignancies, which are difficult to distinguish from CPs [6, 32]. Histopathology is not necessary for the diagnosis and performing a biopsy may even be very dangerous due to the high degree of tumour vascularisation [21, 29].

DISCUSSION

Carotid paragangliomas generally affect women [1, 19, 28, 30, 34], are bilateral in about 10% of cases [6], and the involvement of hereditary factors is described in 4–9% of cases [28, 30, 34].

From a clinical standpoint, CPs are slow-evolving tumours which may remain painless and generally asymptomatic and for a long period of time, and are located anteriorly to the lateral sternocleidomastoid muscle, showing mobility in the lateral plane, but fixed in the cephalocaudal plane (Fontaine's sign) [31]. CPs significantly alter the loco-regional anatomy, both through their dimensions and their position. Therefore, any lesion that develops adjacent to the terminal bifurcation of the common carotid artery will induce changes in the muscular, vascular, and nervous anatomical relations. Taking into account the vascular nature of the lesion in question, the most apparent altered index could be the angle between the origins of the internal and external carotid arteries. As carotid body tumours grow in size they can invade the parapharyngeal space causing a bulging of the lateral oropharyngeal wall inducing dysphagia, odynophagia, or syndromes associated with cranial nerves IX–XII disorders [35].

Carotid body tumours are paragangliomas that show high malignant capacity, a feature that occurs in 6–12% of cases [14, 19, 28, 34]. In the absence of specific histopathological criteria, malignancy is marked by the anatomical presence of metastases [10], with a predilection for regional lymph nodes, and very rare distant metastases [3]. The therapeutic method of choice for carotid body tumours is surgical removal, which in select cases may be preceded by angiographic embolisation [8, 25]. Embolisation may reduce the size of the tumour and promote its disconnection from the vascular system, thereby reducing intraoperative bleeding [13, 36]. Among the significant complications of surgical treatment are secondary bleeding, cranial nerve deficiency, and perioperative stroke; therefore, the intervention requires caution in aged patients, especially in patients with cardio-ischaemic pathology despite the general addressability of the surgery [7, 8, 13, 25, 36].

The key element in choosing the right therapeutic conduit is the assessment of the extent of tumoural vascular involvement through medical imaging, a method that also provides insight regarding the prognosis and possible complications. As such, a classification system for CP was proposed by Shamblin et al. [27] in 1971 and is currently in use despite its shortcomings regarding the degree of tumour infiltration into the carotid wall, a critical element to be factored when the preservation of the arteries is considered. According to Shamblin et al. [27], type I tumours are located at the bifurcation of the common carotid artery, with minimal contact area with blood vessels, type II encompasses tumours that have a diameter generally less than 5 cm, and include about 50% of the circumference of the main arterial axis, entailing difficulties for the surgical cure, while type III is reserved for generally large tumours with a diameter greater than 5 cm, that completely enclose the main arterial axis [27].

Luna-Ortiz et al. [16] emphasizes that imaging by axial sections does not accurately approximate the carotid wall tumour infiltration preoperatively, but it highlights the circumferential ratio of the tumour to the adjacent vascular structures. Thus, in 2006, Luna-Ortiz et al. [16] proposed the introduction of a grade IIIb to the carotid paragangliomas, which, regardless of their size, infiltrate the carotid wall. According to Luna-Ortiz et al. [16], type IIIa is superimposed on the old (Shamblin) type III, respectively CPs that include the vessels without infiltrating them.

A study by Arya et al. [2] sustains a good correlation between the radiological aspects of the Shamblin classification and surgical results, and concludes that without taking into account the tumour size, the maximum degree of circumferential tumour/artery contact should be the only criterion for the Shamblin classification, therefore predicting the degree of vascular viability [2].

Radiation therapy, alone or associated with surgery, is another therapeutic strategy that can be chosen in the case of carotid glomus tumours. The treatment is based on the induction of local fibrosis, which can stop tumour development and is indicated in inoperable cases or postoperative relapses [4, 11].

CONCLUSIONS

Carotid paragangliomas are hypervascular tumours, with imaging features of a soft tissue mass with intense enhancement and "salt and pepper" appearance on MRI in conventional spin-echo sequences.

The radiological examination is essential for diagnosis and establishing of the therapeutic strategy. Firstly, the tumour must be detected and characterised, and secondly, the lesion extension must be appreciated in regard to the surrounding vascular structures. Last but not least, the presence of concomitant tumours should be verified, considering that paragangliomas are multifocal lesions in 30% of patients.

Considering all the information presented, the medical team managing a CP case should benefit from a mindful preoperative planning and a correct selection of patients, in order to obtain a successful therapeutic result.

Compliance with ethical standards and informed consent

The study was performed in compliance with the local institutional research ethics committee and was carried out in accordance with the ethical standards of the Declaration of Helsinki and its later amendments. Informed consent was obtained from all participants included in the study.

Conflict of interest: None declared

REFERENCES

1. Albsoul NM, Alsmady MM, Al-Aardah MI, et al. Carotid body paraganglioma management and outcome. Eur J Sci Res. 2009; 37(4): 567–574.
2. Arya S, Rao V, Juvekar S, et al. Carotid body tumors: objective criteria to predict the Shamblin group on MR imaging. Am J Neuroradiol. 2008; 29(7): 1349–1354, doi: 10.3174/ajnr.A1092, indexed in Pubmed: 18417602.
3. Boedeker CC, Neumann HPH, Maier W, et al. Malignant head and neck paragangliomas in SDHB mutation carriers. Otolaryngol Head Neck Surg. 2007; 137(1): 126–129, doi: 10.1016/j.otohns.2007.01.015, indexed in Pubmed: 17599579.
4. Carroll W, Stenson K, Stringer S. Malignant carotid body tumor. Head Neck. 2004; 26(3): 301–306, doi: 10.1002/hed.20017, indexed in Pubmed: 14999807.
5. Dahia PLM. Pheochromocytoma and paraganglioma pathogenesis: learning from genetic heterogeneity. Nat

Rev Cancer. 2014; 14(2): 108–119, doi: 10.1038/nrc3648, indexed in Pubmed: 24442145.
6. Davidovic LB, Djukic VB, Vasic DM, et al. Diagnosis and treatment of carotid body paraganglioma: 21 years of experience at a clinical center of Serbia. World J Surg Oncol. 2005; 3(1): 10, doi: 10.1186/1477-7819-3-10, indexed in Pubmed: 15707500.
7. Davila VJ, Chang JM, Stone WM, et al. Current surgical management of carotid body tumors. J Vasc Surg. 2016; 64(6): 1703–1710, doi: 10.1016/j.jvs.2016.05.076, indexed in Pubmed: 27871494.
8. Dixon JL, Atkins MD, Bohannon WT, et al. Surgical management of carotid body tumors: a 15-year single institution experience employing an interdisciplinary approach. Proc (Bayl Univ Med Cent). 2016; 29(1): 16–20, doi: 10.1080/08998280.2016.11929343, indexed in Pubmed: 26722157.
9. Farımaz M, Çelik HH, Ergun KM, et al. The morphometry of the cavernous part of the internal carotid artery. Folia Morphol. 2019; 78(1): 54–62, doi: 10.5603/FM.a2018.0045, indexed in Pubmed: 29802716.
10. Fliedner SMJ, Lehnert H, Pacak K. Metastatic paraganglioma. Semin Oncol. 2010; 37(6): 627–637, doi: 10.1053/j.seminoncol.2010.10.017, indexed in Pubmed: 21167381.
11. Gilbo P, Morris CG, Amdur RJ, et al. Radiotherapy for benign head and neck paragangliomas: a 45-year experience. Cancer. 2014; 120(23): 3738–3743, doi: 10.1002/cncr.28923, indexed in Pubmed: 25060724.
12. Itawi SA, Buehler M, Mrak RE, et al. A unique case of carotid splaying by a cervical vagal neurofibroma and the role of neuroradiology in surgical management. Cureus. 2017; 9(9): e1658, doi: 10.7759/cureus.1658, indexed in Pubmed: 29147633.
13. Jackson RS, Myhill JA, Padhya TA, et al. The effects of preoperative embolization on carotid body paraganglioma surgery: a systematic review and meta-analysis. Otolaryngol Head Neck Surg. 2015; 153(6): 943–950, doi: 10.1177/0194599815605323, indexed in Pubmed: 26378186.
14. Lee JH, Barich F, Karnell LH, et al. National Cancer Data Base report on malignant paragangliomas of the head and neck. Cancer. 2002; 94(3): 730–737, doi: 10.1002/cncr.10252, indexed in Pubmed: 11857306.
15. Lee KiY, Oh YW, Noh HJ, et al. Extraadrenal paragangliomas of the body: imaging features. Am J Roentgenol. 2006; 187(2): 492–504, doi: 10.2214/AJR.05.0370, indexed in Pubmed: 16861555.
16. Luna-Ortiz K, Rascon-Ortiz M, Villavicencio-Valencia V, et al. Does Shamblin's classification predict postoperative morbidity in carotid body tumors? A proposal to modify Shamblin's classification. Eur Arch Otorhinolaryngol. 2006; 263(2): 171–175, doi: 10.1007/s00405-005-0968-4, indexed in Pubmed: 16010570.
17. Malec K, Cenda P, Brzewski P, et al. Paragangliomas of head and neck: A surgical challenge. J Craniomaxillofac Surg. 2017; 45(1): 127–130, doi: 10.1016/j.jcms.2016.10.003, indexed in Pubmed: 27842922.
18. Mannelli M, Castellano M, Schiavi F, et al. Clinically guided genetic screening in a large cohort of italian patients with pheochromocytomas and/or functional or nonfunctional paragangliomas. J Clin Endocrinol Metab. 2009; 94(5): 1541–1547, doi: 10.1210/jc.2008-2419, indexed in Pubmed: 19223516.
19. McCrary HC, Babajanian E, Calquin M, et al. Characterization of malignant head and neck paragangliomas at a single institution across multiple decades. JAMA Otolaryngol Head Neck Surg. 2019; 145(7): 641–646, doi: 10.1001/jamaoto.2019.1110, indexed in Pubmed: 31194233.
20. Moore MG, Netterville JL, Mendenhall WM, et al. Head and neck paragangliomas: an update on evaluation and management. Otolaryngol Head Neck Surg. 2016; 154(4): 597–605, doi: 10.1177/0194599815627667, indexed in Pubmed: 26861230.
21. Muhm M, Polterauer P, Gstöttner W, et al. Diagnostic and therapeutic approaches to carotid body tumors. Review of 24 patients. Arch Surg. 1997; 132(3): 279–284, doi: 10.1001/archsurg.1997.01430270065013, indexed in Pubmed: 9125028.
22. Obholzer RJ, Hornigold R, Connor S, et al. Classification and management of cervical paragangliomas. Ann R Coll Surg Engl. 2011; 93(8): 596–602, doi: 10.1308/147870811X13137608455172, indexed in Pubmed: 22041235.
23. Offergeld C, Brase C, Yaremchuk S, et al. Head and neck paragangliomas: clinical and molecular genetic classification. Clinics. 2012; 67(S1): 19–28, doi: 10.6061/clinics/2012(sup01)05.
24. Olsen WL, Dillon WP, Kelly WM, et al. MR imaging of paragangliomas. Am J Roentgenol. 1987; 148(1): 201–204, doi: 10.2214/ajr.148.1.201, indexed in Pubmed: 3024473.
25. Pacheco-Ojeda LA. Carotid body tumors: Surgical experience in 215 cases. J Craniomaxillofac Surg. 2017; 45(9): 1472–1477, doi: 10.1016/j.jcms.2017.06.007, indexed in Pubmed: 28687470.
26. Rush BF. Jr. Current concepts in the treatment of carotid body tumors. Surgery. 1962; 52: 679–684, indexed in Pubmed: 14495345.
27. Shamblin WR, ReMine WH, Sheps SG, et al. Carotid body tumor (chemodectoma). Am J Surg. 1971; 122(6): 732–739, doi: 10.1016/0002-9610(71)90436-3.
28. Sobol SM, Dailey JC. Familial multiple cervical paragangliomas: report of a kindred and review of the literature. Otolaryngol Head Neck Surg. 1990; 102(4): 382–390, doi: 10.1177/019459989010200413, indexed in Pubmed: 2113266.
29. Somasundar P, Krouse R, Hostetter R, et al. Paragangliomas? A decade of clinical experience. J Surg Oncol. 2000; 74(4): 286–290, doi: 10.1002/1096-9098(200008)74:4<286::aid-jso9>3.0.co;2-c.
30. Sykes J, Ossoff R. Paragangliomas of the Head and Neck. Otolaryngol Clin North Am. 1986; 19(4): 755–767, doi: 10.1016/s0030-6665(20)31720-5.
31. Thelen J, Bhatt AA. Multimodality imaging of paragangliomas of the head and neck. Insights Imaging. 2019; 10(1): 29, doi: 10.1186/s13244-019-0701-2, indexed in Pubmed: 30830483.
32. van den Berg R. Imaging and management of head and neck paragangliomas. Eur Radiol. 2005; 15(7): 1310–1318, doi: 10.1007/s00330-005-2743-8, indexed in Pubmed: 15809825.
33. West CT, Brassett C, Gaunt ME. Variations in carotid sinus anatomy and their relevance to carotid interventions. Folia Morphol. 2018; 77(4): 693–697, doi: 10.5603/FM.a2018.0017, indexed in Pubmed: 29500893.
34. Williams MD. Paragangliomas of the head and neck: an overview from diagnosis to genetics. Head Neck Pathol. 2017; 11(3): 278–287, doi: 10.1007/s12105-017-0803-4, indexed in Pubmed: 28321772.
35. Woolen S, Gemmete JJ. Paragangliomas of the Head and Neck. Neuroimaging Clin N Am. 2016; 26(2): 259–278, doi: 10.1016/j.nic.2015.12.005, indexed in Pubmed: 27154608.
36. Zeitler DM, Glick J, Har-El G. Preoperative embolization in carotid body tumor surgery: is it required? Ann Otol Rhinol Laryngol. 2010; 119(5): 279–283, doi: 10.1177/000348941011900501, indexed in Pubmed: 20524570.

VIA MEDICA

CASE REPORT

Folia Morphol.
Vol. 80, No. 3, pp. 707–713
DOI: 10.5603/FM.a2020.0085

ISSN 0015–5659
eISSN 1644–3284
journals.viamedica.pl

Potential compression of the musculocutaneous, median and ulnar nerves by a very rare variant of the coracobrachialis longus muscle

Ł. Olewnik[1], F. Paulsen[2, 3], R. Shane Tubbs[4, 5, 6], N. Zielińska[1], B. Szewczyk[1], P. Karauda[1], M. Polguj[7]

[1]*Department of Anatomical Dissection and Donation, Medical University of Lodz, Poland*
[2]*Institute of Functional and Clinical Anatomy, Friedrich Alexander University Erlangen-Nürnberg, Erlangen, Germany*
[3]*Department of Topographic Anatomy and Operative Surgery, Sechenov University, Moscow, Russia*
[4]*Department of Neurosurgery, Tulane University School of Medicine, New Orleans, LA, United States*
[5]*Department of Neurosurgery and Ochsner Neuroscience Institute, Ochsner Health System, New Orleans, LA, United States*
[6]*Department of Anatomical Sciences, St. George's University, Grenada*
[7]*Department of Normal and Clinical Anatomy, Medical University of Lodz, Poland*

[Received: 18 July 2020; Accepted: 21 July 2020; Early publication date: 22 August 2020]

The coracobrachialis longus muscle (CBL) is an extremely rare variant of the coracobrachialis muscle (CRM). The CBL originates from the apex of the coracoid process together with the short head of the biceps brachii and inserts on the olecranon of the ulna. The CBL consists of three parts: a superior part (classical CRM — length 137.88 mm), a middle fibrous layer (23.41 mm), and an inferior part (185.37 mm). A rare relationship between the CBL and median, musculocutaneous and ulnar nerves was observed with potential compression at these three parts. In addition, this case report describes a connection between CBL and the medial head of the triceps brachii, as well as a third head of the biceps brachii, which originate from the fibrous layer. This case report highlights the relationships between the CBL and the median, ulnar and musculocutaneous nerves. (Folia Morphol 2021; 80, 3: 707–713)

Key words: anatomical variations, coracobrachialis longus muscle, median nerve, musculocutaneous nerve, ulnar nerve

INTRODUCTION

The coracobrachialis muscle (CRM) originates from the apex of the coracoid process of the scapula in common with the short head of the biceps brachii muscle. It inserts by means of a flat, short tendon into the medial surface of the humerus, between the attachments of the triceps brachii and brachialis muscles [36].

The musculocutaneous nerve (MCN) arises from the lateral cord of the brachial plexus and contains fibres from the C5-C7 ventral rami. The MCN passes through the CRM and descends between the biceps brachii and brachialis muscles both of which it innervates [35]. The median nerve (MN) arises from the medial and lateral cords of the brachial plexus and is innervated by the C6, C7, C8 and T1 ventral rami [35]. The MN provides motor and sensory function to the forearm and hand [35]. The ulnar nerve (UN) is comprised of C8 and T1 ventral rami. The UN innervates

Address for correspondence: Ł. Olewnik, MD, PhD, Department of Normal and Clinical Anatomy, Interfaculty Chair of Anatomy and Histology, Medical University of Lodz, ul. Narutowicza 60, 90–136 Łódź, Poland, e-mail: lukasz.olewnik@umed.lodz.pl

two muscles of the forearm, the flexor carpi ulnaris and ulnar half of the flexor digitorum profundus. It has branches extending to the hand over the distal forearm and wrist [35].

Many earlier works describe the various types of morphological variations occurring within this CRM. They mainly concern the morphological variability of the proximal and distal attachment, but also additional bands or the occurrence of additional muscle bellies or heads [4, 16–18, 24, 27, 32]. However, little is reported for one of its variants, the coracobrachialis longus muscle (CBL). While Wood [51] was probably the first to describe such a variant in 1867, a similar discovery was made by Kyou-Jouffroy et al. [30]. A description of the CBL was more recently made by Georgiev et al. [18].

Morphological variations have been previously observed between the CRM and even the MCN or MN. The presence of an extra muscle head or belly can place pressure on the MCN or proximal MN. More importantly, the presence of the CBL can place pressure on the MCN, MN or UN.

Peripheral neuropathies can be classified as compressive/entrapment and non-compressive forms [2, 11]. Although peripheral nerve compression or entrapment is possible anywhere along the course of a nerve, it tends to occur more often where the nerve passes through fibro-osseous or fibromuscular tunnels or penetrates muscles [11, 26].

This study describes a very rare and undescribed variation of the CBL and its extremely rare relationship with the MN, MCN and UN. Knowledge of such a very rare type can make it easier to understand disease in this region and improve its treatment.

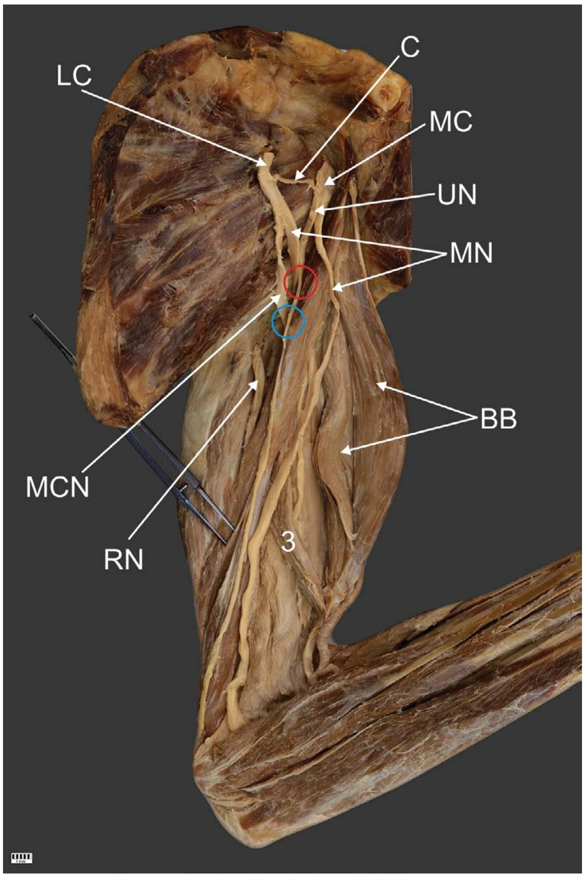

Figure 1. The coracobrachialis longus muscle and relation to the median and musculocutaneous nerve; LC — lateral cord of the brachial plexus; MC — medial cord of the brachial plexus; C — communicating branch; UN — ulnar nerve; MN — median nerve; MCN — musculocutaneous nerve; RN — radial nerve; BB — biceps brachii; 3 — third head of the biceps brachii. The red circle shows the potential compression site of the median nerve, while the blue circle shows the potential compression site of the musculocutaneous nerve.

CASE REPORT

The left upper limb from a male cadaver that was 78-year-old at death underwent routine anatomical dissection for research and teaching purposes in the Department of Anatomical Dissection and Donation, Medical University of Lodz, Poland [38, 45, 46].

Morphology of the coracobrachialis longus muscle

The proximal part of the CRM corresponded to the classical description, and originated from the apex of the coracoid process together with the short head of the biceps brachii. The width of the muscle belly origin was 9.94 mm, while the thickness was 4.13 mm. The length of the belly muscle was 137.88 mm. The muscle then inserted on the medial surface of the shaft of the humerus between the attachments of the triceps brachii and brachialis muscles. This part continued as a thin fibrous layer (length — 23.41 mm) with the second part of the muscle (Fig. 1). The length of the muscle belly was 185.37 mm; the muscle belly passed the tendon (13.95 mm length) and inserted on the olecranon of the ulna. The distal part of the CBL connected with the brachii triceps tendon (Fig. 2). The thin fibrous layer included an accessory band (length 25.83 mm) that connected to the medial head of the triceps brachii, and the thin fibrous layer was the origin of the third head of the biceps brachii muscle (Figs. 1, 3).

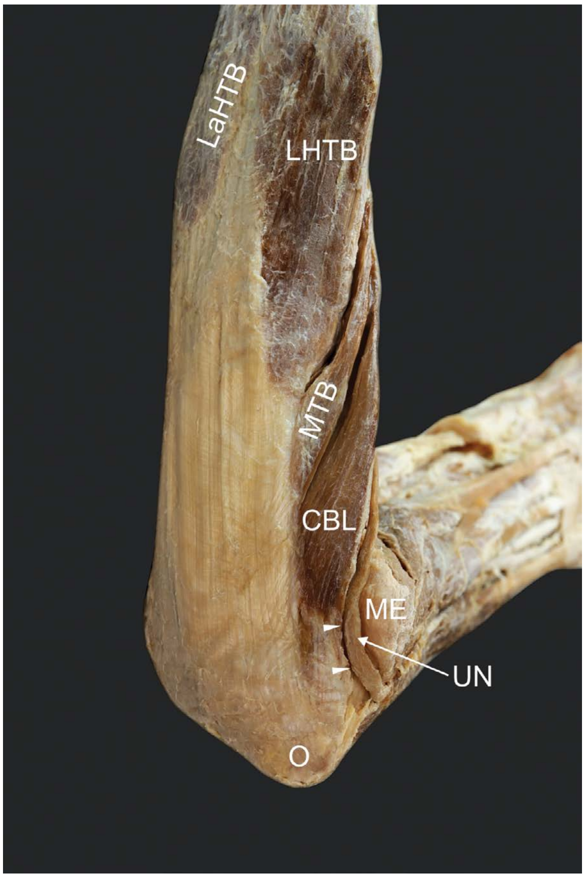

Figure 2. Distal part of the arm. Insertion of the coracobrachialis longus muscle; LaHTB — lateral head of the triceps brachii; LHTB — long head of the triceps brachii; MTB — medial head of the triceps brachii; CBL — coracobrachialis longus muscle; O — olecranon of the ulna; ME — medial epicondyle; UN — ulnar nerve. The white arrowheads show the potential compression site of the ulnar nerve.

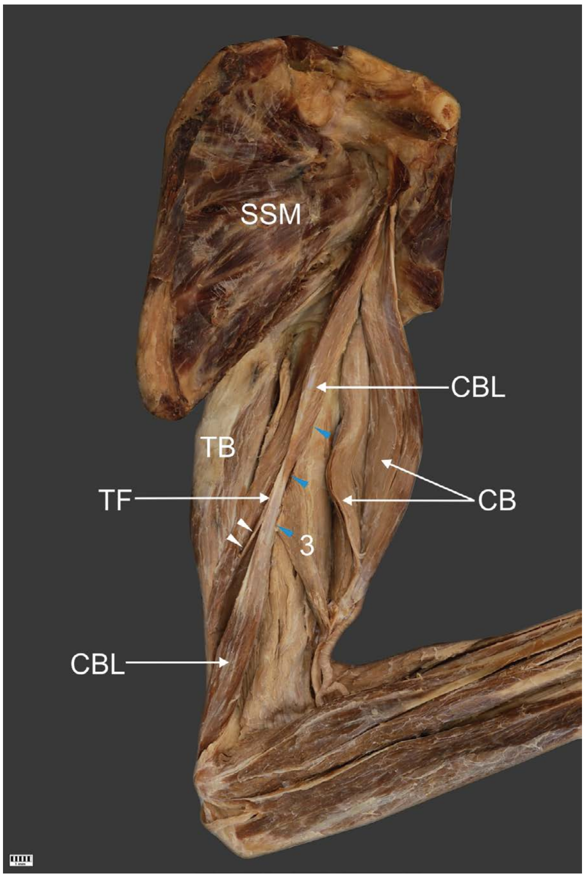

Figure 3. Coracobrachialis longus muscle. Nerves are removed to reveal the coracobrachialis longus muscle; SSM — subscapularis muscle; CBL — coracobrachialis longus muscle; BB — biceps brachii; 3 — third head of the biceps brachii; TB — triceps brachii; TF — tendinous fibrous. The white arrowheads show the slip of the coracobrachialis longus muscle which attaches to the medial head of the triceps brachii. Blue arrowheads show the place of origin of the third head of the biceps brachii.

CBL relation to MN, MCN and UN

Median nerve. The MN arose from both the lateral and medial cords of the brachial plexus. The lateral cord fibres travelled under the CBL and then connected with those arising from the medial cord of the brachial plexus. After 100.09 mm, the lateral cord fibres combined with the medial cord fibres. The medial cord fibres were 97.2 mm in length. The CBL was in the characteristic *loop* of the MN. The MN passed under the muscle and had a diameter of 5.10 mm, while the CBL at this point was 28.36 mm wide and 3.31 mm thick (Fig. 1).

Musculocutaneous nerve. The MCN arose from the lateral cord of the brachial plexus and passed under the CBL at a point 53.25 mm from the place of origin. The MCN passed under the muscle and had a diameter of 4.95 mm, while the CBL at this point was 21.95 mm wide and 3.19 mm thick (Fig. 1).

Ulnar nerve. The UN arose from the medial cord of the brachial plexus, and ran along the CRM, lying exactly on top of it; in the distal part, it was located between the CBL and medial epicondyle, with a diameter of 2.85 mm, while the CBL at this point was 8.90 mm wide and was 3.31 thick (Fig. 2).

Detailed morphometric measurements were taken. After photographic documentation, the CRM was carefully dissected in order to minimise any errors in measurement. The measurements were performed using two methods:

— with an electronic calliper (Mitutoyo Corporation, Kawasaki-shi, Kanagawa, Japan). Each measurement was carried out twice with an accuracy of up to 0.1 mm;

— an analysis of digital photographic images was processed using MultiScanBase 18.03 (Computer

Scanning System II, Warsaw, Poland). The value and precision of this method have been confirmed in previous studies [20, 29, 40, 42].

The posterior cord of the brachial plexus was removed to more accurately visualise the neuromuscular structures described in this case. The variant muscle was innervated by the MCN. No medical or surgical history of the cadaver was available. No similar variation was observed in the contralateral upper limb.

DISCUSSION

Embryologically, the biceps brachii, CRM, and brachialis muscle are intimately fused together at a very early stage and probably arise from a common premuscle mass. The origins of the two heads of the biceps brachii at this early stage are close together and only become separated with the later growth of the scapula. The three muscles can be recognized in embryos 14 to 16 mm in length, and the tendon of the long head in embryos of 14 mm in length. The distal end of the common muscle mass differentiates later than the proximal end [3, 47]. The presence of the CBL could be explained as a result of the premature termination of this regression process.

The CRM is characterised by variability in both proximal and distal attachments. Variations regarding additional heads of this muscle are uncommon [8, 12–14, 17, 18, 24, 51] and the CBL itself has been described much less often [5, 18, 51, 52]. The CBL might attach to the humerus, to a fibrous band of the medial intramuscular septum, i.e. Struthers' ligament, or to the medial epicondyle [5, 18, 51, 52], it may also insert to the tendinous part of the latissimus dorsi [5, 51].

The current study describes an extremely rare type of CBL. The proximal attachment was identical to the normal CRM; however, its distal attachment was not located on the humerus, medial intramuscular septum, Struthers' ligament, medial epicondyle or latissimus dorsi but only on the olecranon of the ulna. In the present study, the thin fibrous layer is characteristic, from which an additional CBL band begins, connecting it to the medial head of the triceps brachii, and gives rise to the origin of the third head of the biceps brachii (Figs. 1, 3).

Recent years have seen a growth in the diagnosis of neuropathies occurring as a consequence of nerve entrapment or compression by muscles. These conditions are most commonly observed in the upper limb and most commonly involve the MN, UN, radial nerve or MCN [6, 9–11, 19, 21–23, 33, 38, 39, 41, 43].

Musculocutaneous nerve neuropathy is not as common as MN or UN neuropathy. Most often, it is due to muscular compression by the CRM, biceps brachii, or brachialis muscles [1, 5, 7, 12–14, 28, 37, 49, 50]. The course of the MCN is closely related to that of the CRM. The MCN can pierce or pass deep to the CRM [12, 15, 24, 31, 48]. It is believed that the CRM is the most common site of MCN entrapment and additional heads can place pressure on the MCN [4, 14, 16, 17, 27, 32]. A potential site of MCN entrapment was also observed in the present case: at this point, 53.25 mm from its origin, the MCN (4.95 mm in diameter) passed under the CBL with the CRM being 21.95 mm in width and 3.19 mm. MN entrapment within the CRM muscle leads to weakness and atrophy of the biceps brachii and brachialis muscles and a loss of sensation in the lateral forearm. Active young individuals that frequently engage in shoulder and elbow flexion with the forearm in a pronated position are most susceptible [44]. It also often occurs following chronic overuse of the CRM and consequent hypertrophy. The nerve compressed within the CRM has already given off its motor branch to the CRM, therefore no loss of CRM muscle function will be observed.

Median nerve compression can occur at various sites along its course [2, 33]. The most common type of MN neuropathy is carpal tunnel syndrome [11, 33]. The next most common site of MN compression is at the pronator teres i.e., pronator teres syndrome, symptoms of which can be manifested by entrapment of MN between the humeral and ulnar heads of the pronator teres muscle [38]. MN compression in the arm is much less common and when present, is due to compression by Struthers' ligament i.e., supracondylar process syndrome [25, 38]. Supracondylar process syndrome is one of the rarest types of MN neuropathy at about 0.5% [33, 34]. MN compression can also occur with the presence of a third head of the biceps brachii [53]; lastly, MN compression can occur more proximal in the arm, with additional heads of the CRM [13, 31], and the additional head of the CRM causing compression of the lateral cord of the brachial plexus [16].

Another potential site of MN entrapment was also identified in the present study. The MN had a diameter of 5.10 mm when passing under the muscle, while the CBL at this point was 28.36 mm wide and

3.31 mm thick. Complaints from compression of the MN by a CBL include loss of fine motor skills and a burning sensation or numbness in the palm.

The second most commonly seen entrapment neuropathy of the upper limb after carpal tunnel syndrome is UN neuropathies. The UN passes over the lateral wall of the axilla and passes to the medial side of the arm. It enters into the groove for the UN behind the medial epicondyle [5, 35]. This groove is the most common entrapment site of the UN. Interestingly, in the current case, the distal part of the CBL might also cause UN compression at the level of the medial epicondyle. At this location, the UN was found to have a diameter of 2.85 mm, while the CBL at this point was 8.90 mm wide and 3.31 thick; any hypertrophy of this muscle could cause compression. UN neuropathy at the elbow can be recognized by numbness of the 4th and 5th digits, hypoesthesia of the medial palm, atrophy and paraesthesia of the hand muscles innervated by the UN.

CONCLUSIONS

The present case report describes a very rare variant of the CBL and its relationship between the MN, MCN and UN. Unfortunately, due to the lack of an adequate number of descriptions of such a rare muscle, confusion may occur during surgery, and the assessment of imaging of this region may be complicated. A greater understanding of the potential compression sites of individual nerves is needed for the correct diagnosis of unrecognised compression sites, and such knowledge of rare variations is an essential part of every clinician's daily practice.

The CBL can have anatomical variants. Along its course, compression of the MN, MCN and UN can occur. Knowledge of such rare muscle variations and their relation to the MN, UN and MCN is required for effective daily clinical practice.

Ethical approval and consent to participate

The cadaver belonged to the Department of Anatomical Dissection and Donation, Medical University of Lodz, Poland.

Conflict of interest: None declared

REFERENCES

1. Abu-Hijleh MF. Three-headed biceps brachii muscle associated with duplicated musculocutaneous nerve. Clin Anat. 2005; 18(5): 376–379, doi: 10.1002/ca.20100, indexed in Pubmed: 15971222.
2. Andreisek G, Crook DW, Burg D, et al. Peripheral neuropathies of the median, radial, and ulnar nerves: MR imaging features. Radiographics. 2006; 26(5): 1267–1287, doi: 10.1148/rg.265055712, indexed in Pubmed: 16973765.
3. Bardeen C. Studies of the development of the human skeleton. Am J Anat. 1905: 265–302.
4. Bauones S, Moraux A. The accessory coracobrachialis muscle: ultrasound and MR features. Skeletal Radiol. 2015; 44(9): 1273–1278, doi: 10.1007/s00256-015-2153-1, indexed in Pubmed: 25924580.
5. Bergman R, Afifi A, Miyauchi R. Illustrated encyclopedia of human anatomic variations. Anatomy Atlas 2017.
6. Besleaga D, Castellano V, Lutz C, et al. Musculocutaneous neuropathy: case report and discussion. HSS J. 2010; 6(1): 112–116, doi: 10.1007/s11420-009-9143-6, indexed in Pubmed: 20013159.
7. Catli MM, Ozsoy U, Kaya Y, et al. Four-headed biceps brachii, three-headed coracobrachialis muscles associated with arterial and nervous anomalies in the upper limb. Anat Cell Biol. 2012; 45(2): 136–139, doi: 10.5115/acb.2012.45.2.136, indexed in Pubmed: 22822469.
8. Chouke KS. Variation of the coracobrachialis muscle. Anat Rec. 1924; 27(3): 157–163, doi: 10.1002/ar.1090270303.
9. Claassen H, Schmitt O, Wree A, et al. Variations in brachial plexus with respect to concomitant accompanying aberrant arm arteries. Ann Anat. 2016; 208: 40–48, doi: 10.1016/j.aanat.2016.07.007, indexed in Pubmed: 27507152.
10. Davidson JJ, Bassett FH, Nunley JA. Musculocutaneous nerve entrapment revisited. J Shoulder Elbow Surg. 1998; 7(3): 250–255, doi: 10.1016/s1058-2746(98)90053-2, indexed in Pubmed: 9658350.
11. Dong Q, Jacobson JA, Jamadar DA, et al. Entrapment neuropathies in the upper and lower limbs: anatomy and MRI features. Radiol Res Pract. 2012; 2012: 230679, doi: 10.1155/2012/230679, indexed in Pubmed: 23125929.
12. El-Naggar MM. A study on the morphology of the coracobrachialis muscle and its relationship with the musculocutaneous nerve. Folia Morphol. 2001; 60(3): 217–224, indexed in Pubmed: 11552663.
13. El-Naggar MM, Al-Saggaf S. Variant of the coracobrachialis muscle with a tunnel for the median nerve and brachial artery. Clin Anat. 2004; 17(2): 139–143, doi: 10.1002/ca.10213, indexed in Pubmed: 14974102.
14. El-Naggar MM, Zahir FI. Two bellies of the coracobrachialis muscle associated with a third head of the biceps brachii muscle. Clin Anat. 2001; 14(5): 379–382, doi: 10.1002/ca.1067, indexed in Pubmed: 11754228.
15. Flatow EL, Bigliani LU, April EW. An anatomic study of the musculocutaneous nerve and its relationship to the coracoid process. Clin Orthop Relat Res. 1989; NA(244): 166–171, doi: 10.1097/00003086-198907000-00014.
16. Garbelotti SA, Marques SR, Rocha PR, et al. An unusual case of accessory head of coracobrachialis muscle involving lateral cord of brachial plexus and its clinical significance. Folia Morphol. 2017; 76(4): 762–765, doi: 10.5603/FM.a2017.0033, indexed in Pubmed: 28353299.
17. Georgiev GP, Landzhov B, Tubbs RS. A novel type of coracobrachialis muscle variation and a proposed new classification. Cureus. 2017; 9(7): e1466, doi: 10.7759/cureus.1466, indexed in Pubmed: 28936378.

18. Georgiev GP, Tubbs RS, Landzhov B. Coracobrachialis longus muscle: humeroepitrochlearis. Cureus. 2018; 10(5): e2615, doi: 10.7759/cureus.2615, indexed in Pubmed: 30027007.
19. Gillingham BL, Mack GR. Compression of the lateral antebrachial cutaneous nerve by the biceps tendon. J Shoulder Elbow Surg. 1996; 5(4): 330–332, doi: 10.1016/s1058-2746(96)80062-0, indexed in Pubmed: 8872933.
20. Gonera B, Kurtys K, Karauda P, et al. Possible effect of morphological variations of plantaris muscle tendon on harvesting at reconstruction surgery-case report. Surg Radiol Anat. 2020; 42(10): 1183–1188, doi: 10.1007/s00276-020-02463-1, indexed in Pubmed: 32248255.
21. Green JR, Rayan GM. The cubital tunnel: anatomic, histologic, and biomechanical study. J Shoulder Elbow Surg. 1999; 8(5): 466–470, doi: 10.1016/s1058-2746(99)90078-2, indexed in Pubmed: 10543601.
22. Halac G, Topaloglu P, Demir S, et al. Ulnar nerve entrapment neuropathy at the elbow: relationship between the electrophysiological findings and neuropathic pain. J Phys Ther Sci. 2015; 27(7): 2213–2216, doi: 10.1589/jpts.27.2213, indexed in Pubmed: 26311956.
23. Hayashi M, Shionoya K, Hayashi S, et al. A novel classification of musculocutaneous nerve variations: The relationship between the communicating branch and transposed innervation of the brachial flexors to the median nerve. Ann Anat. 2017; 209: 45–50, doi: 10.1016/j.aanat.2016.08.004, indexed in Pubmed: 27765675.
24. Ilayperuma I, Nanayakkara BG, Hasan R, et al. Coracobrachialis muscle: morphology, morphometry and gender differences. Surg Radiol Anat. 2016; 38(3): 335–340, doi: 10.1007/s00276-015-1564-y, indexed in Pubmed: 26464302.
25. De Jesus R, Dellon AL. Historic origin of the "Arcade of Struthers". J Hand Surg Am. 2003; 28(3): 528–531, doi: 10.1053/jhsu.2003.50071, indexed in Pubmed: 12772116.
26. Kim SJ, Hong SH, Jun WS, et al. MR imaging mapping of skeletal muscle denervation in entrapment and compressive neuropathies. Radiographics. 2011; 31(2): 319–332, doi: 10.1148/rg.312105122, indexed in Pubmed: 21415181.
27. Kopuz C, Içten N, Yildirim M. A rare accessory coracobrachialis muscle: a review of the literature. Surg Radiol Anat. 2003; 24(6): 406–410, doi: 10.1007/s00276-002-0079-5, indexed in Pubmed: 12652369.
28. Kosugi K, Shibata S, Yamashita H. Supernumerary head of biceps brachii and branching pattern of the musculocutaneus nerve in Japanese. Surg Radiol Anat. 1992; 14(2): 175–185, doi: 10.1007/BF01794898, indexed in Pubmed: 1641744.
29. Kurtys K, Gonera B, Olewnik Ł, et al. A highly complex variant of the plantaris tendon insertion and its potential clinical relevance. Anat Sci Int. 2020; 95(4): 553–558, doi: 10.1007/s12565-020-00540-4, indexed in Pubmed: 32248353.
30. Kyo-Jouffroy M, Lessertisseur J, Saban R, Souteyrand-Boulenger J. Musculature des membres, membre pectoral, groupe branchial ventral. In: Traite de zoologie, mammiferes. Masson, Paris 1971.
31. Loukas M, Aqueelah H. Musculocutaneous and median nerve connections within, proximal and distal to the coracobrachialis muscle. Folia Morphol. 2005; 64(2): 101–108, indexed in Pubmed: 16121328.
32. Mestdagh H, Maynou C, Cassagnaud X. Accessory coracobrachialis muscle as a cause of anterior impingement syndrome of the rotator cuff in an athlete. Eur J Orthop Surg Traumatol. 2002; 12(2): 96–98, doi: 10.1007/s00590-002-0021-x, indexed in Pubmed: 24570160.
33. Meyer P, Lintingre PF, Pesquer L, et al. The median nerve at the carpal tunnel … and elsewhere. J Belg Soc Radiol. 2018; 102(1): 17, doi: 10.5334/jbsr.1354, indexed in Pubmed: 30039031.
34. Miller TT, Reinus WR. Nerve entrapment syndromes of the elbow, forearm, and wrist. Am J Roentgenol. 2010; 195(3): 585–594, doi: 10.2214/AJR.10.4817, indexed in Pubmed: 20729434.
35. Moore KL, Dalley AF, Agur AMR. Clinically Oriented Anatomy. Lippincott Williams&Wilkins, Philadelphia 2013.
36. Moore KL, Dalley AF. Clinical Oriented Anatomy. Lippincott Williams&Wilkins, Philadeplphia 1999.
37. Nakatani T, Tanaka S, Mizukami S. Bilateral four-headed biceps brachii muscles: the median nerve and brachial artery passing through a tunnel formed by a muscle slip from the accessory head. Clin Anat. 1998; 11(3): 209–212, doi: 10.1002/(SICI)1098-2353(1998)11:3<209::AID-CA10>3.0.CO;2-N, indexed in Pubmed: 9579595.
38. Olewnik Ł, Podgórski M, Polguj M, et al. Anatomical variations of the pronator teres muscle in a Central European population and its clinical significance. Anat Sci Int. 2018; 93: 299–306.
39. Olewnik Ł, Waśniewska A, Polguj M, et al. Morphological variability of the palmaris longus muscle in human fetuses. Surg Radiol Anat. 2018; 40(11): 1283–1291, doi: 10.1007/s00276-018-2069-2, indexed in Pubmed: 30022223.
40. Olewnik Ł, Waśniewska A, Polguj M, et al. Rare combined variations of renal, suprarenal, phrenic and accessory hepatic arteries. Surg Radiol Anat. 2018; 40(7): 743–748, doi: 10.1007/s00276-018-2026-0, indexed in Pubmed: 29667030.
41. Olewnik Ł, Wysiadecki G, Polguj M, et al. Anatomical variations of the palmaris longus muscle including its relation to the median nerve - a proposal for a new classification. BMC Musculoskelet Disord. 2017; 18(1): 539, doi: 10.1186/s12891-017-1901-x, indexed in Pubmed: 29258498.
42. Olewnik Ł, Wysiadecki G, Polguj M, et al. A rare anastomosis between the common hepatic artery and the superior mesenteric artery: a case report. Surg Radiol Anat. 2017; 39(10): 1175–1179, doi: 10.1007/s00276-017-1859-2, indexed in Pubmed: 28432408.
43. Pai MM, Nayak SR, Krishnamurthy A, et al. The accessory heads of flexor pollicis longus and flexor digitorum profundus: Incidence and morphology. Clin Anat. 2008; 21(3): 252–258, doi: 10.1002/ca.20612, indexed in Pubmed: 18351652.
44. Pećina M, Bojanić I. Musculocutaneous nerve entrapment in the upper arm. Int Orthop. 1993; 17(4): 232–234, doi: 10.1007/BF00194185, indexed in Pubmed: 8407039.
45. Podgórski M, Olewnik Ł, Rusinek M, et al. 'Superior biceps aponeurosis': Morphological characteristics of the origin of the short head of the biceps brachii muscle. Ann Anat. 2019; 223: 85–89, doi: 10.1016/j.aanat.2019.01.014, indexed in Pubmed: 30797975.

46. Podgórski MT, Olewnik Ł, Grzelak P, et al. Rotator cable in pathological shoulders: comparison with normal anatomy in a cadaveric study. Anat Sci Int. 2019; 94(1): 53–57, doi: 10.1007/s12565-018-0447-9, indexed in Pubmed: 29987440.
47. R.Bardeen C. Development and variation of the musculature of the inferior extremity and the neighboring regions of the trunk in man. Am J Anat. 1907; 6(1): 259–390, doi: 10.1002/aja.1000060108.
48. Remerand F, Laulan J, Couvret C, et al. Is the musculocutaneous nerve really in the coracobrachialis muscle when performing an axillary block? An ultrasound study. Anesth Analg. 2010; 110: 1729–1734.
49. Rodríguez-Niedenführ M, Vázquez T, Choi D, et al. Supernumerary humeral heads of the biceps brachii muscle revisited. Clin Anat. 2003; 16(3): 197–203, doi: 10.1002/ca.10060, indexed in Pubmed: 12673814.
50. Sargon MF, Tuncali D, Celik HH. An unusual origin for the accessory head of biceps brachii muscle. Clin Anat. 1996; 9(3): 160–162, doi: 10.1002/(SICI)1098-2353(1996)9:3<160::AID-CA4>3.0.CO;2-K, indexed in Pubmed: 8740475.
51. Wood J. On human muscular variations and their relation to comperative anatomy. J Anat Physiol. 1867; 1: 44–59.
52. Wood J. On some varieties in human myology. Proc R Soc, London 1864: 299–303.
53. Yershov D, Hudák R. Unusual Variation of the Biceps Brachii with Possible Median Nerve Entrapment. Prague Med Rep. 2015; 116(2): 167–172, doi: 10.14712/23362936.2015.55, indexed in Pubmed: 26093671.

VIA MEDICA

CASE REPORT

Folia Morphol.
Vol. 80, No. 3, pp. 714–717
DOI: 10.5603/FM.a2021.0059

ISSN 0015–5659
eISSN 1644–3284
journals.viamedica.pl

Unusual echocardiographic evidence of hypercoagulation in usual left atrial appendage as the first and only sign of COVID-19

M. Świątczak, R. Nowak, A. Faran, E. Wabich, G. Raczak, M. Klimkiewicz, L. Daniłowicz-Szymanowicz

Department of Cardiology and Electrotherapy, Medical University of Gdansk, Poland

[Received: 14 April 2021; Accepted: 20 May 2021; Early publication date: 25 May 2021]

Coronavirus disease 2019 (COVID-19) is a condition caused by a novel virus, severe acute respiratory syndrome coronavirus 2 (SARS-CoV-2). The disease's course ranges from entirely asymptomatic to severely ill patients. Hypercoagulation is often a complication of this disease, worsening the prognosis, which is extremely important in patients at higher risk of thromboembolic events, such as atrial fibrillation (AF), where thrombus formation in the left atrial appendage (LAA) is frequent. LAA could be of various sizes, volumes, and shapes, distinguish several morphologies, from which the WindSock LAA is the most frequent. In contrast, thromboembolic complications occur most frequently in patients with AF and the Cactus LAA. We present a clinical case of a 70-year-old woman with an initial negative real-time polymerase chain reaction (RT-PCR) test for SARS--CoV-2, suspicion of device-related infection after dual pacemaker implantation, AF, and LAA without thrombus in the initial transoesophageal echocardiography (TEE). Despite apixaban treatment, spontaneous restoration of sinus rhythm, and WindSock LAA morphology, the sludge in LAA was diagnosed in control TEE. The patient did not present any typical clinical COVID-19 symptoms but re-checked the RT-PCR test for SARS-CoV-2 infection was positive. The described case presents echocardiographic evidence of hypercoagulation as the first and only feature of SARS-CoV-2 condition besides the usual morphological presentation of the WindSock LAA. (Folia Morphol 2021; 80, 3: 714–717)

Key words: COVID-19, SARS-CoV-2, coronavirus, atrial fibrillation, left atrial appendage

INTRODUCTION

Coronavirus disease 2019 (COVID-19) is a condition caused by a novel virus, severe acute respiratory syndrome coronavirus 2 (SARS-CoV-2) [10]. The real-time polymerase chain reaction (RT-PCR) test is the most reliable in diagnosing COVID-19. The disease's course ranges from entirely asymptomatic to severely ill patients. Hypercoagulation is often a complication of this disease, worsening the prognosis [3]. This complication seems to be aggravated in patients at higher risk of thromboembolic events, such as patients with atrial fibrillation (AF), in whom a thrombus formation in the left atrial appendage (LAA) is frequent. Additional factors that increase

Address for correspondence: Ludmiła Daniłowicz-Szymanowicz, MD, PhD, Department of Cardiology and Electrotherapy, Medical University of Gdansk, ul. Dębinki 7, 80–211 Gdańsk, Poland, tel: +58 349 39 10, fax: +58 349 39 20, e-mail: ludwik@gumed.edu.pl

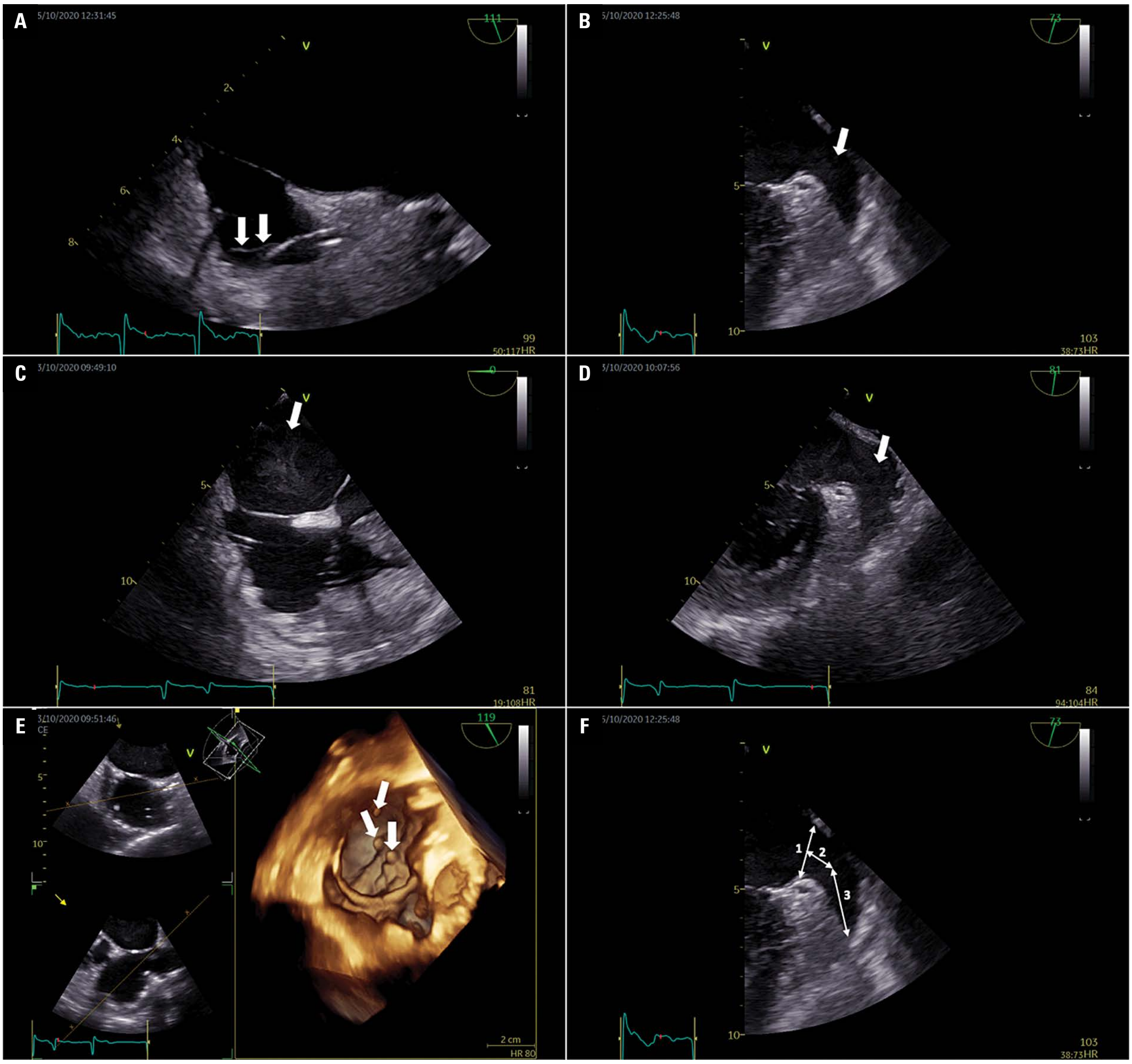

Figure 1. The figures visualise the image in transoesophageal echocardiography performed twice in the described patient. On admission to the Cardiology Department, the patient had linear echoes on the atrial electrode (**panel A** — arrows) and a clean left atrial appendage (LAA) (**panel B** — arrow). In a follow-up study after the spontaneous return of sinus rhythm and a week of apixaban (5 mg BID) therapy, the linear echoes on the atrial lead disappeared, while the left atrium filled with highly hyperechogenic blood (**panel C** — arrow) and LAA with the sludge (**panel D** — arrow) were visualised. Additionally, the long persistence of the bubbles of midazolam in the right atrium was observed (**panel E** — arrows). **Panel F** presents the dimensions of the LAA in the described patient; 1 — 1.7 cm, 2 — 0.8 cm, 3 — 2.4 cm.

the risk of formation of thrombus in the LAA are the specific anatomy of the LAA and the low left ventricular ejection fraction. We present a clinical case that presents SARS-CoV-2 infection as an additional cause of LAA thrombus formation.

CASE PRESENTATION

A 70-year-old woman with AF and negative RT-PCR test for SARS-CoV-2 was transferred from the district hospital to the Cardiology Department with suspicion of device-related infection after dual pacemaker implantation, performed 1 week before the admission. Additionally, the urinary tract infection was diagnosed, and empirical antimicrobial therapy was initiated, leading to a quick reduction of inflammatory markers. There were no pathologies connected with ventricle lead; however, in transoesophageal echocardiography (TEE), using two- and three-dimensional techniques, linear echoes associated with the atrial electrode were visualised (Fig. 1A). Due to the short time after the implantation and negative blood culture results, the thrombus was anticipated,

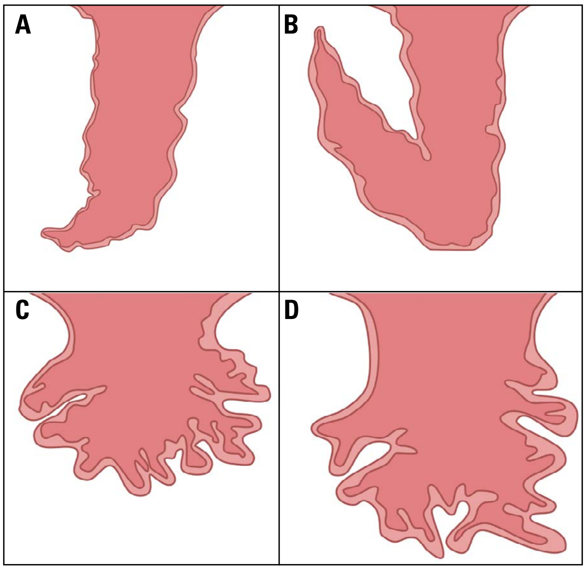

Figure 2. General scheme showing the four most common types of the left atrial appendage (LAA); **A.** The WindSock LAA; **B.** The ChickenWing LAA; **C.** The Cauliflower LAA; **D.** The Cactus LAA.

not bacterial vegetation. The LAA had typical morphology and sizes, as presented in Figure 1. Despite AF, there was no sludge or thrombus in the LAA (Fig. 1B). The spontaneous restoration of sinus rhythm was observed. The treatment with apixaban (5 mg BID) was initiated, and empirical antibiotic therapy was continued. After 1 week of the treatment, TEE was repeated with no linear echoes within the atrial electrode. Interestingly, despite permanent sinus rhythm and anticoagulation therapy with apixaban, the left atrium was filled with highly hyperechogenic blood (Fig. 1C) and the LAA with a sludge (Fig. 1D). Moreover, the long persistence of the bubbles of midazolam in the right atrium has been observed (Fig. 1E). The patient did not present any typical clinical COVID-19 symptoms [2], but had neutropenia, lymphopenia, low procalcitonin, hypoalbuminaemia, and increased C-reactive protein. We re-checked the RT-PCR test for SARS-CoV-2 infection, and the result was positive.

DISCUSSION

The LAA lies within the pericardium, in the left atrioventricular sulcus atop the left circumflex artery's proximal part and extends between the anterior and the lateral walls of the LA near the left pulmonary veins [11]. The LAA could be of various sizes, volumes, and shapes and often has several lobes [5, 8, 11]. Veinot et al. [11] found that the most common is the presence of 2 (54%) lobes, the second most frequent are an LAA with 3 (23%) lobes, then with 1 (20%) lobe and the least frequent is the presence of 4 (3%) lobes. The orifice of the LAA leads through the neck to the central appendage cavity, which can have a different shape depending on the type of an LAA. According to Wang et al. [12], the most frequent LAA anatomy is the WindSock LAA (Fig. 2A), which has no obvious bands, and one dominant lobe of sufficient length is the basic structure. Variations of this type of LAA appear with the different locations and number of secondary lobes descending downward from the dominant lobe. The second most frequent anatomy is the Cauliflower LAA (Fig. 2C), which, like the previous type, does not have obvious bands; an LAA is characterized by a limited overall length and more complex internal features. Its varieties are described by a more irregular shape of the orifice of the LAA, the number of significant lobes, and the lack of the dominant lobe. The ChickenWing LAA (Fig. 2B) is the third most common type; the main feature of that type of LAA is an obvious band in the proximal or middle part of the dominant lobe or a backward fold of the LAA at some distance from the orifice of the LAA. This type may differ in the presence or absence of additional lobes or twigs, with a different measured distance to this bend, and with different orientations of the bends to the main lobe. The last most common type is the Cactus LAA (Fig. 2D); its main feature is the dominant lobe with secondary lobes extending from the dominant lobe to the superior and inferior directions [12].

According to the literature, thromboembolic complications occur most frequently in patients with AF and the Cactus LAA [4]. Additionally, the small size of LAA, the presence of secondary lobes, the narrow orifice of the LAA, and excessive trabeculations result in low LAA peak flow velocities that could significantly increase the risk of thrombus formation LAA [1]. It should also be emphasized that the large size of the left atrium and the reduced left ventricular ejection fraction are additional risk factors for the development of thromboembolic complications.

In the described case, we presented echocardiographic evidence of hypercoagulation as the first and only feature of SARS-CoV-2 infection in the usual morphological presentation of the WindSock LAA (Fig. 1F). Despite the use of apixaban treatment, the lack of features promoting thrombus formation in the LAA (Fig. 1D), such as excessive trabeculations, a narrow junction of the proximal lobe of the LAA, a narrow junction between the distal lobe of the LAA and its proximal lobe, or the presence of additional LAA lobes, there has been a sludge in the LAA. The coagulation abnormalities in COVID-19 are postulated to result from acute inflammation in the organism and increased activity of inflammatory mediators [7]. The urinary tract infection could additionally attenuate the hypercoagulation status in our patient.

CONCLUSIONS

The connection between hypercoagulation features and COVID-19 in a patient without other typical infection indicators seems to be particularly difficult, as in the presented case. Based on the available literature about COVID-19 management, low-molecular-weight heparin should be considered for thromboembolic complications prophylaxis [6]. In contrast, oral anticoagulant therapy is not recommended due to its limited effectiveness, confirmed in our patient. The LAA in the case presented above did not show any features predisposing to thrombus formation; the LAA was of standard size and not narrow. Besides, a thrombus developed despite the patient's persistent sinus rhythm and anticoagulant treatment, which suggests a hypercoagulability state in the course of COVID-19. The presented case additionally shows that a negative test for SARS-CoV-2 infection does not always give a full guarantee that the patient is not infected, and the patient's clinical manifestation should be taken into account in further clinical decisions. It is worth emphasizing that modern echocardiography, including three-dimensional techniques, can be recognised as a part of comprehensive imaging technology that could be helpful in COVID-19 diagnosis [9].

Conflict of interest: None declared

REFERENCES

1. Al-Saady NM, Obel OA, Camm AJ. Left atrial appendage: structure, function, and role in thromboembolism. Heart. 1999; 82(5): 547–554, doi: 10.1136/hrt.82.5.547, indexed in Pubmed: 10525506.
2. Carfì A, Bernabei R, Landi F, et al. Persistent symptoms in patients after acute COVID-19. JAMA. 2020; 324(6): 603, doi: 10.1001/jama.2020.12603.
3. Connors J, Levy J. Thromboinflammation and the hypercoagulability of COVID-19. J Thromb Haemost. 2020; 18(7): 1559–1561, doi: 10.1111/jth.14849.
4. Di Biase L, Santangeli P, Anselmino M, et al. Does the left atrial appendage morphology correlate with the risk of stroke in patients with atrial fibrillation? Results from a multicenter study. J Am Coll Cardiol. 2012; 60(6): 531–538, doi: 10.1016/j.jacc.2012.04.032, indexed in Pubmed: 22858289.
5. Kamiński R, Kosiński A, Brala M, et al. Variability of the left atrial appendage in human hearts. PLoS One. 2015; 10(11): e0141901, doi: 10.1371/journal.pone.0141901, indexed in Pubmed: 26544191.
6. Marietta M, Vandelli P, Mighali P, et al. COVID-19 HD Study Group. Randomised controlled trial comparing efficacy and safety of high versus low Low-Molecular Weight Heparin dosages in hospitalized patients with severe COVID-19 pneumonia and coagulopathy not requiring invasive mechanical ventilation (COVID-19 HD): a structured summary of a study protocol. Trials. 2020; 21(1): 574, doi: 10.1186/s13063-020-04475-z, indexed in Pubmed: 32586394.
7. Panigada M, Bottino N, Tagliabue P, et al. Hypercoagulability of COVID-19 patients in intensive care unit: A report of thromboelastography findings and other parameters of hemostasis. J Thromb Haemost. 2020; 18(7): 1738–1742, doi: 10.1111/jth.14850, indexed in Pubmed: 32302438.
8. Panyawongkhanti M, Fuktongphan P, Chentanez V. Morphometric study of the left atrial appendage related to closure device deployment: a cadaveric study in Thai population. Folia Morphol. 2020; 79(1): 79–85, doi: 10.5603/FM.a2019.0066, indexed in Pubmed: 31162625.
9. Rozwadowska K, Raczak G, Sikorska K, et al. Influence of hereditary haemochromatosis on left ventricular wall thickness: does iron overload exacerbate cardiac hypertrophy? Folia Morphol. 2019; 78(4): 746–753, doi: 10.5603/FM.a2019.0025, indexed in Pubmed: 30835340.
10. Sławiński G, Lewicka E. What should a cardiologist know about coronavirus disease 2019? Kardiol Pol. 2020; 78(4): 278–283, doi: 10.33963/KP.15302, indexed in Pubmed: 32336069.
11. Veinot JP, Harrity PJ, Gentile F, et al. Anatomy of the normal left atrial appendage: a quantitative study of age-related changes in 500 autopsy hearts: implications for echocardiographic examination. Circulation. 1997; 96(9): 3112–3115, doi: 10.1161/01.cir.96.9.3112, indexed in Pubmed: 9386182.
12. Wang Y, Di Biase L, Horton RP, et al. Left atrial appendage studied by computed tomography to help planning for appendage closure device placement. J Cardiovasc Electrophysiol. 2010; 21(9): 973–982, doi: 10.1111/j.1540-8167.2010.01814.x, indexed in Pubmed: 20550614.

VIA MEDICA

CASE REPORT

Folia Morphol.
Vol. 80, No. 3, pp. 718–721
DOI: 10.5603/FM.a2020.0093

ISSN 0015–5659
eISSN 1644–3284
journals.viamedica.pl

Agenesis of the coeliac trunk: a case report and review of the literature

M. Karamanidi[1], D. Chrysikos[1], A. Samolis[1], V. Protogerou[1], N. Fourla[1], I. Michalis[1], G. Papaioannou[2], T. Troupis[1]

[1]*Department of Anatomy, Medical School, National and Kapodistrian University of Athens, Greece*
[2]*Department of Surgery, "Thriasio" General Hospital, Athens, Greece*

[Received: 9 June 2020; Accepted: 11 July 2020; Early publication date: 14 August 2020]

Vascular anatomical variations of the abdomen are very common. Awareness of these variations is of paramount importance in clinical practice mainly in achieving best results in minimal invasive or surgical vascular procedures. From surgical point of view, the preoperative knowledge of vascular anatomy and the relations to the surrounding structures and tissues aims to minimise inadvertent complications. Agenesis of the coeliac trunk is one of the rare anatomical variations of the abdominal aorta. Limited number of cases have been reported in the medical literature, most of which are based on angiographic and cadaveric studies of adult humans. In this paper, we report a case of absence of the coeliac trunk that has been detected as an incidental radiological finding in a female patient who was admitted with abdominal pain. (Folia Morphol 2021; 80, 3: 718–721)

Key words: coeliac trunk agenesis, tripus Halleri absence, anatomical variation

INTRODUCTION

Albrecht von Haller, a Swiss anatomist and physiologist described the trifurcation of the coeliac trunk in 1756, also known as tripus Halleri and it is still considered to be the normal appearance of the coeliac trunk, although numerous variation patterns have been described [27].

Anatomical variations of the unpaired branches of the coeliac trunk may be the result of anomalous embryogenesis of primitive ventral segmental (splanchnic) arteries which supply the gut and its derivatives based on Tandler's hypothesis in 1904 [24]. The 10^{th} primitive root of the ventral segmental artery becomes the left gastric artery, the 11^{th} becomes the splenic artery and the 13^{th} becomes the common hepatic artery. In case of agenesis of the coeliac trunk, the roots of the ventral segmental arteries do not regress and the longitudinal anastomoses regress completely [4, 11, 25].

The coeliac trunk, also known as the coeliac artery, is the first branch of the abdominal aorta arising anteriorly at the level of T12–L1 vertebral body. It is 1.5–2 cm in length and trifurcates into the left gastric artery, the common hepatic artery and the splenic artery which supply the liver, the stomach, the abdominal oesophagus, the spleen, the superior duodenum and the pancreas [23].

The tripus Halleri is still considered to be the normal appearance of the coeliac trunk, although numerous anatomical variations have been reported such as bifurcation or incomplete coeliac trunk, common origin with superior mesenteric artery, additional branches and common origin with superior or inferior mesenteric arteries.

Address for correspondence: Prof. T. Troupis, Department of Anatomy, School of Medicine, Faculty of Health Sciences, National and Kapodistrian University of Athens, 75 Mikras Asias str., Goudi, 11527 Athens, Greece, tel: +30-210-7462388, fax: +30-210-7462398, e-mail: ttroupis@med.uoa.gr

CASE REPORT

A 69-year-old female with no prior history of abdominal surgery was presented in the Out-patient Department of Surgery of our Hospital complaining of a 10 hour abdominal pain of sudden onset. Her examination was unremarkable except for epigastric tenderness with no presentation of rebound sign. Ultrasonogram was undertaken without significant results. An abdominal computed tomography (CT), enhanced with oral and intra venous medium contrast was performed without remarkable findings. However, a complete agenesis of the coeliac trunk was revealed incidentally (type V according to Morita's classification). In this case the left gastric, the common hepatic and the splenic artery arose independently from the abdominal aorta (Fig. 1). In three-dimensional (3D) reconstruction we clarified that the left gastric artery arose from the anterior wall of the abdominal aorta (diameter 4 mm) while the splenic (diameter 3.5 mm) and common hepatic artery (diameter 3.3 mm) were arising lower from the abdominal aorta (Fig. 2).

Although we consider this incidental finding unrelated, the patient's symptoms were attributed to indigestion and she was treated with proton pump inhibitors. A gastroscopy was arranged on a regular basis, in order to exclude peptic ulcer disease.

Figure 1. Abdominal computer tomography depicting separate origin of the left gastric, splenic artery (arrow 1) and common hepatic artery (arrow 2) from the abdominal aorta.

Figure 2. Abdominal computer tomography with three-dimensional reconstruction depicting absence of the coeliac trunk. Left gastric, diameter 4 mm (arrow 1), common hepatic, diameter 3.3 mm (arrow 2) and splenic artery, diameter 3.5 mm (arrow 3) arising directly from the abdominal aorta.

DISCUSSION

Awareness of vascular anatomical variations in the abdominal cavity is important either from topographical anatomy or from a surgical perspective due to their relations with the surrounding structures.

Knowing the anatomy preoperatively assists surgeons during hepatobiliary and pancreatic surgery in order to dissect the coeliac trunk branches during liver and pancreatic resections. Any vascular variation could complicate any operation due to inadvertent vascular injury. Furthermore, oesophagogastric resection and total gastrectomy involve the ligation of left gastric vessels near their origin.

Lymph node dissection performed due to oesophageal, gastric, hepatobiliary or pancreatic cancer requires accurate knowledge of the vascular anatomy, in order to be performed meticulously avoiding any possible and preventable complications.

Transplant surgeons must be extremely cautious in order to dissect and preserve the common hepatic artery and the coeliac trunk integrity when they perform liver transplantation. The risk of damaging these arteries is higher during the cold phase of dissection and if there is a case any arterial anomaly the involved vessel may have to be reconstructed before proceeding to implantation. In the case of pancreatic transplantation the gastroduodenal, the splenic and the superior mesenteric arteries are vital as they provide its blood supply [11, 17].

Moreover, preoperative knowledge of coeliac trunk anatomy and its possible variations is extremely important during vascular operations, performed for thoracoabdominal aneurysm repair. The two therapeutic surgical options for this disease are an open and an endovascular procedure. Both, for technically different reasons demand preoperative topographic information of the involved vessels, to avoid intraoperative complications.

Interventional radiologists should be aware of the coeliac trunk variations when performing a diagnostic or a therapeutic angiography. Pseudoaneurysms can be treated by selective embolisation and possible arterial variations should always be taken into account during the procedure [17].

There are numerous classifications of the coeliac trunk morphology (Lipshutz 1917, Adachi 1928, Morita 1935, Michels 1955) [1, 9, 12, 14].

The pattern of tripus Halleri is considered to be normal and any abnormal branching is considered as an anatomical variation. Agenesis of the coeliac trunk was not described in Adachi's classification [1] though Morita in 1935 [14] proposed five types for the coeliac trunk where type I is normal coeliac trunk, type II — hepatogastric trunk, type III — gastrosplenic trunk, type IV — hepatogastric trunk, and type V — the absence of the coeliac trunk [14]. The anatomical variation reported in our case is of the fifth type (V) in Morita's classification and it is considered to be extremely rare (0–2.6%) [10, 19, 22, 25, 26, 29].

Geofry Saint-Hillaire reported the first case of this rare variation in 1832 as described by Okada in 1983 [15]. Rossi and Cova in 1904 [21] reported such a case and one was reported by Picquand in 1910 according to the statements by Eaton in 1917 [5] and Morita in 1935 [14]. In 1969, Itoh reported the first cadaveric case [7]. Petrella et al. in 2007 [18] reported 1 case of agenesis of the coeliac trunk in a study of 69 (1.12%) cadavers. Yi et al. [29] described such a case during routine gross dissection in 2008 where the coeliac trunk was absent and the arteries arose independently from the abdominal aorta. Yadav et al. [28] reported a case of a female cadaver in 2014 while another case of an adult male cadaver was reported by Badagabettu et al. in 2016 [2]. Lee et al. [8] reported a case of a male cadaver in 2016. However since the first report of Saint-Hillaire only 31 reported cases of such variation have been demonstrated by Iacob et al. 2014 [6]. Since then 4 additional cases have been reported to the best of our knowledge [2, 8, 20, 28]. The majority of these cases reported worldwide were observed during anatomical dissections in cadaveric studies, while others were detected by imaging studies. In 1965, Morettin et al. [13] reported a case based on arteriography prior to surgical exploration. Basar et al. [3] reported a case presented in angiography in 1995. In 2011, Matusz et al. [11] reported a case based on multidetector-row CT while another case was reported by Rastogi et al. in 2016 [20].

Agenesis of the coeliac trunk was observed in 0.19% of cases according to Matusz et al. [11] based on a large series of 10,750 cases from 19 studies including anatomical dissection, surgical procedures and radiological studies. The reported prevalence of the case reports noted above varies from 0.1% according to Vandamme and Bonte [25] to 2.6% according to Venieratos et al. [26] in cadaveric studies of adult humans. The latest cadaveric study by Olewnik et al. [16] in 2017 reported a prevalence of 2.5% of agenesis of the coeliac trunk. In this study the left gastric artery, the common hepatic artery and the splenic artery arose directly from the abdominal aorta, as reported in accordance with our case as well.

Finally, in comparison to most of the previous reported studies, this rare anatomical variation is mainly detected in post-mortem examinations or during cadaveric anatomical dissections. In our case, the agenesis of the coeliac trunk was an incidental finding with clinical significance, revealed during an abdominal CT with 3D reconstruction.

CONCLUSIONS

The knowledge of vascular anatomical variations of the coeliac artery and its branching pattern is of paramount importance during various operative, diagnostic and endovascular procedures. Agenesis of the coeliac trunk is a rare anatomical variation.

Preoperative awareness of coeliac trunk absence is of paramount importance assisting hepatobiliary, pancreatic, upper gastrointestinal and vascular surgeons to perform meticulously a wide range of operations in the coeliac trunk.

Conflict of interest: None declared

REFERENCES

1. Adachi B. Das Arteriensystem der Japaner. I Maruzen 1928.
2. Badagabettu SN, Padur AA, Kumar N, et al. Absence of the celiac trunk and trifurcation of the common hepatic artery: a case report. J Vasc Bras. 2016; 15(3): 259–262,

doi: 10.1590/1677-5449.004016, indexed in Pubmed: 29930600.
3. Başar R, Onderoğul S, Cumhur T, et al. Agenesis of the celiac trunk: an angiographic case. Kaibogaku Zasshi. 1995; 70(2): 180–182, indexed in Pubmed: 7785416.
4. Douard R, Chevallier JM, Delmas V, et al. Clinical interest of digestive arterial trunk anastomoses. Surg Radiol Anat. 2006; 28(3): 219–227, doi: 10.1007/s00276-006-0098-8, indexed in Pubmed: 16547602.
5. Eaton P. The coeliac axis. Anat Rec. 1917; 13(6): 369–374, doi: 10.1002/ar.1090130605.
6. Iacob N, Sas I, Joseph SC, et al. Anomalous pattern of origin of the left gastric, splenic, and common hepatic arteries arising independently from the abdominal aorta. Rom J Morphol Embryol. 2014; 55(4): 1449–1453, indexed in Pubmed: 25611280.
7. Itoh SA. case of no common trunk formation in the celiac arterial system. J Jud Med Soc. 1969; 77: 578.
8. Lee JK, Kang SR, Kim J, et al. A rare variation of the incomplete coeliac trunk. Folia Morphol. 2016; 75(1): 122–124, doi: 10.5603/FM.a2015.0074, indexed in Pubmed: 26365854.
9. Lipshutz B. A composite study of the coeliac axis artery. Ann Surg. 1917; 65(2): 159–169, doi: 10.1097/00000658-191702000-00006, indexed in Pubmed: 17863663.
10. Marco-Clement I, Martinez-Barco A, Ahumada N, et al. Anatomical variations of the celiac trunk: cadaveric and radiological study. Surg Radiol Anat. 2016; 38(4): 501–510, doi: 10.1007/s00276-015-1542-4, indexed in Pubmed: 26267305.
11. Matusz P, Miclaus GD, Ples H, et al. Absence of the celiac trunk: case report using MDCT angiography. Surg Radiol Anat. 2012; 34(10): 959–963, doi: 10.1007/s00276-012-0989-9, indexed in Pubmed: 22689084.
12. Michels NA. Blood supply and anatomy of the upper abdominal organs, with a descriptive atlas. Lippincot, Philadelphia 1955.
13. Morettin LB, Baldwin-Price HK, Schreiber MH. Congenital absence of the celiac axis trunk. Am J Roentgenol Radium Ther Nucl Med. 1965; 95(3): 727–730, doi: 10.2214/ajr.95.3.727, indexed in Pubmed: 5844937.
14. Morita M. Reports and conception of three anomalous cases in the area of the celiac and the superior mesenteric arteries. Igaku Kenkyu [Acta Med]. 1935; 9: 159–172.
15. Okada S, Ohta Y, Shimizu T, et al. A rare anomalous case of absence of the celiac trunk--the left gastric, the splenic and the common hepatic arteries arose from the abdominal aorta independently. Okajimas Folia Anat Jpn. 1983; 60(1): 65–71, doi: 10.2535/ofaj1936.60.1_65, indexed in Pubmed: 6634048.
16. Olewnik Ł, Wysiadecki G, Polguj M, et al. Types of coeliac trunk branching including accessory hepatic arteries: a new point of view based on cadaveric study. Folia Morphol. 2017; 76(4): 660–667, doi: 10.5603/FM.a2017.0053, indexed in Pubmed: 28612916.
17. Panagouli E, Venieratos D, Lolis E, et al. Variations in the anatomy of the celiac trunk: A systematic review and clinical implications. Ann Anat. 2013; 195(6): 501–511, doi: 10.1016/j.aanat.2013.06.003, indexed in Pubmed: 23972701.
18. Petrella S, Rodriguez C, Sgrott E, et al. Anatomy and variations of the celiac trunk. Int J Morphol. 2007; 25(2), doi: 10.4067/s0717-95022007000200002.
19. Picquand G. Researches sur l'anatomie du trone coeliaque et de ses branches. Bibliogr Anat. 1910; 19: 159–201.
20. Rastogi R, Meena G, Yuktika G, et al. Agenesis of celiac axis – a rare clinical entity. J Colitis Diverticulitis. 2016; 1(1): 1–2.
21. Rossi G, Cova E. Studio morfologico delle arterie dello stomaco. Arch Ital Anat Embryol. 1904; 3: 485–526.
22. Song SY, Chung JW, Yin YH, et al. Celiac axis and common hepatic artery variations in 5002 patients: systematic analysis with spiral CT and DSA. Radiology. 2010; 255(1): 278–288, doi: 10.1148/radiol.09090389, indexed in Pubmed: 20308464.
23. Standring S. Gray's Anatomy. 40th Ed. Churchill Livingstone Elsevier, London 2008: 1073–1074.
24. Tandler J. über die Varietäten der Arteria coeliaca und deren Entwickelung. Beiträge und Referate zur Anatomie und Entwickelungsgeschichte. 1904; 25(2): 473–500, doi: 10.1007/bf02300762.
25. Vandamme JP, Bonte J. The branches of the celiac trunk. Acta Anat (Basel). 1985; 122(2): 110–114, doi: 10.1159/000145991, indexed in Pubmed: 4013640.
26. Venieratos D, Panagouli E, Lolis E, et al. A morphometric study of the celiac trunk and review of the literature. Clin Anat. 2013; 26(6): 741–750, doi: 10.1002/ca.22136, indexed in Pubmed: 22886953.
27. von Haller A. Icones anatomicae in quibus aliquae partes corporis humani delineatae preponuntur et arteriarum potissimum historia continetur. Gottigen Vandenhoek 1756.
28. Yadav SP, Gangane SD, Borate SM. A case of absent coeliac trunk. Ind J Med Res. 2014; 4: 286–288.
29. Yi SQ, Terayama H, Naito M, et al. Absence of the celiac trunk: case report and review of the literature. Clin Anat. 2008; 21(4): 283–286, doi: 10.1002/ca.20627, indexed in Pubmed: 18428985.

VIA MEDICA

CASE REPORT

Folia Morphol.
Vol. 80, No. 3, pp. 722–725
DOI: 10.5603/FM.a2020.0082

ISSN 0015–5659
eISSN 1644–3284
journals.viamedica.pl

A case of solitary kidney with duplex collecting systems and renal vascular variants in an adult male cadaver

M.S. Salimy, G.A. Luiselli, M. Yuen, R.C. Healy, S.G. Shah, E.L. Giannaris, M. Das, A.E. Wink

University of Massachusetts Medical School, Worcester, MA, United States

[Received: 28 April 2020; Accepted: 7 July 2020; Early publication date: 29 July 2020]

We describe a unique solitary kidney with duplex collecting system and vascular variation observed in an 86-year-old white male formaldehyde- and phenol-fixed cadaver during routine academic dissection. The left renal fossa was empty with an intact adrenal gland, and the right renal fossa contained a fused renal mass with apparent polarity between the superior and inferior regions and two renal pelves converging into a single ureter. There were three right renal arteries supplying the renal mass; the superior and middle arteries were noted to be postcaval and the inferior artery was precaval. There were also two right renal veins draining into the inferior vena cava and following a regional distribution with the superior vein draining the inferior portion of the renal mass. Despite generally being asymptomatic, the detection of renal anatomical variants is clinically important for appropriate patient management and surgical interventions. (Folia Morphol 2021; 80, 3: 722–725)

Key words: renal artery, renal vein, renal pelvis, anatomic variation, multiple renal arteries, multiple renal veins

INTRODUCTION

The kidneys form between weeks 4 and 12 of development. Congenital solitary kidney (CSK), also known as unilateral renal agenesis, is the failure of one kidney to develop. The estimated prevalence of CSK based on autopsy study is 1 in 1000 cases, occurring slightly more frequently in males and on the left side [20]. CSK is typically asymptomatic, but can be associated with contralateral vesicoureteral reflux, hydronephrosis, hydroureteronephrosis, proteinuria, and genital anomalies [15, 20].

Each kidney is typically supplied by a single renal artery arising from the abdominal aorta and one renal vein draining into the inferior vena cava (IVC). Variation in the origin, number, course, division, and penetration of renal arteries is common [15]. The estimated incidence of additional renal arteries arising from the aorta is between 25% and 30% [22, 19], and this incidence varies among populations [7]. Variation in the number of renal veins is less common than in the renal arteries [22]; one study of multiple renal veins showed a prevalence of 21.6% on the right side [4].

We report a unique case of a solitary kidney with two renal pelves draining into a single ureter with accompanying vascular variations.

CASE REPORT

During academic dissection of a formaldehyde- and phenol-fixed 86-year-old white male cadaver, we

Address for correspondence: Dr. A.E. Wink, Department of Radiology, University of Massachusetts Medical School, 55 Lake Avenue North, Worcester, MA 01655, United States, tel: 1-508-856-6920, e-mail: Alexandra.Wink@umassmed.edu

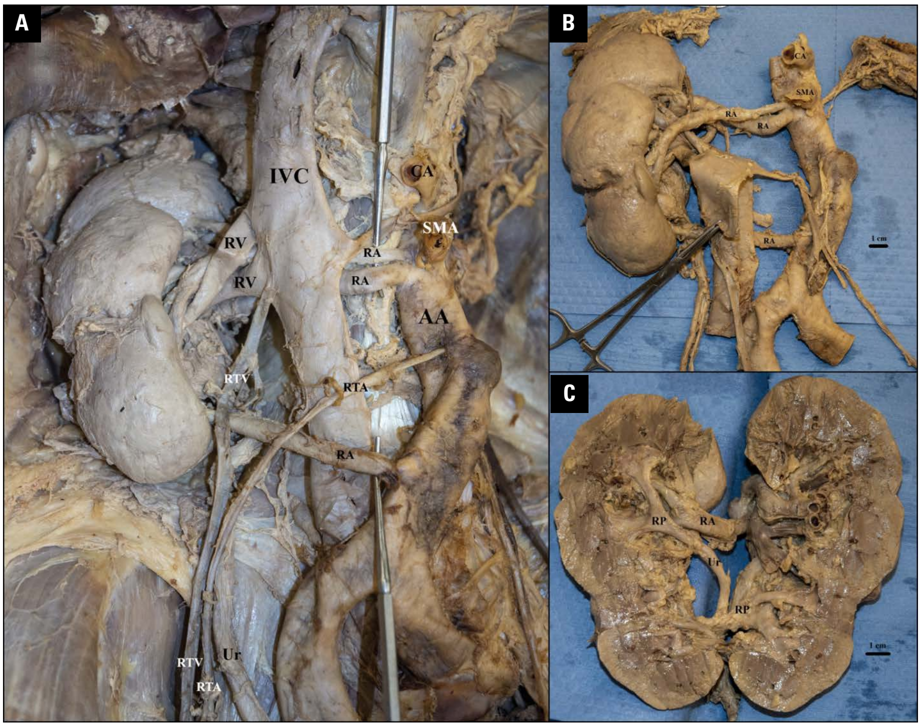

Figure 1. Solitary kidney with dual collecting systems and vascular variation in an adult cadaver. **A.** In-situ photograph of the renal mass and associated vasculature; **B.** Ex-situ photograph of the renal mass and associated vasculature; the inferior vena cava (IVC) has been reflected to demonstrate the course of the two cranial renal arteries; **C.** Sagittal section of the renal mass demonstrating two renal pelves converging into a single ureter; AA — abdominal aorta; CA — coeliac artery; RA — renal artery; RP — renal pelvis; RTA — right testicular artery; RTV — right testicular vein; RV — renal vein; SMA — superior mesenteric artery; Ur — ureter.

noted an empty left renal fossa. The left adrenal gland was present and its vascular supply arose from the abdominal aorta and drained into the IVC. The left testicular vein was not preserved during dissection and its drainage could not be confirmed. The left testicular artery arose from the abdominal aorta. In the right renal fossa, we exposed an enlarged renal mass (Fig. 1), measuring approximately 16 cm from the superior to inferior poles and 5.5 cm from the lateral to medial borders. The renal hilum was below L1, the expected vertebral level. Upon removal of the capsule, we observed a protrusion on the anterior inferior pole of the renal mass.

Further dissection revealed two distinct medially-oriented renal pelves — one draining the upper portion of the kidney and one draining the lower portion of the kidney. Two distinct tributaries converged into a single ureter (Fig. 1C), which descended to the bladder. No additional ureters were encountered in the dissection, and the bladder was not preserved sufficiently to detect the ureteric orifice(s).

Three right renal arteries originated from the abdominal aorta and we refer to them as they arose from the aorta: superior, middle, and inferior. The superior and middle arteries were postcaval and arose from the aorta at approximately the L2 vertebral level, and the inferior artery was precaval and arose from the aorta at approximately the L4 vertebral level. The superior artery crossed anteriorly to the middle artery and bifurcated prior to entering the inferior hilum to supply the more anterior and inferior portion of the kidney. The middle artery crossed posterior to the superior artery and bifurcated into an anterior and posterior branch. The anterior branch gave rise to two polar arteries supplying the superior pole of the kidney before entering the hilum to supply the anterior aspect of the superior (more posterior) portion of the kidney. The posterior branch of the middle artery was distributed to the posterior aspect of the superior portion of the kidney. The inferior artery entered the inferior hilum to supply the anterior inferior portion of the kidney. We identified two right renal veins draining into the IVC. The superior vein crossed anterior to the inferior vein and drained the inferior portion of the kidney, while the inferior vein drained the superior portion. The sagittal dissection of the kidney precluded any attempt to trace the vessels more distally.

DISCUSSION

We report a unique case of CSK with duplex collecting system and atypical vasculature (i.e., three right renal arteries and two right renal veins) in an elderly male cadaver. There has been one other reported case of CSK with multiple renal arteries in a female patient with uterine didelphys [15]. This report did not comment on the renal veins, renal pelves, or ureters. The combination of bifid ureters or duplex collecting systems and renal vascular variants (multiple renal arteries and/or renal veins) has been previously reported, but with both kidneys present [2, 10, 21]. The combination of variants described in our report, namely CSK, multiple renal arteries and veins, and two renal pelves converging into a single ureter, has not been reported previously to our knowledge.

An alternative explanation for this morphology is cross-fused renal ectopia (CFRE) with a single ureter. This phenomenon that has been described elsewhere in various contexts [8, 9, 12]; however, these reports exhibited characteristics not seen in our case, namely "pancake morphology", anterior orientation of the renal pelves, and atypical location of the renal mass. The presence of multiple renal vessels is also common in cross-fused renal ectopia [11, 16–18], with many cases reporting atypical origins of the renal arteries, such as the common iliac artery [7]. We report all renal arteries arising from the right side of the abdominal aorta. In CFRE with a single ureter, a scar for the second ureteric orifice is still present on the internal surface of the urinary bladder [8]. The urinary bladder was not preserved sufficiently to detect a second ureteric orifice on the left side; thus, we cannot confirm that our case is one of CFRE. Nonetheless, many of the clinical implications and possible complications of CFRE are similar to those related to general anomalies of upper urinary tract anatomy [13, 18].

Ureteral duplication has a reported frequency of 0.6–1.0% [1]. The ureteric bud, an extension of the mesonephric duct, is the precursor to the ureter. The ureteric bud penetrates the primitive kidney by day 32 of development and elongates and bifurcates to form the ureter, renal pelvis, and major and minor calyces by week 7. The duplicated pelvis and partially bifid ureter described here could be the result of early bifurcation of the ureteric bud. Bifid ureters are typically asymptomatic, though recurrent urinary infections, flank pain, incontinence, and haematuria may arise as a result of stagnation or reflux of urine from one collecting system into another [5, 21].

Clinicians should be aware of these renal anomalies and understand that genitourinary complications may arise from them. There may also be associations between urinary tract anomalies and anomalies of the cardiovascular, central nervous, genital tract, skeletal system, and the gastrointestinal tract. Despite requiring a unique surgical approach, bifid ureters do not affect the complication rate or outcomes of renal transplantation [1].

We also report vascular variation in this donor specimen: two twisting, more cranially-located renal arteries and one additional caudal, precaval renal artery. During development, the kidneys are supplied by transient aortic branches. As the kidneys ascend during weeks six through nine of gestation, these transient branches disintegrate and reform repeatedly to accommodate the ascent. The final pair of arteries to form becomes the renal arteries. If one or more pairs of transient renal arteries fail to regress, they remain as accessory renal arteries. The presence of additional renal arteries can also be explained by genetic background, oxygenation, and haemodynamic changes [3].

Co-occurrence of renal artery and renal vein variations is likely: Cinar and Türkvatan found an association of renal artery and renal vein variation in 15.5% of 504 patients [4]. The renal veins are formed by the anastomosis of the supracardinal and subcardinal segments of the primitive IVC. Dorsal and ventral renal veins form, but the dorsal typically regresses and the ventral vein persists as the renal vein [14]. Persistence of the dorsal renal vein could account for the two renal veins seen in this case.

Renal vascular variations are typically asymptomatic but may have clinical symptoms such as ischaemia or hypertension [21]. Multiple renal vessels also create surgical challenges during nephrectomy and during aortic reconstruction surgery. Vascular surgeons should be prepared to preserve or revascularise the anomalous renal arteries [6]. In addition, these variants put patients at risk for catastrophic bleeding, so it is crucial for urologists and pelvic surgeons to be vigilant for variant vasculature [9]. Angiography is recommended prior to any surgical procedure involving renal vasculature.

CONCLUSIONS

Congenital solitary kidney is a renal anomaly that may be asymptomatic throughout life and remain undetected until incidental finding on autopsy, or it may present with genitourinary symptoms, such as vesicoureteral reflux. Physicians should consider the possibility of CSK in the context of unexplained genitourinary complications and conduct imaging studies to identify such cases and prevent further complications. As seen in our case and another report [15], variations in arterial supply and venous drainage is common in CSK, and variation in ureteric anatomy is also possible. If a patient with CSK undergoes invasive surgery, it is important for the surgeon to plan for potential anatomical and vascular variations.

Acknowledgements

We would like to thank the anatomical donors for their contribution to our education. We also acknowledge Ms. Amanda Collins, Dr. Yasmin Carter, and Ms. Elizaveta Reznichenko for their assistance with the dissection and preparation of the donor specimen and Ms. Charlene Baron for preparation of the images.

Conflict of interest: None declared

REFERENCES

1. Alberts VP, Minnee RC, van Donselaar-van der Pant KAMI, et al. Duplicated ureters and renal transplantation: a case-control study and review of the literature. Transplant Proc. 2013; 45(9): 3239–3244, doi: 10.1016/j.transproceed.2013.06.012, indexed in Pubmed: 24182792.
2. Chakravarthi KK, Karuneswari DP, Uma MN. Congenital unilateral double renal pelvis and double ureters associated with triple renal veins and left retro aortic renal vein. Int J Chem Life Sci. 2013; 2(5): 1159–1162.
3. Chawla K, Gupta R, Singh HJ, et al. Bilateral bifid ureter with unilateral renal vasculature variations. Surg Radiol Anat. 2014; 36(4): 393–396, doi: 10.1007/s00276-013-1170-9, indexed in Pubmed: 23873247.
4. Çınar C, Türkvatan A. Prevalence of renal vascular variations: Evaluation with MDCT angiography. Diag Interv Imaging. 2016; 97(9): 891–897, doi: 10.1016/j.diii.2016.04.001.
5. Das S, Dhar P, Mehra RD. Unilateral isolated bifid ureter — a case report. J Anat Soc India. 2001; 50(1): 43–44.
6. de Virgilio C, Gloviczki P, Cherry KJ, et al. Renal artery anomalies in patients with horseshoe or ectopic kidneys: the challenge of aortic reconstruction. Cardiovasc Surg. 1995; 3(4): 413–420, doi: 10.1016/0967-2109(95)94161-o, indexed in Pubmed: 7582997.
7. Gulas E, Wysiadecki G, Cecot T, et al. Accessory (multiple) renal arteries - Differences in frequency according to population, visualizing techniques and stage of morphological development. Vascular. 2016; 24(5): 531–537, doi: 10.1177/1708538116631223, indexed in Pubmed: 26945775.
8. Horai K, Naito M, Yakura T, et al. A case of pancake kidney with a single ureter in the retroperitoneal space. Anat Sci Int. 2018; 93(4): 563–565, doi: 10.1007/s12565-018-0442-1, indexed in Pubmed: 29777511.
9. Kanchan T, Murlimanju BV, Saralaya VV. Pancake kidney with a single ureter: a rare incidental observation at autopsy. Anat Sci Int. 2017; 92(1): 142–146, doi: 10.1007/s12565-016-0329-y, indexed in Pubmed: 26848753.
10. Kannabathula A, Rai G, Singh KC, et al. Unilateral double pelvis bifid ureter associated with multiple variations of renal vessels. Int J Anat Res. 2016; 4(4.2): 3100–3104, doi: 10.16965/ijar.2016.412.
11. Kaufman MH, Findlater GS. An unusual case of complete renal fusion giving rise to a 'cake' or 'lump' kidney. J Anat. 2001; 198(Pt 4): 501–504, doi: 10.1046/j.1469-7580.2001.19840501.x, indexed in Pubmed: 11327213.
12. Khanduri S, Tyagi E, Yadav VK, et al. Crossed fused renal ectopia with single ureter and single renal vein: a rare case. Cureus. 2019; 11(1): e3914, doi: 10.7759/cureus.3914, indexed in Pubmed: 30931185.
13. Loganathan AK, Bal HS. Crossed fused renal ectopia in children: a review of clinical profile, surgical challenges, and outcome. J Pediatr Urol. 2019; 15(4): 315–321, doi: 10.1016/j.jpurol.2019.06.019, indexed in Pubmed: 31331806.
14. Mathews R, Smith PA, Fishman EK, et al. Anomalies of the inferior vena cava and renal veins: embryologic and surgical considerations. Urology. 1999; 53(5): 873–880, doi: 10.1016/s0090-4295(99)00007-2, indexed in Pubmed: 10223477.
15. Matusz P, Miclaus GD, Banciu CD, et al. Congenital solitary kidney with multiple real arteries: case report using MDCT angiography. Rom J Morphol Embryol. 2015; 56(2 Suppl): 823–826.
16. Miclaus GD, Pupca G, Gabriel A, et al. Right lump kidney with varied vasculature and urinary system revealed by multidetector computed tomographic (MDCT) angiography. Surg Radiol Anat. 2015; 37(7): 859–865, doi: 10.1007/s00276-014-1390-7, indexed in Pubmed: 25380828.
17. Palit S, Datta AK, Tapadar AA. Rare presentation of rudimentary ectopic right kidney fused to the lower pole of the left with multiple aberrant renal vessel – a case report. J Anat Soc India. 2008; 57(2): 146–150.
18. Pupca G, et al. Left crossed fused renal ectopia L-shaped kidney type, with double nutcracker syndrome (anterior and posterior). Rom J Morphol Embryol. 2014; 55: 1237–1241.
19. Satyapal KS, Haffejee AA, Singh B, et al. Additional renal arteries: incidence and morphometry. Surg Radiol Anat. 2001; 23(1): 33–38, doi: 10.1007/s00276-001-0033-y, indexed in Pubmed: 11370140.
20. Shapiro E, Goldfarb DA, Ritchey ML. The congenital and acquired solitary kidney. Rev Urol. 2003; 5(1): 2–8, indexed in Pubmed: 16985610.
21. Stojadinovic D, Zivanovic-Macuzic I, Sazdanovic P, et al. Concomitant multiple anomalies of renal vessels and collecting system. Folia Morphol. 2020; 79(3): 627–633, doi: 10.5603/FM.a2019.0108, indexed in Pubmed: 31617578.
22. Tubbs RS, Shoja MM, Loukas M. Bergman's Comprehensive Encyclopedia of Human Anatomic Variation. John Wiley & Sons, Hoboken NJ 2016.

VIA MEDICA

CASE REPORT

Folia Morphol.
Vol. 80, No. 3, pp. 726–729
DOI: 10.5603/FM.a2020.0081

ISSN 0015–5659
eISSN 1644–3284
journals.viamedica.pl

Aberrant right subclavian artery in a cadaver: a case report of an aortic arch anomaly

M.A. Alghamdi[1, 2], L.N. AL-Eitan[3, 4], B. Elsy[1], A.M. Abdalla[1], H. Mutwakil Mohammed[1], A.G.A. Salih[1], S. Al Hilal Al Ghamdi[5]

[1]*Department of Anatomy, College of Medicine, King Khalid University, Abha, Saudi Arabia*
[2]*Genomics and Personalised Medicine Unit, College of Medicine, King Khalid University, Abha, Saudi Arabia*
[3]*Department of Applied Biological Sciences, Jordan University of Science and Technology, Irbid, Jordan*
[4]*Department of Biotechnology and Genetic Engineering, Jordan University of Science and Technology, Irbid, Jordan*
[5]*Department of Surgery, College of Medicine, King Khalid University, Abha, Saudi Arabia*

[Received: 18 April 2020; Accepted: 25 July 2020; Early publication date: 29 July 2020]

In early embryogenesis, aortic anomalies occur as a consequence of disorders in the development of the primitive aortic arches system. Aberrant right subclavian artery, also known as arteria lusoria, is one of the important congenital anomalies of the aortic arch, in which the right subclavian artery arises from the arch of aorta instead of the brachiocephalic trunk. During routine dissection of a female cadaver, we observed retro-oesophageal aberrant right subclavian artery arising as the fourth branch from the aortic arch. In this case, the brachiocephalic trunk was absent. Early detection of aortic arch anomalies through diagnostic interventions is helpful to avoid complications during surgical procedures. (Folia Morphol 2021; 80, 3: 726–729)

Key words: anatomical variant, aortic arch, retro-oesophageal, arteria lusoria

INTRODUCTION

Anatomical variations in the human body do exist externally and internally where the latter may be presenting some pathological consequences or a life-threatening factor during surgical procedures. Aberrant right subclavian artery (ARSA) is the commonest congenital aortic arch anomaly with an incidence of 0.5% to 1.8% [25]. ARSA, or arteria lusoria, is a rare anatomical variation in the general population and has a female predominance [13, 23]. Right subclavian artery (RSA) normally originates from the brachiocephalic trunk, but when this anomaly is present, the brachiocephalic trunk is absent. Therefore, four large arteries (i.e. right common carotid artery, left common carotid artery, left subclavian artery and RSA) arises from the aortic arch, in which the RSA has an aberrant origin arises from the most distal left side [16, 23]. This anomaly is frequently asymptomatic; however, in some cases, it may be associated with clinical symptoms such as compression, dysphagia (dysphagia lusoria), cough, and chest pain [3, 16, 24, 25]. According to Vučurević et al. [27] aortic arch branching classification, type 4 pattern was found in this case report. Here, we report a case of a female cadaver with an ARSA and reviewed the aortic arch branching variations, its embryological development and clinical significances.

Address for correspondence: Dr. M.A. Alghamdi, King Khalid University PO Box 641, Abha, Asir Region, Postcode: 61421, Saudi Arabia, tel: 966 17 241 7866, Mobile: 966 505236044, e-mail: m.alghamdi@kku.edu.sa

This work was conducted at the Anatomy Department of King Khalid University (KKU), Abha, Saudi Arabia.

CASE REPORT

During a routine dissection at the Anatomy Department of King Khalid University, a female cadaver of unknown age was presented with a retro-oesophageal ARSA. The branches were carefully dissected to identify their courses and photographed.

We measured the diameters of the arch of aorta and its branches with a calliper. The diameter of the aortic arch was measured prior to the origin of the right common carotid artery. The descending aorta diameter was performed at a distance of 1 cm from the origin of the branching of ARSA. The diameters of the right common carotid, left common carotid, and left subclavian and aberrant right subclavian were measured at 1 cm from their origins (Table 1).

In the present case, we observed absences of brachiocephalic trunk and presences of four branches namely, right common carotid, left common carotid, left subclavian artery and ARSA from right to left side of the aortic arch (Fig. 1).

Table 1. Measured diameters of the aortic arch and its branches in millimetres

Aortic arch	28
Descending aorta	22
Left common carotid artery	8
Right common carotid artery	8
Left subclavian artery	9
Aberrant right subclavian artery	16

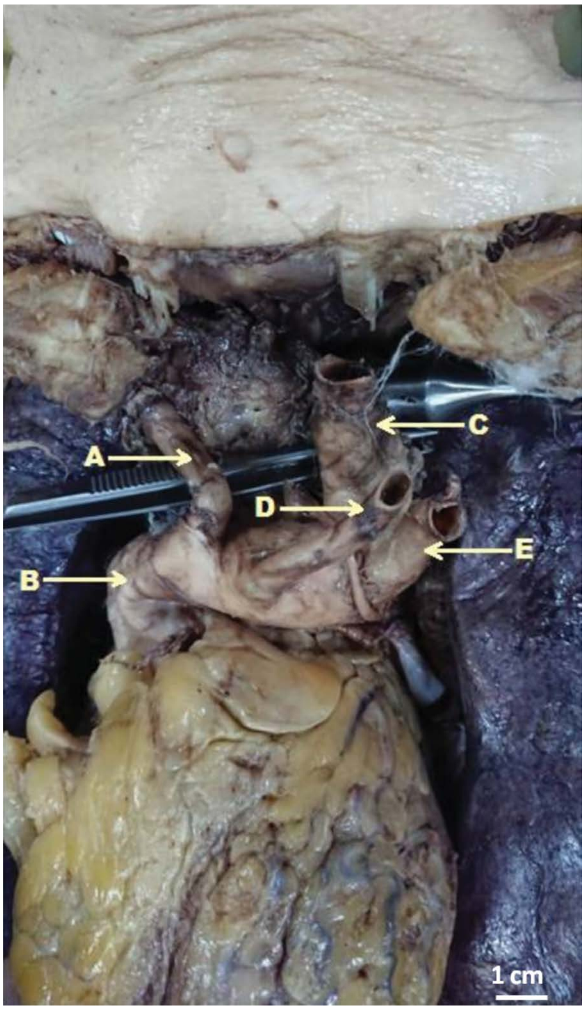

Figure 1. Right common carotid artery (A), aortic arch (B), retro-oesophageal aberrant right subclavian artery (C), left common carotid artery (D) and left subclavian artery (E).

DISCUSSION

Normally during embryological development, the distal right dorsal aorta degenerates in the double aortic arches system. RSA develops from the right 4th aortic arch and 7th cervical intersegmental artery. In the case of ARSA, the right 4th aortic arch, 7th intersegmental artery, proximal and persistent distal right dorsal aorta involve in the formation of this cardiac malformation [3, 25, 26]. When aberrant, the RSA arises from the aortic arch distal to the left subclavian artery and crosses the midline causing compression [19, 25].

Despite the fact that the ARSA is a common aortic developmental anomaly, it is relatively a rare aberration in the general population with a female predominance [20]. The occurrence was more common in females (55.3%) than males (44.7%) [23], which is consistent with other reported studies [13, 18]. In the current case, ARSA arises from the left side of the aortic arch as the last branch and passes behind the oesophagus.

This anomaly is mostly having a retro-oesophageal course (dorsal to the oesophagus) in the reported cases (80%), passes between the trachea and the oesophagus (15%), or anterior to the trachea in 5% of the cases [10, 19]. Although most of the patients (60–70%) are asymptomatic throughout their lives [14, 24], they are frequently diagnosed by incidental evaluations obtained for other reasons (i.e. imaging and aortic dissection) [5, 11, 24]. If symptomatic, in adult patients ARSA usually produces dysphagia (dysphagia lusoria), cough, chest pain, shortness of breath and weight loss due to the compressive effect of the nearby structures [19, 23]. An aneurysmal aortic dilatation, Kommerell's diverticulum occurs at the origin of the ARSA [9, 26]. Increased frequency of pulmonary infections is more common in infants than adult patients; this is due to the absence of tracheal stiffness, in combination with dysphagia and aspiration of food particles [4].

In our case, the ARSA was 16 mm in diameter; same finding had been reported in another study [21]. The calibre of the aortic arch branches depends on the position of their origin. There is an association between the origin of the branches and the diameter of the aortic arch [17].

In right transradial approach for coronary angiography and angioplasty procedures, the presences of the ARSA increase the number of catheters and prolong angiography time. Before proceeding the techniques, the operator must gain a sound knowledge of the anatomical variations to decrease the complication rate [1, 2].

Many studies [6, 7, 15] reported the correlation between foetal ARSA, intracardiac malformations and chromosomal abnormalities such as trisomy 21, 22q11 deletion of the long arm of the chromosome and Turner syndrome. Prenatal diagnosis of the ARSA is a useful marker for the ultrasonographic detection of foetal chromosomal abnormalities. In such cases, prenatal cytogenetic analysis is strongly recommended.

Treatment options such as conservative measures and surgical intervention mainly depend on the severity of the patient's symptoms and the presence of aneurysms [22]. Conservative measures are non-invasive treatments including dietary and lifestyle modifications often used for patients with mild to moderate symptoms [19, 22]. This includes reducing or avoiding exacerbating foods, eating small bites of the food at a slower rate with adequate chewing, and having more liquids [22].

Several non-invasive angiography methods such as multislice and multidetector computed tomography, Doppler sonography, transthoracic echocardiography and the magnetic resonance imaging are essential for preoperative diagnosis of the ARSA. These methods help to avoid unintentional injury of this artery during surgical procedures [8, 12, 28]. Patients with severe symptoms, consideration for surgery should be taken as a variety of safe and effective surgical approaches have been proposed [22, 23].

CONCLUSIONS

Conclusively, anatomical variations are frequent, and the ARSA is a well-known anomalous with or without pathological consequences. Prenatal diagnosis of the ARSA through non-invasive angiography methods helps to detect the foetal chromosomal abnormalities. Sound knowledge of the course and relations of the ARSA is helpful to reduce the risk and complications in surgical procedures.

Funding

The authors would like to extend their appreciation to the Deanship of Scientific Research at King Khalid University for funding this project through general research program under grant number (G.R.P. 220/41).

Acknowledgements

The authors would like to express their gratitude to King Khalid University, Saudi Arabia, for providing administrative and technical support.

Conflict of interest: None declared

REFERENCES

1. Abhaichand RK, Louvard Y, Gobeil JF, et al. The problem of arteria lusoria in right transradial coronary angiography and angioplasty. Catheter Cardiovasc Interv. 2001; 54(2): 196–201, doi: 10.1002/ccd.1266, indexed in Pubmed: 11590683.
2. Allen D, Bews H, Vo M, et al. Arteria lusoria: an anomalous finding during right transradial coronary intervention. Case Rep Cardiol. 2016; 2016: 8079856, doi: 10.1155/2016/8079856, indexed in Pubmed: 27478652.
3. Aslan S, Elmalı M. An unusual cause of late-onset dysphagia; Aberrant right subclavian artery. South Clin Ist Euras. 2019; 30(3): 277–279, doi: 10.14744/scie.2019.44127.
4. Atay Y, Engin C, Posacioglu H, et al. Surgical approaches to the aberrant right subclavian artery. Tex Heart Inst J. 2006; 33(4): 477–481, indexed in Pubmed: 17215974.
5. Battaloglu B, Secici S, Colak C, et al. Aberrant right subclavian artery and axillary artery cannulation in type a aortic dissection repair. Ann Thorac Surg. 2013; 96(1): e1–e2, doi: 10.1016/j.athoracsur.2013.01.044, indexed in Pubmed: 23816108.
6. Borenstein M, Minekawa R, Zidere V, et al. Aberrant right subclavian artery at 16 to 23 + 6 weeks of gestation: a marker for chromosomal abnormality. Ultrasound Obstet Gynecol. 2010; 36(5): 548–552, doi: 10.1002/uog.7683, indexed in Pubmed: 20503237.
7. Chaoui R, Thiel G, Heling KS. Prevalence of an aberrant right subclavian artery (ARSA) in fetuses with chromosomal aberrations. Ultrasound Obstet Gynecol. 2006; 28(4): 414–415, doi: 10.1002/uog.3047.
8. Chen X, Qu YJ, Peng ZY, et al. Diagnosis of congenital aortic arch anomalies in chinese children by multi-detector computed tomography angiography. J Huazhong Univ Sci Technolog Med Sci. 2013; 33(3): 447–451, doi: 10.1007/s11596-013-1140-9, indexed in Pubmed: 23771676.

9. Cinà CS, Althani H, Pasenau J, et al. Kommerell's diverticulum and right-sided aortic arch: a cohort study and review of the literature. J Vasc Surg. 2004; 39(1): 131–139, doi: 10.1016/j.jvs.2003.07.021, indexed in Pubmed: 14718830.
10. Domínguez EF, Corredera BM. Anomalies associated with aberrant right subclavian arteries. A case report. Eur J Anat. 2009; 13(1): 43–46.
11. Fernando RJ, Altman JM, Farmer B, et al. Aberrant right subclavian artery: an important variant of the aortic arch. Anesthesiology. 2019; 130(4): 615–616, doi: 10.1097/ALN.0000000000002567, indexed in Pubmed: 30875358.
12. Hart PA, Kamath PS. Dysphagia lusoria. Mayo Clin Proc. 2012; 87(3): e17, indexed in Pubmed: 3497995.
13. Jain KK, Braze AJ, Shapiro MA, et al. Aberrant right subclavian artery-esophageal fistula and severe gastrointestinal bleeding after surgical correction of scimitar syndrome. Tex Heart Inst J. 2012; 39(4): 571–574, indexed in Pubmed: 22949782.
14. Janssen M, Baggen MG, Veen HF, et al. Dysphagia lusoria: clinical aspects, manometric findings, diagnosis, and therapy. Am J Gastroenterol. 2000; 95(6): 1411–1416, doi: 10.1111/j.1572-0241.2000.02071.x, indexed in Pubmed: 10894572.
15. Lee SH, Jung JiMi, Song MS, et al. Evaluation of cardiovascular anomalies in patients with asymptomatic turner syndrome using multidetector computed tomography. J Korean Med Sci. 2013; 28(8): 1169–1173, doi: 10.3346/jkms.2013.28.8.1169, indexed in Pubmed: 23960443.
16. Mahmodlou R, Sepehrvand N, Hatami S. Aberrant right subclavian artery: a life-threatening anomaly that should be considered during esophagectomy. J Surg Tech Case Rep. 2014; 6(2): 61–63, doi: 10.4103/2006-8808.147262, indexed in Pubmed: 25598945.
17. Manole AM, Iliescu DM, Rusali A, et al. Morphometry of the aortic arch and its branches. ARS Medica Tomitana. 2013; 19(3): 154–159, doi: 10.2478/arsm-2013-0027.
18. Molz G, Burri B. Aberrant subclavian artery (arteria lusoria): sex differences in the prevalence of various forms of the malformation. Evaluation of 1378 observations. Virchows Arch A Pathol Anat Histol. 1978; 380(4): 303–315, doi: 10.1007/BF00431315, indexed in Pubmed: 153045.
19. Naqvi SE, Beg MH, Thingam SK, et al. Aberrant right subclavian artery presenting as tracheoesophagial fistula in a 50-year-old lady: Case report of a rare presentation of a common arch anomaly. Ann Pediatr Cardiol. 2017; 10(2): 190–193, doi: 10.4103/apc.APC_158_16, indexed in Pubmed: 28566828.
20. Natsis K, Didagelos M, Gkiouliava A, et al. The aberrant right subclavian artery: cadaveric study and literature review. Surg Radiol Anat. 2017; 39(5): 559–565, doi: 10.1007/s00276-016-1796-5, indexed in Pubmed: 27999944.
21. Natsis K, Didagelos M, Manoli SM, et al. A bicarotid trunk in association with an aberrant right subclavian artery. Report of two cases, clinical impact, and review of the literature. Folia Morphol. 2011; 70(2): 68–73, indexed in Pubmed: 21630225.
22. Nik Qisti F, Shahrun Niza AS, Razrim R. Lusoria: a case report. Dysphagia. 2016; 15(2): 7376, doi: 10.31436/imjm.v15i2.393 .
23. Polguj M, Chrzanowski Ł, Kasprzak JD, et al. The aberrant right subclavian artery (arteria lusoria): the morphological and clinical aspects of one of the most important variations: a systematic study of 141 reports. Sci World J. 2014; 2014: 292734, doi: 10.1155/2014/292734, indexed in Pubmed: 25105156.
24. Rosa P, Gillespie DL, Goff JM, et al. Aberrant right subclavian artery syndrome: a case of chronic cough. J Vasc Surg. 2003; 37(6): 1318–1321, doi: 10.1016/s0741-5214(02)75464-5, indexed in Pubmed: 12764282.
25. Saraceni C, Kwan WC, Joshi T, et al. Aberrant Right Subclavian Artery: A Rare Cause of Dysphagia. Am J Gastroenterol. 2018; 113(Suppl): S982–S983, doi: 10.14309/00000434-201810001-01720.
26. van Son JA, Konstantinov IE, Burckhard F. Kommerell and Kommerell's diverticulum. Tex Heart Inst J. 2002; 29(2): 109–112, indexed in Pubmed: 116736.
27. Vučurević G, Marinković S, Puškaš L, et al. Anatomy and radiology of the variations of aortic arch branches in 1,266 patients. Folia Morphol. 2013; 72(2): 113–122, doi: 10.5603/fm.2013.0019, indexed in Pubmed: 23740497.
28. Yang M, Mo X, Jin J, et al. [Diagnostic value of 64 multislice CT in typing of congenital aortic anomaly in neonates and infants]. Zhonghua Yi Xue Za Zhi. 2010; 90(31): 2167–2171, indexed in Pubmed: 21029654.

VIA MEDICA

CASE REPORT

Folia Morphol.
Vol. 80, No. 3, pp. 730–734
DOI: 10.5603/FM.a2020.0090

ISSN 0015–5659
eISSN 1644–3284
journals.viamedica.pl

Case report of a bifurcated fibular (lateral) collateral ligament: which band is the dominant one?

K. Kurtys[1], B. Gonera[1], Ł. Olewnik[1], P. Karauda[1], R. Shane Tubbs[3, 4, 5], M. Polguj[2]

[1]*Department of Anatomical Dissection and Donation, Medical University of Lodz, Poland*
[2]*Department of Normal and Clinical Anatomy, Medical University of Lodz, Poland*
[3]*Department of Neurosurgery, Tulane University School of Medicine, New Orleans, LA, United States*
[4]*Department of Neurosurgery and Ochsner Neuroscience Institute, Ochsner Health System, New Orleans, LA, United States*
[5]*Department of Anatomical Sciences, St. George's University, Grenada*

[Received: 29 June 2020; Accepted: 10 July 2020; Early publication date: 7 August 2020]

Background: *The fibular collateral ligament is a permanent and extracapsular ligament of the knee joint. It is located on the lateral aspect of the knee and extends from the lateral epicondyle of the femur to the lateral surface of the head of the fibula. As one of the main knee joint ligaments it is a stabilizer of the posterolateral corner of the knee and resists varus stress. The case report displays the bifurcated variant of the fibular collateral ligament. The aim of this study is to determine which of those bands should be considered dominant.*
Materials and methods: *Classical anatomical dissection was performed on the left knee joint. The fibular collateral ligament was thoroughly cleansed around its origin, distal attachments, and course. Appropriate morphometric measurements were collected.*
Results: *A bifurcated variant of the fibular collateral ligament with inverted proportions of its two bands (main and accessory one) constitutes our findings. It originated on the lateral epicondyle of the femur. Then it divided into two bands (A1 and A2). Band A1 inserted to the head of the fibula. A bony attachment of band A2 was located on the lateral aspect of the lateral condyle of the tibia.*
Conclusions: *Although the fibular collateral ligament is a permanent structure it presents morphological variations. It is important to constantly extend morphological knowledge for all scientists concerned in anatomy.* (Folia Morphol 2021; 80, 3: 730–734)

Key words: fibular collateral ligament, lateral collateral ligament, knee, knee joint, case report

INTRODUCTION

The knee joint is considered the biggest and one of the most complex joints in the human body. It consists of various structures including many ligaments, which are divided into two main groups, *extracapsular* and *intracapsular*. It is due to these ligaments that the knee joint can maintain proper stabilisation during different movements.

Address for correspondence: Dr. K. Kurtys, Department of Anatomical Dissection and Donation, Medical University of Lodz, ul. Żeligowskiego 7/9, 90–136 Łódź, Poland; tel: + 48 42 630 4949, +48 42 630 0749, e-mail: kurtyskonrad@gmail.com

The fibular collateral ligament (FCL) is one of the main extracapsular knee joint ligaments. It is located within the lateral aspect of the knee and originates, traditionally, on the lateral epicondyle of the femur. It then runs distally and attaches to the lateral surface of the head of the fibula [3, 17, 28]. There is no connection between it and the knee joint capsule [3]. The biomechanical functions of the FCL are well known and the most important of them is to resist varus forces. Additionally, it can preclude excessive posterolateral rotation of the tibia relative to the femur [8, 10, 15].

Lesions of the FCL are not rare, especially among athletes [16]. However, isolated FCL injuries seldom occur, so clinicians have to face so-called multi-ligament knee injuries. Co-occurrence of lesions of both cruciate ligaments of the knee, anterior and posterior, and structures of the posterolateral corner of the knee, are most frequent [19]. Those in most danger of FCL rupture are sportsmen exposed to shifting strains on a fully extended knee [16]. The FCL can tear as a result of hyperextension, direct varus stress, or twisting movement when a foot is fixed on the ground and the athlete rapidly changes direction of movement [14].

Anatomical structures tend to vary and can surprise us with their morphological variations [12, 26, 27]. Such fluctuations are quite common among ligaments, muscles, and their tendons [1, 6, 7, 11, 21–25]. Although scientists know a lot about the morphology of the FCL, it can still present some new features. Therefore, a proper and accurate classification system of the FCL based on morphological variations has been created [23].

This study presents a case of the bifurcated FCL with inverted size proportions of its two bands. It is important to collect such knowledge for all scientists involved in anatomy.

CASE REPORT

The cadaver of a 71-year-old female was subjected to routine anatomical dissection at the Department of Normal and Clinical Anatomy, Medical University of Lodz, for the purposes of research and the education of medical students. The knee joint was dissected using standard techniques according to a strictly specified protocol [22, 23].

During dissection of the lateral aspect of the knee joint, a bifurcated FCL was recognised. The whole ligament was thoroughly cleansed around its origin, distal attachments, and course. It originated on the lateral epicondyle of the femur. Then the common part (band A) divided into two bands (A1 and A2). After the cleansing, it was noted that two bands differed in their proportions.

- band A1 ran towards the lateral surface of the head of the fibula and inserted at this point;
- band A2 descended anterior to A1, went under the deep fascia of leg and presented a broad bony attachment on the lateral aspect of the lateral condyle of the tibia.

There were no other morphological abnormalities (Fig. 1).

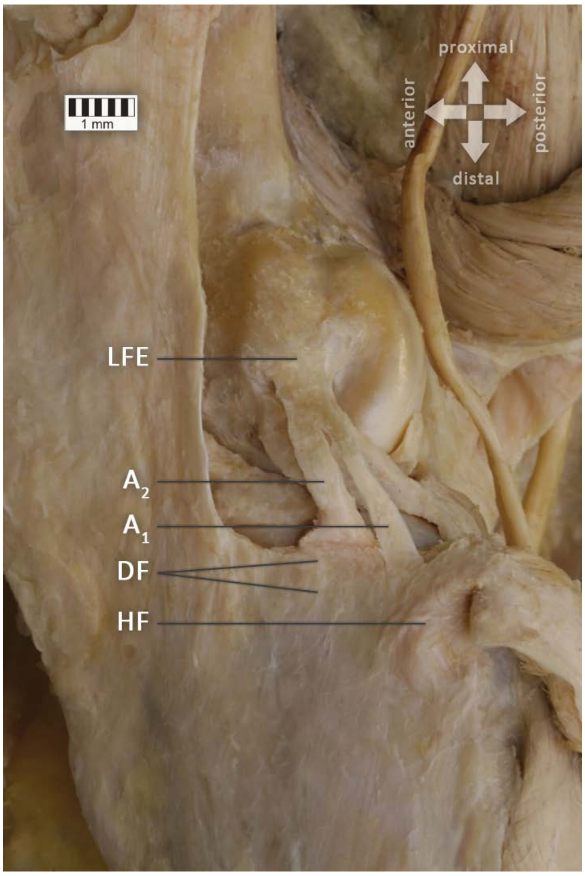

Figure 1. The presented variant of the fibular collateral ligament; a lateral view of the left knee joint; LFE — the lateral femoral epicondyle; DF — the deep fascia of leg; HF — the head of the fibula; A_1 — the main band of the fibular collateral ligament; A_2 — the accessory band of the fibular collateral ligament.

Appropriate morphometric measurements were acquired. Length and width were taken from digital photographic images and processed through MultiScanBase 18.03 (Computer Scanning System II, Warsaw, Poland), while thickness was measured with an electronic calliper (Mitutoyo Corporation, Kawasaki-shi, Kanagawa, Japan). All results are presented in Table 1.

Table 1. Measurements of the fibular collateral ligament bands

	Band	
	A1	A2
Length from the bifurcation point [mm]	24.34	18.40
Width at the bifurcation point [mm]	2.59	4.63
Width at the middle point [mm]	3.05	4.98
Width of the insertion [mm]	5.21	11.33
Thickness at the bifurcation point [mm]	0.32	0.41
Thickness at the middle point [mm]	0.34	0.40
Thickness of the insertion [mm]	0.29	0.40

DISCUSSION

Among clinicians, including orthopaedists, there is increasing interest in and hence awareness of anatomical variations. Many morphological classification systems have been published to facilitate better diagnosis and plan more advanced treatment approaches [22–24].

The fibular collateral ligament is a variable structure as demonstrated in some studies. Most of these have focused on abnormalities of its origin around the lateral epicondyle of the femur [2, 5, 13, 17, 29]. Nevertheless, some have presented morphological variations involving different numbers of FCL bands and points of distal attachments. Specifically, bifurcated and trifurcated FCLs have been recognised [3, 4, 23]. One study even presented a double FCL [23]. According to Olewnik et al. [23], there are four types of FCL (I, IIa, IIb, III, IV). Among the types that occur as multibands, we can distinguish a *main* band and one or two *accessory* band(s). The *main* band always inserts to the head of the fibula, while the *accessory* band(s) has/have two points of insertion, the deep fascia of the leg and the styloid process of the fibula. Chappell et al. [3] found all *additional* bands attached to the anterior or posterior aspect of the head of the fibula. In our study, we recognised two bands, A1 and A2. A1 inserted to the lateral surface of the head of the fibula, while A2 inserted to the lateral aspect of the tibial lateral condyle. The FCL described in this study appeared to be similar to type IIa described by Olewnik et al. [23] because of the bifurcation and the descending direction of the bands. However, there was a difference in the attachment point of the *accessory* band (A2); it presented a bony attachment, while in Olewnik et al. [23] the *accessory* band inserted to the deep fascia of the leg. On the basis of this information about the insertional points, we could consider band A1 the *main* one and band A2 an *accessory* one. The question arises whether it is appropriate reasoning in each case and whether the *main* band is always dominant. In our work, all measurements revealed (Table 1) that the band attached to the lateral aspect of the lateral condyle of the tibia (A2) was more massive than A1. This could imply that despite the atypical "non-main" insertion in such cases, the *accessory* band can be functionally dominant.

An embryological study found the mesenchymal condensation that provides rise to the FCL in 7-week--old embryos. At 9 weeks it was described as a thin but well-defined cellular band which descended from the lateral epicondyle of the femur to merge with the perichondrium of the head of the fibula. The FCL reached a structural similarity with the adult knee at 14 weeks, presenting groups of cells separated by a lot of bundles consists of collagenous fibres [9]. According to Merida-Velasco et al. [18], the FCL develops independently from the knee joint capsule in contrast to the medial collateral ligament. It is interesting whether, in the case of bifurcated variants of the FCL, both bands (*main* and *accessory*) develop simultaneously.

The FCL is a significant knee joint stabilizer. It resists varus forces at all knee flexion angles and stabilises the posterolateral corner of the knee. Moreover, it resists external rotation of the knee over the flexion span 0°–30°. Above 30° it loses tension and becomes insufficient as a stabilizer of external rotation of the knee [5, 8, 10, 15, 20]. It is possible that some kinds of multibanded FCL can provide extra stabilisation functions, but specialist biomechanical examination will be needed to establish this.

Although injuries to the FCL are less common than injuries to the medial collateral ligament, appropriate diagnosis, treatment, and rehabilitation are key to ensuring sufficient recovery and postoperative stabilisation [15, 29]. The treatment method depends on the "grade" of FCL injury, and surgical procedures include primary repair and total reconstruction. Primary repair is used in acute bony avulsions around the proximal or distal attachment of the FCL, while total reconstruction is preferable for midsubstance tears or chronic lateral knee instability after the FCL injury [19, 20]. Our findings suggest that in some surgical treatment approaches to ligaments or tendons with *accessory* bands, surgeons should be more careful and verify which band is truly dominant; this should be given most focus in order to restore the primary and essential function.

Limitations of the study

The study has some limitations. Although the anatomical examination was thorough, this is only a case report, presenting the topic for the first time. Further anatomical, biomechanical, and imaging examinations are required to investigate the variation more deeply and create useful tips for clinicians specialising in treatment of ligaments and tendons. Nevertheless, we think it important to collect all new morphological information, and to enrich and integrate anatomical knowledge for all anatomists.

CONCLUSIONS

The fibular collateral ligament is an anatomical structure with the potential for novel, extremely rare morphological variations. Besides bifurcated, trifurcated, or double FCLs, the size proportions between the *main* and *accessory* bands can be inverted. Assembling complete anatomical knowledge, even including such rare cases, is valuable for clinicians involved in anatomy.

Ethics approval and consent to participate

The protocol of the study was accepted by Bioethics Committee of Medical University of Lodz (resolution RNN/297/17/KE). The cadavers belong to the Department of Normal and Clinical Anatomy of the Medical University of Lodz.

Acknowledgements

The authors wish to express their gratitude to all those who donated their bodies to medical science.

Conflict of interest: None declared

REFERENCES

1. Ahmed SN, Murudkar P, Ahmed M, et al. A morphological study of plantaris muscle and its surgical perspective. Int J Anat Res. 2017; 5(1.3): 3560–3566, doi: 10.16965/ijar.2016.506.
2. Brinkman JM, Schwering PJA, Blankevoort L, et al. The insertion geometry of the posterolateral corner of the knee. J Bone Joint Surg Br. 2005; 87(10): 1364–1368, doi: 10.1302/0301-620X.87B10.16536, indexed in Pubmed: 16189309.
3. Chappell TM, Panchani PN, Moore GD, et al. Morphometry of the fibular collateral ligament: anatomic study with comprehensive review of the literature. Clin Anat. 2014; 27(7): 1089–1096, doi: 10.1002/ca.22416, indexed in Pubmed: 24840861.
4. Diamantopoulos A, Tokis A, Tzurbakis M, et al. The posterolateral corner of the knee: evaluation under microsurgical dissection. Arthroscopy. 2005; 21(7): 826–833, doi: 10.1016/j.arthro.2005.03.021, indexed in Pubmed: 16012496.
5. Espregueira-Mendes V, da Silva MV. Anatomy of the lateral collateral ligament: a cadaver and histological study. Knee Surg Sports Traumatol Arthrosc. 2006; 14(3): 221–228, doi: 10.1007/s00167-005-0681-2, indexed in Pubmed: 16220313.
6. Georgiev GP, Landzhov B, Tubbs RS. A novel type of coracobrachialis muscle variation and a proposed new classification. Cureus. 2017; 9(7): e1466, doi: 10.7759/cureus.1466, indexed in Pubmed: 28936378.
7. Georgiev GP, Tubbs RS, Iliev A, et al. Extensor indicis proprius muscle and its variants together with the extensor digitorum brevis manus muscle: a common classification. Clinical significance in hand and reconstructive surgery. Surg Radiol Anat. 2018; 40(3): 271–280, doi: 10.1007/s00276-018-1981-9, indexed in Pubmed: 29383419.
8. Gollehon DL, Torzilli PA, Warren RF. The role of the posterolateral and cruciate ligaments in the stability of the human knee. A biomechanical study. J Bone Joint Surg. 1987; 69(2): 233–242, doi: 10.2106/00004623-198769020-00010.
9. Gray DJ, Gardner E. Prenatal development of the human knee and superior tibiofibular joints. Am J Anat. 1950; 86(2): 235–287, doi: 10.1002/aja.1000860204, indexed in Pubmed: 15410671.
10. Grood ES, Stowers SF, Noyes FR. Limits of movement in the human knee. Effect of sectioning the posterior cruciate ligament and posterolateral structures. J Bone Joint Surg Am. 1988; 70(1): 88–97, indexed in Pubmed: 3335577.
11. Karauda P, Olewnik Ł, Podgórski M, et al. Anatomical variations of the abductor pollicis longus: a pilot study. Folia Morphol. 2020; 79(4): 817–822, doi: 10.5603/FM.a2019.0134, indexed in Pubmed: 31802470.
12. Kurtys K, Gonera B, Olewnik Ł, et al. A highly complex variant of the plantaris tendon insertion and its potential clinical relevance. Anat Sci Int. 2020; 95(4): 553–558, doi: 10.1007/s12565-020-00540-4, indexed in Pubmed: 32248353.
13. LaPrade RF, Ly TV, Wentorf FA, et al. The posterolateral attachments of the knee: a qualitative and quantitative morphologic analysis of the fibular collateral ligament, popliteus tendon, popliteofibular ligament, and lateral gastrocnemius tendon. Am J Sports Med. 2003; 31(6): 854–860, doi: 10.1177/03635465030310062101, indexed in Pubmed: 14623649.
14. LaPrade RF, Terry GC. Injuries to the posterolateral aspect of the knee. Association of anatomic injury patterns with clinical instability. Am J Sports Med. 1997; 25(4): 433–438, doi: 10.1177/036354659702500403, indexed in Pubmed: 9240974.
15. LaPrade RF, Tso A, Wentorf FA. Force measurements on the fibular collateral ligament, popliteofibular ligament, and popliteus tendon to applied loads. Am J Sports Med. 2004; 32(7): 1695–1701, doi: 10.1177/0363546503262694, indexed in Pubmed: 15494335.
16. Majewski M, Susanne H, Klaus S. Epidemiology of athletic knee injuries: A 10-year study. Knee. 2006; 13(3): 184–188, doi: 10.1016/j.knee.2006.01.005, indexed in Pubmed: 16603363.

17. Meister BR, Michael SP, Moyer RA, et al. Anatomy and kinematics of the lateral collateral ligament of the knee. Am J Sports Med. 2000; 28(6): 869–878, doi: 10.1177/03635465000280061601, indexed in Pubmed: 11101111.
18. Mérida-Velasco JA, Sánchez-Montesinos I, Espín-Ferra J, et al. Development of the human knee joint ligaments. Anat Rec. 1997; 248(2): 259–268, doi: 10.1002/(SICI)1097-0185(199706)248:2<259::AID-AR13>3.0.CO;2-O, indexed in Pubmed: 9185992.
19. Moatshe G, Dean CS, Chahla J, et al. Anatomic fibular collateral ligament reconstruction. Arthrosc Tech. 2016; 5(2): e309–e314, doi: 10.1016/j.eats.2016.01.007, indexed in Pubmed: 27354951.
20. Moulton SG, Matheny LM, James EW, et al. Outcomes following anatomic fibular (lateral) collateral ligament reconstruction. Knee Surg Sports Traumatol Arthrosc. 2015; 23(10): 2960–2966, doi: 10.1007/s00167-015-3634-4, indexed in Pubmed: 25986095.
21. Olewnik Ł, Karauda P, Gonera B, et al. Intramuscular innervation of plantaris muscle evaluated using a modified Sihler's staining protocol - Proposal for a new classification. Ann Anat. 2020; 230: 151504, doi: 10.1016/j.aanat.2020.151504, indexed in Pubmed: 32173561.
22. Olewnik Ł, Gonera B, Kurtys K, et al. The anterolateral ligament of the knee: a proposed classification system. Clin Anat. 2018; 31(7): 966–973, doi: 10.1002/ca.23267, indexed in Pubmed: 30144325.
23. Olewnik Ł, Gonera B, Kurtys K, et al. A proposal for a new classification of the fibular (lateral) collateral ligament based on morphological variations. Ann Anat. 2019; 222: 1–11, doi: 10.1016/j.aanat.2018.10.009, indexed in Pubmed: 30408521.
24. Olewnik Ł, Gonera B, Podgórski M, et al. A proposal for a new classification of pes anserinus morphology. Knee Surg Sports Traumatol Arthrosc. 2019; 27(9): 2984–2993, doi: 10.1007/s00167-018-5318-3, indexed in Pubmed: 30535546.
25. Olewnik Ł, Kurtys K, Gonera B, et al. Proposal for a new classification of plantaris muscle origin and its potential effect on the knee joint. Ann Anat. 2020; 231: 151506, doi: 10.1016/j.aanat.2020.151506, indexed in Pubmed: 32173563.
26. Olewnik Ł, Wysiadecki G, Polguj M, et al. The report on the co-occurrence of two different rare anatomic variations of the plantaris muscle tendon on both sides of an individual. Folia Morphol. 2017; 76(2): 331–333, doi: 10.5603/FM.a2016.0069, indexed in Pubmed: 27813626.
27. Olewnik Ł, Podgórski M, Polguj M, et al. The plantaris muscle - rare relations to the neurovascular bundle in the popliteal fossa. Folia Morphol. 2018; 77(4): 785–788, doi: 10.5603/FM.a2018.0039, indexed in Pubmed: 29651792.
28. Recondo JA, Salvador E, Villanúa JA, et al. Lateral stabilizing structures of the knee: functional anatomy and injuries assessed with MR imaging. Radiographics. 2000; 20 (Spec No.): S91–S9S102, doi: 10.1148/radiographics.20.suppl_1.g00oc02s91, indexed in Pubmed: 11046165.
29. Terry GC, LaPrade RF. The posterolateral aspect of the knee. Anatomy and surgical approach. Am J Sports Med. 1996; 24(6): 732–739, doi: 10.1177/036354659602400606, indexed in Pubmed: 8947393.

VIA MEDICA

CASE REPORT

Folia Morphol.
Vol. 80, No. 3, pp. 735–738
DOI: 10.5603/FM.a2020.0089

ISSN 0015–5659
eISSN 1644–3284
journals.viamedica.pl

Bilateral double-layered patella in a patient with advanced knee osteoarthritis

P. Przybylski[1], M. Skoczyński[1], P. Tarkowski[1], M. Tarczyńska[2], K. Gawęda[2], A. Drop[1]

[1]1st Department of Radiology, Medical University of Lublin, Poland
[2]Department and Clinic of Orthopaedics and Traumatology, Medical University of Lublin, Poland

[Received: 6 May 2020; Accepted: 28 July 2020; Early publication date: 7 August 2020]

Double layered patella (DLP) is a rare anomaly of the patella that may go undiagnosed, especially in patients with progressive knee dysfunction and early degenerative changes. Clinical symptoms such as motion-dependent pain and anterior knee pain most typically occur in adolescents or young adults; however, gradually increasing pain and early generalised degenerative changes have also been seen in patients over 40 years old.
Diagnosis of DLP could be difficult, especially in cases with coexisting arthrosis. DLP is considered to be pathognomonic for the diagnosis of multiple epiphyseal dysplasia and usually coexists with other anomalies seen in this syndrome, such as hip dysplasia. In extremely rare cases, DLP can occur as a solitary disorder. The prevalence of such cases, however, is unknown, and they could be easily misdiagnosed. Computed tomography and magnetic resonance imaging are the most sensitive radiological methods used in DLP diagnosis. This case report presents a case of a bilateral DLP incidentally found in a 47-year-old patient with advanced arthritis referred for arthroplasty because of increasing symptoms of knee joint failure with no other abnormalities recorded. An important goal of our case study is to raise the awareness of this abnormality with radiologists and orthopaedic surgeons. (Folia Morphol 2021; 80, 3: 735–738)

Key words: bilateral double-layered patella, osteoarthritis

INTRODUCTION

Medical literature reports only a few cases of double layered patella (DLP). DLP is considered to be pathognomonic for the diagnosis of multiple epiphyseal dysplasia (MED) [7].

Early onset of clinical symptoms, such as increasing anterior knee pain and motion-dependent pain, are characteristic of young patients; however, dysfunctions as well as early, generalised degenerative changes have also been seen in patients over 40 years old with no history of trauma [10]. Because there are therapeutic implications to distinguishing DLP from other causes of knee failure in non-traumatic painful patients, imaging findings should be used to guide differential diagnosis.

This case report presents a case of an incidentally found bilateral DLP in a 47-year-old patient with advanced arthritis referred for arthroplasty because of increasing symptoms of knee joint failure with no other abnormalities recorded.

CASE REPORT

The patient (M.G.), aged 47, was referred from a county health centre to the Orthopaedic Clinic of the Medical University in Lublin, Poland, with in-

Address for correspondence: P. Przybylski, PhD, 1st Department of Radiology, Medical University of Lublin, ul. Jaczewskiego 8, 20–954 Lublin, Poland, tel: +48 81 7244660, fax: +48 81 7244543, e-mail: dr.przybylski@gmail.com

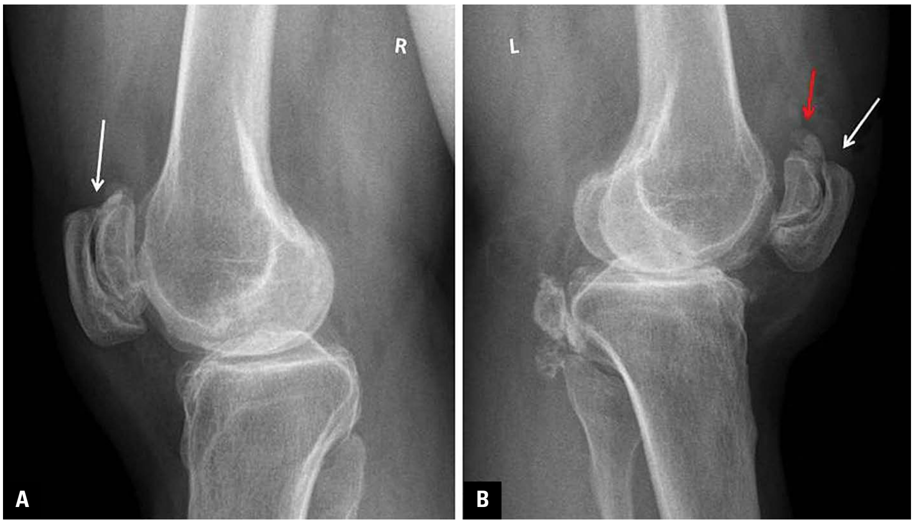

Figure 1. Lateral X-ray views of double-layered patella; **A.** Right patella (white arrow); **B.** Left (white arrow), additional separated segment in upper part of left patella (red arrow).

creasing symptoms of knee dysfunction and pain. On physical examination, the patient felt severe pain in both knees during movement and physical effort, especially the left knee, with a slight contracture in flexion and motor impairment of the left leg extension resulting in abnormal gait. The patient had not been diagnosed previously for these complaints. Physical examination also revealed a limited range of motion of 0 to 100 degrees of flexion for the right knee and 0 to 70 degrees for the left knee. The patient reported pain in both compartments in the area of the joint space. Antero-posterior and lateral view radiographs of both knees showed advanced arthritis, with more advanced lesions in the left knee. In lateral views two separated, parallel segments of both patellas were found (Fig. 1). The patient was referred for arthroplasty of the left knee. Computed tomography (CT) was performed a month later to assess bone structure. CT scans confirmed the presence of advanced degenerative changes in both knees and coexisting bilateral double-layered patella (Fig. 2). Additionally, several small segments were detected in the upper outer quadrant of the superficial surface of the left knee patella (Fig. 2B, D). During the arthroplasty, patellar segments were removed or fused. The articular surfaces of the distal femur and proximal tibia were replaced with prosthesis. Osteophytes that had formed on the patella and the edges of both bones were reduced. Following surgery, the patient underwent standard postoperative rehabilitation. Despite reminders, the patient never reported for follow-up.

DISCUSSION AND CONCLUSIONS

The patella, being the largest sesamoid bone in the human body, serves as an anatomic pulley (trochlea) for the quadriceps tendon. One of the most common patellar abnormalities is multipartite patella, which occurs in 0.2–6% of the population. A bipartite patella is the most prevalent form of this condition [12]. The partition is most often considered to be the consequence of a failed fusion of patellar ossification centres, but, other causes, such as trauma, tendon pulling on the patella, or insufficient vascular supply have also been proposed in the literature [11]. Available classifications of multipartite patella do not include a DLP [9]. DLP is currently considered to be pathognomonic for the diagnosis of MED, but single cases of this anomaly without coexistence of MED have also been described [1, 7]. The dominant form of MED occurs in 0.01% of the population, but the prevalence of the recessive form is unknown [1]. It has been suggested that mutations in the *COMP*, *DTDST*, *MATN3*, *COL9A1*, *COL9A2*, and *COL9A3* MED genes may be responsible for the occurrence of MED, while mutations in the *DTDST* and *COL9A2* genes have been shown to coexist with the DLP phenotype [1, 5, 10].

It is extremely difficult to estimate the prevalence of solitary DLP, because until now only a few cases have been reported in the literature available to the authors. First described by Buttner in 1925, DLP is an anomaly in which there are two patellar segments separated by a coronal septum: an anterior segment which is embedded in the quadriceps femoris tendon

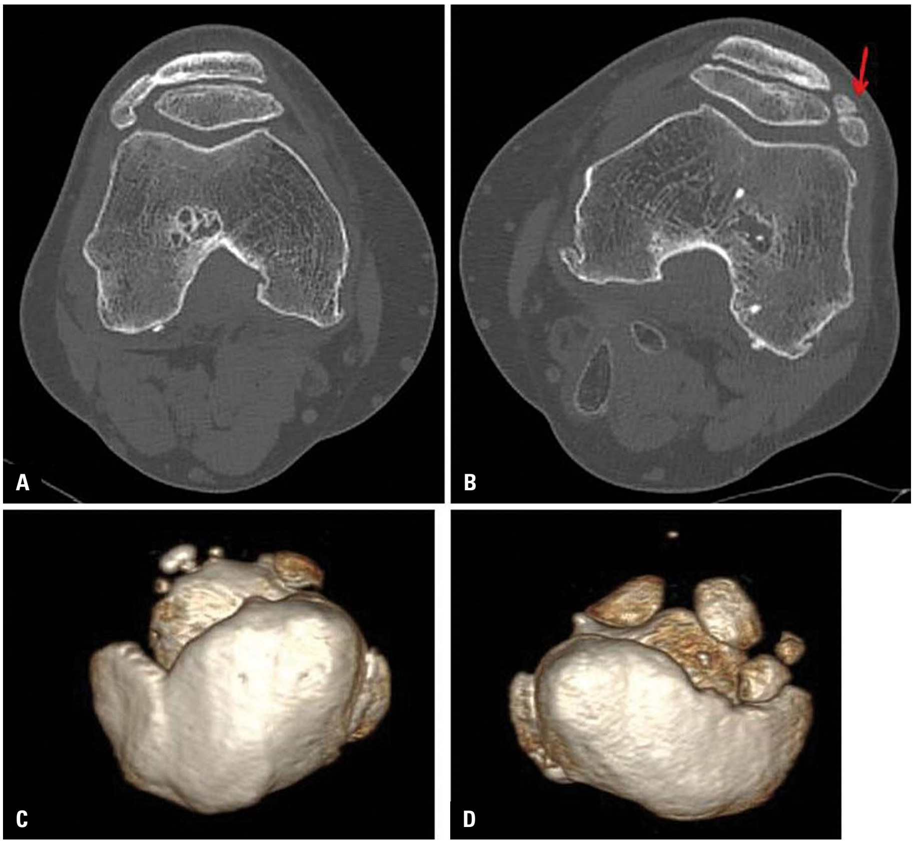

Figure 2. Computed tomography scans reconstructions; **A.** Axial view of right knee; **B.** Axial view of left knee, multiple segments in upper part of anterior layer are seen (red arrow); **C.** Three-dimensional reconstruction of right patella; **D.** Three-dimensional reconstruction of left patella.

and patellar tendons, and a posterior segment, which forms the articulating surface for the femur [7]. It is thought that DLP is bilateral in up to 40% of patients [3]. The interface between the two segments is cartilaginous [4, 7]. Apart from complete DLPs, partial DLPs have also been described in the literature, often in association with fracture [5]. A partial DLP can also occur in patients without MED [3].

Double layered patella is sometimes asymptomatic, but it can also cause a variety of clinical problems. Clinical symptoms such as motion-dependent pain and anterior knee pain, clicking, locking or patellar dislocation most typically occur in adolescents or young adults [4, 7]; however, gradually increasing pain and early, generalised degenerative changes have also been seen in patients over 40 years old [10]. A delayed and painful movement of the posterior patellar segment that has no tendinous insertions, which causes painful snapping of the patella has also been reported [4]. DLP can be suspected based on clinical examination, especially in patients with a history of MED [7]. The diagnosis is confirmed following imaging (X-ray, CT or magnetic resonance imaging [MRI] scans) [8]. CT and MRI are the only modalities that enable precise morphological evaluation of both patellar segments. As a method that allows performing multiplanar and three-dimensional reconstructions, CT is an important preoperative tool. The layers can also be seen in ultrasound images, because the posterior segment is not entirely covered by the anterior segment.

Because DLP is a very rare abnormality, no standard treatment has been established so far. This means that therapeutic interventions are individually tailored to the patients' needs. Surgery has been performed in symptomatic patients both with and without a history of trauma. Resection of the posterior segment was proposed previously [2]; however, more recent work describes a good clinical outcome in patients who have undergone a surgery involving decortication of the separated bone segments and fixation using multiple stabilising elements [4, 5] or a single screw [6].

Patients who are referred for surgery may need a more extensive evaluation, including CT scanning, as CT scans can be used for planning treatment and printing three-dimensional models of the patella.

Conflict of interest: None declared

REFERENCES

1. Dahlqvist J, Orlén H, Matsson H, et al. Multiple epiphyseal dysplasia. Acta Orthop. 2009; 80(6): 711–715, doi: 10.3109/17453670903473032, indexed in Pubmed: 19995321.
2. Dahners LE, Francisco WD, Halleran WJ. Findings at arthrotomy in a case of double layered patellae associated with multiple epiphyseal dysplasia. J Pediatr Orthop. 1982; 2(1): 67–70, doi: 10.1097/01241398-198202010-00010, indexed in Pubmed: 7076836.
3. García-Mata S, Hidalgo-Ovejero A. Partial double-layered patella in a nondysplasic adolescent. J Pediatr Orthop B. 2016; 25(6): 561–563, doi: 10.1097/BPB.0000000000000361, indexed in Pubmed: 27392305.
4. Goebel S, Steinert AF, Barthel T. Surgical management of a double-layered patella: a case report. Arch Orthop Trauma Surg. 2009; 129(8): 1071–1075, doi: 10.1007/s00402-008-0701-z, indexed in Pubmed: 18677496.
5. Jørgensen A, Brandt E, Ulstrup A. Traumatic separation of osseous segments in a double-layered patella. Int J Surg Case Rep. 2017; 41: 352–355, doi: 10.1016/j.ijscr.2017.11.006, indexed in Pubmed: 29145110.
6. Leng HC, Foster P, Templeton PA. Fusion of double-layered patella using a single small fragment partially threaded screw: a case report. J Pediatr Orthop. 2011; 31(2): e9––e12, doi: 10.1097/BPO.0b013e318207454b, indexed in Pubmed: 21307701.
7. Milants A, De Maeseneer M, De Mey J. Double-layered patella (DLP) in multiple epiphyseal dysplasia (MED). J Belg Soc Radiol. 2017; 101(1): 8, doi: 10.5334/jbr-btr.1219, indexed in Pubmed: 30039000.
8. Nguyen MD, Everhart JS, May MM, et al. Bilateral double-layered patella: MRI findings and fusion with multiple headless screws: a case report. JBJS Case Connect. 2013; 3(2): e50, doi: 10.2106/JBJS.CC.L.00314, indexed in Pubmed: 29252402.
9. Oohashi Y, Koshino T, Oohashi Y. Clinical features and classification of bipartite or tripartite patella. Knee Surg Sports Traumatol Arthrosc. 2010; 18(11): 1465–1469, doi: 10.1007/s00167-010-1047-y, indexed in Pubmed: 20111951.
10. Sayilir S, Ekiz T. Early osteoarthritis and double-layered patella in a patient with multiple epiphyseal dysplasia. Arch Rheumatol. 2017; 32(3): 260–263, doi: 10.5606/ArchRheumatol.2018.6415, indexed in Pubmed: 30375546.
11. Smillie IS. Injuries of extensor apparatus. In: Injuries of the Knee Joint. 3rd Ed. Williams & Wilkins, Baltimore, MD 1962: 272–277.
12. Weckström M, Parviainen M, Pihlajamäki HK. Excision of painful bipartite patella: good long-term outcome in young adults. Clin Orthop Relat Res. 2008; 466(11): 2848–2855, doi: 10.1007/s11999-008-0367-4, indexed in Pubmed: 18607662.

VIA MEDICA

CASE REPORT

Folia Morphol.
Vol. 80, No. 3, pp. 739–744
DOI: 10.5603/FM.a2020.0101

ISSN 0015–5659
eISSN 1644–3284
journals.viamedica.pl

A bifurcated plantaris muscle: another confirmation of its high morphological variability? Another type of plantaris muscle

A. Smędra[1], Ł. Olewnik[2], P. Łabętowicz[1, 2], D. Danowska-Klonowska[3], M. Polguj[4], J. Berent[1]

[1]*Department of Forensic Medicine, Medical University of Lodz, Poland*
[2]*Department of Anatomical Dissection and Donation, Medical University of Lodz, Poland*
[3]*Department of Histology and Embryology, Medical University of Lodz, Poland*
[4]*Department of Normal and Clinical Anatomy, Medical University of Lodz, Poland*

[Received: 6 August 2020; Accepted: 18 August 2020; Early publication date: 22 August 2020]

The plantaris muscle usually begins with a short, narrow belly in the popliteal fossa at the lateral supracondylar line of the femur and the knee joint capsule. Then it forms a long and slender tendon and usually inserts into the calcaneal tuberosity on the medial side of Achilles tendon. Nevertheless, many anatomical variations of distal attachment have been described. Cases of atypical proximal origin are reported less frequently. In this paper, we have presented a case of a two headed plantaris muscle. First head attached to the condyle of the femoral bone, medially and inferiorly to the lateral head of the gastrocnemius muscle. The second one originated from the popliteal surface of the femur, just above the intercondylar fossa. According to present literature, no such case with atypical proximal origin was presented. Such information has potentially clinical significance during the surgical procedures performed in the area of the popliteal fossa. (Folia Morphol 2021; 80, 3: 739–744)

Key words: anatomical variations, plantaris muscle, plantaris tendon, rare variant

INTRODUCTION

The plantaris muscle (PM) is a small, flat, spindle-shaped muscle located in the posterior region of the knee, slightly above and medially to the lateral head of the gastrocnemius muscle (GM) [16]. The proximal attachment is located on the popliteal surface of the femoral bone above the lateral condyle on the articular capsule [16]. From this origin, the short muscle belly develops into a long, thin tendon, which usually runs in the "space" between the GM and the soleus muscle inserting on to the medial calcaneus and adjacent fibrous tissues [28].

Due to its attachments, it is involved in plantar flexion of the foot at the ankle joint and in knee flexion at the knee joint. In reality, however, it weakly assists the gastrocnemius and soleus muscles to perform these two movements. The PM contains a large number of muscle spindles, so it's considered as a proprioceptive organ for the larger, more powerful flexors of the ankle joint, transferring information about the position of the foot and about movement [16, 28].

But still, since neither proprioceptive or flexor functions are affected when plantaris is absent or

Address for correspondence: A. Smędra, MD, PhD, Chair and Department of Forensic Medicine, Medical University of Lodz, ul. Sędziowska 18a, 91–304 Łódź, Poland, tel: +48 508257657, fax: +48 426544293, e-mail: karolanka@wp.pl

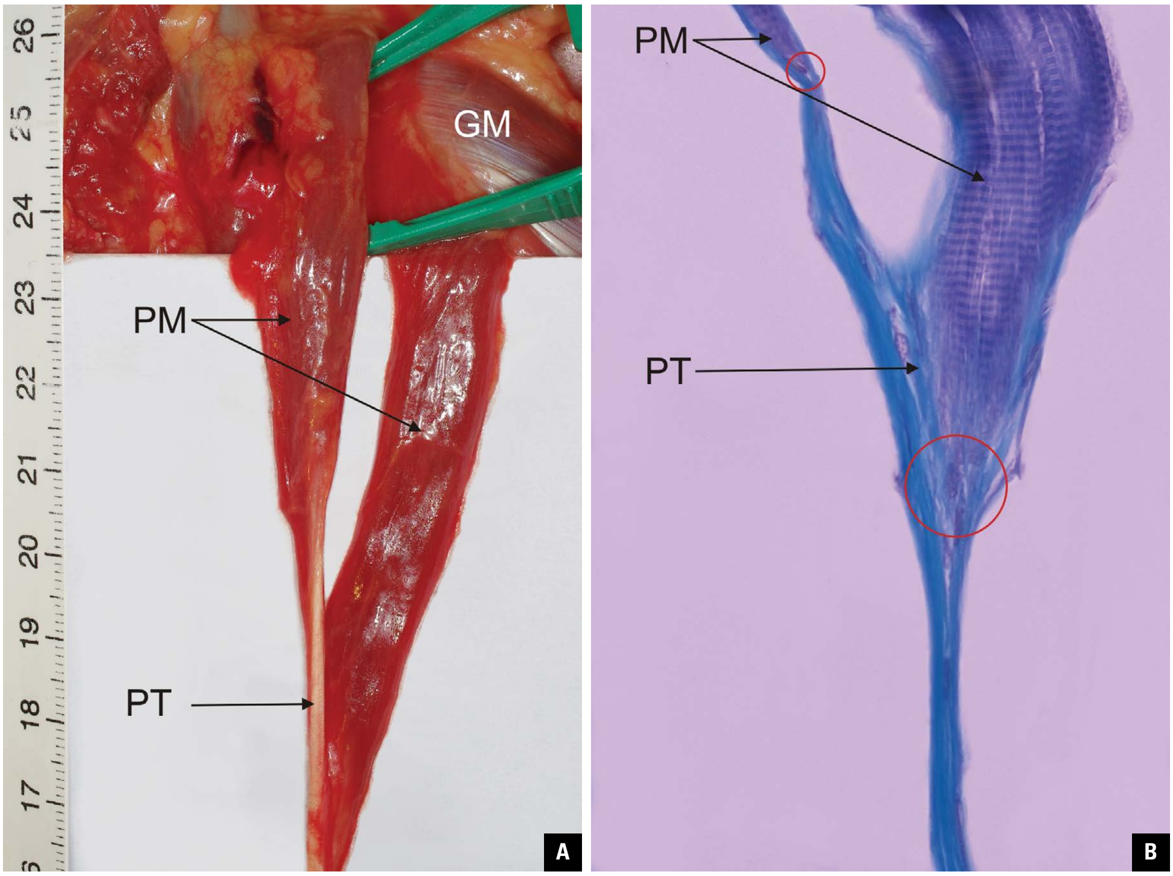

Figure 1. A. Right plantaris muscle with two bellies (PM — plantaris muscle, PT — plantaris tendon); GM — gastrocnemius muscle; **B.** The plantaris muscle, Mallory staining, mag. 400 ×. Muscle transitions to the tendon are marked (red circles).

removed, some authors consider this muscle to be vestigial in humans.

It should be noted that PM is not always present. According to different data, this muscle is not present in 4–20% of subjects [3, 7, 21, 26]. Cases of a double PM, unilaterally [11] or bilaterally [10], have also been reported.

Anatomical variability in the morphology of the muscle and its attachments may affect both the function of the lower limb (potential predisposition to Achilles tendon tendinopathy) [21, 30] and the surgical procedures, including those involving the use of the plantaris tendon for reconstruction procedures. The tendon of this muscle is long and can be used for the reconstruction of anterior talofibular ligaments, calcaneofibular ligaments and flexor tendons in the lower extremities. Removal of the PM does not typically hinder the patient's lower extremity function in the presence of a normal soleus and gastrocnemius. Injury to the PM either on its own, or in combination with gastrocnemius, or soleus damage, can represent the cause of the clinical condition known as tennis leg [6]. It must be noted that some cases of the use of this tendon for the repair of the atrioventricular valve have also been reported [25].

Findings related to deep venous thrombosis in the calf can be mistaken for those of tennis leg and thus must be kept in mind in the differential diagnosis of clinical findings suggestive of this condition. Other differentials may include a ruptured Baker's cyst, and calf neoplasms [13].

In the present paper, we describe a case of a PM with two completely separate heads, which confirms the introduced classification of origin (rare cases) by Olewnik et al. [22].

CASE REPORT

In the Chair and Department of Forensic Medicine, a forensic autopsy of a 68-year-old woman was carried out. During the dissection of the muscles, it was found that the right PM had two heads (Fig. 1A). The heads were carefully assessed in situ with respect to their length and width, as were the proximal and distal attachment and the course of the tendon.

Table 1. Measurement results in millimetres

	I	II
Belly length	63.64	58.21
Tendon length to the connection point	8.21	2.21
Tendon width at muscle-tendon junction	1.96	1.10
Whole tendon length	328.21	328.21

The first (lateral) head was attached to the lateral condyle of the femur and to the lateral head of the GM, whereas the second (medial) head originated from the femoral popliteal surface, just above the intercondylar fossa. The bellies then passed into a long tendon oriented towards the medial side of the calf. Photographic documentation with a measuring tape was prepared. The muscle was cut and measured using an electronic calliper (Mitutoyo Corporation, Kawasaki-shi, Kanagawa, Japan). Measurement results are given in the Table 1.

The muscle was then fixed in 4% buffered formalin solution for histological investigations. After fixation, the microscopic specimens stained with haematoxylin and eosin as well as with Mallory's method were prepared. Inspection under the microscope revealed that the heads of the investigated muscle had a normal histological structure (Fig. 1B).

DISCUSSION

Based on the literature, the PM may be a residual structure, a remnant of the primitive flexor of the toes. According to this assumption, the tuberosity of the calcaneus bone has then become a junction between the two parts of the primary flexor (plantaris tendon and plantaris aponeurosis), which are attached to it but not connected with each other. According to Cruveilhier [4], the change in the position of the foot relative to the remainder of the extremity was the result of the loss of connection between the PM and the plantaris aponeurosis. It is worth noting that the situation is different in the case of the palmaris longus, which has not lost connection with the palmar fascia [23].

The loss of the plantaris tendon connection to the plantaris aponeurosis gave rise to the secondary connection to the calcaneus [4]. In many mammals, including apes, the plantaris is attached to the plantar aponeurosis. In most ruminants and horses; however, the plantaris attaches to the Achilles tendon similar as in humans. A study of the comparative anatomy of mammals reveals no phylogenetically coherent story based on either the size or the location of the attachments of the plantaris. Embryological development in man supports the idea supported by McMurrich that the plantaris is a derivative of the deeper portion of the lateral head of the gastrocnemius. When absent, it is likely that this separation has failed to take place during ontogeny [15].

While the human PM is clearly in a position to flex the knee and to plantarflex the foot at the ankle, its motor functions are obviously trivial. A point often overlooked in the assessment of a muscle's function; however, is that most muscles have a sensory function in addition to their more obvious motor function. While all muscles contain scattered muscle spindles among their more numerous and larger motor fibres, some small muscles have an exceptionally high number of spindles and should be thought of as sensory or proprioceptive organs rather than as motor organs. Often these small sensory muscles are found to be in close association with much larger motor muscles — PM goes together with gastrocnemius and soleus.

The PM is a structure characterized by high anatomic variability. First, it may not be present at all, second, there are many variations in its attachments and third, it can have two or even three bellies (heads) [22].

As it was previously mentioned, according to different data, this muscle is not present in 4–20% of subjects. Studies usually do not show significant statistical differences in occurrence between sexes and body sides.

The plantaris is exceedingly variable in origin. It may take origin from the inferior extremity of the lateral limb of the linea aspera; the posterior ligament of the knee at the intercondylar space; the fascial covering of the popliteus; the fibula, between the flexor hallucis longus and the peroneus longus; the oblique line of the tibia, under cover of the soleus; the fascia of the leg; the lateral condyle of the femur above the origin of the lateral head of the gastrocnemius and when bicipital, any two of the above mentioned areas [5]. With regard to the differences in proximal attachment, Olewnik et al. [18] described six types of origin and proposed a new classification of plantaris origin. The most common was type I (48.4%) divided into two subtypes (A-B): subtype A, attaching to the lateral head of the GM, lateral femoral condyle and to the capsule of the knee joint, and subtype B, attaching to the lateral head of the GM, the lateral femoral condyle, knee joint capsule and the popliteal surface of the femur. The second most common type was type II (25%), attaching to the capsule of the knee joint and, indirectly, to the lateral head of the GM through the lateral femoral condyle. The third most common type was type III (10.15%), attaching to the lateral femoral condyle and the knee joint capsule. Type IV (6.25%), the rarest type, attached to the lateral femoral condyle, knee joint capsule and to the iliotibial band. Type V (8.6%) originated only from the lateral condyle of the femur. Type VI (1.6%) was separated for "rare cases" [18].

The distal attachment of the plantaris varies — it usually inserts into the posterosuperior aspect of the calcaneus via the Achilles tendon; however, it can insert into neighbouring structures along it's normal course deep to the gastrocnemius and superficial to the medial aspect of the gastrocnemius and soleus, the flexor retinaculum, the dorsomedial border of the calcaneal tendon near or at its insertion, or distally into the fascia overlying the calcaneus or the plantar aponeurosis [1, 12, 17, 20, 21, 24, 27, 29]. The specific course of the PT and type of insertion may significantly affect the onset of Achilles midportion tendinopathy. Especially type II (characterised by insertion to the calcaneal tuberosity on the medial side, along with the Achilles tendon of the plantaris tendon which was beaded in common parathendon with the calcaneal tendon) may predispose a patient to this condition [20].

Regarding the cases of bifurcated PM, it has been reported to occur unilaterally [11] and bilaterally [10]. According to Herzog (2011) [8], PM with accessory belly has a prevalence of 6.3% in 1000 consecutive magnetic resonance imaging exams of the knee. However, cadaveric studies suggest a much lower incidence [10, 24]. In fact, in autopsy study of 750 bodies, Daseler and Anson (1943) [5] did not report the identification of such muscle. When the muscle has two bellies, one of them may have a typical attachment, and the other may be attached in a different area; both bellies can be attached typically or both atypically. Christy and Sathialakshmi [3] described a case in which one of the bellies was attached on the supracondylar line above the lateral condyle, while the other was attached to the oblique popliteal ligament. The popliteal artery was medial to the PM attachment [3]. By contrast Sawant et al. [24] described a rare variation of the muscle with presence of two heads taking origin together from lower part of lateral supracondylar line and oblique popliteal ligament [17]. In the present case, the muscle with two bellies was located unilaterally, as in the publication of Christy and Sathialakshmi (2019) [3]. However, such a case, in which one of the heads is attached to the lateral femoral condyle, medially and below the lateral head of the GM and the other originates on the popliteal surface of the femoral bone just above the intercondylar fossa, has not yet been described. The cases described so far relate to attachments located in other areas. For example, Kotian et al. (2013) [9] described a case in which the muscle had a typical origin on the lateral condyle and then bifurcated into two bellies, one superior and one inferior, whose location differed in relation to the popliteal vessels and the sciatic nerve. The superior head ran in front of these structures, and the inferior head was posterior to them [9]. It should be added that in the case in question, a histological examination was performed, which revealed that there were actually two bellies — two areas of muscle transition to the tendon were clearly visible. Previous publications also did not describe the histological structure of the identified bifurcated PM, which may raise doubts since macroscopic assessment might not always be accurate.

Using the classification prepared by Olewnik et al. 2020 [18], this type should be allocated in type VI — "rare cases". However, it should be emphasized that such type has not yet been described.

According to the authors, the second belly size, location and potential impact on adjacent structures determine how its presence affects the function of the extremity. The presence of the second belly may be mistaken for the presence of a tumour during the examination, so orthopaedists and rehabilitation specialists should be aware that a patient may present such anatomical variation. In the authors' opinion, it would be necessary to consider whether the PM with two bellies may be more prone to disruption. As is known from the literature, plantaris tendon rupture may cause symptoms similar to deep vein thrombosis [14], which can be a significant clinical problem. The second belly may also interfere with the structures located in its vicinity, other muscles, vessels and nerves, especially when muscular hypertrophy occurs. In cases of compression of the vessels or nerves, symptoms suggesting other conditions such as neuropathy, varicose veins or the aforementioned thrombosis may occur. It should be noted that any anatomical variability may affect the functioning of the patient. With regard to the differences in proximal attachment, Olewnik et al. [19] described a case in which the PM was attached to the capsule of the knee joint, medially to the lateral head of the crural GM, which resulted in abnormalities in the further course of the muscle.

The presence of a two-headed PM may result in symptoms and disorders that normally do not occur, hinder the diagnostics of the popliteal region and affect the surgical procedures performed in that area (e.g. the tibial nerve, the common fibular nerve, and the popliteal artery and vein). In the authors' opinion, all cases of anatomical variations, not only in the vicinity of the distal attachment but also in that of the initial attachment, should be published, as this may be essential for clinicians, for example, in connection with planned surgical procedures in the popliteal area.

CONCLUSIONS

The PM is characterised by high morphological variability. The presence of two bellies may potentially affect the surgical procedures performed in the area of the popliteal fossa. Knowledge of anatomical variants of the PM is crucial during surgery in that region. The classification of the PM origin should be extended to include described variant in "type VI".

Conflict of interest: None declared

REFERENCES

1. Alfredson H. Midportion Achilles tendinosis and the plantaris tendon. Br J Sports Med. 2011; 45(13): 1023–1025, doi: 10.1136/bjsports-2011-090217.
2. Bergman RA, Afifi AK, Miyauchi R. Illustrated encyclopedia of human anatomic variation. 2020. https://www.anatomyatlases.org/AnatomicVariants/AnatomyHP.shtml.
3. Christy JA, Sathialakshmi V. Unilateral two headed plantaris muscle — a rare variation. Int J Anat Var. 2019; 12(1): 015–016.
4. Cruveilhier J. Anatomie descriptive. 1st ed. Bechet Jeune, Paris 1834: 262–263.
5. Daseler EH, Anson BJ. The plantaris muscle: an anatomical study of 750 specimens. J Bone Joint Surg Am. 1943; 25: 822–827.
6. Gilbert TJ, Bullis BR, Griffiths HJ. Tennis calf or tennis leg. Orthopedics. 1996; 19(2): 179, 182, 184, indexed in Pubmed: 8834295.
7. Harvey FJ, Chu G, Harvey PM. Surgical availability of the plantaris tendon. J Hand Surg Am. 1983; 8(3): 243–247, doi: 10.1016/s0363-5023(83)80151-8, indexed in Pubmed: 6875222.
8. Herzog RJ. Accessory plantaris muscle: anatomy and prevalence. HSS J. 2011; 7(1): 52–56, doi: 10.1007/s11420-010-9175-y, indexed in Pubmed: 22294958.
9. Kotian SR, Sachin KS, Bhat KMR. Bifurcated plantaris with rare relations to the neurovascular bundle in the popliteal fossa. Anat Sci Int. 2013; 88(4): 239–241, doi: 10.1007/s12565-013-0184-z, indexed in Pubmed: 23771697.
10. Rana K, Das S, Verma R. Double plantaris muscle: a cadaveric study with clinical importance. Int J Morphol. 2006; 24(3): 495–498, doi: 10.4067/s0717-95022006000400032.
11. Kwinter D, Lagrew J, Kretzer J, et al. Unilateral double plantaris muscle: a rare anatomical variation. Int J Morphol. 2010; 28(4): 1097–1099, doi: 10.4067/s0717-95022010000400018.
12. Le Double AF. Traite des variations du systeme musculaire de l`hommeet de leur signification au point de vue de l` anthropologie zoologique. Tome II. Schleicher frères, Paris 1897.
13. Leekam RN, Agur AM, McKee NH. Using sonography to diagnose injury of plantaris muscles and tendons. Am J Roentgenol. 1999; 172(1): 185–189, doi: 10.2214/ajr.172.1.9888765, indexed in Pubmed: 9888765.
14. Lopez GJ, Hoffman RS, Davenport M. Plantaris rupture: a mimic of deep venous thrombosis. J Emerg Med. 2011; 40(2): e27–e30, doi: 10.1016/j.jemermed.2007.12.027, indexed in Pubmed: 19150191.
15. McMurrich J. The phylogeny of the crural flexors. Am J Anat. 1905; 4(1): 33–76, doi: 10.1002/aja.1000040104.
16. Moore KL, Agur AMR, Dalley AF. Clinically Oriented Anatomy. 7th ed. Lippincott Williams&Wilkins, Philadelphia 2013.
17. Nayak SR, Krishnamurthy A, Prabhu LV, et al. Additional tendinous origin and entrapment of the plantaris muscle. Clinics (Sao Paulo). 2009; 64(1): 67–68, doi: 10.1590/s1807-59322009000100012, indexed in Pubmed: 19142554.
18. Olewnik Ł, Kurtys K, Gonera B, et al. Proposal for a new classification of plantaris muscle origin and its potential effect on the knee joint. Ann Anat. 2020; 231: 151506, doi: 10.1016/j.aanat.2020.151506, indexed in Pubmed: 32173563.
19. Olewnik Ł, Podgórski M, Polguj M, et al. The plantaris muscle — rare relations to the neurovascular bundle in the popliteal fossa. Folia Morphol. 2018; 77(4): 785–788, doi: 10.5603/FM.a2018.0039, indexed in Pubmed: 29651792.
20. Olewnik Ł, Wysiadecki G, Podgórski M, et al. The plantaris muscle tendon and its relationship with the achilles tendinopathy. Biomed Res Int. 2018; 2018: 9623579, doi: 10.1155/2018/9623579, indexed in Pubmed: 29955614.
21. Olewnik Ł, Wysiadecki G, Polguj M, et al. Anatomic study suggests that the morphology of the plantaris tendon may be related to Achilles tendonitis. Surg Radiol Anat. 2017; 39(1): 69–75, doi: 10.1007/s00276-016-1682-1, indexed in Pubmed: 27155667.
22. Olewnik Ł, Zielinska N, Karauda P, et al. A three-headed plantaris muscle: evidence that the plantaris is not a vestigial muscle? Surg Radiol Anat. 2020; 42(10): 1189–1193, doi: 10.1007/s00276-020-02478-8, indexed in Pubmed: 32382814.
23. Pękala PA, Kaythampillai L, Skinningsrud B, et al. Anatomical variations of the plantar fascia's origin with respect to

age and sex-an MRI based study. Clin Anat. 2019; 32(4): 597–602, doi: 10.1002/ca.23342, indexed in Pubmed: 30701591.
24. Sawant SP, Shaikh ST, More RMA. rare variation of plantaris muscle. Int J Biol Med Res. 2012; 3(4): 2437–2440.
25. Shuhaiber JH, Shuhaiber HH. Plantaris tendon graft for atrioventricular valve repair: a novel hypothetical technique. Tex Heart Inst J. 2003; 30(1): 42–44, indexed in Pubmed: 12638670.
26. Simpson SL, Hertzog MS, Barja RH. The plantaris tendon graft: an ultrasound study. J Hand Surg Am. 1991; 16(4): 708–711, doi: 10.1016/0363-5023(91)90198-k, indexed in Pubmed: 1880370.
27. Smith J, Alfredson H, Masci L, et al. Differential plantaris-Achilles tendon motion: a sonographic and cadaveric investigation. PMR. 2017; 9(7): 691–698, doi: 10.1016/j.pmrj.2016.10.013, indexed in Pubmed: 27789336.
28. Spina AA. The plantaris muscle: anatomy, injury, imaging, and treatment. J Can Chiropr Assoc. 2007; 51(3): 158–165, indexed in Pubmed: 17885678.
29. van Sterkenburg MN, Kerkhoffs GM, Kleipool RP, et al. The plantaris tendon and a potential role in mid-portion Achilles tendinopathy: an observational anatomical study. J Anat. 2011; 218(3): 336–341, doi: 10.1111/j.1469-7580.2011.01335.x, indexed in Pubmed: 21323916.
30. van Sterkenburg MN, Kerkhoffs GM, van Dijk CN. Good outcome after stripping the plantaris tendon in patients with chronic mid-portion Achilles tendinopathy. Knee Surg Sports Traumatol Arthrosc. 2011; 19(8): 1362–1366, doi: 10.1007/s00167-011-1514-0, indexed in Pubmed: 21541711.

CASE REPORTS

FOLIA MORPHOLOGICA

Folia Morphol. Vol. 80, No. 3, August 2021

C O N T E N T S

←

INDEXED in: BIOSIS Previews, CAS, CINAHL, CrossRef, Dental Abstracts, EBSCO, Elsevier BIOBASE, EMBIOLOGY, FMJ, Google Scholar, Index Copernicus (154.80), Index Medicus/MEDLINE, Index Scholar, Polish Ministry of Education and Science (70), NCBI/National Center for Biotechnology Information, Polish Medical Bibliography, Scopus, SJR, Thomson Reuters, Thomson Scientific Products — Biological Abstracts, Ulrich's Periodicals Directory, Veterinary Bulletin, WorldCat and Zoological Record.

Cover picture: Type 1 — the RIPA and LIPA originate from the abdominal aorta. PHA — proper hepatic artery; GDA — gastro-duodenal artery; RIPA — right inferior phrenic artery; CHA — common hepatic artery; LGA — left gastric artery; SA — splenic artery; LIPA — left inferior phrenic artery; CT — coeliac trunk; SMA — superior mesentery artery; St — stomach; Li — liver; AA — abdominal aorta. For details see: Szewczyk et al., Folia Morphol 2021; 80, 3: 567–574.